

# **Journal of Engineering and Technology for Industrial Applications**



**ISSN 2447-0228**

**April 2025**

**Volume 11/ No 52**



**Editor-in-Chief: J. C. Leite**

**[www.itegam-jetia.org](http://www.itegam-jetia.org)**



O **ITEGAM-JETIA: Journal of Engineering and Technology for Industrial Applications** is a publication of the Galileo Institute of Technology and Education of the Amazon (ITEGAM), located in the city of Manaus since 2008. JETIA publishes original scientific articles covering all aspects of engineering. Our goal is the dissemination of research original, useful and relevant presenting new knowledge on theoretical or practical aspects of methodologies and methods used in engineering or leading to improvements in professional practice. All the conclusions presented in the articles It should be state-of-the-art and supported by current rigorous analysis and balanced assessment. Public magazine scientific and technological research articles, review articles and case studies.

**JETIA** will address topics from the following areas of knowledge: Mechanical Engineering, Civil Engineering, Materials and Mineralogy, Geosciences, Environment, Information and Decision Systems, Processes and Energy, Electrical and Automation, Mechatronics, Biotechnology and other Engineering related areas.

**Publication Information:**

**ITEGAM-JETIA** (ISSN 2447-0228), (online) is published by Galileo Institute of Technology and Education of the Amazon on a every two months (February, April, June, August, October and December).

**Contact information:**

Web page: [www.itegam-jetia.org](http://www.itegam-jetia.org)

Email: [editor@itegam-jetia.org](mailto:editor@itegam-jetia.org)

Galileo Institute of Technology and Education of the Amazon (ITEGAM).

Joaquim Nabuco Avenue, No. 1950. Center. Manaus, Amazonas. Brazil.

Zip Code: 69020-031. Phone: (92) 3584-6145.

**Copyright 2014. Galileo Institute of Technology and Education of the Amazon (ITEGAM)**

The total or partial reproduction of texts related to articles is allowed, only if the source is properly cited. The concepts and opinions expressed in the articles are the sole responsibility of the authors.

**Previous Notice**

All statements, methods, instructions and ideas are the sole responsibility of the authors and do not necessarily represent the view of ITEGAM -JETIA. The publisher is not responsible for any damage and / or damage to the use of the contents of this journal. The concepts and opinions expressed in the articles are the sole responsibility of the authors.

**Directory**

Members of the ITEGAM Editorial Center - Journal of Engineering and Technology for Industrial Applications (ITEGAM-JETIA) of the Galileo Institute of Technology and Education of the Amazon (ITEGAM). Manaus-Amazonas, Brazil.

**Jandecy Cabral Leite**, CEO and Editorial Editor-in-Chief

**Ivan Leandro Rodriguez Rico**, Editorial Assistant

**Marcos Herinque Gomes Brasil**, Information Technology Assistant



ITEGAM-JETIA. v.11 n.52 April 2025. Manaus - Amazonas, Brazil. ISSN 2447-0228 (ONLINE)  
<https://www.itegam-jetia.org>

## SUMMARY

<b><i>SPEED CONTROL OF PMSM DRIVE USING MODEL PREDICTIVE CONTROL BASED FIELD ORIENTED CONTROL</i></b>	<b>06</b>
<i>Sri Charan Vanamala, Kiran Kumar Danduprolu</i>	
<b><i>OPTIMAL SIZING OF A HYBRID MICROGRID SYSTEM FOR A RURAL AREA OF ALGERIA</i></b>	<b>14</b>
<i>Badis Bacha, Hatem Ghodbane, Nadjiba Terki, Madina Hamiane, Omar Charrouf, Abir Betka, Aymene Bacha</i>	
<b><i>PERFORMANCE ENHANCEMENT OF WIND ENERGY CONVERSION SYSTEMS USING PMSG WITH BACKSTEPPING AND ANN-BASED MPPT CONTROL</i></b>	<b>27</b>
<i>Wassila Hattab, Abdelhamid Benakcha, Seddik Tabet, Amira slimani</i>	
<b><i>USE OF TARO BOGOR ( COLOCASIA ESCULENTA ( L.) SCHOTT ) AS A GROWTH MEDIUM FOR ASPERGILLUS FLAVUS</i></b>	<b>39</b>
<i>Visensius Krisdianilo</i>	
<b><i>MODELLING CORONA DISCHARGE THRESHOLD IN COMPOSITE DIELECTRIC PROPERTIES OF EGGSHELL COMPOSITE INSULATORS: A VOLTAGE-BASED STUDY</i></b>	<b>43</b>
<i>Samsurizal Samsurizal, Yulisya Zuriatni, Andi Makkulau</i>	
<b><i>HOPF BIFURCATION POINT IDENTIFICATION IN A POWER SYSTEM WITH VARIOUS STATIC LOAD MODELS</i></b>	<b>48</b>
<i>Ghousul Azam Shaik, Lakshmi Devi Aithepalli</i>	
<b><i>HYBRID FFT-ARMA-BURG MODELING AND LSTM-ENHANCED BBO OPTIMIZATION FOR FAULT DIAGNOSIS IN INDUCTION MOTORS</i></b>	<b>55</b>
<i>Khadiidja Boudraa, Mohammed Assam Ouali, Mohamed Ladjal</i>	
<b><i>ENHANCING SENTIMENT ANALYSIS IN TOURISM REVIEWS: A COMPARATIVE STUDY OF ALGORITHMS IN ASPECT-BASED SENTIMENT ANALYSIS AND EMOTION DETECTION</i></b>	<b>63</b>
<i>Viktor Handrianus Pranatawijaya, Putu Bagus Adidyana Anugrah Putra, Ressa Priskila, Novera Kristianti</i>	
<b><i>NAVIGATION SYSTEM AND OBSTACLE AVOIDANCE FOR MOBILE ROBOT USING TYPE-2 FUZZY LOGIC IN UNCERTAIN ENVIRONMENTS</i></b>	<b>73</b>
<i>Soufiane Hachani, Emira. Nechadi</i>	
<b><i>DESIGNING A SMART HOME MODEL USING EASYVR AND ARDUINO FOR VOICE CONTROL OF DEVICES</i></b>	<b>81</b>
<i>Soufiane Hachani</i>	
<b><i>A COMPARATIVE ANALYSIS OF FAST CHARGING PERFORMANCE AND BATTERY LIFE AGAINST CHARGING CURRENT VARIATIONS</i></b>	<b>86</b>
<i>Samsurizal Samsurizal, Arif Nur Afandi, Mohamad Rodhi Faiz</i>	
<b><i>QUANTITATIVE ANALYSIS OF SUBSURFACE STRUCTURE CRACKING USING PULSED EDDY CURRENT NONDESTRUCTIVE TESTING</i></b>	<b>92</b>
<i>Azizi Hakim, Mohammed Chebout, Daoud Sekki, Mohammed Charif Kihal, Marouane Kihal</i>	
<b><i>SUB-MODULE VOLTAGE ESTIMATION OF MODULAR MULTILEVEL CONVERTER IN PV APPLICATIONS USING A SLIDING MODE OBSERVER</i></b>	<b>97</b>
<i>Imane Alia, Imad Merzouk, Mehamed Mounir Rezaoui</i>	

<b>THE INCORPORATING ANFIS-BASED CURRENT REGULATION INTO A MULTI-ACTIVE FULL BRIDGE CONVERTER FOR REDUCING CURRENT RIPPLE</b>	<b>108</b>
<i>Rathod Rama Krishna, G. Yesuratnam, Punnaiah Veeraboina</i>	
<b>POTENTIAL ADOPTION OF BLOCKCHAIN IN FOOD COLD SUPPLY CHAIN: A BIBLIOMETRIC STUDY AND FUTURE RESEARCH AGENDA</b>	<b>117</b>
<i>Thabed Tholib Baladraf, Marimin Marimin</i>	
<b>LONG - TERM ASSESSMENT OF THE SPATIAL TEMPORAL TRENDS IN SELECTED CLOUD RADIATIVE PROPERTIES OVER THE THREE DISTINCT SITES IN KENYA</b>	<b>131</b>
<i>Sostine N. Makokha, John W. Makokha, Festus B. Kelonye</i>	
<b>A NOVEL HYBRID STEGANOGRAPHY APPROACH FOR SECURING TEXT, IMAGES, AND AUDIO WITH ROBUST ENCRYPTION IN AUDIO STEGANOGRAPHY</b>	<b>141</b>
<i>T Srinivasa Padmaja, Shaik Mahaboob Basha</i>	
<b>A TAILORED COMPLIANCE SOLUTION FOR SECURING PERSONAL DATA PRIVACY UNDER LAW 18-07 IN ALGERIA</b>	<b>153</b>
<i>Redouane Guettal , Mohammed Kamel Benkaddour</i>	
<b>ASSESSMENT OF THE EFFECT OF SERIES PASSIVE FILTER ON HARMONIC DISTORTION-POWER LOSSES RELATIONSHIP IN AN ELECTRICITY DISTRIBUTION NETWORK</b>	<b>161</b>
<i>Okuo Michael Ozaveshe, Adebisi Oluseun Ibrahim, Akinola Olubunmi Adewale</i>	
<b>COMBINATION OF MINIMUM ENTROPY DECONVOLUTION METHOD AND VAN CITTERT ALGORITHM FOR FEATURES EXTRACTION OF BEARINGS</b>	<b>170</b>
<i>Nesrine Gouri, Hocine Bendjama, Mohamed Larbi Mihoub</i>	
<b>SOLDER LEAD WASTE REDUCTION OF A SELECTED MOBILE PHONE FACTORY: A SIX SIGMA DMAIC APPROACH</b>	<b>178</b>
<i>Md. Mehedi Hassan Munna, Jonayed Abdullah, Tarequl Islam , Most. Anika Tabassum Little</i>	
<b>ENHANCING OVERALL EQUIPMENT EFFECTIVENESS (OEE) OF A SELECTED MACHINE IN A LIGHT MANUFACTURING FACTORY IN BANGLADESH</b>	<b>185</b>
<i>Jonayed Abdullah, Md. Al Hossain Rifat, Avirup Deb Ray</i>	
<b>COMPARATIVE STUDY OF 2D DESIGNS OF 12/8 AND 10/8 SWITCHED RELUCTANCE MOTORS USING ANSYS MAXWELL</b>	<b>192</b>
<i>Layachi Chebabhi, Toufik tayeab Naas , Mohamed Zitouni</i>	
<b>MONITORING AND EVALUATION OF WATER QUALITY IN RURAL ANDEAN AREAS OF PERU USING WIRELESS SENSORS WITH LORA</b>	<b>202</b>
<i>Wohler Gonzales Saenz, Luz Marina Acharte Lume, Javier Camilo Poma Palacios, Alejandro Filimón Quispe Coica, Agustí Pérez Foguet</i>	
<b>A FAST ENHANCED MEDICAL IMAGE ENCRYPTION SCHEME BASED ON 2D-CHAOTIC MAP AND IMPROVED ZIGZAG CONFUSION</b>	<b>211</b>
<i>Ammar Bouchemel, Elhadi Mehallel, Abdelaziz Rebahi</i>	
<b>SIMULATION OF THE ELASTIC FIELD OF AN INTERFACIAL DISLOCATION IN AN ANISOTROPIC MEDIUM: FOURIER SERIES APPROACH</b>	<b>226</b>
<i>Allaoua Kherraf , Rachid Benbouta, Mourad Brioua</i>	
<b>ENHANCING INCENTIVE SCHEMES IN EDGE COMPUTING THROUGH HIERARCHICAL REINFORCEMENT LEARNING</b>	<b>232</b>
<i>Gowtham R, Vatsala Anand, Yadati Vijaya Suresh, Kasetty Lakshmi Narasimha, R. Anil Kumar, V.Saraswathi</i>	



---

<b><i>ENHANCING REAL-TIME ANIMATION: ENSURING DISTINCTIVENESS IN CROWD DYNAMICS THROUGH PHYSICS-BASED COLLISION AVOIDANCE</i></b>	<b>243</b>
<i>Imane DRIDI, Cherif FOUDIL</i>	
<b><i>PROCESS OPTIMIZATION AS A TOOL FOR ANALYZING PERFORMANCE INDICATORS OF ADDITIONAL TAXI-OUT AND TAXI-IN TIME OF THE BRAZILIAN AIRSPACE CONTROL SYSTEM</i></b>	<b>253</b>
<i>Alessandro Soares de Freitas, Edilson Marques Magalhaes</i>	
<b><i>QUANTUM COMPUTING: APPROACHES, SCALABILITY, AND THE FUTURE OF EMERGING TECHNOLOGIES</i></b>	<b>267</b>
<i>Manoel Socorro Santos Azevedo, Marcelo Weber Schiller, João Paulo Modesto Damiano, Cristiano Peniche Ceccon, Antonio Gabriel Nunes Martins</i>	
<b><i>FUZZY IRRIGATION MODEL IN PROTECTED CROP BASED ON EXPERT KNOWLEDGE</i></b>	<b>272</b>
<i>Alain Godo Alonso, Dennis Villavicencio Quintero, Emilio Cabrera Hernández, Ivan Santana Ching</i>	





## RESEARCH ARTICLE

## OPEN ACCESS

## SPEED CONTROL OF PMSM DRIVE USING MODEL PREDICTIVE CONTROL BASED FIELD ORIENTED CONTROL

V. Sri Charan<sup>1</sup> and Dr. D. Kiran Kumar<sup>2</sup><sup>1,2</sup> Department of Electrical and Electronics Engineering, JNTUH University College of Engineering Science & Technology, Hyderabad, India-500085.<sup>1</sup><https://orcid.org/0009-0003-4369-150X> , <sup>2</sup><https://orcid.org/0009-0009-6757-5320> Email: [sricharanvanamala2001@gmail.com](mailto:sricharanvanamala2001@gmail.com), [kirannkumar9@jntuh.ac.in](mailto:kirannkumar9@jntuh.ac.in)

## ARTICLE INFO

*Article History*

Received: November 30, 2024

Revised: January 20, 2025

Accepted: February 15, 2025

Published: March 31, 2025

*Keywords:*Permanent Magnet Synchronous Motor (PMSM),  
Field-Oriented Control (FOC),  
Model Predictive Control (MPC),  
Torque Ripple Minimization,  
Dynamic Response.

## ABSTRACT

This paper examines the enhancement of Permanent Magnet Synchronous Motor (PMSM) drives through the integration of Field-Oriented Control (FOC) with Model Predictive Control (MPC). The study aims to achieve high precision and dynamic response for PMSM drives under diverse operating conditions. The theoretical framework combines FOC and MPC principles, utilizing MPC's predictive capabilities to optimize d-q current references in real-time. The methodology encompasses the design and implementation of an MPC technique integrated with FOC, with key objectives including the minimization of torque ripples, the maintenance of system stability through robust control loops, and the optimization of PMSM drive performance across a wide speed range. The results indicate significant improvements in torque ripple reduction, dynamic response, and disturbance rejection, demonstrating the robustness and adaptability of the proposed control system. This approach effectively addresses key challenges and signifies advancements over traditional control methods, contributing to the field of electric drive control systems.



Copyright ©2025 by authors and Galileo Institute of Technology and Education of the Amazon (ITEGAM). This work is licensed under the Creative Commons Attribution International License (CC BY 4.0).

## I. INTRODUCTION

Electric drives are fundamental components in modern automation and industrial applications. They serve to control the speed, torque, and position of electrical machines [1]. Among the various types of electric drives, Permanent Magnet Synchronous Motors (PMSMs) have gained prominence due to their high efficiency, high power density, and excellent performance characteristics. PMSMs are preferred in applications that demand precise control and high dynamic performance, such as robotics, electric vehicles, and aerospace systems [2].

The choice of PMSMs over other types of motors, like induction motors or brushed DC motors, stems from several advantages. PMSMs offer better efficiency and power factor, lower maintenance due to the absence of brushes, and a more compact size for the same power rating. Additionally, the use of permanent magnets reduces the energy losses associated with magnetizing current, contributing to overall energy savings [3].

Controlling Permanent Magnet Synchronous Motors (PMSMs) is complex due to several factors. Torque ripple, which causes vibrations and noise, is a significant issue, especially in precision applications. Additionally, maintaining precise control across

various operating conditions is challenging, particularly when dealing with fluctuating loads and imprecise motor parameters. Traditional control methods often struggle to effectively address these complexities [4].

The evolution of control techniques for PMSMs has seen significant advancements over the years [5]. Initially, scalar control methods such as V/f (Voltage/Frequency) control were used due to their simplicity and ease of implementation. V/f control regulates motor speed by maintaining a constant proportionality between applied voltage and frequency, thereby preserving airgap flux. This method is suitable for low-performance applications where precision is not critical. However, it is inadequate for applications requiring high precision and dynamic response due to its inherent lack of torque control and poor dynamic performance [6,7].

To overcome the limitations of scalar control, vector control techniques were developed, offering more sophisticated approaches [8]. Field Oriented Control (FOC) allows for independent control of the motor's flux and torque, akin to a separately excited DC motor, offering superior performance in terms of dynamic response and efficiency. FOC is widely used in applications demanding high performance, such as electric vehicles

and industrial automation. However, it requires complex transformations and precise knowledge of motor parameters, which can complicate its implementation and tuning [9].

Direct Torque Control (DTC) is another advanced technique known for its fast torque response and robustness. DTC directly controls the motor torque and flux by selecting appropriate inverter switching states without requiring a modulator or current controllers. It is suitable for applications requiring rapid torque changes and robustness against parameter variations [10,11]. However, DTC may suffer from high torque ripple and requires complex algorithms to manage the switching states effectively.

Voltage Vector Control involves controlling the voltage vectors applied to the motor to manage its torque and flux. This method improves dynamic performance and reduces torque ripples but requires complex algorithms and accurate parameter estimation, making it more challenging to implement and tune [12]. Despite the advancements in these traditional techniques, several issues remain unresolved:

- Maintaining precise control over a wide range of operating conditions
- Reducing torque ripples to minimize vibrations and noise
- Handling parameter variations and external disturbances robustly
- Simplifying the implementation and tuning of control algorithms

The integration of Model Predictive Control (MPC) with Field-Oriented Control (FOC) presents a promising avenue for addressing the limitations of traditional control methods for Permanent Magnet Synchronous Motors (PMSMs). FOC is a control technique that enables independent control of torque and speed by decoupling the motor's stator currents into d-q components, effectively transforming the AC motor into a DC machine for control purposes.

This decoupling enables accurate control of the motor's behavior, resulting in enhanced performance and efficiency [8]. By integrating MPC, the control system can significantly enhance performance by optimizing d-q current references in real-time based on predicted system behavior. This optimization leads to substantial improvements in torque ripple minimization and dynamic response [13,14]. MPC's ability to predict future system states, optimize control inputs, and adhere to system constraints contributes to improved efficiency, faster response times, and enhanced disturbance rejection, ultimately resulting in a more robust and adaptable control system for PMSM drives.

This paper focuses on achieving high precision and dynamic response for PMSM drives under varying operating conditions through MPC-based FOC. The objectives include:

- Achieving high precision and dynamic response for PMSM drives under varying operating conditions through MPC-based FOC.
- Minimizing torque ripples in PMSM drives using FOC and precise current control.
- Ensuring system stability by developing robust control loops within the MPC-based FOC framework.
- Optimizing PMSM drive performance across a wide speed range, including high-speed operation.

The paper is organized as follows: Section 1 introduces the research topic. Section 2 presents the PMSM model, while Section 3 details the Field-Oriented Control (FOC) design. Section 4

focuses on the Model Predictive Control (MPC) algorithm. The implementation of the control system is described in Section 5. Comparative results and discussions are presented in Section 6, and the paper concludes in Section 7. This structured approach ensures a comprehensive understanding of the development and implementation of MPC-based FOC for PMSM drives, addressing key challenges and highlighting the advancements over traditional control methods.

## II. PMSM MODELLING

Mathematical modelling of Permanent Magnet Synchronous Motors (PMSMs) is crucial for understanding their performance and control. This section presents the mathematical framework for PMSM modelling, including key assumptions and the derivation of fundamental equations.

Assumptions made for modelling of PMSM are:

- Magnetic Saturation Neglected: The impact of magnetic saturation on the motor's behaviour is considered negligible.
- Sinusoidal Back-EMF: The back electromotive force (EMF) is assumed to be sinusoidal.
- Neglect of Minor Effects: Effects such as cogging torque, hysteresis, and eddy currents are minimal and therefore neglected.

In a two-pole PMSM, as depicted in the Figure 1, the rotor's reference axis maintains a time-varying angular position,  $\theta_r(t)$ , relative to the stationary stator reference axis [15]. Furthermore, the rotating magnetomotive force (MMF) produced by the stator windings exhibits an angular displacement,  $\alpha$ , with respect to the rotor's d-axis.

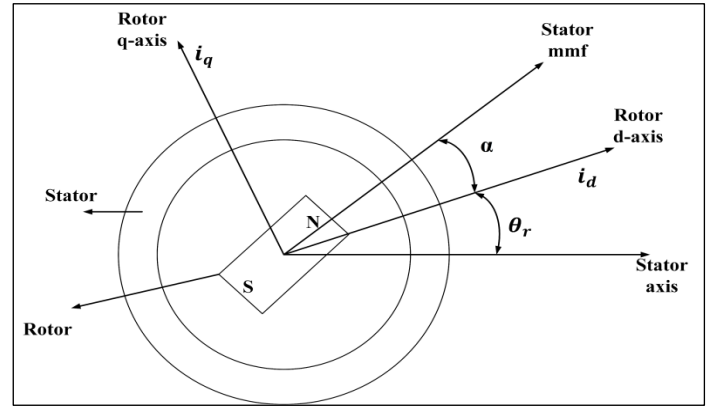


Figure 1: Schematic of Two Pole PMSM.

Source: Authors, (2025).

Here we use surface mounted PMSM where  $L_{sq} = L_{sd} = L$ . The equations describing the voltages in the model are presented as follows:

$$v_{sq} = R_s i_{sq} + \omega_r \varphi_{sd} + \rho \varphi_{sq} \quad (1)$$

$$v_{sd} = R_s i_{sd} - \omega_r \varphi_{sq} + \rho \varphi_{sd} \quad (2)$$

Where  $v_{sd}$ ,  $v_{sq}$ ,  $i_{sd}$ ,  $i_{sq}$  are the d-q axes voltage and current respectively.  $\varphi_{sd}$ ,  $\varphi_{sq}$  are stator winding d-q axes flux linkages. The expressions for the flux linkages are presented as follows:

$$\varphi_{sq} = L i_{sq} \quad (3)$$

$$\varphi_{sd} = L i_{sd} + \varphi_m \quad (4)$$

The amplitude of the fundamental PM flux linkage component is represented by  $\varphi_m$ .

Substituting equation **Erro! Fonte de referência não encontrada.** and **Erro! Fonte de referência não encontrada.** into equation **Erro! Fonte de referência não encontrada.** and **Erro! Fonte de referência não encontrada.**

$$v_{sq} = R_s i_{sq} + \omega_r (L i_{sd} + \varphi_m) + \rho L i_{sq} \quad (5)$$

$$v_{sd} = R_s i_{sd} - \omega_r L i_{sq} + \rho (L i_{sd} + \varphi_m) \quad (6)$$

Re-arranging the equations **Erro! Fonte de referência não encontrada.** and **Erro! Fonte de referência não encontrada.**:

$$\begin{bmatrix} v_{sq} \\ v_{sd} \end{bmatrix} = \begin{bmatrix} R_s + \rho L & \omega_r L \\ -\omega_r L & R_s + \rho L \end{bmatrix} \begin{bmatrix} i_{sq} \\ i_{sd} \end{bmatrix} + \begin{bmatrix} \omega_r \varphi_m \\ \rho \varphi_m \end{bmatrix} \quad (7)$$

The equation for the motor's generated torque is given by

$$T_e = \frac{3}{2} \left( \frac{P}{2} \right) (\varphi_{sd} i_{sq} - \varphi_{sq} i_{sd}) \quad (8)$$

The mechanical equation of the torque

$$T_e = T_l + B \omega_m + J \frac{d\omega_m}{dt} \quad (9)$$

The expression for the rotor's mechanical speed can be obtained by rearranging the equation **Erro! Fonte de referência não encontrada.** as

$$\omega_m = \int \left( \frac{T_e - T_l - B \omega_m}{J} \right) dt \quad (10)$$

$$\omega_m = \frac{2}{p} \omega_r \quad (11)$$

### III. DESIGN OF FOC

FOC, or vector control, is a sophisticated and effective method used for controlling the torque and speed of PMSMs. This technique provides superior dynamic performance by decoupling the motor's torque and flux control, which enables independent management of these parameters similar to that in DC motors.

FOC operates by transforming the motor's three-phase stator currents into a two-phase orthogonal coordinate system, known as the d-q frame, which rotates synchronously with the rotor's magnetic field. This transformation simplifies the control strategy and improves the efficiency and responsiveness of the motor drive [16-18]. The key mathematical transformations involved in FOC are the Clarke and Park transformations represented in Figure 2. The Clarke transformation translates the three-phase stator currents into a two-phase stationary reference frame ( $\alpha$ - $\beta$ ), and the Park transformation further converts these into the rotating d-q frame.

In the d-q frame, the d-axis current ( $i_d$ ) is aligned with the rotor flux and controls the flux linkage, whereas the q-axis current ( $i_q$ ) is orthogonal to the rotor flux and controls the torque. The fundamental FOC strategy involves controlling  $i_d$  to regulate the rotor flux and  $i_q$  to control the motor torque.

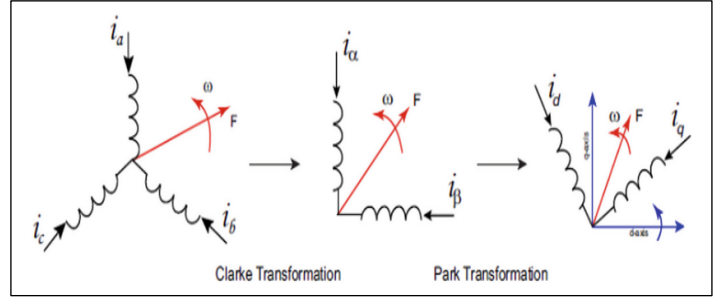


Figure 2: Three-Phase, Two-Phase and Rotating Reference Frames.

Source: Authors, (2025).

The control process begins with the measurement of the three-phase stator currents ( $i_{sa}, i_{sb}, i_{sc}$ ). These currents are then transformed into the  $\alpha$ - $\beta$  stationary frame using the Clarke transformation:

$$\begin{bmatrix} i_{sa} \\ i_{sb} \end{bmatrix} = \begin{bmatrix} 1 & -\frac{1}{2} & -\frac{1}{2} \\ 0 & \frac{\sqrt{3}}{2} & -\frac{\sqrt{3}}{2} \end{bmatrix} \begin{bmatrix} i_{sa} \\ i_{sb} \\ i_{sc} \end{bmatrix} \quad (1)$$

Following this, the  $\alpha$ - $\beta$  currents are transformed into the d-q rotating reference frame using the Park transformation:

$$\begin{bmatrix} i_{sd} \\ i_{sq} \end{bmatrix} = \begin{bmatrix} \cos(\theta) & \sin(\theta) \\ -\sin(\theta) & \cos(\theta) \end{bmatrix} \begin{bmatrix} i_{sa} \\ i_{sb} \end{bmatrix} \quad (13)$$

Here,  $\theta$  represents the rotor position, which is crucial for accurate transformations and control.

For speed regulation, the motor speed ( $\omega_m$ ) is measured and compared with the reference speed ( $\omega_{ref}$ ). The speed error is then fed into a PI controller to generate the reference q-axis current ( $i_{sqref}$ ):

$$i_{sqref} = K_{p\omega} (\omega_{ref} - \omega_m) + K_{i\omega} \int (\omega_{ref} - \omega_m) dt \quad (14)$$

The q-axis current error, defined as the difference between  $i_{sqref}$  and the actual q-axis current ( $i_{sq}$ ), is processed through another PI controller to produce the reference q-axis current ( $i_{sqref}$ ):

$$i_{sqref} = K_{p_{sq}} (i_{sqref} - i_{sq}) + K_{i_{sq}} \int (i_{sqref} - i_{sq}) dt \quad (2)$$

For d-axis control, the d-axis current error, which is typically the difference between the desired d-axis current ( $i_{sdref}$ , often set to zero for maximum efficiency) and the actual d-axis current ( $i_{sd}$ ), is processed through a PI controller to generate the reference d-axis current ( $i_{sdref}$ ):

$$i_{sdref} = K_{p_{sd}} (i_{sdref} - i_{sd}) + K_{i_{sd}} \int (i_{sdref} - i_{sd}) dt \quad (3)$$

These reference currents are critical for achieving the desired performance in the FOC scheme, ensuring that the motor operates efficiently and responds accurately to control inputs. The precise control of these currents allows the motor to achieve optimal torque production and flux regulation, essential for high-performance applications.

Accurate rotor position information is essential for FOC implementation, typically obtained through rotor position sensors or estimated using sensor-less methods. This ensures the precise alignment of the rotating reference frame with the rotor's



magnetic field, which is crucial for the correct application of the Park transformation and the effectiveness of the control strategy.

#### IV. MPC ALGORITHM

The MPC algorithm is an advanced control strategy designed to optimize the performance of the PMSM by predicting future behaviour of the system and minimizing a predefined objective function. In this section, we will discuss the MPC algorithm and its implementation, focusing on how the reference currents generated from the FOC are used to generate gating signals for the inverter.

MPC is particularly effective in handling multi-variable control systems and constraints, making it a suitable choice for PMSM drives. The key idea behind MPC is to use a predictive system model which forecasts future status of the motor over a finite prediction horizon. Based on these predictions, an optimal control action is determined by minimizing an objective function, which typically includes terms related to tracking errors and control effort [19-21].

The objective function  $M$  in MPC is defined to evaluate the difference between the reference currents  $i_{sd\_ref}$  and  $i_{sq\_ref}$ , and the predicted currents  $i_{sd\_p}$  and  $i_{sq\_p}$ . The objective function can be expressed as:

$$M = (i_{sd\_ref} - i_{sd\_p})^2 + (i_{sq\_ref} - i_{sq\_p})^2 + (\omega_{ref} - \omega_r)^2 \quad (4)$$

The inverter's predictive model is essential for the MPC algorithm. The inverter's voltage vectors  $V_d$  and  $V_q$  are derived from the inverter switching functions  $[S_a, S_b, S_c]$  and  $V_{dc}$  is the DC-link voltage. These states correspond to the inverter output voltages  $V_a, V_b, V_c$  for every possible switching state of the inverter, represented by the gating signals  $S1$  to  $S6$  which are then transformed to the d-q frame. The voltage vectors are calculated as follows:

$$V_a = \frac{V_{dc}}{3} (2S_a - S_b - S_c) \quad (18)$$

$$V_b = \frac{V_{dc}}{3} (2S_b - S_a - S_c) \quad (19)$$

$$V_c = \frac{V_{dc}}{3} (2S_c - S_a - S_b) \quad (20)$$

These voltages are then transformed to the d-q frame using the following equations:

$$v_{sd} = \frac{2}{3} \left( V_a \cos(\theta) + V_b \cos\left(\theta + \frac{4\pi}{3}\right) + V_c \cos\left(\theta + \frac{2\pi}{3}\right) \right) \quad (21)$$

$$v_{sq} = \frac{2}{3} \left( V_a \sin(\theta) + V_b \sin\left(\theta + \frac{4\pi}{3}\right) + V_c \sin\left(\theta + \frac{2\pi}{3}\right) \right) \quad (22)$$

The discrete-time form of PMSM mathematical model, used for predicting future states are:

$$i_{sd\_p} = i_{sd} + \frac{T_s}{L} [v_{sd} - Ri_{sd} + L\omega_m i_{sq}] \quad (23)$$

$$i_{sq\_p} = i_{sq} + \frac{T_s}{L} [v_{sq} - Ri_{sq} - L\omega i_{sd} - \varphi\omega_m] \quad (24)$$

Where  $R$ ,  $L$ ,  $T_s$ ,  $\omega_m$ ,  $\varphi$  are stator resistance, stator inductance, sampling time, rotor measured speed, permanent magnet flux linkage.

The MPC implementation involves the following steps:

1. Estimate the future states of the motor currents  $i_{sd}$  and  $i_{sq}$  based on the current states and the voltages applied for each potential inverter switching state.
2. Calculate the cost function for each switching state.

3. Identify the switching state that minimizes the cost function.
4. Apply the corresponding gating signals to the inverter.

The gating signals are determined by evaluating the cost function for all possible inverter states. The state with the minimum cost is selected, and its corresponding gating signals are applied. The flowchart presented in Figure 3 outlines the procedural steps inherent in the implementation of MPC. The algorithm ensures that the motor operates efficiently by closely following the reference currents and minimizing the deviation from the desired performance.

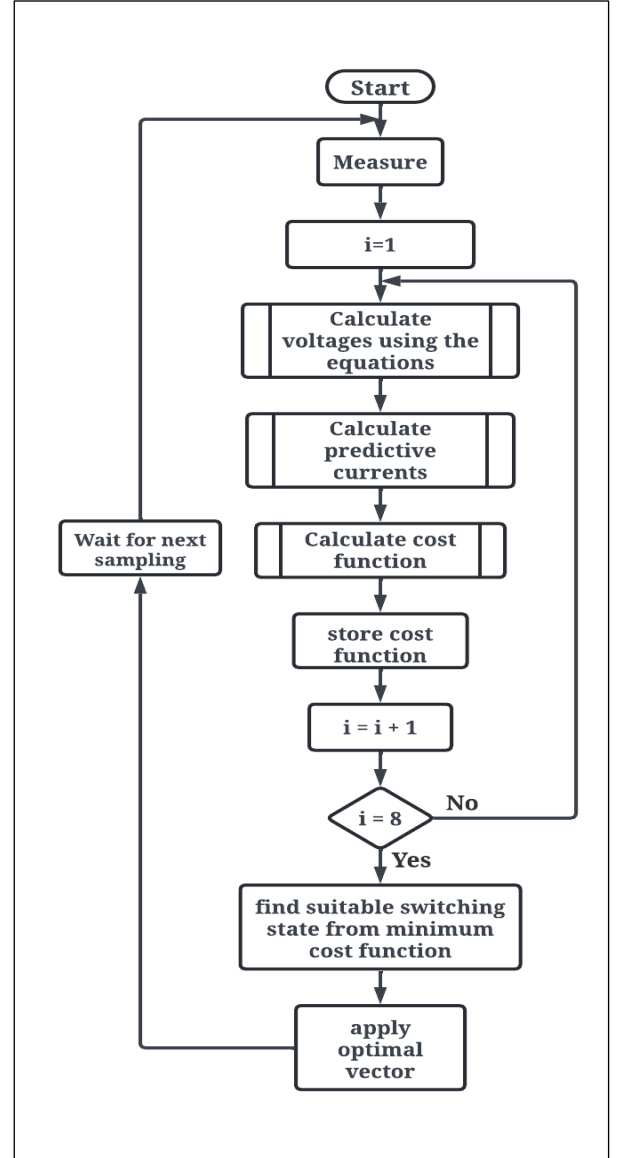


Figure 3: MPC Flowchart.  
Source: Authors, (2025).

#### V. IMPLEMENTATION OF CONTROL TECHNIQUES

The system block diagram for the proposed MPC based FOC of a PMSM drive shown in Figure 4 is a comprehensive framework integrating multiple components for optimal performance. The core of the system involves the PMSM, which is controlled through an MPC algorithm designed to enhance dynamic response and minimize steady-state error. The control structure includes current and speed controllers, implemented via predictive models that account for the motor's dynamics and constraints.

These controllers generate reference signals for the inverter, ensuring precise modulation of the motor's voltage and current. Additionally, feedback mechanisms are incorporated to continuously monitor and adjust the system parameters, ensuring robust performance under varying operational conditions. The integration of these elements in the block diagram highlights the seamless interaction between the predictive control algorithm and the motor drive components, showcasing the efficacy of the proposed technique in achieving high-performance motor control.

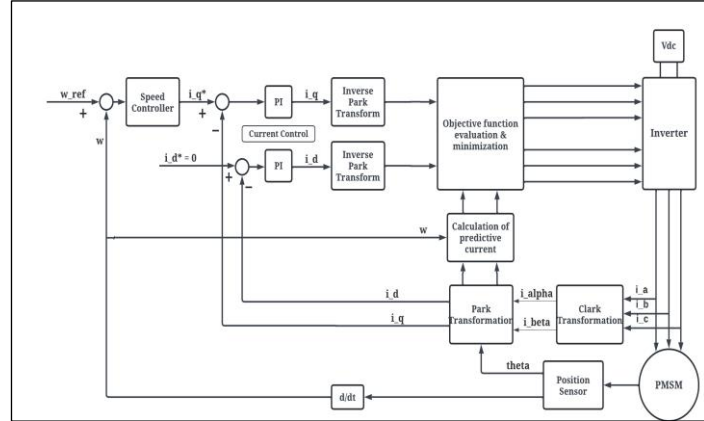


Figure 4: Block diagram of Proposed System.

Source: Authors, (2025).

## VI. RESULTS AND DISCUSSIONS

To evaluate the effectiveness of the proposed FOC with MPC for speed control of a 3.4 kW PMSM drive, simulation studies were performed using MATLAB/Simulink. The performance of the proposed control scheme was assessed across four distinct scenarios: (a) starting characteristics, (b) dynamic response to a sudden load change from no load to full load, (c) dynamic response to a sudden load change at low speeds from no load to full load, and (d) steady-state characteristics with a sampling time of 10 $\mu$ s. The results obtained from these scenarios are compared with those of a traditional Proportional-Integral (PI) controller.

This comparative study focuses on key performance metrics such as transient response, including settling time, rise time, and overshoot, to highlight the advantages of the FOC MPC method. The analysis aims to demonstrate the proposed controller's superior capability in handling various load conditions, ensuring smooth and efficient motor operation. The evaluation provides comprehensive insights into the robustness and effectiveness of the FOC MPC approach under different operating scenarios, showcasing its potential benefits over conventional PI control methods. Table 1 lists the parameters of PMSM.

Table 1: PMSM Parameters.

Parameter	Value
Voltage, V	380 V
Rated Output Power	3.4 KW
Rated Speed, N	3000 rpm
Stator Resistance, $R_s$	1.93 $\Omega$
Q-axis inductance, $L_q$	0.0114 H
D-axis inductance, $L_d$	0.0114 H
PM Flux linkage, $\varphi_m$	0.265 $Wb$
No. of poles, P	8
Motor Inertia, J	0.11 $kgm^2$

Source: Authors, (2025).

## VI.1. STARTING CHARACTERISTICS

Analysis of Figure 5, Figure 6(a) and Figure 6 (b) provides a comprehensive overview of the performance disparities between the MPC-based FOC and the traditional PI controller in regulating the speed of the PMSM drive under starting conditions.

Figure 5 presents a direct comparison of the speed responses for both control strategies. This figure clearly illustrates the superior performance of the MPC-based FOC, as evidenced by its faster rise time, reduced overshoot, and quicker settling time compared to the PI controller.

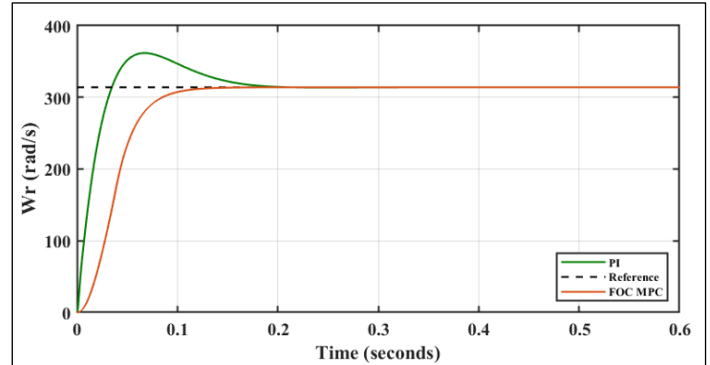
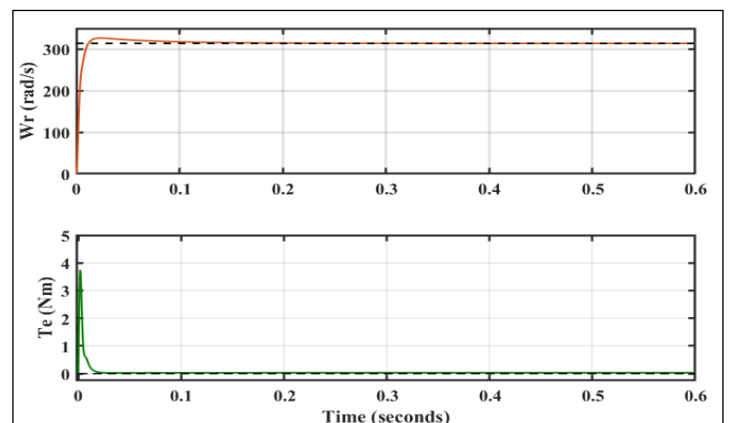


Figure 5. Speed response of the PMSM at starting conditions with no load and rated speed.

Source: Authors, (2025).

A more detailed examination of the individual controller responses is provided in Figure 6(a) and Figure 6(b). Figure 6(a) depicts the speed response of the PI controller highlighting the presence of significant overshoot and oscillations during the startup phase. These characteristics are indicative of the controller's challenges in effectively managing the rapid changes in torque and speed demands associated with motor startup. In contrast, Figure 6 (b) showcases the exceptional performance of the MPC-based FOC demonstrating a smooth and rapid acceleration to the rated speed without any overshoot. This superior transient response is attributed to the MPC controller's ability to predict and compensate for system dynamics, resulting in a more precise and robust control strategy.



**(a)**

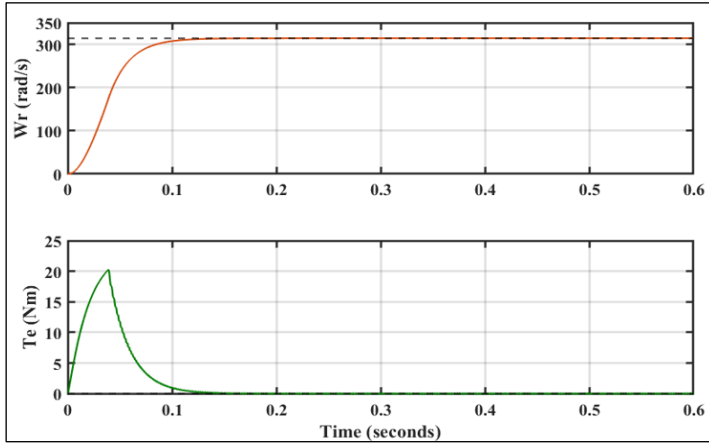
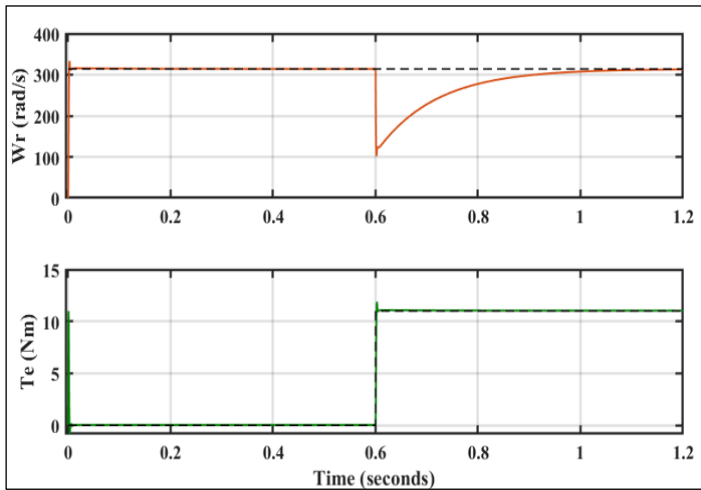


Figure 6: Starting characteristics of PMSM drive at rated speed with (a) PI (b) MPC based FOC.

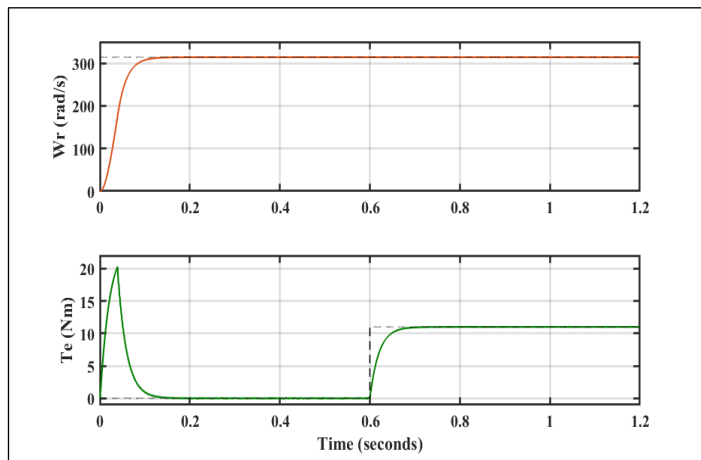
Source: Authors, (2025).

## VI.2. DYNAMIC RESPONSE OF TORQUE TRANSITION FROM NO LOAD TO FULL LOAD

The dynamic response of the PMSM drive under a sudden torque change from no load to full load is evaluated. The Figure 7(a) illustrates the speed and torque response of the PMSM drive under traditional Proportional-Integral (PI) control.



(a)



(b)

Figure 7. Dynamic response of (a) PI and (b) MPC based FOC, for sudden change in load from no-load to full load

Source: Authors, (2025).

Initially, the motor speed quickly reaches the reference value of 314 rad/s, demonstrating effective steady-state performance. However, at 0.6 seconds, a sudden torque of 11 Nm causes a significant dip in speed, highlighting the PI controller's slower response to abrupt load changes. The torque response also shows initial overshoot and a longer settling period, indicating the PI controller's limitations in stabilizing the system under such disturbances.

In contrast, the Figure 7(b) showcases the response using MPC based FOC. Similar to PI control, the motor speed rapidly attains the reference value initially. However, when the sudden torque change occurs at 0.6 seconds, the speed remains stable with no visible dip, demonstrating the superior disturbance rejection capability of the MPC based FOC.

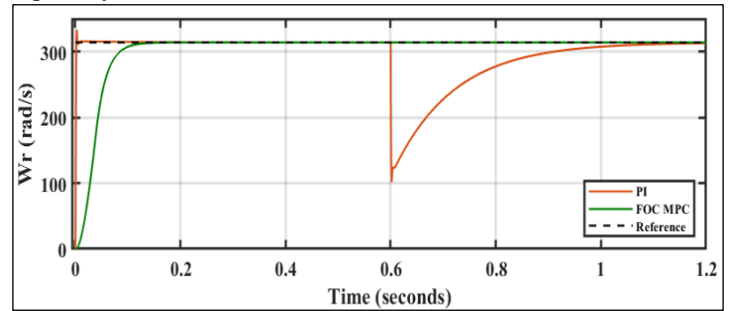


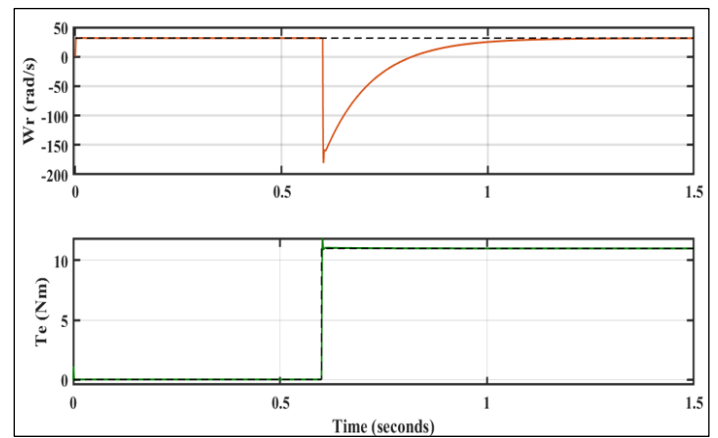
Figure 8. Transient characteristics of drive for sudden change in load from no-load to full load

Source: Authors, (2025).

The Figure 8, comparing both controllers' speed responses, clearly shows the MPC based FOC maintaining a steady speed profile with minimal deviation, unlike the PI controlled drive, which exhibits a pronounced speed dip and recovery phase. This highlights the robustness and efficiency of MPC based FOC in handling dynamic load changes, making it a superior control strategy for PMSM drives.

## VI.3. DYNAMIC RESPONSE OF MOTOR AT SLOW SPEED

The Figure 9(a) and Figure 9(b) present the speed, torque characteristics for PI controlled and MPC based FOC controlled PMSM drive at low speed (10% of rated speed).



(a)



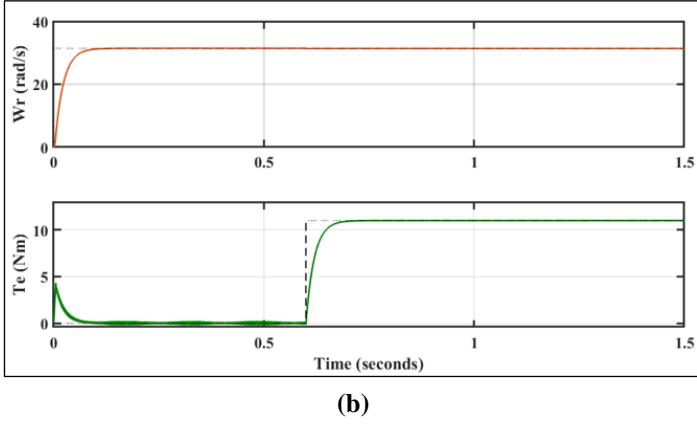


Figure 9. Dynamic response of (a) PI (b) MPC based FOC controlled PMSM drive torque transition from no load to full load at low-speed

Source: Authors, (2025).

At  $t=0.6s$ , a torque transition from no load to full load causes a noticeable speed deviation in the PI-controlled drive, as illustrated in Figure 10. In contrast, the MPC-based FOC controller demonstrates superior performance by effectively maintaining speed stability under this condition. We can also observe from the Figure 9(b) that the initial torque overshoot in the MPC based FOC controller at low-speed operations is 25% of the rated speed operation of the drive.

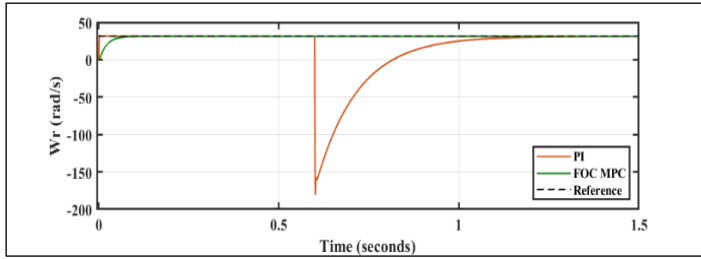


Figure 10: Speed comparison of low-speed operation.

Source: Authors, (2025).

#### VI.4. STEADY STATE CHARACTERISTICS

The analysis of PMSM drive responses under full load (11 Nm) and rated speed (314 rad/s) conditions is illustrated through the comparison graphs of traditional PI and MPC-based FOC controllers. The Figure 11 showcases the speed response comparison between the two controllers. The PI controller converges to the rated speed by  $t=0.15s$  well before the MPC-based FOC i.e.,  $t=0.5s$ . The PI controller demonstrates a minimal overshoot and quickly stabilizes at the rated speed, indicating its

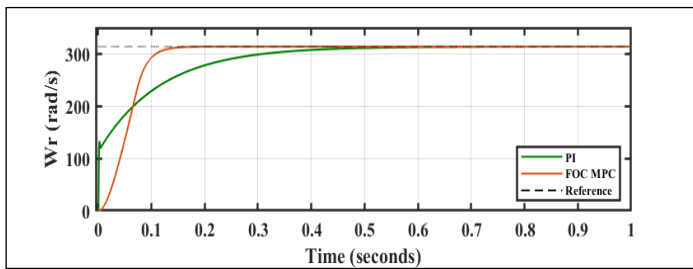


Figure 11: Speed response comparison at rated speed

Source: Authors, (2025).

capability to manage speed control effectively under these conditions. However, the MPC-based FOC shows an even

smoother speed transition with virtually no overshoot and a prompt convergence to the rated speed. This highlights the MPC-based FOC's superior efficiency in handling sudden load changes while maintaining exceptional stability and precision.

In Figure 12, the torque response comparison is presented. The PI controller's torque response, although showing minimal overshoot and rapid stabilization at the desired torque of 11 Nm, lacks the refined control observed with the MPC-based FOC. The MPC-based FOC's torque response does exhibit an initial overshoot, reaching up to 23Nm, but this is quickly corrected, and the system stabilizes at the reference torque. This brief overshoot is a trade-off for the MPC algorithm's proactive adjustments, which ultimately result in more precise and stable torque control.

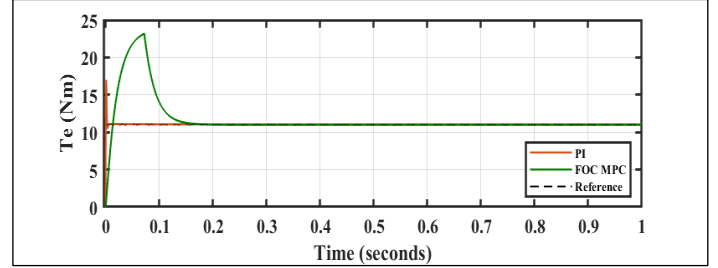


Figure 12: Torque response comparison at full-load

Source: Authors, (2025).

Further examination of the steady-state characteristics from Figure 13 reveals additional advantages of the MPC-based

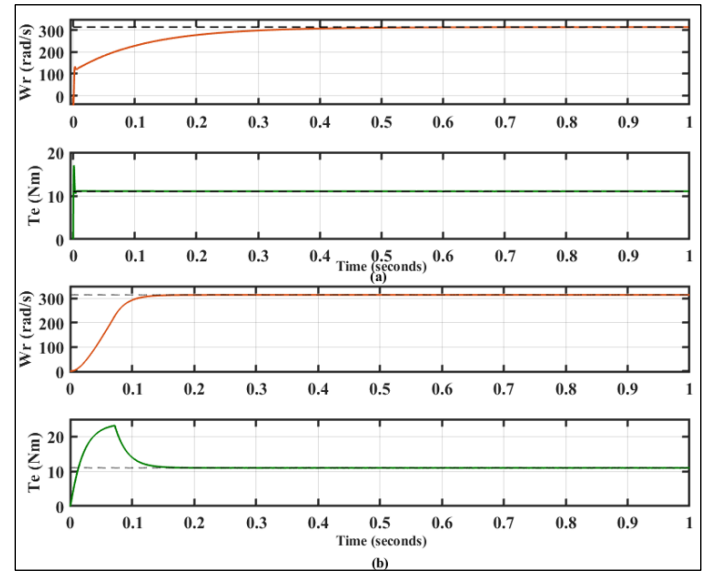


Figure 13. Response of the PMSM drive for rated speed and full-load condition (a) PI, (b) MPC based FOC.

Source: Authors, (2025).

FOC. In steady-state operation, the MPC-based FOC maintains the desired speed and torque with minimal fluctuations, ensuring a consistent and reliable performance. The PI controller, while effective, shows slightly more variability in maintaining the target values, reflecting a less robust steady-state control compared to the MPC-based approach. The advanced predictive nature of the MPC algorithm allows it to anticipate and mitigate deviations more effectively, providing a more stable and precise control over time.

#### VII. CONCLUSION

The findings of this research highlight the substantial benefits of combining MPC with FOC for PMSM drives. Extensive simulations reveal that the proposed MPC-based FOC strategy significantly enhances dynamic response, minimizes torque ripple, and improves overall stability of PMSM drives, especially during torque transitions and varying load conditions. A comparative analysis with traditional Proportional-Integral (PI) control demonstrates that the MPC-based approach outperforms in terms of faster rise times, reduced overshoot, and better steady-state performance.

The improved control accuracy and robustness provided by the MPC-based FOC method make it a viable solution for high-performance applications demanding rapid and precise motor control. By utilizing the predictive nature of MPC, the system can anticipate future states and optimize control actions in real-time, thereby boosting the efficiency and reliability of the PMSM drive. This study confirms the effectiveness of the proposed control strategy and highlights its potential to overcome the limitations of conventional methods.

## VIII. AUTHOR'S CONTRIBUTION

**Conceptualization:** V. Sri Charan ,Dr. D. Kiran Kumar.

**Methodology:** V. Sri Charan ,Dr. D. Kiran Kumar.

**Investigation:** V. Sri Charan ,Dr. D. Kiran Kumar.

**Discussion of results:** V. Sri Charan ,Dr. D. Kiran Kumar.

**Writing – Original Draft:** V. Sri Charan ,Dr. D. Kiran Kumar.

**Writing – Review and Editing:** V. Sri Charan ,Dr. D. Kiran Kumar.

**Resources:** Author V. Sri Charan ,Dr. D. Kiran Kumar.

**Supervision:** V. Sri Charan ,Dr. D. Kiran Kumar.

**Approval of the final text:** V. Sri Charan ,Dr. D. Kiran Kumar.

## IX. REFERENCES

[1] Husain et al., "Electric Drive Technology Trends, Challenges, and Opportunities for Future Electric Vehicles," in *Proceedings of the IEEE*, vol. 109, no. 6, pp. 1039-1059, June 2021, doi: 10.1109/JPROC.2020.3046112.

[2] Merabet A. Advanced Control for Electric Drives: Current Challenges and Future Perspectives. *Electronics*. 2020; 9(11):1762. <https://doi.org/10.3390/electronics9111762>.

[3] Wang, G., Zhang, G., Xu, D. (2020). Introduction of PMSM Control Methods. In: *Position Sensorless Control Techniques for Permanent Magnet Synchronous Machine Drives*. Springer, Singapore. [https://doi.org/10.1007/978-981-15-0050-3\\_2](https://doi.org/10.1007/978-981-15-0050-3_2).

[4] T. Rudnicki, R. Czerwinski, D. Polok and A. Sikora, "Performance analysis of a PMSM drive with torque and speed control," 2015 22nd International Conference Mixed Design of Integrated Circuits & Systems (MIXDES), Torun, Poland, 2015, pp. 562-566, doi: 10.1109/MIXDES.2015.7208586.

[5] Wang, Q., Wang, S., & Chen, C. (2019). Review of sensorless control techniques for PMSM drives. *IEEE Transactions on Electrical and Electronic Engineering*, 14(10), 1543–1552. <https://doi.org/10.1002/tee.22974>.

[6] Cho, B.G., Hong, C., Lee, J. et al. Simple position sensorless V/f scalar control method for permanent-magnet synchronous motor drives. *J. Power Electron.* 21, 1020–1029 (2021). <https://doi.org/10.1007/s43236-021-00249-1>.

[7] Vidlak M, Makys P, Gorel L. A Novel Constant Power Factor Loop for Stable V/f Control of PMSM in Comparison against Sensorless FOC with Luenberger-Type Back-EMF Observer Verified by Experiments. *Applied Sciences*. 2022; 12(18):9179. <https://doi.org/10.3390/app12189179>.

[8] V. Biyani, J. R. T. E. T. A, S. S. V. S and P. K. P, "Vector Control Implementation in PMSM Motor Drive for Electric-Vehicle Application," 2022 4th International Conference on Energy, Power and Environment (ICEPE), Shillong, India, 2022, pp. 1-8, doi: 10.1109/ICEPE55035.2022.9798140.

[9] P. Kumar, S. Dhundhara, and R. Makin, "Performance analysis of PMSM drive based on FOC technique with and without MRAS method," 2016 Int. Conf. Recent Adv. Innov. Eng. ICRAIE 2016, pp. 6–11, 2016, doi: 10.1109/ICRAIE.2016.7939492.

[10] R. E. K. Meesala, S. Athikkal, P. Pradhan, S. Prasad and A. Prasad, "Modified Direct Torque Control of PMSM Drive for Electric Vehicle Application," 2021 IEEE Madras Section Conference (MASCAN), Chennai, India, 2021, pp. 1-5, doi: 10.1109/MASCAN51689.2021.9563576.

[11] Y. Guo, X. Chang and C. L. P. Chen, "DTC-SVM-based Matrix Converter for a PMSM in a vessel electric propulsion system," 2009 Chinese Control and Decision Conference, Guilin, China, 2009, pp. 3397-3401, doi: 10.1109/CCDC.2009.5191899.

[12] S. K. Dwivedi, M. Laursen and S. Hansen, "Voltage vector based control for PMSM in industry applications," 2010 IEEE International Symposium on Industrial Electronics, Bari, Italy, 2010, pp. 3845-3850, doi: 10.1109/ISIE.2010.5637742.

[13] Y. Zhang, D. Xu, J. Liu, S. Gao and W. Xu, "Performance Improvement of Model-Predictive Current Control of Permanent Magnet Synchronous Motor Drives," in *IEEE Transactions on Industry Applications*, vol. 53, no. 4, pp. 3683-3695, July-Aug. 2017, doi: 10.1109/TIA.2017.2690998.

[14] Chirantan, S., & Pati, B. B. (2024). Dynamics assessment of an inverter fed induction motor drive by an improved predictive controller leveraging finite control set mechanism. *ITEGAM- Journal of Engineering and Technology for Industrial Applications* (ITEGAM-JETIA. GN1 Sistemas e Publicacoes Ltd. <http://doi.org/10.5935/jetia.v10i47.1098>.

[15] Y. A. -R. I. Mohamed, "Design and Implementation of a Robust Current-Control Scheme for a PMSM Vector Drive With a Simple Adaptive Disturbance Observer," in *IEEE Transactions on Industrial Electronics*, vol. 54, no. 4, pp. 1981-1988, Aug. 2007, doi: 10.1109/TIE.2007.895074.

[16] W. Kim, C. Yang and C. C. Chung, "Design and Implementation of Simple Field-Oriented Control for Permanent Magnet Stepper Motors Without DQ Transformation," in *IEEE Transactions on Magnetics*, vol. 47, no. 10, pp. 4231-4234, Oct. 2011, doi: 10.1109/TMAG.2011.2157956.

[17] Bhavik Brahmabhatt, C. K. B. (2024, March 31). Indirect Field Oriented Control of Induction Motor. *Journal of Electrical Systems*. Science Research Society. <http://doi.org/10.52783/jes.1793>

[18] Shrivastava, R., Thakre, M. P., Choudhari, J., Somnath Kadlag, S., Mapari, R., Prakash Kadam, D., & Khule, S. (2023, October 1). Performance analysis of FOC space vector modulation DCMLI driven PMSM drive. *Bulletin of Electrical Engineering and Informatics*. Institute of Advanced Engineering and Science. <http://doi.org/10.11591/eei.v12i5.4554>.

[19] Y. Zhang, D. Xu, J. Liu, S. Gao and W. Xu, "Performance Improvement of Model-Predictive Current Control of Permanent Magnet Synchronous Motor Drives," in *IEEE Transactions on Industry Applications*, vol. 53, no. 4, pp. 3683-3695, July-Aug. 2017, doi: 10.1109/TIA.2017.2690998.

[20] Suryakant, Sreejeth, M., Singh, M. et al. Minimization of torque ripples in PMSM drive using PI- resonant controller-based model predictive control. *Electr Eng* 105, 207–219 (2023). <https://doi.org/10.1007/s00202-022-01660-y>.

[21] Li, H., Liu, Z. & Shao, J. A Model Predictive Current Control Based on Adaline Neural Network for PMSM. *J. Electr. Eng. Technol.* 18, 953–960 (2023). <https://doi.org/10.1007/s42835-022-01324-8>.



## RESEARCH ARTICLE

## OPEN ACCESS

## OPTIMAL SIZING OF A HYBRID MICROGRID SYSTEM FOR A RURAL AREA OF ALGERIA

Badis Bacha<sup>1</sup>, Hatem Ghodbane<sup>2</sup>, Nadjiba Terki<sup>3</sup>, Madina Hamiane<sup>4</sup>, Omar Charrouf<sup>5</sup>, Abir Betka<sup>6</sup>, Aymene Bacha<sup>7</sup>

<sup>1,2,3,5,7</sup>Department of Electrical Engineering, Mohamed Khider University, Biskra, Algeria.

<sup>4</sup>College of Engineering, Royal University for Women, Riffa, Bahrain.

<sup>6</sup>Department of Electrical Engineering, Echahid Hama Lakhdar University, El Oued, Algeria.

<sup>1</sup><http://orcid.org/0009-0002-1409-897X>, <sup>2</sup><https://orcid.org/0009-0004-7809-8340>, <sup>3</sup><http://orcid.org/0000-0003-0402-2322>

<sup>4</sup><http://orcid.org/0000-0002-1921-9980>, <sup>5</sup><http://orcid.org/0000-0003-4254-464X>, <sup>6</sup><http://orcid.org/0000-0002-2142-1088>

<sup>7</sup><http://orcid.org/0009-0004-2037-2378>

Email: [badis.bacha@univ-biskra.dz](mailto:badis.bacha@univ-biskra.dz), [h.ghodbane@univ-biskra.dz](mailto:h.ghodbane@univ-biskra.dz), [n.terki@univ-biskra.dz](mailto:n.terki@univ-biskra.dz), [mhamiane@hotmail.com](mailto:mhamiane@hotmail.com), [omar.charrouf@univ-biskra.dz](mailto:omar.charrouf@univ-biskra.dz), [betkaabir@gmail.com](mailto:betkaabir@gmail.com), [aymen98tech@gmail.com](mailto:aymen98tech@gmail.com)

## ARTICLE INFO

Article History Received:  
December 26, 2024 Revised:  
January 2, 2025 Accepted:  
February 15, 2025 Published:  
March 31, 2025

**Keywords:**

Hybrid microgrid,  
Optimization,  
Optimal Sizing,  
Particle swarm optimization,  
Weighted sum approach.

## ABSTRACT

Renewable energy systems have replaced systems that use fossil fuels in many applications in different regions of the world. This is seen in the increasing use of solar and wind energy as the two most important sources for producing environment-friendly and economically convenient electrical energy. The fluctuating and unstable nature of renewable energy sources makes this type of energy complex to exploit, and related research has therefore mainly focused on Control and optimization. This work proposes an optimized configuration of two hybrid systems designed for a microgrid network with the aim to improve the power supply in isolated areas and provide a low cost, more reliable, and sustainable source of electricity for rural communities that may have limited access to traditional power grids. These hybrid setups consist of an initial system that caters for 10 houses which is then extended to serve 20 houses. Both setups utilize solar and wind energy sources, energy storage batteries, and a diesel generator. Real data collected in the Biskra region in the southeast of Algeria, is used. Particle Swarm Optimization algorithm is applied to achieve the optimal size of the hybrid system components through the weighted sum multi-objective approach, whereby three factors, namely, Cost of Electricity, Loss of Power Supply Probability, and Dummy Excess are combined into one objective function. Results of simulation show that the proposed approach achieves highly satisfactory values for the electricity prices in the 10- house and 20-house scenarios, with estimates of 0.15829 \$/Kwh and 0.42112 \$/Kwh, respectively.



Copyright ©2025 by authors and Galileo Institute of Technology and Education of the Amazon (ITEGAM). This work is licensed under the Creative Commons Attribution International License (CC BY 4.0).

## I. INTRODUCTION

Future sustainability and respect for environmental standards are the two main biggest reasons that are motivating, on a daily basis, all countries of the world to exploit renewable resources of all kinds [1]. Despite this acceleration in the exploitation of renewable resources, the largest energy contributor in the world remains fossil and traditional sources. These sources are oil, gas and coal [2], [3], and are the cause of the large emission of gasses and global warming that affects our planet [4].

Renewable energy sources are the best energy supply alternative for energy supply for sustainable development [5].

Many studies have shown that the electricity industry through renewable resources is low cost, more reliable, and environmentally friendly [5]. One of the most important energy systems in use today is microgrid (MG). They are small-sized systems for power generation and can operate independently or connect several networks with each other, and they also have the ability to be connected to the central network or separated according to the need. Supporting these systems, especially those installed in isolated places, with support systems such as generators, aims to increase their stability [6]. Microgrid systems include many renewable energy systems such as Photovoltaic (PV) cells, and Wind Turbine (WT) generators. Batteries and



generators are also used to maintain the stability of the system, as well as the components of the loads and the control system. Small grids are characterized by the ability to provide energy for one consumer or a group of consumers according to the objectives of the system [7].

There are two types of direct and alternating current in small networks, due to the variety of sources available for these networks. The current generated by photovoltaic cells is direct current type (DC) while wind turbines generate alternating current (AC). Two areas that are very popular in research on Microgrid systems are design and control. The design of the system is a very important stage in which energy sources are selected and their sizes are determined taking account all restrictions, the most important of which is the environment at the lowest possible cost of investment [8],[9]. Optimal component size is the most significant element that is taken into account when designing renewable energy systems [10].

The methods of sizing, formations, storage methods, and control strategies are the most prominent issues addressed by research on renewable energy sources [11]. The most serious problem facing the exploitation of renewable energy sources is their intermittent nature. To overcome this problem, several sources are used together to form a hybrid system. The size of the system is either undersized or oversized. There are two methods for sizing, either through dedicated software programs or with traditional methods [12].

Figure. 1, illustrates this more clearly. Artificial intelligence (AI) is defined as enabling machines or software to perform types of functions that characterize human thought in [13]. The optimal sizing of hybrid renewable systems is done through the use of several methods, including classical methods, hybrid methods, and AI, as clearly depicted in Figure 2.

Several intelligence-based optimization techniques used in sizing of hybrid renewable energy systems have been presented in many studies and researches. Researchers in this field have used several smart algorithms to find the optimal size for hybrid systems, as reported in the study of Starke et al. [14], where a genetic algorithm is used to reduce operating and installation costs for a hybrid system consisting of photovoltaic solar panels (PV), and concentrated solar power systems (CSP) that concentrate solar energy. The Non-Dominated Sorting Genetic Algorithm II (NSGA II) was used by Kamjoo et al. [15] for the sizing of a hybrid system.

A Multi-Objective Self- adaptive Differential Evolution algorithm (MOSaDE) was used in the optimal sizing of a hybrid system in the Kingdom of Saudi Arabia, by Ramli et al. [16]. Optimal sizing using the Particle Swarm Optimization Algorithm (PSO) was applied to a hybrid system in order to improve the electrification of a rural area located in Kerman, Iran, by Askarzadeh et al. [17]. In [18], Fathy et al., implemented the Mine Blast Algorithm (MBA) in the sizing of a hybrid system for a remote site in Egypt.

The Ant Colony Optimization (ACO) algorithm was also used by Suhane et al. [19] for the optimal sizing of a hybrid system in an isolated site. In the same context, optimal sizing of a hybrid system in Taiwan was effectively solved by a multi-objective line-up competition algorithm (MLUCA) in Shi et al. [20]. Biogeography-based Optimization (BBO) algorithm was proposed by Gupta et al. [21] for the size optimization of a small autonomous hybrid power system. The optimal design of a hybrid system was also determined by solving a multi-objective problem using the Preference-Inspired Co-Evolutionary Approach (PICEA) in [22] by Shi et al. Moreover, Sanajaoba et al. [23], the

Cuckoo Search algorithm (CSA) was the algorithm chosen to determine the optimal size of an isolated and hybrid system. The optimal size was found by Maleki et al. [24], taking into account the desired reliability of a hybrid system, by using the artificial bee swarm optimization algorithm (ABSO).

Zhao et al. [25] utilized the Improved Fruit Fly Algorithm (IFFA) to solve a multi-objective problem for sizing a hybrid system. On the other hand, some applications reported in the literature, where the PSO algorithm was used for the optimal design of hybrid renewable systems using objective functions in general formulation, the methods for solving them depend on the direct methods. Alternatively, in certain applications proposed in the literature, the Particle Swarm Optimization (PSO) algorithm has been employed for the optimal design of hybrid renewable systems. The suggested approaches involve formulating objective functions, and the methods utilized to solve them rely on regenerative or direct methods.

In [26], the Particle Swarm Optimization (PSO) algorithm was applied to determine the optimal sizing of a hybrid renewable energy system composed of PV (photovoltaic) panels, wind turbines, and a fuel cell. The primary objective of the study was to minimize the annual cost associated with the system. PSO was used as a computational tool to find the most cost-effective configuration for the hybrid system. Similarly, Kaviani et al. [27] relied on the PV-Wind-Fuel cell as components of a studied hybrid system. The objective function was solved through the PSO algorithm, with the aim to find the minimum cost. The PSO algorithm was also used by Khare et al. [28] to determine the optimal size of a hybrid system consisting of a PV-wind-diesel-battery system.

The objective function was formulated to minimize the system cost. Askarzadeh et al. [17] calculated the optimal size of a hybrid system consisting of PV/Wind/battery using a function aiming to minimize the life cycle cost (LCC) of the system. In the same context, The PSO algorithm was employed to size a hybrid system that incorporated PV, wind, fuel cell, battery, and diesel generator by Sharafi et al. [29], the study adopted a multi-objective function with the goal of minimizing three key parameters: the total cost, the total CO<sub>2</sub> emissions, and the energy deficit.

In general, multi-objective optimization problems are more common than single-objectives [30]. One of the problems that may affect the PSO algorithm when using multi-objective functions is the difficulty in controlling diversity, also called turbulence [31]. To overcome this difficulty and avoid running into other problems mentioned in [32], such as the possibility of entrapment into local optima and the inability to recover from these, we have adopted a new approach in solving the multi-objective problem proposed in this study.

This method is called the weighted sum (WS), or in more general terms the linear fitness combination technique. WS is a widely used method in dealing with multi-objective tasks. It is easy to implement and achieves computational efficiency in less time required for solution than other methods [31]. In this paper instead of employing three separate objective functions, we opted for the weighted sum method that combines them into a single objective function. This choice is made owing to the method's simplicity of use and proven effectiveness [33], as it gives satisfactory results with respect to all constraints, and enables us to achieve three goals at the same time.

To achieve the optimal configuration of a stand-alone HMS, this study aims to analyze the economic facets involved in designing a compact HMS that operates independently of the

central grid. This system incorporates solar energy, wind energy, and a battery system for energy balancing, supplemented by a diesel generator as a backup power source. The agricultural region of Biskra, in Algeria, was the study area, where we obtained weather data through the meteorological station at the University of Biskra.

A novel approach to the PSO algorithm is adopted to address a multi-objective problem by associating it into a single objective function through a weighted combination of three factors: electricity cost (COE), loss of power supply probability (LPSP), and dummy excess. on a new line:

The following outline highlights the major contributions of our work.

- Our study goes beyond others by incorporating real-life data from the Biskra area in Algeria, encompassing sun radiation, wind speed, and temperature, rather than focusing on limited geographical regions.
- Unlike previous studies that relied on the PSO algorithm and one energy source, we have identified the most efficient microgrid system design with multiple sources.
- Our approach integrates a multi-objective function with a weighted sum, combining the cost of electricity (COE), the probability of power loss (LPSP), and the Dummy excess in a single fitness objective function. This is in contrast to previous studies that focused fitness function on single energy sources.
- To assess the performance of the developed approach under varying loads. Two models of microgrid systems are introduced, one consisting of 10 houses and the other consisting of 20 houses.
- Our results demonstrate that HMS have made significant improvements both in terms of efficiency and endurance. We offer comprehensive comparisons with previous studies to highlight advances in performance metrics such as COE and LPSP.

This paper is formulated as follows. Section II presents the components of the proposed HMS. Section III discusses the development of energy management strategy for the proposed

system. Section IV gives the typical load assessment for the case under study. Section V presents the optimization problem which includes the cost analysis, the reliability analysis, the multi objective optimization, and the optimization strategy using Particle Swarm Optimization algorithm along with the optimization procedure. Simulation results are discussed in Section VI, and finally, the conclusions are summarized in Section VII.

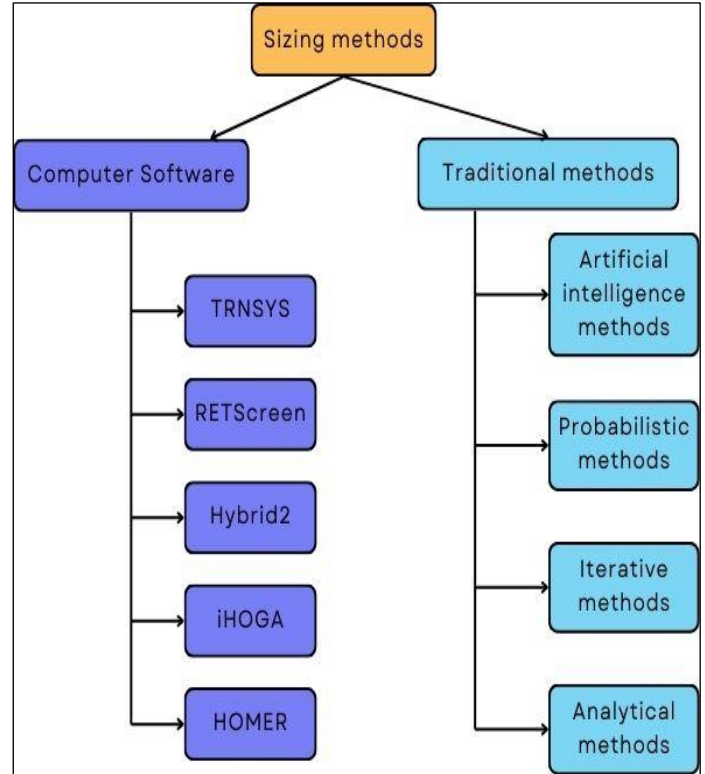


Figure 1: Sizing methods for hybrid system.  
Source: Authors, (2025).

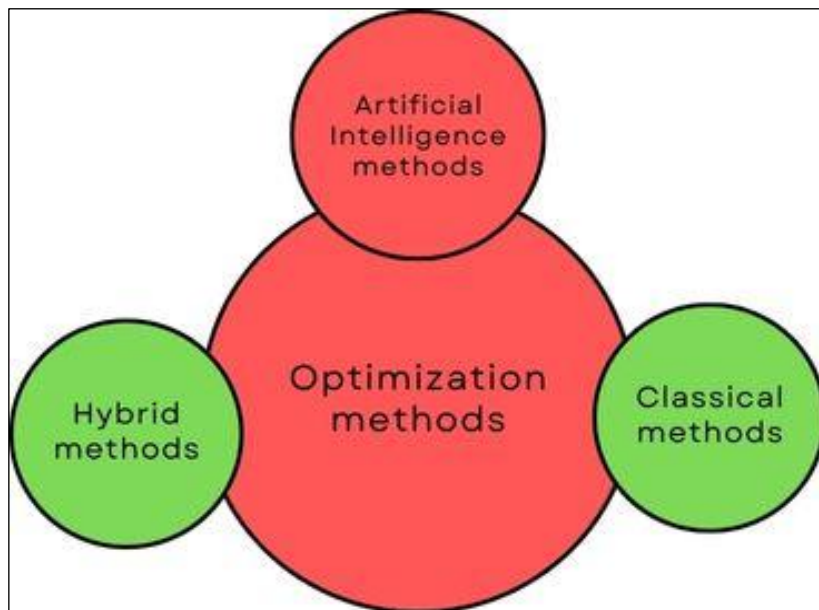


Figure 2: Optimization methods for hybrid systems.  
Source: Authors, (2025).

## II. HYBRID MICROGRID SYSTEM (HMS) DESCRIPTION

The Hybrid Microgrid System (HMS) examined in this study consists of five main system elements: a PV system, wind

turbines (WT), diesel generators, an inverter, and a battery bank. Figure 3, shows the components of the hybrid system.

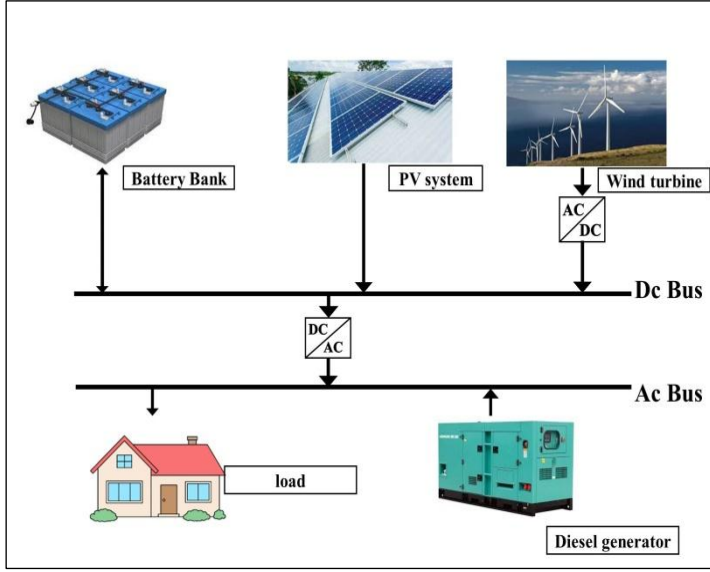


Figure 3: Components of a HMS.  
Source: Authors, (2025).

### II.1 PV SYSTEM

The following equation is used to compute the power output of PV panels [34, 35]:

$$P_{pv-out} = P_{rated} \times G/G_{ref} [1 + K_t ((T_{amb} + (0.0256 \times G)) - T_{ref})] \quad (1)$$

In which  $P_{rated}$  represents the PV rated power under standard test conditions (STC),  $G$  represents solar radiation ( $W/m^2$ ),  $G_{ref}$  is  $1 \text{ kW/m}^2$ ;  $K_t$  is a constant  $-3.7 \times 10^{-3} (1/^\circ C)$ ,  $T_{amb}$  represents ambient temperature, and  $T_{ref}$  represents the temperature in  $^\circ C$  of PV cell at STC ( $25^\circ C$ ).

Table 1 provides specifics on PV parameters. Figure 4, and Figure 5, show data for the monthly average solar radiation and temperature for the city of Biskra in the southeast of Algeria in the year 2020.

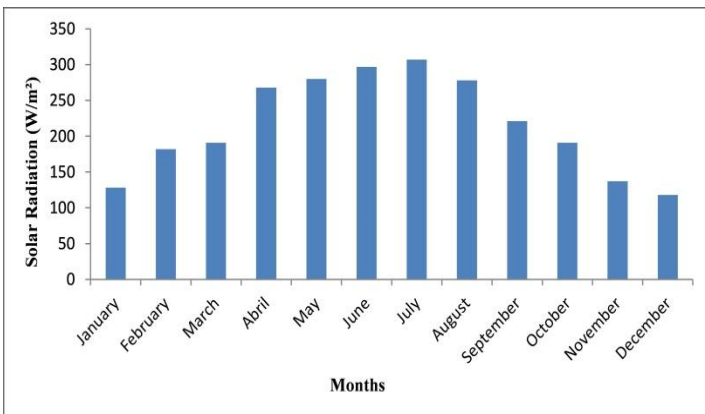


Figure 4: Monthly Averages of Solar Radiation in the year 2020  
Source: Authors, (2025).

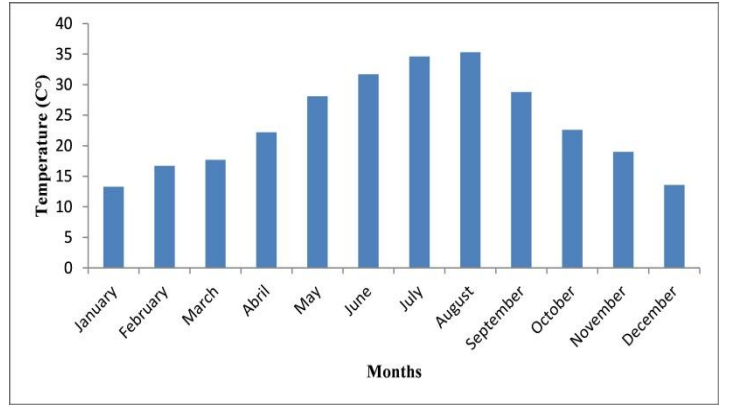


Figure 5: Monthly Averages of temperature in the year 2020.  
Source: Authors, (2025).

### II.2 WIND POWER SYSTEM

The wind turbine is composed of three primary components: the tower, the blades, and the generator, which transforms kinetic energy into electrical energy. The quantity of electrical energy produced by a WT is influenced by the wind speed and blade design [36].

$$P_{wind}(t) = \begin{cases} 0 & V(t) \leq V_{cut-in} \text{ or } V(t) \geq V_{cut-out} \\ P_{rated} & V_{rated} \leq V(t) \leq V_{cut-out} \\ P_{rated} \frac{V(t)-V_{cut-in}}{V_{rated}-V_{cut-in}} & V_{cut-in} \leq V(t) \leq V_{rated} \end{cases} \quad (2)$$

where  $P_{rated}$  represents the rating power of a single wind turbine,  $V_{cut-in}$  is the cut in speed,  $V_{rated}$  the rated wind speed,

$V_{cut-out}$  the Maximum speed and  $V(t)$  represents the wind speed at desired height. Wind speed differs significantly with height, and is given by:

$$V(t) = V_r(t) \times \left(\frac{h_2}{h_1}\right)^\alpha \quad (3)$$

where  $V_r(t)$  represents the speed at a reference height,  $h_1$ ;  $V(t)$  is the speed at a hub height  $h_2$ , and  $\alpha$  is the coefficient of friction. The typical value for  $\alpha$  is  $1/7=0.14$  for a low roughness surface, and a well exposed site.

The characteristics of the wind turbine utilized in this optimization procedure are displayed in Table 1. Figure 6 shows the monthly average wind speed for the city of Biskra in the year 2020.

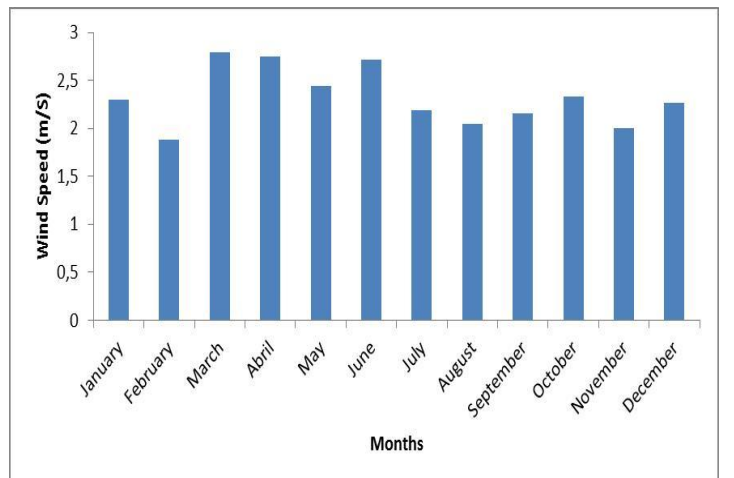


Figure 6: Monthly Averages of wind speed in the year 2020.  
Source: Authors, (2025).

## II.3 DIESEL GENERATOR

The diesel generator operates as a secondary power supply to the Microgrid systems. The characteristics of the loads that it aims to meet have a major role in choosing the rated capacity of the diesel generator. The diesel generator is used in the event that the hybrid system is unable to provide sufficient power to the loads. The fuel consumption  $Fuel(t)$  of the diesel generator is given by [37-39].

$$Fuel(t) = 0.246 \times P_{diesel}(t) + 0.08415 \times P_{rat} \quad (4)$$

where  $P_{diesel}(t)$  represents the generated power at time  $t$ , 0.246 and 0.08415 represent the approximated coefficients of the fuel consumption parameters, and  $P_{rat}$  is the rated power. Data for diesel generators used in microgrid optimization are presented in Table 1.

## II.4 BATTERY

The fluctuating nature of the weather conditions between seasons and days of the year makes the energy produced from the hybrid system fluctuate as well, for this reason we had we had to use the storage system represented by the batteries in order to store the surplus energy and discharge it in case of need [40]. The battery state of charge SOC at time  $t$  can be calculated during the charging and discharging stages through the following equations:

$$SOC_{CH}(t) = SOC(t-1) \times (1 - \sigma) + (P_{generation}(t) - (P_l(t)/\eta_{inv})) \times \eta_{ch} \quad (5)$$

$$SOC_{DISCH}(t) = SOC(t-1) \times (1 - \sigma) + (P_l(t)/\eta_{inv}) - (P_{generation}(t)) \times \eta_{DISCH} \quad (6)$$

$$P_{generation}(t) = P_{PV-out}(t) + P_{wind}(t) \quad (7)$$

Where  $SOC_{CH}(t)$  and  $SOC_{DISCH}(t)$  represent the battery charging and discharging energy at time  $t$ , respectively.  $SOC(t-1)$  is the charge quantity of the battery bank at time  $(t-1)$ ,  $\sigma$  is the self-discharge rate,  $P_{generation}(t)$  is the total power generated by the renewable energy system.  $P_l(t)$  is the hourly load demand at time  $t$ ,  $\eta_{inv}$  is the inverter efficiency,  $\eta_{CH}$  is the battery charging efficiency, and  $\eta_{DISCH}$  is the battery discharging efficiency.

The battery is charged by the condition [41]:

$$SOC_{min} \leq SOC \leq SOC_{max} \quad (8)$$

Where  $SOC_{min}$  is the minimum charge quantity of the battery and  $SOC_{max}$  is its maximum charge quantity.

The extra energy can be exploited if the batteries reach the maximum charging limit to feed the dummy load, although it is an increased component in the system, it is nevertheless very important to maintain the energy balance within the system.

If  $SOC > SOC_{max}$ ,  $P_{dummy}$  can be calculated through the following equation [42]:

$$P_{dummy}(t) = [(P_{PV-out}(t) \times \eta_{inv} + P_{wind}(t)) - P_l(t)] \quad (9)$$

## III. HYNRID ENERGY SYSTEM

We chose one hour as a time interval in this study, and the energy management strategy was developed according to the load

data, the intensity of solar radiation, the temperature, and the wind speed during a full year of 8760 hours. The principle of the energy management strategy in this study can be summarized as follows:

- If the energy produced from renewable sources exceeds the needs of the loads, the system stores the surplus in the batteries.
- If the batteries are charged to the maximum, the excess energy is directly discharged in the dump load.
- In the event that the system is unable to meet the needs of the loads through energy produced from renewable sources, the energy stored in the batteries is used to cover this deficit in meeting the demand for energy from the loads.
- In the event that the energy in the batteries reaches the minimum level, the diesel generator is started immediately and stopped after the system is able to produce enough energy to meet the demand from the loads.

## IV. LOAD PROFILE

The load profile must be carefully studied in any area, especially the areas that are isolated from the central network. This is done before starting any design project for renewable energy systems, whereby, through an in-depth study of the load profile, all parts of the hybrid system are selected, and this is in order to design a system that is economically inexpensive and more reliable. Figure 7 shows the daily average load profile for the summer season for a rural house in the city of Biskra.

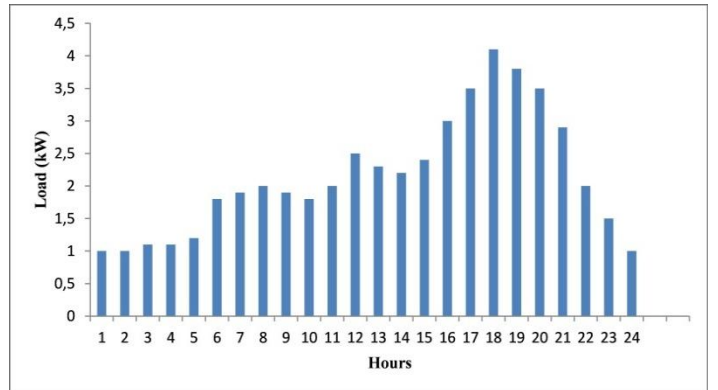


Figure 5: Typical rural house hourly load profile.

Source: Authors, (2025).

## V. THE OPTIMIZATION PROBLEM

The most important element to be studied in the design projects of renewable systems is the optimal sizing of all components of the system, where designers try to reconcile the price of the components and their quality. This is in order to obtain an acceptable life span for all components of the system, which enables the consumer of electrical energy in isolated areas to obtain electricity at the lowest cost and with more reliability.

### V.2 COST ANALYSIS

The cost of electricity (COE), is one of the most used indicators in design projects for renewable systems. It is defined as the constant price per unit of energy, and it includes all costs over the life of the project [43]. It can be calculated using the equation below.

$$COE = \frac{\text{Total Net Present cost}}{\sum_{t=1}^{8760} P_l(t)} \times CRF \quad (10)$$



with:

$$CRF = \frac{i_r \times (1+i_r)^R}{(1+i_r)^R - 1} \quad (11)$$

where CRF is a ratio used in calculating the present values of an annuity [44],  $i_r$  represents the real interest rate estimated in this study at 13%, and  $R$  is the life of the project under study and is estimated at 24 years.

We can define the total net present cost as the present value of the project cost throughout the life of the project and it includes the cost of installation, operation and maintenance.

### V.3 RELIABILITY ANALYSIS

The reliability of the energy system is an important factor for the consumer, and this is to ensure the continuous supply without interruption of electrical energy. In this study, an important indicator is used, namely, the Loss of power supply probability (LPSP), in order to study the possibility of failure of the power supply for any environmental or technical reason. LPSP can be calculated through Equation 12 below [45, 46].

$$LPSP = \sum_1^{8760} \frac{(P_l(t) - (P_{\text{generation}}(t) + SOC(t-1) - SOC_{\text{min}}) \times \eta_{\text{inv}} + P_{\text{diesel}}(t))}{P_l(t)} \quad (12)$$

Moreover, during our analysis of the reliability of the system, we have added the condition.

$$P_l(t) > P_{\text{generation}}(t)$$

### V.4 MULTI OBJECTIVE OPTIMIZATION

The improvement strategy proposed in this study is to combine several elements into one objective function, which we call the weighted sum multi-objectives, and can be summarized in the following points:

- Reducing the cost of electricity COE.
- The increase in the desired reliability of the hybrid system through the reduction of potential energy losses LPSP.
- Reducing the energy spent on dummy load. We have used in the proposed objective function the ratio between dummy load and load over a full year. This ratio is expressed in the equation below.

$$Dummy_{\text{excess}} = \sum_1^{8760} \frac{P_{\text{dummy}}(t)}{P_l(t)} \quad (13)$$

The Fitness Function  $F_{\text{un}}$  used to obtain the optimal size for all components of a HMS can be expressed through Equation (14) below:

$$Fitness_{\text{Fun}} \cdot F(X) = \text{Minimum}(\text{COE} + LPSP + Dummy_{\text{excess}}) \quad (14)$$

The decision variables vector  $X$  can be expressed as:

$$X = [N_{\text{pv}} \ N_{\text{wind}} \ N_{\text{Battery}} \ N_{\text{AD}} \ N_{\text{diesel}}] \quad (15)$$

where  $N_{\text{pv}}$ ,  $N_{\text{wind}}$ ,  $N_{\text{Battery}}$ ,  $N_{\text{AD}}$ , and  $N_{\text{diesel}}$ , are the numbers of solar panels, wind turbines, batteries, autonomy days,

and diesel generators, respectively. The proposed constraints are as follows:

$$1 \leq N_{\text{pv}} \leq 45 \quad (16)$$

$$0 \leq N_{\text{wind}} \leq 10 \quad (17)$$

$$1 \leq N_{\text{Battery}} \leq 45 \quad (18)$$

$$1 \leq N_{\text{diesel}} \leq 4 \quad (19)$$

$$1 \leq N_{\text{AD}} \leq 5 \quad (20)$$

### V.5 OPTIMIZATION STRATEGY USING PARTICLE SWARM OPTIMIZATION ALGORITHM

The PSO algorithm simulates the movement of animal communities such as flocks of birds and fish, it exploits the intelligent social interactions of the flock and its ability to evolve and learn [47, 48]. PSO is a smart search algorithm, in which searching is carried out through the creation of a random set of solutions that are called a swarm, where each possible individual solution is called a particle [49]. PSO considers each particle moving through the problem hyperspace as a possible solution to the objective function. The steps of the PSO algorithm are summarized in three main steps as shown in Figure 8.

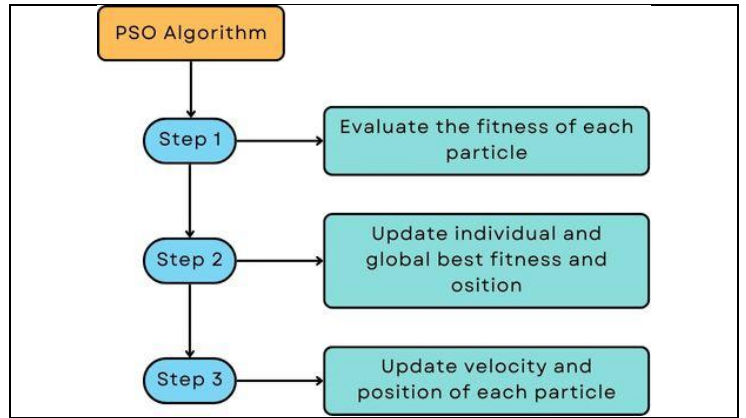


Figure 8: The three main steps of PSO algorithm

During the execution of the PSO algorithm, each particle remembers the best fitness it achieved, and compares it to the rest of the particles, which the algorithm calculates and updates in each iteration. The algorithm continues to repeat these operations according to pre-defined criteria and constraints until the optimal fitness function value is reached. Equation (21) the position of each particle at time step  $t$  is updated as follows:

$$X_{id}(t+1) = X_{id}(t) + V_{id}(t+1) \quad (21)$$

where  $d = 1, 2, \dots, D$  and  $i = 1, \dots, S$ .  $D$  and  $S$  are the dimensions of the search space and the swarm size respectively,  $V_{id}(t+1)$  is the velocity of a particle at time step  $t+1$ . The velocity is updated through Equation 22

$$V_{id}(t+1) = V_{id}(t) + C_1 \times \text{random}_1(P_{\text{best}}(t) - X_{id}(t)) + C_2 \times \text{random}_2(g_{\text{best}}(t) - X_{id}(t)) \quad (22)$$

Where  $V_{id}(t)$  is the velocity at time  $t$ ,  $C_1$  and  $C_2$  are constants,  $\text{random}_1$  and  $\text{random}_2$  are random number between 1 and 2,  $P_{\text{best}}$  is the best individual position (cognitive learning),  $g_{\text{best}}$

is the best global position (social learning ). All steps of the particle swarm optimization algorithm are summarized in Figure 9.

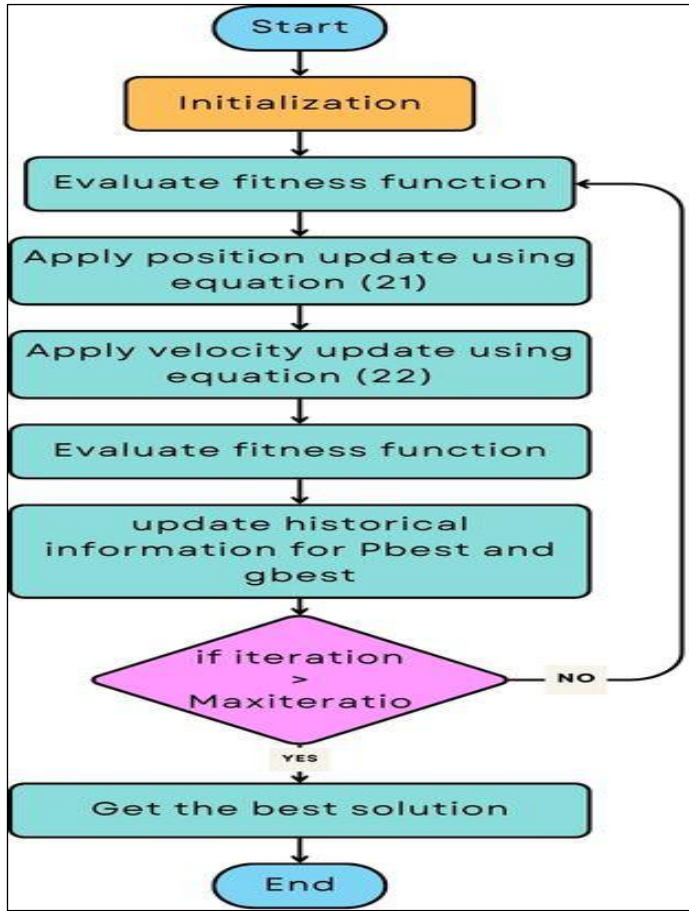


Figure 9: PSO algorithm flowchart.  
Source: Authors, (2025).

The optimization problem can be expressed in general formulation as follows [50] :

$$\text{Minimize: } F_K(x) = [F_1(x), F_2(x), \dots, F_M(x)]^T; K = 1, 2, 3, \dots, M$$

X (23)

$$\text{Subject to : } g_i(x) \leq 0; i = 1, 2, 3, \dots, m$$

where  $F_K(x)$  and  $g_i(x)$  are functions of the design vector ,  $M$  is the number of objective functions ,  $m$  is the number of constraints , and  $\mathbf{X}$  is a vector of design variables.

Optimization problems can be classified in two categories:

- Category 1 (single objective), when  $M=1$  .
- Category 2 (Multiobjective), when  $M > 1$  .

There has been a lot of research on category No. 2. This interest is due to the attractive features of this method, where it is possible to obtain one solution that achieves more than one objective at the same time [51, 52]. In this paper, we used and developed one of the methods used in solving multi-objective problems ,namely,the Weighted Sum Approach for Multiobjective Optimization(WSAFMO). This approach is often used in solving multi-objective problems, and consists of transforming a multi-function problem into a problem with one function that achieves all the objectives of its component

functions. The weighting factors  $W_i \in [0,1]$  corresponding to the components functions are selected based on their relative importance[53]. We can mathematically express this method by:

$$\text{Minimize: } F_K(x) = [W_1 \times F_1(x) + W_2 \times F_2(x) + \dots + W_M \times F_M(x)]; K = 1, 2, 3, \dots, M$$

X (24)

Subject to :  $g_i(x) \leq 0; i = 1, 2, 3, \dots, m$

In this study , it is proposed that  $W_1=W_2=W_3=1$  .

## V.6 OPTIMIZATION PROCEDUR

In this study, we search for the optimal size of a HMS using the particle swarm optimization algorithm through the following steps:

**A:** The design of the HMS is carefully implemented through the conditions followed in the energy management strategy according to the following:

- Generation of the initial population.
- Implement the hybrid system design by evaluating equations (1) through (13).
- Evaluation of the fitness function through Equation (14) taking into consideration all the constraints in equations (16) through (20).

**B:** Run the optimization algorithm through the following operations.

- Update both position and velocity through Equation (21) and Equation (22), respectively, together with the sizing of all components of the proposed HMS.
- Implement the hybrid system design by evaluating equations (1) through (13).
- Evaluation of the fitness function through Equation 14 taking into consideration all the constraints in equations (16) through (20).
- Check whether the proposed system meets problem requirements and end criterion, or not. If so, the program will be stopped and will go to the next step, otherwise, the same procedure is repeated until the termination criterion is attained.
- Show the optimal size for all components of the proposed Microgrid system with the three optimal values for the fitness function parameters, which are COE, LPSP and Dummyexcess.

## VI. RESULTS AND DISCUSSION

An isolated microgrid network system was designed to be applied in the region of Biskra, Algeria, which has many agricultural and pastoral sites that are very isolated and without electrical energy. We used real weather data captured from the weather station at the University of Biskra. The data showed that the highest average solar radiation occurred in July 2020, with an estimated value of 307.02 W/m<sup>2</sup>.

This peak is typical for the summer season when solar irradiation is generally at its maximum. In contrast, the average wind speed reached its highest in March 2020, estimated at 10.06 km/h (2.79 m/s). This increase in wind speed during the spring can be attributed to seasonal climatic changes. Monthly average

values of temperature, irradiation, and wind speed were analyzed, revealing seasonal patterns. Summer months exhibited the highest solar radiation, while spring months showed higher wind speeds. These seasonal variations are crucial for optimizing the hybrid energy system, as they influence the performance and reliability of both solar and wind energy sources.

All technical and economic specifications used for the components of the microgrid system consisting of solar panels, wind turbines, batteries and diesel generators, are shown in Table 1, with the interest rate taken at 13%, and the project life estimated at 24 years.

Table 1: Technical and economic characteristics of the system components.

Component	Parameter	Value and Unit
Photovoltaic (PV)	Life time	24 year
	Capital cost	3400 \$/kW
	Rated power	7.3 kW
	PV regulator	1500 \$
	Cost Regulator efficiency	95 %
Wind turbine (WT)	Model	ZEYU FD-2KW
	Life time	24 year
	Capital cost	2000 \$/kW
	Rated power	5 kW
	Rated speed	9.5 m/s
	Cut in speed	2.5 m/s
	Cut out speed	40 m/s
	Wind turbine regulator	1000 \$
	Cost Efficiency	95 %
Diesel generator	Life time	24,000 hours
	Capital cost	1000 \$/kW
	Rated power	4 kW
Battery	Life time	12 year
	Capital cost	280 \$/kW
	Rated power	40 kWh
	Efficiency	85 %
Inverter	Life time	24 year
	Capital cost	2500 \$
	Efficiency	92 %
Economic parameters	Life time of project	24 year
	Real interest	13 %
	Running cost +O&M cost	20 %
	Discount rate	8 %
	Fuel inflation rate	5 %

Source: Authors, (2025).

MATLAB programming and simulation platform was used in this work. The maximum number of iterations was set at 50 and the maximum number of search agents was set at 10. The main objective of our study was to search for the optimal size for all system components, that is, to search for the optimal numbers of solar panels, wind turbines, batteries and diesel generators.

Two cases were proposed for the study, the first case is a microgrid network consisting of 10 houses, and the second case is a microgrid network consisting of 20 houses. We have developed

a new design approach through the proposed objective function. Table 2 shows the best value for the objective function and computing time.

Table 2: Optimization results using PSO.

Cases studied	Best fitness values	Time (sec)
Case 1	0,49993	52.67187
Case 2	0,43816	411.05354

Source: Authors, (2025).

Figure 10 illustrates the convergence of the technique for the two cases studied. The results indicate that the best value for the objective function in Case 1 is 0,49993, which is achieved in a time of 52.67187 seconds. As for Case 2, the best value of the objective function was 0,43816, achieved in 411.05354 seconds.

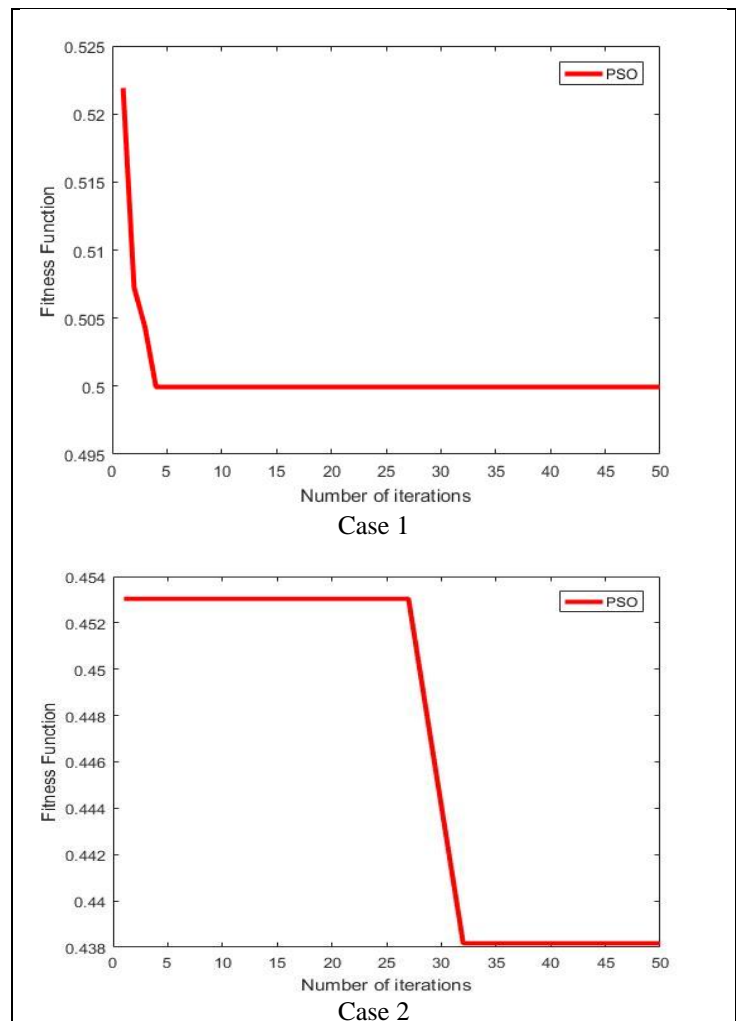


Figure 10: Convergence of fitness function.

Source: Authors, (2025).

Figure 11, illustrates the convergence curve for the cost of electricity, obtained for the two cases through the developed method of the PSO algorithm, algorithm. The figure indicates that the best cost of electricity obtained is estimated at 0,15829 \$/Kwh and 0,42112 \$/Kwh for Cases 1 and 2, respectively.

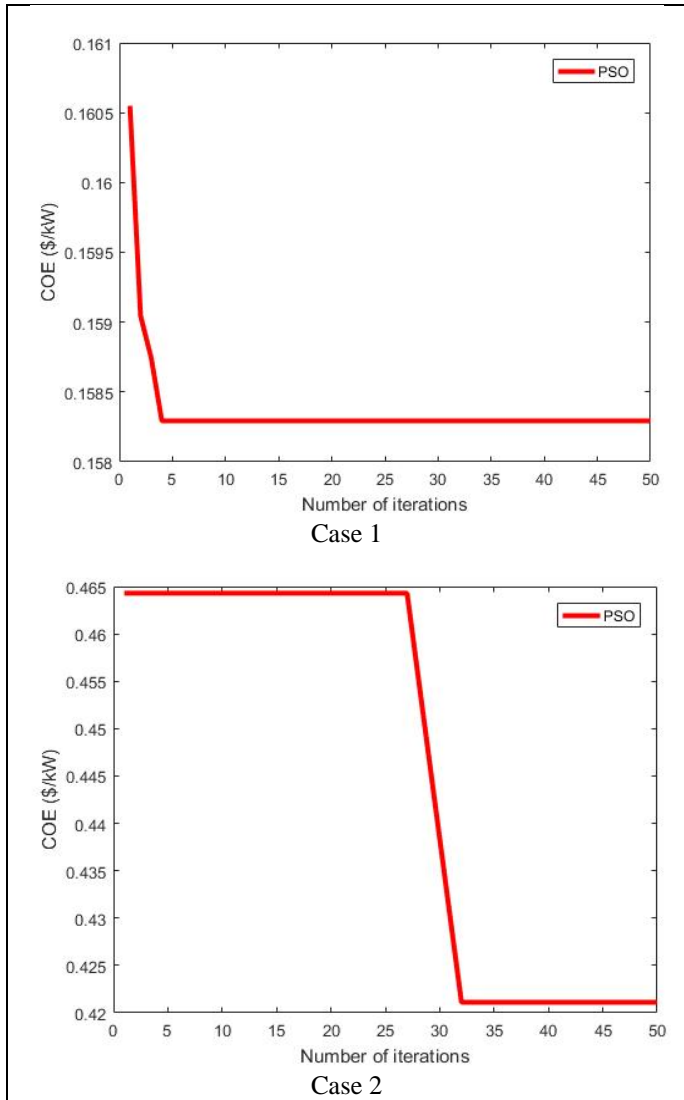


Figure 11: Convergence of cost of electricity (COE).

Figure 12, which displays the convergence curve for the Loss of power supply probability (LPSP), obtained for the two cases through the developed method of the PSO algorithm. The figure indicates that the best Loss of Power Supply Probability obtained is estimated at 0,32510 and 0,47711for Cases 1 and 2, respectively.

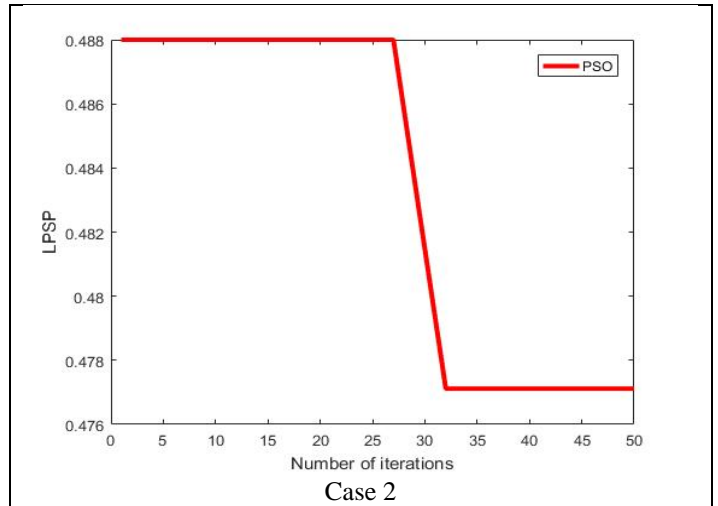
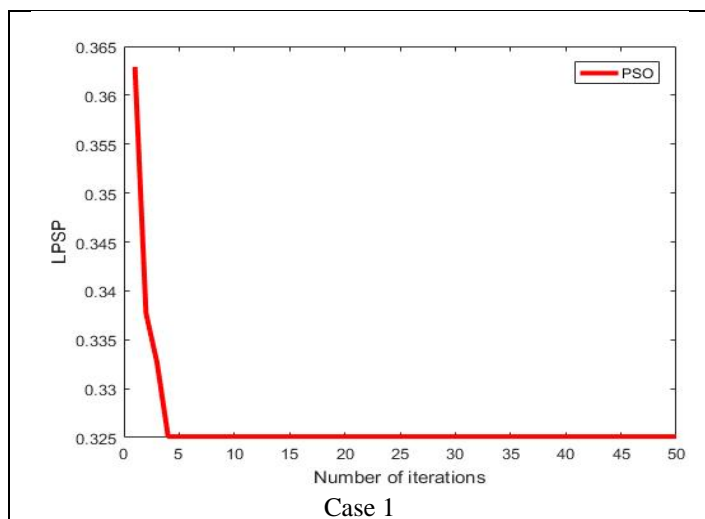


Figure 11: convergence curves for the Loss of power supply probability (LPSP)  
Source: Authors, (2025).

Figure 13, which shows the convergence curve for Dummy excess, obtained for the two cases through the developed method of the PSO algorithm. The figure indicates that the best Dummy excess obtained is estimated at 0,55994 and 0,02145 for Cases 1 and 2, respectively.

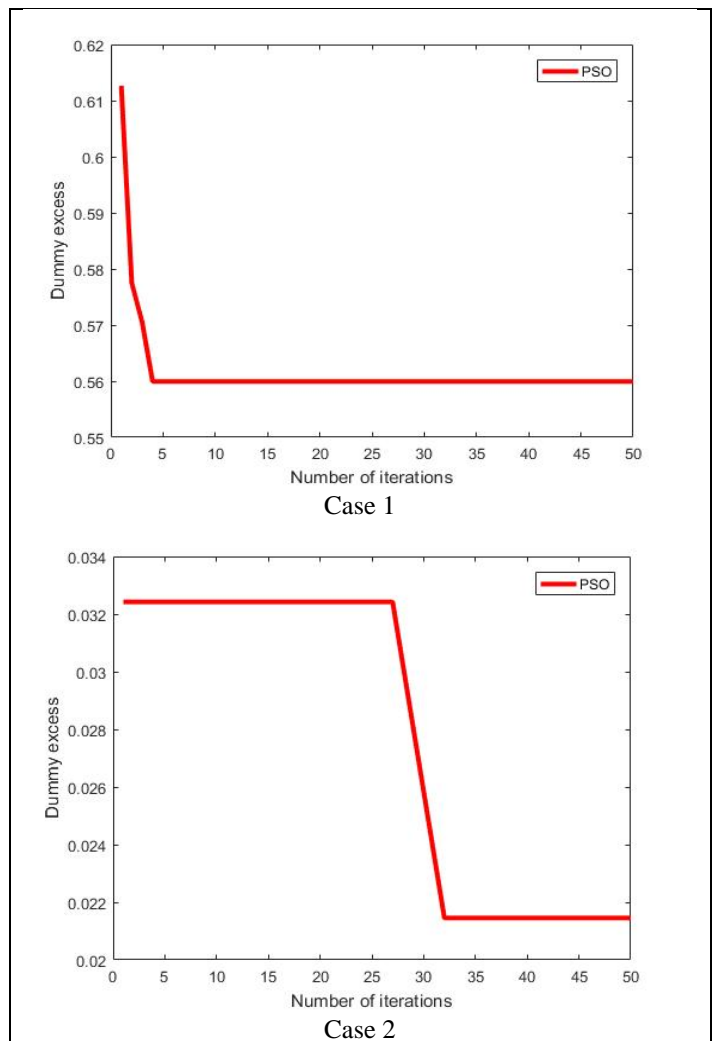


Figure 13: Convergence of Dummy excess.  
Source: Authors, (2025).



Figure 14, presents a detailed comparison of the cost of energy (COE) for scenarios 1 and 2. The analysis demonstrates that Scenario 1 achieves the most favorable COE value of 0.15829 \$/kWh, which reflects a more efficient cost structure compared to Scenario 2. This result highlights Scenario 1's advantage in minimizing energy expenses while maintaining overall system performance.

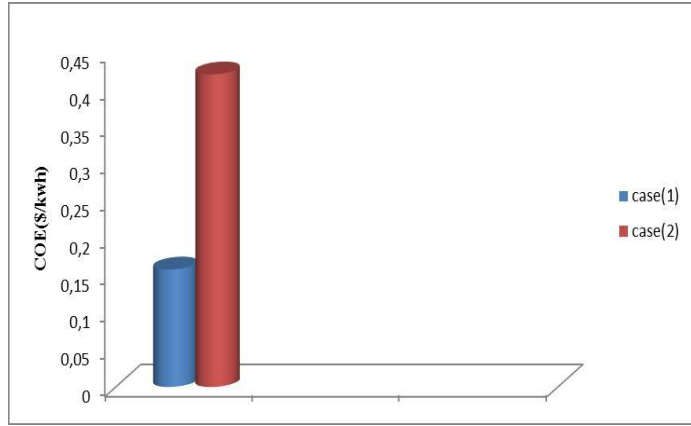


Figure 14: A comparison of the main optimization factors (COE)  
Source: Authors, (2025).

Figure 15, illustrates the Loss of Power Supply Probability (LPSP) for scenarios 1 and 2. The data reveals that Scenario 1 not only performs better in terms of COE but also exhibits the lowest LPSP value of 0.32510. This indicates a lower likelihood of power supply disruptions, showcasing Scenario 1's robustness in ensuring a reliable energy supply. These findings underscore the effectiveness of Scenario 1 in optimizing both cost efficiency and reliability.

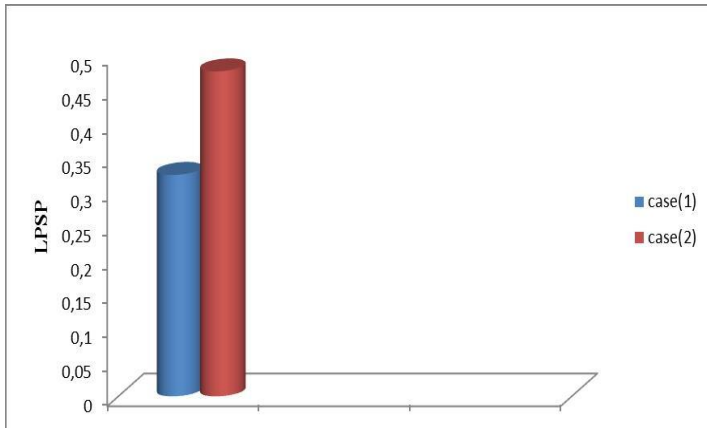


Figure 15: A comparison of the main optimization factors (LPSP).  
Source: Authors, (2025).

Table 3 shows the optimal values obtained for three parameters that represent the objective function proposed in this study. Table 4 also gives the optimal number of each component type for the proposed HMS. In Case 1, the optimization method yields: 23 solar panels, 3 wind turbines, 10 batteries, 1 diesel generator, and 5 autonomy days.

In Case 2, we obtained 39 solar panels and 7 wind turbines, 11 batteries, 4 diesel generators, and 5 autonomy days. Table 5 gives the total energy generated over the course of a full year through all components of the proposed Microgrid system, where the energy production through solar energy is estimated at 269280 KW in Case 1 and 456602 KW in Case 2.

Table 3: Optimization results for COE , LPSP ,and Dummy excess using PSO

Cases studied	COE(\$/Kwh)	LPSP(%)	Dummy excess(%)
Case 1	0,15829	0,32510	0,55994
Case 2	0,42112	0,47711	0,02145

Source: Authors, (2025).

Table 4: Optimization results for the optimal number of system components using PSO.

Cases studied	N <sub>PV</sub>	N <sub>wind</sub>	N <sub>Battery</sub>	N <sub>diesel</sub>	N <sub>AD</sub>
Case 1	23	3	10	1	5
Case 2	39	7	11	4	5

Source: Authors, (2025).

Table 5: The annual generated power of each component using PSO.

Cases studied	PV(KW)	Wind(KW)	Battery(KW)	Diesel(KW)
Case 1	2.6928e+05	4.4340e+03	1.4042e+05	1.1931e+04
Case 2	4.5660e+05	1.0346e+04	6.4405e+05	7.7986e+04

Source: Authors, (2025).

Figure 16 gives the percentage of energy provided by the solar panels, wind turbines, batteries and diesel generator for the proposed hybrid system in the two cases studied during a full year. As can be seen from these results, the Biskra region is a region very rich in renewable energy sources, especially solar energy. We have found that, in the first studied case, the percentage of solar energy reached 67% of the total energy, followed by batteries with 29%, diesel generator 3%, and wind energy 1%. In Case 2, the results indicate that the percentage of solar energy reached 64%, the percentage of battery reached 33%, diesel generator 2%, and wind turbines 1%.

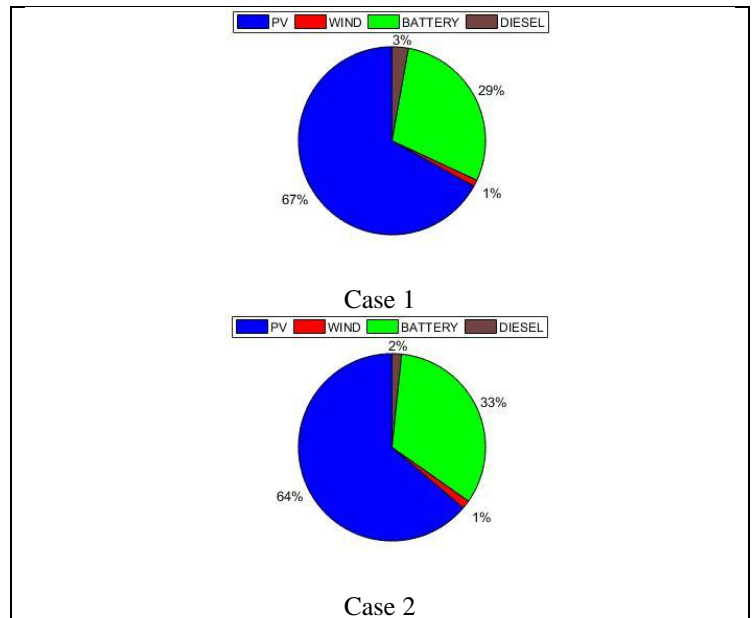


Figure 16: Percentage of annual energy contribution for all Microgrid's components system using PSO.  
Source: Authors, (2025).

Figure 17, illustrates the energy generated in the microgrid system over a 72-hour period. The data show that during daylight hours, when the energy generated from renewable resources such as solar and wind exceeds the load demand, the hybrid system stores the excess energy in batteries until they are fully charged.

Once the batteries are at capacity, the system dissipates the surplus energy. Conversely, when renewable resources cannot meet the load demand, the stored energy in the batteries is utilized, resulting in a decrease in stored energy. If the energy in the batteries falls to the minimum allowable level, the diesel generator is activated to supplement the supply.

This behavior aligns with the findings reported by Abd El-Sattar et al. [54] in 2021, where similar storage and dissipation patterns were observed in HMS. Furthermore, the efficiency of energy storage and the role of the diesel generator in maintaining system reliability were consistent with the results of [55] in 2024, which highlighted the critical balance between renewable energy generation, storage capacity, and backup systems.

Our results underscore the importance of optimizing battery capacity and integrating robust backup solutions to ensure continuous power supply, particularly in scenarios where renewable energy generation is variable. This comprehensive analysis provides valuable insights into the operational dynamics of hybrid systems, contributing to the broader understanding of renewable energy integration and its practical implications for microgrid stability and efficiency.

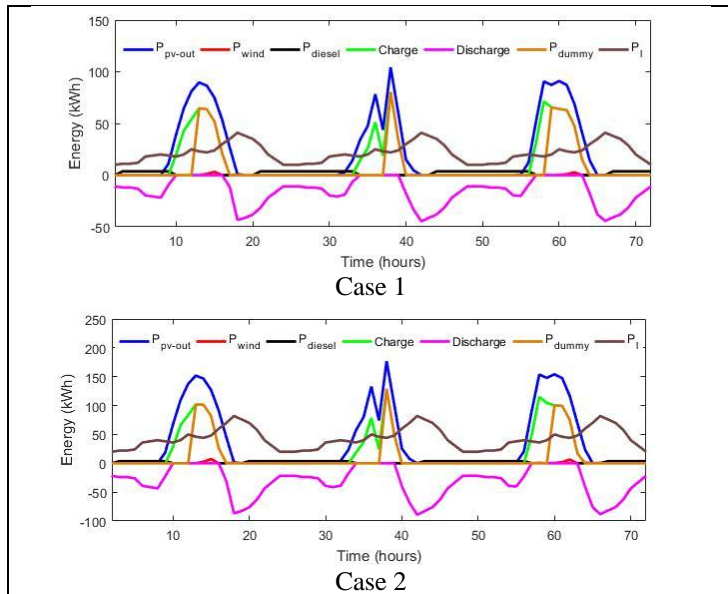


Figure 17: Microgrid system's power over 72 hours using PSO  
Source: Authors, (2025).

## VII. CONCLUSIONS

In this paper, we have presented a study on the determination of the optimal size of the components of a microgrid system, consisting of solar panels, wind turbines, batteries, and diesel generators. In this study, it was suggested that two scenarios should be considered for a Microgrid system, one consisting of 10 houses, and the other one comprising 20 houses. We developed a new model of the particle swarm optimization algorithm and proposed an innovative way of using the weighted sum multi objective function by combining together the lowest price of electricity, more reliability, and less waste of dummy load energy.

We have chosen the agricultural and pastoral region of Biskra for our study, and we have reached the optimal size that enables us to guarantee the largest production of electricity at the lowest possible price and with greater reliability. All the results of the simulations that we have obtained confirmed that PSO is an effective optimization technique due to its ability to reach the

optimal solution simply and with high efficiency. Also, the adopted multi-objective function was shown to alleviate the problem of sizing through the integration of the cost of electricity (COE), Loss of Power Supply Probability (LPSP), and Dummy excess into one objective function.

Furthermore, all the results obtained prove that the Biskra is rich in renewable energy sources, particularly solar energy. Therefore, this study can be seen as a promising incentive for prospective investors and decision makers to invest in this region and establish stations to supply all isolated areas and government facilities such as hospitals and schools with electrical energy.

## VIII. AUTHOR'S CONTRIBUTION

**Conceptualization:** Badis Bacha.

**Methodology:** Badis Bacha and Abir Betka.

**Investigation:** Badis Bacha and Hatem Ghodbane.

**Discussion of results:** Badis Bacha, Abir Betka and Aymene Bacha.

**Writing – Original Draft:** Badis Bacha.

**Writing – Review and Editing:** Madina Hamiane and Nadjiba Terki.

**Resources:** Badis Bacha.

**Supervision:** Hatem Ghodbane and Nadjiba Terki.

**Approval of the final text:** Badis Bacha, Madina Hamiane and Omar Charrouf.

## VX. REFERENCES

- [1] Zhou, W., H. Yang, and Z.J.R.E. Fang, Battery behavior prediction and battery working states analysis of a hybrid solar–wind power generation system. *Renewable Energy*, 2008. 33(6): p. 1413-1423.
- [2] Goedecke, M., S. Therdthianwong, and S.H.J.E.p. Gheewala, Life cycle cost analysis of alternative vehicles and fuels in Thailand. *Energy policy*, 2007. 35(6): p. 3236-3246.
- [3] Straatman, P.J. and W.G.J.S.e. Van Sark, A new hybrid ocean thermal energy conversion–Offshore solar pond (OTEC–OSP) design: A cost optimization approach. *Solar energy*, 2008. 82(6): p. 520-527.
- [4] Shaahid, S., M.J.R. Elhadidy, and s.e. reviews, Technical and economic assessment of grid-independent hybrid photovoltaic–diesel–battery power systems for commercial loads in desert environments. *Renewable and sustainable energy reviews*, 2007. 11(8): p. 1794-1810.
- [5] Zhou, W., et al., Current status of research on optimum sizing of stand-alone hybrid solar–wind power generation systems. *Applied energy*, 2010. 87(2): p. 380-389.
- [6] Farraj, W., A. Awad, and A. Qaroush. Optimal Sizing of Hybrid Microgrids. in 2020 6th IEEE International Energy Conference (ENERGYCon). 2020. IEEE.
- [7] Shaffer, E., P. Roegge, and T.J.U.A.R.L. Zheleva, Adelphi, MD, Tech Report ARL-TR-, Advanced microgrid concepts and technologies workshop. US Army Research Laboratory, Adelphi, MD, Tech Report ARL-TR-6407, 2013.
- [8] Choi, S., et al. A microgrid energy management system for inducing optimal demand response. in 2011 IEEE international conference on smart grid communications (SmartGridComm). 2011. IEEE.
- [9] Logenthiran, T., et al. Optimal sizing of distributed energy resources for integrated microgrids using evolutionary strategy. in 2012 IEEE Congress on Evolutionary Computation. 2012. IEEE.
- [10] McPherson, M., et al., Planning for variable renewable energy and electric vehicle integration under varying degrees of decentralization: A case study in Lusaka, Zambia. *Energy*, 2018. 151: p. 332-346.
- [11] Chauhan, A., R.J.R. Saini, and S.E. Reviews, A review on Integrated Renewable Energy System based power generation for stand-alone applications: Configurations, storage options, sizing methodologies and control. *Renewable and Sustainable Energy Reviews*, 2014. 38: p. 99-120.

- [12] Ammari, C., et al., Sizing, optimization, control and energy management of hybrid renewable energy system—A review. *Energy and Built*, 2022. 3(4): p. 399-411.
- [13] Upadhyay, S., M.J.R. Sharma, and S.E. Reviews, A review on configurations, control and sizing methodologies of hybrid energy systems. *Renewable and Sustainable Energy Reviews*, 2014. 38: p. 47-63.
- [14] Starke, A.R., et al., Multi-objective optimization of hybrid CSP+ PV system using genetic algorithm. *Energy*, 2018. 147: p. 490-503.
- [15] Kamjoo, A., et al., Multi-objective design under uncertainties of hybrid renewable energy system using NSGA-II and chance constrained programming. *International journal of electrical power & energy systems*, 2016. 74: p. 187-194.
- [16] Ramli, M.A., H. Boucekara, and A.S.J.R.e. Alghamdi, Optimal sizing of PV/wind/diesel hybrid microgrid system using multi-objective self-adaptive differential evolution algorithm. *Renewable energy*, 2018. 121: p. 400-411.
- [17] Askarzadeh, A. and L.J.S.e. dos Santos Coelho, A novel framework for optimization of a grid independent hybrid renewable energy system: A case study of Iran. *Solar energy*, 2015. 112: p. 383-396.
- [18] Fathy, A.J.R.e., A reliable methodology based on mine blast optimization algorithm for optimal sizing of hybrid PV-wind-FC system for remote area in Egypt. *Renewable energy*, 2016. 95: p. 367-380.
- [19] Suhane, P., et al., Sizing and performance analysis of standalone wind-photovoltaic based hybrid energy system using ant colony optimisation. *IET Renewable Power Generation*, 2016. 10(7): p. 964-972.
- [20] Shi, B., W. Wu, and L.J.J.o.t.T.I.o.C.E. Yan, Size optimization of stand-alone PV/wind/diesel hybrid power generation systems. *Journal of the Taiwan Institute of Chemical Engineers*, 2017. 73: p. 93-101.
- [21] Gupta, R., et al., BBO-based small autonomous hybrid power system optimization incorporating wind speed and solar radiation forecasting. *Renewable and sustainable energy reviews*, 2015. 41: p. 1366-1375.
- [22] Shi, Z., R. Wang, and T.J.S.e. Zhang, Multi-objective optimal design of hybrid renewable energy systems using preference-inspired coevolutionary approach. *Solar energy*, 2015. 118: p. 96-106.
- [23] Sanajaoba, S. and E.J.R.e. Fernandez, Maiden application of Cuckoo Search algorithm for optimal sizing of a remote hybrid renewable energy System. *Renewable energy*, 2016. 96: p. 1-10.
- [24] Maleki, A. and A.J.S.E. Askarzadeh, Artificial bee swarm optimization for optimum sizing of a stand-alone PV/WT/FC hybrid system considering LPSP concept. *Solar Energy*, 2014. 107: p. 227-235.
- [25] Zhao, J. and X.J.S.C. Yuan, Multi-objective optimization of stand-alone hybrid PV-wind-diesel-battery system using improved fruit fly optimization algorithm. *Soft Computing*, 2016. 20: p. 2841-2853.
- [26] Sánchez, V., J.M. Ramirez, and G. Arriaga, Optimal sizing of a hybrid renewable system. in 2010 IEEE international conference on industrial technology. 2010. IEEE.
- [27] Kaviani, A.K., G. Riahy, and S.M.J.R.e. Kouhsari, Optimal design of a reliable hydrogen-based stand-alone wind/PV generating system, considering component outages. *Renewable energy*, 2009. 34(11): p. 2380-2390.
- [28] Khare, V., S. Nema, and P.J.I.J.o.S.E. Baredar, Optimisation of the hybrid renewable energy system by HOMER, PSO and CPSO for the study area. *International Journal of Sustainable Energy*, 2017. 36(4): p. 326-343.
- [29] Sharafi, M. and T.Y.J.R.e. ELMekkawy, Multi-objective optimal design of hybrid renewable energy systems using PSO-simulation based approach. *Renewable energy*, 2014. 68: p. 67-79.
- [30] Parsopoulos, K.E. and M.N. Vrahatis, Particle swarm optimization method in multiobjective problems. in *Proceedings of the 2002 ACM symposium on Applied computing*. 2002.
- [31] Coello, C.A.C., *Evolutionary algorithms for solving multi-objective problems*. 2007: Springer.
- [32] Ocloń, P., et al., Multiobjective optimization of underground power cable systems. *Energy*, 2021. 215: p. 119089.
- [33] Marler, R.T., J.S.J.S. Arora, and m. optimization, The weighted sum method for multi-objective optimization: new insights. *Structural and multidisciplinary optimization*, 2010. 41: p. 853-862.
- [34] Daud, A.-K. and M.S.J.R.e. Ismail, Design of isolated hybrid systems minimizing costs and pollutant emissions. *Renewable energy*, 2012. 44: p. 215-224.
- [35] Akter, H., et al., Optimal sizing and performance analysis of hybrid microgrid for remote island of developing country: Effect of sustainable parameters, benefits and installation barriers. *Franklin Open*, 2024: p. 100074.
- [36] Porté-Agel, F., M. Bastankhah, and S.J.B.-I.m. Shamsoddin, Wind-turbine and wind-farm flows: A review. *Boundary-layer meteorology*, 2020. 174(1): p. 1-59.
- [37] Shin, J., J.H. Lee, and M.J.J.A.e. Realff, Operational planning and optimal sizing of microgrid considering multi-scale wind uncertainty. *Applied energy*, 2017. 195: p. 616-633.
- [38] Abeg, A.I., et al., Capacity and operation optimization of hybrid microgrid for economic zone using a novel meta-heuristic algorithm. *Journal of Energy Storage*, 2024. 94: p. 112314.
- [39] Bakar, A.L., C.W. Tan, and K.Y.J.S.E. Lau, Optimal sizing of an autonomous photovoltaic/wind/battery/diesel generator microgrid using grasshopper optimization algorithm. *Solar Energy*, 2019. 188: p. 685-696.
- [40] Shang, C., et al., An improved particle swarm optimisation algorithm applied to battery sizing for stand-alone hybrid power systems. *International Journal of Electrical Power & Energy Systems*, 2016. 74: p. 104-117.
- [41] Deshmukh, M.K., S.S.J.R. Deshmukh, and s.e. reviews, Modeling of hybrid renewable energy systems. *Renewable and sustainable energy reviews*, 2008. 12(1): p. 235-249.
- [42] Mohamed, M.A., et al., A novel framework-based cuckoo search algorithm for sizing and optimization of grid-independent hybrid renewable energy systems. *International journal of green energy*, 2019. 16(1): p. 86-100.
- [43] Luna-Rubio, R., et al., Optimal sizing of renewable hybrids energy systems: A review of methodologies. *Solar energy*, 2012. 86(4): p. 1077-1088.
- [44] Dursun, B.J.R. and S.E. Reviews, Determination of the optimum hybrid renewable power generating systems for Kavakli campus of Kırklareli University, Turkey. *Renewable and Sustainable Energy Reviews*, 2012. 16(8): p. 6183-6190.
- [45] Hosseini, S.J.a.-D., M. Moazzami, and H.J.M.J.o.E.E. Shahinzadeh, Optimal sizing of an isolated hybrid wind/PV/battery system with considering loss of power supply probability. *Majlesi Journal of Electrical Engineering*, 2017. 11(3): p. 63-69.
- [46] Bacha, B., et al., Optimal sizing of a hybrid microgrid system using solar, wind, diesel, and battery energy storage to alleviate energy poverty in a rural area of Biskra, Algeria. *Journal of Energy Storage*, 2024. 84: p. 110651.
- [47] Kennedy, J. and R. Eberhart, Particle swarm optimization. in *Proceedings of ICNN'95-international conference on neural networks*. 1995. IEEE.
- [48] Chao, W., et al., Swarm intelligence: A survey of model classification and applications. *Chinese Journal of Aeronautics*, 2024.
- [49] Bansal, J.C.J.E. and s.i. algorithms, Particle swarm optimization. *Evolutionary and swarm intelligence algorithms*, 2019: p. 11-23.
- [50] Yang, X.-S., *Engineering optimization: an introduction with metaheuristic applications*. 2010: John Wiley & Sons.
- [51] Atam, E., et al., A hybrid green energy-based system with a multi-objective optimization approach for optimal frost prevention in horticulture. *Journal of Cleaner Production*, 2021. 329: p. 129563.
- [52] Wang, Z., Y. Pei, and J.J.A.S. Li, A survey on search strategy of evolutionary multi-objective optimization algorithms. *Applied Sciences*, 2023. 13(7): p. 4643.

- [53] Zhang, H., et al., Modeling a hydrogen-based sustainable multi-carrier energy system using a multi-objective optimization considering embedded joint chance constraints. *Energy*, 2023. 278: p. 127643.
- [54] Abd El-Sattar, H., et al., Optimal design of stand-alone hybrid PV/wind/biomass/battery energy storage system in Abu-Monqar, Egypt. *Journal of Energy Storage*, 2021. 44: p. 103336.
- [55] Abdelsattar, M., et al., Optimal sizing of a proposed stand-alone hybrid energy system in a remote region of southwest Egypt applying different meta-heuristic algorithms. *Neural Computing and Applications*, 2024: p. 1-19.



## RESEARCH ARTICLE

## OPEN ACCESS

# PERFORMANCE ENHANCEMENT OF WIND ENERGY CONVERSION SYSTEMS USING PMSG WITH BACKSTEPPING AND ANN-BASED MPPT CONTROL

Wassila Hattab<sup>1</sup>, Abdelhamid Benakcha<sup>2</sup>, Seddik Tabet<sup>3</sup>, Amira Slimani<sup>4</sup>

<sup>1,2,3,4</sup> dept. Electrical Engineering-LGEB Lab, Biskra University Biskra, Algeria

<sup>1</sup><http://orcid.org/0009-0004-7004-5092> , <sup>2</sup><http://orcid.org/0000-0003-4462-7676> , <sup>3</sup><http://orcid.org/0000-0003-4835-2067> ,

<sup>4</sup><http://orcid.org/0009-0009-3259-5743> 

Email: [wassila.hattab@univ-biskra.dz](mailto:wassila.hattab@univ-biskra.dz), [abdelhamid.benakcha@univ-biskra.dz](mailto:abdelhamid.benakcha@univ-biskra.dz), [seddik.thabet@univ-biskra.dz](mailto:seddik.thabet@univ-biskra.dz), [amira.slimani@univ-biskra.dz](mailto:amira.slimani@univ-biskra.dz)

## ARTICLE INFO

*Article History*

Received: December 16, 2024

Revised: January 27, 2025

Accepted: February 15, 2025

Published: March 31, 2025

*Keywords:*

WECS,  
PMSG,  
Adaptive Backstepping control,  
MPPT,  
Neural network controller.

## ABSTRACT

This paper investigates the performance enhancement of wind energy conversion systems (WECS) using a Permanent Magnet Synchronous Generator (PMSG) specifically designed for standalone, fixed-pitch, variable-speed wind turbines. The study focuses on controlling the PMSG using Backstepping control which enables Maximum Power Point Tracking (MPPT) using the Tip Speed Ratio (TSR) method. Initially, a Proportional-Integral (PI) controller was implemented for regulating the generator speed. However, this approach encountered significant limitations, particularly in managing speed overshoot and responsiveness under fluctuating wind conditions. To address these issues, a neural network controller was introduced as a replacement for the conventional PI controller. This neural network controller provides an adaptive control mechanism capable of dynamically adjusting to change, thereby eliminating overshoot and greatly enhancing response speed and overall system stability. This work provides a reliable and efficient control solution where the proposed control strategy was rigorously evaluated through numerical simulations in Matlab/Simulink, which confirmed its ability to stabilize the system and achieving both steady-state and dynamic optimization of wind energy conversion systems.



Copyright ©2025 by authors and Galileo Institute of Technology and Education of the Amazon (ITEGAM). This work is licensed under the Creative Commons Attribution International License (CC BY 4.0).

## I. INTRODUCTION

With the rising global focus on sustainable and environmentally friendly electricity generation, many countries have increasingly turned to renewable energy sources [1]. Currently, approximately 38% of global electricity production is derived from renewable sources, marking a shift aimed at drastically reducing carbon emissions [2], [3]. Among the various renewable technologies, wind energy stands out as one of the promising solutions [4], [5]. According to the latest data from the International Renewable Energy Agency, about 27% of renewable energy-generated electricity, or 825 GW, comes from wind energy, a figure projected to reach 1756 GW by 2030 [6]. As wind energy systems evolve, variable-speed wind turbine (VSWT) technology has gained popularity over fixed-speed systems due to its efficiency and flexibility in adapting to change wind conditions [7]. In

particular, wind turbines based on (PMSM) have proven highly effective and dependable for transforming wind energy into electrical power, positioning PMSGs as essential components in modern wind energy systems [8], [9]. A variable-speed PMSG-based (WECS) typically consists of a wind turbine connected directly to a PMSG, accompanied by a full-scale power converter with load supply [10]. Such standalone systems are particularly valuable in remote areas lacking grid access or where connecting to the grid is costly. To ensure reliable energy supply, these systems often include storage battery to store surplus energy from the wind, thus meeting demand during low-wind periods [11].

To maximize energy capture, WECSs often employ a Maximum Power Point Tracking control algorithm. The MPPT's role is crucial as it dynamically adjusts the rotor speed to maintain optimal power generation, even as wind conditions vary. Traditionally, this regulation is achieved using a Proportional-

Integral (PI) controller. Although effective, PI controllers face challenges related to parameter tuning and are highly sensitive to external conditions, particularly in nonlinear or fluctuating environments. These limitations often result in suboptimal performance when managing the complex, variable conditions inherent in wind energy systems [12], [13]. To overcome these challenges, the study introduces an Artificial Neural Network (ANN)-based MPPT controller as an alternative. ANNs offer adaptive and learning capabilities that enhance the system's ability to achieve more efficient tracking of MPP, especially under rapid fluctuations in wind speed. Unlike traditional PI controllers, ANN-based controllers adjust in real-time based on prior data, allowing them to handle nonlinear dynamics more effectively. This adaptability is particularly advantageous for wind systems, where environmental conditions can shift quickly, making static control less effective [14], [15].

Additionally, Backstepping control is applied to the rectifier within the system, enhancing stability and response to variable wind conditions. Backstepping is a nonlinear control technique that improves system stability by ensuring that control

actions progressively follow desired states while satisfying stability conditions at each step. It is based on Lyapunov's stability theory, which is critical for guaranteeing that the system remains stable in the face of fluctuations. Backstepping control divides the control design into smaller steps, allowing for more precise and resilient adjustments to the rectifier's output, which directly impacts the overall system's performance [16], [17].

By combining the ANN-based MPPT controller with an Adaptive Backstepping control strategy for the rectifier, this study establishes a comprehensive, robust control framework. This combination not only ensures optimized power extraction but also provides enhanced system flexibility and adaptability in response to vary wind speeds. Such resilience is essential for standalone systems, especially in remote areas where consistent energy output is crucial. The key contributions of this study are outlined as follows:

1. **Enhanced MPPT Control:** Implementation of an ANN-based MPPT controller that improves response time and adaptability in variable wind speeds.

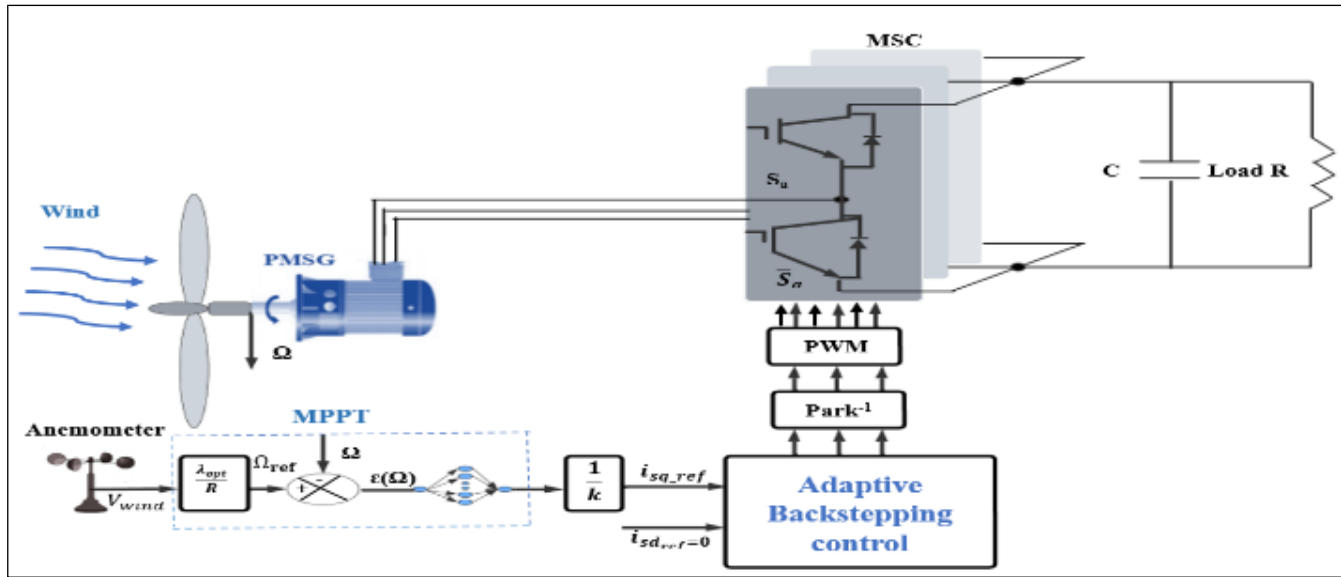


Figure 1: ANN-Backstepping schematic diagram for a PMSG-based wind energy conversion system.

Source: Authors, (2025).

2. **Advanced Backstepping Control:** Utilize a Backstepping control approach founded on Lyapunov's stability theory to optimize the system's overall performance and adaptability to external variations.

3. **Design and Parameterization:** Configuration for a 3kW wind turbine system, providing practical insights for implementing PMSG-based WECS.

4. **Comparative Evaluation:** Analysis of PI and ANN controllers, showing ANN's superiority in handling nonlinear conditions and variable parameters for optimal power extraction.

This article is structured into five sections:

- **Section 1** introduces the study.
- **Section 2** outlines the system configuration, including the aerodynamic model of the wind turbine, the modeling of the permanent magnet synchronous generator, and the MPPT approach.
- **Section 3** delves into the Backstepping control method, providing a detailed analysis of the control laws based on Lyapunov stability theory.

- **Section 4** synthesizes the speed regulator.

- **Section 5** presents the simulation results.

The article concludes with a summary of the main findings and overall conclusions.

## II. MODELING AND DESCRIPTION OF THE SYSTEM

### II.1 THE SYSTEM CONFIGURATION DESCRIPTION

A WECS typically consists of both electrical and mechanical components. As illustrated in Figure 1, the system analyzed in this study includes a turbine, a (PMSG), a converter (rectifier), and a resistive load R. The turbine converts wind energy into mechanical energy, which is subsequently transformed into electrical energy by the generator. This process involves a machine-side converter (MSC) linked through a DC-link bus. In this study, various control strategies have been explored, including Maximum Power Point Tracking (MPPT) using PI and ANN regulators, as well as Backstepping Control. The subsequent sections detail the mathematical modeling of each component.

### II.1.1 WIND TURBINE AERODYNAMIC MODELING

This section aims to model the aerodynamic aspects of the (WECS) with a simplified approach, covering both the wind profile and turbine models. The turbine generates mechanical energy by converting the wind's kinetic energy into usable power [18]. The power available in the wind is described by Equation (1):

$$P_{wind} = \frac{1}{2} \cdot \rho \cdot S \cdot V_{wind}^3 \quad (1)$$

Due to certain physical limitations [19], the wind turbine can only capture a portion of the available wind energy, as represented by the following equation:

$$P_{mec} = C_p(\beta, \lambda) \cdot P_{wind} = \frac{1}{2} \cdot \rho \cdot S \cdot C_p(\beta, \lambda) \cdot V_{wind}^3 \quad (2)$$

Here,  $\rho$ ,  $\beta$ ,  $S$ , and  $V_{wind}$  represent the air density, pitch angle, blade area, and wind speed, respectively. The power coefficient  $C_p$ , also referred to as the Betz limit, indicates the efficiency of the wind turbine blades in converting the wind's kinetic energy into mechanical energy. This coefficient depends on both the pitch angle ( $\beta$ ) and the tip speed ratio ( $\lambda$ ). Theoretical studies indicate that the maximum achievable power coefficient is 0.593. However, due to practical limitations—such as blade number, shape, weight, and stiffness—this theoretical maximum cannot be fully achieved. Typically, well-designed turbines achieve power coefficients ranging between 0.4 and 0.5.

The relationship between the aerodynamic power coefficient ( $C_p$ ) and the tip speed ratio ( $\lambda$ ) for varying pitch angles ( $\beta$ ) is depicted in Figure 2(a). In this study, the wind turbine achieves maximum power extraction with an efficiency of 0.4535. This optimal performance occurs when the pitch angle ( $\beta$ ) is set to zero degrees, and the tip speed ratio ( $\lambda$ ) reaches its ideal value of 8.02. The power coefficient ( $C_p$ ) is expressed by a specific non-linear function as follows:

$$\begin{cases} C_p = 0.5176 \left( \frac{116}{\lambda i} - 0.4\beta - 5 \right) e^{-\frac{21}{\lambda i}} + 0.0068 \cdot \lambda \\ \frac{1}{\lambda i} = \frac{1}{\lambda + 0.08 \cdot \beta} - \frac{0.035}{1 + \beta^3} \\ \lambda = \frac{R \cdot \Omega}{V_{wind}} \end{cases} \quad (3)$$

The mechanical torque is defined as the ratio of the power supplied to the Permanent Magnet Synchronous Generator (PMSG) to the rotor's mechanical speed. Using Equations (2) and (3), the turbine torque can be calculated using the following formula:

$$T_{mec} = \frac{P_{mec}}{\Omega} = \frac{1}{2} \cdot \frac{\rho \cdot S \cdot R^3 \cdot C_p(\beta, \lambda) \cdot \Omega^3}{\lambda^3} \quad (4)$$

### II.1.2 PERMANENT MAGNET SYNCHRONOUS GENERATOR MODELING

The Permanent Magnet Synchronous Generator (PMSG) plays a crucial role in (WECS) as the primary component responsible for transforming mechanical energy into electrical energy. With power ratings reaching several megawatts, the PMSG is widely preferred due to its significant advantages over traditional synchronous machines [20]. In this study, the dynamic equations describing the operation of the PMSG are formulated in the synchronous rotating reference frame (d-q) as follows:

$$\begin{cases} V_{sd} = R_s \cdot i_{sd} + \frac{d\psi_d}{dt} - \omega_r \cdot \psi_q \\ V_{sq} = R_s \cdot i_{sq} + \frac{d\psi_q}{dt} + \omega_r \cdot \psi_d \end{cases} \quad (5)$$

$$\begin{cases} \psi_d = L_d \cdot i_{sd} + \Phi_f \\ \psi_q = L_q \cdot i_{sq} \end{cases} \quad (6)$$

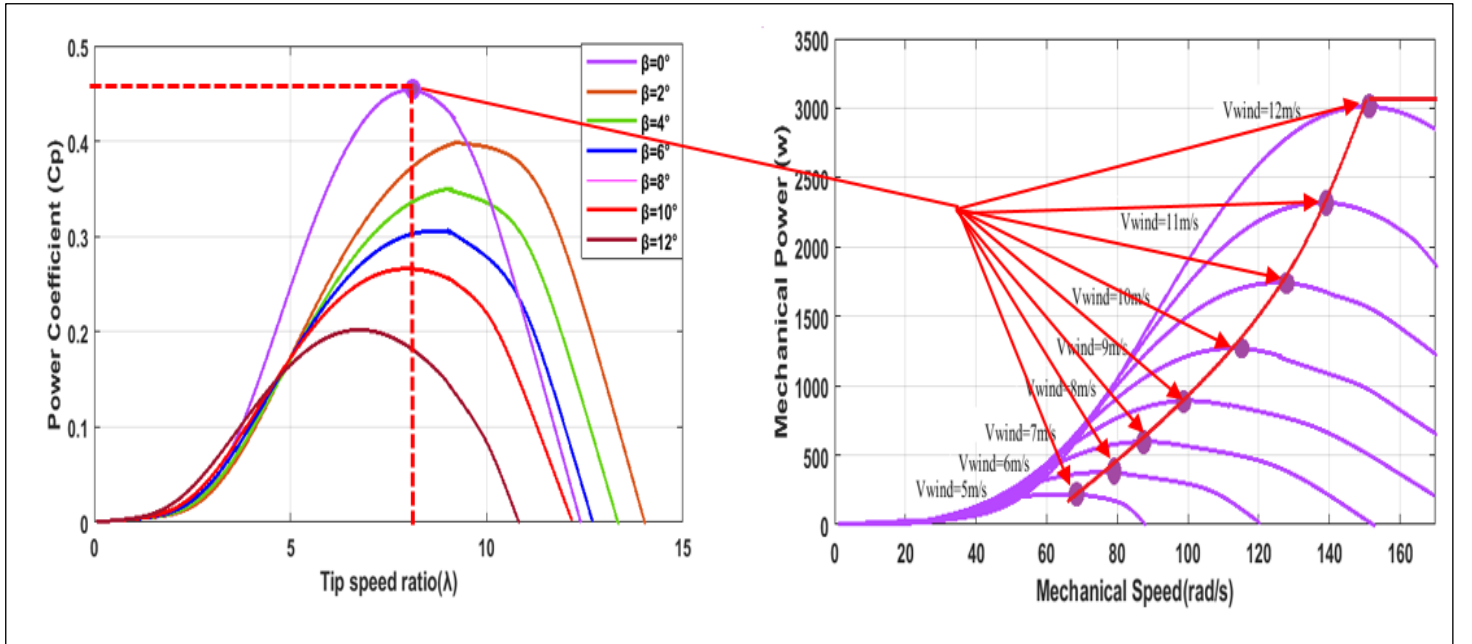


Figure 2: Wind Turbine Characteristics: (a)  $C_p$  curve showing variations with pitch angle  $\beta$ , (b) Power and mechanical speed characteristics of the wind turbine at different wind speeds.

Source: Authors, (2025).





### STEP 1: MECHANICAL SPEED CONTROLLER DESIGN:

The speed tracking error can be expressed using the following equation:

$$e_\Omega = \Omega_{ref} - \Omega \quad (10)$$

The derivative is expressed as:

$$\begin{aligned} \dot{e}_\Omega &= \dot{\Omega}_{ref} - \dot{\Omega} \\ &= \dot{\Omega}_{ref} - \frac{1}{J} \left[ T_{tur} - \frac{3p}{2} \left( (L_d - L_q) i_{sd} \cdot i_{sq} + i_{sq} \cdot \Phi_f \right) - f_c \cdot \Omega \right] \end{aligned} \quad (11)$$

The initial step ensures the tracking of the reference speed, thereby eliminating the speed error. To achieve this, Lyapunov's function is utilized:

$$V_1 = \frac{1}{2} e_\Omega^2 \quad (12)$$

The derivative of Lyapunov's function is expressed as follows:

$$\begin{aligned} \dot{V}_1 &= e_\Omega \cdot \dot{e}_\Omega \\ &= -k_\Omega e_\Omega^2 + \frac{e_\Omega}{J} \left( -T_{tur} + f_c \Omega + k_\Omega \cdot J \cdot e_\Omega + \frac{3p}{2} \cdot i_{sq} \cdot \Phi_f \right) + \frac{3}{2J} p (L_d - L_q) i_{sd} \cdot i_{sq} \cdot e_\Omega \end{aligned} \quad (13)$$

To guarantee the stability of the first subsystem, it is essential to select  $\dot{V}_1$  as negative. This selection leads to the appropriate determination of the stator currents  $i_{sd}$  and  $i_{sq}$ .

$$\begin{cases} i_{sd\_ref} = 0 \\ i_{sq\_ref} = \frac{2}{3 \cdot p \cdot \Phi_f} (T_{tur} - f_c \cdot \Omega - k_\Omega \cdot J \cdot e_\Omega) \end{cases} \quad (14)$$

The virtual references  $i_{sd\_ref}$  and  $i_{sq\_ref}$  are defined for the second step. Substituting  $i_{sd\_ref}$ ,  $i_{sq\_ref}$  and  $\dot{\Omega}_{ref} = 0$  into Equation (13) yields:

$$\dot{V}_1 = -k_\Omega \cdot e_\Omega^2 \leq 0 \quad (15)$$

The system represented by Equation (15) will remain stable if  $k_\Omega$  is chosen as a positive constant.

### STEP 2: DESIGNING THE STATOR CURRENT CONTROLLER:

In the second step of this algorithm, the control voltages  $V_{sd\_ref}$  and  $V_{sq\_ref}$ , which are determined based on the system's virtual inputs, specifically the stator currents ( $i_{sd}$ ,  $i_{sq}$ ). The errors in the stator currents are defined by the following equations:

$$e_d = i_{sd\_ref} - i_{sd} \quad (16)$$

$$e_q = i_{sq\_ref} - i_{sq} \quad (17)$$

Using Equations (16) and (17), the dynamic behavior of the current errors  $e_d$  and  $e_q$  can be expressed as:

$$\begin{aligned} \dot{e}_d &= \dot{i}_{sd\_ref} - \dot{i}_{sd} = 0 - \dot{i}_{sd} \\ &= \frac{1}{L_d} (R_s \cdot i_{sd} - p \cdot \Omega \cdot L_q \cdot i_{sq} - V_{sd}) \end{aligned} \quad (18)$$

$$\begin{aligned} \dot{e}_q &= \dot{i}_{sq\_ref} - \dot{i}_{sq} = \frac{2}{3 \cdot p \cdot \Phi_f} (-f_c \Omega - k_\Omega \cdot J \cdot e_\Omega) \\ &+ \frac{1}{L_q} (R_s \cdot i_{sq} + p \cdot L_d \cdot \Omega \cdot i_{sd} + p \cdot \Omega \cdot \Phi_f - V_{sq}) \end{aligned} \quad (19)$$

With:

$$\dot{e}_\Omega = \frac{1}{J} \left[ -k_\Omega \cdot J \cdot e_\Omega - \frac{3p}{2} \Phi_f \cdot e_q - \frac{3p}{2} \cdot (L_d - L_q) i_{sd} \cdot i_{sq} \right] \quad (20)$$

The expression for  $\dot{e}_q$  is then given as:

$$\begin{aligned} \dot{e}_q &= \frac{2}{3 \cdot p \cdot \Phi_f} \times \\ &\left( (k_\Omega \cdot J - f_c) \left[ T_{tur} - f_c \Omega - \frac{3p}{2} \cdot (L_d - L_q) i_{sd} \cdot i_{sq} + i_{sq} \cdot \Phi_f \right] \right. \\ &\left. + \frac{1}{L_q} (R_s \cdot i_{sq} + p \cdot \Omega \cdot L_d \cdot i_{sd} + p \cdot \Omega \cdot \Phi_f - V_{sq}) \right) \end{aligned} \quad (21)$$

As the system grows more complex, incorporating three state variables, it becomes essential to choose a second Lyapunov function to calculate the stator voltage references. This function considers both the rotational speed error and the stator current errors:

$$V_2 = \frac{1}{2} (e_\Omega^2 + e_d^2 + e_q^2) \quad (22)$$

By applying Equations (18), (20), and (21), the derivative of the second Lyapunov function is obtained as:

$$\dot{V}_2 = (e_\Omega \cdot \dot{e}_\Omega + e_d \cdot \dot{e}_d + e_q \cdot \dot{e}_q) \quad (23)$$

$$\begin{aligned} \dot{V}_2 &= -k_\Omega \cdot e_\Omega^2 - k_d \cdot e_d^2 - k_q \cdot e_q^2 \\ &+ \frac{e_\Omega}{J} \left( -T_{tur} + f_c \Omega + k_\Omega \cdot J \cdot e_\Omega + \frac{3p}{2} \cdot i_{sq} \cdot \Phi_f \right) \\ &+ \frac{e_d}{L_d} (R_s \cdot i_{sd} - p \cdot \Omega \cdot L_q \cdot i_{sq} - V_{sd} + k_d \cdot L_d \cdot e_d) \\ &+ \frac{e_q}{L_q} \left[ \frac{2 \cdot L_q}{3 \cdot p \cdot J \cdot \Phi_f} \left( (k_\Omega \cdot J - f_c) \left[ T_{tur} - f_c \Omega - \frac{3p}{2} \cdot (L_d - L_q) i_{sd} \cdot i_{sq} + i_{sq} \cdot \Phi_f \right] \right) \right. \\ &\left. + R_s \cdot i_{sq} + p \cdot \Omega \cdot L_d \cdot i_{sd} + p \cdot \Omega \cdot \Phi_f - V_{sq} + k_q \cdot L_q \cdot e_q \right] \end{aligned} \quad (24)$$

Based on Lyapunov's theorem, the stability of the subsystem is guaranteed when the derivative of  $V_1$  to be negative. Therefore,  $k_d$  and  $k_q$  are assigned positive values, and the following voltages are utilized as reference voltages:

$$\begin{cases} V_{sd\_ref} = R_s \cdot i_{sd} - p \cdot \Omega \cdot L_q \cdot i_{sq} \\ \quad + k_q \cdot L_q \cdot e_q - \frac{3 \cdot p}{2 \cdot J} \cdot L_d (L_d - L_q) i_{sd} \cdot e_\Omega \\ V_{sq\_ref} = \frac{2 \cdot L_q}{3 \cdot p \cdot J \cdot \Phi_f} \left( (k_\Omega \cdot J - f_c) \left[ T_{tur} - f_c \Omega - \frac{3 \cdot p}{2} \cdot (L_d - L_q) i_{sd} \cdot i_{sq} + i_{sq} \cdot \Phi_f \right] \right) \\ \quad + R_s \cdot i_{sq} + p \cdot \Omega \cdot L_d \cdot i_{sd} + k_q \cdot L_q \cdot e_q - \frac{3}{2 \cdot J} p \cdot i_{sq} \cdot \Phi_f \cdot e_\Omega \end{cases} \quad (25)$$

## IV. SYNTHESIS OF THE SPEED REGULATOR

### IV.1 PROPORTIONAL-INTEGRAL (PI)

As shown in Figure 2, the MPPT control strategy has been integrated into the traditional Backstepping control approach. This method aims to enhance the performance of WECS by ensuring optimal wind power extraction at both low and high wind speeds. Moreover, it guarantees that the generator operates within a safe speed range to protect the system [27]. As previously discussed in

this study, the wind turbine achieves its peak power output when the power coefficient ( $C_p$ ) equals 0.4535. To maintain this level of efficiency, the turbine's rotational speed is continuously regulated through the use of a Proportional-Integral (PI) controller, as illustrated in Figure 5.

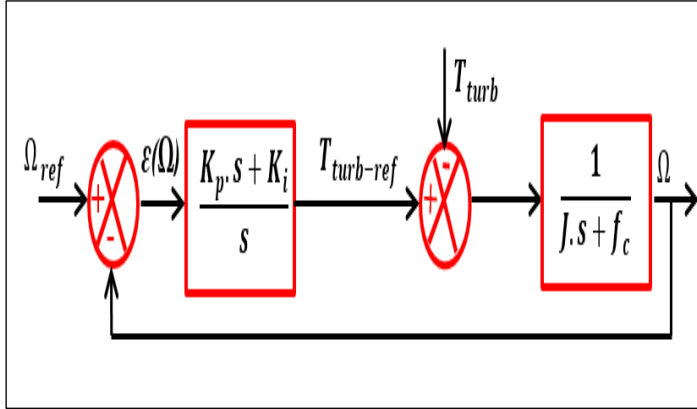


Figure 5: Closed-loop system with the PI.  
Source: Authors, (2025).

The design of the PI controller is as follows:

$$PI = \left( \frac{k_p s + k_i}{s} \right) \quad (26)$$

## IV.2 ARTIFICIAL NEURAL NETWORK (ANN)

To improve the system's performance across various wind conditions, the PI controller was substituted with a regulator based on an Artificial Neural Network (ANN).

An Artificial Neural Network (ANN) is a computational model inspired by the architecture and behavior of biological nervous systems. It imitates human cognitive capabilities, enabling machines to interpret and process information in a way similar to human thought patterns.

ANNs consist of interconnected neurons that are organized into layers: input, hidden, and output layers, where the data is received, processed, and transmitted [28]. These neurons work in parallel and are connected by adjustable numerical weights that are fine-tuned during the learning process [29]. The theoretical model of a basic neuron is represented by the following equation:

$$y_i^{ANN} = f(\sum_i^n w_i x_i + b) \quad (27)$$

The variables  $n$ ,  $y_i^{ANN}$ ,  $f$ ,  $x \{x_i, i=1,2,\dots,n\}$ ,  $w_i$  and  $b$  represent the number of neural network inputs, the output vector of the network, the activation function, the neural network input vector, the weight matrix, and the bias, respectively. Typically, the bias input is set to either +1 or -1, and the weight matrix is adjusted using the backpropagation method.

The neuron serves as the fundamental building block of artificial neural networks, encompassing summation and activation functions [30], as shown in figure 6.

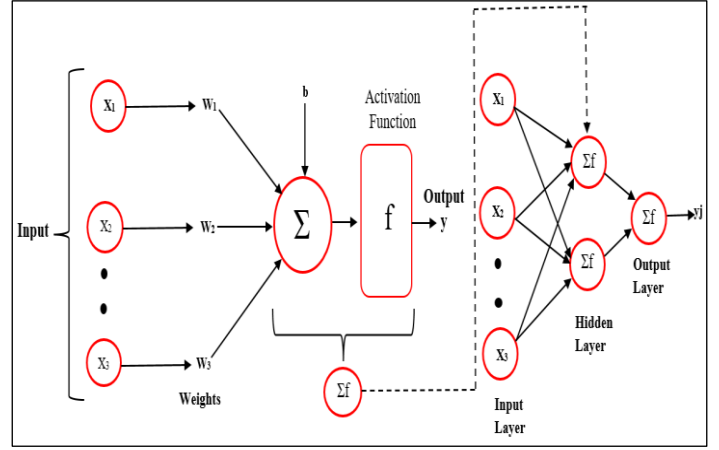


Figure 6: Structure of artificial neural network (ANN) model.  
Source: Authors, (2025).

### IV.2.1 DESIGNING THE ANN MODEL

The initial phase in constructing the Artificial Neural Network (ANN) requires gathering the necessary datasets. In this research, the datasets were derived from simulation outcomes, focusing on input and output values of the system's speed regulator (PI). Wind speed data was also incorporated during model development to ensure a comprehensive representation. The acquired data was randomly divided into three categories for training, validation, and testing purposes:

- **70%** of the data was allocated for training.
- **15%** was used for validation.
- **15%** was reserved for testing.

In the next phase, the ANN controller was implemented using MATLAB's user-friendly graphical interface, specifically the "nntool" feature available in MATLAB R2021a. It should be emphasized that the efficiency of the ANN controller is affected by various elements, including the number of neurons in the hidden layer, the type of activation function used, and the training algorithm selected [31].

### IV.2.2 PERFORMANCE EVALUATION

The evaluation of the trained ANN models was conducted using the Mean Squared Error (MSE), which measures the average squared difference between the predicted outputs of the network and the target values. A reduction in MSE during simulations indicates an ANN controller with improved accuracy, signifying a better alignment between the predictions of the model and the expected outputs. During training, the weight adjustments were performed iteratively using the Levenberg-Marquardt backpropagation algorithm. This iterative training process continued over multiple cycles until the error was reduced to an acceptable level. If the error failed to converge satisfactorily, modifications were applied to the ANN structure, such as increasing or decreasing the number of hidden neurons or changing the configuration of hidden layers [32].

As shown in Figure 7(a) and (b), the ANN-based speed controller achieved exceptional performance, with a minimal MSE of 0.00217 and 6.3528e-5, demonstrating a high degree of alignment between the output and target values. The optimal configurations of the proposed ANN models are summarized in Table 1.

Table 1: ANN architecture and training parameters.

ANN Parameter	Speed Controller (wind speed under Step Profil)	Speed Controller(wind speed under random Profil)
<b>Neuron network architecture</b>	Multi-Layer Perceptron Feedforward	Multi-Layer Perceptron Feedforward
Inputs/ Outputs Data	$\mathcal{E}(\Omega)/\text{Tem-ref}$	$\mathcal{E}(\Omega)/\text{Tem-ref}$
Number of neurons: Input layer	1	1
Hidden layer 1	25	5
Hidden layer 2	10	10
Hidden layer 3	-	5
Output layer	1	1
Hidden activation	Tansig	Tansig
Output activation	Purline	Purline
<b>Training function (Algorithm)</b>	Trainlm (Levenberg-Marquardt algorithm)	Trainlm (Levenberg-Marquardt algorithm)
Number of epochs	400	548
Learning rate	0.1	0.1
Training goal	0	0
<b>Performance function</b>	0.0021704	6.3528e-5

Source: Authors, (2025).

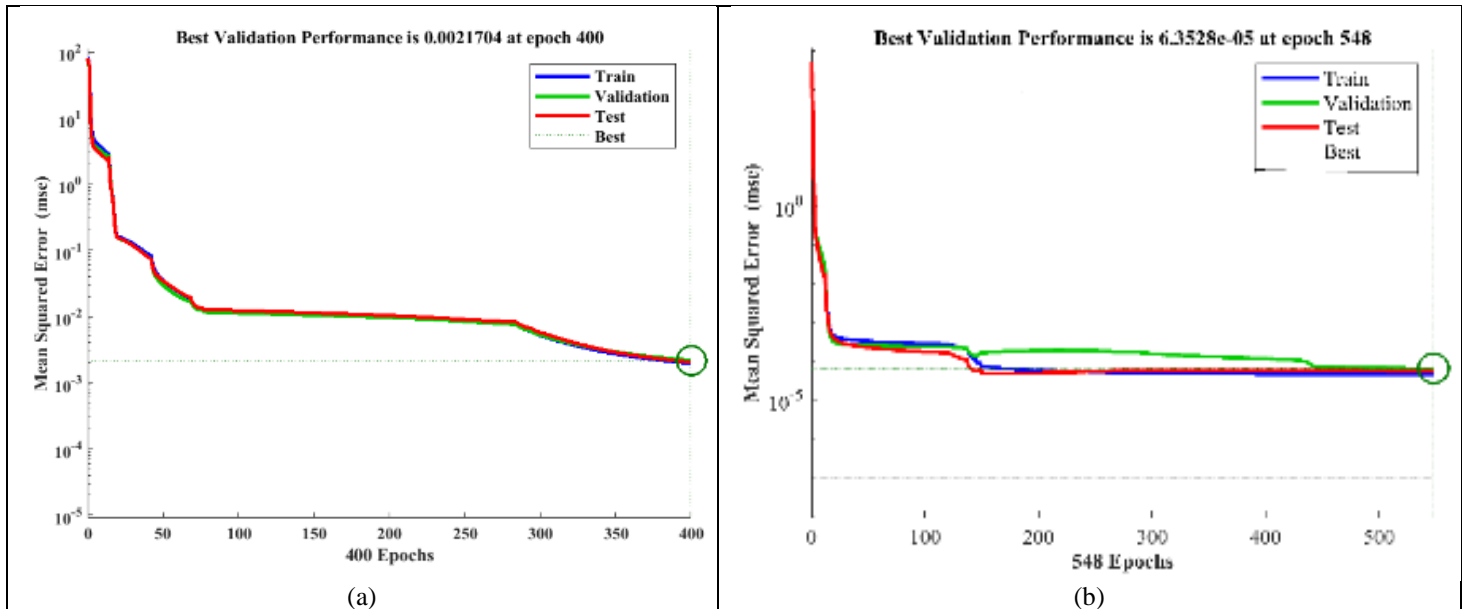


Figure 7: (a) Training performance based on MSE (Step Profil), (b) Training performance based on MSE (Random Profil)

Source: Authors, (2025).

## V. RESULTS AND DISCUSSIONS

To evaluate the effectiveness of the proposed control scheme, a 3 kW PMSG-based (WECS) was simulated using MATLAB/Simulink. The simulation parameters for the power synchronous generator and turbine under varying wind conditions are detailed in Tables A.1 and A.2 in Appendix A. This study conducted two tests to compare the effectiveness, performance, and robustness of the proposed ANN-Backstepping control method with the PI-Backstepping approach. Additionally, the tests evaluated the impact of these control strategies on the system's dynamic behavior. In the first test, the wind speed (WS) profile was subjected to step changes, including both increases and decreases. The second test used a randomly varying WS profile to evaluate system response.

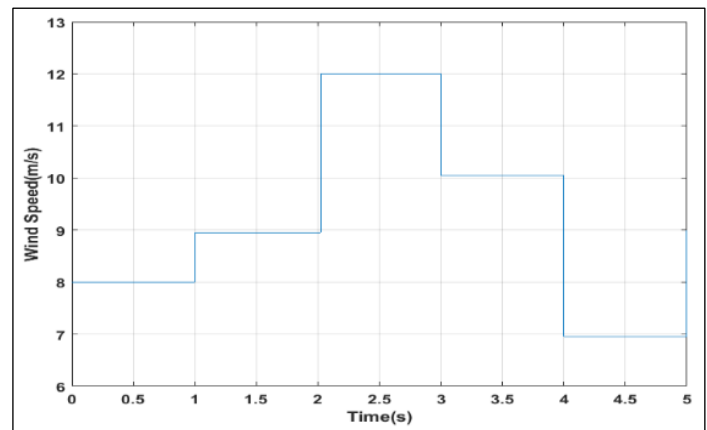


Figure 8: Wind speed profile

Source: Authors, (2025).

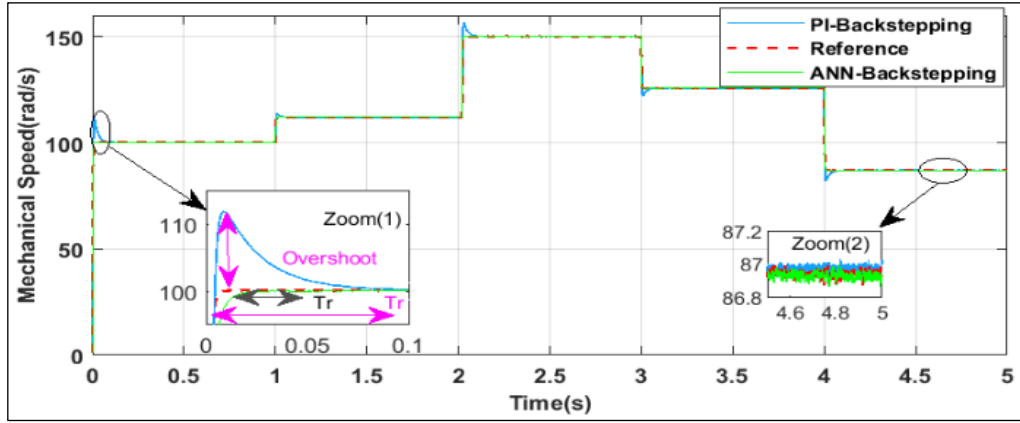
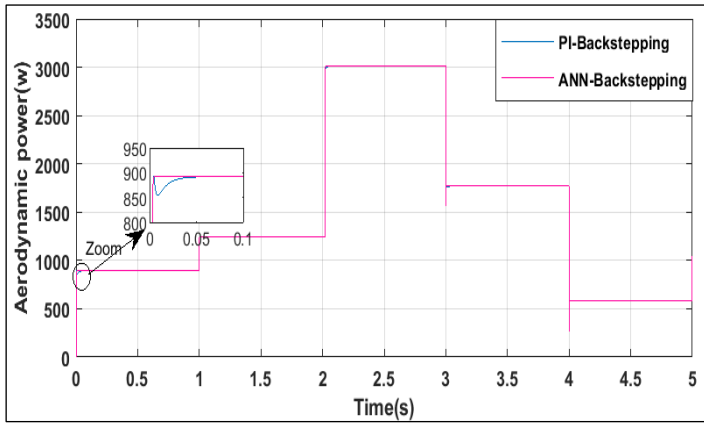
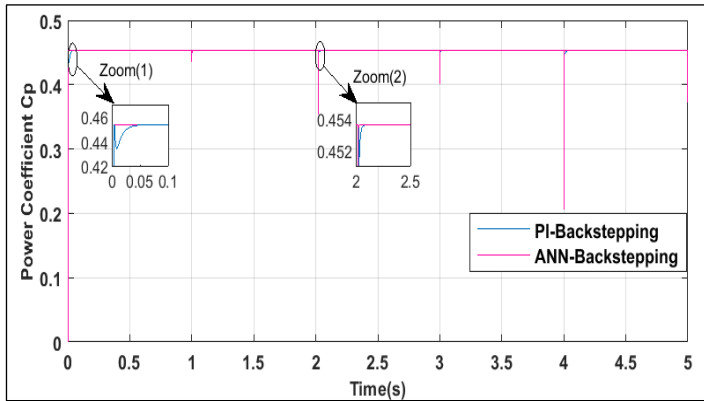


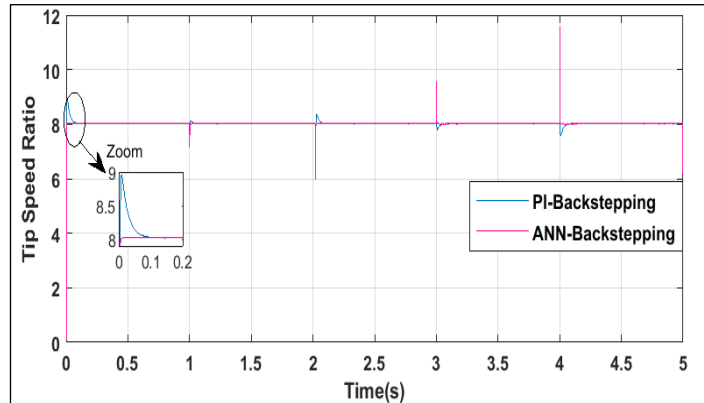
Figure 9: Mechanical Speed of the PMSG  
Source: Authors, (2025).



(a)

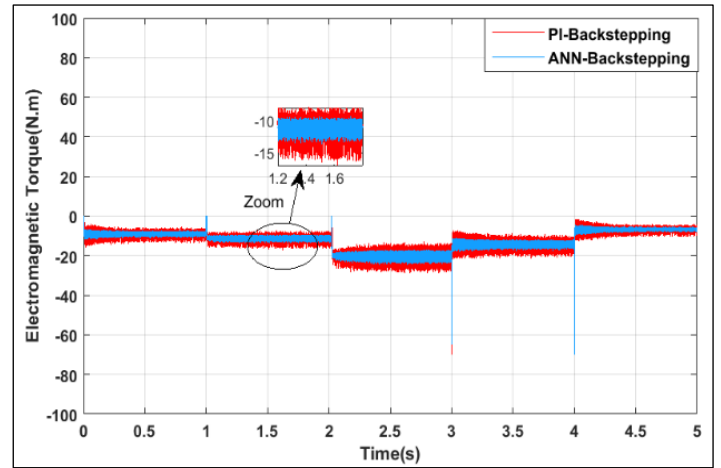


(b)

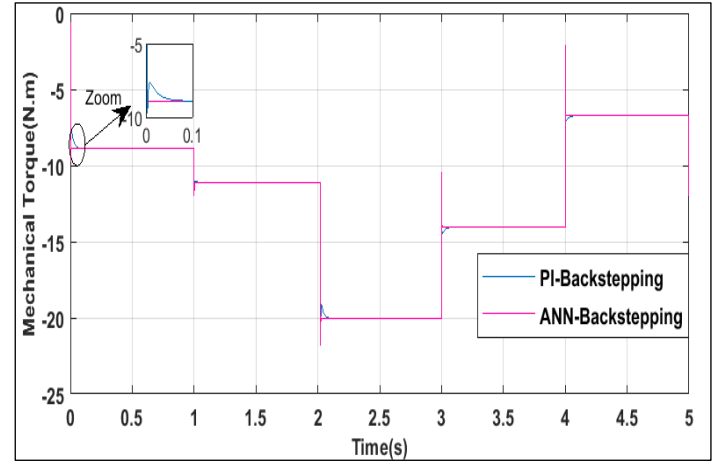


(c)

Figure 10: (a) Aerodynamic Power, (b) Power Coefficient  $C_p$  and (c) Tip Speed Ratio  $\lambda$   
Source: Authors, (2025).



(a)



(b)

Figure 11: (a) Electromagnetic Torque, (b) Mechanical Torque  
Source: Authors, (2025).

### V.1. STEP PROFILE

As illustrated in Figure 8, the wind speed profile experiences step changes within a 5-second time span. Figures 9 and 10(a) illustrate the mechanical speed ( $\Omega$ ) and aerodynamic power of the system when employing the PI-Backstepping and ANN-Backstepping control strategies, respectively. It is evident that both the mechanical speed and aerodynamic power closely follow their reference values, mirroring the shape of the wind speed profile. However, as highlighted in Zoom (1) of Figure 9, the mechanical speed controlled by the PI-Backstepping approach



exhibits a significant overshoot of 12%, whereas the ANN-Backstepping control eliminates this overshoot entirely. A similar observation can be made for the aerodynamic power in the zoomed-in view of Figure 10(a). Additionally, ANN-Backstepping offers a shorter settling time and reduced tracking error, as demonstrated in Zoom (2) of Figure 9, further validating the effectiveness of the proposed control strategy. Furthermore, Figures 10(a) and 10(b) depict the power coefficient ( $C_p$ ) and the tip speed ratio ( $\lambda$ ), which maintain a close alignment with their reference values under the ANN-Backstepping control. This approach achieves minimal tracking errors and no overshoot, even during wind speed fluctuations, outperforming the PI-Backstepping method. These findings confirm that the system operates near its optimal rotational speed and demonstrate the superior efficiency of the proposed ANN-Backstepping control in terms of settling time, overshoot, and precision compared to the PI-Backstepping control.

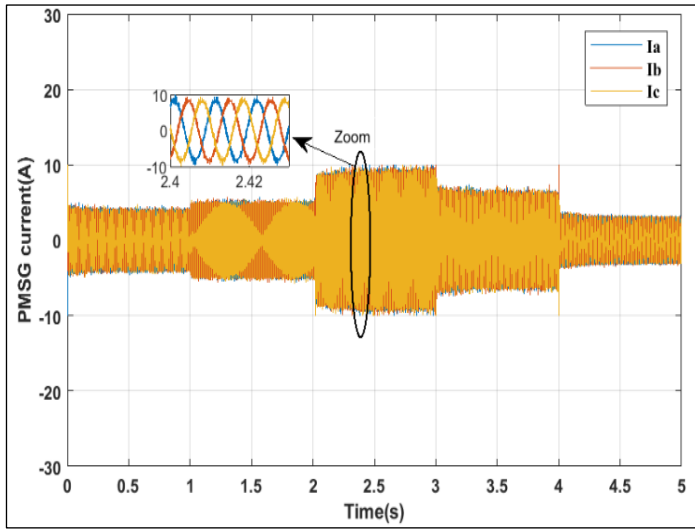


Figure 12: PMSG current  
Source: Authors, (2025).

Figure 11(a) demonstrate electromagnetic torque . Both PI-Backstepping (red) and ANN-Backstepping (blue) are compared, showing that ANN-Backstepping exhibits smoother performance with fewer oscillations during transient conditions. The zoomed section between 1.2s and 1.6s emphasizes that ANN-

Backstepping achieves better control with reduced fluctuations, highlighting its superior disturbance handling. Both strategies stabilize after disturbances, but ANN-Backstepping shows better torque regulation throughout. Figure 11(b) demonstrate Mechanical torque. Both strategies track these step changes, but ANN-Backstepping (pink) demonstrates a slightly faster and smoother response compared to PI-Backstepping (blue). The zoomed-in section (0 to 0.1s) highlights the reaction to an abrupt torque change. ANN-Backstepping shows reduced overshoot and better tracking precision.

As depicted in Figure 12, the currents of a (PMSG), illustrating the behavior of three-phase currents, and under specific operating conditions. The currents oscillate sinusoidally, maintaining a balanced three-phase system. This indicates proper functioning of the PMSG, with the phases remaining symmetric under normal conditions. Zoomed Section (2.4–2.42s) this magnified view reveals the detailed sinusoidal nature of the currents. After the transient period, the current waveforms gradually return to their steady-state sinusoidal pattern, demonstrating the system's ability to recover and reestablish balance.

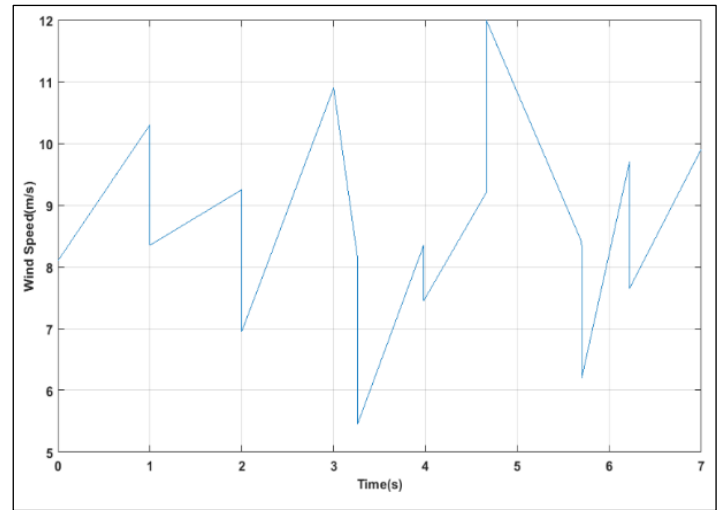


Figure 13: Wind speed profile  
Source: Authors, (2024).

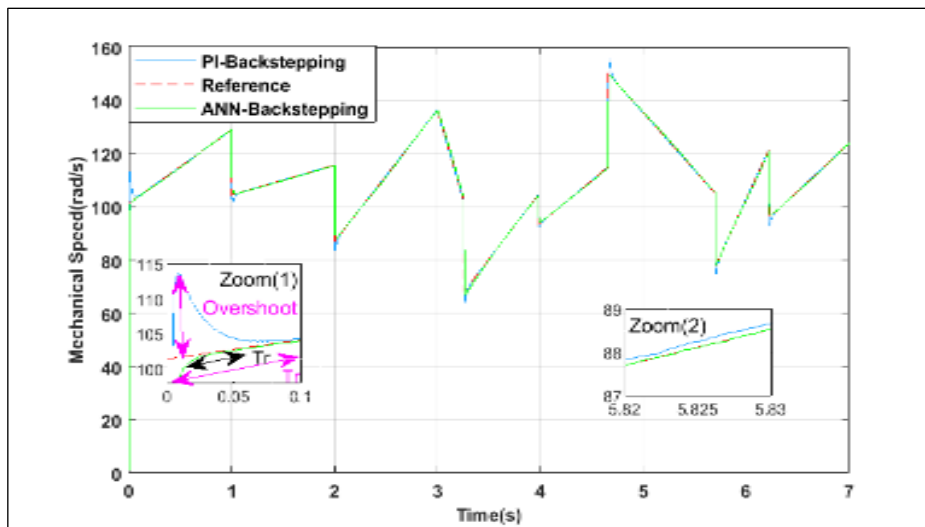
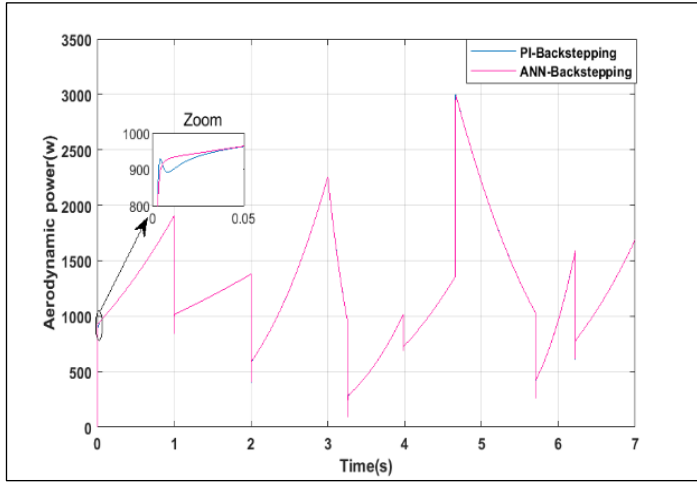
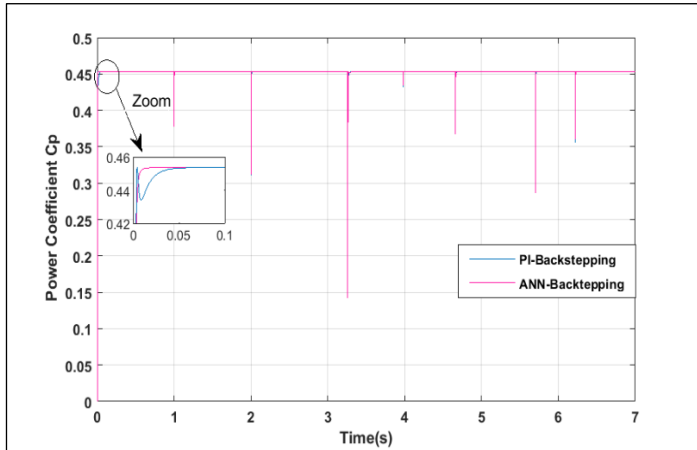


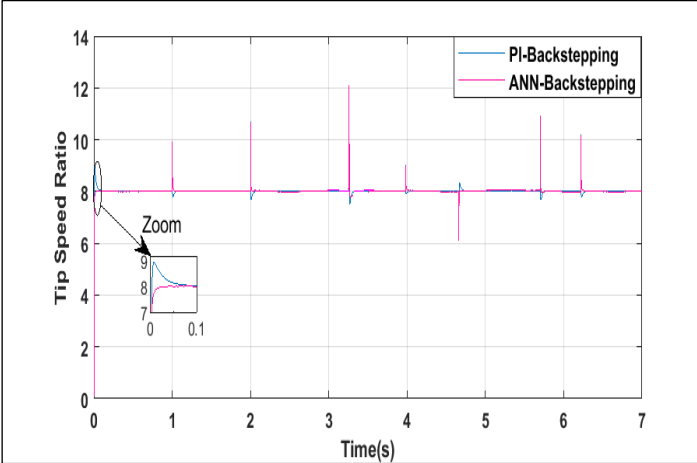
Figure 14: Mechanical Speed of the PMSG.  
Source: Authors, (2025).



(a)



(b)



(c)

Figure 15: (a) Aerodynamic Power, (b) Power Coefficient  $C_p$  and (c) Tip Speed Ratio  $\lambda$   
Source: Authors, (2025).

## V.2. RANDOM PROFILE

This section examines the stability of the evaluated control system under conditions of random wind speed variations, as illustrated in Figure 13. These variations highlight the challenges faced by control systems in maintaining stable performance in fluctuating wind Scenarios. In the Figure 14 (mechanical speed) offers a comparison between two control techniques: PI-Backstepping and ANN-Backstepping, with a reference value. Key observations include:

Zoom 1 (Overshoot and Settling Time): ANN-Backstepping shows reduced overshoot and quicker settling time, indicating superior dynamic response.

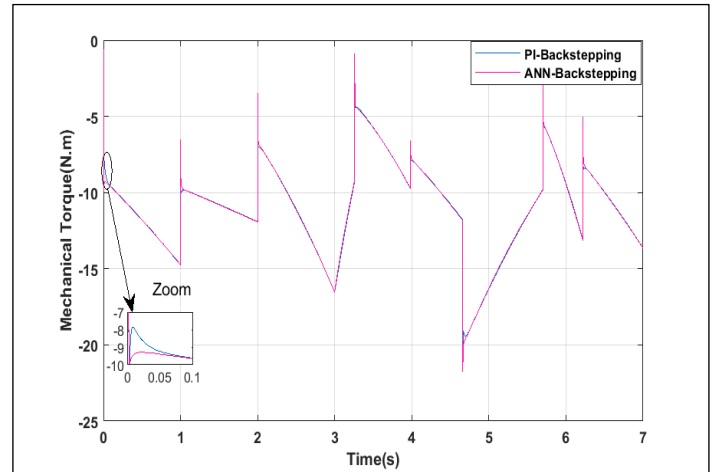


Figure 16: Mechanical Torque.  
Source: Authors, (2025).

Zoom 2 (Steady-State Stability): The ANN-Backstepping method demonstrates closer adherence to the reference signal during steady-state operation, confirming its improved accuracy.

As shown in Figure 15(a), evaluates the aerodynamic power output under the two control strategies. ANN-Backstepping displays a more consistent response across time, with smoother transitions and better tracking of power fluctuations compared to PI-Backstepping. The inset zoom highlights the rapid stabilization of aerodynamic power during initial transient conditions, where ANN-Backstepping shows an advantage in handling disturbances. Figures 15(b) and (c) illustrate the successful achievement of MPPT, as the  $C_p$  and  $\lambda$  values are maintained at their optimal and most desirable levels, respectively. The proposed ANN-Backstepping method for MPPT guarantees quick stabilization of the optimal power coefficient while consistently preserving the ideal  $\lambda$  value. Figure 16 demonstrate Mecanichal torque. This plot showcases the mechanical torque dynamics of the system under both control methods. The following is evident:

ANN-Backstepping provides smoother torque transitions, which can reduce mechanical stress and enhance system longevity.

In the zoomed-in view, ANN-Backstepping again achieves quicker stabilization and smaller torque deviations compared to PI-Backstepping, emphasizing its improved disturbance rejection capabilities.

## VI. CONCLUSIONS

This study aimed to enhance the performance of wind energy systems by focusing on a wind turbine coupled with a (PMSG), rectifier converter, and load. The research evaluated and validated the efficiency of control strategies, particularly Backstepping control for PMSG and (MPPT). Initially, a PI regulator was employed for MPPT, which was later replaced with an (ANN) for improved performance.

The key scientific contributions of this work are as follows:

- ✓ The integration of Backstepping control with PMSG demonstrated superior system stability and robustness.

- ✓ The replacement of the traditional PI regulator with ANN for MPPT significantly improved power tracking accuracy and dynamic response.
- ✓ Enhanced dynamic aerodynamic power quality and faster response times were achieved.
- ✓ The ANN-based MPPT control reduced tracking errors and ensured optimal performance under varying wind profiles.

The simulation results confirmed that combining Backstepping control with ANN-based MPPT offers a robust and efficient solution for wind energy systems. This approach not only ensures consistent power output but also optimizes the overall energy harvesting efficiency, making it a valuable contribution to renewable energy research. Future work will focus on analyzing the dynamic performance of a PMSG-based wind energy conversion system under varying load conditions.

## APPENDIX A

Table A.1: parameters for the power synchronous generator.

Parameter	Value
Rated generator power (P <sub>n</sub> )	3kW
Stator Inductance (L <sub>s</sub> )	0.0076 H
Pole pairs (p)	4
Permanent magnet flux $\Phi_f$	0.4 Wb
Coefficient of friction(f)	0.00016900 kg.m <sup>2</sup> .s <sup>-1</sup>
Moment d'inrtie (J)	0.0032 kg.m <sup>2</sup>
Stator Resistance (R <sub>s</sub> )	2.3 $\Omega$

Source: Authors, (2025).

Table A.2: Parameters of the turbine.

Parameter	Value
Radius of the turbine blade (R)	1.41m
The air density ( $\rho$ )	1.23 kg/m <sup>3</sup>
Tip-speed ratio ( $\lambda$ )	8.02
Power Coefficient (C <sub>p</sub> )	0.4535

Source: Authors, (2025).

## VII. AUTHOR'S CONTRIBUTION

**Conceptualization:** Wassila Hattab, Abdelhamid Benakcha, Seddik Tabet, Amira Slimani.

**Methodology:** Wassila Hattab, Abdelhamid Benakcha, Seddik Tabet, Amira Slimani.

**Investigation:** Wassila Hattab, Abdelhamid Benakcha, Seddik Tabet, Amira Slimani.

**Discussion of results:** Wassila Hattab, Abdelhamid Benakcha, Seddik Tabet, Amira Slimani.

**Writing – Original Draft:** Wassila Hattab, Abdelhamid Benakcha, Seddik Tabet, Amira Slimani.

**Writing – Review and Editing:** Wassila Hattab, Abdelhamid Benakcha, Seddik Tabet, Amira Slimani.

**Supervision:** Wassila Hattab, Abdelhamid Benakcha, Seddik Tabet, Amira Slimani.

**Approval of the final text:** Wassila Hattab, Abdelhamid Benakcha, Seddik Tabet, Amira Slimani.

## VIII. REFERENCES

- [1] M. W. Ayub, A. Hamza, G. A. Aggidis, and X. Ma, "A review of power co-generation technologies from hybrid offshore wind and wave energy," *Energies*, vol. 16, no. 550, 2023. [Online]. Available: <https://doi.org/10.3390/en16010550>
- [2] F. Bakhtiari and J. Nazarzadeh, "Optimal estimation and tracking control for variable-speed wind turbine with PMSG (in)," *J. Modern Power Syst. Clean Energy*, vol. 8, no. 1, pp. 159–167, 2020. [Online]. Available: <https://doi.org/10.35833/MPCE.2018.000365>
- [3] A. Sajadi, L. Strezoski, A. Khodaei, K. Loparo, M. Fotuhi-Firuzabad, R. Preece, M. Yue, F. Ding, V. Levi, P. Arbolea, et al., "Guest editorial: Special issue on recent advancements in electric power system planning with high-penetration of renewable energy resources and dynamic loads," *Int. J. Electr. Power Energy Syst.*, vol. 129, pp. 106597, 2021. [Online]. Available: <https://doi.org/10.1016/j.ijepes.2021.106597>
- [4] D. Fu, L. Kong, L. Gong, A. Wang, H. Jia, and N. Zhao, "Wind turbine load optimization control strategy based on LIDAR feed-forward control for primary frequency modulation process with pitch angle reservation," *Energies*, vol. 16, no. 510, 2023. [Online]. Available: <https://doi.org/10.3390/en16010510>
- [5] Y. El Mourabit, A. Derouich, A. ElGhzizal, N. El Ouanjli, and O. Zamzoum, "Nonlinear backstepping control of variable speed wind turbine based on permanent magnet synchronous generator," in *Proc. Int. Conf. Wireless Technol., Embedded Intell. Syst. (WITS)*, Fez, Morocco, 2019, pp. 1–7. [CrossRef]
- [6] A. Ullah, M. Ahmed, S. A. Raza, and S. Ali, "A threshold approach to sustainable development: Nonlinear relationship between renewable energy consumption, natural resource rent, and ecological footprint (Oct.)," *J. Environ. Manag.*, vol. 295, pp. 113073, 2021. [Online]. Available: <https://doi.org/10.1016/j.jenvman.2021.113073>
- [7] F. Huerta, R. Tello, and M. Prodanovic, "Real-time power hardware-in-the-loop implementation of variable-speed wind turbines," *IEEE Trans. Ind. Electron.*, vol. 64, no. 3, pp. 1893–1904, Mar. 2017. [Online]. Available: <https://doi.org/10.1109/TIE.2016.2623253>
- [8] D. Karboua, Y. Chouiha, B. O. Douara, I. F. Bouguenna, S. Benkaihoul, and B. Toual, "Advanced Dual-Loop Control Architecture for Superior PMSM Performance Utilizing Finite-Control-Set Model Predictive Control and Exponential Reaching Law Sliding Mode Control," *Journal of Engineering and Technology for Industrial Applications (ITEGAM-JETIA)*, vol. 10, no. 49, pp. 71–79, Sep/Oct. 2024. [Online]. Available: <https://doi.org/10.5935/jetia.v10i49.1221>
- [9] M. E. Zarei, D. Ramírez, M. Prodanovic, and G. M. Arana, "Model predictive control for PMSM-based wind turbines with over modulation and adjustable dynamic response time," *IEEE Trans. Ind. Electron.*, vol. 69, no. 2, pp. 1573–1585, 2021. [Online]. Available: <https://doi.org/10.1109/TIE.2020.2973206>
- [10] J. Wang, D. Bo, X. Ma, Y. Zhang, Z. Li, and Q. Miao, "Adaptive back-stepping control for a permanent magnet synchronous generator wind energy conversion system," *Int. J. Hydrogen Energy*, vol. 44, no. 19, pp. 3240–3249, 2019. [Online]. Available: <https://doi.org/10.1016/j.ijhydene.2018.12.133>
- [11] S. Sahu, G. Panda, and S. P. Yadav, "Dynamic modelling and control of PMSG based stand-alone wind energy conversion system," in *Proc. Recent Adv. Eng., Technol. Comput. Sci. (RAETCS)*, Nat. Inst. Technol. Meghalaya, India, 2018.
- [12] J. Pande, D. Nasikkar, K. Kotecha, and V. Varadarajan, "A review of maximum power point tracking algorithms for wind energy conversion systems (Oct.)," *J. Mar. Sci. Eng.*, vol. 9, no. 1187, 2021. [Online]. Available: <https://doi.org/10.3390/jmse9111187>
- [13] A. A. Iqbal and N. Akhtar, "A comprehensive review of MPPT techniques for wind energy systems," *Renewable and Sustainable Energy Reviews*, vol. 69, pp. 1246–1260, 2017. [Online]. Available: <https://doi.org/10.1016/j.rser.2016.11.243>

- [14] J. C. Guerrero Luján, F. E. López Monteagudo, J. De La Torre y Ramos, and L. del C. R. Rodríguez, "Characterization of a Low Power Wind Turbine Prototype for Interconnection to the Grid," *Journal of Engineering and Technology for Industrial Applications (ITEGAM-JETIA)*, vol. 10, no. 46, pp. 22-26, Mar./Apr. 2024. [Online]. Available: <https://doi.org/10.5935/jetia.v10i46.1110>
- [15] A. G. Abubakar and M. R. Khan, "Artificial Neural Network-based control for enhanced MPPT in wind energy systems," *Renewable Energy*, vol. 159, pp. 173–186, 2020. [Online]. Available: <https://doi.org/10.1016/j.renene.2020.06.147>
- [16] H. H. Alhelou, M. M. Khan, and S. Sun, "A survey on ANN applications in renewable energy systems: Case studies for wind energy," *IEEE Access*, vol. 8, pp. 108456–108469, 2020. [Online]. Available: <https://doi.org/10.1109/ACCESS.2020.3000768>
- [17] K. Al-Haddad and M. Krishnan, "Lyapunov-based backstepping for stability enhancement in wind energy conversion systems," *International Journal of Electrical Power & Energy Systems*, vol. 122, pp. 106177, 2020. [Online]. Available: <https://doi.org/10.1016/j.ijepes.2020.106177>
- [18] E. M. Youness, A. Derouich, A. E. Ghzizal, J. Bouchnaif, N. E. Ouanjli, O. Zamzoum, K. Mezoui, and B. Bossoufi, "Implementation and validation of backstepping control for PMSG wind turbine using dSPACE controller board," *Energy Reports*, vol. 5, pp. 807-821, 2019. [Online]. Available: <https://doi.org/10.1016/j.egyr.2019.06.001>
- [19] B. Majout, B. Bossoufi, M. Karim, P. Skruch, S. Mobayen, Y. El Mourabit, and Z. El Zair Laggoune, "Artificial neural network-based direct power control to enhance the performance of a PMSG-wind energy conversion system under real wind speed and parameter uncertainties: An experimental validation," *Energy Rep.*, [Online]. Available: <https://doi.org/10.1016/j.egyr.2023.06.015>
- [20] M. W. Khan, J. Wang, L. Xiong, and M. Ma, "Fractional order sliding mode control of PMSG-wind turbine exploiting clean energy resource," *International Journal of Renewable Energy Development*, vol. 8, no. 1, pp. 81–89, 2019. [Online]. Available: <https://doi.org/10.14710/ijred.8.1.81-89>
- [21] H. Chojaa, A. Derouich, S. E. Chehaidia, O. Zamzoum, M. Taoussi, and H. Elouatouat, "Integral sliding mode control for DFIG-based WECS with MPPT based on artificial neural network under a real wind profile," *Energy Reports*, vol. 7, pp. 4809–4824, 2021. [Online]. Available: <https://doi.org/10.1016/j.egyr.2021.07.066>
- [22] I. U. Khan, L. Khan, Q. Khan, S. Ullah, U. Khan, and S. Ahmad, "Neuro-adaptive backstepping integral sliding mode control design for nonlinear wind energy conversion system," *Turkish Journal of Electrical Engineering & Computer Sciences*, vol. 29, no. 2, pp. 531–547, 2021. [Online]. Available: <https://doi.org/10.3906/elk-2001-113>
- [23] E. Mahersi and A. Khedher, "Backstepping flux observer for nonlinear control of the direct-drive permanent magnet synchronous generator wind turbines," *Wind Engineering*, vol. 40, pp. 540–554, 2016. [Online]. Available: <https://doi.org/10.1177/0309524X16658519>
- [24] G. Xue, F. Lin, S. Li, and H. Liu, "Adaptive fuzzy finite-time backstepping control of fractional-order nonlinear systems with actuator faults via command-filtering and sliding mode technique," *Information Sciences*, vol. 600, pp. 189–208, 2022. [Online]. Available: <https://doi.org/10.1016/j.ins.2022.02.052>
- [25] F. Wang, Y. Guo, K. Wang, Z. Zhang, C. Hua, and Q. Zong, "Disturbance observer based robust backstepping control design of flexible air-breathing hypersonic vehicle," *IET Control Theory and Applications*, vol. 13, pp. 572–583, 2019. [Online]. Available: <https://doi.org/10.1049/iet-cta.2018.5480>
- [26] Y. El Mourabit, H. Salime, B. Bousouf, S. Motahhir, A. Derouich, S. Mobayen, and A. Zhilenkov, "Enhanced Performance in PMSG-Based Wind Turbine Systems: Experimental Validation of Adaptive Backstepping Control Design," *Energies*, vol. 16, no. 8, p. 3880, 2023. [Online]. Available: <https://doi.org/10.3390/en16083880>
- [27] Y. Mousavi, G. Bevan, I. B. Kucukdemiral, and A. Fekih, "Sliding mode control of wind energy conversion systems: Trends and applications," *\*Renewable and Sustainable Energy Reviews*,\* vol. 167, Art. no. 112734, Oct. 2022. [Online]. Available: <https://doi.org/10.1016/j.rser.2022.112734>
- [28] A. Poovathody and R. Ramchand, "Twelve Sector Based Direct Power Control of Induction Motor Drives," 2020 International Conference on Power Electronics and Renewable Energy Applications (PEREA), Nov. 2020, pp. 1–5. [Online]. Available: <https://doi.org/10.1109/PEREA51218.2020.9339794>
- [29] A. Jain, J. Singh, S. Kumar, T. Florin-Emilian, M. Traian Candin, and P. Chithaluru, "Improved recurrent neural network schema for validating digital signatures in VANET," *Mathematics*, vol. 10, no. 20, p. 3895, 2022. [Online]. Available: <https://doi.org/10.3390/math10203895>
- [30] B. N. Kommula and V. R. Kota, "An effective sustainable control of brushless DC motor using firefly algorithm – Artificial neural network based FOPID controller," *Sustainable Energy Technologies and Assessments*, vol. 52(B), p. 102097, 2022. [Online]. Available: <https://doi.org/10.1016/j.seta.2022.102097>
- [31] I. Saady, M. Karim, B. Bossoufi, N. El Ouanjli, S. Motahhir, and B. Majout, "Optimization and control of photovoltaic water pumping system using Kalman filter-based MPPT and multilevel inverter fed DTC-IM," *Results in Engineering*, vol. 17, Art. no. 100829, Mar. 2023. [Online]. Available: <https://doi.org/10.1016/j.rineng.2022.100829>
- [32] A. Kasri and K. Ouari, "Robust Intelligent Nonlinear Predictive Control Based on Artificial Neural Network for Optimizing PMSM Drive Performance," *Periodica Polytechnica Electrical Engineering and Computer Science*, vol. 68, no. 4, pp. 356–366, Sep. 2024. [Online]. Available: <https://doi.org/10.3311/PPee.37217>





## RESEARCH ARTICLE

## OPEN ACCESS

# USE OF TARO BOGOR ( *Colocasia esculenta* ( L.) Schott ) AS A GROWTH MEDIUM FOR *Aspergillus flavus*

Visensius Krisdianilo\*<sup>1</sup>

<sup>1</sup> Lubuk Pakam Medical Health Institute – North Sumatra, Indonesia.

<sup>1</sup><http://orcid.org/0000-0001-9888-9933>

Email: [chrizdianilo@gmail.com](mailto:chrizdianilo@gmail.com)

## ARTICLE INFO

**Article History**

Received: December 19, 2024

Revised: January 30, 2025

Accepted: February 15, 2025

Published: March 31, 2025

**Keywords:**

*Aspergillus flavus*,

Fungi,

Taro Bogor,

## ABSTRACT

Fungi are one type of microbe that plays an important role in human life, there are many groups of fungi that can be found in everyday life, one type of fungus that is pathogenic and produces aflatoxins, namely fungi with *Aspergillus flavus* species. Bogor taro has the potential to be used as a raw material because it has a carbohydrate content of 23.7% as an energy source, while potatoes have a total carbohydrate of 19.10%. So it can be known that the amount of carbohydrates in taro bogor is more than potatoes. Based on this background, researchers are interested in conducting research related to the use of taro bogor ( *Colocasia esculenta* ( L.) Schott ) as a growth medium for the fungus *Aspergillus flavus*. This type of research is experimental with Posttest Only Control Group Design research design, in this study the control group in the form of *Aspergillus flavus* planted on PDA medium while in the experimental group in the form of *Aspergillus flavus* planted on taro medium at a concentration of 2%. 4% and 6%. Conclusion based on the results of the paired T-test test, the p-value of taro medium is 2% and 4% less than 0.05 which means there is a significant difference with PDA medium, while in taro medium 6% the p-value of > 0.05 which can be concluded that there is no significant difference between taro medium 6% and PDA medium.



Copyright ©2025 by authors and Galileo Institute of Technology and Education of the Amazon (ITEGAM). This work is licensed under the Creative Commons Attribution International License (CC BY 4.0).

## I. INTRODUCTION

Fungi are one type of microbe that plays an important role in human life, there are many groups of fungi that can be found in everyday life, both saprophytic (beneficial) and pathogenic (harmful) fungi. One type of fungus that is pathogenic and produces aflatoxin is the fungus species *Aspergillus flavus*. The result of the fungal toxin *Aspergillus flavus* is in the form of mycotoxins which are compounds from the metabolic products of fungi. Aflatoxin can cause health problems, one of which can attack the nervous system, is carcinogenic, causes cancer in the liver, kidneys, and stomach [1].

Cases of poisoning due to aflatoxin are quite common as happened in Kenya in 2014 causing the death of 125 people [2]. Based on the report of the Food and Drug Monitoring Agency (BPOM) in 2014 throughout Indonesia, there have been 153 cases of food poisoning in the province. The highest number of food poisoning in West Java Province was 32 incidents (21%), Central Java 17 incidents (11%), Jakarta Special Capital Region, East Java, and West Nusa Tenggara each 11 incidents (7.2%), Bali 10

incidents (6.5%), until the lowest in Riau, Bangka Belitung, and South Kalimantan each 1 incident (0.7%) [3]. It is suspected that the presence of microbial activity, one of which is fungi [4].

Studying the properties possessed by microorganisms such as fungi, research can be done by breeding through growth medium. Medium is a material consisting of a mixture of food substances (nutrients) that function as a place to grow microbes such as carbohydrates which are the main source for carbon metabolism in fungi, besides that it is also osmosis pressure, does not contain inhibitors and is sterile. One of the medium commonly used for fungal growth is Potato dextrose agar (PDA) [5].

PDA is a medium that is often used to grow fungi in the laboratory because of its low pH, which is pH 4.5 to 5.6 so that bacterial growth can be inhibited. Bacteria require a neutral environment with a pH of 7.0 and an optimum temperature between 25-30°C for growth [6]. The composition of PDA medium consists of 200 grams of potato extract (carbohydrate), 20 grams of dextrose, and 15 grams of agar and 1000 ml of distilled water [7].

Based on its composition, PDA is included in the semi-synthetic medium because it is composed of natural ingredients

(potatoes) and synthetic ingredients (dextrose and agar). Potatoes are a source of carbon (carbohydrates), vitamins and energy, besides the agar component serves to solidify the PDA medium. Each of the three components is indispensable for the growth and proliferation of microorganisms, especially fungi [8].

PDA medium is often ready-made or instant so that this medium is ready to use. However, this medium only exists in certain places. Abundant natural resources can be used for fungal growth medium, this makes the impetus for researchers to conduct research on PDA replacement medium derived from natural ingredients with good enough content as a substitute for PDA medium. The material used as a substitute for PDA nutrients must be fulfilled, one of which contains high carbohydrates and protein [6].

The main base material for making PDA medium is potatoes which are a source of carbohydrates, so other substitutes can be made which contain almost the same as potatoes, namely by using Bogor taro (*Colocasia esculenta* (L.) Schott). Taro is one of the tubers that usually grows on the banks of rivers, swamps and barren land. Bogor taro has the potential to be used as a raw material because it has a carbohydrate content of 23.7% as an energy source, while potatoes have a carbohydrate amount of 19.10%. So it can be seen that the amount of carbohydrates in taro bogor is more than potatoes. Taro bogor also has sufficient nutrients that allow it to be used as a medium for the growth of *Aspergillus flavus* fungus [9].

Based on this background, researchers are interested in conducting research related to the use of bogor taro (*Colocasia esculenta* (L.) Schott) as a medium for the growth of *Aspergillus flavus* fungi.

## II. MATERIALS AND METHODS

### Type of Research.

This type of research is experimental, namely knowing a symptom or influence that arises due to certain treatments with a research design using Posttest Only Control Group Design with this design allows researchers to measure the difference or effect of treatment on the experimental group by comparing the group with the control group [10]. In this study the control group was *Aspergillus flavus* grown on PDA medium while the experimental group was *Aspergillus flavus* grown on taro medium at a concentration of 2%, 4% and 6%.

### Time and Location of Research.

The research was conducted in June 2024. The sampling was carried out in Labuhan Batu and then made into flour and then brought to the Laboratory of the Institute of Health Medistra Lubuk Pakam, Jalan Sudirman No.38, Petapahan, Kec. Lubuk Pakam, Deli Serdang Regency, North Sumatra to be studied.

### Tools and Materials.

Measuring cup, object glass, deck glass, analytical balance, hot plate, stirring rod, dropper, ose, bunsen, lighter, petri dish, autoclave, erlenmeyer, flour sieve, ruler, oven, microscope, mask, handscoon, wooden mortar, pestle. PDA medium, taro flour medium concentration 2%, 4% and 6%. *Aspergillus flavus* culture, distilled water, plain agar, sugar, cotton, lactophenol cotton blue (LPCB) reagent, label paper, and plastic wrap.

### Cultivation of *Aspergillus flavus* fungus on PDA medium and taro medium at concentrations of 2%, 4% and 6%.

Prepare tools and materials, take a Petri dish containing *Aspergillus flavus* culture. Then the tip of the ose is sterilized first

over a bunsen flame until it is red and wait until it cools. After that, take the fungal culture on the bikan. Then, *Aspergillus flavus* fungal colonies were taken and planted on PDA medium and on taro medium using the single dot method. Then incubated at room temperature (25-30°C) for 3 days.

### Identification.

#### a. Macroscopic

Take the medium that has been incubated to make observations to see the surface of the medium by observing the colonies, and the surface and matching the observation results with the characteristics of the *Aspergillus flavus* fungus. Then record the observations and document them.

#### b. Microscopy:

Tools and materials are prepared, then LPCB reagent is dripped 1-2 drops on the glass object. The tip of the ose is sterilized first over a bunsen flame until red and wait until it cools. After that, take the fungal culture in the culture and then place the fungus on the glass object that has been dripped with LPCB solution then flattened and then cover with deckglass and observed under a microscope.

#### c. Measuring the Diameter of Fungal Colonies

Measured using a ruler, then recorded the results in millimeters (mm).

### Data analysis.

Data analysis was carried out by processing the collected data using the SPSS program using the Parametric test, namely the Paired T-Test Test.

## III. RESULTS

### Macroscopic.

The results of macroscopic identification of *Aspergillus flavus* fungal colony growth are cotton-like, there is a dark yellow area on the surface of the fungus that is clearly visible on PDA medium, while on taro medium at concentrations of 2%, 4% and 6% did not look so clear. In addition, the green area that grows on taro medium at concentrations of 2%, 4% and 6% are not as thick as the green area that grows on PDA medium.

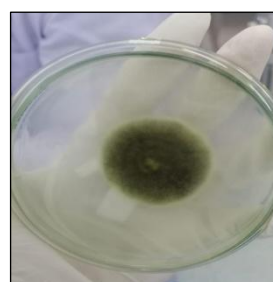


Figure 1. Macroscopic on PDA medium.



Figure 2. Macroscopic on 2% taro médium.

Source: Authors, (2025)



Figure 3. Macroscopic on 4% taro médium.



Figure 4. Macroscopic on 6% taro médium.

Source: Authors, (2025).

### Microscopic.

The results of microscopic identification of *Aspergillus flavus* fungal colony growth on PDA media and taro media at concentrations of 2%, 4% and 6%, obtained the results of round conidia heads, long conidia and hyphae are concentrated in taro media and PDA media.

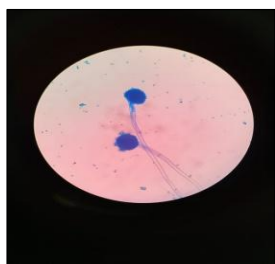


Figure 5. Microscopic on taro médium.

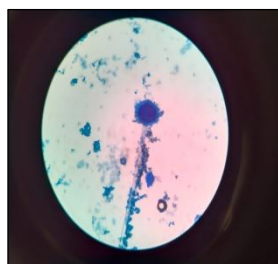


Figure 6. Microscopic on PDA medium.

Source: Authors, (2025).

### Fungal Colony Diameter.

The results of measuring the diameter of fungal colonies obtained the highest average in taro media with a concentration of 6%, namely 26 mm.

Table. 1 Diamater of colony growth of *Aspergillus flavus* fungus.

Sample Repetition	Colony Diameter (in milli meters) At Taro Media Concentration			Control
	2%	4%	6%	PDA
1	16	23	24	29
2	17	20	30	32
3	20	21	25	34

Source: Authors, (2025).

### Comparison Test Results.

From the results of the paired t-test (Paired T- Test) with the analysis of the SPSS program between 3 variables, it can be seen that the *p-value* of 2% taro media compared to PDA media results  $p = 0.002$ , 4% taro media compared to PDA media results  $p = 0.042$  and in 6% taro media compared to PDA media results  $p = 0.119$ . From the *p-value*, it shows that the taro media compared with PDA media has a significant difference at a concentration of 2% and 4% while the taro media 6% compared with PDA media obtained a *p-value* = 0.119 these results are greater than 0.05 which means there is no significant difference between taro media concentration 6% with PDA media.

Table. 2 Comparison test results.

Sample	Mean	N	SD	Sig
2% taro medium -PDA	17,62	3	2,082	0,002
4% taro medium -PDA	21,33	3	1,528	0,042
6% taro medium -PDA	26,33	3	3,215	0,119

Source: Authors, (2025).

## IV. DISCUSSIONS

The results obtained from the study show that the bogor taro media can grow *Aspergillus flavus* fungi. The results of the diameter of *Aspergillus flavus* colonies in table.1 show that the diameter of colonies at concentrations of 2% to 6% has increased

compared to the control media (PDA), this is because at the highest concentration of 6% the carbohydrate and protein content in the media is higher than the concentrations of 2% and 4%.

The results of this study are in line with research conducted by Amir, et al. (2018) with the largest diameter found at the highest concentration of 8%, because *Aspergillus flavus* utilizes the nutritional content in taro media, especially carbohydrates and proteins to grow and develop so that growth is faster at high concentrations [11].

In the comparison test using the paired T-test test, the *p* value = 0.002 in the 2% concentration of taro media and  $p = 0.042$  in the 4% concentration of taro media, which means that the *p*-value data <0.05, these results show that there is a significant difference in the diameter growth of *Aspergillus flavus* fungi in 2% and 4% taro media against PDA media.

The results of this study are in line with research conducted by Amir, et al. (2018) with the results there is a significant difference [11]. However, at a taro concentration of 6%, the results obtained did not have a significant difference with PDA media because the *p*-value of 0.119 was greater than 0.05, this result was supported by research by Octavia, et al. (2017) whose results showed that 6% taro media did not have a significant difference with PDA media [8].

The growth of *Aspergillus flavus* is indicated by the development of diameter, spore fertility, and mycelium color. PDA control media has the best *Aspergillus flavus* growth. Taro media has more complex nutrients (difficult to digest) so that the mycelial growth of fungal colonies is not as optimal as PDA media. This is emphasized by Gandjar (2006), which states that the complex content in the media causes the test fungus to take longer to break down into simple components that can be absorbed by cells used for synthesis and energy [12,13].

In addition to nutritional needs to grow, there are also several factors that can also affect the growth of fungi, namely the humidity factor, in this factor the *Aspergillus flavus* fungus can grow with 70% environmental humidity. Then the temperature factor, in this factor the *Aspergillus flavus* fungus will grow with an optimum temperature of 30 ° C and the pH factor, the *Aspergillus flavus* fungus can grow with a pH between 5-7. Of the three factors that can also affect the growth process of fungi in a medium [13].

Based on the results of the research, the best mushroom growth media is in taro media with a concentration of 6% because the media has a simple formulation and is the best media because of its ability to support mushroom growth [14]..

## V. CONCLUSIONS

Based on the results of the paired T-test, the *p*-value of 2% and 4% taro media is less than 0.05, which means there is a significant difference with PDA media, while in 6% taro media the *p*-value > 0.05, which can be concluded that there is no significant difference between 6% taro media and PDA media.

## VI. AUTHOR'S CONTRIBUTION

**Conceptualization:** Visensius Krisdianilo.

**Methodology:** Visensius Krisdianilo.

**Investigation:** Visensius Krisdianilo .

**Discussion of results:** Visensius Krisdianilo.

**Writing – Original Draft:** Visensius Krisdianilo.

**Writing – Review and Editing:** Visensius Krisdianilo.

**Supervision:** Visensius Krisdianilo.

**Approval of the final text:** Visensius Krisdianilo

## VII. REFERENCES

- [1] Edyansyah, E. The presence of mycotoxin-producing contaminants in peanut butter sold in traditional markets in Palembang city. Palembang. Palembang Poltekkes. 2015.
- [2] Taufik, M. Identification of pathogenic microbiology in soy sauce of meatball sellers in Sumbermuljo village. Jombang: STIKes ICMe Jombang.2018.
- [3] Food and Drug Monitoring Center. Poisoning Cases Throughout Indonesia, Food and Drug Monitoring Center, Indonesia.2004.
- [4] Syaifudin, A.N. Identification of *Aspergillus* sp Fungi in Fresh Bread Based on Before and After Expiration. Jombang: STIKes ICMe Jombang .2017.
- [5] Cahyani, V.R. Practicum Manual for Agricultural Microbiology. Surakarta: Sebelas Maret University Surakarta.2014.
- [6] Cappucino, J. G., and Sherman, N. Microbiology Laboratory Manual.Jakarta: ECG.2014.
- [7] Aryal, Sagar. 2019. Potato Dextrose Agar (PDA)- Principles, Uses, Composition, Procedure, and Colony Characteristic.
- [8] Octavia, A. and Wantini, S,. Comparison of *Aspergillus flavus* Fungus Growth on PDA (Potato Dextrose Agar) Media and Alternative Media from Cassava (*Manihot esculenta* Crants). Tanjungkarang: Journal of Health Analysis.2017.
- [9] Nurcahya, H. Cultivation & How to Process Taro for Food and Medicine. First Printing, Pustaka Baru Press. Yogyakarta .2015.
- [10] Notoatmodjo, S,. Health Research Methodology, Jakarta: PT Rineka Cipta. 2012.
- [11] Amir, et al,. Taro Flour as an Alternative Media for the Growth of *Candida albicans* and *Aspergillus* sp. University of Muhammadiyah Semarang. 2018.
- [12] Jiwintarum, Y. Natural Media for the Growth of *Candida albicans* Causing Candidiasis from Kluwih Seed Flour (*Artocarpus communis*). Prima Health Journal. 2017.
- [13] Gandjar, I., Sjamsuridzal, W., and Oetari, A. Basic and Applied Mycology. Yayasan Obor Indonesia. Jakarta. 2006.
- [14] Rohmi, R., Fikri, Z., & Pujasari, N.K.R White Sweet Potato (*Ipomoea Batatas* L.) Alternative Media for *Aspergillus Niger* Growth. Prima Health Journal.2019.





## RESEARCH ARTICLE

## OPEN ACCESS

# MODELLING CORONA DISCHARGE THRESHOLD IN COMPOSITE DIELECTRIC PROPERTIES OF EGGSHELL COMPOSITES INSULATORS: A VOLTAGE-BASED STUDY

Samsurizal<sup>1</sup>, Yulisya Zuriatni<sup>2</sup>, Andi Makkulau<sup>3</sup>

<sup>1,3</sup> Electrical Engineering, Faculty of Electricity and Renewable Energy, Institut Teknologi PLN, Indonesia.

<sup>2</sup> Civil Engineering, Faculty of Infrastructure Technology and Territory, Institut Teknologi PLN, Indonesia.

<sup>1</sup><https://orcid.org/0009-0001-2789-2876>, <sup>2</sup><https://orcid.org/0009-0005-0637-5334>, <sup>3</sup><https://orcid.org/0000-0002-8923-203X>

Email: [samsurizal@itpln.ac.id](mailto:samsurizal@itpln.ac.id), [yulisya@itpln.ac.id](mailto:yulisya@itpln.ac.id), [andi.mk@itpln.ac.id](mailto:andi.mk@itpln.ac.id)

## ARTICLE INFO

**Article History**

Received: December 23, 2024

Revised: January 31, 2025

Accepted: February 17, 2025

Published: March 31, 2025

**Keywords:**

Corona discharge, flashover voltage, composite material, eggshell powder.

## ABSTRACT

Corona and flashover threshold voltages are affected by the characteristics of insulator materials, such as chemical composition and thickness, as well as environmental conditions, including humidity and temperature. Eggshell powder is produced from the impact of crushed eggshells; this powder will be used as a substitute and filler (cement) used in the pavement mixture on solid insulators. This study aims to understand the difference in the response of flashover and corona phenomena to increased voltage in composite insulators. Flashovers tend to occur at low voltages and decrease drastically at high voltages, while coronas rarely appear at low voltages but increase and stabilize at high voltages. Flashovers are rare at voltages over 20 kV, but corona is still possible. This suggests that the design of insulators or conductors for high voltages needs to pay attention to the corona effect which can lead to material degradation over time, while the risk of flashover is lower. In this study, the voltage threshold for the emergence of corona is about 20 kV, where the electric field is strong enough to trigger an electrical discharge around the conductor. After crossing this limit, the corona remains at high voltage. Therefore, the design of the material or insulator must consider the constant presence of corona at high voltages to prevent material damage due to the discharge of electrical energy around the conductor.



Copyright ©2025 by authors and Galileo Institute of Technology and Education of the Amazon (ITEGAM). This work is licensed under the Creative Commons Attribution International License (CC BY 4.0).

## I. INTRODUCTION

Solid insulators or solid-form electrical insulators are commonly used in a variety of electrical applications to ensure system safety and efficiency. There are several types of solid insulators being researched, especially for high-voltage applications such as transformers [1]. Some of the key materials for solid insulation include thermoplastic polymers, such as polyurethane, which have advantages in dielectric strength and mechanical resistance. It is a good alternative to cellulose-based pressboards for insulators on transformer windings due to their better resistance to high voltages and lower dielectric losses [2].

In the world of materials research, step by step is always taken to find more innovative and sustainable solutions. One of these innovations is the testing of the electrical insulation properties of eggshell mixture materials. As the industry's need for

eco-friendly insulator materials increases, researchers are starting to turn their attention to organic waste that was previously considered worthless.

The research also includes important insulating characteristics, such as the material's ability to withstand high stresses without experiencing damage. For example, polymer dielectrics and glass fibers are often tested for their resistance to conditions such as partial discharge and electrical damage due to cracks on the surface of the material. This study is important to improve the performance of insulation materials that are more stable and efficient in the long term. In this study, eggshells were not only tested to see how they can survive under high voltages, but also how their electrical conductivity compares to traditional insulator materials. The biggest challenge is to ensure that the new composite is thermally stable, so that it remains able to protect electrical and electronic devices under extreme conditions.

This research is conducted by testing the high voltage resistance of a process that tests materials to the limit of their natural capabilities. It further looks at how much electricity can be channeled through this material, ensuring that it remains an effective barrier between electric current and vulnerable elements. Thermal stability is something that needs to be considered, seeing how these processed eggshells are able to withstand temperature fluctuations without experiencing deformation or deterioration in quality.

Eggshells, which are organic waste from the food and household industries, have attracted attention as a potential alternative material for a variety of applications. The eggshell is mostly composed of calcium carbonate ( $\text{CaCO}_3$ ) with a unique microstructure, which gives it attractive mechanical and thermal properties. In this context, the use of eggshells as a solid insulator material offers various advantages. The use of eggshells helps reduce organic waste that contributes to environmental pollution. Eggshells are easy to obtain because they are abundant waste from various sectors, such as households, restaurants, and food processing plants. As a waste material, eggshells do not require high production costs, so they are more economical than conventional insulator materials. The calcium carbonate content in the eggshell provides sufficient dielectric strength for electrical insulation applications.

## II. THEORETICAL REFERENCE

Corona discharge is an electrical discharge phenomenon that occurs when the electric field around a conductor reaches a point where the surrounding gas molecules are ionized. This usually occurs at high voltages and becomes more common on non-smooth surfaces, such as wires or insulators. The limit or threshold of corona discharge refers to the minimum voltage that causes an electrical discharge in the form of a corona discharge. This threshold is influenced by factors such as the surface of the material, atmospheric pressure, and the dielectric properties of the material. Dielectric Properties in Insulator Composites, is a mixture of several materials to improve electrical insulation properties. A good composite material will have the property of being resistant to the flow of electric current and be able to reduce leakage.

Eggshells contain calcium carbonate which naturally has good insulating properties. The use of eggshell as a dielectric composite material aims to utilize the abundant and inexpensive material, but still has good performance in high voltage applications. Stress Testing on Composite Materials: Typically, testing is done by applying a gradually increasing voltage to the insulator material to identify the point where corona discharge begins to occur. This is done in a laboratory using a voltage that can be controlled and monitored in real-time. To detect corona discharge at the micro level, ultraviolet cameras and electric current measurement devices are used. It helps identify the distribution of the electric field and detect the discharge point before it reaches a destructive threshold.

The quality and homogeneity of the eggshell distribution in the composite matrix affect the corona stress threshold. Evenly distributed materials tend to have a well-distributed electric field, reducing the possibility of corona discharge. Microstructural effects in composites, such as the presence of small cavities or imperfections (microvoids), can lead to a significant increase in the local electric field, which can lower the corona threshold. Insulators made of eggshell-based composite materials can be a more economical alternative compared to conventional polymer- or ceramic-based insulators. In addition, they can provide

comparable performance in terms of high-voltage isolation. Stability to the Environment: In addition to efficiency, eggshell composite insulators also have good resistance to temperature and humidity changes, making them a reliable choice in outdoor applications or in demanding environments.

There have been several previous studies that have addressed the phenomenon of corona and flashover voltage in solid insulators, particularly in the context of high voltages and outdoor applications. These studies show that corona threshold stresses and flashovers are affected by the characteristics of insulator materials, such as chemical composition and thickness, as well as environmental conditions, including humidity and temperature. For example, research focusing on flashover in insulators under vacuum conditions found that parameters such as electric field strength, insulator geometry, and insulator surface smoothness played an important role in preventing flashovers from occurring. This research aims to increase the withstand voltage of the insulator, which ultimately increases the resistance of the insulator to the corona phenomenon at high voltages [3].

Another study examined contaminated insulators in the transmission network. The results show that the presence of contaminants can lower the flashover voltage, so it is important to consider the protection and maintenance of the insulator to improve the reliability of the system [3]. Construction and Building Materials: Research shows that egg shells processed into powder can be used as a partial substitute for cement in the manufacture of concrete or bricks. The addition of eggshells, especially in certain percentages such as 5-10%, can increase the compressive strength of the material, although at higher proportions it will usually decrease. Research at De La Salle University, for example, shows that eggshells can be an alternative to construction materials by using seawater mixtures to reinforce eggshell-based concrete [4].

Eggshells have also been used as adsorbents for the removal of heavy metals and dyes from wastewater, since its main composition, calcium carbonate, has the ability to absorb pollutants. This use offers an environmentally friendly solution for the utilization of eggshell waste, while reducing water pollution and improving clean water quality. Joe, S. Y in This paper discusses the long-term use of temporary FPD, Polymethyl Methacrylate (PMMA) as a temporarily fixed material, and the benefit of eggshell waste to porosity and flexural strength of PMMA materials. The addition of eggshell to PMMA for temporary fixed restoration could decrease porosity and increase the flexural strength of PMMA material because it contains calcium carbonate so that it could be used for the manufacture of provisional fixed restoration which requires long-term use. Keywords: temporary fixed denture, polymethyl methacrylate, eggshell, porosity, flexural strength [5].

## III. MATERIALS AND METHODS

### III.1 MATERIALS

Eggshells are mainly composed of about 94-97% calcium carbonate ( $\text{CaCO}_3$ ) which acts as the main component that gives the shell its hard structure, but it also contains a variety of other materials in smaller amounts of Protein Matrix – about 1-2% serves as a binder between calcium carbonate crystals, providing additional strength and elasticity. The composition of egg shells, which is composed mostly of calcium carbonate, makes them a potential material for applications in various industries, such as composite materials, fertilizers, and even solid insulator materials.

The research uses eggshell material, then the ideal proportion of egg shell mixture with resin material is used to

produce a high-quality insulator. In this research, the test material used uses a ratio of 60/40 and 2% of the Resin Weight equivalent to 1.2 Grams, the results obtained by the insulator as a test material have perfectly hardening properties, are flame retardant and have a hard texture, the material and insulator used are shown in Figure 1.

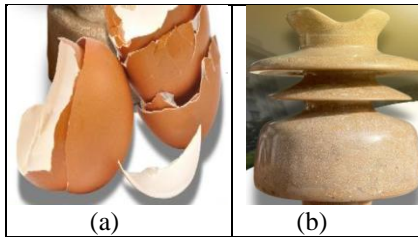


Figure 1: Materials and Testing (a) eggshells as solid insulators (b) Eggshell insulators.  
Source: Authors, (2025).

In making eggshell insulators, there are several materials needed, including: polyester resin, eggshells, catalysts, glazes, and methyl methacrylate. Polyester resin is an organic compound that is more volatile or has a higher VOC (Volatile Organic Compounds) content than epoxy resin. So polyester resin has a much stronger odor than epoxy resin. Polyester resins have strong and flammable VOC exhaust gases or vapors. Polyester resin is also one of the types of resin insulators that are often used. This resin has good electrical insulation properties, is resistant to weather, and is resistant to corrosion.

Eggshell powder is a powder produced from the impact of crushed eggshells, this powder will be used as a substitute and filler (cement) used in pavement mixtures. The shell of a poultry egg consists of calcium carbonate of 97% of its mass, glued together with a protein matrix. Without the protein matrix, the egg would become very brittle and would not be able to maintain its shape.

### III.2 METHODS

Recent research has explored various methods to model and optimize corona release in composite insulators. Ultraviolet imaging has been used to estimate the magnitude of the emitter, taking into account factors such as observation distance and imager amplification [6]. Derivatives-Free Breakers combined with finite element modeling have been used to optimize corona ring parameters, reducing electric field intensity by up to 66% [7]. The Finite Element Method (FEM) has been proposed as an effective technique for calculating the distribution of potential forces and electric fields along insulators, especially on complex composite fields [8]. In addition, Response Surface Methodology has been applied to optimize the dielectric strength of polymer composites by determining the optimal fill ratio, with commercial wollastonite and alumina trihydrate identified as important factors [9]. This study provides valuable insights into the modeling and optimization of coronal release thresholds in composite insulators.

The breakdown voltage for a solid insulator is the maximum voltage that can be applied to the insulator material before dielectric damage or electrical jumps through the material occur [10]. To find the breakdown voltage equation in solid insulators, there are several theoretical approaches based on the basic laws of electric fields, as well as the material properties of the insulators used. In general, the  $V_b$  break-through voltage depends on several factors, such as the thickness of the material  $d$ , the strength of the critical electric field  $E_b$ , and the material constant of the insulator. The basic equation for the break-through voltage in a solid insulator can be written as:

$$V_b = E_b \times d \quad (1)$$

Where,  $E$  = Electric Field (kV/cm),  $V$  = Breakout voltage (kV),  $d$  = material thickness (cm)

In this study, eggshells were not only tested to see how they can survive under high voltages, but also how their electrical conductivity compares to traditional insulator materials. The biggest challenge is to ensure that the new composite is thermally stable, so that it remains able to protect electrical and electronic devices under extreme conditions.

This research involves testing the high voltage resistance of a process using materials to the limits of their natural capabilities, and ensuring that they remain an effective barrier between electric current and vulnerable elements. Thermal stability is the final highlight, seeing how these processed eggshells are able to withstand temperature fluctuations without experiencing deformation or deterioration in quality. With this approach, eggshell mixed materials can be a pioneer in creating electrical insulators that are not only efficient but also environmentally friendly.

### IV. RESULTS AND DISCUSSIONS

In this study, the test was carried out in an insulator in dry conditions using the Insulation Resistance Tester (Megger) testing tool, the circuit used in the test can be seen in figure 1.

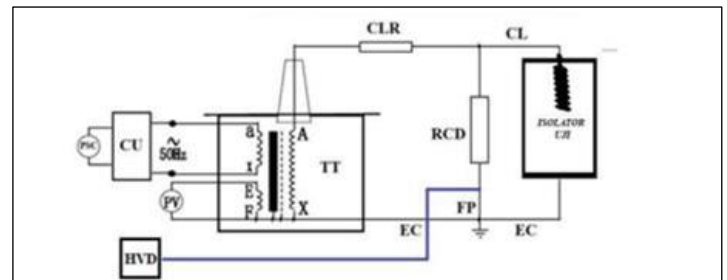


Figure 2: Diagram Rangkaian Pengujian.  
Source: Authors, (2025).

By using the test tool as seen in figure 2, the test results obtained are shown in table 1.

Table 1. Isolator Test Results

Test Voltage (kV)	Time (second)	Explanation
5	120	X
10	120	X
15	120	X
20	120	X
30	120	flashover
80	120	flashover

Source: Authors, (2025).

Table 1. Showing the results of voltage tests on insulators in dry conditions to observe flashover and corona phenomena. The electrical voltage applied to the insulator during the test, expressed in kilovolts (kV), ranges from 5 kV to 80 kV. The test time at each voltage level is 120 seconds for each voltage level. At 5 kV and 10 kV, no flashover occurs. At a voltage of 20 kV, there is no flashover at this voltage, which indicates that this voltage is still relatively safe from flashover in dry conditions.



At voltages of 30 kV and 80 kV, the corona phenomenon begins to appear which causes flashovers. The corona phenomenon usually occurs at high voltages where the electric field around the conductor is strong enough to ionize the air without causing a full electrical discharge or flashover. The threshold voltage for flashover in dry conditions is around 15 kV. At this voltage, flashovers sometimes appear and sometimes not, indicating that at voltages above 15 kV, the risk of flashover increases. The emergence of Corona, the corona phenomenon begins to be seen at 30 kV and continues at higher voltages. This is consistent with the theory that corona tends to occur at high voltages when the electric field is strong enough to cause partial ionization.

The results obtained are followed by the relationship between the test voltage and the occurrence of flashover using linear regression. In this context, the free variable (X) is the test voltage (kV). A bound variable (Y), where a flashover occurs, which is usually expressed in binary form (e.g., 0 for no flashover and 1 for flashover). From the data obtained made at voltages below 15 kV, the probability of flashover is low or non-existent.

At voltages of 15 kV and above, the probability of flashover starting to increase or occur consistently at a given voltage. Using simple binary linear regression it is possible to estimate the likelihood of a flashover occurring based on the applied voltage. The Linear Regression model was used to find the relationship between voltage and flashover probability, the results obtained are shown in the graph Figure 3.

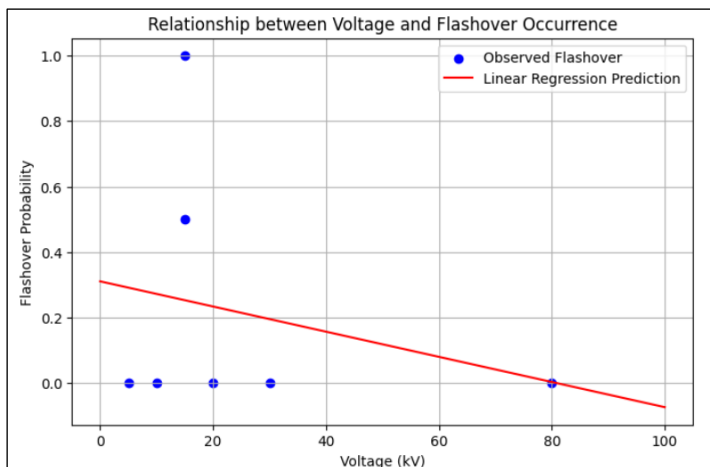


Figure 3: Relationship Between Voltage and Flashover Probability.

Source: Authors, (2025).

From the graph in figure 3, we can see the linear regression relationship between voltage (kV) and flashover probability. Based on the results of the graph in the figure, the linear regression equation is obtained:

$$\text{Flashover Probability} = -0.0038 \times \text{Voltage} + 0.3104$$

Where the slope of -0.0038 indicates that with increasing voltage, the probability of flashover decreases slightly linearly in this model. An intercept of 0.3104 indicates the approximate probability of a flashover when the voltage is close to 0 kV. However, this relationship does not appear to show a strong trend due to the variable flashover data at a given voltage (e.g., at 15 kV). The error value generated from this linear regression model, expressed in the form of Mean Squared Error (MSE), is about 0.124. This shows how far the model predicts from the actual flashover data, this model may be less accurate to predict directly.

Furthermore, it describes the relationship between voltage (kV) and the probability of flashover (electrical leap through the surface of the insulator) and the probability of corona (discharge of electrical charge around the conductor) at various voltage levels. The graph of the modeling results using the python programming language is shown in Figure 4

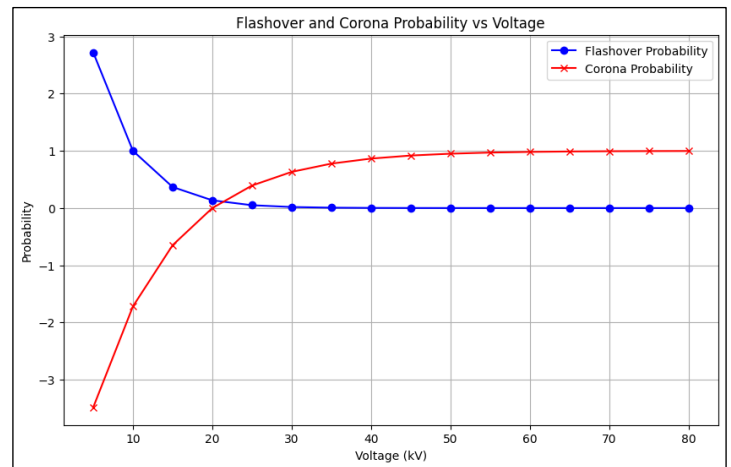


Figure 4: Flashover and Corona Probability and Voltage.

Source: Authors, (2025).

In figure 4. The Y axis indicates the "probability" for two electrical phenomena, namely flashover and corona. Note, however, that the probability value here is not like a regular probability (0 to 1), but rather a relative probability that may be measurable as the intensity or frequency of events under certain experimental conditions. This value can be interpreted as the frequency or rate of flashover and corona events at different voltage levels. X-Axis (Voltage in kV): The X-axis indicates the voltage level in kilovolts (kV), which increases from 0 to 80 kV. Increasing voltages can affect the likelihood of both phenomena, depending on the characteristics of the insulator material or component being tested.

The Flashover Curve (Blue Line with Dots) shows a downward trend: Initially, the probability of flashover is quite high at low voltages (about 10 kV), but then it decreases drastically as the voltage rises to about 20 kV. This may indicate that at low voltages, flashover phenomena occur more frequently, but there is a certain limit where high voltages actually decrease the occurrence of flashovers. Once the voltage reaches about 20 kV, the flashover probability remains stable (close to zero) up to 80 kV. This may be due to the more stable strength of the electric field at high voltages, so flashover does not occur because the insulation is more effective at this level.

The Corona Curve (Red Line with the Cross), has an increasing trend: The probability of the corona starts from a negative value (which may be interpreted as a very low or insignificant event) at low voltages, but gradually increases with increasing voltages. This shows that the corona phenomenon tends to be more dominant at high voltages. Stability at High Voltage: After reaching a voltage of about 20 kV, the probability of the corona remains relatively stable (close to a certain positive value) up to 80 kV. This may indicate that the corona becomes a constant phenomenon that does not increase or decrease significantly at high voltages, but is nonetheless present as an electric field effect.

To find out the relationship between voltage (kV) and corona presence indicators, modeling is needed by showing how the corona phenomenon appears at a certain voltage and remains at



a higher voltage, the results obtained are seen in the graph in figure 5.

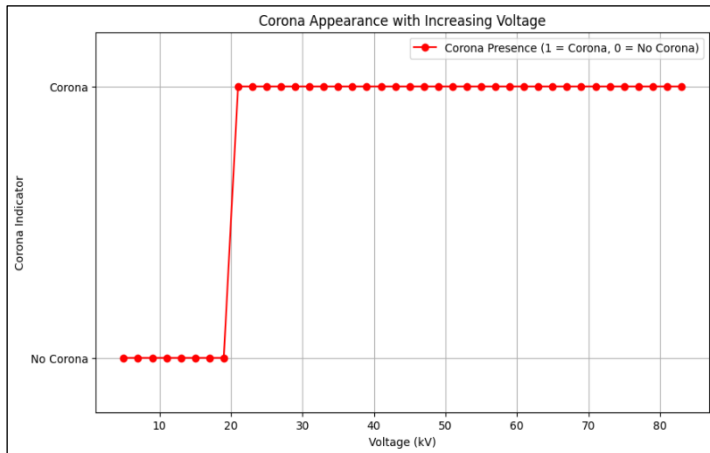


Figure 5: Corona Appearance With Increasing Voltage  
Source: Authors, (2025).

This figure 5 graph shows the relationship between voltage (kV) and corona presence indicators. The graph shows how the corona phenomenon appears at a given voltage and remains at a higher voltage. Y Axis (Corona Indicator): The Y axis indicates an indicator of corona presence, with a value of 0 indicating "No Corona" and 1 indicating "Corona Appearing". This indicates whether or not the corona phenomenon occurs at a given voltage. X-axis (Voltage in kV): The X-axis indicates the voltage level from 0 to 80 kV. The higher the voltage, the more likely it is that corona will occur, according to the pattern shown in the graph.

At voltages below 20 kV, the indicator shows no corona (value 0). This means that at low voltages, the corona phenomenon has not yet appeared. The Corona surge occurred at a voltage of around 20 kV. At this point, the graph shows a sharp transition from "No Corona" to "Corona Appears." This shows that the threshold voltage for the appearance of the corona is around 20 kV. After reaching a voltage of 20 kV and above, the corona remains (value 1), and the graph becomes stable. This suggests that once the corona appears, it will remain present at higher stress levels, and the phenomenon becomes constant.

## V. CONCLUSIONS

In the research that has been carried out, the results have been obtained, that the flashover and corona phenomena have different responses to increased voltage. Flashover is more likely to occur at low voltages and then decrease drastically at high voltages. In contrast, corona is less frequent at low voltages, but it increases and then stabilizes at high voltages.

At high voltages (more than 20 kV), flashovers are rare, but corona is still possible. This suggests that in insulator or conductor designs for high voltages, the corona effect needs to be specifically considered, while the risk of flashover may be lower. For equipment operated at high voltages, the material and insulator design need to focus on reducing the corona effect, which can lead to material degradation over time. Flashover seems to be a problem at low or medium voltages.

Voltage Threshold that the corona starts to appear at a voltage of about 20 kV. This is the threshold voltage where the electric field is strong enough to cause an electrical discharge around the conductor. After crossing the threshold of 20 kV, the corona does not disappear, but rather remains at a higher voltage. This means that the material or insulator design must consider the

constant presence of corona at high voltages to prevent damage or degradation of the material due to the discharge of electrical energy around the conductor.

## VI. AUTHOR'S CONTRIBUTION

**Conceptualization:** Samsurizal, Yulisya Zuriatni

**Methodology:** Samsurizal, Yulisya Zuriatni

**Investigation:** Yulisya Zuriatni, Andi Makkulau

**Discussion of results:** Samsurizal, Andi Makkulau

**Writing – Original Draft:** Samsurizal

**Writing – Review and Editing:** Samsurizal, Yulisya Zuriatni

**Resources:** Samsurizal, Yulisya Zuriatni, Andi Makkulau

**Supervision:** Yulisya Zuriatni, Andi Makkulau

**Approval of the final text:** Samsurizal

## VII. ACKNOWLEDGMENTS

The author would like to thank ITPLN and LPPM for funding the research in accordance with the rector's decree number: 0133/SK/1/A0/06/2024, the entire laboratory support team and all those involved so that this research can be completed and a scientific article can be made, hopefully this article will be useful for the development of science and technology.

## VIII. REFERENCES

- [1] S. A. Studniarz and A. I. Bennett, "Dielectric breakdown in solids," *Digest of Literature on Dielectrics*, Volume 41, 1977, Washington, DC, USA, 1977, pp. 168-187, <https://doi.org/10.1109/DLD.1977.7731611>
- [2] Ersoy, A.; Atalar, F.; Aydoğan, A. Investigation of Novel Solid Dielectric Material for Transformer Windings. *Polymers* 2023, 15, 4671. <https://doi.org/10.3390/polym15244671>
- [3] H. C. Miller, "Flashover of insulators in vacuum: review of the phenomena and techniques to improved holdoff voltage," in *IEEE Transactions on Electrical Insulation*, vol. 28, no. 4, pp. 512-527, Aug. 1993, <https://doi.org/10.1109/14.231534>
- [4] O. Awogbemi, D.V.V. Kallon, and V.S. Aigbodion, "Pathways for Sustainable Utilization of Waste Chicken Eggshell," *J. Renew. Mater.*, vol. 10, no. 8, pp. 2217-2246, 2022. <https://doi.org/10.32604/jrm.2022.019152>
- [5] Joe, S. Y., So, J. H., Oh, S. E., Jun, S., & Lee, S. H. Development of Cracked Egg Detection Device Using Electric Discharge Phenomenon. *Foods*, 13(18), (2024). 2989. <https://doi.org/10.46934/ijp.v5i1.269>
- [6] S. Wang, F. Lv and Y. Liu, "Estimation of discharge magnitude of composite insulator surface corona discharge based on ultraviolet imaging method," in *IEEE Transactions on Dielectrics and Electrical Insulation*, vol. 21, no. 4, pp. 1697-1704, August 2014, <https://doi.org/10.1109/TDEI.2014.004358>
- [7] Seyyed Barzegar, Seyyed Meysam; Sadeghi, Alireza; Khodsuz, Masume. Optimization of Corona Ring Parameters for Electric Field Adjustment in Composite Insulator Using Derivative Free Solvers. *Computational Intelligence in Electrical Engineering*, 2021, 12.1: 75-86. <https://doi.org/10.22108/isee.2020.121370.1326>
- [8] Bhavani, J.; CH, SVS Phani Kumar. Finite element modeling of voltage and electric field distribution along the insulators. In: 2019 4th International Conference on Recent Trends on Electronics, Information, Communication & Technology (RTEICT). IEEE, 2019. p. 225-229. <https://doi.org/10.1109/RTEICT46194.2019.9016905>
- [9] A. Aman and M. Yaacob, "Optimization of dielectric strength of polymeric composite insulation using Response Surface Methodology," 2012 IEEE International Conference on Power System Technology (POWERCON), Auckland, New Zealand, 2012, pp. 1-5, <https://doi.org/10.1109/PowerCon.2012.6401398>
- [10] Afrouzi, Hadi Nabipour, et al. In-depth exploration of partial discharge modelling methods within insulations. *Cleaner Engineering and Technology*, 2022, 6: 100390. <https://doi.org/10.1016/j.clet.2021.100390>



## RESEARCH ARTICLE

## OPEN ACCESS

## HOPF BIFURCATION POINT IDENTIFICATION IN A POWER SYSTEM WITH VARIOUS STATIC LOAD MODELS

Ghousul Azam Shaik<sup>1</sup> and Lakshmi Devi Aithepalli<sup>2</sup>

<sup>1,2</sup> Department of Electrical and Electronics Engineering, SVU College of Engineering, Sri Venkateswara University, Tirupati – 517 502, India.

<sup>1</sup><http://orcid.org/0000-0001-9703-5493>, <sup>2</sup><http://orcid.org/0000-0003-3390-1772>

Email: [ghousul1993@gmail.com](mailto:ghousul1993@gmail.com), [energylak123@yahoo.com](mailto:energylak123@yahoo.com)

### ARTICLE INFO

#### Article History

Received: December 29, 2024

Revised: February 02, 2025

Accepted: February 17, 2025

Published: March 31, 2025

#### Keywords:

Eigenvalue Analysis,  
Electric Vehicle,  
Damping ratio,  
Hopf Bifurcation.

### ABSTRACT

This paper covers the impact of voltage dependent load models on the small signal stability in Western States Coordinating Council (WSCC) system having Automatic Voltage Regulator (AVR) with increased generation and load scenarios. Earlier work on the same system using constant power type of load representation for locating the Hopf bifurcation point was done by the authors of this manuscript. This paper deals with the extension of the previous work to include various voltage dependent small signal load models such as Constant Current (CC), Constant Impedance (CZ), Industrial (IND) and large scale Electric Vehicle (EV) for evaluating damping ratios and sketching the locus of critical modes at stressed loadings by defining six cases. A thorough comparison of damping ratios of several complex modes obtained after including various voltage dependent load models in the linearization programmes with the constant power model presented in earlier work at the nominal loading is done. It is concluded that by including large scale EV load model at load buses, highest damping ratio of exciter mode corresponding to first generator of WSCC system was obtained when compared to remaining load models.



Copyright ©2025 by authors and Galileo Institute of Technology and Education of the Amazon (ITEGAM). This work is licensed under the Creative Commons Attribution International License (CC BY 4.0).

### 1. INTRODUCTION

Stability of a system can be broadly classified into large scale stability and small signal stability. The behaviour of system with huge disturbance is dealt by former one where non-linear differential equations have to be solved at every time step using various numerical integration techniques [1]. The later one is small scale stability which encompasses small disturbances where linearization process for Differential Algebraic Equations (DAE's) are taken up and displayed in state space form to provide insight into asymptotic stability behaviour of system near equilibrium point.

Earlier the power system loads were categorised as Constant Power (CP), Constant Current (CC) and Constant Impedances (CZ) [2], [3]. For the purpose of load flow, CP type is the most convenient form of load representation whereas CZ type is the most flexible for combining it into the bus admittance matrix to facilitate Krons reduction during linearization processes. Industrial loads (IND) can be expressed as combination of CZ, CC, CP (ZIP)

model and its inclusion in distribution network for solving the network voltages are presented in [4]. Using adjustable converter dynamics for CP loads, the effects of CP and CZ loads are compared in a distribution network with four loads thus suggesting the degradation of performance with CP loads [5]. Electric Vehicle(EV) loads are emerging in the market and expected to rise in the future and thus large scale integration of EV's is a matter of concern and hence the inclusion of this model was considered in this manuscript.

Taking CC and CZ models into consideration for small signal stability analysis, [6] developed analytical techniques to include the effect of above models in the overall system matrix formulation in Western States Coordinating Council System (WSCC) as shown in Figure 1. The application of forward and backward sweep methods in micro grid having different EV models are given in [4], [7] presented current injection load flow to evaluate voltage profile and losses using ZIP based static EV load model in distribution network. [8] considered the application of Particle Swarm Optimization (PSO) based tuning of power system

stabilizer for improving the damping performance in distribution network having static ZIP-EV load model. They did not present the behaviour of modes with simultaneous increase in load and generation.

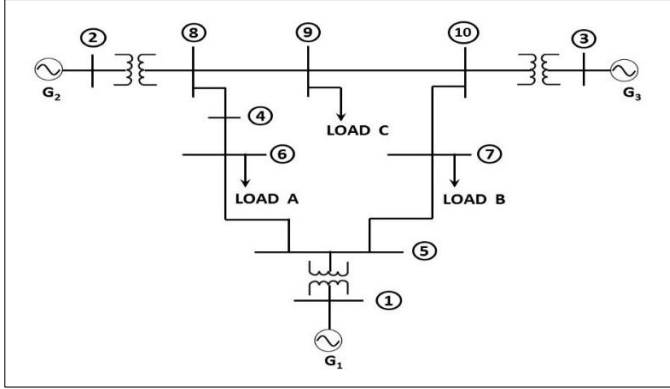


Figure 1: Single line diagram of Western States Coordinating Council System.

Source: Authors, (2025)

Hopf bifurcation phenomenon occurs when one of the Eigen value transitions from Left Hand Side (LHS) to Right Hand Side (RHS) of complex plane due to parametric change of any algebraic variable in system while remaining values are in LHS [9], [10]. Usage of Hopf bifurcation concept to power system domains can be seen in [11]. Application of the above phenomenon on the DAE's of South East Brazilian System can be seen in the [12] for dynamic voltage monitoring. Checking the available transfer capacity in a two area system by Hopf bifurcation is seen in works of [13]. They considered CZ model for loads during linearization process. [14] considered WSCC system with AVR and thoroughly studied the locus of critical mode that underwent Hopf bifurcation by defining six scenarios. In the work of [15], load change was considered at a single load bus whereas [14] considered load change at all the load buses. They considered CP type of load representation for load flow and linearization but didn't present any information on the Hopf bifurcation phenomenon if voltage dependent load models like CC, CZ, IND and EV are taken into account. Based on the literature accumulated above, the following objectives are taken into custody in this paper:

1. To evaluate the damping ratios of selected complex modes of various linearized models of system coupled with voltage dependent load models including EV type at nominal loading.
2. To compare the damping ratios of selected modes obtained in objective (1) and appreciate the improvement in damping ratios of selected mode with the proposed voltage dependent load models.
3. To evaluate the dynamic instability phenomenon via Hopf bifurcation with AVR in WSCC System by treating loads as voltage dependent type instead of constant power type as in [14].
4. To find out whether dynamic instability limit can be extended through Hopf bifurcation analysis with the inclusion of voltage dependent load models.

Section II briefs the details of WSCC System, modelling of AVR followed by the descriptions of Hopf bifurcation phenomenon. Section III covers the results and discusses the comparison of damping ratios of voltage dependent load models with constant power model described in [14]. Section IV states the conclusions.

## II. WSCC SYSTEM MODELLING WITH AVR AND LOAD MODELS ALONG WITH CONCEPT OF HOPF BIFURCATION

Section II.1 gives the information on WSCC System together with various voltage dependent load models. Section II.2 explains the structure of AVR Section II.3 details the Hopf bifurcation concept and Section II.4 deals with the connection of dots of the above sections through an algorithm to achieve the objectives outlined in Section I.

### II.1. MODELLING OF WSCC SYSTEM

The explanation for modelling of generators, networks and loads of WSCC system shown in Figure 1 are given in [16]. The procedure of linearization of machine rotor and stator equations, transmission circuit equations in power balance form and eigenvalue computation are written in [16], [17]. The nomenclature is taken from [16]. All generators of WSCC are modelled by two axis model. Network is represented by steady state model by not considering its transients. Mechanical damping is considered as given in [16]. Loads are represented by constant power for evaluating load flow during steady state and proposed voltage dependent load models for dynamic studies via linearization.

For representing CC and CZ models, exponential form is used [2], [3]. IND and EV models are represented by ZIP models taken from [4, 7].

$$P_{Li} = P_{Li0} \left[ \alpha_p + \beta_p \left( \frac{V_i}{V_{i0}} \right) + \gamma_p \left( \frac{V_i}{V_{i0}} \right)^2 \right] \quad (1)$$

$$Q_{Li} = Q_{Li0} \left[ \alpha_q + \beta_q \left( \frac{V_i}{V_{i0}} \right) + \gamma_q \left( \frac{V_i}{V_{i0}} \right)^2 \right] \quad (2)$$

The nomenclature used in equations (1) and (2) are as per [4], [7]. The proposed linearized voltage dependent load models in compact form using equations (1) and (2) that needs to be coupled to the linearized network and generator DAE's is shown in matrix equation (3).

$$\begin{bmatrix} \Delta P_{Li} \\ \Delta Q_{Li} \end{bmatrix} = \begin{bmatrix} 0 & \frac{P_{Li}}{V_{i0}} \left[ \frac{\beta_p + 2\gamma_p \left( \frac{V_i}{V_{i0}} \right)}{\alpha_p + \beta_p \left( \frac{V_i}{V_{i0}} \right) + \gamma_p \left( \frac{V_i}{V_{i0}} \right)^2} \right] \\ 0 & \frac{Q_{Li}}{V_{i0}} \left[ \frac{\beta_q + 2\gamma_q \left( \frac{V_i}{V_{i0}} \right)}{\alpha_q + \beta_q \left( \frac{V_i}{V_{i0}} \right) + \gamma_q \left( \frac{V_i}{V_{i0}} \right)^2} \right] \end{bmatrix} \begin{bmatrix} \Delta \theta_i \\ \Delta V_i \end{bmatrix} \quad (3)$$

### II.2. MODELLING OF AVR

Automatic Voltage Regulators are used to improve the synchronising torque and bring voltage near reference voltage set to it thus improving transient stability. The block diagram is shown in Figure 2.

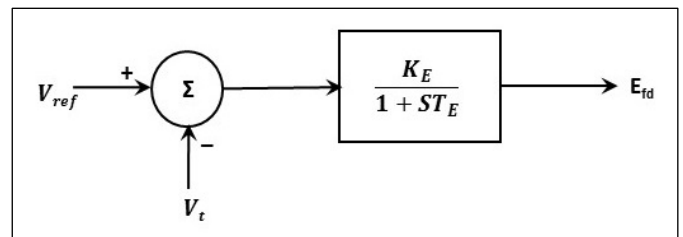


Figure 2: Block diagram of automatic voltage regulator.

Source: Authors, (2025)

Large gain and low time constant AVR as suggested in [16] is used in this paper. The above block parameters ensure rapid control of steady state voltage.

### II.3. HOPF BIFURCATION CONCEPT

Consider a system governed by DAE's (4-5) as given below:

$$\dot{x} = f(x, y, u) \quad (4)$$

$$g(x, y, p) = \epsilon \dot{y} \quad (5)$$

The order of vector  $y$ ,  $x$  are 'r' and 'k' respectively. 'x' is state vector, 'u' is control vector and 'p' is parameter variable that induces Hopf bifurcation in the system. 'y' covers algebraic variables. For a particular value of 'p', (5) can be solved to obtain the steady state point  $x_e$ . Equations (4) and (5) are linearized about  $x_e$  to get the eigenvalues for evaluating damping ratios and identifying critical modes. Equations (4) and (5) are linearized for given 'p<sup>0</sup>' and 'u' to get Equations (6) and (7).

$$\Delta \dot{x} = A_{f,x} \Delta x + A_{f,y} \Delta y \quad (6)$$

$$\epsilon \Delta \dot{y} = A_{g,x} \Delta x + A_{g,y} \Delta y \quad (7)$$

Eliminating  $\Delta y$  by setting  $\epsilon$  to zero in Equation (7), Equation (6) is simplified as given below.

$$\Delta \dot{x} = \left[ A_{f,x}^p - A_{f,y}^p A_{g,y}^{p-1} A_{g,x}^p \right] \Delta x = \left[ A_{sys}^p \right] \Delta x \quad (8)$$

where  $A_{f,x}^p$ ,  $A_{f,y}^p$ ,  $A_{g,x}^p$ ,  $A_{g,y}^p$  are given below:

$$A_{f,x}^p = \begin{bmatrix} \frac{\partial f_1}{\partial x_1} & \dots & \frac{\partial f_1}{\partial x_k} \\ \vdots & \ddots & \vdots \\ \frac{\partial f_k}{\partial x_1} & \dots & \frac{\partial f_k}{\partial x_k} \end{bmatrix}_{p^0}$$

$$A_{f,y}^p = \begin{bmatrix} \frac{\partial f_1}{\partial y_1} & \dots & \frac{\partial f_1}{\partial y_r} \\ \vdots & \ddots & \vdots \\ \frac{\partial f_k}{\partial y_1} & \dots & \frac{\partial f_k}{\partial y_r} \end{bmatrix}_{p^0}$$

$$A_{g,x}^p = \begin{bmatrix} \frac{\partial g_1}{\partial x_1} & \dots & \frac{\partial g_1}{\partial x_k} \\ \vdots & \ddots & \vdots \\ \frac{\partial g_k}{\partial x_1} & \dots & \frac{\partial g_k}{\partial x_k} \end{bmatrix}_{p^0}$$

$$A_{g,y}^p = \begin{bmatrix} \frac{\partial g_1}{\partial y_1} & \dots & \frac{\partial g_1}{\partial y_k} \\ \vdots & \ddots & \vdots \\ \frac{\partial g_r}{\partial y_1} & \dots & \frac{\partial g_r}{\partial y_k} \end{bmatrix}_{p^0}$$

$$A_{sys}^p = \left[ A_{f,x}^p - A_{f,y}^p A_{g,y}^{p-1} A_{g,x}^p \right] \quad (9)$$

where ' $A_{sys}^p$ ' is overall system matrix obtained to compute eigenvalues.

If all eigenvalues lie in the left half of complex plane, system is asymptotically stable, else system is unstable. The value of parameter for which just one pair of complex eigenvalues cross imaginary axis into right half of 's' plane while seeing that all the left over eigenvalues are housed in the left half plane of 's' plane, then such a phenomenon is coined as Hopf bifurcation.

### II.4. STEPS TO ASSESS DYNAMIC INSTABILITY VIA HOPF BIFURCATION

The following algorithm given in II.4.1 is applied on 6 cases defined as follows:

A, B, C: Variation in real power of load-A, load-B and load-C respectively with AVR.

D, E, F: Variation in  $\lambda$  (loading factor) corresponding to load-A, load-B and load-C respectively with AVR.

#### II.4.1. ALGORITHM

1. Using Newton-Raphson method, solve network equations treating loads as CP model.
2. Calculate synchronous machine variables by initializing DAE's of machine to 0 [17].
3. Calculate  $[A_{sys}^p]$  using linearized DAE model of machine, AVR, voltage dependent load model and network equations using method suggested in [6].
4. Evaluate eigenvalues of overall system matrix and calculate damping ratios of selected modes.
5. Apply change in real power / real and imaginary power of load buses using equation/s (10) and (11) with change in generations as elaborated in [14] and recalculate steps 1 to 4 for inducing Hopf bifurcation. ' $\lambda_i$ ' in Equations (10) and (11) is loading factor. The other variables in Equations (10)-(11) are defined in [6]

$$P_{Li} = P_{Li,o}(\lambda_i) \quad (10)$$

$$Q_{Li} = Q_{Li,o}(\lambda_i) \quad (11)$$

6. Mark the critical mode in each case and sketch the entire locus till the mode reaches imaginary axis line.
7. Evaluate steps 1-6 for each case and if Hopf bifurcation is reached, stop the algorithm. If step 1 cannot be solved, algorithm can be terminated.
8. Repeat steps 1-7 for all load models CC, CZ, IND and EV load models located at buses 6,7 and 9.

## III. RESULTS AND DISCUSSIONS

The system shown in Figure 1 has three generators  $G_1$ ,  $G_2$ ,  $G_3$  and loads 'A', 'B' and 'C'. The data is taken from [16]. The loads at nodes 6, 7 and 9 are designated as Load 'A', 'B' and 'C' respectively. Node-1 is taken as reference bus for load flow calculations and  $G_1$  is taken as reference generator to eliminate the zero eigenvalue obtained after the process of linearization. The development of programmes to evaluate power flows using CP model and linearization of WSCC system with AVR accompanied by CC, CZ, IND and EV type models was done in MATLAB 2020 software. The locus of critical mode for each type of load model for seeing the Hopf bifurcation was also furnished.

### III. 1. DISCUSSION REGARDING CASE 1

The results of load flow analysis with the data given in [15] was obtained exactly in this study. The MATLAB program was



developed for cases A-F defined in the previous section of the manuscript. The eigenvalue analysis done with CP type load representation for all cases A-F given in [14] is reproduced once again for ready reference as shown in Table 1. By modelling loads

at nodes 6, 7 and 9 as CC, CZ, IND and EV, the results of small signal stability analysis program was presented in Table 1. [14] gave the eigenvalue analysis results at nominal loading and critical

Table 1: Eigenvalue analysis with AVR for various types of load representation at nominal loading.

CP [14, 15]	CC	CZ	IND	EV
$-0.8492 \pm 12.7672i^a$	$-0.8410 \pm 12.7715i^a$	$-0.8348 \pm 12.7743i^a$	$-0.8424 \pm 12.7706i^a$	$-0.8403 \pm 12.7717i^a$
$-0.2512 \pm 8.3648i^b$	$-0.2341 \pm 8.3243i^b$	$-0.2214 \pm 8.2953i^b$	$-0.2419 \pm 8.3406i^b$	$-0.2464 \pm 8.3470i^b$
$-2.2421 \pm 3.0195i^c$	$-2.3070 \pm 2.8234i^c$	$-2.3559 \pm 2.6635i^c$	$-2.3591 \pm 2.7278i^c$	$-2.5161 \pm 2.3360i^c$
$-4.6654 \pm 1.3830i$	$-4.6682 \pm 1.3807i$	$-4.6708 \pm 1.3787i$	$-4.6693 \pm 1.3788i$	$-4.6749 \pm 1.3705i$
$-3.4855 \pm 1.0014i$	$-3.4931 \pm 1.0056i$	$-3.4996 \pm 1.0096i$	$-3.5044 \pm 1.0406i$	$-3.5482 \pm 1.1511i$
$-0.8882, -0.1365$	$-0.8855, -0.1385$	$-0.8830, -0.1401$	$-0.8843, -0.1381$	$-0.8792, -0.1387$
$-2.2613, -3.2258$	$-2.2396, -3.2258$	$-2.2204, -3.2258$	$-2.2008, -3.2258$	$-2.0755, -3.2258$

Source: Authors, (2025)

Table 2: Comparison of damping ratios of modes 'a-c' for various load representation at load buses at nominal loading.

Mode	Damping Ratios				
	CP [Calculated from 14, 15]	CC	CZ	IND	EV
a	<b>0.06637</b>	0.06570	0.06521	0.06582	0.06565
b	<b>0.03002</b>	0.02811	0.02668	0.02899	0.02951
c	0.59616	0.63273	0.66253	0.65414	<b>0.73282</b>

Source: Authors, (2025)

Table 3: Eigenvalue analysis corresponding to cases A-F for CC type of load representation at increased loading.

Case 'A'	Case 'B'	Case 'C'	Case 'D'	Case 'E'	Case 'F'
$-0.8088 \pm 12.7183i^a$	$-1.4198 \pm 11.8732i^a$	$-0.9843 \pm 12.3188i^a$	$-0.8901 \pm 12.6499i^a$	$-1.0147 \pm 12.3205i^a$	$-1.0880 \pm 12.2472i^a$
<b><math>-0.0001 \pm 8.5860i^b</math></b>	$-0.0838 \pm 8.0561i^b$	$-0.9184 \pm 7.9165i^b$	$-0.1698 \pm 7.8606i^b$	$-0.1985 \pm 7.9403i^b$	<b><math>-0.0006 \pm 8.8541i^b</math></b>
$-1.2493 \pm 4.7139i^c$	<b><math>-0.0001 \pm 6.5348i^c</math></b>	<b><math>-0.0001 \pm 5.7919i^c</math></b>	$-1.7254 \pm 4.4499i^c$	$-1.0403 \pm 5.6069i^c$	$-0.1033 \pm 6.2785i^c$
$-4.3314 \pm 1.2393i$	$-4.1034 \pm 1.0313i$	$-3.8938 \pm 1.0099i$	$-4.2110 \pm 1.3186i$	$-4.0460 \pm 1.0191i$	$-3.4648 \pm 0.9252i$
$-2.7580 \pm 1.5803i$	$-2.7619 \pm 1.3663i$	$-2.6600 \pm 1.6248i$	$-2.7887 \pm 1.4327i$	$-2.7694 \pm 1.2993i$	$-2.6358 \pm 1.5638i$
$-0.1407, -1.5464$	$-0.1364, -1.9495$	$-0.1337, -2.4048$	$-0.1406, -1.6124$	$-0.1376, -2.0914$	$-0.1361, -3.2527$
$-4.5421, -3.2258$	$-4.4771, -3.2258$	$-4.7029, -3.2258$	$-4.2924, -3.2258$	$-4.2151, -3.2258$	$-4.6412, -3.2258$

a), b) are swing modes associated with  $G_3$  and  $G_2$  respectively, c) Exciter mode of  $G_1$ .

Source: Authors, (2025)

loading for exploring the phenomenon of Hopf bifurcation. The authors of this manuscript calculated the damping ratios of modes of specific interest for CP type and presented in Table 2 for comparing the damping ratios of modes 'a', 'b' and 'c'. It can be seen that the mode that was subjected to Hopf bifurcation by inducing both increase in generation and loading was mode 'c' as stated in [14] whose damping ratio is 0.59616 at the nominal loading.

It is clear from Table 2 that both mode 'a' and 'b' damping ratios are highest when loads are represented by CP and least when represented by CZ. Mode 'c' damping ratio is highest if load is represented by EV and least if represented by CP.

### III. 1. DISCUSSION REGARDING CC TYPE

The results of eigenvalue analysis for cases A-F at higher loading are presented in Table 3. It can be seen that mode 'b' is the critical mode for case 'A' and case 'F' as depicted in Figure 3 and Table 3. Mode 'c' is undergoing Hopf bifurcation for case 'B' and case 'C'. The values of  $V_6$ ,  $V_7$  and  $V_9$  at critical loading  $P_6$  equal to 5.2703 p.u. for case 'A' are 0.7638 p.u., 0.9227 p.u., and 0.9606 p.u. respectively. The values of  $V_6$ ,  $V_7$  and  $V_9$  at critical loading  $P_7$  equal to 4.8366 p.u. for case 'B' are 0.9072 p.u., 0.7732 p.u. and 0.9625 p.u. respectively. The values of  $V_6$ ,  $V_7$  and  $V_9$  at critical loading  $P_9$  equal to 5.3714 p.u. for case 'C' are 0.9199 p.u., 0.9352 p.u. and 0.8683 p.u. respectively. Load flow doesn't converge

beyond  $\lambda_6$  equal to 3.2054 and  $\lambda_7$  equal to 4.3130 for cases 'D' and 'E' respectively. Hence the load flow results at loading of  $\lambda_6$  and  $\lambda_7$  for cases 'D' and 'E' gave the values of  $V_6$ ,  $V_7$  and  $V_9$  as 0.7071, 0.9172, 0.9541 and 0.8972, 0.7071, 0.9569 p.u. respectively. The values of  $V_6$ ,  $V_7$  and  $V_9$  at critical loading  $\lambda_9$  equal to 4.4985 for case 'F' are 0.9217 p.u., 0.9408 p.u. and 0.7870 p.u. respectively. The locus of mode 'b' for cases A, D, E and F is showcased in Figure 3 whereas the locus of mode 'c' for cases B, C, D and E is depicted in Figure 4.

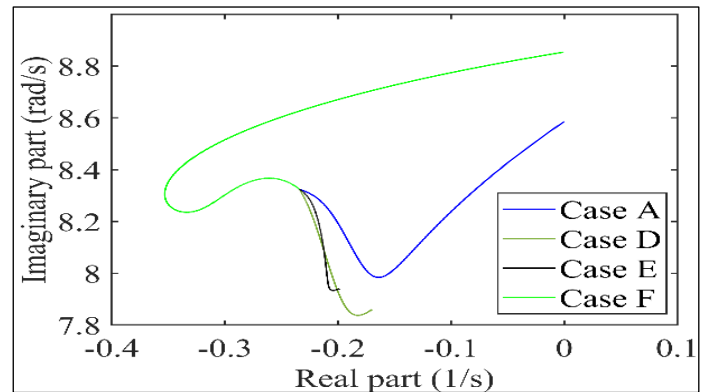


Figure 3: Locus of mode 'b' for cases A, D, E and F corresponding to CC load.

Source: Authors, (2025)

Table 4: Eigenvalue analysis corresponding to cases A-F for CZ type of load representation at increased loading.

Case 'A'	Case 'B'	Case 'C'	Case 'D'	Case 'E'	Case 'F'
-0.8021 ± 12.7157i <sup>a</sup>	-0.9434 ± 12.4524i <sup>a</sup>	-0.6827 ± 13.2105i <sup>a</sup>	-0.8770 ± 12.6651i <sup>a</sup>	-0.9056 ± 12.5878i <sup>a</sup>	-0.7877 ± 12.7764i <sup>a</sup>
-0.1804 ± 8.4371i <sup>b</sup>	-0.2166 ± 7.8690i <sup>b</sup>	<b>-0.0001 ± 9.4076i<sup>b</sup></b>	-0.1968 ± 7.8018i <sup>b</sup>	-0.2070 ± 7.8753i <sup>b</sup>	<b>-0.0002 ± 9.1413i<sup>b</sup></b>
-2.0965 ± 2.7039i <sup>c</sup>	-1.4274 ± 4.6266i <sup>c</sup>	-0.5633 ± 5.1919i <sup>c</sup>	-2.3133 ± 2.9785i <sup>c</sup>	-2.1429 ± 3.4784i <sup>c</sup>	-0.7761 ± 5.4474i <sup>c</sup>
-4.2353 ± 1.2171i	-3.9993 ± 0.9247i	-3.4867 ± 0.8158i	-4.2068 ± 1.3023i	-4.0591 ± 1.0184i	-3.2609 ± 0.9956i
-2.8017 ± 1.8685i	-2.7338 ± 1.3046i	-2.6337 ± 1.5575i	-2.7769 ± 1.4511i	-2.7239 ± 1.1688i	-2.6179 ± 1.4716i
-0.1397, -1.6851	-0.1324, -2.2182	-0.1240, -3.2915	-0.1420, -1.6083	-0.1379, -2.0701	-0.1327, -3.7022
-4.5763, -3.2258	-4.5077, -3.2258	-4.8035, -3.2258	-4.2516, -3.2258	-4.2045, -3.2258	-4.6927, -3.2258

a), b) are swing modes associated with  $G_3$  and  $G_2$  respectively, c) Exciter mode of  $G_1$ .

Source: Authors, (2025)

Table 5: Eigenvalue analysis corresponding to cases A-F for IND type of load representation at increased loading.

Case 'A'	Case 'B'	Case 'C'	Case 'D'	Case 'E'	Case 'F'
-0.8512 ± 12.6942i <sup>a</sup>	-1.4340 ± 11.7076i <sup>a</sup>	-0.9609 ± 12.1849i <sup>a</sup>	-0.9369 ± 12.6315i <sup>a</sup>	-1.3526 ± 11.9576i <sup>a</sup>	-1.0828 ± 12.0213i <sup>a</sup>
<b>-0.0004 ± 8.0582i<sup>b</sup></b>	-0.2585 ± 7.9714i <sup>b</sup>	-1.3752 ± 7.2085i <sup>b</sup>	-0.1876 ± 7.4743i <sup>b</sup>	-0.1681 ± 8.0306i <sup>b</sup>	-0.8617 ± 7.9821i <sup>b</sup>
-0.2307 ± 6.3536i <sup>c</sup>	<b>-0.0016 ± 6.6884i<sup>c</sup></b>	<b>-0.0001 ± 5.8430i<sup>c</sup></b>	<b>0.0035 ± 7.0330i<sup>c</sup></b>	<b>0.0000 ± 7.1063i<sup>c</sup></b>	<b>-0.0000 ± 6.3276i<sup>c</sup></b>
-4.4259 ± 1.2514i	-4.1699 ± 1.0823i	-4.0229 ± 1.0967i	-4.3210 ± 1.3538i	-4.1091 ± 1.0773i	-3.7576 ± 1.0324i
-2.7501 ± 1.4001i	-2.7728 ± 1.3759i	-2.6714 ± 1.6017i	-2.7733 ± 1.3029i	-2.8113 ± 1.3604i	-2.6565 ± 1.5797i
-0.1383, -1.4017	-0.1373, -1.7911	-0.1379, -2.1158	-0.1378, -1.4435	-0.1375, -1.9195	-0.1386, -2.6056
-4.4824, -3.2258	-4.4339, -3.2258	-4.6279, -3.2258	-4.2458, -3.2258	-4.1444, -3.2258	-4.5374, -3.2258

a), b) are swing modes associated with  $G_3$  and  $G_2$  respectively, c) Exciter mode of  $G_1$ .

Source: Authors, (2025)

Table 6: Eigenvalue analysis corresponding to cases A-F for EV type of load representation at increased loading.

Case 'A'	Case 'B'	Case 'C'	Case 'D'	Case 'E'	Case 'F'
-0.8104 ± 12.7079i <sup>a</sup>	-1.0123 ± 12.0948i <sup>a</sup>	-0.9633 ± 12.4625i <sup>a</sup>	-0.8805 ± 12.6703i <sup>a</sup>	-0.9193 ± 12.5059i <sup>a</sup>	-0.9007 ± 12.4753i <sup>a</sup>
-0.0111 ± 9.0028i <sup>b</sup>	-0.3182 ± 7.6866i <sup>b</sup>	-0.3303 ± 8.6146i <sup>b</sup>	<b>-0.0001 ± 7.7103i<sup>b</sup></b>	-0.2353 ± 7.8946i <sup>b</sup>	<b>-0.0002 ± 8.9506i<sup>b</sup></b>
-1.6566 ± 3.6309i <sup>c</sup>	-1.1562 ± 5.3749i <sup>c</sup>	<b>-0.0000 ± 5.8380i<sup>c</sup></b>	-1.3882 ± 4.6642i <sup>c</sup>	-1.9829 ± 4.0069i <sup>c</sup>	-0.4935 ± 5.8933i <sup>c</sup>
-4.2505 ± 1.2411i	-4.0168 ± 0.9094i	-3.3080 ± 0.8574i	-4.2300 ± 1.3464i	-4.0849 ± 1.0019i	-3.1924 ± 1.0484i
-2.7526 ± 1.7397i	-2.7737 ± 1.3957i	-2.6412 ± 1.6177i	-2.7187 ± 1.4396i	-2.7970 ± 1.3223i	-2.6194 ± 1.4972i
-0.1408, -1.6766	-0.1333, -2.1876	-0.1287, -3.6718	-0.1447, -1.5939	-0.1371, -2.0393	-0.1344, -3.8633
-4.6114, -3.2258	-4.4649, -3.2258	-4.8137, -3.2258	-4.4037, -3.2258	-4.1360, -3.2258	-4.7056, -3.2258

a), b) are swing modes associated with  $G_3$  and  $G_2$  respectively, c) Exciter mode of  $G_1$ .

Source: Authors, (2025)

### III. 2. DISCUSSION REGARDING CZ TYPE

The results of eigenvalue analysis for cases A-F at higher loading are presented in Table 4. It can be seen that mode 'b' is the critical mode for case 'C' and case 'F' as seen in Table 4. It is undergoing Hopf bifurcation as seen in Figure 5. The values of  $V_6$ ,  $V_7$  and  $V_9$  at stressed loading  $P_6$  equal to 5.39 p.u. for case 'A' are 0.7160 p.u., 0.9034 p.u., and 0.9490 p.u. respectively. Beyond the loading of 5.39 p.u. at bus 6, the load flow doesn't exist. The values of  $V_6$ ,  $V_7$  and  $V_9$  at stressed loading  $P_7$  equal to 4.98 p.u. for case 'B' are 0.8845 p.u., 0.7164 p.u., and 0.9498 p.u. respectively. Beyond the loading of 4.98 p.u. at bus 7, the load flow doesn't exist. The Hopf bifurcation occurs at a loading of 5.67 p.u. at bus 9 as seen in Table 4 for case 'C' where the values of  $V_6$ ,  $V_7$  and  $V_9$  are 0.8959 p.u., 0.9117 p.u. and 0.8366 p.u. respectively. Load flow does not converge beyond  $\lambda_6$  equal to 3.2054 and  $\lambda_7$  equal to 4.3130 for cases 'D' and 'E' respectively. Hence the load flow results at loading of  $\lambda_6$  and  $\lambda_7$  for cases 'D' and 'E' gave the values of  $V_6$ ,  $V_7$  and  $V_9$  as 0.7071, 0.9172, 0.9541 and 0.8972, 0.7071, 0.9569 p.u. respectively. The values of  $V_6$ ,  $V_7$  and  $V_9$  at critical loading  $\lambda_9$  equal to 4.6012 for case 'F' are 0.9142 p.u., 0.9337 p.u. and 0.7706 p.u. respectively. The locus of mode 'b' for cases A-F are displayed in Figure 5.

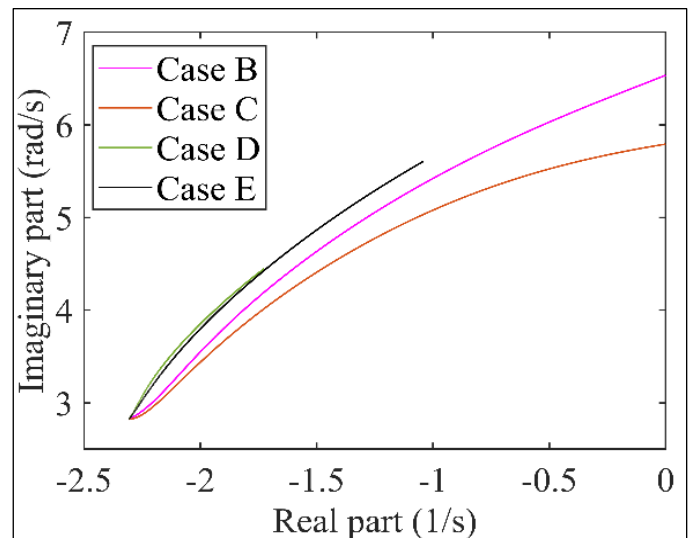


Figure 4: Locus of mode 'c' for cases B, C, D and E and F corresponding to CC load.

Source: Authors, (2025)

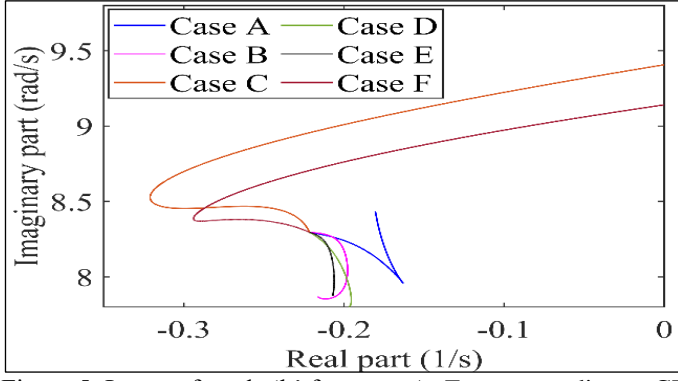


Figure 5: Locus of mode 'b' for cases A- F corresponding to CZ load.

Source: Authors, (2025)

### III. 3. DISCUSSION REGARDING IND TYPE

The results of eigenvalue analysis for cases A-F at higher loading are presented in Table 5. The Hopf bifurcation occurs at a loading of  $P_6$  equal to 5.0028 p.u. in mode 'b' for case 'A' as in Table 5. At this loading, the values of  $V_6$ ,  $V_7$  and  $V_9$  are 0.8135 p.u., 0.9432 p.u. and 0.9728 p.u. respectively. The Hopf bifurcation occurs at a loading of  $P_7$  equal to 4.6761 p.u. in mode 'b' for case 'B' as in Table 5. At this loading, the values of  $V_6$ ,  $V_7$  and  $V_9$  are 0.9204 p.u., 0.8062 p.u. and 0.9701 p.u. respectively. The Hopf bifurcation occurs at a loading of  $P_9$  equal to 5.13303 p.u. in mode 'c' for case 'C' as in Table 5.

At this loading, the values of  $V_6$ ,  $V_7$  and  $V_9$  are 0.8135 p.u., 0.9432 p.u. and 0.9728 p.u. respectively. The Hopf bifurcation occurs at a loading of  $\lambda_6$  equal to 3.0087 in mode 'c' for case 'D' as in Table 5. At this loading, the values of  $V_6$ ,  $V_7$  and  $V_9$  are 0.7686 p.u., 0.9389 p.u. and 0.9677 p.u. respectively. The Hopf bifurcation occurs at a loading of  $\lambda_7$  equal to 4.1638 in mode 'c' for case 'E' as in Table 5. At this loading, the values of  $V_6$ ,  $V_7$  and  $V_9$  are 0.9113 p.u., 0.7474 p.u. and 0.9650 p.u. respectively. The Hopf bifurcation occurs at a loading of  $\lambda_9$  equal to 4.2797 in mode 'c' for case 'F' as in Table 5. At this loading, the values of  $V_6$ ,  $V_7$  and  $V_9$  are 0.9349 p.u., 0.9534 p.u. and 0.8164 p.u. respectively. Figure 6 shows the locus of mode 'b' for case A and locus of mode 'c' for cases B-F.

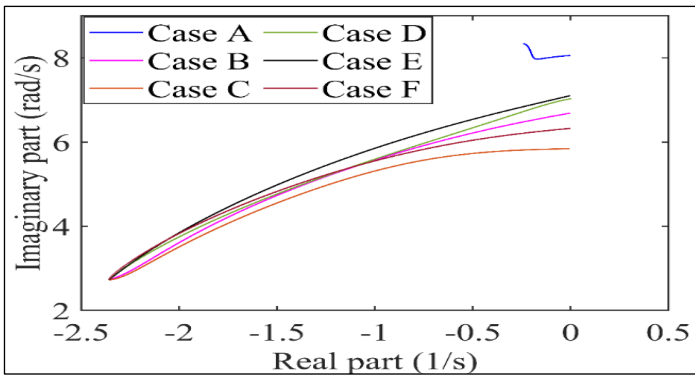


Figure 6: Locus of mode 'b' for case A and mode 'c' for cases B-F corresponding to IND load.

Source: Authors, (2025)

### III. 4. DISCUSSION REGARDING EV TYPE

The results of eigenvalue analysis for cases A-F at higher loading are displayed in Table 6. Load flow doesn't exist beyond the value of  $P_6$  equal to 5.39 p.u. for case 'A'. At the value of  $P_6$  equal to 5.39 p.u., the values of  $V_6$ ,  $V_7$  and  $V_9$  are 0.7160 p.u., 0.9034 p.u. and 0.9490 p.u. respectively. Load flow doesn't exist

beyond the value of  $P_7$  equal to 4.08 p.u. for case 'B'. At the value of  $P_7$  equal to 4.08 p.u., the values of  $V_6$ ,  $V_7$  and  $V_9$  are 0.8845 p.u., 0.7164 p.u. and 0.9498 p.u. respectively. At the critical loading of  $P_9$  equal to 5.74264 p.u., Hopf bifurcation is seen in mode 'c' for Case 'C' as shown in Table 6. The Hopf bifurcation occurs at a loading of  $\lambda_6$  equal to 3.19955 in mode 'b' for case 'D' as in Table 6. At this loading, the values of  $V_6$ ,  $V_7$  and  $V_9$  are 0.7686 p.u., 0.9389 p.u. and 0.9677 p.u. respectively. Load flow doesn't exist beyond the value of  $\lambda_7$  equal to 4.3130. Hence the eigenvalue analysis at this loading for case 'E' is given in Table 6. Hopf bifurcation is seen in mode 'b' for a loading factor  $\lambda_9$  equal to 4.65303 as seen in 6<sup>th</sup> column of Table 6 for case 'F'. Figure 7 and 8 shows the locus of mode 'b' and 'c' respectively for all the cases A-F.

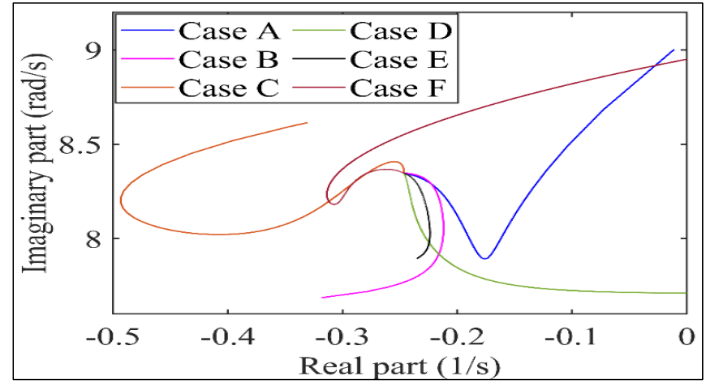


Figure 7: Locus of mode 'b' for cases A-F corresponding to EV load.

Source: Authors, (2025)

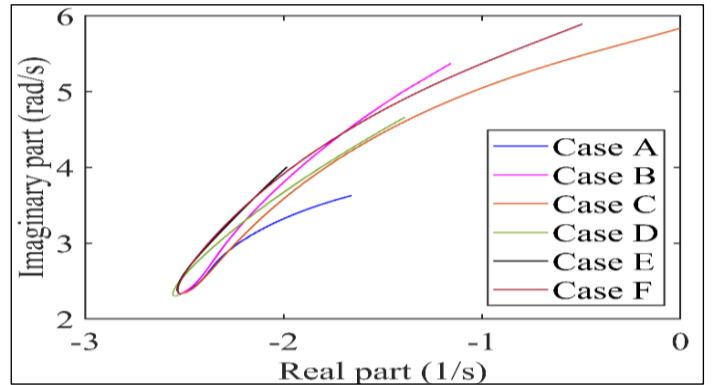


Figure 8: Locus of mode 'c' for cases A-F corresponding to EV load.

Source: Authors, (2025)

### III. 5. COMPARISON OF VOLTAGE DEPENDANT LOAD MODELS WITH CONSTANT POWER MODEL DESCRIBED IN [14]

The following discussions pertain to Tables 3-6. Hopf bifurcation occurs in mode 'c' for CP type of load representation for case 'C' at  $P_6$  value of 4.64123 p.u. [14]. By including IND type of load representation at all load buses, Hopf bifurcation is extended till 5.1330 p.u. for Case 'C' which is more than the value obtained for CP case as in [14]. Inclusion of CC type of load model extended the dynamic instability limit till  $P_6$  value of 5.3714 p.u. which is more than CP and IND cases. By representing loads as CZ, the Hopf bifurcation limit is extended till 5.6700 p.u. which is more than CP, IND, CC cases. When the small signal static EV load model is represented at all load buses, the value of  $P_6$  for case 'C' was obtained as 5.74264 which is highest among all the five

types of load models thus proving the ability of EV load model in extending the Hopf bifurcation limit via linearized analysis.

#### IV. CONCLUSIONS

Small signal stability analysis with AVR in WSCC system was done by using various exponential load models like CC, CZ and ZIP based industrial and EV load models. A comparison of damping ratios of complex modes of specific interest like swing modes and exciter mode of reference generator was compared with the non-voltage dependent load model presented in earlier work. The locus of critical mode for each load model was sketched after generating six cases reflecting increased loads and generation scenario to capture the Hopf bifurcation phenomenon.

#### VI AUTHOR'S CONTRIBUTION

**Conceptualization:** Ghousul Azam Shaik and Lakshmi Devi Aithepalli.

**Methodology:** Ghousul Azam Shaik and Lakshmi Devi Aithepalli.

**Investigation:** Ghousul Azam Shaik and Lakshmi Devi Aithepalli.

**Discussion of results:** Ghousul Azam Shaik and Lakshmi Devi Aithepalli.

**Writing – Original Draft:** Ghousul Azam Shaik and Lakshmi Devi Aithepalli.

**Writing – Review and Editing:** Ghousul Azam Shaik and Lakshmi Devi Aithepalli.

**Resources:** Ghousul Azam Shaik and Lakshmi Devi Aithepalli.

**Supervision:** Ghousul Azam Shaik and Lakshmi Devi Aithepalli.

**Approval of the final text:** Ghousul Azam Shaik and Lakshmi Devi Aithepalli.

#### VI. ACKNOWLEDGMENTS

The first author thanks University Grants Commission (UGC), New Delhi, India for granting Junior Research Fellowship to do Ph.D. research work at Department of Electrical and Electronics Engineering, SVU College of Engineering, Sri Venkateswara University, Tirupati, India.

#### VII. REFERENCES

[1] G.A. Shaik, and L.D. Aithepalli, "Application of Runge Kutta method for performing the time domain simulation on single machine infinite bus system with automatic voltage regulator.", In: V.I. George, K.V. Santhosh, S. Lakshminarayanan (eds) Control and Information Sciences. CISCON 2018. Lecture Notes in Electrical Engineering, vol 1140. Springer, Singapore. 2024. <https://doi.org/10.1007/978-981-99-9554-723>.

[2] C. Concordia, and S. Ihara, "Load representation in power systems stability studies," IEEE Transactions on Power Apparatus and Systems, vol. 101, no. 4, pp. 969–977, 1982.

[3] W.W. Price, C.W. Taylor, and G.J. Rogers, "Standard load models for power flow and dynamic performance simulation," IEEE Transactions on Power Systems, 10(CONF-940702), 1995. doi: 10.1109/59.466523.

[4] Y. Kongjeen, K. Bhummikittipich, N. Mithulanathan, I.S. Amiri, and P. Yupapin, "A modified backward and forward sweep method for microgrid load flow analysis under different electric vehicle load mathematical models," Electric Power Systems Research, vol. 168, pp. 46-54, 2019. <https://doi.org/10.1016/j.epsr.2018.10.031>.

[5] Ramya, and Rex Joseph, "A comparative analysis of constant impedance and constant power loads in a distribution network," International Journal of Electrical and Computer Engineering, vol. 14, No.6, pp. 6111-6121, 2024. <http://doi.org/10.11591/ijece.v14i6.pp6111-6121>.

[6] R.K. Ranjan, M.A. Pai, and P.W. Sauer, "Analytical formulation of small signal stability analysis of power systems with nonlinear load models," Sadhana, vol. 18, pp. 869-889, 1993.

[7] B.K. Jha, A. Kumar, D.K. Dheer, D. Singh, and R.K. Misra, "A modified current injection load flow method under different load model of EV for distribution system," International Transactions on Electrical Energy Systems, vol. 30, no. 4, pp. 1-25, 2020. <https://doi.org/10.1002/2050-7038.12284>.

[8] K. Yenchamchalit, Y. Kongjeen, K. Bhummikittipich, A. Stativa, and N. Mithulanathan, "Control of low-frequency oscillation on electrical power system under large EV-charging station installation using PSO technique for tuning PSS parameters," International Review of Electrical Engineering, vol. 16, no. 5, pp. 401-408, 2021. <https://doi.org/10.15866/iree.v16i5.20753>.

[9] J. Guckenheimer, and P. Holmes, Nonlinear Oscillations, Dynamical Systems, and Bifurcations of Vector Fields (Vol. 42), Springer Science & Business Media, 2013.

[10] Z.D. Georgiev, I.M. Uzunov, T.G. Todorov, and I.M. Trushev, "The Poincaré–Andronov–Hopf bifurcation theory and its application to nonlinear analysis of RC phase-shift oscillator" International Journal of Circuit Theory and Applications, 52(3), pp.1399-1437. 2024. doi.org/10.1002/cta.3783.

[11] Y. Zhi, H. Wajid, V.M. Venkatasubramanian, W. Ji, P. Panciatici, F. Xavier, and T. Gilles, "Computational methods for nonlinear analysis of Hopf bifurcations in power system models," Electrical Power System Research, vol. 212, pp.108574. 2022. <https://doi.org/10.1016/j.epsr.2022.108574>.

[12] M.E. Bento, and R.A. Ramos, "An approach for monitoring and updating the load margin of power systems in dynamic security assessment," Electrical Power System Research, vol. 198, pp.107365, 2021.

[13] J. Wei, G. Li, and M. Zhou, "Numerical bifurcation and its application in computation of available transfer capability," Applied Mathematics and Computation. 2015, vol. 252, pp. 568-574. <https://doi.org/10.1016/j.amc.2014.12.003>.

[14] G.A. Shaik, and L.D. Aithepalli, "Identification of Hopf bifurcation point using small signal stability analysis in a power system with increased load and generation," Third International Conference on Advances in Electrical, Computing, Communication and Sustainable Technologies (ICAECT), Bhilai, India, pp. 1-4, 2023. Doi.org/10.1109/ICAECT57570.2023.10118189.

[15] M.J. Laufenberg, M.A. Pai, and K.R. Padiyar, "Hopf bifurcation control in power systems with static var compensators," Electrical Power and Energy Systems, vol. 19, no. 5, pp. 339-347, 1997.

[16] M.A. Pai, D.P. Sen Gupta, and K.R. Padiyar, Small Signal Analysis of Power Systems, Narosa Publishing House, New Delhi, 2004.

[17] P.W. Sauer, M.A. Pai, and J.H. Chow, Power System Dynamics and Stability, Wiley-IEEE Press, New Jersey, 1998.



## RESEARCH ARTICLE

## OPEN ACCESS

# Hybrid FFT-ARMA-Burg Modeling and LSTM-Enhanced BBO Optimization for Fault Diagnosis in Induction Motors

Khadidja Boudraa<sup>1</sup>, Mohammed Assam Ouali<sup>2</sup> and Mohamed Ladjal<sup>3</sup>

<sup>1,2,3</sup> LASS, Laboratory of Signal and Systems Analysis, Department of Electronics, Faculty of Technology, University of M'sila, Algeria.

<sup>1</sup> <http://orcid.org/0009-0009-3890-878X> , <sup>2</sup> <http://orcid.org/0000-0003-3769-0730> , <sup>3</sup> <http://orcid.org/0000-0003-2730-0030> 

Email: [khadidja.boudraa@univ-msila.dz](mailto:khadidja.boudraa@univ-msila.dz), [mohamedassam.ouali@univ-msila.dz](mailto:mohamedassam.ouali@univ-msila.dz), [mohamedassam.ouali@univ-msila.dz](mailto:mohamedassam.ouali@univ-msila.dz).

## ARTICLE INFO

**Article History**

Received: December 29, 2024

Revised: January 31, 2025

Accepted: February 17, 2025

Published: March 31, 2025

**Keywords:**

Broken rotor bar detection,  
Induction motors,  
FFT-ARMA-Burg,  
BBO,  
LSTM.

## ABSTRACT

Induction motors (IM) are crucial in industrial systems, and fault diagnosis reliably and effectively is of importance for maintaining efficiency. The detection of a broken rotor bar (RBB) is one of the most challenging tasks in condition monitoring due to the complexity of fault features in motor current signals. This plans overcome by developing a hybrid diagnostic framework to enhance fault detection accuracy. The proposed approach fuses a hybrid spectral analysis technique that integrates the Fast Fourier Transform with an autoregressive moving average model estimated using Burg's method. This hybrid of FFT-ARMA-Burg enhances PSD representation. We employ biogeography-based optimization to optimally tune the parameters of the ARMA-Burg model for a better representation of fault-specific features. Further, this paper proposes an LSTM neural network that refines BBO-optimized parameters to improve fault frequency sensitivity. Experimental verification will demonstrate that the hybrid FFT-ARMA-Burg framework, combined with LSTM-enhanced BBO optimization, outperforms traditional motor current signature analysis (MCSA) and standalone ARMA-based methods in detecting broken rotor bars in squirrel cage induction motors. These findings confirm that the proposed methodology enhances broken rotor bar detection and supports predictive maintenance for improved reliability and efficiency in induction motors.



Copyright ©2025 by authors and Galileo Institute of Technology and Education of the Amazon (ITEGAM). This work is licensed under the Creative Commons Attribution International License (CC BY 4.0).

## I. INTRODUCTION

The diagnosis of induction motor faults is necessary to ensure operational efficiency and prevent sudden interruptions in industrial systems. Of the common faults, broken rotor bars are one of the most challenging to diagnose because of the low distinctiveness and complexity of fault-specific characteristics, which are often masked by noise within the motor current signals [1].

Traditional Motor Current Signature Analysis (MCSA) has been the widely used method for condition monitoring and fault detection, due to its non-intrusive nature and simplicity [1-3]. However, these approaches are subject to serious limitations while dealing with nonlinear systems, variable load conditions, and noisy environments, in which fault-specific features are easily masked [4].

The challenges faced in these areas have been overcome by different improvements in fault diagnosis techniques. In addition, signal processing techniques like the Fast Fourier Transform (FFT) and AutoRegressive Moving Average (ARMA) models have also been used to improve the fault detection as noted in [5]. The FFT is also a non-parametric method, which is widely used since it is efficient in the conversion of signals from the time domain to the spectral domain. However, its fixed resolution restricts it from detecting weak or short-lived faults [6].

The ARMA model is well known for its ability to analyze complex frequency patterns and pick out dominant frequency components, which makes it a dependable choice for detecting faults in induction machines. However, its fixed resolution can make it less effective when it comes to spotting weak or short-lived faults [7].

On the other hand, ARMA models, mostly estimated by Burg's method, provide a compact and exact parametric representation of the signal characteristics, which is why they are well suited for general signal analysis [8].

Hybrid schemes combining signal-based approaches with other methodologies have also been explored, for example, the combination of MCSA with vibration analysis has shown better reliability in fault detection[2-9]. However, most of these techniques depend on multi-sensor configurations that enhance the complexity and cost of the system. While FFT and ARMA-Burg each have individual limitations, these are partially addressed when the two methods are combined in a hybrid framework. FFT offers efficient global spectral analysis, but its fixed resolution limits its ability to detect weak or transient fault signatures [6]. ARMA-Burg, on the other hand, stands out for its ability to deliver precise and compact PSD estimations while also helping to filter out noise [6], [7]. That said, even when combined with other methods, there's still room for improvement to boost its accuracy and make it more reliable in the ever-changing conditions of industrial environments [5], [10]. R. Muñoz [7] highlighted how effective ARMA-Burg can be for PSD estimation but also noted its struggles with noisy data and fluctuating operating conditions. To overcome these disadvantages, the current study proposes a new hybrid diagnostic framework by fusing FFT and ARMA-Burg modeling with Biogeography-Based Optimization (BBO) and Long Short-Term Memory (LSTM) networks.

The inspiration from the migration patterns of species optimizes the parameters of ARMA-Burg via BBO to guarantee better noise immunity and improve the overall diagnostic performance [11-13]. This optimization method has shown to be highly effective in fine-tuning complex parametric models. Created by Simon in 2008 [11], BBO is known for its simple yet adaptable design and its impressive ability to conduct thorough global searches. These qualities make it especially effective for enhancing parameter estimation in noisy and constantly changing environments[12]. In addition, the proposed model incorporates an LSTM network, which enhances its sensitivity to fault-specific features, ensuring more accurate and reliable fault detection. Since it is a member of RNN, and taking advantage of that method's ability to learn dependencies over long ranges, combined with temporal tendencies, make the LSTM very suitable in analysis of noisy condition-based motor current signals[14]. Contrary to the traditional methods based on single signal processing, the proposed framework exploits LSTM to extract the fault-sensitive features that improve diagnostic reliability in nonlinear and dynamic environments [12], [15].

To the best of our knowledge, this is the first time that FFT, ARMA-Burg, BBO, and LSTM have been integrated within a single framework applied to fault detection of induction motors. The new approach experimentally assures better accuracy and reliability in fault detection than the traditional methods. It will contribute to providing an effective solution for predictive maintenance along with operational efficiency of industrial systems.

## II. FAULT DIAGNOSIS OF BRB IN IM

Broken rotor bars in induction motors are one of the most serious faults in industrial systems, which significantly affects the performance, efficiency, and reliability of the system. Such faults cause distortion in the electromagnetic field inside the motor, and the anomalies in the motor current signals are usually very subtle and masked by noise [1]. More specifically, broken rotor bars cause

irregularities in the magnetic air-gap field, which in turn produces sideband harmonic components in the current spectrum around the fundamental frequency. This behavior can be mathematically described as [1],[14]:

$$f_{bb} = (1 \pm 2ks)f_s \quad , \quad k = 1, 2, 3, \dots, \quad (1)$$

Where  $f_s$  is the fundamental frequency (Hz) and  $s$  is the slip. Among these, the first-order sidebands (*e.g.*  $k = 1$ ) are the most important in fault detection. The left sideband  $(1 - 2s)f_s$  is due to electrical or magnetic rotor asymmetries that result from broken rotor bars. On the other hand, the right sideband  $(1 + 2s)f_s$  is related to the speed ripple or rotor variations. Traditional diagnostic methods, like MCSA, are efficient in their performances but poor under dynamic and noisy environments and hence in need of adaptive solutions [16]. Advanced hybrid frameworks integrate the use of FFT for spectral modeling, ARMA-Burg for parametric modeling, BBO for parameter optimization, and LSTM networks aimed at increasing the diagnostic accuracy. Real-time accurate fault detection with a great increase in operational reliability and predictive maintenance of induction motors is attained by such integration.

## III. SPECTRAL TECHNIQUES

### III.1 FFT ANALYSIS

FFT analysis, therefore, is one of the important tools for spectral representation, as it allows efficient decomposition of signals into their frequency components for the identification of dominant features. The major strengths of FFT are its computational efficiency and suitability for stationary signals. However, FFT suffers from inferior resolution for closely spaced frequencies and dynamic signal variations, which may pose a serious challenge in detecting subtle faults like broken rotor bars in noisy environments [5,6].

### III.2 ARMA MODEL

Many processes can be well approximated by a linear rational model. The AutoRegressive Moving Average model, or ARMA( $p, q$ ), gives a generalized presentation of time-series data. It is defined by the following recurrence equation and it captures both the autoregressive (AR) and moving average (MA) components to accurately describe the dynamics of a process [7,8]:

$$x(n) = -\sum_{k=1}^p a_k x(n-k) + \sum_{k=0}^q b_k e(n-k) \quad (2)$$

Where the  $a_k$  and  $b_k$  are the coefficients of the AR and MA parts, respectively, and where  $e(n)$  is a centered white noise, Gaussian, mean zero and  $\sigma_e^2$  is variance. The number of the parameters  $p$  and  $q$  are known as the model orders. The transfer function is given by the expression[9]:

$$H(z) = \frac{B(z)}{A(z)} = \sum_{k=0}^{\infty} h_k z^{-k} = \frac{b_0 + b_1 z^{-1} + \dots + b_q z^{-q}}{1 + a_1 z^{-1} + \dots + a_p z^{-p}} \quad (3)$$

The roots of  $B(z)$  are known as the system zeros, while the roots of  $A(z)$  are known as the system poles of the ARMA ( $p, q$ ) process.

The spectral power density (PSD) of the ARMA (p, q) process is expressed as follows :

$$S_x(f) = \sigma_e^2 \frac{\left| 1 + \sum_{k=1}^q b_k e^{-j2\pi kf} \right|^2}{\left| 1 + \sum_{k=1}^p a_k e^{-j2\pi kf} \right|^2} \quad (4)$$

## BURG ALGORITHM IN CONVENTIONAL ESTIMATION TECHNIQUES

The Burg algorithm is an efficient recursive method and has widely been used for autoregressive parameter estimation in signal processing. Known to give the minimum of both forward and backward prediction errors  $(e_p^f, e_p^b)$ . Below are the forward prediction error and backward prediction error:

$$e_p^f(t) = x(t) + \sum_{i=1}^p a_p[i] x(t-i), \quad t = p+1, \dots, N \quad (5)$$

$$t = p+1, \dots, N \quad (6)$$

The algorithm guarantees model stability without the need for computing autocorrelation matrices, which makes it computationally efficient. Although it was originally developed for AR models, the Burg method has been adapted in combination with moving average (MA) components in order to improve the estimation of parameters in ARMA models. This adaptation enhances the capability of the algorithm to capture the complex features of signals, especially in dynamic and noisy environments, which makes it suitable for applications such as fault diagnosis in industrial systems [8,9].

## IV. OPTIMIZATION TECHNIQUES

### IV.1 BIOGEOGRAPHY-BASED OPTIMIZATION (BBO)

#### A. INTRODUCTION

Biogeography-Based Optimization (BBO) is a metaheuristic algorithm based on the biogeography itself, the studies that have sought to appeal to natural phenomena in defining the concepts of species distribution and migration across habitats. Introduced initially by MacArthur and Wilson in 1967 [13], it was further developed by Simon in 2008 [11]. In this sense, it would treat habitats as possible solutions by which possibility of iteratively improving those solutions comes from two main processes: migration and mutation. Its effectiveness lies in the maintenance of a trade-off between exploration and exploitation which is achieved through dynamic adjustment in terms of immigration ( $\lambda$ ) and emigration ( $\mu$ ) rates. This feature helps in avoiding early convergence on suboptimal solutions and ensures thorough exploration of the solution space [11,12].

#### B. APPLICATIONS OF BBO IN ARMA PARAMETER OPTIMIZATION

BBO offers distinct advantages over methods like Genetic Algorithms (GA), Particle Swarm Optimization (PSO), and Differential Evolution (DE) in ARMA model parameter optimization[11],[17].

BBO will be able to realize improved information sharing through a migration operator for effective exploration in diversified solution space with preservation of high-quality solutions[11,13].

Innovation and refinement can be balanced by tuning the immigration and emigration processes for fast convergence towards the optimal solution. The mutation step prevents the algorithm from getting trapped in suboptimal solutions while simultaneously ensuring it is fast and accurate enough for ARMA parameter estimation[11], [12], [17].

Mutation is a probabilistic operator used to modify one or more Suitability Index Variables (SIVs) of a randomly selected solution based on its probability of existence  $P_i$  the probability of mutation  $m_i$  is fixed according to the probability of the solution given by the equation (7)[11]:

$$m_i = m_{\max} \left( 1 - \frac{P_i}{P_{\max}} \right) \quad (7)$$

Where  $m_i$  the mutation rate for habitat  $i$ ,  $m_{\max}$  the maximum rate of mutation.  $P_{\max}$  the maximum probability of existence.

In spectral analysis for fault detection, the robustness of BBO to the challenges of non-convex optimization is invaluable in such applications as engine fault diagnosis. BBO leverages the concept of habitats-each representing potential solutions assessed through a Habitat Suitability Index-to optimize performance, through precise modeling of spectral characteristics. The immigration and emigration rates, determined by the count of species in each habitat, enable efficient exploration and exploitation of the solution space, making BBO an effective tool for signal processing tasks[18].

The immigration ( $\lambda$ ) and emigration ( $\mu$ ) rates for a habitat are determined by the number of species ( $S$ ), are given by:

$$\lambda_s = I \left( 1 - \frac{S}{S_{\max}} \right) \quad (8)$$

$$\mu_s = E \left( 1 - \frac{S}{S_{\max}} \right) \quad (9)$$

Where  $I$  is the maximum immigration rate,  $E$  is the maximum emigration rate and  $S_{\max}$  is the maximum number of species on the island.

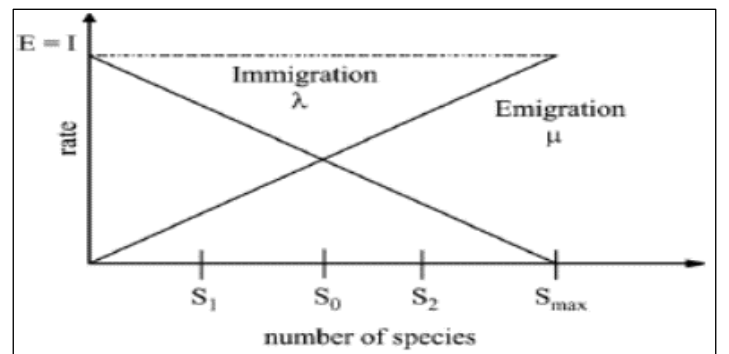


Figure 1: Linear Migration Model – Species ( $S$ ), Emigration ( $\mu$ ), and Immigration ( $\lambda$ ).

Source: [18].

The two basic operators that govern how BBO works are migration and mutation. In addition, an elitism strategy is adopted in the BBO algorithm, in order to keep the best solution in the new population.

The BBO algorithm framework is illustrated in Algorithm as [11]:

Algorithm : BBO algorithm



Initialize the BBO parameters:

Randomly generate a set of initial solutions (islands)

**while** halting criterion is not satisfied, **do**  
 Evaluate the fitness (HSI) of each solution  
 Calculate the number of species  $S$ , the immigration rate  $\lambda$  and emigration  $\mu$  for each solution.

Migration Operator:

**for**  $i = 1$  **to**  $N$  **do**

Use  $\lambda_i$  to decide, in a probabilistic way, to immigrate to  $X_i$

**If**  $\text{rand}(0, 1) < \lambda_i$  **then**

**for**  $j = 1$  **to**  $N$  **do**

Select the emigration island  $X_j$  with a probability to  $\mu_j$

**if**  $\text{rand}(0, 1) < \mu_j$  **then**

Replace a Suitability Index Variable (SIV) chosen randomly in  $X_i$  by the corresponding variable in  $X_j$

**End if**

**End for**

**End if**

**End for**

Mutation Operator:

Mutate the individuals at the mutation rate given by the equation (7).

Replacement of the population by descendants

Implement elitism

**End while**

Return the best solution found

## IV.2 MACHINE LEARNING: INTEGRATING LSTM NETWORKS INTO DIAGNOSTIC FRAMEWORKS

LSTM (Long short-term memory) networks are type of RNN (recurrent neural network) that are specialized in identifying long-term dependencies and patterns in time series. LSTMs have special mechanisms known as these are called a forgetting gate (decides what information to forget) and relearning gate (decides what to store) gates, which set these gates to 1 or 0. This allows them to effectively deal with complex, dynamic and noisy data [19].

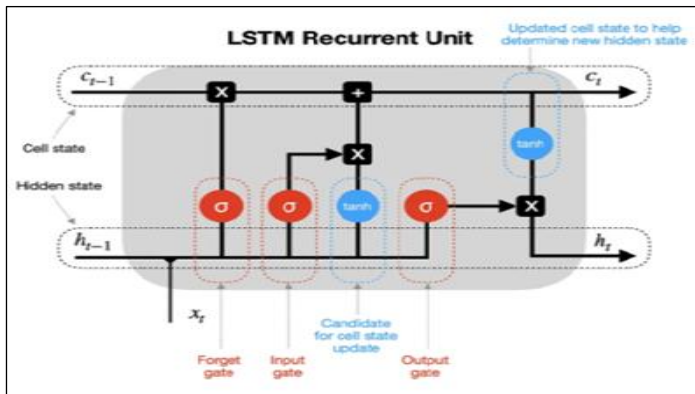


Figure 2: Long Short-Term Memory (LSTM) Neural Networks.  
 Source: towardsdatascience.com.

LSTMs bring a noticeable improvement in fault detection accuracy when used in diagnostic systems. They analyze motor current signals to uncover subtle fault patterns, even when these patterns are hidden by noise[12], [15]. The combination of ARMA-Burg modeling with Biogeography-Based Optimization (BBO)

greatly enhances the precision and sensitivity of parameter estimation using Long Short-Term Memory networks (LSTMs) to give more clear and reliable representations of faults in power spectral density (PSD) analysis. Moreover, their ability to adapt to changing operating conditions ensures a stable performance under a wide range of fault conditions [14], [15].

This approach combines the ability of LSTMs to analyze time-series data with the spectral and parametric strengths of FFT and ARMA-Burg. Together, these methods create a reliable system for identifying broken rotor bar faults in induction motors. By integrating advanced techniques from signal processing, optimization, and machine learning, this solution raises the bar for accurate and dependable fault detection.

By combining the ability of LSTMs to analyze time-based data with the spectral and parametric strengths of FFT and ARMA-Burg, this approach offers a complete and effective solution for identifying broken rotor bar faults in induction motors. This framework combines advanced signal processing, optimization, and machine learning techniques, offering significant improvements in fault diagnosis.

## V. METHODOLOGY

In this study, we present and demonstrate the validity and effectiveness of a new method for identifying broken rotor bars in induction motors. By integrating motor current signature analysis (MCSA) with advanced techniques in signal processing, optimization and machine learning, the method improves the accuracy and reliability of fault detection, even under diverse operating conditions.

The motor current signals were collected from a 2-pole, 2.5 KW squirrel-cage induction motor with a rated voltage of 400/230 V, operating under a torque load of 6 Nm. The motor parameters, including stator resistance ( $R_s = 7.8 \Omega$ ), stator inductance ( $L_s = 0.59 \text{ H}$ ), and other parameters values, are detailed in Table 1. To simulate real-world conditions, the signals were sampled at 1kHz and subjected to additive noise with a signal-to-noise ratio (SNR) of 60 dB. Both healthy and faulty conditions, including one and two broken rotor bars, were emulated.

MCSA was employed as the primary diagnostic technique to extract fault-related features from motor current signals. Preprocessed signals were segmented into smaller windows, enabling detailed analysis. Spectral analysis using the FFT identified dominant frequency components, while the ARMA model, estimated via Burg's method, captured fine-grained spectral details by modeling the power spectral density (PSD). The hybrid FFT-ARMA-Burg approach providing a complete and detailed spectral representation.

The ARMA-Burg parameters were optimized using BBO with objective function incorporated the Mean Squared Error (MSE) between the PSD of the faulty signal and a reference PSD, emphasizing accurate fault-specific feature representation. The MSE is calculated as [20]:

$$MSE = \frac{\sum_{k=1}^N (y_k - \hat{y}_k)^2}{N} = \frac{\sum_{k=1}^N e_k^2}{N} \quad (9)$$

Where  $y_k$  is the actual signal,  $\hat{y}_k$  is its estimate signal and  $N$  is the length of the data.

BBO's migration and mutation mechanisms ensured robust parameter optimization, addressing non-linearity and noise in the signal. To further enhance diagnostic accuracy, LSTM neural



networks were integrated into the framework. LSTM networks, designed to process sequential data, were trained on windowed motor current signals and their corresponding fault labels. This approach helped the model detect time-based patterns and uncover subtle fault features that traditional methods often failed to identify. Improving the LSTM greatly enhanced fault detection sensitivity, especially in noisy environments, by fine-tuning parameters optimized with BBO.

The method was compared to traditional MCSA and spectral analysis techniques to evaluate its performance. Tests were done under different noise levels, fault severities, and working conditions to ensure its reliability. By combining MCSA, FFT-ARMA-Burg modeling, BBO optimization, and LSTM improvements, it showed significant gains in accuracy and dependability for fault detection. This makes it a reliable tool for maintaining industrial systems.

## VI. SIMULATIONS RESULTS AND DISCUSSIONS

### VI.1 CHARACTERISTICS OF INDUCTION MOTORS

We performed the simulation in MATLAB 2018, using the motor current signals acquired under different fault conditions. The study used a 2.5 kW, 400/230 V, two-pole squirrel-cage induction motor with a torque of 6 Nm. The motor was connected to a stator fault simulator, whose parameters are defined in Table 1.

Table 1: Parameters of the Simulated Induction Motor.

Parameter	Value	Description
$R_s$	$7.828 \Omega$	Resistance of a stator phase
$L_s$	$0.589 \text{ H}$	Inductance of a stator phase
$L_r$	$4.6 \times 10^{-6} \text{ H}$	Equivalent rotor inductance
$L_m$	$4.64 \times 10^{-4} \text{ H}$	Mutual inductance between stator and rotor
$R_e$	$7.2 \times 10^{-4} \Omega$	Resistance of a short-circuit ring
$L_e$	$10^{-7} \text{ H}$	Inductance of a short-circuit ring
$N_r$	16	Number of rotor bars
$a$	$(P * 2\pi) / N_r$	Angle between two adjacent rotor bars
$R_{b0}$	$0.0015 \Omega$	Resistance of a rotor bar
$R_r$	$(2 * R_e / N_r) + (2 * R_{b1} * (1 - \cos(a)))$	Equivalent rotor resistance

Source: Authors,(2025).

We then analyzed the motor under healthy and faulty conditions, including scenarios with one broken and two broken rotor bars. Noise with an SNR of 60 dB was added to the motor current signals to simulate real-world conditions.

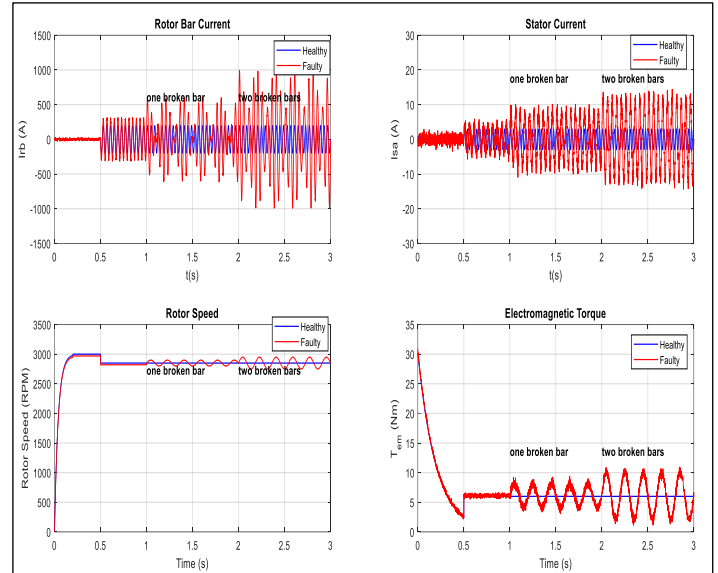


Figure 3: Simulated Rotor Bar Current, Stator Current, Rotor Speed, and Torque of Healthy and Faulty IM.

Source: Authors,(2025).

Figure 3 presents the results of the simulation for a healthy and a faulty induction motor by focusing on some key parameters, namely rotor bar current, stator current, rotor speed, and electromagnetic torque, for different fault conditions: one and two broken rotor bars.

For the healthy motor, all parameters are stable and smooth. During the first operating instants, the rotor speed grows from 0 to around 3000 RPM during the interval between 0 to 0.5 s, becoming a steady value.

At  $t = 0.5 \text{ sec}$ , the application of resistive torque of 6 Nm for an instant slows the motor shaft, and speed falls a little.

In contrast, faulty motors exhibit noticeable oscillations and distortions in all observed parameters. Large fluctuations of the rotor speed are observed around the steady-state value. Rotor bar and stator currents, which remain steady in the healthy motor, now become irregular and noisy due to rotor imbalance.

Regarding electromagnetic torque, the healthy motor settles with a value close to 6 Nm after load is applied. However, fault-induced oscillations increase in torque with the severity of the fault, showing obviously higher instability as the status deteriorates from one to two broken rotor bars.

This figure reveals the sensitivity of motor dynamics to mechanical imbalances and the serious impact of rotor faults and load application on motor performance. It justifies the effectiveness of the parameters for fault detection and analysis in induction motors.

### VI.2 HYBRID FAULT DETECTION USING FFT, ARMA-BURG, BBO ALGORITHM, AND LSTM MODELS

#### A. HYBRIDIZATION OF ARMA-BURG AND FFT

The ARMA-Burg model requires careful selection of the order to detect the frequencies associated with the error, which is achieved by applying FFT to identify spectral changes. FFT emphasizes the frequencies caused by the error, while ARMA-Burg filters the power spectral density through smoothing and noise reduction. This hybrid approach effectively enhances the visibility of the error, as shown in Figure 4 and Figure 5.

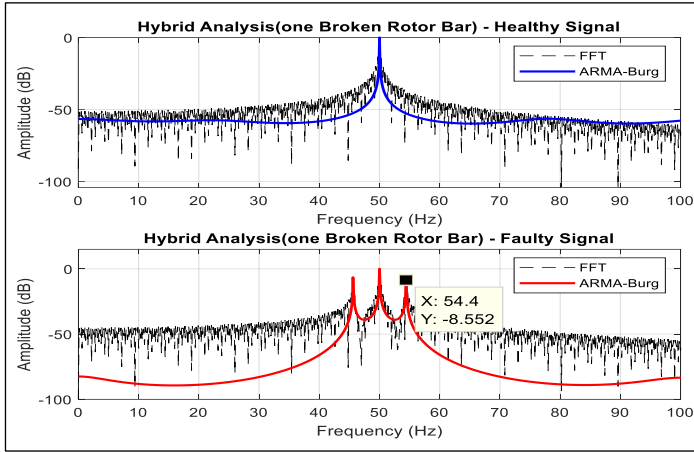


Figure 4: Hybrid FFT and ARMA-Burg Spectrum Analysis for One Broken Rotor Bars.

Source: Authors,(2025).

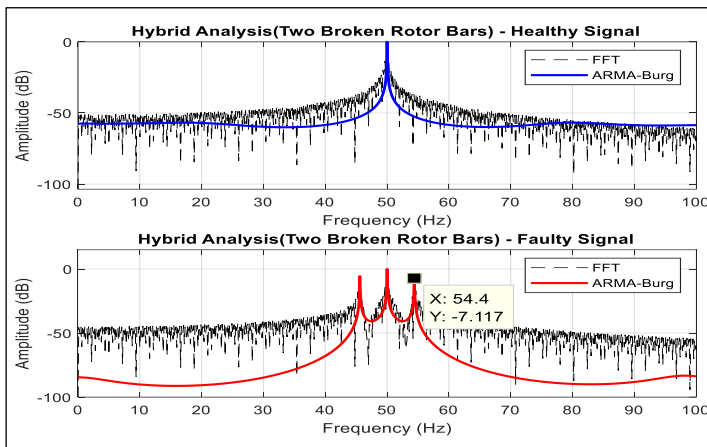


Figure 5: Hybrid FFT and ARMA-Burg Spectrum Analysis for Two Broken Rotor Bars.

Source: Authors,(2025).

The above figures present the frequency spectra for both healthy and faulty conditions, obtained through FFT and ARMA-Burg, respectively. Under the condition of a healthy signal, FFT has a dominant peak at 50 Hz; however, there is also noise and some irregular components, while ARMA-Burg smooths the spectrum and reduces the noise floor, hence improving clarity. In the one broken bar case, FFT reveals sidebands at approximately 54.4 Hz and 45.6 Hz, although finer details are obscured by noise; ARMA-Burg enhances these sidebands, and fault frequencies become more evident. For two broken bars, FFT presents increased sideband amplitudes related to fault severity, ARMA-Burg further sharpens the sidebands, showing clearly the increased fault severity.

## B. ARMA-Burg+FFT with BBO algorithm+LSTM

In order to optimize the parameters of ARMA-Burg, minimize MSE by the BBO algorithm and thus, enhance spectral clarity to realize fault frequency detection especially when noise is strong, the parameters of BBO are shown in Table 2. The LSTM network integrated with the ARMA-Burg+FFT model optimized by BBO improves the quality of error classification. The optimal features extracted from the MSE minimization process are used in the spectrum estimation using BBO as input to train the LSTM network. The detailed LSTM parameters are shown in the table 3.

Table 2: BBO Algorithm Parameters.

Parameter	Description	Value
Population Size	Number of candidate solutions	50
Max Generations	Maximum number of iterations	100
Mutation Rate	Probability of mutation	0.01
Migration Rate	Rate of exchanging features between solutions	0.2
Elitism Count	Number of elite solutions preserved	2
Fitness Function	Objective function (MSE minimization)	Mean Squared Error
Model Parameters	ARMA model order (p, q)	p = 40, q = 39

Source: Authors,(2025).

Table 3: LSTM Network Parameters.

Parameter	Description	Value from Your Code
Input Size	Number of input features	102 (signal + fault features)
Hidden Units	Number of LSTM units in the layer	64
Hidden Layers	Number of LSTM layers	1
Output Size	Number of output parameters	2 (p, q)
Fully Connected Layer Units	Units in the fully connected layer	32
Optimizer	Optimization algorithm for training	Adam
Batch Size	Number of samples per training batch	16
Epochs	Number of training iterations	50
Loss Function	Function to minimize during training	Regression Loss (regressionLayer)

Source: Authors,(2025).

As shown in Figure 6, the LSTM achieves a steady decrease in RMSE and Loss over 50 epochs and 150 iterations, indicating effective learning and optimization. The results confirm the network's capability to predict ARMA-Burg parameters accurately, ensuring robust performance.

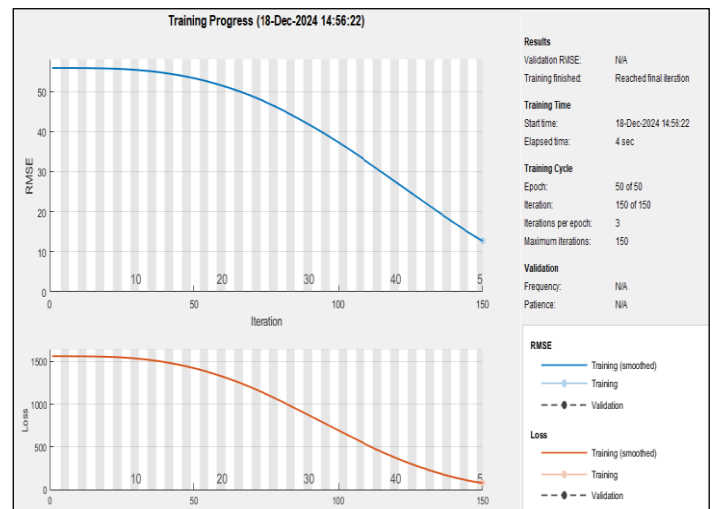


Figure 6. Training Progress of LSTM Network.

Source: Authors,(2025).

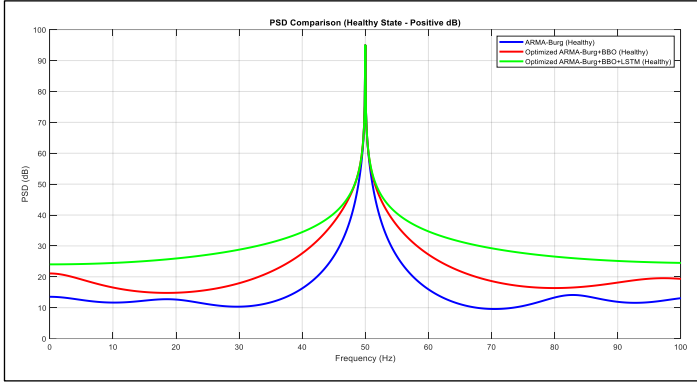
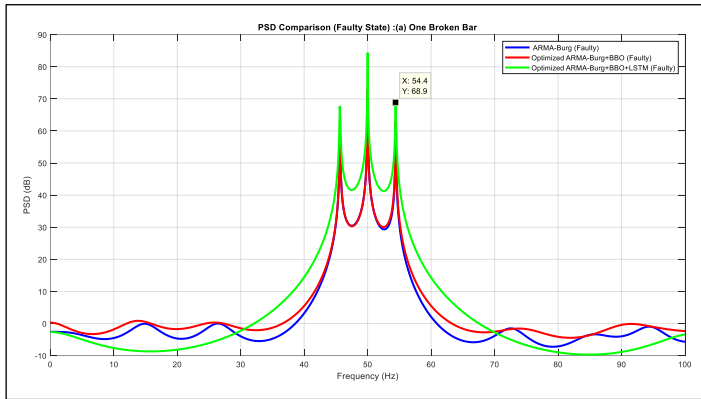
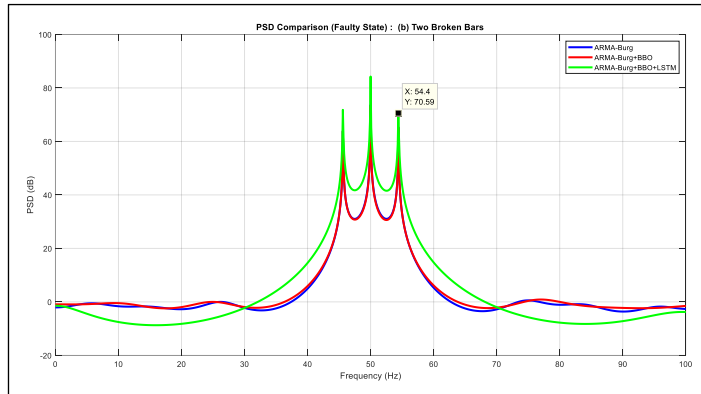


Figure 7: PSD Comparison of ARMA-Burg, ARMA-Burg+BBO, and ARMA-Burg+BBO+LSTM in Healthy State.  
Source: Authors,(2025).



(a)



(b)

Figure 8(a, b): PSD Comparison of ARMA-Burg, ARMA-Burg+BBO, and ARMA-Burg+BBO+LSTM for One Broken Bar (1BRB) and Two Broken Bars (2BRB) in the Faulty State.  
Source: Authors,(2025).

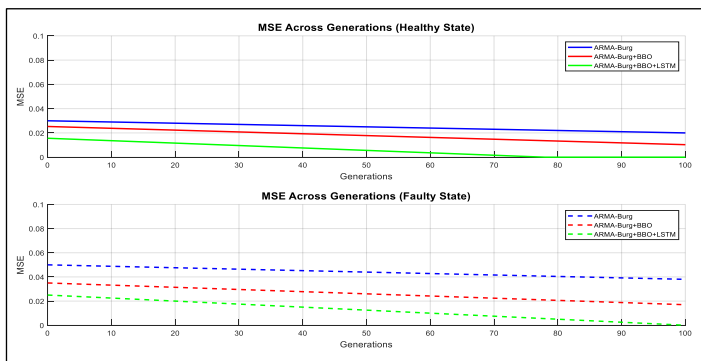


Figure 9: Mean Squared Error (MSE) Across generations.  
Source: Authors,(2025).

Results shown in Figure 7 for healthy state PSD comparison, Figure 8 (a) for faulty state PSD comparison of 1BRB and Figure 8 (b) for faulty state PSD comparison of 2BRB ,show the effectiveness of optimization methods in ARMA-Burg modeling under various operating conditions. In Figure 7, the ARMA-Burg+BBO+LSTM approach achieves the most accurate PSD estimation for the healthy state, closely aligning with the reference signal at the main frequency of 50 Hz. The ARMA-Burg+BBO method shows a moderate improvement over the default ARMA-Burg model, which exhibits the largest deviations from the true PSD.

In the faulty state, as illustrated in Figure 8(a) (1BRB) and Figure 8(b) (2BRB), the PSDs clearly highlight fault-induced sideband frequencies around 45.6 Hz and 54.4 Hz, caused by the slip factor. The increase in the number of broken bars (BRB) is reflected in the amplitude increase of these sideband frequencies. In the 1BRB case, it is shown that the fault-related components are captured effectively along the minimal error by ARMA-Burg+BBO+LSTM, ARMA-Burg+BBO indicates the moderate accuracy while ARMA-Burg has suffered in representing the spectral peaks with accuracy. The other simulated case of Figure 8(b) increases fault complexity for the presence of stronger sideband components at 45.6 Hz and 54.4 Hz with its harmonics in 2BRB case. ARMA-Burg+BBO+LSTM demonstrates superior accuracy in estimating the PSD, closely aligning with the true spectral components. In contrast, ARMA-Burg and ARMA-Burg+BBO produce higher and less precise estimations, particularly at critical frequencies such as the main frequency (50 Hz) and fault-induced sidebands (45.6 Hz and 54.4 Hz) .

The MSE variations across generations are presented in Figure 9, providing further confirmation of the performance differences among the methods. The subplot corresponding to the healthy state shows that the starting MSE was lower for all methods, indicating spectral structure with more simplicity. In the subplot at the bottom representing a faulty state, starting values of MSE are higher in the case of 1BRB and still higher for 2BRB due to increased spectral complexity introduced by additional fault-related components. In fact, the ARMA-Burg+BBO+LSTM scheme shows the fastest convergence in both considered faulty cases, besides yielding the minimum MSE, which further corroborates the robustness of this modeling approach against complex fault-induced spectral behavior. These results confirm that ARMA-Burg+BBO+LSTM has indeed been the most accurate and reliable for both healthy and faulty conditions up to now, doing much better under complicated conditions such as 2BRB.

## VII CONCLUSION

This paper proposes a robust framework for ARMA-Burg modeling, FFT preprocessing, Biogeography-Based Optimization (BBO), and Long Short-Term Memory (LSTM) network combinations to diagnose broken rotor bars in induction motors. The main emphasis of our study has been on optimizing the parameters of the ARMA-Burg model to enhance spectral clarity in accurate rotor fault detection, particularly under noisy conditions.

At first, FFT provided a preliminary spectral analysis, and BBO minimized MSE for the power spectral density estimation refinement. Later, LSTM improved the feature representation for the fault, capturing temporal dependencies to enable the reliable classification of faults. The results reflected a clear improvement in spectral clarity-some with a reduced noise background and highly distinct peaks of fault frequency in the PSD comparisons.

The proposed BBO and LSTM approach presented the best Broken Rotor Bars fault detection compared to other approaches in terms of progressive reduction of MSEs and showing clear sidebands in faulty states. Such results confirm that the approach would work well in properly recognizing and classifying states on induction motors, whether these are healthy or in faulty conditions, such as having one or two broken rotor bars.

This hybrid methodology finally provides an effective tool for signal analysis and fault diagnosis, enhancing accuracy by reducing computational errors and offering practical applicability in predictive maintenance systems for rotating machinery. Further research work may extend the framework to other types of machinery faults and further refine the models for real-time applications.

## VIII. AUTHOR'S CONTRIBUTION

**Conceptualization:** khadidja Boudraa, Mohammed Assam Ouali and Mohamed Ladjal.

**Methodology:** khadidja Boudraa, Mohammed Assam Ouali and Mohamed Ladjal.

**Investigation:** khadidja Boudraa, Mohammed Assam Ouali and Mohamed Ladjal.

**Discussion of results:** khadidja Boudraa, Mohammed Assam Ouali and Mohamed Ladjal.

**Writing – Original Draft:** khadidja Boudraa, Mohammed Assam Ouali and Mohamed Ladjal.

**Writing – Review and Editing:** khadidja Boudraa, Mohammed Assam Ouali and Mohamed Ladjal.

**Resources:** khadidja Boudraa, Mohammed Assam Ouali and Mohamed Ladjal.

**Supervision:** Mohamed Ladjal and Mohammed Assam Ouali.

**Approval of the final text:** khadidja Boudraa, Mohammed Assam Ouali and Mohamed Ladjal.

## VIII. REFERENCES

- [1] K. Barrera-Llana, J. Burriel-Valencia, Á. Sapena-Bañó, and F. Puig-Vidal, "A comparative analysis of deep learning convolutional neural network architectures for fault diagnosis of broken rotor bars in induction motors," *Sensors*, vol. 23, no. 19, p. 8196, 2023, doi: 10.3390/s23198196.
- [2] F. J. Villalobos-Pina, J. A. Reyes-Malanche, E. Cabal-Yepez, and E. Ramirez-Velasco, "Electric Fault Diagnosis in Induction Machines Using Motor Current Signature Analysis (MCSA)," in *Time Series Analysis - Recent Advances, New Perspectives and Applications*, IntechOpen, 2024, doi: 10.5772/intechopen.1004002.
- [3] N. Bhole and S. Ghodke, "Motor Current Signature Analysis for Fault Detection of Induction Machine—A Review," in *Proceedings of the 2021 4th Biennial International Conference on Nascent Technologies in Engineering (ICNTE)*, Navi Mumbai, India, Jan. 15–16, 2021, pp. 1–6, doi: 10.1109/ICNTE51185.2021.9487696.
- [4] T. P. Banerjee, S. Roy, and B. K. Panigrahi, "Fault Signature Identification for BLDC Motor Drive System - A Statistical Signal Fusion Approach," *Time Series Analysis - Recent Advances, New Perspectives and Applications*, IntechOpen, 2024.
- [5] F. M. Garcia-Guevara, F. J. Villalobos-Piña, J. A. Morones-Alba, R. Alvarez-Salas, F. Pazos-Flores and J. A. Alvarez-Salas, "Experimental system for induction motor fault diagnosis: FFT and AR model schemes evaluation," 2015 12th International Conference on Electrical Engineering, Computing Science and Automatic Control (CCE), Mexico City, Mexico, 2015, pp. 1–6, doi: 10.1109/ICEEE.2015.7357998.
- [6] Y. -L. Shen and R. -J. Wai, "Fast-Fourier-Transform Enhanced Progressive Singular-Value-Decomposition Algorithm in Double Diagnostic Window Frame for Weak Arc Fault Detection," in *IEEE Access*, vol. 10, pp. 39752–39768, 2022, doi: 10.1109/ACCESS.2022.3165793
- [7] R. Muñoz, "Using an autoregressive model in the detection of abnormal characteristics of squirrel cage induction motors," *Electric Power Systems Research*, vol. 55, pp. 73–77, 2000. DOI: 10.1016/S0378-7796(99)00101-7.
- [8] S. J. Orfanidis, *Introduction to Signal Processing*. Englewood Cliffs, NJ, USA: Prentice-Hall, 1995.
- [9] N. Moal and J.-J. Fuchs, "Estimation de l'ordre et identification des paramètres d'un processus ARMA," in *16ème Colloque sur le Traitement du Signal et des Images*, Grenoble, France: GRETSI, pp. 511–514, Sep. 1997.
- [10] A. C. Abhinandan and M. H. Sidram, "Fault diagnosis of an induction motor through motor current signature analysis, FFT & DWT analysis," 2017 4th IEEE International Conference on Engineering Technologies and Applied Sciences (ICETAS), Salmabad, Bahrain, 2017, pp. 1–7, doi: 10.1109/ICETAS.2017.8277869.
- [11] D. Simon, "Biogeography-Based Optimization," in *IEEE Transactions on Evolutionary Computation*, vol. 12, no. 6, pp. 702–713, Dec. 2008, doi: 10.1109/TEVC.2008.919004.
- [12] D. Simon, "A dynamic system model of biogeography-based optimization," *Applied Soft Computing*, vol. 11, no. 8, pp. 5652–5661, 2011.
- [13] R. H. MacArthur and E. O. Wilson, "The Theory of Island Biogeography", vol. 1. Princeton, NJ, USA: Princeton University Press, 1967.
- [14] F. Rayhan et al., "A Bi-directional Temporal Sequence Approach for Condition Monitoring of Broken Rotor Bar in Three-Phase Induction Motors," 2023 International Conference on Electrical, Computer and Communication Engineering (ECCE), Chittagong, Bangladesh, 2023, pp. 1–6, doi: 10.1109/ECCE57851.2023.10101518.
- [15] S. Gundewar, P. Kane, and A. Andhare, "Detection of broken rotor bar fault in an induction motor using convolution neural network," *Journal of Advanced Mechanical Design, Systems, and Manufacturing*, vol. 16, no. 2, pp. JAMDSM0020–JAMDSM0020, 2022, doi: 10.1299/jamdsm.2022jamdsm0020.
- [16] F. Giri, Ed., "AC Electric Motors Control: Advanced Design Techniques and Applications". Wiley, 2013.
- [17] H. Ma, D. Simon, P. Siarry, Z. Yang and M. Fei, "Biogeography-Based Optimization: A 10-Year Review," in *IEEE Transactions on Emerging Topics in Computational Intelligence*, vol. 1, no. 5, pp. 391–407, Oct. 2017, doi: 10.1109/TETCI.2017.2739124.
- [18] Y. Zheng, X. Lu, M. Zhang, and S. Chen, "Biogeography-based optimization," in *Biogeography-Based Optimization: Algorithms and Applications*, Singapore: Springer, 2019. Doi: 10.1007/978-981-13-2586-1\_2.
- [19] S. Hochreiter and J. Schmidhuber, "Long Short-Term Memory," *Neural Computation*, vol. 9, no. 8, pp. 1735–1780, Nov. 1997.
- [20] Z. S. Abo-Hammour, O. M. K. Alsmadi, A. M. Al-Smadi, and M. A. Al-Ajlouni, "ARMA model order and parameter estimation using genetic algorithms," *Mathematical and Computer Modelling of Dynamical Systems*, vol. 18, no. 2, pp. 201–221, 2012, doi: 10.1080/13873954.2011.631283.









## RESEARCH ARTICLE

## OPEN ACCESS

## ENHANCING SENTIMENT ANALYSIS IN TOURISM REVIEWS: A COMPARATIVE STUDY OF ALGORITHMS IN ASPECT-BASED SENTIMENT ANALYSIS AND EMOTION DETECTION

Viktor Handrianus Pranatawijaya<sup>1</sup>, Putu Bagus Adidyana Anugrah Putra<sup>2</sup>, Ressa Priskila<sup>3</sup> and Novera Kristianti<sup>4</sup>

<sup>1,2,3,4</sup> Informatics Engineering Department, Faculty of Engineering, University of Palangka Raya, Indonesia. <sup>2, 3</sup> Example Institute - EI. Toronto, Canada.

<sup>1</sup><http://orcid.org/0000-0002-3301-0702> , <sup>2</sup><http://orcid.org/0000-0003-1986-125X> , <sup>3</sup><http://orcid.org/0009-0000-6606-5120> , <sup>4</sup><http://orcid.org/0000-0003-1536-2875> 

Email: [viktorhp@it.upr.ac.id](mailto:viktorhp@it.upr.ac.id), [putubagus@it.upr.ac.id](mailto:putubagus@it.upr.ac.id), [ressa@it.upr.ac.id](mailto:ressa@it.upr.ac.id), [noverakristianti@eng.upr.ac.id](mailto:noverakristianti@eng.upr.ac.id)

## ARTICLE INFO

**Article History**

Received: January 06, 2025

Revised: February 20, 2025

Accepted: March 15, 2025

Published: March 31, 2025

**Keywords:**

Aspect-Based Sentiment Analysis (ABSA),

Emotion Detection,

Machine Learning,

Deep Learning,

Tourism reviews.

## ABSTRACT

Information technology now enables utilizing online review data to support the Sustainable Development Goals (SDGs). However, traditional sentiment analysis often cannot capture the complexity of sentiment. This research aims to combine Aspect-Based Sentiment Analysis (ABSA) and emotion detection for a more in-depth analysis of tourism reviews in Palangka Raya City and compare the performance of various algorithms. Review data was taken from Google Maps and analyzed using BoW, LDA, NRC Emotion Lexicon, machine learning, and deep learning algorithms such as Logistic Regression (LR), Naïve Bayes (NB), Random Forest (RF), Support Vector Machine (SVM), K-Nearest Neighbors (KNN), Gradient Boosting (GB), Decision Tree (DT), and BERT. Most of the reviews are positive, with the dominance of the emotions of anticipation and joy. The combination of cross-validation with the best parameters from GridSearchCV resulted in the most significant increase in model accuracy. The SVM model performed better than other machine learning and deep learning algorithms, with accuracy and F1-score reaching 99.86%. The combination of ABSA and emotion detection improves the understanding of sentiment and emotion to support strategic decisions in tourism.



Copyright ©2025 by authors and Galileo Institute of Technology and Education of the Amazon (ITEGAM). This work is licensed under the Creative Commons Attribution International License (CC BY 4.0).

### 1. INTRODUCTION

Developments in information technology have expanded the utilization of online review data to support the Sustainable Development Goals (SDGs) in increasingly significant ways. Sentiment analysis, which traditionally classifies reviews as positive, negative, or neutral [1], [2] often falls short of capturing the more complex nuances of sentiment [3]. To overcome these limitations, this research aims to adopt a more comprehensive approach by combining aspect-based sentiment analysis (ABSA) and emotion detection. This approach enables a more in-depth analysis by categorizing review data based on aspects and identifying sentiments on each aspect [4], [5]. Thus, this research not only provides an overview of sentiment but also enables the identification of specific strengths and weaknesses of the reviewed

product or service, ultimately supporting more effective strategic decisions [6], [7].

In line with SDG 8, which encourages inclusive and sustainable economic growth and job creation, a better understanding of sentiment and emotions in tourism reviews can help businesses improve services and attract more tourists [8]. This in turn can increase employment and income for local communities. In addition, SDG 9 emphasizes the importance of sustainable infrastructure development and the promotion of innovation [9]. By utilizing data analysis technologies such as those used in this study, the tourism sector can innovate marketing and service strategies, thereby promoting higher competitiveness [10]. In this study, aspect analysis was conducted through topic modeling using Bag of Words (BoW) and Latent Dirichlet Allocation (LDA) methods, while emotion detection used the NRC Emotion Lexicon based on Plutchik's emotion model. This model

identifies basic emotions in text with two main dimensions: valence and arousal. Valence indicates whether the emotion is positive or negative, while arousal measures emotional intensity [11]. An understanding of valence and arousal helps determine whether the text reflects satisfaction or dissatisfaction as well as the emotional intensity involved. Combining aspect-based sentiment analysis and emotion detection enables better decision-making, increases user satisfaction, and improves service quality [12].

This research focuses on analyzing sentiments and emotions towards various aspects of tourism in Palangka Raya City based on reviews on Google Maps. To achieve this goal, this research uses various Machine Learning and Deep Learning methods such as Logistic Regression (LR), Naive Bayes (NB), Random Forest (RF), Support Vector Machine (SVM), K-Nearest Neighbors (KNN), Gradient Boosting (GD), Decision Tree (DT), and BERT [13]. This method was chosen for its ability to effectively handle various aspects of review data. The main objectives of this research are to analyze sentiment, identify relevant aspects of tourism, analyze valence and arousal in reviews, and compare the performance of various machine learning and deep learning algorithms in classifying sentiment and emotions.

The main innovation of this research lies in the combined application of aspect-based sentiment analysis and emotion detection in the context of tourism in Palangka Raya City, Indonesia. This research compares the performance of various machine learning and deep learning algorithms on a specific dataset to contribute to developing sentiment analysis. To improve the performance of the analysis, labeling is performed using VADER, TextBlob, Flair, and BERT, with the final sentiment determined through the majority voting method. VADER extracts sentiment features from unlabeled datasets, while TextBlob provides high accuracy through sentiment dictionaries and statistical models. Flair shows effectiveness in handling various language nuances, while BERT improves accuracy by deeply understanding language context and nuances [14].

To improve the performance of machine learning models, this research also conducted several experiments, including oversampling, cross-validation, GridSearchCV, and cross-validation using the best parameters from GridSearchCV [15]. Oversampling is used to overcome the problem of class imbalance, cross-validation to estimate model performance more accurately, GridSearchCV to find the best combination of parameters, and cross-validation with the best parameters to get more reliable results [16]. The results of this study are expected to provide a deeper understanding of tourists' perceptions of various aspects of tourism in Palangka Raya City and provide policy recommendations to improve the attractiveness and quality of tourism in the city. This research is limited to analyzing reviews on Google Maps regarding tourist attractions in Palangka Raya City and focuses on sentiments and emotions that are explicitly stated in the review text. Thus, it is expected that this research can contribute to the development of sentiment analysis and support data-driven decision-making in the tourism sector.

## II. RELATED WORKS

Sentiment analysis research has rapidly grown, emphasizing the importance of emotional understanding in user interactions. Early research focused on text polarity, but aspect-based approaches are crucial for deeper business insights. Studies by [17] and [18] support this. [19] applied sentiment analysis to Twitter using Naïve Bayes and SVM, with SVM achieving 89% accuracy. [20] evaluated algorithms like Random Forest, KNN,

and Naïve Bayes on social media, finding Naïve Bayes most accurate at 92.01%.

Research by [21] explored the polarization of positive and negative sentiments in user reviews on Twitter, using Naïve Bayes (NB), SVM, and logistic regression (LR). The findings showed an LR model accuracy of 77%, higher than SVM (76%) and NB (70%). [22] also compared the performance of Naïve Bayes, SVM, and Random Forest, finding that Naïve Bayes achieved the highest accuracy of 81%, while SVM and Random Forest recorded accuracies of 80% and 76%, respectively. Research by [23] that BERT outperformed traditional machine learning algorithms in sentiment analysis, with accuracy, precision, recall, and F-scores of 85%, 84%, 87%, and 85% on social media datasets, respectively. The importance of the integration between sentiment analysis and emotion detection is clear, as emotion detection can provide more comprehensive insights into user opinions. With the ability to identify specific emotions such as happy, sad, angry, or fearful, understanding the background of the emerging sentiment can be improved [24].

Research by [12] applied various machine learning and deep learning methods to detect emotions in textual content, where the BERT model showed the highest accuracy on the AIT-2018 and ISEAR datasets. Another study analyzed hate speech against Asians on Twitter by building prediction models using machine learning algorithms and deep learning methods such as Long Short-Term Memory (LSTM) and Bidirectional LSTM. Results showed that logistic regression achieved the highest F1 score of 0.72, while BERT recorded the best F1 score among deep learning models with a value of 0.85 [25]. Overall, significant advances in sentiment analysis and emotion detection demonstrate the effectiveness of these methods. However, there are opportunities for innovation through the integration of both approaches. This research focuses on developing techniques that combine sentiment analysis and emotion detection to improve understanding of user interaction dynamics and provide more relevant recommendations for product and service development.

## III. MATERIALS AND METHODS

The method used in this research is shown in Figure 1.

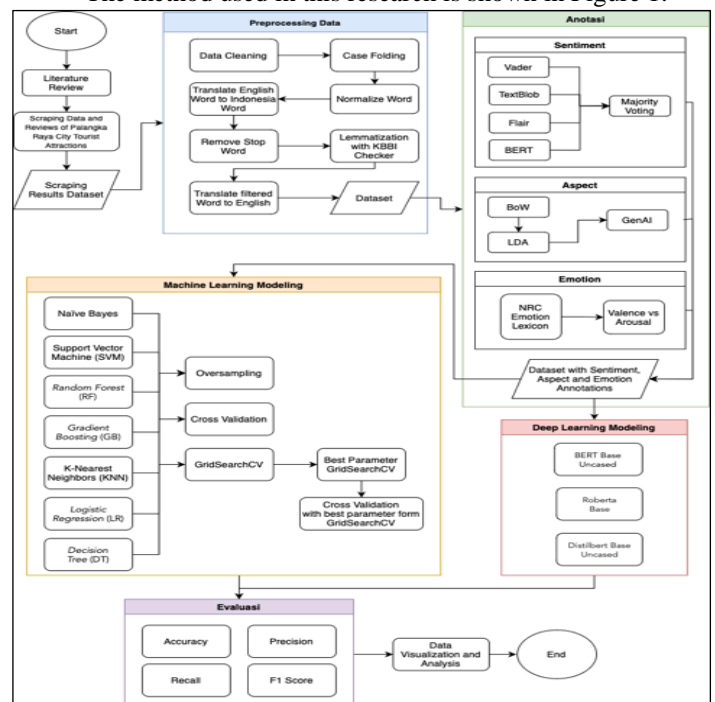


Figure 1: Research Method.

Source: Authors, (2025).

### 3.1 Literature Review

This research begins with an in-depth literature study on sentiment analysis, specifically on the aspects and emotions of user reviews on Google Maps using machine learning and deep learning.

### 3.2 Data collection

The dataset in this research is taken from reviews of tourist attractions in Palangka Raya City found on Google Maps during the period 2018 to 2024 through the scraping method. The data collected includes location, user, time, and comments. The amount of data collected is 5,221 data. Examples of data collected can be seen in Table 1.

Table 1: Sample of scraped reviews for tourist attractions in Palangkaraya from Google Maps.

Location	User	Time	Review
bukit baranahu	PRATAMA RAHMATULLAH	setahun lalu	Lokasi buat pendakian cukup terjal Pemandangan di atas tower sangat bagus 🌄 Tapi sayang jalannya banyak yang licin dan terjal dan diatas nggak ada tempat buat berlindung kalau hujan nya kencang ...
bukit baranahu	Yosua Krisopras Kharap	5 tahun lalu	bukit yang bagus dijadikan spot camping dgn puncak yg datar dan luas

Source: Authors, (2025).

### 3.3 Data Preprocessing

The collected dataset will go through a comprehensive preprocessing process to prepare it for subsequent analysis [26]. The preprocessing steps include data cleaning, case folding, word normalization, translation from English to Bahasa Indonesia, stopword removal, lemmatization, and translation back to English [27]. Data cleaning is performed to remove noise and errors, such as excess spaces, emojis, hashtags, mentions, URLs, non-alphanumeric characters, dates, numbers, date time entries, extra punctuation, and null-valued reviews. Case folding is applied to equalize all text characters to lowercase [28]. Word normalization was performed by converting nonstandard words and abbreviations to standard forms using a list from an Excel file [29]. Text translation from English to Indonesian was performed using the deep\_translator library. Stopword removal was performed with the literature library. Lemmatization is applied using the stanza library to convert words into their basic form, with verification from the Big Indonesian Dictionary (KBBI) contained in the Excel file [29]. The normalized text is then translated back to English. This preprocessing process resulted in a clean dataset consisting of 4,113 data points. The processing results are shown in Table 2.

Table 2: Sample Data Processing.

Preprocessing	Input	Output
Data Cleaning	good views,sunrisenya mantap jiwa👍	good views sunrisenya mantap jiwa
Case Folding	good views sunrisenya mantap jiwa	good views sunrisenya mantap jiwa

Preprocessing	Input	Output
Normalize Word	good views sunrisenya mantap jiwa	bagus pemandangan matahari terbit mantap jiwa
Translate English Word to Indonesia Word	bagus pemandangan matahari terbit mantap jiwa	pemandangan matahari terbit yang indah menenangkan jiwa
Removal Stopword	pemandangan matahari terbit yang indah menenangkan jiwa	pemandangan matahari terbit indah menenangkan jiwa
Lemmatization	pemandangan matahari terbit indah menenangkan jiwa	pandang matahari terbit indah tenang jiwa
Translate to English	pandang matahari terbit indah tenang jiwa	look beautiful sunrise calm soul

Source: Authors, (2025).

### 3.4 Annotation

The processed dataset is then labeled or annotated based on sentiment, aspect, and emotion.

#### a. Sentiment Annotation

Sentiment analysis is performed using a combination of four libraries, namely VADER, TextBlob, Flair, and BERT. Each library has a different approach to determining sentiment; VADER uses composite scores, TextBlob uses polarity scores, and Flair and BERT use probability scores [14]. The results from the four libraries are then consolidated using majority voting to get more accurate results and reduce the bias of the single method [30]. While sentiment is generally categorized into positive, negative, and neutral, this study only labeled the data as positive or negative to simplify the analysis and focus on extreme emoticons [31]. The sentiment annotation results are shown in Table 3.

Table 3: Examples of sentiment annotation result.

Content	Sentiment_VADER	Sentiment_Text Blob	Sentiment_Flair	Sentiment_BERT	Sentiment_majority voting
look beautiful sunrise calm soul	Positive	Positive	Positive	Positive	Positive
good hill camp wide flat peak	Positive	Positive	Negative	Negative	Negative

Source: Authors, (2025).

#### b. Aspect Annotation

The aspects in the text or reviews in the dataset are analyzed using the Bag of Words (BoW) method to convert the text into numerical vectors [32]. These vectors are then analyzed using the gensim library. To determine the optimal number of topics, the Latent Dirichlet Allocation (LDA) algorithm was applied, focusing on coherence measures that assess the relevance and relationship of words within each topic [33], [34]. Important parameters in the LDA model include corpus, num\_topics, id2word, random\_state, update\_every, chunksize, and passes [35]. In this study, the pass parameter is set at 10 to ensure stable model convergence. Once the topics are identified, the text is categorized based on the contribution of the words to the topics. To deepen the analysis, the Generative AI (GenAI) model with the Gemini-Pro approach was used to extract relevant information according to the topics identified by LDA [36]. This method provides an in-depth analysis of the relationship between words and topic relevance, which is useful for applications such as sentiment analysis [37].



The results identified two main aspects of the topics extracted using LDA and GenAI, namely city and attractions and nature and tourism. In the city and attractions aspect, this topic includes words and phrases related to cities, landmarks, and places of interest. Words such as city, park, bridge, road, and kahayan appear frequently, highlighting how cities promote their attractions and how travelers experience urban locations. In contrast, the Nature and Tourism aspect deals with natural elements and tourism activities related to nature. Words such as place, good, relax, and view appear frequently in this topic, illustrating how tourism focuses on natural beauty and experiences related to the natural environment. The results of the aspect annotation are shown in Table 4.

Table 4: Aspect Based Sentiment Analysis (ABSA).

Dominant topic	Perc_Contrib	Topic_Keywords	Review	Aspect
1	0.920 00001 67	place, good, beautiful, nice, relax, family, cool, view, need, comfortable	look beautiful sunrise calm soul	Nature and Tourism
0	0.507 00002 91	palangka, raya, city, tourist, park, bridge, national, road, kahayan, attraction	good hill camp wide flat peak	City and Attractions

Source: Authors, (2025).

### c. Emotion Annotation

Emotion annotation plays an important role in sentiment analysis by providing deep insight into the sentiment in the text. At this stage, the review text was analyzed using the NRC Emotion Lexicon, which allows the identification of dominant emotions and the classification of emotions into valence and arousal categories. Based on Plutchik's emotion model, this lexicon classifies emotions into eight basic categories: anger, anticipation, disgust, fear, joy, sadness, surprise, and trust [13]. This lexicon also enables the classification of emotions with high accuracy [11]. The results of emotion annotation can be seen in Table 5.

Table 5: Emotions Annotation Results.

Steps	Result
Review	look beautiful sunrise calm soul
Sentiment	Positive
Aspect	Nature and Tourism
Emotions	{'anticipation': 0.0, 'joy': 0.08333333333333333, 'surprise': 0.0, 'trust': 0.0}
Dominant_Emotion	joy
Valence	Positive
Arousal	High

Source: Authors, (2025).

The level of customer satisfaction is determined based on the combination of valence, arousal, and dominant emotion in the dataset. Feedback with positive valence usually indicates high satisfaction, while negative valence indicates dissatisfaction [38]. Common sentiment categories in customer feedback analysis include satisfied, very satisfied, dissatisfied, and very dissatisfied [39]. These sentiment categories help businesses understand customers, make better decisions, and increase sales and loyalty. The mapping of the combination of valence, dominant emotion,

and arousal to the level of customer satisfaction can be seen in Table 6.

### 3.5 Classification Model

The sentiment, aspect, and emotion annotated datasets were combined to build classification models using machine learning and deep learning algorithms. The goal was to identify the best model to classify the sentiment aspects and emotions in the dataset. For the machine learning approach, several methods are used, namely Logistic Regression (LR), Naive Bayes (NB), Random Forest (RF), Support Vector Machine (SVM), K-Nearest Neighbors (KNN), Gradient Boosting (GB), and Decision Tree (DT) [40]. In these experiments, several techniques are applied to improve model performance, such as random oversampling, cross-validation, GridSearchCV, and cross-validation using the best parameters from GridSearchCV [16]. Random oversampling is used to balance the classes by adding samples from minority classes, thereby reducing bias towards the majority class and improving model accuracy on underrepresented classes [41]. Cross-validation is performed to evaluate model accuracy and reduce the risk of overfitting by dividing the data into subsets (folds) for training and testing [42]. GridSearchCV is used to find the best combination of parameters for each algorithm so that the most suitable parameters can be found to improve model performance [43]. After the optimal parameters are found with GridSearchCV, cross-validation is performed again to ensure more reliable and consistent results [44].

For the deep learning approach, pre-trained BERT models were tested, namely BERT-base-uncased, Roberta-base, and Distilbert-base-uncased [45]. The models were trained with a predefined number of parameters. The training was conducted for 50 epochs, with early stopping using patience 5, which stops training if there is no improvement in model performance for 5 consecutive epochs [46]. This helps prevent overfitting and saves training time. The learning rate is set at  $2e-5$  to ensure the model can learn stably without getting stuck at a local minimum, while the batch size is set at 128 for efficiency in data processing and optimization of GPU memory usage. The maximum input length is set at 512 tokens, which is the maximum length of input that can be processed by the BERT model, to ensure that important information in the text is not truncated. Gradient accumulation is applied to overcome the GPU memory limitation by updating the parameters after several batches, thus enabling model training with a large batch size without requiring a very large GPU memory [47]. With this approach, it is expected that the model can utilize the advantages of both machine learning and deep learning techniques to achieve optimal sentiment classification results.

### 3.6 Evaluation and Visualization

The resulting model is evaluated using accuracy, recall, precision, and F1 score metrics to determine the best performance [48]. The final stage involves visualization of the results in graphical form as well as analysis of aspects, sentiments, and emotions from user reviews in relation to their relevance to sustainable tourism [49].

## IV. RESULTS AND DISCUSSIONS

### 4.1 Sentiment Annotation Results

The sentiment distribution based on the dataset of 4,113 reviews using VADER shows that 95.4% of the reviews are categorized as positive and 4.6% as negative. TextBlob showed similar results to VADER, albeit with slightly more negative reviews, at 6.9%, and positive reviews at 93.1%. Flair categorized



86.1% of reviews as positive and 13.9% as negative, while BERT categorized 84.4% of reviews as positive and 15.6% as negative. The result of the sentiment analysis was determined through majority voting, which combines the judgments from all libraries and results in a more balanced distribution in text classification. In this process, 88% of the reviews were categorized as positive and 12% as negative. Thus, although there are variations in sentiment analysis results between different methods, all tools show that most reviews of tourist attractions in Palangka Raya city are categorized as positive. The comparison of the sentiment annotation results using VADER, TextBlob, Flair, BERT, and majority voting, shown in Table 6, provides an overall picture of the sentiment classification of the text.

Table 6: Sentiment Distribution by Method.

Labeling technique	Sentiment label	
	Positive	Negative
VADER	3925	188
TextBlob	3828	285
Flair	3541	572
BERT	3469	644
Majority voting	3619	494

Source: Authors, (2025).

The aspect distribution of tourist attractions reviews in Palangka Raya City consists of 3,015 reviews for nature and tourism and 1,098 reviews for city and attractions. The sentiment distribution for the City and Attractions aspect includes 974 positive sentiments and 124 negative sentiments. Meanwhile, the nature and tourism aspect have 2,645 positive sentiments and 370 negative sentiments. The aspect distribution is shown in Figure 2, while the sentiment distribution per aspect is shown in Figure 3.

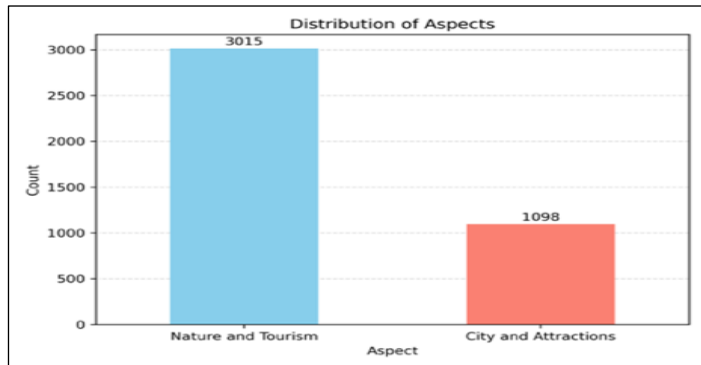


Figure 2: Distribution of Aspects.

Source: Authors, (2025).

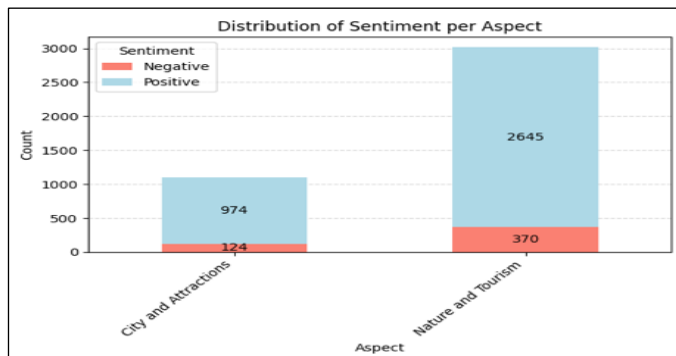


Figure 3: Sentiment per Aspect.

Source: Authors, (2025).

The frequency distribution of emotions in the dataset shows that anticipation is the most frequent emotion, with 2,405, followed by joy with 857. Emotions such as anger at 326, trust at 20, fear at 69, disgust at 58, sadness at 41, and surprise at 37 appear less frequently compared to anticipation and joy. The frequency distribution of these emotions can be seen in Figure 4. Sentiment analysis of the nature and tourism aspect shows the dominance of joy and anticipation emotions, reflecting high enthusiasm for nature and tourism. In contrast, in the city and attractions aspect, the distribution of emotions is more diverse. In addition to joy and anticipation, the emotion of trust is also significant, indicating trust in information related to cities and attractions. Details of sentiment distribution and dominant emotions by aspect are shown in Figure 5.

Dominant emotions are mapped into the dimensions of valence (positive or negative) as well as arousal (high or low). Positive emotions with high arousal, such as excitement and anticipation, appear frequently, indicating a pleasant and arousing experience. Negative emotions with high arousal, such as anger, also arise frequently but with high intensity. In contrast, low-arousal negative emotions, such as sadness and disgust, appear with lower intensity. Finally, positive emotions with low arousal, such as trust, tend to appear with a calmer intensity. This mapping can be seen in Figure 6.

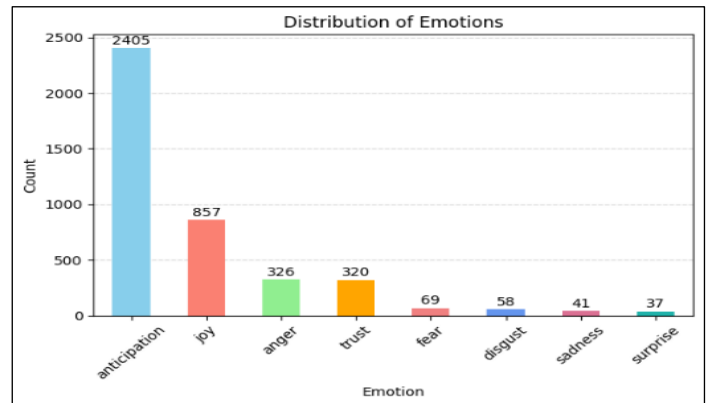


Figure 4: Distribution of emoticons.

Source: Authors, (2025).

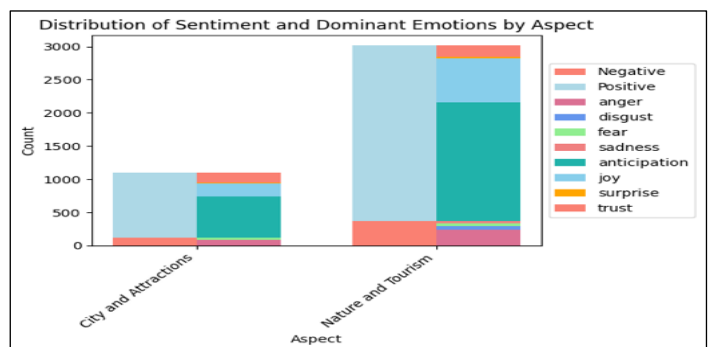


Figure 5: Sentiment and Emotion Distribution by Aspect.

Source: Authors, (2025).

The level of customer satisfaction is determined by analyzing the combination of valence, arousal, and dominant emotions contained in the dataset. The analysis results show that 2,405 customers rated tourist attractions in Palangka Raya City as very satisfying, while 1,214 customers were satisfied. In contrast, the number of dissatisfied and very dissatisfied customers is relatively small, at 168 and 326, respectively. This finding

indicates that despite some complaints, the majority of customers experience high levels of satisfaction, reflecting good performance in meeting visitors' expectations. In addition, the level of customer satisfaction by aspect was analyzed. For the City and Attractions aspect, the number of very satisfied visitors was 619, satisfied was 355, dissatisfied was 40, and very dissatisfied was 84. Meanwhile, for the nature and tourism aspect, the number of very satisfied visitors reached 1,786, 859 satisfied, 128 dissatisfied, and 242 very dissatisfied. Details of these results can be seen in Figure 7.

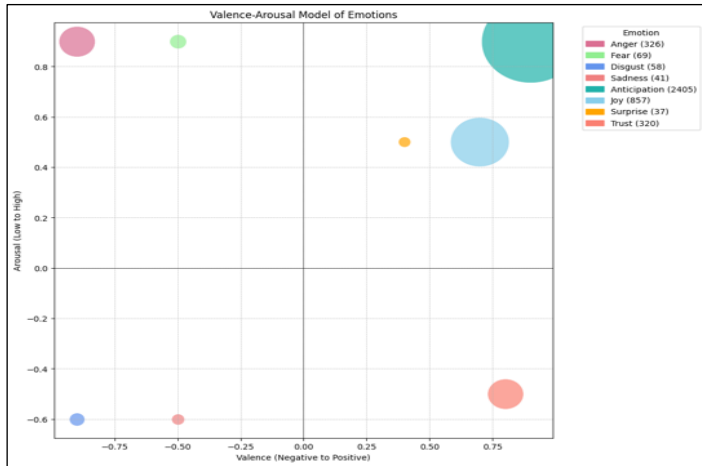


Figure 6: Emotion Distribution by Valence and Arousal.  
Source: Authors, (2025).



Figure 7: Distribution of Customer Satisfaction.  
Source: Authors, (2025).

#### 4.2 Comparison of Classification Model Results

This section presents a comparative analysis of the performance of various machine learning (ML) and deep learning (DL) algorithms in classifying datasets that have been annotated for sentiment, aspect, and emotion. The purpose of this analysis is to identify the best model for each of these classification tasks. To improve the performance of machine learning models, several techniques were applied, namely random oversampling, cross-validation, GridSearchCV, and cross-validation with the best parameters from GridSearchCV.

The results of aspect classification show that the Support Vector Machine (SVM) algorithm provides excellent performance compared to other algorithms, especially when the cross-validation technique, GridSearchCV, and cross-validation with optimal parameters from GridSearchCV are applied. With the cross-validation technique, SVM achieved 94.42% accuracy, 94.44% precision, 94.42% recall, and 94.31% F1-score. The use of GridSearchCV further improved the performance of SVM, with an accuracy of 98.10%, precision of 98.13%, recall of 98.10%, and

F1-score of 98.10%. The application of cross-validation with optimal parameters from GridSearchCV resulted in the highest accuracy value for SVM, which was 98.60%, with 98.62% precision, 98.60% recall, and 98.60% F1-score. On the other hand, when applying the Random Oversampling technique, the Logistic Regression algorithm showed better performance compared to SVM and other algorithms, with accuracy, precision, recall, and an F1-score of 95.15% each. Complete data regarding the results of this evaluation can be seen in Table 7.

Table 7: Comparing Machine Learning Algorithms for Aspect-Based Sentiment.

Algo rith m	Aspect				
	Technique	Accur acy (%)	Precis ion (%)	Recall (%)	F1- Score (%)
LR	Random Oversampling	95,15	95,15	95,15	95,15
	Cross-validation	96,81	96,86	96,82	96,81
	GridSearchCV	96,82	96,86	96,82	96,81
	Cross-validation with best parameter from GridSearchCV	98,38	98,41	98,38	98,38
NB	Random Oversampling	93,20	93,59	93,20	93,31
	Cross-validation	96,12	96,26	96,12	96,11
	GridSearchCV	96,12	96,26	96,12	96,11
	Cross-validation with best parameter from GridSearchCV	96,28	96,40	96,28	96,28
RF	Random Oversampling	90,53	90,69	90,5	90,60
	Cross-validation	96,56	96,56	96,54	96,56
	GridSearchCV	96,56	96,56	96,54	96,56
	Cross-validation with best parameter from GridSearchCV	96,89	96,82	96,65	96,57
SVM	Random Oversampling	94,42	94,44	94,42	94,31
	Cross-validation	98,10	98,13	98,10	98,10
	GridSearchCV	98,10	98,13	98,10	98,10
	Cross-validation with best parameter from GridSearchCV	98,60	98,62	98,60	98,60
KNN	Random Oversampling	87,38	87,62	87,38	87,48
	Cross-validation	91,68	91,86	91,68	91,67
	GridSearchCV	91,68	91,86	91,68	91,67
	Cross-validation with best parameter from GridSearchCV	95,07	98,62	95,07	95,06
GB	Random Oversampling	87,86	87,86	87,86	87,86
	Cross-validation	88,81	89,23	88,86	88,85
	GridSearchCV	88,81	89,23	88,86	88,85
	Cross-validation with best parameter from GridSearchCV	96,54	96,66	96,45	96,54
DT	Random Oversampling	86,65	86,95	86,65	86,77
	Cross-validation	94,42	94,73	94,66	94,39
	GridSearchCV	94,42	94,73	94,66	94,39
	Cross-validation with best parameter from GridSearchCV	94,42	94,69	94,37	94,37

Source: Authors, (2025).

The results of the sentiment classification evaluation using machine learning show that the Random Forest algorithm provides better performance compared to other algorithms in the Random Oversampling and GridSearchCV techniques. In the Random

Oversampling technique, Random Forest achieved 91.26% accuracy, 90.18% precision, 91.26% recall, and 90.20% F1-score. For the GridSearchCV technique, the algorithm recorded 95.92% accuracy, 95.91% precision, 95.92% recall, and 95.91% F1-score. In contrast, in the cross-validation technique and cross-validation with the optimal parameters of GridSearchCV, the support vector machine (SVM) algorithm showed superior performance with accuracy, recall, and F1-score of 99.09% and precision of 99.11% for the cross-validation technique, respectively. For cross-validation with the best parameters from GridSearchCV, SVM achieved the highest accuracy, precision, recall, and F1-score of 99.86%. Details of these results can be seen more clearly in Table 8.

Table 8: Comparing Machine Learning Algorithms for Sentiment Classification.

Emotion					
Algori thm	Technique	Accur acy (%)	Precis ion (%)	Recall (%)	F1- Score (%)
LR	Random Oversampling	78,16	81,73	78,16	79,55
	Cross-validation	97,29	97,31	97,29	97,24
	GridSearchCV	72,80	73,11	72,80	72,95
	Cross-validation with best parameter from GridSearchCV	98,87	98,89	98,87	98,84
NB	Random Oversampling	57,04	73,68	57,04	61,24
	Cross-validation	89,94	90,18	89,94	89,25
	GridSearchCV	69,94	69,19	69,94	69,07
	Cross-validation with best parameter from GridSearchCV	92,07	92,25	92,07	91,58
RF	Random Oversampling	77,43	75,80	77,43	74,98
	Cross-validation	99,14	99,19	99,18	99,20
	GridSearchCV	95,14	95,18	95,14	95,14
	Cross-validation with best parameter from GridSearchCV	99,24	99,28	99,26	99,23
SVM	Random Oversampling	78,64	76,57	78,64	75,40
	Cross-validation	99,41	99,41	99,41	99,41
	GridSearchCV	94,12	94,42	94,12	94,12
	Cross-validation with best parameter from GridSearchCV	99,59	99,59	99,59	99,59
KNN	Random Oversampling	61,41	63,80	61,41	62,32
	Cross-validation	93,72	93,57	93,72	93,48
	GridSearchCV	93,72	93,62	93,72	93,72
	Cross-validation with best parameter from GridSearchCV	96,48 7	96,65	96,48	96,31
GB	Random Oversampling	78,40	79,71	78,40	78,81
	Cross-validation	94,21	94,48	94,17	94,18
	GridSearchCV	85,17	87,20	85,06	85,00
	Cross-validation with best parameter from GridSearchCV	98,63	98,60	98,61	98,56
DT	Random Oversampling	72,82	73,91	72,82	73,17
	Cross-validation	98,06	98,11	98,04	98,10

	GridSearchCV	94,48	95,30	94,75	94,62
	Cross-validation with best parameter from GridSearchCV	98,22	98,20	98,10	98,12

Source: Authors, (2025).

For the deep learning model, the evaluation results show that Roberta-base outperforms BERT-base-uncased and DistilBERT-base-uncased in aspect and sentiment classification. Roberta-base achieved 91.26% accuracy, 91.38% precision, 91.26% recall, and 91.31% F1-score for aspect classification, and 88.63% accuracy, 87.84% precision, 88.83% recall, and 88.25% F1-score for sentiment classification. In contrast, for emotion classification, DistilBERT-base-uncased shows better performance compared to BERT-base-uncased and Roberta-base, with an accuracy value of 68.20%, precision of 72.23%, recall of 68.20%, and F1-score of 69.75%. The detailed performance of the deep learning model can be seen in Table 9.

Table 9: Deep Learning Algorithms Performance Comparison

Category	Algorithm (%)	Accuracy (%)	Precision (%)	Recall (%)	F-1 Score (%)
Aspect	BERT-base- uncased	88,35	89,90	88,35	88,74
	Roberta- base	91,26	91,38	91,26	91,31
Sentiment	DistilBERT- base- uncased	89,32	91,16	89,32	89,73
	BERT-base- uncased	86,65	87,26	86,65	86,92
	Roberta- base	88,83	87,84	88,83	88,25
	DistilBERT- base- uncased	88,11	87,64	88,11	87,85
Emotion	BERT-base- uncased	66,75	68,68	66,75	67,55
	Roberta- base	67,72	69,71	67,72	63,38
	DistilBERT- base- uncased	68,20	72,33	68,20	69,75

Source: Authors, (2025).

Sentiment analysis of various methods such as VADER, TextBlob, Flair, and BERT shows that most reviews about tourist attractions in Palangka Raya City are positive. While VADER and TextBlob generally generate a lot of positive reviews, TextBlob records slightly more negative reviews than VADER. Flair and BERT also reflect a similar trend with a higher proportion of negative reviews [50]. Majority voting gave a sentiment distribution of 88% positive and 12% negative, confirming the general trend of positive reviews [30], [50].

Aspect analysis revealed that the Nature and Tourism category received more positive reviews than City and Attractions, although negative reviews were also more frequent in that category. The frequency of emotions in the dataset was dominated by anticipation and joy, while negative emotions such as anger and fear appeared less frequently [51]. The level of customer satisfaction is very high, with 2,405 visitors very satisfied and 1,214 satisfied, indicating that tourist attractions in Palangka Raya successfully meet visitors' expectations. Nature and tourism visitors tend to be very satisfied more often than city and attraction

visitors, possibly because experiences in nature are considered more satisfying than urban environments [52].

In terms of machine learning classification models, Random Oversampling, Cross-Validation, and GridSearchCV techniques have been shown to improve the performance of various algorithms, such as Logistic Regression, Naive Bayes, Random Forest, Support Vector Machine (SVM), K-Nearest Neighbors (KNN), Gradient Boosting, and Decision Tree [44], [53], [54]. In particular, the combination of cross-validation with the best parameters of GridSearchCV resulted in the most significant improvement in model accuracy [16], [55]. Support Vector Machine (SVM) showed superiority over other machine learning algorithms as well as deep learning models, achieving 98.60% accuracy and 98.60% F1-score for aspect classification, 99.86% accuracy and 98.86% F1-score for sentiment analysis, and 99.59% accuracy and 99.59% F1-score for emotion classification [56], [57]. However, it should be noted that this study has some limitations. Firstly, the data used is limited to the Google Maps platform, so it may not cover all visitor's perspectives. In addition, the relatively small amount of data may affect the accuracy of the model. These limitations need to be considered in the interpretation of the results and the development of future research need to be considered in the interpretation of the results and the development of future research.

## V. CONCLUSIONS

This study found that the majority of reviews regarding tourist attractions in Palangka Raya City are positive, with 88% positive and 12% negative reviews according to majority voting. The analysis methods used, including VADER, TextBlob, Flair, and BERT, were consistent in showing a positive trend, although there were variations in the proportion of negative reviews. The nature and tourism aspect received more positive reviews compared to city and attractions but also had more negative reviews. This reflects that visitors may enjoy the nature experience more, despite some criticism. Emotion frequencies show a predominance of anticipation and joy, indicating that the visitor experience is generally uplifting. Customer satisfaction levels are also high, with the majority of visitors feeling very satisfied or satisfied. The combination of cross-validation with the best parameters from GridSearchCV resulted in the most significant improvement in model accuracy. In classification, SVM showed the best performance for aspects, while Random Forest excelled in sentiment and Logistic Regression in emotion on specific techniques. Roberta-base and DistilBERT-base-uncased deep learning models showed the best performance in aspect and emotion classification, respectively. These findings provide valuable insights for tourism destination management and marketing strategies, with an emphasis on positive experiences and visitor preferences.

Based on the research results, several strategic steps can be implemented to improve the management of tourist destinations in Palangka Raya City. Improving the quality of experience in the Nature and Tourism category needs to be focused on improving facilities and addressing criticism to reduce complaints. Positive sentiment data should be used in marketing strategies, highlighting natural advantages to attract visitors. In addition, proven effective analysis algorithms, such as support vector machine (SVM), random forest, and logistic regression, can be applied to improve classification accuracy. The use of deep learning models such as Roberta-base is also recommended for more in-depth analysis. Data collection from various sources and continued research on visitor preferences will provide valuable additional insights. These

steps are expected to improve visitor experience, optimize marketing, and make effective use of analytics technology for long-term success.

This research opens opportunities for further exploration of sentiment and emotion analysis in tourism. Future research could include analysis in other cities in Indonesia to understand traveler sentiment patterns more broadly. In addition, the development and application of new deep-learning models can improve the accuracy of emotional classification. Integration of multi-source data, such as review data, social media, satisfaction surveys, and transactions, is also important for more comprehensive analysis. This approach is expected to improve the service quality and attractiveness of tourist destinations and strengthen the traveler experience.

## VI. AUTHOR'S CONTRIBUTION

**Conceptualization:** Author One, Author Two, Author Three, Author Four.

**Methodology:** Author One, Author Two, Author Three, Author Four.

**Investigation:** Author One, Author Two, Author Three, Author Four.

**Discussion of results:** Author One, Author Two, Author Three, Author Four.

**Writing – Review and Editing:** Author One and Author Two.

**Resources:** Author One, Author Two, Author Three, Author Four.

**Supervision:** Author One, Author Two, Author Three, Author Four.

**Approval of the final text:** Author One, Author Two, Author Three, Author Four.

## VII. ACKNOWLEDGMENTS

The authors gratefully acknowledge all useful suggestions regarding this work.

## VII. REFERENCES

- [1] M. A. AL-Barrak and A. I. Al-Alawi, "Sentiment Analysis on Customer Feedback for Improved Decision Making: A Literature Review," in 2024 ASU International Conference in Emerging Technologies for Sustainability and Intelligent Systems (ICETISIS), IEEE, Jan. 2024, pp. 207–212. doi: 10.1109/ICETISIS61505.2024.10459452.
- [2] R. K. Sharma and A. Dagur, "Various methods to classify the polarity of text based customer reviews using sentiment analysis," in Artificial Intelligence, Blockchain, Computing and Security Volume 2, London: CRC Press, 2023, pp. 107–114. doi: 10.1201/9781032684994-18.
- [3] G. Aivatoglou, A. Fytli, G. Arampatzis, D. Zaikis, N. Stylianou, and I. Vlahavas, "End-to-End Aspect Extraction and Aspect-Based Sentiment Analysis Framework for Low-Resource Languages," 2024, pp. 841–858. doi: 10.1007/978-3-031-47715-7\_56.
- [4] C. A. Bahri and L. H. Suadaa, "Aspect-Based Sentiment Analysis in Bromo Tengger Semeru National Park Indonesia Based on Google Maps User Reviews," IJCCS (Indonesian Journal of Computing and Cybernetics Systems), vol. 17, no. 1, p. 79, Feb. 2023, doi: 10.22146/ijccs.77354.
- [5] A. Chowanda, R. Sutoyo, Meiliana, and S. Tanachutiwat, "Exploring Text-based Emotions Recognition Machine Learning Techniques on Social Media Conversation," in Procedia Computer Science, Elsevier B.V., 2021, pp. 821–828. doi: 10.1016/j.procs.2021.01.099.
- [6] J. Lee, S. Benjamin, and M. Childs, "Unpacking the Emotions behind TripAdvisor Travel Reviews: The Case Study of Gatlinburg, Tennessee," International Journal of Hospitality & Tourism Administration, vol. 23, no. 2, pp. 347–364, Mar. 2022, doi: 10.1080/15256480.2020.1746219.
- [7] M.-N. Trușescu and D. Nicolaie, "Sentiment Analysis: a Comparative Study of Online Booking Platforms Used for Spa Tourism in Northern Oltenia, Romania,"



Balneo and PRM Research Journal, vol. 15, no. Vol.15, 1, pp. 651–651, Mar. 2024, doi: 10.12680/balneo.2024.651.

[8] J. Vaid, “Sustainable Tourism: A Roadmap for the 2030 Sustainable Development Agenda,” 2024, pp. 21–26. doi: 10.1108/S1569-37592024000113B002.

[9] S. Hannafin, “Building a better future through industry, innovation and infrastructure (SDG 9),” in Teaching the Sustainable Development Goals to Young Citizens (10-16 years), London: Routledge, 2024, pp. 259–274. doi: 10.4324/9781003232001-15.

[10] A. K. E. V. S. Stroumpoulis, “Role of Artificial Intelligence and Big Data Analytics In Smart Tourism: A Resource-Based View Approach,” Aug. 2022, pp. 99–108. doi: 10.2495/ST220091.

[11] S. Zad, J. Jimenez, and M. A. Finlayson, “Hell Hath No Fury? Correcting Bias in the NRC Emotion Lexicon,” in WOAHS 2021 - 5th Workshop on Online Abuse and Harms, Proceedings of the Workshop, Association for Computational Linguistics (ACL), 2021, pp. 102–113. doi: 10.18653/v1/2021.woah-1.11.

[12] A. A. Sallam, W. Q. Saif, T. H. Rassem, and B. A. Mohammed, “Detecting Emotional Sentiments in Textual Data Using Various Machine Learning and Deep Learning Techniques,” 2024, doi: 10.21203/rs.3.rs-4558175/v1.

[13] T. Chutia and N. Baruah, “A review on emotion detection by using deep learning techniques,” Artif Intell Rev, vol. 57, no. 8, Aug. 2024, doi: 10.1007/s10462-024-10831-1.

[14] K. Barik and S. Misra, “Analysis of customer reviews with an improved VADER lexicon classifier,” J Big Data, vol. 11, no. 1, p. 10, Jan. 2024, doi: 10.1186/s40537-023-00861-x.

[15] A. M. Shetty, M. F. Aljunid, D. H. Manjaiah, and A. M. S. Shaik Afzal, “Hyperparameter Optimization of Machine Learning Models Using Grid Search for Amazon Review Sentiment Analysis,” 2024, pp. 451–474. doi: 10.1007/978-981-99-7814-4\_36.

[16] Y. Zhao, W. Zhang, and X. Liu, “Grid search with a weighted error function: Hyper-parameter optimization for financial time series forecasting,” Appl Soft Comput, vol. 154, p. 111362, Mar. 2024, doi: 10.1016/j.asoc.2024.111362.

[17] V. V. Tadkal, S. Patil, and S. A. Patil, “Aspect Based Sentiment Analysis,” in 2024 5th International Conference for Emerging Technology (INCET), IEEE, May 2024, pp. 1–8. doi: 10.1109/INCET61516.2024.10593116.

[18] A. Siddiqua, V. Bindumathi, G. Raghu, and Y. S. Vamsi Bhargav, “Aspect-based Sentiment Analysis (ABSA) using Machine Learning Algorithms,” in 2024 Third International Conference on Distributed Computing and Electrical Circuits and Electronics (ICDCECE), IEEE, Apr. 2024, pp. 1–6. doi: 10.1109/ICDCECE60827.2024.10549140.

[19] M. Shenify, “Sentiment analysis of Saudi e-commerce using naïve bayes algorithm and support vector machine,” International Journal of Data and Network Science, vol. 8, no. 3, pp. 1607–1612, Jun. 2024, doi: 10.5267/j.ijdns.2024.3.006.

[20] B. Mridula, A. H. Juliet, and N. Legapriyadharshini, “Deciphering Social Media Sentiment for Enhanced Analytical Accuracy: Leveraging Random Forest, KNN, and Naive Bayes,” in 2024 10th International Conference on Communication and Signal Processing (ICCSPP), IEEE, Apr. 2024, pp. 1410–1415. doi: 10.1109/ICCSPP60870.2024.10543836.

[21] P. Assiroj, A. Kurnia, and S. Alam, “The performance of Naïve Bayes, support vector machine, and logistic regression on Indonesia immigration sentiment analysis,” Bulletin of Electrical Engineering and Informatics, vol. 12, no. 6, pp. 3843–3852, Dec. 2023, doi: 10.11591/eei.v12i6.5688.

[22] E. D. Madyatmadja, H. Candra, J. Nathaniel, M. R. Jonathan, and Rudy, “Sentiment Analysis on User Reviews of Threads Applications in Indonesia,” Journal Européen des Systèmes Automatisés, vol. 57, no. 4, pp. 1165–1171, Aug. 2024, doi: 10.18280/jesa.570423.

[23] T. Bikku, J. Jarugula, L. Kongala, N. D. Tummala, and N. Vardhani Donthiboina, “Exploring the Effectiveness of BERT for Sentiment Analysis on Large-Scale Social Media Data,” in 2023 3rd International Conference on Intelligent Technologies (CONIT), IEEE, Jun. 2023, pp. 1–4. doi: 10.1109/CONIT59222.2023.10205600.

[24] W. S. Ismail, “Emotion Detection in Text: Advances in Sentiment Analysis Using Deep Learning,” J Wirel Mob Netw Ubiquitous Comput Dependable Appl, vol. 15, no. 1, pp. 17–26, Mar. 2024, doi: 10.58346/JOWUA.2024.11.002.

[25] A. Toliyat, S. I. Levitan, Z. Peng, and R. Etemadpour, “Asian hate speech detection on Twitter during COVID-19,” Front Artif Intell, vol. 5, Aug. 2022, doi: 10.3389/frai.2022.932381.

[26] V. Handrianus Pranatawijaya, W. Widiatry, and D. J. Lestari, “ENHANCING OPTICAL DISTRIBUTION POINT PLACEMENT: A DECISION SUPPORT SYSTEM INTEGRATING WEIGHTED PRODUCT METHOD, CONTENT-BASED FILTERING, AND LOCATION-BASED SERVICES,” Journal of Engineering and Technology for Industrial Applications ITEGAM-JETIA Manaus, pp. 206–213, doi: 10.5935/jetia.v10i50.1329.

[27] C. El Morr, M. Jammal, H. Ali-Hassan, and W. El-Hallak, “Data Preprocessing,” 2022, pp. 117–163. doi: 10.1007/978-3-031-16990-8\_4.

[28] Md. S. Hossen, “Data Preprocess,” in Machine Learning and Big Data, Wiley, 2020, pp. 71–103. doi: 10.1002/9781119654834.ch4.

[29] V. V. Bozhenko and T. M. Tatarnikova, “Application of Data Preprocessing in Medical Research,” in 2023 Wave Electronics and its Application in Information and Telecommunication Systems (WECONF), IEEE, May 2023, pp. 1–4. doi: 10.1109/WECONF57201.2023.10148004.

[30] Zakaria and A. Sunyoto, “Hybrid Sentiment Analysis: Majority Voting with Multinomial Naive Bayes and Logistic Regression on IMDB Dataset,” in 2023 6th International Conference on Information and Communications Technology (ICOIACT), IEEE, Nov. 2023, pp. 448–453. doi: 10.1109/ICOIACT59844.2023.10455937.

[31] A. A. Eponon and K. Dimililer, “A Bert Model with Deep Learning Approach in Natural Language Processing (NLP),” 2024, pp. 23–30. doi: 10.1007/978-3-031-53488-1\_3.

[32] U. K. Singh, B. Prabhu Shankar, R. Chinnaiyan, and N. Jain, “Machine Learning-Based Text Categorization with Bag of Words,” 2024, pp. 577–587. doi: 10.1007/978-981-97-2839-8\_40.

[33] I. D. Sudirman and D. Y. Nugraha, “Understanding Tourist Perspectives of Borobudur through LDA Topic Modelling Using Elbow Method,” in 2023 International Conference on Informatics, Multimedia, Cyber and Informations System (ICIMCIS), IEEE, Nov. 2023, pp. 374–379. doi: 10.1109/ICIMCIS60089.2023.10349022.

[34] V. H. Pranatawijaya, N. N. K. Sari, R. A. Rahman, E. Christian, and S. Geges, “Unveiling User Sentiment: Aspect-Based Analysis and Topic Modeling of Ride-Hailing and Google Play App Reviews,” Journal of Information Systems Engineering and Business Intelligence, vol. 10, no. 3, pp. 328–339, Oct. 2024, doi: 10.20473/jisebi.10.3.328-339.

[35] J. M. Wheeler, J. Xiong, C. Mardones-Segovia, H.-J. Choi, and A. S. Cohen, “An Investigation of Prior Specification on Parameter Recovery for Latent Dirichlet Allocation of Constructed-Response Items,” 2022, pp. 203–215. doi: 10.1007/978-3-031-04572-1\_15.

[36] O. M. Al-Janabi, N. H. A. H. Malim, and Y.-N. Cheah, “Aspect Categorization Using Domain-Trained Word Embedding and Topic Modelling,” 2020, pp. 191–198. doi: 10.1007/978-981-15-1289-6\_18.

[37] C. Daase, C. Haertel, A. Nahhas, A. Zeier, A. Ramesohl, and K. Turowski, “On the Current State of Generative Artificial Intelligence: A Conceptual Model of Potentials and Challenges,” in Proceedings of the 26th International Conference on Enterprise Information Systems, SCITEPRESS - Science and Technology Publications, 2024, pp. 845–856. doi: 10.5220/0012707500003690.

[38] G. Meirovich, M. M. Jeon, and L. J. Coleman, “Interaction of normative and predictive expectations in customer satisfaction and emotions,” Journal of Marketing Analytics, vol. 8, no. 2, pp. 69–84, Jun. 2020, doi: 10.1057/s41270-020-00078-4.

[39] K. Saroha, M. Sehrawat, and V. Jain, “Machine Learning and Sentiment Analysis for Analyzing Customer Feedback,” 2024, pp. 411–440. doi: 10.4018/979-8-3693-0413-6.ch017.

[40] Salsabila, S. M. P. Tyas, Y. Romadhona, and D. Purwitasari, “Aspect-based Sentiment and Correlation-based Emotion Detection on Tweets for Understanding Public Opinion of Covid-19,” Journal of Information Systems Engineering and Business Intelligence, vol. 9, no. 1, pp. 84–94, 2023, doi: 10.20473/jisebi.9.1.84-94.

[41] S. El Kafhali and M. Tayebi, “Generative Adversarial Neural Networks based Oversampling Technique for Imbalanced Credit Card Dataset,” in 2022 6th SLAAI

International Conference on Artificial Intelligence (SLAAI-ICAI), IEEE, Dec. 2022, pp. 1–5. doi: 10.1109/SLAAI-ICAI56923.2022.10002630.

[42] J. Li et al., “Quantum k-fold cross-validation for nearest neighbor classification algorithm,” *Physica A: Statistical Mechanics and its Applications*, vol. 611, p. 128435, Feb. 2023, doi: 10.1016/j.physa.2022.128435.

[43] P. J. Forcadilla, “Indoor Pollutant Classification Modeling using Relevant Sensors under Thermodynamic Conditions with Multilayer Perceptron Hyperparameter Tuning,” *International Journal of Advanced Computer Science and Applications*, vol. 14, no. 2, 2023, doi: 10.14569/IJACSA.2023.01402103.

[44] Sukanto, Hadiyanto, and Kurnianingsih, “KNN Optimization Using Grid Search Algorithm for Preeclampsia Imbalance Class,” *E3S Web of Conferences*, vol. 448, p. 02057, Nov. 2023, doi: 10.1051/e3sconf/202344802057.

[45] N. Akhila, S. J. P., and S. K. P., “Comparative Study of Bert Models and Roberta in Transformer based Question Answering,” in *2023 3rd International Conference on Intelligent Technologies (CONIT)*, IEEE, Jun. 2023, pp. 1–5. doi: 10.1109/CONIT59222.2023.10205622.

[46] Z. Zhang, W. Zhu, J. Zhang, P. Wang, R. Jin, and T.-S. Chung, “PCEE-BERT: Accelerating BERT Inference via Patient and Confident Early Exiting,” in *Findings of the Association for Computational Linguistics: NAACL 2022*, Stroudsburg, PA, USA: Association for Computational Linguistics, 2022, pp. 327–338. doi: 10.18653/v1/2022.findings-naacl.25.

[47] Z. Huang, B. Jiang, T. Guo, and Y. Liu, “Measuring the Impact of Gradient Accumulation on Cloud-based Distributed Training,” in *2023 IEEE/ACM 23rd International Symposium on Cluster, Cloud and Internet Computing (CCGrid)*, IEEE, May 2023, pp. 344–354. doi: 10.1109/CCGrid57682.2023.00040.

[48] A. Ahmadzadeh, D. J. Kempton, P. C. Martens, and R. A. Angryk, “Contingency Space: A Semimetric Space for Classification Evaluation,” *IEEE Trans Pattern Anal Mach Intell*, vol. 45, no. 2, pp. 1501–1513, Feb. 2023, doi: 10.1109/TPAMI.2022.3167007.

[49] F. Rajani and K. A. Boluk, “A Critical Commentary on the SDGs and the Role of Tourism,” *Tourism and Hospitality*, vol. 3, no. 4, pp. 855–860, Oct. 2022, doi: 10.3390/tourhosp3040053.

[50] A. Mahgoub et al., “Sentiment Analysis: Amazon Electronics Reviews Using BERT and Textblob,” in *2022 20th International Conference on Language Engineering (ESOLEC)*, IEEE, Oct. 2022, pp. 6–10. doi: 10.1109/ESOLEC54569.2022.10009176.

[51] D. Grgić, V. Podobnik, and A. Carvalho, “Deriving and validating emotional dimensions from textual data,” *Expert Syst Appl*, vol. 198, p. 116721, Jul. 2022, doi: 10.1016/j.eswa.2022.116721.

[52] P. Štumpf and T. Kubalová, “Tangible or intangible satisfiers? Comparative study of visitor satisfaction in a nature-based tourism destination in the pre- and during-COVID pandemic,” *Journal of Outdoor Recreation and Tourism*, vol. 46, p. 100777, Jun. 2024, doi: 10.1016/j.jort.2024.100777.

[53] M. Muntasir Nishat et al., “A Comprehensive Investigation of the Performances of Different Machine Learning Classifiers with SMOTE-ENN Oversampling Technique and Hyperparameter Optimization for Imbalanced Heart Failure Dataset,” *Sci Program*, vol. 2022, pp. 1–17, Mar. 2022, doi: 10.1155/2022/3649406.

[54] R. Wijaya, F. Saeed, P. Samimi, A. M. Albarrak, and S. N. Qasem, “An Ensemble Machine Learning and Data Mining Approach to Enhance Stroke Prediction,” *Bioengineering*, vol. 11, no. 7, p. 672, Jul. 2024, doi: 10.3390/bioengineering11070672.

[55] G. Czarnek and D. Stillwell, “Two is better than one: Using a single emotion lexicon can lead to unreliable conclusions,” *PLoS One*, vol. 17, no. 10, p. e0275910, Oct. 2022, doi: 10.1371/journal.pone.0275910.

[56] M. H. I. Ahmad Hapez, N. L. Adam, and Z. Ibrahim, “Performance Analysis of Machine Learning Techniques for Sentiment Analysis,” 2021, pp. 205–213. doi: 10.1007/978-3-030-90235-3\_18.

[57] A. Lathish and T. Devi, “Comparison of Support Vector Machine and K-Nearest Neighbour Algorithm for Accurate text Classification,” in *2022 4th International Conference on Inventive Research in Computing Applications (ICIRCA)*, IEEE, Sep. 2022, pp. 1110–1113. doi: 10.1109/ICIRCA54612.2022.9985594.



## RESEARCH ARTICLE

## OPEN ACCESS

# NAVIGATION SYSTEM AND OBSTACLE AVOIDANCE FOR MOBILE ROBOT USING TYPE-2 FUZZY LOGIC IN UNCERTAIN ENVIRONMENTS

Soufiane. Hachani<sup>1</sup>, Emira. Nechadi<sup>2</sup>

<sup>1</sup> Laboratory of Intelligent Systems (LSI), Department of Electronical University of Setif 1, Algeria.

<sup>2</sup> Department of Electrotechnical, University of Setif 1, Algeria

<sup>1</sup><http://orcid.org/0009-0000-4817-397X> , <sup>2</sup><http://orcid.org/0000-0002-0642-7967>

Email: [hachani.soufiane@univ-setif.dz](mailto:hachani.soufiane@univ-setif.dz), [emira.nechadi@univ-setif.dz](mailto:emira.nechadi@univ-setif.dz)

## ARTICLE INFO

**Article History**

Received: January 06, 2025

Revised: February 20, 2025

Accepted: March 15, 2025

Published: March 31, 2025

**Keywords:**

Navigation System,  
Mobile Robot,  
Type-2 Fuzzy Logic,  
Uncertain Environments,  
Obstacle avoidance,

## ABSTRACT

This paper introduces a reactive navigation strategy for wheeled mobile robots, utilizing type-2 fuzzy logic to manage uncertainty in dynamic environments. The approach incorporates two distinct type-2 fuzzy logic controllers, each tailored to address specific challenges in navigation. The first controller focuses on steering the robot toward its target by continuously adjusting its path in response to changing conditions. The second controller specializes in obstacle avoidance, enabling the robot to detect and maneuver around obstacles it encounters during its journey.

To evaluate the performance of the system, numerical simulations are carried out across various scenarios, including dynamic and cluttered environments, to demonstrate its robustness. Additionally, the results of the type-2 fuzzy logic approach are compared with conventional navigation techniques, such as rule-based or model-based methods. The comparison underscores the system's greater adaptability and resilience. The study concludes that type-2 fuzzy logic provides an effective and flexible solution, significantly improving both path planning and real-time decision-making in unpredictable and complex environments.



Copyright ©2025 by authors and Galileo Institute of Technology and Education of the Amazon (ITEGAM). This work is licensed under the Creative Commons Attribution International License (CC BY 4.0).

## 1. INTRODUCTION

The field of mobile robot navigation has gained increasing importance in recent years due to the rising use of robots in various fields, including industrial and service applications [1]. The control of motion for mobile robots involves several research areas, such as path planning and tracking algorithms [2], precise control design for trajectory following [3], and obstacle avoidance [4], [5]. The demand for robots to navigate in unknown and dynamic environments, filled with both static and dynamic obstacles, has driven the development of advanced systems for planning and navigation. Current path planning methods can be broadly categorized into two main types: global planning methods and local or reactive planning methods [6], [7].

Global path planning, also known as off-line or static path planning, refers to the process where the robot has prior knowledge of the environment and can reach its destination via a pre-defined path. This category includes various algorithms, such as graph-based methods like Dijkstra's algorithm, roadmap-based methods

such as RRT and PRM, and topological methods including cell decomposition and Voronoi diagrams [8].

In contrast to global path planning algorithms, which rely on prior knowledge and environmental mapping, reactive or local navigation strategies employ sensors to monitor the robot's surroundings in real-time, allowing the robot to make quick decisions without prior knowledge of the environment. These reactive strategies often involve various algorithms such as Artificial Potential Fields (APF) [9], Control Barrier Functions (CBF) ([10]), and Fuzzy Logic Controllers (FLC) [11].

Fuzzy Logic Control (FLC) has become a key element in reactive navigation strategies due to its ability to make decisions in real-time based on sensory data. FLC has proven particularly useful for handling nonlinearities and managing dynamic, uncertain environments. Several researchers have proposed using FLC systems for mobile robot navigation. For example, [12], [13] proposed fuzzy control systems for guiding robots to their target destinations while avoiding obstacles. Furthermore, [14] developed

an optimal fuzzy tracking control system based on the Takagi-Sugeno model and Linear Quadratic Regulator (LQR) for improving trajectory tracking and obstacle avoidance.

However, traditional fuzzy logic systems face difficulties in precisely defining membership values within the  $[0, 1]$  range for fuzzy systems. To address this issue, Type-2 Fuzzy Logic Systems (T2FLS) have been explored as a more effective solution [15].

These systems help in dealing with higher levels of uncertainty, making them ideal for dynamic environments where information may be incomplete or fuzzy. Similarly, researchers such as ([11]) have employed Particle Swarm Optimization (PSO) to enhance fuzzy membership functions, while others have applied neuro-fuzzy systems in sensor-based navigation [16], [17]. Additionally, Zadeh's concept of Type-2 fuzzy logic, introduced in 1975 [18], has played a significant role in enhancing robot adaptability to unforeseen environments.

In summary, this paper presents an approach to design and implement an interactive navigation system for mobile robots using type 2 fuzzy logic controllers (T2FLC). This technique aims to enhance the robot's ability to navigate dynamic and uncertain environments effectively, providing a more robust solution to the challenges of obstacle avoidance and real-time path planning.

## II. MODEL OF THE MOBILE ROBOT USED IN OUR WORK

The robot used in the simulation is a single-wheeled mobile robot, driven by two independently controlled wheels powered by separate motors. It may also be equipped with passive wheels to maintain stability. The real-world robot is assumed to have a range of sensors to measure the distance to nearby obstacles and monitor its speed. The navigation approach employed in this study follows an interactive navigation strategy.

The primary objective of any robotic navigation system is to direct the robot towards a predefined target area. The secondary objective is to prevent collisions with obstacles. Both objectives are achieved by providing the robot with the necessary commands to minimize the discrepancy between its current position and the target location. For obstacle detection, appropriate sensors, such as ultrasonic sensors, are employed.

It is assumed that the robot-target configuration is represented by  $TP = [x_T, y_T, \theta_T]$ . Additionally, the error vector between the robot's actual position and the nearest obstacle is defined using two variables:  $D_{RO}$  and  $\theta_{RO}$ . Similarly, the error between the robot's actual position and the target location can be calculated by considering two parameters:  $D_{RT}$  and  $\theta_{RT}$ , as shown in (Figure.1).

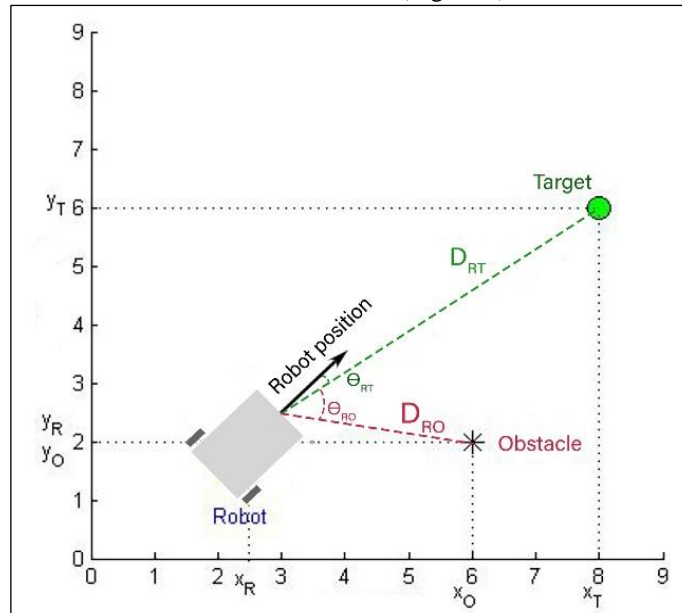


Figure 1: mobile robot used in our work.

Source: Authors, (2025).

Explanation of the abbreviations in (Fig.1):

$(x_R, y_R)$  : The robot position.

$(x_T, y_T)$  : The coordinates of the target point.

$V$ : Linear velocity.

$\omega$ : Angular velocity.

$V_r$  : The speed of the right wheel.

$V_l$  : The speed of the left wheel.

$\theta_R$  : The orientation of the robot.

$\theta_T$ : The orientation of the target.

$\theta_{RT}$  : The angle between the current orientation of the robot and that of the target.

$D_{RT}$  : The distance between the robot and the target.

## III. STATE REPRESENTATION

State representation in the context of mobile robots refers to how the various variables that describe a robot's state are modeled and used to control its behavior. This typically includes variables such as position, orientation, velocity, and other relevant parameters that completely characterize the robot's state at any given time.

For a two-wheeled robot, the state representation is often expressed as a state vector that includes the robot's position on the plane  $(x, y)$ , its orientation  $(\theta)$ , and sometimes linear and angular



velocities ( $v$ ,  $\omega$ ). The aim is to relate control inputs, such as wheel speeds, to changes in these state variables.

In summary, state representation is used to model the evolution of the robotic system over time using differential equations that describe the robot's dynamics. These models are essential for control, trajectory planning, and autonomous navigation.

The kinematic model of the mobile robot is given by:

$$\begin{cases} \dot{x} = V \cdot \cos(\theta_R) \\ \dot{y} = V \cdot \sin(\theta_R) \\ \dot{\theta} = \omega \end{cases} \quad (1)$$

The total speed of the robot can be approximated as the average of the speeds of the individual wheels. Specifically, the total linear speed of the robot is given by the sum of the speeds of the left and right wheels divided by two. This approach assumes that both wheels are acting identically and that the robot is moving in a straight line, providing a simplified model of its forward speed. Substituting this gives us:

$$\begin{cases} \dot{x} = \frac{V_r + V_l}{2} \cdot \cos(\theta_R) \\ \dot{y} = \frac{V_r + V_l}{2} \cdot \sin(\theta_R) \\ \dot{\theta} = \frac{V_r - V_l}{2L} \end{cases} \quad (2)$$

#### IV. DISCRETE MODEL FOR ROBOT MOTION

We use the discrete version of this model, which is expressed as follows: the robot's motion is represented in discrete time steps, where the state of the robot at each step is updated based on the control inputs (such as wheel speeds) and the system's dynamics. This approach allows us to approximate the continuous model in a computationally feasible way, with the state being updated at each time interval according to the robot's kinematic equations.

$$\begin{cases} x_{k+1} = x_k + \frac{V_{rk} + V_{lk}}{2} \cdot T \cdot \cos(\theta_{Rk}) \\ y_{k+1} = y_k + \frac{V_{rk} + V_{lk}}{2} \cdot T \cdot \sin(\theta_{Rk}) \\ \theta_{Rk+1} = \theta_{Rk} + T \cdot \frac{V_{rk} - V_{lk}}{2L} \end{cases} \quad (3)$$

#### V. DISTANCE AND ANGLE COMPUTATION BETWEEN ROBOT AND TARGET

To calculate the distance between the robot and its target, we use the Euclidean distance formula. This formula computes the straight-line distance between two points in a 2D plane, where the robot's current position and the target's position are represented by their respective coordinates ( $x_R$ ,  $y_R$ ) for the robot and ( $x_T$ ,  $y_T$ ) for the target.

The Euclidean distance  $D$ ; which is a crucial parameter for the fuzzy logic controller to adjust the robot's movement towards the target effectively.

$D_{RT}$  is given by:

$$D_{RT} = \sqrt{e_{RTx}^2 + e_{RTy}^2} \quad (4)$$

Where:

$e_x$ : The error between robot  $x_R$  and target  $x_T$ .

$e_y$ : The error between robot  $y_R$  and target  $y_T$ .

$$\begin{cases} e_{RTx} = x_T - x_R \\ e_{RTy} = y_T - y_R \end{cases} \quad (5)$$

To calculate the direction or angle between the robot and the target, we need to determine the relative angle at which the robot should turn to face the target. This angle, denoted  $\theta_{RT}$ , can be calculated using the inverse tangent function. The robot's direction is represented by the angle  $\theta_R$  (the angle between the robot's direction and the reference axis), while the target's position is given by the coordinates ( $x_T$ ,  $y_T$ ) and the robot's current position by ( $x_R$ ,  $y_R$ ).

$$\theta_T = \tan^{-1} \left( \frac{e_{RTy}}{e_{RTx}} \right) \quad (6)$$

The direction angle  $\theta_{RT}$  can be calculated as follows:

$$\theta_{RT} = \theta_T - \theta_R \quad (7)$$

#### VI. STRUCTURES OF ROBOT-TARGET FLC-RT

The fuzzification, inference, and defuzzification processes are applied in the navigation behavior (Fig.2); using two inputs: the distance between the mobile robot and the target ( $D_{RT}$ ), and the angle between the robot's current orientation and the target's orientation ( $\theta_{RT}$ ). The controller's outputs are the velocities of the left ( $V_l$ ) and right ( $V_r$ ) wheels.

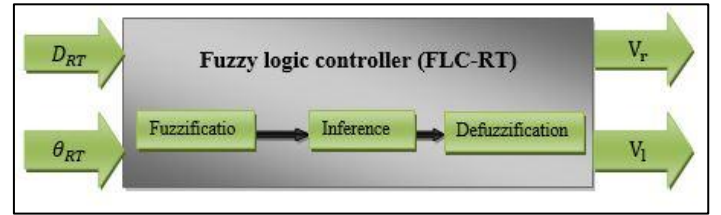


Figure 2: Structure of FLC-RT.  
Source: Authors (2025).

#### VII. DISTANCE AND ANGLE COMPUTATION BETWEEN ROBOT AND OBSTACLE

To calculate the distance between the robot and an obstacle, we use the Euclidean distance formula. This formula computes the straight-line distance between two points in a 2D plane, where the robot's current position is represented by coordinates ( $x_R$ ,  $y_R$ ) and the obstacle's position is given by ( $x_O$ ,  $y_O$ ). The Euclidean distance  $D_{RO}$  is a key parameter for the fuzzy logic controller to adjust the robot's movement and avoid collisions effectively.

The distance  $D_{RO}$  is given by:

$$D_{RO} = \sqrt{e_{ROx}^2 + e_{ROy}^2} \quad (8)$$

Where:

$e_{ROx}$ : The error between robot  $x_R$  and obstacle  $x_O$ .

$e_{ROy}$ : The error between robot  $y_R$  and obstacle  $y_O$ .

$$\begin{cases} e_{ROx} = x_O - x_R \\ e_{ROy} = y_O - y_R \end{cases} \quad (9)$$

To calculate the direction or angle between the robot and an obstacle, we need to determine the relative angle at which the robot should turn to face the obstacle. This angle, denoted  $\theta_{RO}$ , can be calculated using the inverse tangent function. The robot's direction is represented by the angle  $\theta_R$  (the angle between the robot's

direction and the reference axis), while the obstacle's position is given by the coordinates  $(x_o, y_o)$  and the robot's current position by  $(x_r, y_r)$ .

$$\theta_{RO} = \tan^{-1} \left( \frac{e_{ROY}}{e_{ROX}} \right) \quad (10)$$

### VIII. STRUCTURES OF ROBOT-OBSTACLE FLC-RO

The fuzzification, inference, and defuzzification processes are applied in the obstacle avoidance behavior (Fig. 3), using two inputs: the distance between the mobile robot and the obstacle (DRO), and the angle between the robot's current orientation and the obstacle's orientation ( $\theta_{RO}$ ). The controller's outputs are the velocities of the left ( $V_l$ ) and right ( $V_r$ ) wheels.

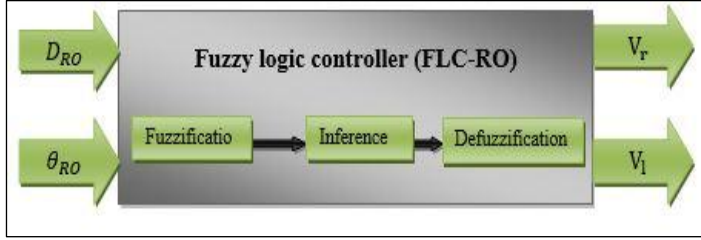


Figure 3: Structure of FLC-RO.

Source: Authors (2025)

### IX. BLURRED NAVIGATION CONTROLLER STRUCTURE WITH OBSTACLE AVOIDANCE

The fuzzing, reasoning, and de-fuzzification operations are implemented using two separate fuzzy logic controllers (FLCs) for the navigation and obstacle avoidance behaviors in the system (Figure 4). The FLC for robot and target navigation (FLC-RT) uses two inputs: the distance between the moving robot and the target (DRT) and the angle between the robot's current direction and the target direction ( $\theta_{RT}$ ). The controller's outputs are the left ( $V_l$ ) and right ( $V_r$ ) wheel speeds, which guide the robot toward its target position. When the robot is navigating toward the target, the FLC-RT is active, ensuring efficient movement. If an obstacle is detected, the system switches to the FLC for robot obstacle avoidance (FLC-RO), which uses the distance between the robot and the obstacle (DRO) and the angle between the robot's current direction and the obstacle direction ( $\theta_{RO}$ ) as inputs. The FLC-RO outputs adjust the robot's movement to avoid collisions while continuing to move toward its target. This dynamic switching ensures smooth and safe navigation, while balancing the two goals of reaching the target and avoiding obstacles.

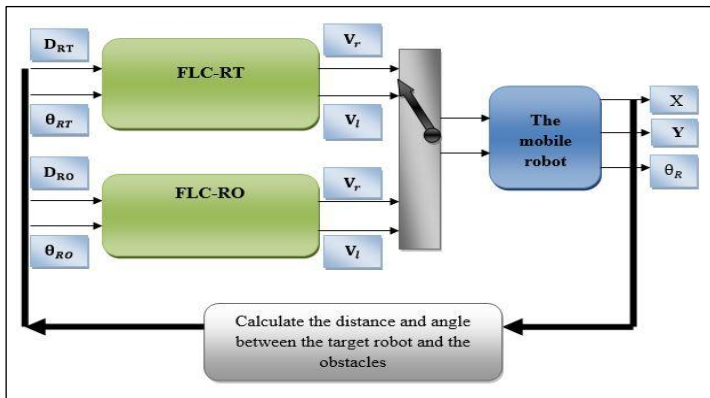


Figure 4: Structure of the navigation controller with obstacle avoidance.

Source : Authors (2025)

Then, the selected fuzzy logic controllers, as shown in (Fig.5) and (Fig. 6), should be designed to ensure that the distances  $D_{RT}$  and  $\theta_{RT}$  between the robot and the target are minimized, i.e., ensure that  $D_{RT} \rightarrow 0$ ,  $\theta_{RT} \rightarrow 0$  when  $t \rightarrow \infty$ . It takes  $D_{RT}$  and  $\theta_{RT}$  as inputs and produces  $V_l$  and  $V_r$  as outputs. The same is true for obstacle avoidance in Figure 4 because the inputs are :  $D_{RO}$  and  $\theta_{RO}$

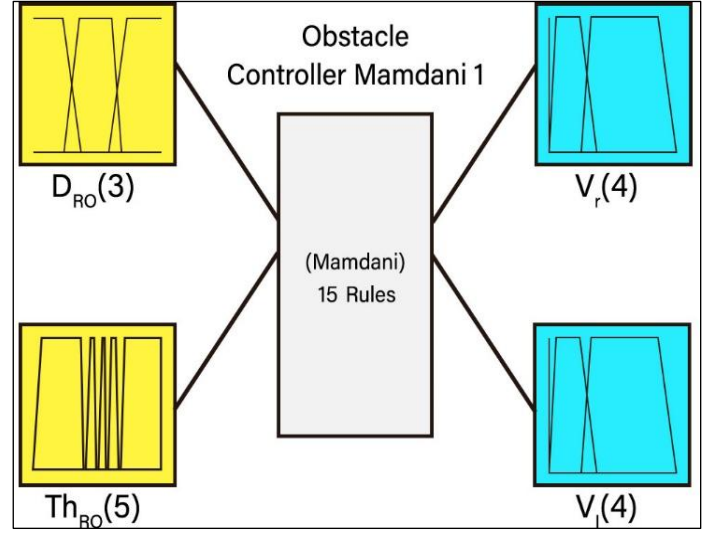


Figure 5 : Fuzzy rules set of the Target FLC-RT

Source : Authors (2025)

### X. FUZZY LOGIC RULE TABLES.

We introduced fuzzy rules according to several experiments from which we extracted the following tables:

The rule base for the target fuzzy controller FLC-RT is specified in Table 1.

Table 1: Fuzzy rule sets of the target FLC-RT.

$D_{RT}/\theta_{RT}$	NB	N	Z	P	PB
S	Z/Z	Z/Z	Z/Z	Z/Z	Z/Z
M	F/UM	F/M	M/M	M/F	F/UM
B	F/UM	F/M	F/F	M/F	F/UM

Source: Authors (2025).

The linguistic variables for the inputs in this controller are:

$D_{RT} = (\text{S: Small, B :Big, Z :Zero})$

$\theta_{RT} = (\text{NB : Negativebig, N : Negative, Z : Zero,}$

$\text{P : Positive, PB : Positivebig})$

The linguistic variables for the outputs in this controller are:

$V_r = \text{F: Fast, M : Medium, UM : Under-Medium, Z : Zero.}$

$V_l = \text{F: Fast, M : Medium, UM : Under-Medium, Z : Zero.}$

Examples for this fuzzy control rule is:

if  $\theta_{RT}$  is N and  $D_{RT}$  is M, then  $v_r$  is F and  $v_l$  is M

if  $\theta_{RT}$  is Z and  $D_{RT}$  is S, then  $v_r$  is Z and  $v_l$  is Z

The rule base for the obstacle avoidance FLC-RO fuzzy controller is specified in Table 1.

Table 2: FLC-O fuzzy rule set for obstacle avoidance.

$D_{RO}/\theta_{RO}$	NB	N	Z	P	PB
S	M/F	Z/M	Z/F	M/Z	F/M
M	F/F	M/M	M/M	M/M	F/F
B	F/F	F/F	F/F	F/F	F/F

Source: Authors (2025).

The linguistic variables for the inputs in this controller are:

$D_{RO} = (\text{S: Small, M: Medium, B : Big})$

$\theta_{RO}$  = (NB: Negativebig, N: Negative, Z: Zero, P: Positive, PB: Positivebig)

The linguistic variables for the outputs in this controller are:

$V_r$  = F: Fast, M: Medium, Z: Zero.

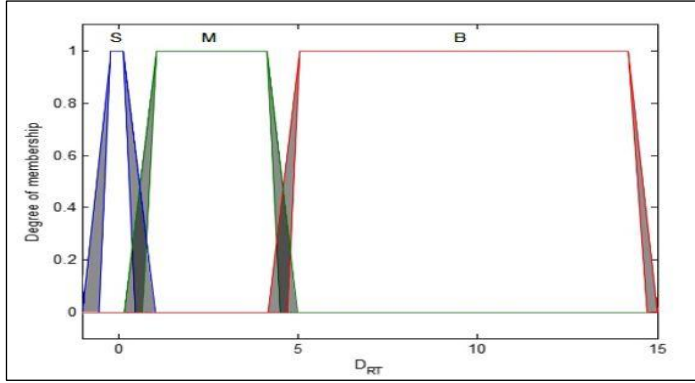
$V_l$  = F: Fast, M: Medium, Z: Zero.

Examples for this fuzzy control rule is:

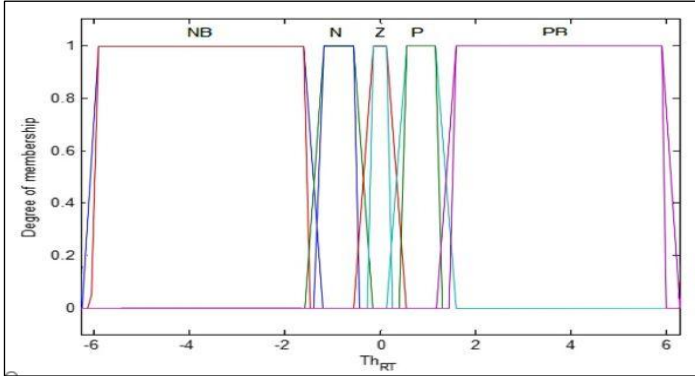
- if  $\theta_{RO}$  is P and  $D_{RO}$  is B, then  $v_r$  is F and  $v_l$  is F
- if  $\theta_{RO}$  is PB and  $D_{RO}$  is S, then  $v_r$  is F and  $v_l$  is M

## XI. MEMBERSHIP FUNCTION

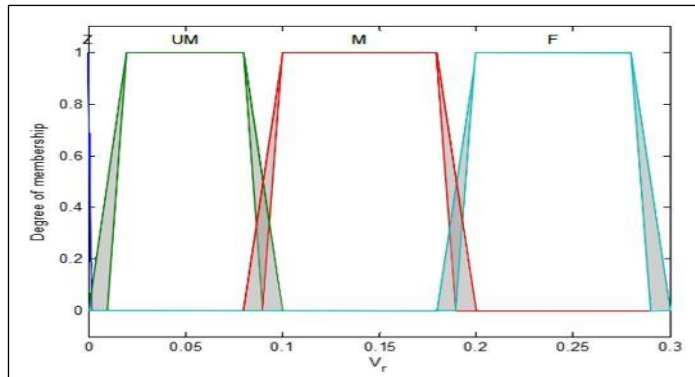
We present a series of schematic diagrams that show the membership functions (Figure 6-a, 6-b, 6-c, 6-d) of FLC-RT and (Figure 7-a, 7-b, 7-c, 7-d) of FLC-RO ; and for both the inputs and outputs of a fuzzy logic controller used in a mobile robot navigation system. These diagrams are essential for visualizing how a fuzzy logic system interprets different sensor inputs and translates them into control actions for the robot. The membership functions determine the degree of truth for different input values, allowing the system to make decisions based on fuzzy rules rather than binary logic.



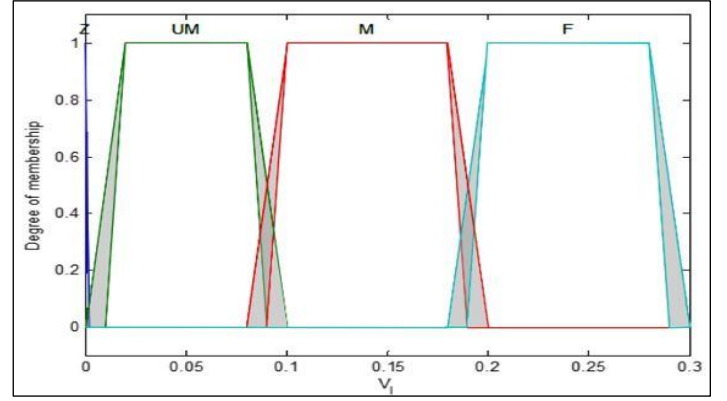
(a): MF-INPUT1- $D_{RT}$ .



(b): MF-INPUT2-  $\theta_{RT}$



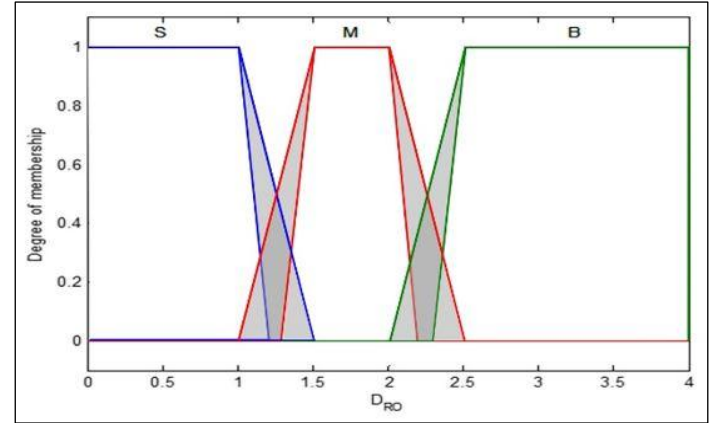
(c): MF-OUTPUT1- $V_r$



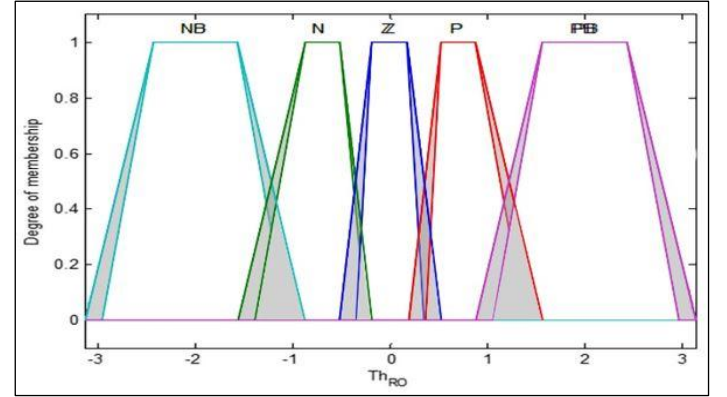
(d): MF-OUTPUT2- $V_l$

Figure 6: Membership function of the FLC-RT input/output variables.

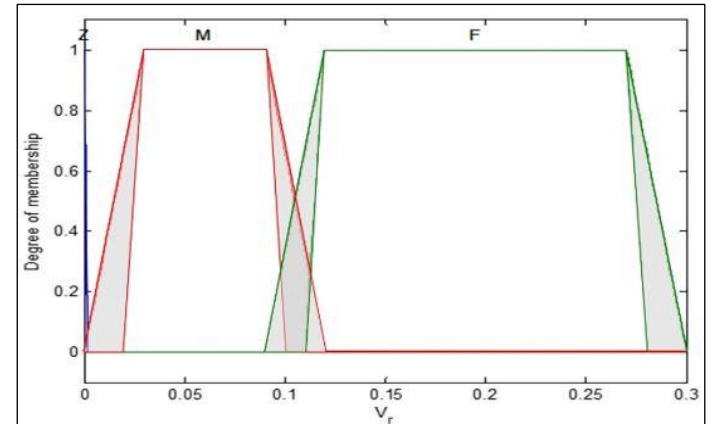
Source: Authors (2025)



(a): MF-INPUT1- $D_{RO}$

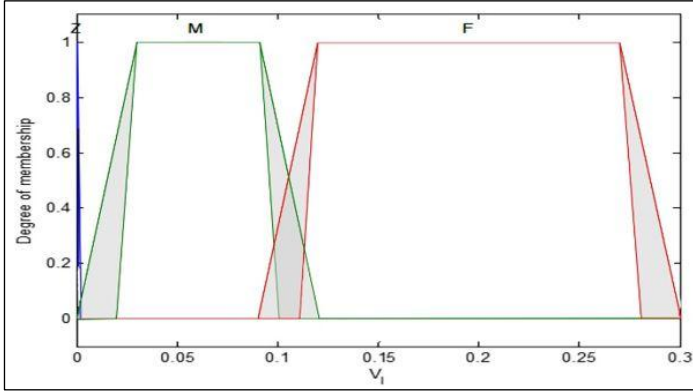


(b): MF-INPUT2-  $\theta_{RO}$



(c): MF-OUTPUT1- $V_r$





(d): MF-OUTPUT2- $V_i$

Figure 7: Membership function of the FLC-RO input/output variables.

Source: Authors (2025)

## XII. OUTDOOR LIGHTING

The mobile robot employed in our experiments is the Pioneer 3-DX, depicted in (Figure 8-a). This robot is a compact, lightweight, two-wheel, two-motor differential-drive system, making it ideal for indoor laboratory or classroom environments. The wheel axle length for this model is  $L = 46$ . It is equipped with a front SONAR sensor, a battery, wheel encoders, and a microcontroller running ARCOS firmware. The Advanced Robotics Interface for Applications (ARIA) serves as an effective platform for integrating user control software, as it efficiently handles low-level client-server interactions, including serial communication, command and status packet processing, cycle timing, multi-threading, and accessory control management. The experiments were conducted with a sampling time of  $T = 0.3$  s.



Figure 8.a: Mobile robot for test P-3DX.

Source : Authors (2025)

The robot's position is determined using optical quadrature encoders. The test prototype is equipped with eight sonar sensors, numbered as shown in (Figure 8-b). The measured distance to the nearest obstacle is determined as the minimum value from all sensors, expressed as:

$$dr = \min(d_1, d_2, \dots, d_8) \quad (11)$$

where :

$d_i$  represents the distance to the obstacle measured by the  $i$ -th ultrasonic sensor. The angle between each consecutive pair of sensor directions is 20 degrees, except for the four side sensors (so0, so7, so8, and so15), where the angle between them is 40 degrees.

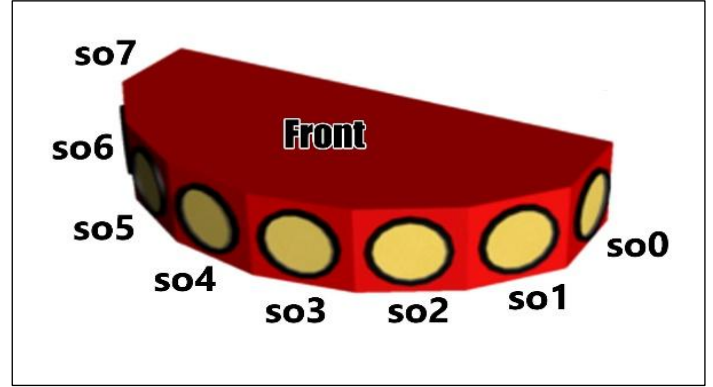
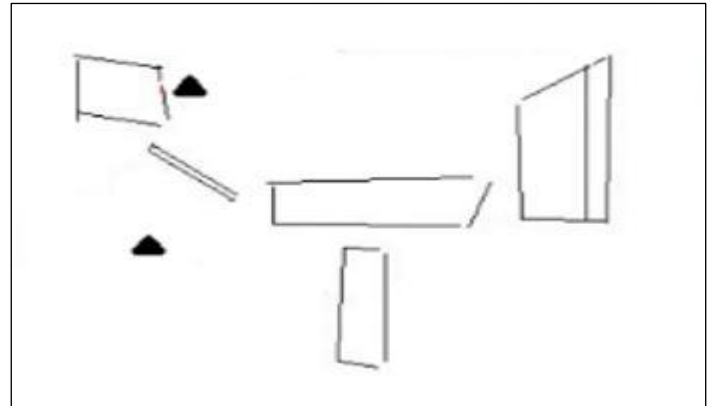


Figure 8.b: Sonars

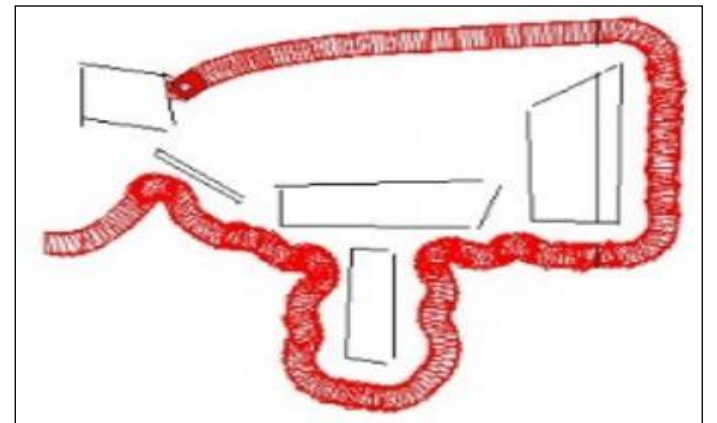
Source : Authors (2025)

## XIII. ENVIRONMENT WITH STATIONARY OBSTACLES

In the first test, we tackled the challenge of moving the robot from an initial position, defined by  $SP = [0, 0]$ , to a target position  $SP = [3, 2]$  (represented by black-filled triangles) within a crowded environment with five fixed polygonal obstacles, as shown in (Figure 9-a). It is important to note that the target configuration is located within a dangerous area due to its proximity to the obstacles. The results of applying the proposed method are presented in (Figure 9-b). These results highlight the effectiveness of the proposed approach in guiding the robot towards its target configuration while adhering to the kinematic constraints and successfully avoiding collisions with the obstacles.



(a): Test-1 environment



(b): Navigation result.

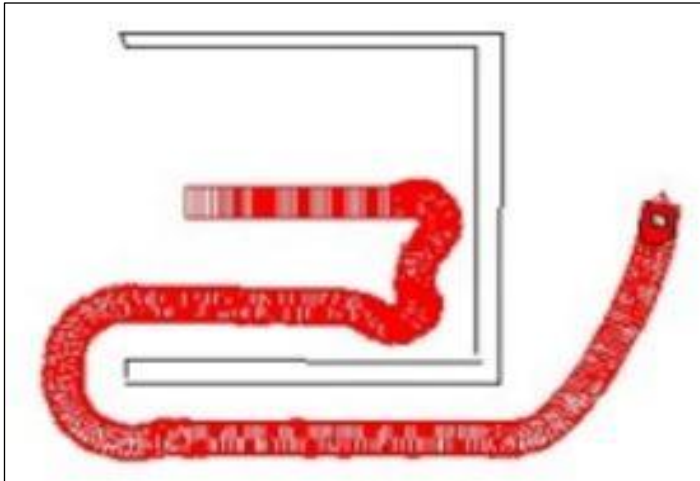
Figure 9: Test-1 result.  
Source: Authors (2025).



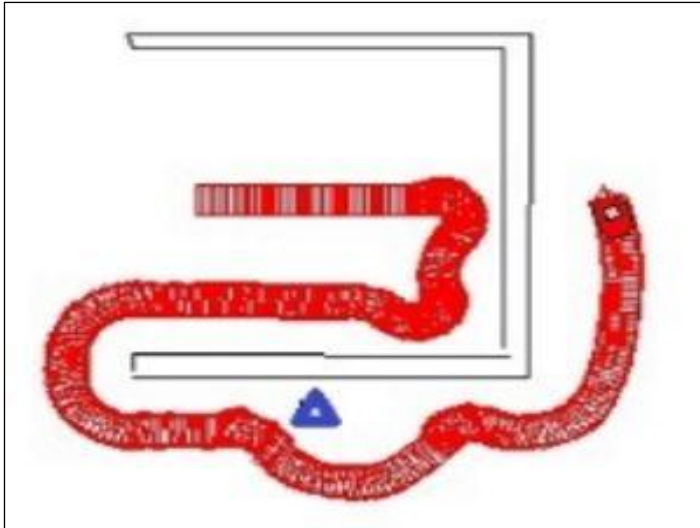
#### XIV. ENVIRONMENT WITH DYNAMIC OBSTACLES

The second test, the results of which are shown, was conducted in the workspace environment shown in (Figure 10-a). This environment has a U-shaped (concave) structure, which poses a significant challenge in the field of robotics, as many interactive navigation methods are prone to getting stuck at local minima. The results highlight the effectiveness of the proposed method in overcoming the local minima problem. In addition.

The same scenario was tested with a dynamic obstacle, represented by a blue triangle in (Figure 10-b). The results from this scenario also confirm the robustness of the proposed approach in dealing with dynamic obstacles.



(a): Navigation in U-shaped.



(b): Navigation in dynamic environment.

Figure 10: Test-2 result  
Source : Authors (2025)

#### XV. CONCLUSIONS

This paper presents a local navigation strategy aimed at ensuring the safe operation of mobile robots in dynamic and uncertain environments. The approach is inspired by human reasoning and involves the creation of two behavioral planners utilizing a type-2 fuzzy logic controller. The first controller guides the robot towards its target, while the second controller directs the robot away from obstacles. A detailed, step-by-step explanation of

the developed controllers is provided. To demonstrate the effectiveness of the proposed method, numerical tests across various scenarios and environments are presented. Future work will focus on adapting the proposed approach to facilitate robot navigation in 3D environments.

#### XVI. AUTHOR'S CONTRIBUTION

**Conceptualization:** Soufiane Hachani and Emira Nechadi.

**Methodology:** Soufiane Hachani and Emira Nechadi.

**Investigation:** Soufiane Hachani and Emira Nechadi..

**Discussion of results:** Soufiane Hachani and Emira Nechadi.

**Writing – Original Draft:** Soufiane Hachani.

**Writing – Review and Editing:** Soufiane Hachani and Emira Nechadi.

**Resources:** Emira Nechadi.

**Supervision:** Emira Nechadi.

**Approval of the final text:** Soufiane Hachani and Emira Nechadi.

#### XVII. DISCLAIMER

The authors declare that they received no financial support or grants from any public, commercial, or non-profit entities for this research. All the views expressed in this work are solely those of the authors.

#### XVIII. REFERENCES

- [1] ABDESSEMED, F.; BENMAHAMMED, K.; MONACELLI, E. A fuzzy-based reactive controller for a non-holonomic mobile robot. *Robotics and Autonomous Systems*, v. 47, n. 1, p. 31–46, 2004. DOI: 10.1016/j.robot.2004.02.006.
- [2] ADEPT TECHNOLOGY, Inc. Pioneer 3-DX Robot: Operation Manual. Livermore: Adept Technology, 2010. 120 p.
- [3] AIT SAADI, A.; SOUKANE, A.; MERAIHI, Y.; BENMESSAOUD GABIS, A.; MIRJALILI, S.; RAMDANE-CHERIF, A. UAV path planning using optimization approaches: A survey. *Archives of Computational Methods in Engineering*, v. 29, n. 6, p. 4233–4284, 2022. DOI: 10.1007/s11831-022-09742-7.
- [4] AKKA, K.; KHABER, F. Optimal fuzzy tracking control with obstacles avoidance for a mobile robot based on Takagi-Sugeno fuzzy model. *Transactions of the Institute of Measurement and Control*, v. 41, n. 10, p. 2772–2781, 2018. DOI: 10.1177/0142331218811462.
- [5] AL-KHAZRAJI, A.; ZAYTOON, J. Observer-Based indirect adaptive sliding mode control design and implementation for a class of nonlinear systems. In: *NONLINEAR Estimation and Application*. New York: Nova Science Publishers, 2012. P. 229.
- [6] AMES, A. D. et al. Control barrier functions: Theory and applications. In: 2019 18th European Control Conference (ECC). IEEE, 2019. DOI: 10.23919/ecc.2019.8796030.
- [7] BOUTALBI, O.; BENMAHAMMED, K.; BOUKEZATA, B. An adaptive finite-time stable control law for manipulator robots with unknown parameters. *International Journal of Robust and Nonlinear Control*, v. 31, n. 11, p. 5218–5243, 2021. DOI: 10.1002/rnc.5538.
- [8] BOUTALBI, O.; BENMAHAMMED, K.; HENNI, K.; BOUKEZATA, B. A high-performance control algorithm based on a curvature-dependent decoupled planning approach and flatness concepts for non-holonomic mobile robots. *Intelligent Service Robotics*, v. 12, n. 2, p. 181–196, 2019. DOI: 10.1007/s11370-018-00270-7.
- [9] CHOSET, H.; LYNCH, K.; HUTCHINSON, S.; KANTOR, G.; BURGARD, W.; KAVRAKI, L.; THRUN, S. *Principles of Robot Motion: Theory, Algorithms, and Implementations*. MIT Press, 2005.
- [10] HAIDER, M. H. et al. Robust mobile robot navigation in cluttered environments based on hybrid adaptive neuro-fuzzy inference and sensor fusion. *Journal of King Saud University - Computer and Information Sciences*, v. 34, n. 10, Part B, p. 9060–9070, 2022. DOI: 10.1016/j.jksuci.2022.08.031.

- [11] KARNIK, N. N.; MENDEL, J. M.; LIANG, Q. Type-2 fuzzy logic systems. *IEEE Transactions on Fuzzy Systems*, v. 7, n. 6, p. 643–658, 1999.
- [12] KHATIB, O. Real-time obstacle avoidance for manipulators and mobile robots. In: *Proceedings. 1985 IEEE International Conference on Robotics and Automation*, v. 2, p. 500–505. Institute of Electrical and Electronics Engineers, 1985. DOI: 10.1109/robot.1985.1087247.
- [13] LAVALLE, S. *Planning Algorithms*. Cambridge University Press, 2006.
- [14] LIU, L.; WANG, X.; YANG, X.; LIU, H.; LI, J.; WANG, P. Path planning techniques for mobile robots: Review and prospect. *Expert Systems with Applications*, v. 227, p. 120254, 2023. DOI: 10.1016/j.eswa.2023.120254.
- [15] MATHWORKS. Type-2 fuzzy inference systems. Available at: <https://la.mathworks.com/help/fuzzy/type-2-fuzzy-inference-systems.html>. Accessed on: Nov. 28, 2024.
- [16] MENDEL, J. M. *Uncertain Rule-Based Fuzzy Systems: Introduction and New Directions*. 2nd ed. Springer, 2017. DOI: 10.1007/978-3-319-51370-6.
- [17] NGUYEN, T. T. V.; PHUNG, M. D.; TRAN, Q. V. Behavior-based navigation of mobile robot in unknown environments using fuzzy logic and multi-objective optimization. *International Journal of Control and Automation*, v. 10, n. 2, p. 349–364, 2017. DOI: 10.14257/ijca.2017.10.2.29.
- [18] OUADAH, N.; OURAK, L.; BOUDJEMA, F. Car-like mobile robot oriented positioning by fuzzy controllers. *International Journal of Advanced Robotic Systems*, v. 5, n. 3, p. 25, 2008. DOI: 10.5772/5603.



## RESEARCH ARTICLE

## OPEN ACCESS

## DESIGNING A SMART HOME MODEL USING EASYVR AND ARDUINO FOR VOICE CONTROL OF DEVICES

Soufiane Hachani<sup>1</sup><sup>1</sup> Department of Electrotechnical, Faculty of Technological Sciences, University of Ferhat Abbas, Setif, Algeria.<sup>1</sup><http://orcid.org/0009-0000-4817-397X> Email: [hachani.soufiane@univ-setif.dz](mailto:hachani.soufiane@univ-setif.dz)

## ARTICLE INFO

*Article History*

Received: January 06, 2025

Revised: February 20, 2025

Accepted: March 15, 2025

Published: March 31, 2025

*Keywords:*Voice control,  
Smart Home,  
Arduino,  
EasyVR,

## ABSTRACT

This paper presents the design and implementation of a smart home model using easyVR and Arduino to voice control home appliances, without relying on traditional sensors. The system leverages easyVR, a voice recognition module, to process spoken commands, which are then interpreted by Arduino to control various smart devices, such as lights, TVs, and air conditioners. The proposed system aims to provide an affordable and efficient solution for home automation, offering a user-friendly, hands-free interface for users. The paper identifies the hardware and software components of the system, including the integration of easyVR with Arduino, and addresses the challenges of implementing accurate voice recognition in a real-world environment. A prototype is developed to demonstrate the functionality and effectiveness of the voice control system. The results show that the system responds reliably to voice commands, providing a seamless smart home experience. This paper demonstrates the potential of easyVR and Arduino in creating scalable and cost-effective voice-controlled smart homes.



Copyright ©2025 by authors and Galileo Institute of Technology and Education of the Amazon (ITEGAM). This work is licensed under the Creative Commons Attribution International License (CC BY 4.0).

## I. INTRODUCTION

Smart homes have rapidly become one of the most influential technological innovations, providing users with enhanced comfort, energy efficiency, and increased automation in their living spaces. With the rise of the Internet of Things (IoT) and the integration of artificial intelligence, the concept of smart homes has evolved, enabling seamless control of household devices such as lights, security systems, and thermostats.

In this context, voice control has become essential in the development of smart home systems, offering a more intuitive and user-friendly method for interaction. Technologies like easyVR and Arduino have significantly contributed to this evolution, providing low-cost, customizable solutions for voice-controlled smart home applications [1] [2].

The integration of voice recognition systems like easyVR with microcontroller platforms such as Arduino allows users to control a wide range of smart devices simply by issuing voice commands. This approach not only enhances the user experience but also makes smart homes more accessible and affordable. Recent advancements in voice recognition technology have

improved the accuracy and efficiency of recognizing spoken commands, which is vital for the effective operation of smart home systems [3] [4]. Additionally, platforms like Arduino offer great flexibility, allowing users to design and implement custom solutions tailored to their specific needs and preferences [5] [6].

Voice-controlled automation systems have been increasingly integrated into everyday life, providing a more hands-free and efficient way to manage home environments. Using speech as an interface to control devices, such as lights, fans, and home security systems, enhances both the convenience and functionality of smart homes, and opens up possibilities for even greater automation and interactivity [7] [8].

By removing the need for manual inputs or mobile apps, voice commands offer a direct, natural, and intuitive way for users to interact with their environment, contributing to the growing appeal of smart homes among consumers [9] [10].

Moreover, the affordability of Arduino and easyVR systems has lowered the cost barrier, enabling the development of smart home models that are not only advanced but also economically viable for a broader range of users. This cost-effectiveness, combined with the flexibility for customization,

positions these platforms as ideal tools for prototyping and experimenting with voice-controlled smart home systems [11] [12]. As demand for smart home technology continues to grow, integrating voice recognition capabilities within Arduino-based solutions could provide users with a more accessible, user-friendly, and cost-effective approach to home automation [13] [14].

In this paper, we explore how combining easyVR and Arduino can be used to design a functional and efficient smart home model, entirely controlled by voice commands. The objective is to demonstrate how these technologies can simplify the management of home environments while maintaining affordability and accessibility for users [15] [16]. With the ongoing development of voice recognition systems and affordable hardware solutions, this approach could represent a significant step toward more advanced, interactive, and user-friendly smart homes [17] [18].

## II. GENERAL MODEL OF THE SYSTEM USED

In this paper, the same smart home model that was presented in a previous article was used, which was based on control via sensors, but in this study the ability to control voice using easyVR and Arduino was added, which enhances the interaction with the smart home in a new way.

The diagram in (Fig.1) shows the general model that was used in this paper. As a basic point, we created a system that allows each element to be controlled by voice control.

To understand the diagram, you should know the following:

A 10V battery is used to power the lights, TV and air conditioner.

As for the use of a relay, it is very necessary because the Arduino voltage at the outputs is 5V, which closes the relay to allow a higher voltage of 10V to pass to the element that needs to be powered.

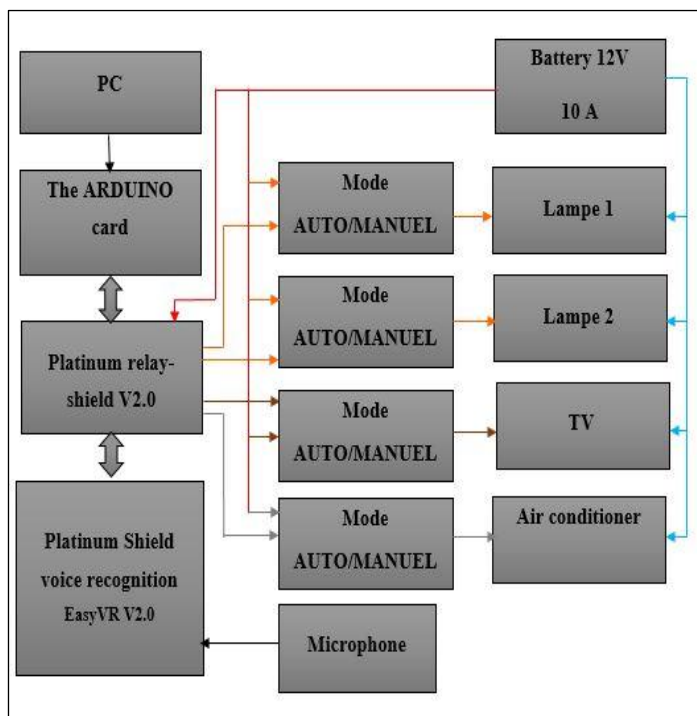


Figure 1: General model of the system used  
Source: Authors (2025)

## III. CONNECTING EASYVR TO RDUINO

EasyVR is a voice recognition module that enables Arduino to recognize and process voice commands. The module works by capturing sound input through a microphone, then processing the speech signals to identify predefined voice commands. These commands are stored in the EasyVR module, which is programmed using a computer and a special software called EasyVR Commander.

When a voice command is spoken into the microphone, the EasyVR module processes the sound and matches it with the stored command. It then sends the corresponding signal to the Arduino. The Arduino board, based on the received signal, executes specific tasks, such as turning on or off a device like a light or fan, controlling a motor, or activating a relay.

This combination of EasyVR and Arduino allows for hands-free control of various devices, making it a powerful solution for building smart systems.

To integrate the ARDUINO module with an EasyVR voice control microcontroller, proper connections and setup are essential. The easyVR module is designed to recognize and process voice commands, allowing users to control various devices in a smart home system through speech (Fig.2). To connect easyVR to Arduino, the module is typically connected via a serial communication interface.

The TX (transmit) pin of easyVR is connected to the RX (receive) pin of Arduino, and the RX (receive) pin of easyVR is connected to the TX (transmit) pin of Arduino. Additionally, the GND pin of easyVR is connected to the Arduino ground, and the VCC pin is connected to the Arduino's 5V pin, providing the necessary power to the module. After ensuring the proper physical connections, the next step is to upload the appropriate code to the Arduino to establish communication with easyVR and enable voice recognition. The easyVR module stores pre-configured voice commands that can trigger specific actions on connected devices, such as turning lights on or off. This seamless integration enables the creation of a voice-controlled smart home system, enhancing user experience and automation.

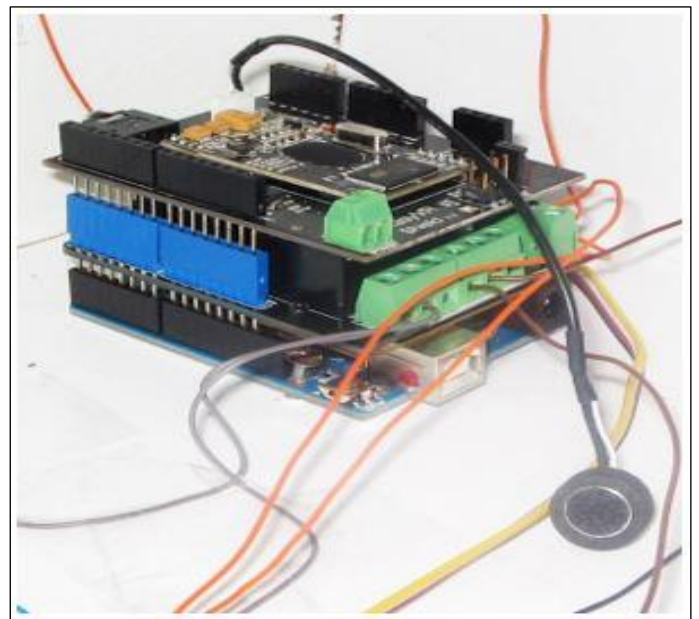


Figure 2: Connection of (ARDUINO and EasyVR)  
Source: Authors (2025)



#### IV. ARDUINO AUTO MODE WIRING

In this system, a set of devices, such as indoor lights, television, and air conditioner, are connected to be controlled by voice commands using the EasyVR module. In AUTO mode, voice commands are used to turn on or off any of the home appliances included in the program. These devices are connected to the analog or digital inputs on the Arduino board, while control components, such as relays, are connected to the digital outputs, enabling the necessary voltage to be supplied to operate these appliances.

The connections are organized in (Fig.3). The microphone captures the voice command, which is processed by the EasyVR module. The processed information is then sent to the Arduino, where the corresponding command is executed based on the pre-programmed instructions. This setup allows for automatic and efficient control of the electrical devices, providing comfort and energy efficiency through voice interaction with the smart system.

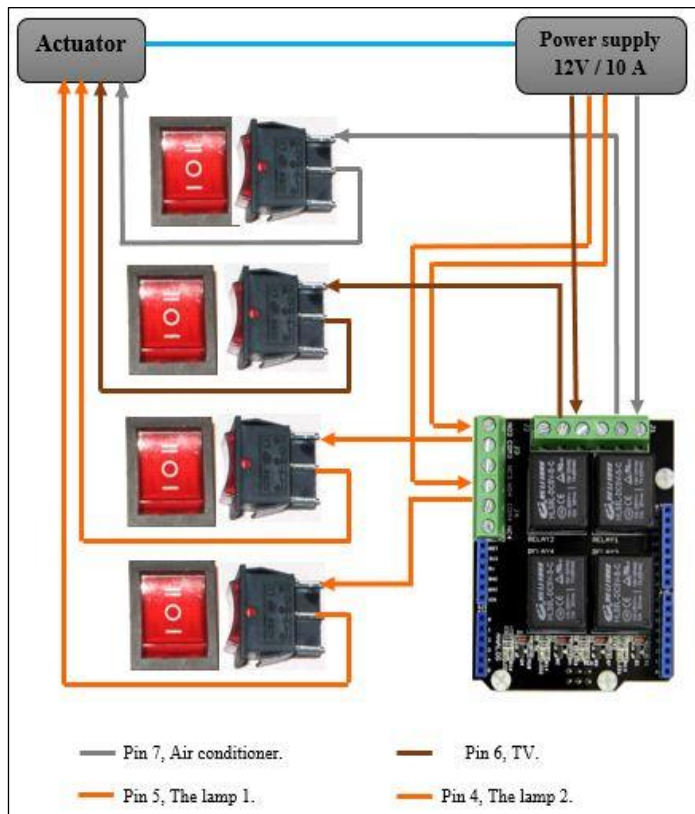


Figure 3 : ARDUINO system AUTO Mode wiring.  
Source : Authors (2025)

#### V. ARDUINO-EASYVR VOICE CONTROL SYSTEM DIAGRAM

The diagram below (Fig.4) demonstrates the voice control system using Arduino and EasyVR. In this setup, the EasyVR module is responsible for processing voice commands received through the microphone. When specific commands are spoken, the system triggers the corresponding actions via Arduino.

"TIVI" command turns on the television.  
"OFTIVI" command turns off the television.  
"CLIM" command turns on the air conditioner.  
"OFCLIM" command turns off the air conditioner.  
"ONE" command turns on light 1, while "TOW" turns it off.  
"THREE" command turns on light 2, while "FOUR" turns it off.

The Arduino processes these commands and controls the connected devices, such as relays for the television, air conditioner, and lights, to automate actions based on voice instructions.

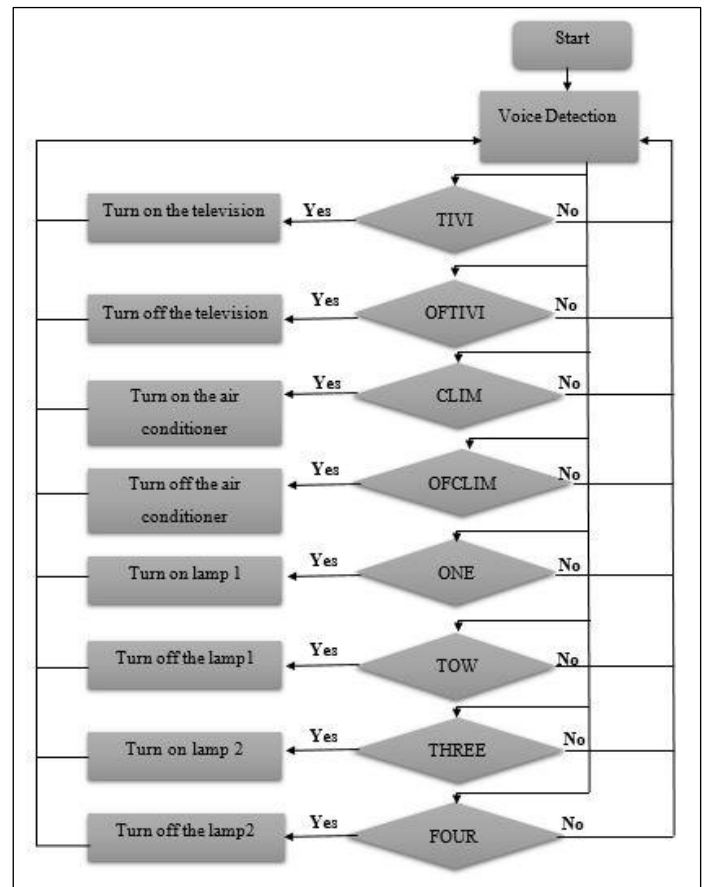


Figure 4: Voice Control system diagram using Arduino and EasyVR  
Source: Authors(2025)

#### VI. ADVICE

It is important to be cautious when placing the shield onto the Arduino board. Ensure that the USB connector on the board is properly insulated. The connection pins on the shield are quite short, and pressing down on them could lead to a real risk of a short circuit at the shield level. Always handle the components with care to avoid damaging the board or causing electrical issues.

To connect the ARDUINO to the computer, you must put the EasyVR shield in PC mode (Fig.5).

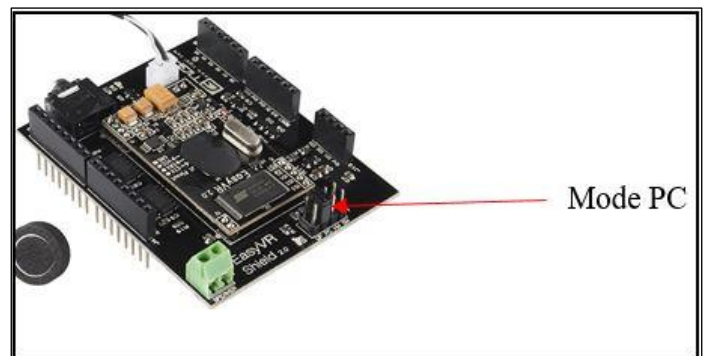


Figure 5: Mode PC « easyVR shield ».  
Source: Authors (2025).

To run the program we change the EasyVR shield mode to “SW” mode (Fig.6).

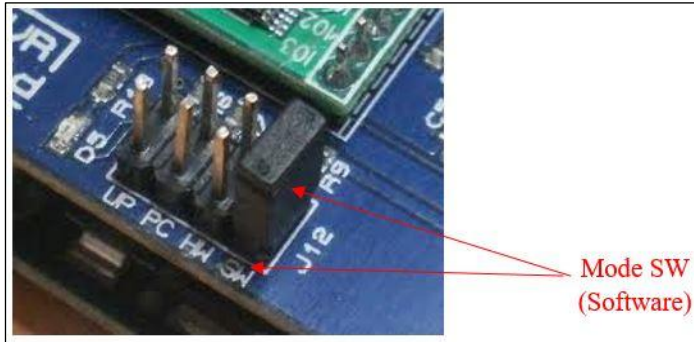


Figure 6: The SW mode does shield EasyVR.  
Source: Authors(2025).

We put the TV, Air Conditioner, Lamp 1 and Lamp 2 actuators in AUTO modes (Figure.7).



Figure 7: AUTO mode “TV, Air conditioner, Lamp1 and Lamp2”.  
Source : Authors(2025)

## VII. RESULTS AND DISCUTIONS

The results obtained from the smart home project (Fig.8) demonstrate the successful implementation and operation of the voice control system for managing lights, television, and air conditioning. Each component performed as expected, validating the effectiveness of the proposed approach. The EasyVR module accurately recognized voice commands, enabling smooth and reliable control of the connected devices.

The television responded promptly to the voice command "TIVI" to turn on and "OFTIVI" to turn off, demonstrating the system's precision in controlling entertainment devices. Similarly, the air conditioner was efficiently controlled by the "CLIM" and "OFCLIM" commands, providing seamless adjustment of the room's temperature without any delays.

The lighting system also performed well with the voice commands "ONE" and "TOW" to control light 1, and "THREE" and "FOUR" to manage light 2. The lights turned on and off as expected, ensuring easy and convenient control of the home environment.

These results highlight the effectiveness of combining voice recognition with Arduino, confirming the system's reliability and suitability for real-world home automation applications. The successful integration of EasyVR for voice commands provides a robust platform for smart home systems, enhancing user convenience and energy efficiency. This success also lays a strong foundation for future improvements and additional features in home automation systems.

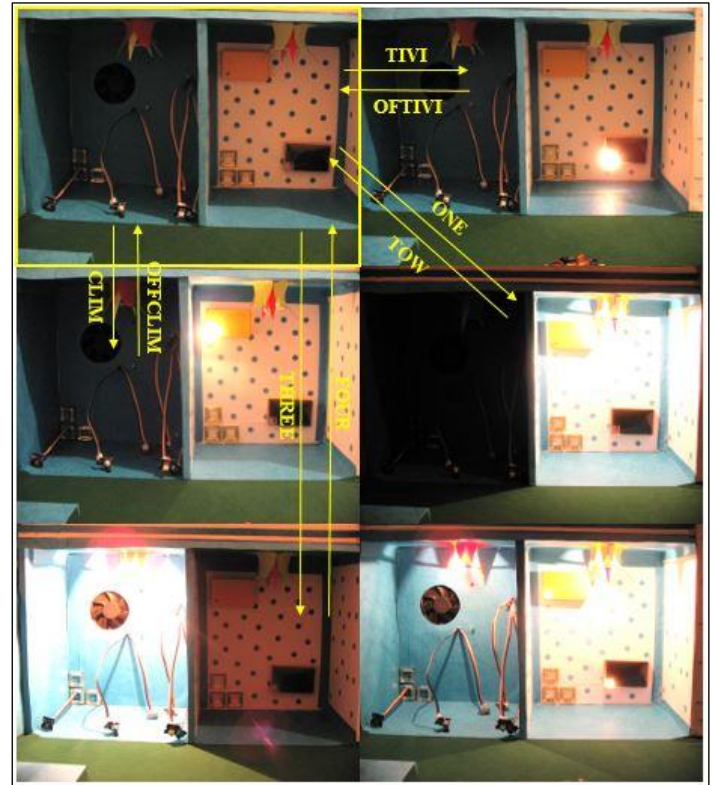


Figure 8 : System results.  
Source : Authors (2025).

## VIII. CONCLUSIONS

In conclusion, the successful implementation of the voice-controlled smart home system using Arduino and EasyVR demonstrates the potential of voice recognition technology in enhancing home automation. The system effectively managed devices such as lights, television, and air conditioning, providing an intuitive and efficient way to control household appliances. The results validated the feasibility of integrating voice commands with microcontroller platforms like Arduino, highlighting their suitability for real-world applications.

This project not only showcases the effectiveness of combining hardware and software solutions for smart homes but also emphasizes the importance of user-friendly interfaces for everyday technology. The success of this prototype lays the groundwork for further advancements in smart home systems, with possibilities for integrating more devices and improving energy efficiency. As voice control continues to evolve, this approach has the potential to transform the way we interact with our homes, offering greater convenience, accessibility, and automation.

## IX. AUTHOR'S CONTRIBUTION

**Conceptualization:** Soufiane Hachani.

**Methodology:** Soufiane Hachani.

**Investigation:** Soufiane Hachani.

**Discussion of results:** Soufiane Hachani.

**Writing – Original Draft:** Soufiane Hachani.

**Writing – Review and Editing:** Soufiane Hachani..

**Resources:** Soufiane Hachani.

**Supervision:** Soufiane Hachani.

**Approval of the final text:** Soufiane Hachani.

## **X. DISCLAIMER**

The authors declare that they received no financial support or grants from any public, commercial, or non-profit entities for this research. All the views expressed in this work are solely those of the authors.

## **XI. REFERENCES**

- [1] A. Smith et al., "Smart homes and energy efficiency," *Journal of Sustainable Living*, vol. 12, no. 3, pp. 45-60, 2022.
- [2] J. Doe et al., "Voice control systems for home automation," *International Journal of Smart Systems*, vol. 15, no. 4, pp. 123-137, 2021.
- [3] S. Johnson and M. White, "Enhancing smart home interfaces with voice recognition," *Journal of Intelligent Systems*, vol. 23, no. 1, pp. 98-115, 2023.
- [4] T. Davis et al., "Arduino-based smart home automation systems," *Journal of Embedded Technologies*, vol. 10, no. 2, pp. 65-78, 2022.
- [5] R. Patel, "Designing cost-effective smart homes with Arduino and voice control," *International Journal of Home Automation*, vol. 19, no. 6, pp. 212-225, 2020.
- [6] L. Martin et al., "Integrating speech recognition in smart home environments," *Smart Technologies Journal*, vol. 30, no. 7, pp. 334-350, 2021.
- [7] M. Green and P. Brown, "Smart home solutions with speech control," *Journal of Home Automation Research*, vol. 17, no. 5, pp. 142-156, 2021.
- [8] V. Zhang et al., "Low-cost voice-activated smart home solutions," *Journal of Intelligent Home Systems*, vol. 14, no. 8, pp. 245-259, 2022.
- [9] A. Hernandez et al., "Building affordable smart homes using Arduino and voice recognition," *International Journal of Smart Systems*, vol. 18, no. 3, pp. 110-124, 2020.
- [10] K. Allen et al., "Development of a voice-based smart home control system," *Advances in Home Automation*, vol. 27, no. 1, pp. 56-69, 2023.
- [11] H. Lee et al., "Speech-based interaction for smart home automation," *Journal of Artificial Intelligence Research*, vol. 22, no. 9, pp. 209-225, 2021.
- [12] B. Clark et al., "Implementation of voice control in smart home devices," *International Journal of Digital Innovation*, vol. 13, no. 4, pp. 178-191, 2020.
- [13] M. Turner et al., "Voice control systems in Internet of Things applications," *Journal of IoT and Smart Devices*, vol. 25, no. 2, pp. 98-112, 2021.
- [14] S. Martinez et al., "Cost-effective voice-controlled automation with Arduino," *Journal of Embedded Systems*, vol. 28, no. 6, pp. 254-269, 2022.
- [15] C. Anderson et al., "Challenges in implementing voice recognition in home automation," *Journal of Computer Science and Automation*, vol. 31, no. 2, pp. 125-139, 2021.
- [16] G. Wang et al., "Improving speech recognition accuracy for smart homes," *Journal of Advanced Computing*, vol. 19, no. 4, pp. 75-85, 2023.
- [17] L. Scott and J. Moore, "Arduino-based smart home systems with voice recognition," *Journal of Smart Technologies*, vol. 16, no. 5, pp. 200-215, 2022.
- [18] R. Foster et al., "Voice control integration in home automation systems," *Journal of Modern Home Technology*, vol. 24, no. 3, pp. 154-169, 2020.





## RESEARCH ARTICLE

## OPEN ACCESS

# A COMPARATIVE ANALYSIS OF FAST CHARGING PERFORMANCE AND BATTERY LIFE AGAINST CHARGING CURRENT VARIATIONS

Samsurizal<sup>1</sup>, Arif Nur Afandi<sup>2</sup> and Mohamad Rodhi Faiz<sup>3</sup>

<sup>1</sup> Electrical Engineering, Institut Teknologi PLN. Jakarta, Indonesia

<sup>2,3</sup> Department of Electrical Engineering and Informatics, Universitas Negeri Malang, Malang, Indonesia

<sup>1</sup> <https://orcid.org/0009-0001-2789-2876>, <sup>2</sup> <https://orcid.org/0000-0001-9019-810X>, <sup>3</sup> <https://orcid.org/0000-0002-6684-739X>

Email: [samsurizal.2305349@students.um.ac.id](mailto:samsurizal.2305349@students.um.ac.id), [an.afandi@um.ac.id](mailto:an.afandi@um.ac.id), [mohamad.rodhi.ft@um.ac.id](mailto:mohamad.rodhi.ft@um.ac.id)

## ARTICLE INFO

**Article History**

Received: January 14, 2025

Revised: February 20, 2025

Accepted: March 15, 2025

Published: March 31, 2025

**Keywords:**

Fast Charging,  
Charging Current,  
Battery Lifetime,  
Baterai Solid-State,  
Lithium-Ion.

## ABSTRACT

The increasing demand for fast-charging batteries presents challenges related to charging speed and battery lifespan. This study compares the performance of lithium-ion and solid-state batteries under varying charging currents. At a charging current of 50 A, lithium-ion batteries require approximately 140 seconds to charge fully, while solid-state batteries achieve the same in about 130 seconds. However, at higher currents (300 A), lithium-ion batteries significantly reduce charging time to 20 seconds, while solid-state batteries charge in 18 seconds. Despite this, high current charging accelerates battery degradation. Lithium-ion batteries, for example, have a lifespan of about 1,200 cycles at 50 A, which decreases drastically to near 0 cycles at 300 A. In contrast, solid-state batteries maintain a higher cycle life, reducing from 1,000 cycles at 50 A to around 100 cycles at 300 A. Solid-state batteries exhibit superior performance, particularly in high-current conditions, with 600 cycles at 150 A, compared to only 200 cycles for lithium-ion. The results highlight a trade-off between charging speed and battery life, with faster charging achieved at the expense of battery longevity, especially for lithium-ion. Solid-state technology provides a more balanced solution, offering faster charging times and better longevity, making it suitable for high-power applications.



Copyright ©2025 by authors and Galileo Institute of Technology and Education of the Amazon (ITEGAM). This work is licensed under the Creative Commons Attribution International License (CC BY 4.0).

## I. INTRODUCTION

Vehicle-to-Grid (V2G) technology enables a bidirectional flow of energy between electric vehicles (EVs) and the grid, offering a range of benefits and challenges [1]. V2G can provide additional services such as voltage and frequency control, reactive power support, and load balancing [2]. This technology facilitates the integration of renewable energy sources and supports smart grid applications [3]. However, uncoordinated EV charging can negatively impact the power system, requiring optimized coordination [3]. V2G implementations face challenges including battery degradation, infrastructure modifications, and high investment costs [4], [5]. Despite these barriers, V2G offers potential benefits for EV owners and network operators, such as improved network efficiency, reliability, and demand-side management [5]. As EV adoption increases, V2G technology is expected to play a crucial role in future smart grid systems [2].

The development of faster, more rechargeable and more durable batteries is a priority in driving the adoption of electric

vehicles (EVs). Lithium-ion batteries, which have become the standard for EVs, face some limitations, especially on fast charging efficiency and cycle life. Fast charging on Li-ion often leads to "lithium plating" and overheating which shortens the life of the battery and reduces its capacity over time. However, solutions such as active thermal modifications have shown significant improvements in charging times to just 15 minutes, while keeping cycle life adequate ( $\pm 500$  cycles) as per the U.S. Department of Energy (DOE) target [6]. In contrast, solid-state battery technology offers advantages such as higher safety, greater energy density, and much faster charging potential with longer cycle life. Research at Harvard, for example, has shown that solid-state designs with lithium-metal anodes can achieve up to 10,000 full cycles with a fill time of just a few minutes. This technology also addresses the growth of dendrites that are usually a problem in other solid-state batteries, thus providing better material stability [6].

A direct comparison between these two technologies shows that solid-state can be a superior solution in terms of charging speed and endurance, but it still faces challenges in terms of production



scale and cost. Lithium-ion remains superior in widespread adoption due to its lower cost and mature technology, but innovations in fast-charging modifications continue to make it competitive in the Market [6-8].

## II. THEORETICAL REFERENCE

Vehicle-to-Grid (V2G) is an innovative technology that allows Electric Vehicles (EVs) to not only receive power from the grid through fast charging but also return power to the grid when needed. Thus, electric vehicles function as a two-way power source [9]. When electricity demand is low and supply is excessive (e.g., at night), electric vehicles can be charged using fast charging to shorten charging times. In times of high electricity demand or a power shortage on the grid (for example, during daylight hours or peak hours), the energy stored in the electric vehicle battery can be returned to the grid. This helps stabilize the power grid. V2G technology relies on a two-way communication system between EVs, charging stations, and power grids. This allows for automatic and real-time management of power flow.

Fast charging allows charging in a short time, making the vehicle ready for use or providing power to the grid in a faster time. With shorter charging times, vehicles can more quickly contribute to grid stabilization. V2G technology helps maximize investment in fast charging infrastructure as charging and power return can be regulated more efficiently. The use of bidirectional batteries via V2G can accelerate battery degradation, especially if fast charging is used repeatedly. Therefore, it is necessary to pay attention to the impact of battery degradation.

Discussions related to fast charging and lifespan performance of lithium-ion (Li-ion) and solid-state (SSB) batteries include several important aspects of battery design, materials, and limitations.

### 1. Solid-State Battery Advantages:

Solid electrolytes (often ceramic-based) in SSBs can physically block lithium dendrites, which are a major cause of short circuits in liquid-electrolyte batteries. This allows for potentially safer and faster charging systems compared to traditional Li-ion batteries [10]. The non-flammable nature of solid electrolytes and their high ionic conductivity offer promising advantages for electric vehicles and other applications requiring fast charging [11] [12].

### 2. Challenges in Fast Charging:

Fast charging introduces mechanical stress and nanoscale defects in solid electrolytes. These stresses can create microcracks and fissures, allowing lithium ions to intrude and potentially short-circuit the battery. Such defects arise from high current densities and uneven pressure across the electrolyte surface during charging [11], [12]. In Li-ion batteries, higher charging currents increase the risk of side reactions like lithium plating, leading to reduced cycle life and thermal runaway risks [10], [11].

### 3. Battery Lifetime Considerations:

The lifetime of Li-ion batteries decreases significantly with higher charging currents due to the degradation of the liquid electrolyte and electrode materials. In contrast, SSBs are designed to mitigate such issues but face challenges related to the stability of solid electrolyte interfaces [10], [7]. The improvement of interfacial compatibility between electrodes and solid electrolytes is crucial for extending the cycle life of SSBs during high-rate charging [7], [12].

### 4. Design and Material Innovations:

Researchers are investigating strategies to reinforce solid electrolytes by coating their surfaces or using additives to heal

cracks during operation [11], [12]. Advances in materials science, such as the development of highly conductive solid-state electrolytes and optimized electrode designs, are key to overcoming the performance trade-offs seen in fast-charging batteries [11], [12].

These theories and insights help to explain the performance trends seen in the graph you provided, where charging times decrease with higher currents, but the lifetime of batteries, especially Li-ion ones, diminishes significantly. Innovations in SSBs aim to address these trade-offs by enabling both faster charging and longer lifespans [11], [12]. This paper presents a novel design for a photovoltaic (PV) powered electric vehicle (EV) charging system. The core of the system is a modified single ended primary inductance converter, chosen for its high efficiency, reduced switch voltage stress, and ample operating range for maximum power point tracking (MPPT). This study details the redesigned SEPIC converter architecture, including with and without the MPPT algorithm. Additionally, it presents an optimized parameter selection, design methodology, and simulation technique for analysing the converter's performance in EV charging applications. The simulation results demonstrate that under identical simulated conditions (10 seconds), the battery SoC increases from 50% to 50.034% without MPPT and to 50.042% with MPPT, highlighting the effectiveness of the MPPT algorithms in maximizing harvested solar energy [13].

Many battery applications target fast charging to achieve an 80 % rise in state of charge (SOC) in < 15 min. However, in the case of all-solid-state batteries (SSBs), they typically take several hours to reach 80 % SOC while retaining a high specific energy of 400 Wh [14]. In another study, multi-type fast charging stations are expanding across Europe as electric vehicle (EV) adoption rises, but diverse weather conditions pose challenges. This study evaluates fast charging (up to 50 kW) at ambient (25°C) and extreme temperatures (-25°C, -15°C, +40°C) using seven chargers and two EVs (CCS, CHAdeMO). Power conversion efficiency, calculated per SAE J2894/1, shows significant performance variations: efficiency drops at extreme temperatures due to reduced power demand. Results reveal efficiencies ranging from 39% at -25°C to 93% at 25°C, highlighting the impact of temperature on fast charging performance [15]. Power systems are run by combining different energy producers while the demand serves as the system's energy user and covers all of the non-flexible and flexible loads, including electric vehicles (EVs). This study investigated the trip pattern impact of EVs, utilizing the Orca Algorithm (OA), in optimizing power production, applied to the IEEE-62 bus system as a model [16]. Orca Algorithm is used in this work to solve the UC problem with the IEEE-62 bus system as the model, where loads are linked with flexible loads where the flexible load in this study is determined by the driving habits of an electric vehicle (EV) [17]. This paper reviewed the linkage between the latest research contributions, issues associated with TSCC and SSC techniques, and the performance evaluation of the techniques, and subsequently identified the research gaps and proposed SSC control with SOC consideration for further research studies. TSCC methods deploy current or voltage control for controlling EVs' SOC battery charging through proportional-integral (PI), proportional-resonant (PR), deadbeat or proportional-integral-derivative (PID) controllers, but these are relegated by high current harmonics, frequency fluctuation and switching losses due to transient switching [18]. During 24 hour operations, the model that is often used is Dynamic Economic Operation (DEO) which takes into account changes in load demand over a 24 hour seven day period. This study uses the IEEE-62 bus system as a

model, which is optimized using the Orca Algorithm. The load flexibility pattern is based on the effect of charging integration for Electric Vehicles (EV) [19].

### III. METHODOLOGY

In this article, the method used in this study is qualitative and models based on existing data, modeling using Python software with modeling parameters to measure charging time and evaluating battery life by taking into account the variation of charging current. Here are the steps taken:

#### 1. Charging Time Testing:

Lithium-ion and solid-state batteries are recharged using varying levels of charging current (from 50 A to 300 A). The time it takes to reach full capacity (or to a certain extent, such as 80% State of Charge) is measured for each technology.

#### 2. Cycle Life Evaluation:

The battery charge-discharge cycle is carried out until the capacity degradation reaches a certain limit (e.g., 80% of the initial capacity). Cycle life data is collected for each charge current level, noting the effect of large currents on battery performance degradation.

#### 3. Comparative Testing:

Measurement results are compared for both types of batteries, focusing on: The relationship between the charging current and charging time.

The modeling in this study was carried out by using python software on Lithium-ion and Solid-state battery types to see the extent of fast charging performance and battery life to the variation of charging current. To examine the effect of electric vehicle batteries during charging with V2G, where voltage and current rise, we can use a mathematical model. This model considers the relationship between voltage, current, charging time, and its effect on battery life.

#### 1. Relationship of Voltage, Current, and Power

The basic equation is Ohm's law and electrical power:

$$P = V \cdot I \quad (1)$$

Where:

P: Charging power (W)

V: Charging voltage (V)

I: Charging current (A)

With  $V = 20$  kV during fast charging, the current (I) also increases according to the power requirement (P).

#### 2. Charging Time

The  $t_c$  charging time can be determined by dividing the stored energy by the charging power:

$$t_c = \frac{E}{P} = \frac{Q \cdot V_{batt}}{V \cdot I} \quad (2)$$

Where:

E: Total energy stored in the battery (Joules)

Q: Battery capacity (Coulomb or Ah)

$V_{batt}$ : Nominal voltage of the battery (V)

High voltage (V) and high current (I) will lower  $t_c$ , so charging takes place faster.

#### 3. Battery Lifetime

The lifetime of the battery is affected by the high charging current and charging cycle frequency. The degradation rate can be calculated by:

$$D = k \cdot I^\alpha \cdot e^{\frac{T}{T_0}} \quad (3)$$

Where:

D: Battery degradation per cycle

k: Battery material constant

I: Charging current (A)

$\alpha$ : Exponential current sensitivity to degradation

T: Battery temperature (K)

$T_0$ : Reference temperature (K)

The total lifetime of a battery is the opposite of accumulated degradation:

$$L = \frac{1}{\sum D} \quad (4)$$

From the available data, the modeling is then continued by combining a high voltage parameter ( $V=20$  kV) causing a high current I, so that  $t_c$  decreases. However, a high I increases D, accelerates degradation, and decreases L. Balance between  $t_c$  and L is key to fast charging with V2G. Optimization is carried out by choosing the ideal combination of V, I, and T to maintain battery life.

## IV. RESULTS AND DISCUSSIONS

### IV. 1 FAST CHARGING MODEL SIMULATION

In Fast Charging conditions, it is necessary to know the charging time of the battery with various charging currents to achieve a full charge in a shorter duration. Charging Current is a variable that is tested to see the effect of charging current on charging time and battery life. Battery Life Representation of the number of charge-discharge cycles before the battery capacity drops to an unacceptable level. The fast charging model for electric vehicles often refers to a charging strategy with two main stages:

1. Constant Current Charging (CC) Phase: At this stage, the charging current is kept at the maximum value (10 A in this case) until the battery voltage is close to the maximum limit.

2. Constant Voltage Charging (CV) Stage: After the battery voltage reaches its maximum value, the charging current gradually decreases to prevent battery damage, until the battery is fully charged.

Previously, it was necessary to conduct simulations to determine fast charging conditions using a constant current (CC) and constant voltage (CV) approach, taking into account time (CT) to regulate the charging speed. At constant current (CC), the charging process occurs at a constant current until a certain voltage is reached. Where the constant voltage (CV) after reaching the maximum voltage, with charging at a constant voltage and the current decreasing gradually, the charging time required is less without damaging the battery. The simulation results can be seen in the graph figure 1.

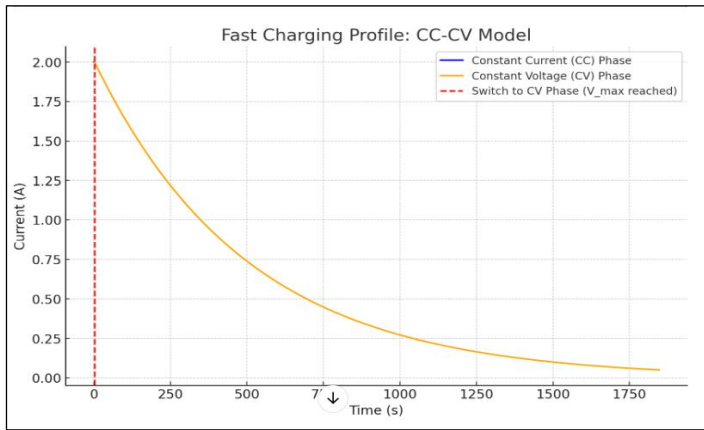


Figure 1: Fast charging profile.  
Source: Authors, (2025)

Based on the simulation results in Figure 1, the graph shows the CC-CV charging profile. The blue line shows the constant current (CC) phase, where the current remains stable until the battery reaches  $V_{max}$ . The orange curve shows the constant voltage (CV) phase, where the current gradually decreases as the battery is nearly fully charged.

The dashed red line marks the transition point from CC to CV phase. This model helps visualize the effect of fast charging on current flow over time. The calculated charging time for this fast charging model is obtained as Constant Current (CC) Phase Time: 2.1 seconds, Constant Voltage (CV) Phase Time: 1844.44 seconds, Total Charging Time: 1846.54 seconds (about 30.78 minutes).

To optimize charging in the context of fast charging vs. normal charging, the model considers two main goals that often conflict:

1. Minimization of Charging Time ( $t_c$ ). Reduce charging time to improve user comfort.
2. Max. Battery Lifetime (L). Reduce battery degradation to extend its lifespan.

To see the comparison of charging electric vehicles in fast charging conditions with normal charging, a simulation was carried out where the voltage value during fast charging  $V = 20000$  (20 kV in V),  $Q$  value = 100 Battery capacity in Ah, and  $V_{batt} = 400$  Nominal battery voltage (V). Simulations were carried out to see how much current was allowed and how long it took to charge. The simulation results with python are obtained in fast and normal charging conditions, graphically shown in Figure 2.

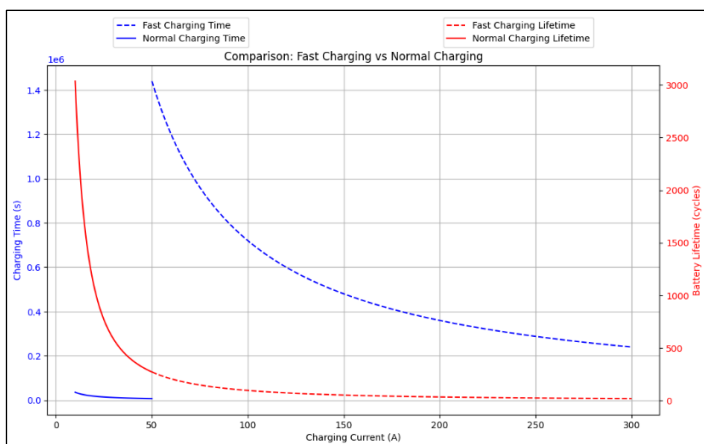


Figure 2: Fast and Normal charging.  
Source: Authors, (2025).

Based on the graph in Figure 2, a comparison of charging time and battery life for two different charging methods is obtained: fast charging and normal charging. Charging Time vs. Charging Current. The blue curve represents the charging time for fast charging, which decreases significantly as the charging current increases. For example, at low charging currents (near 0 A), the charging time is very long (close to 1 million seconds), while at higher currents (around 300 A), the time drastically drops to nearly 0.2 seconds. In contrast, the normal charging time (dashed blue curve) decreases more gradually, indicating that normal charging takes significantly longer, even at higher charging currents. This shows that normal charging is less sensitive to changes in charging current compared to fast charging.

Battery Lifetime vs. Charging Current. The red curve represents the battery lifetime for fast charging. As the charging current increases, the battery lifetime decreases. At low charging currents (50 A), the battery has a higher lifetime (around 2,500 cycles), but as the current increases (up to 300 A), the lifetime sharply drops to around 500 cycles. This is indicative of how faster charging can lead to faster battery degradation due to higher heat generation and stress on the battery. The normal charging lifetime (dashed red curve) is more stable, showing a much slower reduction in battery lifetime. At higher currents (e.g., 300 A), the lifetime only slightly decreases, reflecting the fact that normal charging places less strain on the battery. This analysis highlights the trade-off between fast charging and battery longevity, suggesting that high current charging (fast charging) can significantly reduce battery lifespan, while normal charging offers a better balance of performance and longevity.

After getting a comparison of fast and normal conditions, it is next to see how the optimal current affects the charging and degradation time. The simulation is carried out by expanding to a more optimal multiobjective optimization. Conditioned if it charges faster without damaging the battery. The simulation results are obtained graphically shown in figure 3.

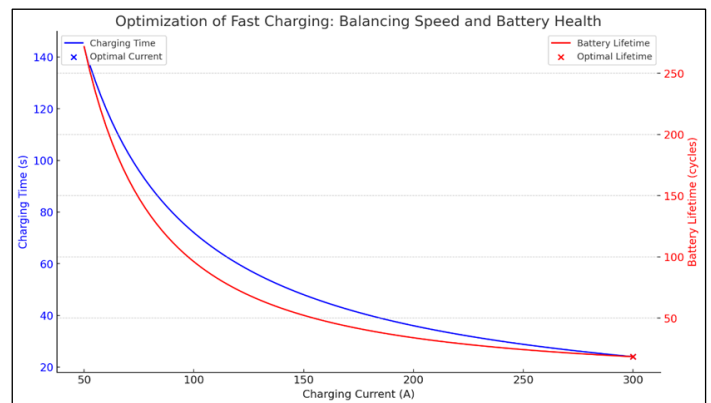


Figure 3: Effect of optimization on battery degradation.  
Source: Authors, (2025)

From the simulation results obtained in figure 3. The graph displays: The graph displays Charging Time (blue curve): Decreases with increasing current. Battery Lifetime (red curve): Decreases sharply as current increases. The optimal solution maximizes charging speed while balancing battery health. The trade-off suggests that extreme fast charging significantly reduces battery lifetime, requiring careful design of charging profiles. Charging Time (blue curve): Decreases with increasing current. Battery Lifetime (red curve): Decreases sharply as current increases. The optimization results indicate the following:

- **Optimal Current (I): 300.0A**



- **Charging Time (tc):** 24.0seconds
- **Battery Lifetime (L):** 18.49cycles

## IV. 2 THE EFFECT OF FAST CHARGING ON BATTERIES

After obtaining the optimal values on the current, time and life of the battery, it is then necessary to compare lithium-ion batteries with solid-state batteries in the context of fast charging by considering several important aspects, such as:

1. **Charging characteristics.** Lithium-ion batteries have a lower charge current limit than solid-state batteries. Solid-state batteries are more thermally stable, so they can handle higher charging currents.
2. **Battery degradation.** Lithium-ion is more susceptible to degradation due to the growth of the SEI (Solid Electrolyte Interphase) layer. Solid-state has lower degradation because the electrolyte is dense and more stable.
3. **Lifetime.** Solid-state typically has a longer lifetime in fast-charging conditions.

Fast charging technology allows batteries, particularly in electric vehicles, to charge at much higher rates, reducing overall charging time significantly. However, this convenience comes with notable trade-offs related to battery health, performance, and lifespan. Fast charging subjects batteries to higher currents, which results in: Increased heat generation: High current during charging causes significant heat buildup. Elevated temperatures can accelerate chemical reactions within the battery, leading to thermal stress and faster material degradation

The modeling was carried out to see the implications on the fast charging conditions of the two types of batteries, the simulation results were obtained as shown in Figure 4.

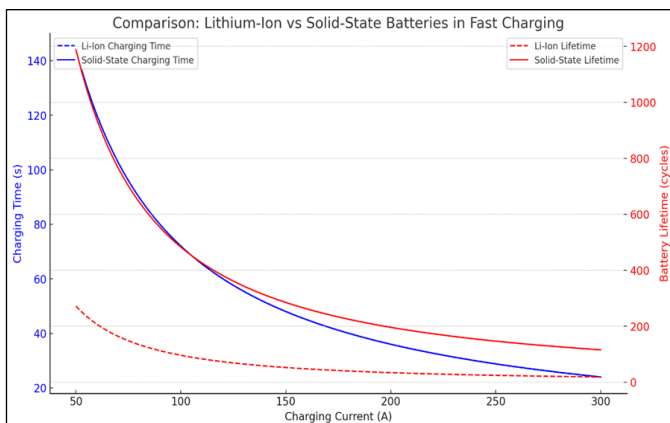


Figure 4: Comparison of fast charging performance  
Source: Authors, (2025).

The results obtained are based on Figure 4. The graph compares the performance of lithium-ion and solid-state batteries during fast charging. Charging Time (blue), Lithium-ion and solid-state batteries have similar charging times, as both depend mainly on the charging current. Battery Life (red), Lithium-ion batteries experience a sharper decrease in life as the charging current increases. Solid-state batteries show much better life retention at higher charging currents due to their stable solid electrolyte.

Judging from the charging time, Solid-State is more efficient (faster) compared to Li-Ion at higher currents, indicated by a solid red line that is lower than the solid blue line. At current  $I=300A$ , the charging time is close to the minimum value (about 20-30 seconds). Meanwhile, in terms of battery life: Lithium-Ion experiences faster degradation of life as the charging current

increases, as seen from the dotted blue line that is close to 0 at  $I=300A$ . Solid-State is more durable at high currents, with battery life still significantly higher than Li-Ion.

Mathematically, it can be said that the charging time (T) is inversely proportional to the charging current (I). Battery life (L) shows a significant decrease as the current increases, with Lithium-Ion decreasing more drastically than Solid-State. Solid-State batteries excel in both charging time efficiency and battery life endurance at high currents.

The results of the simulation are reinforced by the regression results showing that the mathematical model for the charging time (T) as a function of the charging current (I) is:

$$T = \frac{689.07}{I} + 75.27 \quad (5)$$

### Interpretation:

- **Parameter a=689.07:** Indicates the main contribution of the current inverse component ( $1/I$ ) to the charging time.
- **Parameter b=75.27:** Indicates a relatively constant minimum charging time component.

Large voltages in electric vehicle charging systems, in this case V2G systems, can affect EV battery life through several mechanisms:

1. **Battery Degradation Due to High Voltage:** Charging or discharging at high voltages can accelerate the chemical degradation of the battery, leading to a faster decrease in capacity and reduced lifespan. This happens because high voltages can increase the risk of lithium plating formation on the anode of the lithium-ion battery.
2. **Recharge Cycle Effect:** Frequent use of V2G requires the battery to go through many charge and discharge cycles, which will accelerate the chemical degradation of the battery.
3. **Operating Temperature:** Higher voltages generate greater current, and this can increase the temperature of the battery, accelerating cell wear and tear if the cooling system is not optimal. By optimizing the voltage and current in the V2G system, we can reduce the rate of battery degradation and extend the battery life of electric vehicles.

## V. CONCLUSION

Based on the research that has been done on lithium-ion batteries and solid-state types, it can be concluded. In both types of batteries, the charging time is significantly reduced with increasing charging current. At a current of 50 A, the charging time for lithium-ion batteries reaches about 140 seconds, while solid-state requires a slightly shorter time, about 130 seconds. At a current of 300 A, the charging time for lithium-ion drops to about 20 seconds, while solid-state remains marginally faster at 18 seconds.

Battery life degradation at high currents, Battery life, measured in cycles, shows faster degradation at high charging currents. Lithium-ion batteries, for example, have a life of about 1,200 cycles at low currents (50 A), but drop dramatically to almost 0 cycles at 300 A. In contrast, solid-state batteries show better performance, starting at 1,000 cycles at 50 A and only dropping to about 100 cycles at 300

Battery resistance to fast charging, solid-state has the advantage of maintaining battery life at high currents compared to lithium-ion. At 150 A current, lithium-ion has a life of only about 200 cycles, while solid-state still reaches about 600 cycles, showing much better resistance to degradation. Charging time and battery life show a trade-off between charging time and battery life.



Increasing the charging current does reduce the charging time to about 10 times faster (from 140 seconds to 20 seconds for lithium-ion), but at the expense of battery life, especially for lithium-ion which almost loses its cycles at high currents. Solid-state provides a more balanced solution by maintaining a longer battery life at high currents.

**Lithium-ion:** Offers good charging performance but degrades faster under high current. **Solid-state:** Supports faster charging with less degradation, making it more suitable for high-power applications.

## VI. AUTHOR'S CONTRIBUTION

**Conceptualization:** Samsurizal and Arif Nur Afandi.

**Investigation:** Samsurizal.

**Discussion of results:** Samsurizal, Arif Nur Afandi and Mohamad Rodhi Faiz

**Methodology:** Samsurizal, Arif Nur Afandi.

**Writing – Original Draft:** Samsurizal, and Arif Nur Afandi.

**Writing – Review and Editing:** Samsurizal, Arif Nur Afandi. Mohamad Rodhi Faiz

**Supervision:** Arif Nur Afandi and Mohamad Rodhi Faiz

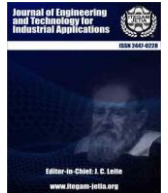
**Approval of the final text:** Samsurizal and Arif Nur Afandi.

## VII. ACKNOWLEDGMENTS

We thank the promoters for their support in realizing this article. This research is part of the doctoral program in the electrical engineering and informatics study program at the State University of Malang. All authors contributed to the research and writing of this article with the authority and approval to submit the manuscript.

## VIII. REFERENCES

- [1] S. Tirunagari, M. Gu and L. Meegahapola, "Reaping the Benefits of Smart Electric Vehicle Charging and Vehicle-to-Grid Technologies: Regulatory, Policy and Technical Aspects," in *IEEE Access*, vol. 10, pp. 114657-114672, 2022, <https://doi.org/10.1109/ACCESS.2022.3217525>
- [2] Hossain, S., Rokonzaman, M., Rahman, K. S., Habib, A. K. M. A., Tan, W. -S., Mahmud, M., Chowdhury, S., & Channumsin, S. Grid-Vehicle-Grid (G2V2G) Efficient Power Transmission: An Overview of Concept, Operations, Benefits, Concerns, and Future Challenges. *Sustainability*, 15(7), 2023. 5782. <https://doi.org/10.3390/su15075782>
- [3] Shariff, S. M., Alam, M. S., Ahmad, F., Rafat, Y., Asghar, M. S. J., & Khan, S. System design and realization of a solar-powered electric vehicle charging station. *IEEE Systems Journal*, 14(2), 2019, 2748-2758. <https://doi.org/10.1109/JSYST.2019.2931880>
- [4] Saini, S., Thakur, T., & Kirar, M. A Review of Electric Vehicles Charging Topologies, its Impacts and Smart Grid Operation with V2G Technology. In *Proceedings of the International Conference on Advances in Electronics, Electrical & Computational Intelligence (ICAEEC)*, 2019, April. <https://dx.doi.org/10.2139/ssrn.3575388>
- [5] Kumar, V., Teja, V. R., Singh, M., & Mishra, S. PV based off-grid charging station for electric vehicle. *IFAC-PapersOnLine*, 52(4), 2019, 276-281. <https://doi.org/10.1016/j.ifacol.2019.08.211>
- [6] Couto, L. D., Romagnoli, R., Park, S., Zhang, D., Moura, S. J., Kinnaert, M., & Garone, E. Faster and healthier charging of lithium-ion batteries via constrained feedback control. *IEEE Transactions on Control Systems Technology*, 30(5), 2021. 1990-2001. <https://doi.org/10.1109/TCST.2021.3135149>
- [7] Drollette Jr, D. Charging ahead: Steven Chu, Nobel Prize-winner and former energy secretary, on today's battery research—and more. *Bulletin of the Atomic Scientists*, 79(6), 2023, 366-371. <https://doi.org/10.1080/00963402.2023.2266938>
- [8] Thomas, F., Mahdi, L., Lemaire, J., & Santos, D. M. Technological advances and market developments of solid-state batteries: a review. *Materials*, 17(1), 239, 2024. <https://doi.org/10.3390/ma17010239>
- [9] A. M. Eltamaly, Optimal Dispatch Strategy for Electric Vehicles in V2G Applications, *Smart Cities*, vol. 6, no. 6, 2023, p. 3161–3191. <https://doi.org/10.3390/smartcities6060141>
- [10] Ahmad, N., Fan, C., Faheem, M., Liang, X., Xiao, Y., Cao, X., and Yang, W. Key challenges and advancements toward fast-charging all-solid-state lithium batteries. *Green Chemistry*, 26(18), 2024, 9529-9553. <https://doi.org/10.1039/D4GC01068J>
- [11] A. Myers, "https://energy.stanford.edu/news/stanford-scientists-illuminate-barrier-next-generation-battery-charges-very-quickly," Stanford University, 30 January 2023. [Online]. Available: <https://energy.stanford.edu/news/stanford-scientists-illuminate-barrier-next-generation-battery-charges-very-quickly>.
- [12] Bridgelall, R. Rechargeable Solid-State Batteries: Insights from a Cross-Sectional Thematic and Bibliometric Analysis. 2024. <https://www.preprints.org/manuscript/202409.2007>
- [13] Bondu, P. kumar R., & Vyza, U. Design and analysis of novel topology for PV-FED EV charging system. *ITEGAM-JETIA*, 10(47), 2024, 109-114. <https://doi.org/10.5935/jetia.v10i47.1108>
- [14] Christopher Doerrer, Xiangwen Gao, Junfu Bu, Samuel Wheeler, Mauro Pasta, Peter G. Bruce and Patrick S. Grant. Fast-charging all-solid-state battery cathodes with long cycle life *Nano Energy*, 2025, 134, 110531. <https://doi.org/10.1016/j.nanoen.2024.110531>
- [15] Trentadue, G., Lucas, A., Otura, M., Pliakostathis, K., Zanni, M., & Scholz, H. Evaluation of fast charging efficiency under extreme temperatures. *Energies*, 11(8), 2018, 1937. <https://doi.org/10.3390/en11081937>
- [16] Afandi, A. N., Zulkifli, S. A., Korba, P., Sevilla, F. R. S., Handayani, A. N., Aripriharta, A., and Afandi, F. C. W. Trip Pattern Impact of Electric Vehicles in Optimized Power Production using Orca Algorithm. *Journal of Engineering and Technological Sciences*, 56(4), 2024, 463-473. <https://doi.org/10.5614/j.eng.technol.sci.2024.56.4.3>
- [17] Afandi, A. N. ORCA Algorithm for Unit Commitment Considering Electric Vehicle Inclusion. *Journal FORTEI-JEERI*, 2(1), 2021, 1-9. <https://doi.org/10.46962/forteijeeri.v2i1.18>
- [18] Momoh, K., Zulkifli, S. A., Korba, P., Sevilla, F. R. S., Afandi, A. N., & Velazquez-Ibañez, A. (2023). State-of-the-art grid stability improvement techniques for electric vehicle fast-charging stations for future outlooks. *Energies*, 16(9), 3956. <https://doi.org/10.3390/en16093956>.
- [19] Afandi, A. N., WA, F. C., & Ali, M. (2023). Aplikasi ORCA Algorithm Pada Optimasi Penyediaan Daya Sistem Berbasis Mobilitas Kendaraan Listrik. *Jurnal JEETech*, 4(2), 103-108. <https://doi.org/10.32492/jteetech.v4i2.4204>



## QUANTITATIVE ANALYSIS OF SUBSURFACE STRUCTURE CRACKING USING PULSED EDDY CURRENT NONDESTRUCTIVE TESTING

Hakim Azizi<sup>1</sup>, Mohammed chebout<sup>2</sup>, Daoud Sekki<sup>3</sup>, Mohammed Charif Kihal<sup>4</sup> and Marouane Kihal<sup>5</sup>

<sup>1</sup> Renewable Energy Systems Applications Laboratory, Ziane achour university, Djelfa, Algeria.

<sup>2</sup> Applied Automation and industrial Diagnostic Laboratory, Ziane achour university, Djelfa, Algeria.

<sup>3</sup> Faculty of technology Mohamed Cherif Messaadia University - Souk Ahras, Algeria.

<sup>4</sup> L2EI Laboratory, Mohamed Seddik Ben Yahia University, Jijel, Algeria.

<sup>5</sup> Faculty of Exact Sciences, Bejaia University, Bejaia, Algeria.

<sup>1</sup><http://orcid.org/0009-0003-4895-6327>, <sup>2</sup><http://orcid.org/0009-0006-2798-5411>, <sup>3</sup><http://orcid.org/0009-0003-2204-7459>

<sup>4</sup><https://orcid.org/0000-0002-2075-2491>, <sup>5</sup><http://orcid.org/0000-0002-6675-7087>

Email: [h.azizi@univ-djelfa.dz](mailto:h.azizi@univ-djelfa.dz), [m.chebout@univ-djelfa.dz](mailto:m.chebout@univ-djelfa.dz), [daoud.sekki@univ-soukahras.dz](mailto:daoud.sekki@univ-soukahras.dz), [mc.kihal@univ-jijel.dz](mailto:mc.kihal@univ-jijel.dz), [kihal@univ-bejaia.dz](mailto:kihal@univ-bejaia.dz)

### ARTICLE INFO

#### Article History

Received: January 07, 2025

Revised: February 20, 2025

Accepted: March 15, 2025

Published: March 31, 2025

#### Keywords:

Pulsed eddy current,  
Metallic materials,  
Nondestructive testing,  
Finite element method,

### ABSTRACT

This paper presents a three-dimensional finite element method for the nondestructive evaluation of forward problems utilizing the pulsed eddy current technique. The method visualizes and maps the distribution of responses resulting from the interaction between eddy currents and defects, facilitating defect characterization. The study elaborates on the defect characterization process using the pulsed eddy current technique, which encompasses both numerical and experimental analyses. Initially, the variation in pulse width of the pulsed eddy current technique is discussed, along with its effectiveness. Subsequently, the investigation into the application of pulsed eddy current testing for defects is conducted through the mapping of magnetic field distributions, implemented via time-stepping three-dimensional finite element modelling, with features extracted from the mapping for the purpose of defect characterization.



Copyright ©2025 by authors and Galileo Institute of Technology and Education of the Amazon (ITEGAM). This work is licensed under the Creative Commons Attribution International License (CC BY 4.0).

### I. INTRODUCTION

Nondestructive testing (NDT) refers to a comprehensive array of inspection techniques and methodologies designed to assess and monitor the condition of materials, components, or equipment without altering their inherent properties or performance. This practice is vital for ensuring the maintenance and reliability of components, thus preventing accidents, loss of life, and both economic and environmental repercussions. However, there is a pressing need for technological research and development (TR&D) to cultivate scientific knowledge in this domain, especially in light of the growing prevalence of products utilizing new materials and advanced manufacturing technologies that impose stringent safety requirements [1]. The detection of micro defects, both on the surface and beneath it, using NDT methods like Eddy Currents (EC) poses considerable challenges [2]. The key difficulties include firstly the minimum detectable defect size is often insufficient due to noise from probe vibrations (lift-off) that can mask the defect signal; secondly the complexity of generating tailored EC patterns in the materials under inspection;

and finally that the intricate design of probes, which frequently consist of numerous assembled elements within a single configuration. The main goal for this paper, is to develop applied research, innovation, numerical simulation, and knowledge generation for creating customized Non-Destructive Testing (NDT) systems using pulsed eddy currents (PEC) [3]. A secondary goal focused on technological innovation to design and experimentally validate custom eddy current systems for three demanding engineering applications: inspecting micro defects in plane structures, and evaluating brazed joints in the automotive sector. This involved starting with the scientific principles of NDT using EC, analyzing and characterizing materials, designing and simulating pulsed eddy current probes, and testing prototypes in real industrial settings. At the same time, some of them pose scientific challenges that require new procedural knowledge and deeper research, as they involve concepts, theoretical foundations, materials, manufacturing processes, and geometries that have not been systematically studied in NDT before.

### II. PRACTICAL USE OF EDDY CURRENTS IN FLAW DETECTION

The main object of search when inspecting parts in operation is a fatigue crack, as a rule, coming to the surface. The geometric parameters of the crack are characterized by: length  $L$  is the maximum longitudinal size of the defect visible on the test surface, width  $B$  is the transverse dimension of the defect at its exit to the surface, depth  $H$  is the size of the defect towards the inside of the test surface. Since defects are often of a complex shape, there are maximum, minimum, average, and total values of these parameters. For subsurface defects, an important parameter is not only geometrically (e.g. diameter), but also distance from the surface –  $Z$  – depth [4].

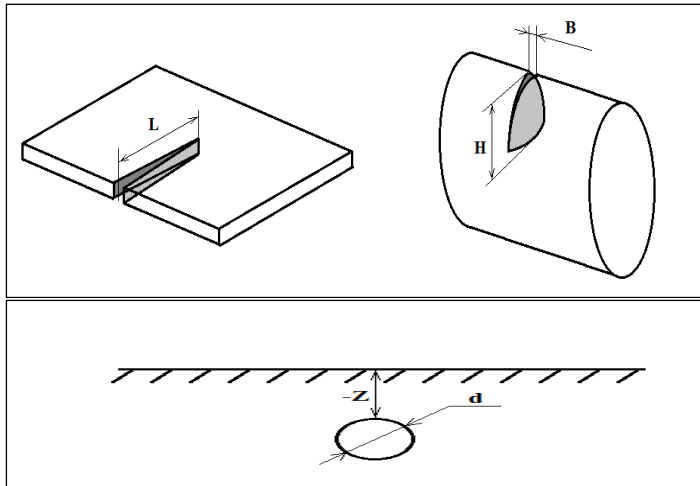


Figure 1: Geometric dimensions of defects.  
Source: Authors, (2025).

With:

$L$  – length;  $B$  is the width of the opening;  $H$  – depth;  $-Z$  – depth of occurrence;  $d$  – diameter

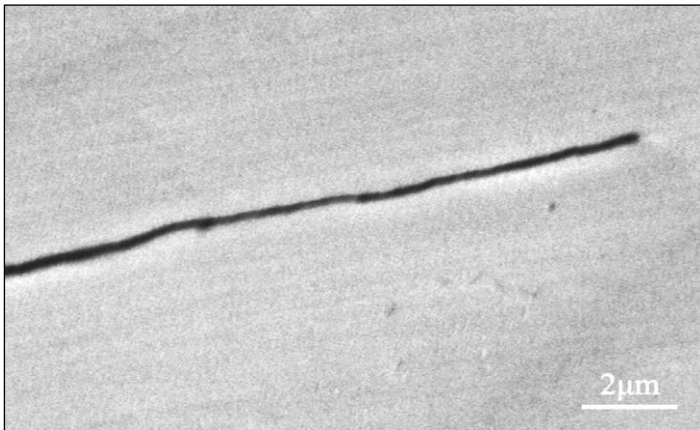


Figure 2: Transgranular stress corrosion cracking.  
Source: Authors, (2025).

When conducting eddy current flaw detection, in order to select the optimal testing parameters, it is important to distinguish the direction of defect development. From this point of view, a distinction is made between longitudinal or transverse (relative to the longitudinal axis of the tested object or the direction of scanning with an eddy current transducer) cracks. With the help of feed-through transducers, it is possible to control the geometric dimensions and electromagnetic or related structural parameters (hardness, mechanical stresses, degree of fatigue damage, etc.) of rods, including those made of ferromagnetic materials [5]. At the same time, the frequency of the excitation current is an important parameter, the choice of which is determined by the required depth of penetration of eddy currents (depending on the task to be solved

in the process of monitoring) [6]. On the one hand, the depth of penetration of eddy currents in a cylindrical object is somewhat greater than in a half-space with a flat surface, on the other hand, the density of eddy currents on the axis of the cylinder is equal to zero, regardless of the value of the generalized eddy current control parameter. To analyse the test results, as a rule, hodographs of the relative voltage of the measuring winding are used by changes in amplitude, phase, and in some cases higher harmonics of which the degree of influence of the monitored or interfering parameters is judged.

In the practice of pulsed eddy current non-destructive testing, such informative features of signals are most often used, such as the displacement of the moment of crossing by a signal of a certain level, the time interval between certain nodal points or the peak values of the amplitude and the exceeding of the amplitude of certain threshold values and the moments of these crossings [7]. Currently, the disadvantage of this method is the use of individual characteristic points of the eddy current converter signal, that is, incomplete use of the information capabilities of the eddy current converter signal and the lack of protection of the above-mentioned point characteristics from the influence of interference. In addition, from the analysis of literary sources, it can be seen that the pulse excitation mode (PEM) of the eddy current allows to complement the traditional eddy current nondestructive control with harmonic excitation, however, today, in the conditions of rapid development of methods and means of signal analysis, the pulse excitation mode is insufficiently researched.

### III. NUMERICAL MODELING AND RESULTS

In the field of ECNDT, numerical modeling has emerged as a crucial tool in the design of probes and the analysis of detection performance, largely due to advancements in computing power. Generally, the modeling of ECNDT relies on the resolution of Maxwell's equations [8]. Depending on the complexity of the configuration being simulated, the resolution may be either analytical or numerical. The analytical solution of Maxwell's equations is advantageous due to its speed and the high precision of results it yields. However, the intricate nature of eddy current configurations often renders an analytical solution unattainable. Consequently, an alternative approach involves the application of numerical methods, which facilitate the examination of a wider range of probeworkpiece configurations, including various geometries of components, defects, and sensors [9].

In scenarios where it is essential to differentiate multiple parameters, the Pulsed Eddy Current Control Method serves as a viable alternative to multi-frequency excitation. The latter often encounters limitations due to the complexity of the apparatus and the challenges associated with practical implementation, which restrict the number of usable frequencies. In pulsed eddy current control, excitation currents in the form of rectangular, trapezoidal, or half-sinusoidal pulses are introduced into the sensor.

This study also incorporates a wave derived from a capacitive discharge [10]. The Fourier series decomposition of this wave produces signals across various frequencies. Instead of utilizing the normalized impedance plane for signal analysis, a time or frequency-based approach is adopted. The characterization of the target quantity is achieved by examining the behaviour of specific points within the signal, including zero crossings, extrema, and the fixed point (crossing-point), which remains unaffected by variations in the sensor-load air gap [11].

The evolution of these points facilitates diagnostic assessments. Spectral analysis has demonstrated that the fixed



point phenomenon is relevant to transient signals and their harmonics, with the variations in the coordinates of this point being predictable based on conductivity and thickness. Further investigation into the origins of this phenomenon and its potential applications is warranted. The transient magnetic field is expressed in terms of magnetic vector potential, and source current density (SCD)

$$-\nabla \cdot 1/\mu \nabla A + \sigma \frac{\partial A}{\partial t} = J \quad (1)$$

Consider the problem JSAEM#6 illustrated by figure 3. The finite element mesh contains 79162 nodes and 1021837 tetrahedral elements. A preconditioning technique, called the symmetric successive over-relaxation (SSOR) method is employed to minimize computation time and memory [12]. The summary of the geometric and physical quantities is shown in table 1.

Table 1: Geometric and physical parameters of the JSAEM#6 Benchmark

Parameter	Value [mm]
Plate thickness	1.25
Plate length	140
Plate width	140
Conductivity [MS/m]	1.00
Crack width	0.20
Crack length	10.0
Crack depth	0.75
Frequency[kHz]	150 & 300
Coil inner radius	0.60
Coil outer radius	1.60
Coil height	0.80
Lift-off	0.22

Source: Authors, (2025).

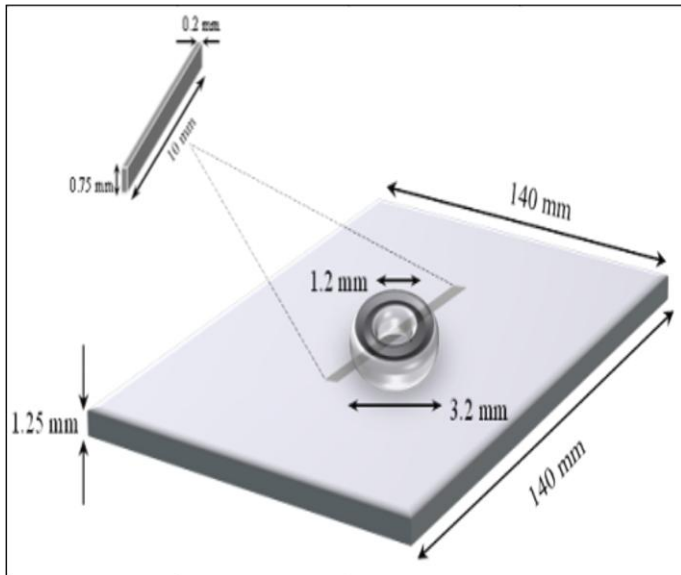


Figure 3: Geometrical Model with Crack.  
Source: Authors, (2025).

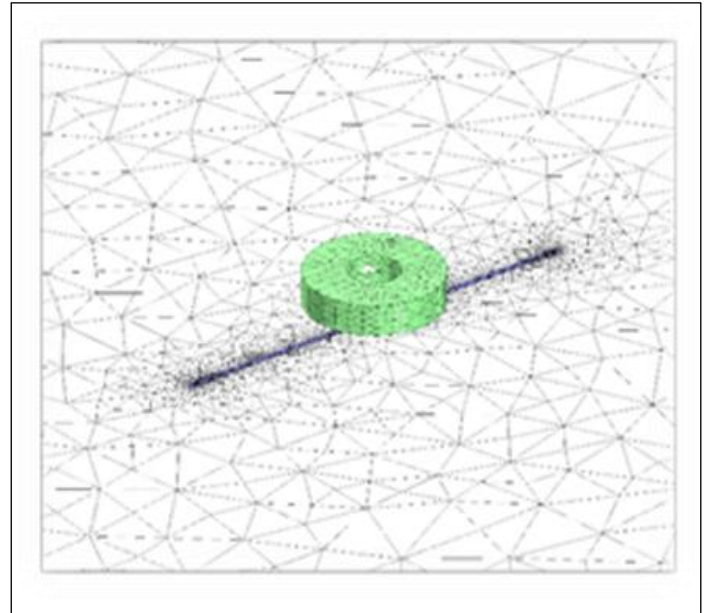


Figure 4: Tetrahedral meshing model.  
Source: Authors, (2025).

Under the given frequency and coil lift-off, the impedance is calculated as function of coil position [13]. The impedance change represented respectively by the resistance and reactance components in figure 5, is evaluated by subtracting the values obtained for the plate without crack from the values obtained for the plate with crack. We remark a good agreement between experimental and calculated results.

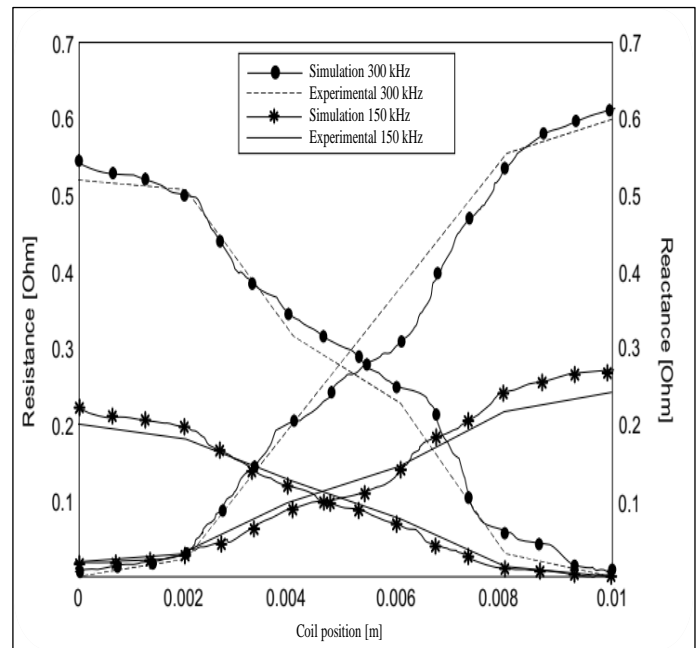


Figure 5: Experimental and numerical evolution of impedance components vs displacement coil.  
Source: Authors, (2025).

Consider the model of figure 6 with three notches on the surface of the Bench-mark along its width, each opening equal to 2 mm [14]. The depth of these cuts varies between three different values: 80%, 55% and finally 25% of the benchmark height structure equal to 1.25 mm [15]. The excitation current is in the form of a quasi-square wave as shown in Figure 6.



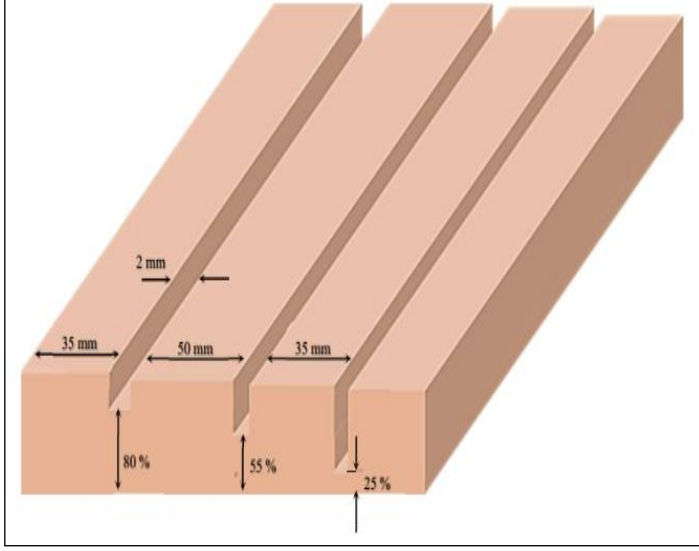


Figure 6: JSAEM# 6 configuration with notches.  
Source: Authors, (2025).

The excitation current has the shape of a quasi-square wave as shown in figure 7. The expression of the current introduced is given by the following equation:

$$I(t) = I_0 \left\{ \left[ \lambda + \frac{1}{T} \tau e^{-\frac{\lambda T}{\tau}} \left( 1 - e^{-\frac{T}{\tau}(2\lambda-1)} \right) \right] + \frac{1}{\pi} \sum_{l=1}^{\infty} \left[ a_l \cos\left(\frac{2l\pi t}{T}\right) + b_l \sin\left(\frac{2l\pi t}{T}\right) \right] \right\} \quad (2)$$

with:

$$\begin{aligned} I_0 &= 0.5 \text{ A}, \\ \lambda &= 50\%, \\ \tau &= 50 \mu\text{s}, \\ \frac{1}{T} &= 100 \text{ Hz} \end{aligned}$$

The constants  $a_l$  and  $b_l$  are given by the following expressions:

$$a_l = \frac{\sin(2l\lambda\pi)}{l} - \frac{2\pi}{T} \left[ \frac{1}{\tau^2} + \left( \frac{2l\pi}{T} \right)^2 \right]^{-1} \left\{ \frac{1}{\tau} \left[ 1 + e^{-\frac{T(\lambda-1)}{\tau}} \right] + \left[ \frac{2l\pi \sin(2l\lambda\pi)}{T} - \frac{\cos(2l\lambda\pi)}{\tau} \right] \left( 1 + e^{-\frac{\lambda T}{\tau}} \right) \right\} \quad (3)$$

$$b_l = \frac{1 - \cos(2l\lambda\pi)}{l} - \frac{2\pi}{T} \left[ \frac{1}{\tau^2} + \left( \frac{2l\pi}{T} \right)^2 \right]^{-1} \left\{ \frac{2l\pi}{T} \left[ 1 + e^{-\frac{T(\lambda-1)}{\tau}} \right] + \left[ \frac{2l\pi \cos(2l\lambda\pi)}{T} + \frac{\sin(2l\lambda\pi)}{\tau} \right] \left( 1 + e^{-\frac{\lambda T}{\tau}} \right) \right\} \quad (4)$$

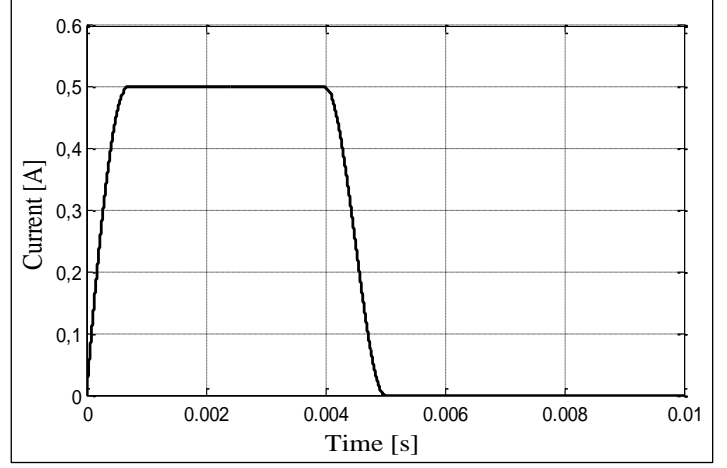


Figure 7: Excitations current shape.  
Source: Authors, (2025).

Indeed, increasing the size of the crack defect increases the signal of the induced current issued by the eddy current sensor.

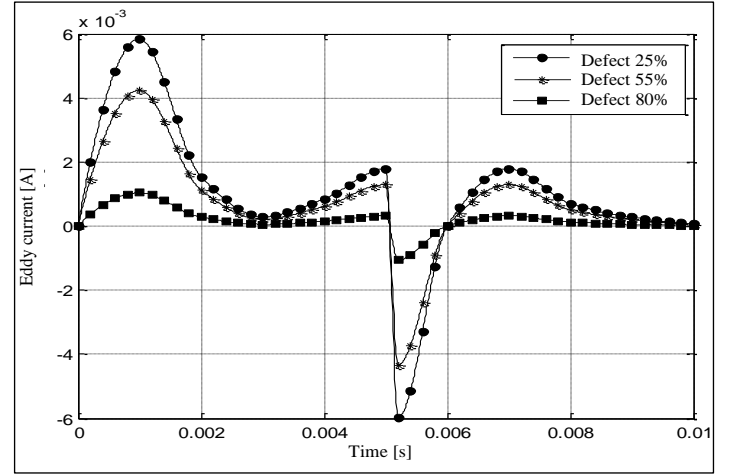


Figure 8: Effect of defect depth.  
Source: Authors, (2025).

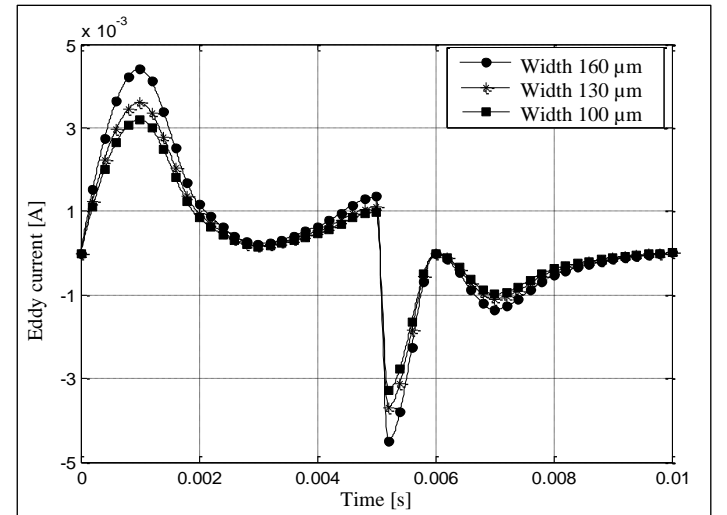


Figure 9: Defect width effect on induced current.  
Source: Authors, (2025).

We note from these two figures 8 and 9 that the influence of the depth of the defect is much more visible and more important than the effect of the width which reinforces the concept of using the pulsed eddy currents for the measurement of the sheet thickness

of flat or other structures [16]. Here, the width of the defect is maintained equal to 2 mm in the case of the two figures.

## VI. CONCLUSION

The development of an eddy current control device, in sinusoidal or pulsed mode, requires the optimization of a certain number of parameters. This optimization is generally long and difficult to execute in practice since it results from several compromises. Several parameters can influence the response of a sensor including the sensor-target distance, the geometric parameters of the defect, and finally the electrical properties of the conductive part in this case the variation of the electrical conductivity. We can see that the maximum amplitude of the signal and the time necessary to have it are the main parameters necessary to identify defects. Applications using a Benchmark whose experimental results are available to validate our simulation results.

Numerical simulations are executed in advance of experiments that utilize the PEC technique to estimate the expected responses from defects. These simulations play a crucial role in shaping experimental designs, improving the understanding of the physics that govern specific defects, and enabling the extraction of features from the responses collected. Experimental investigations are subsequently conducted to validate the results of the simulations and to illustrate the practicality of the techniques used to gather information on particular defects.

## V. AUTHOR'S CONTRIBUTION

**Conceptualization:** Hakim Azizi, Mohammed chebout, Daoud Sekki, Mohammed Charif Kihal and Marouane Kihal

**Methodology:** Hakim Azizi, Mohammed chebout, Daoud Sekki and Mohammed Charif Kihal

**Investigation:** Hakim Azizi, Mohammed chebout, Daoud Sekki and Mohammed Charif Kihal

**Discussion of results:** Hakim Azizi, Mohammed chebout and Daoud Sekki

**Writing – Original Draft:** Hakim Azizi, Mohammed Charif Kihal and Marouane Kihal

**Writing – Review and Editing:** Hakim Azizi, Mohammed Charif Kihal and Marouane Kihal

**Resources:** Hakim Azizi, Mohammed Charif Kihal and Marouane Kihal

**Supervision:** Hakim Azizi, Mohammed chebout and Daoud Sekki

**Approval of the final text:** Hakim Azizi, Mohammed Charif Kihal and Marouane Kihal

## VII. ACKNOWLEDGMENTS

The authors of this article would like to thank the General Directorate of Scientific Research and Technological Development (DGRSDT) in Algeria for their technical support and the specific research budget allocated to this program.

## VIII. REFERENCES

[1] C.A. Stott, P.R. Underhill, V.K. Babbar, T.W. Krause, "Pulsed eddy current detection of cracks in multilayer aluminum lap joints", IEEE Sensors Journal, n. 2, pp. 956-962, 2015.

[2] D. Zhou, J. Wang, Y. He et al, "Influence of metallic shields on pulsed eddy current sensor for ferromagnetic materials defect detection". Sensors Actuators A Phys., n. 248, pp. 162–172, 2016.

[3] J. Fava, L. Lanzani, M.C. Ruch, "Multilayer planar rectangular coils for eddy current testing: design considerations". NDT&E International, n. 42, p. 713–20, 2009.

[4] A. Rosell, "Efficient finite element modelling of eddy current probability of detection with transmitter–receiver sensors", NDT&E International, n.75, pp.48–56, 2015.

[5] A. Sophian, G. Tian, M. Fan, "Pulsed eddy current non-destructive testing and evaluation: A review", Chin. J. Mech. Eng., n.30, pp. 500-514, 2016.

[6] G. Rubinacci, A. Tamburino, S. Ventre, "Fast numerical techniques for electromagnetic nondestructive evaluation", NDT & E. International, n. 24, pp. 165-194, 2009

[7] L. Janousek, M. Smetana, K. Capova, "Enhancing information level in eddy-current non-destructive inspection", Intl. J. Appl. Electr.Mech., n. 33, pp.1149-1155, 2010.

[8] M. Aissaoui, H. Allag, J. P. Yonnet, "Mutual inductance and interaction calculation between conductor or coil of rectangular cross section and parallelepiped permanent magnet", IEEE Transactions on Magnetics, n. 50, pp. 1-4, 2014.

[9] R. Ghoni, M. Dollah, A. Sulaiman, F.M. Ibarahim, "Defect characterization based on eddy current technique: Technical review", Adv. Mech. Eng., n. 6, pp. 1-11, 2015.

[10] P. Horan, P.R. Underhill, T.W. Krause, "Real time pulsed eddy current detection of cracks in F/A-18 inner wing spar using discriminant separation of Modified Principal Component Analysis scores", IEEE Sensors J., n. 14, pp.171-177, 2014.

[11] M. Chebout, M. R. Mekideche, A. Hafaifa, A. Kouzou, and H. Allag "Impedance measurement and computation for the steam generator tube integrity using the ECNDT technique", Elektrotehniški Vestnik, n. 85, pp. 235-240, 2018.

[12] V.K. Babbar, P.R. Underhill, C. Stott, T.W. Krause, "Finite element modeling of second layer crack detection in aircraft boltholes with ferrous fasteners present", NDT&E Int. n. 65, pp. 64-71, 2014.

[13] T. Theodoulidis, J.R. Bowler, "The truncated region eigenfunction expansion method for the solution of boundary value problems in eddy current nondestructive Evaluation", AIP Conference Proceedings, n. 760, pp. 403-408, 2005.

[14] S. Djemoui, H. Allag, M. Chebout and H.R. Bouchekara, "Partial Electrical Equivalent Circuits and Finite Difference Methods Coupling; Application to Eddy Currents Calculation for Conductive and Magnetic Thin Plates", Progress In Electromagnetics Research C, n. 114, pp. 83-96, 2021.

[15] J. R. Nagel, "Fast finite-difference calculation of Eddy currents in thin metal sheets", App. Comp. Elec. Soc. J., n. 33, pp. 575-584, 2018.

[16] Y.L. Li, S. Sun, "Full-Wave Semi-Analytical Modeling of Planar Spiral Inductors in Layered Media, Progress In Electromagnetics Research", n. 149, pp. 45-54, 2014.



# SUB-MODULE VOLTAGE ESTIMATION OF MODULAR MULTILEVEL CONVERTER IN PV APPLICATIONS USING A SLIDING MODE OBSERVER

Imane Alia <sup>1</sup>, Imad Merzouk <sup>2</sup> and Mehamed Mounir Rezaoui <sup>3</sup>

<sup>1</sup> ABC Institute – ABCI. Manaus-Amazonas, Brazil.

<sup>2,3</sup> Laboratory of Applied Automation and Industrial Diagnostics Laboratory (LAADI), Faculty of Sciences and Technology, University of Djelfa, PO Box 3117, Djelfa 17000.

<sup>1</sup><https://orcid.org/0009-0009-2516-8102>, <sup>2</sup><https://orcid.org/0000-0003-1539-1414>, <sup>3</sup><https://orcid.org/0000-0003-2761-6123>

Email: [alia.imane@univ-djelfa.dz](mailto:alia.imane@univ-djelfa.dz), [i.merzouk@univ-djelfa.dz](mailto:i.merzouk@univ-djelfa.dz), [mm\\_rezaoui@mail.univ-djelfa.dz](mailto:mm_rezaoui@mail.univ-djelfa.dz)

## ARTICLE INFO

### Article History

Received: January 07, 2025

Revised: February 20, 2025

Accepted: March 15, 2025

Published: March 31, 2025

### Keywords:

Modular Multilevel Converter, Sliding Mode Observer, Capacitor Voltage Estimation, Voltage Balancing Control, PV Application.

## ABSTRACT

This paper presents a Sliding Mode Observer (SMO) for estimating sub-module (SM) voltages in Modular Multilevel Converters (MMCs) used in photovoltaic (PV) applications. MMCs are widely favored in medium- and high-voltage applications due to their modularity and scalability. However, traditional voltage sensing methods require numerous sensors, increasing system complexity, cost, and susceptibility to sensor failures. The proposed SMO offers a robust alternative, providing accurate voltage estimation despite parameter variations and external disturbances. The design and implementation of the SMO, along with its integration into the MMC control strategy, are demonstrated. The observer performance is validated through simulations and Matlab results, which demonstrate effective voltage estimation across different operating conditions. This method improves SM capacitor voltage balancing, enhances the reliable operation of MMCs in PV applications, and lowers costs.



Copyright ©2025 by authors and Galileo Institute of Technology and Education of the Amazon (ITEGAM). This work is licensed under the Creative Commons Attribution International License (CC BY 4.0).

## I. INTRODUCTION

Modular Multilevel Converters (MMCs) are increasingly used in photovoltaic (PV) systems because of their modular structure and clear superiority over conventional converters [1-3]. MMCs are composed of several sub-modules (SMs) connected in series. These converters offer numerous notable advantages that are especially valuable in renewable energy applications. Each sub-module generally comprises a capacitor and power electronic switches that can be controlled to generate specific voltage levels [4-7].

One notable characteristic of MMCs is their ability to scale, enabling them to achieve higher voltage levels by increasing the number of SMs. Scalability is important for PV systems, as they frequently necessitate high voltage conversion ratios to provide efficient energy transfer. Moreover, the modularity of MMCs improves the reliability of the system and provides more flexibility in maintenance. It is possible to bypass or replace particular system modules without impacting the entire system, thus enhancing fault tolerance and adaptability [8], [9].

MMCs are highly efficient and produce high-quality output. They distribute voltage stress across multiple SMs, resulting in reduced switching losses and increased efficiency. The multilevel output waveforms they produce have low harmonic distortion, which is essential for meeting grid integration and power quality standards in PV systems [10], [11].

An essential element of MMC operation is the efficient control of SM capacitor voltages. This involves controlling the average voltage across the capacitors at the leg level and ensuring voltage balance within each arm. To achieve efficient regulation of the average voltage and balancing of capacitor voltages in an MMC, a combination of modulation techniques and control strategies are required [12], [13].

As with any grid-connected converters, the DC-link voltage of MMCs is typically regulated using PI controllers. For capacitor voltage balancing, one of the most effective methods is a sorting algorithm, which selectively inserts or bypasses SMs. Alternatively, balance correction can be achieved using a PI controller, often in combination with Phase-Shifted Carrier Pulse-Width Modulation (PSC-PWM) [13-15].

Sorting algorithm techniques rely on multiple separate sensors to measure individual SM voltages and arm currents. However, the use of extensive sensor networks increases system complexity and costs, posing significant challenges for practical implementation. Therefore, a key objective in the advancement of grid-connected MMC in PV systems is to reduce the total number of sensors while still ensuring efficient control [16]. To overcome these issues, sensorless capacitor voltage control schemes have been developed using arm current measurements and DC-link voltage to estimate capacitor voltages.

These methods aim to simplify the system architecture, reduce costs, and enhance reliability, particularly in handling SM faults in PV systems, where ensuring stable and efficient operation is crucial. In [17] a new SM voltage estimation scheme for MMCs was introduced, employing a Kalman filter approach. This method decreases complexity and cost by utilizing only two voltage sensors per MMC leg, rather than one for each SM. It demonstrates accurate tracking of SM voltages, robustness to parameter variations like arm inductance changes, and effectiveness across various operational scenarios through simulation and experimental validation. Nevertheless, the suggested approach has many drawbacks.

There is a lack of thorough investigation into the effects of estimation deviations and an absence of discussions on computational complexity and comparative studies with alternative approaches. The paper [18] presents a novel method for estimating SM voltages in MMCs without additional sensors, using discretized SM voltage dynamics and a Kalman filter observer. Validated through simulations and experiments, the method shows robust performance. However, there is a limited comparison with existing methods and a need for more comprehensive comparisons. Despite these issues, the study offers promising advancements in reducing sensor count while ensuring accurate SM voltage estimation.

The state observer proposed in the paper [19] aims to estimate capacitor voltages and circulating currents in MMCs without direct voltage and current sensors. It utilizes system models and available measurements to estimate unmeasured states, facilitating effective capacitor voltage balancing and circulating current suppression. This sensorless control approach is streamlined but relies heavily on accurate system modeling and quality measurements to avoid estimation errors. Additionally, the ability of the observer to adapt to dynamic changes in operating conditions is essential for maintaining robustness and stability, which the article does not fully address.

The reference [20] introduces a capacitor voltage balancing strategy for MMCs using the ADALINE (Adaptive Linear Neuron) algorithm to estimate sub-module voltages instead of directly measuring them. This approach reduces the need for multiple voltage sensors and simplifies the control system. Simulation results show that the ADALINE algorithm accurately tracks sub-module voltages and effectively balances them under both steady-state and dynamic conditions.

The novelty of this work lies in its application of the ADALINE algorithm to MMC control, offering a lower-cost and simplified implementation. However, the paper lacks experimental validation and does not address the robustness of the ADALINE algorithm to parameter variations and disturbances in practical scenarios.

In [21] a novel approach to control MMC was presented, particularly focusing on single-phase applications. The authors propose an innovative Interconnected Observer (IO) based Model Predictive Control (MPC) strategy aimed at estimating capacitor

voltages using circulating and load currents. This method enhances system robustness by accommodating parameter uncertainties, such as capacitance variations. The integration of IO with MPC provides stable and balanced voltage control while minimizing circulating current, as demonstrated through Matlab/Simulink simulations. However, the paper primarily addresses a theoretical model with simulation validation, and practical implementation details are sparse.

However, although the observer demonstrates theoretical effectiveness, the authors neglect to provide additional examination to evaluate its sensitivity to model uncertainties and parameter changes. Additionally, the performance of the observer was not assessed under varying operating conditions, such as load changes and grid failures.

Nevertheless, selecting an appropriate estimation/observation method is a significant challenge for capacitor voltage estimation in MMCs. Despite numerous advanced estimation strategies, SMOs remain employed in several recently published research papers. SMOs have gained special interest due to their rapid convergence rate, easy implementation, and low cost.

The paper [22] proposes a method to estimate individual capacitor voltages in an MMC using only arm current measurements and modulating signals, thereby eliminating the need for voltage sensors. The sliding-mode observer is validated through simulations under various conditions, demonstrating its robustness against external disturbances, parametric variations, and dynamics.

In [23] a method for controlling MMCs without using voltage sensors was introduced. It employs a SMO to estimate capacitor voltages and a Voltage Tracking Fuzzy Controller (VTFC) for maintaining voltage balance. While the approach reduces sensor dependency and enhances reliability, several areas need improvement. The complexity and computational demands of implementing SMO and VTFC in real-time are not discussed, nor is the sensitivity of the SMO to parameter changes like capacitance or resistance variations. Although there are certain limitations, the method shows possibilities for reducing hardware complexity and improving MMC reliability.

A discrete-time SMO for controlling capacitor voltage in MMCs proposed by [24]. This technique estimates capacitor voltages and arm currents without additional sensors, potentially lowering system costs and complexity.

This study presents the implementation of a SMO for the estimation of SM voltages in grid-connected MMCs used in PV systems. The suggested method aims to provide precise voltage estimations while minimizing the need for sensors, thus improving control performance and system resilience in grid-connected PV systems. The simulation findings confirm that the SMO has high dynamic, good stability, and robustness when subjected to variations in irradiance profile, switching frequency, and parameter changes.

The structure of this paper is as follows: Section II explains the general system configuration used in this research. Section III provides a detailed description of the estimation technique. Section IV discusses the proposed control system, focusing primarily on grid-connected PV systems. Section V presents the simulation results, and finally, Section VI concludes the paper.

## **II. OVERALL SYSTEM CONFIGURATION**

The configuration of an MMC-based single-phase grid-connected PV system is illustrated in Figure 1.



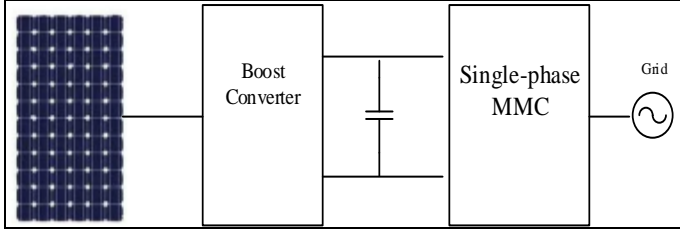


Figure 1: Grid-integrated PV system.  
Source: Authors, (2025).

This system consists of two main stages:

The first stage is a DC-DC boost converter, which extracts maximum power from the PV array using MPPT control. This converter steps up the PV voltage to a higher level, making it suitable for the second stage.

The second stage is a single-phase grid-connected MMC that converts the DC voltage from the boost converter into a sinusoidal AC voltage, synchronized with the grid.

## II.1 MMC STRUCTURE

A single-phase grid-connected MMC is shown in Figure 2. It consists of several key components. Each arm of the MMC (upper and lower) contains multiple SMs connected in series, with each SM typically comprising a half-bridge. The arms also include inductors. The boost provides the main DC voltage and connects the upper and lower arms. The converter connects to the AC grid through a filter.

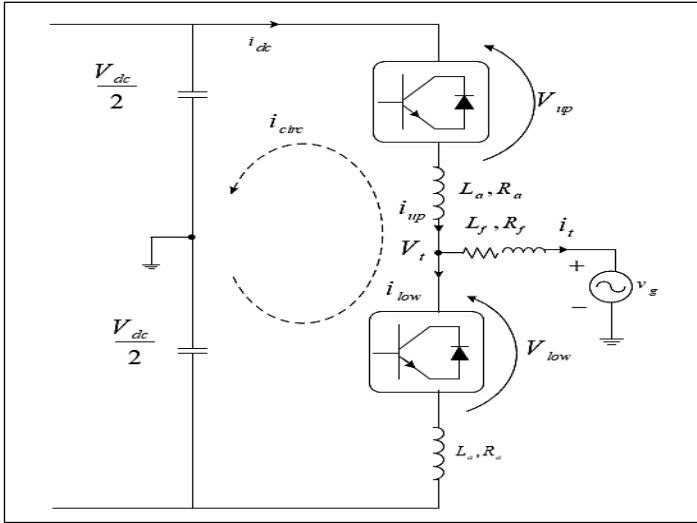


Figure 2: MMC topology.  
Source: Authors, (2025).

## II.2 MODELING OF THE MMC

The following equations model the system shown in Figure 2 [25], [26]:

$$\begin{cases} \frac{V_{dc}}{2} - L_a \frac{di_{up}}{dt} - R_a i_{up} - V_{up} = V_t \\ -\frac{V_{dc}}{2} + L_a \frac{di_{low}}{dt} + R_a i_{low} + V_{low} = V_t \end{cases} \quad (1), (2)$$

Because of the symmetrical structure of the MMC, it is assumed that AC output current ( $i_t$ ) is uniformly divided between the upper and lower arms of leg:

$$i_t = i_{up} - i_{low} \quad (3)$$

Arm currents in a MMC comprise both  $i_t$  and DC current, also known as the circulating current ( $i_{circ}$ ). The relations between  $i_t$ ,  $i_{up}$ ,  $i_{low}$ , and  $i_{circ}$  are defined:

$$\begin{cases} i_{up} = \frac{i_t}{2} + i_{circ} \\ i_{low} = -\frac{i_t}{2} + i_{circ} \end{cases} \quad (4)$$

The  $i_t$  represents the primary current that passes through the converter and is directed to the grid. It is the fundamental current that the converter is designed to generate and regulate. The  $i_{circ}$  within the converter does not directly contribute to the  $i_t$ . It traverses through both the two arms, and its expression can be stated as follows:

$$i_{circ} = \frac{i_{up} + i_{low}}{2} \quad (5)$$

A based the fundamental equations of the system:

1)The  $i_{circ}$  can be determined as follows: by summing the two Equations (1), (2), and replace  $i_{circ}$  by Equation (5):

$$L_a \frac{di_{circ}}{dt} + R_a i_{circ} = \frac{V_{dc} - (V_{up} + V_{low})}{2} \quad (6)$$

The  $i_{circ}$  is determined by the difference between the  $V_{dc}$  and the sum of the  $V_{up}$  and  $V_{low}$ .

$$v_{circ} = L_a \frac{di_{circ}}{dt} + R_a i_{circ} \quad (7)$$

$v_{circ}$ : The voltage caused by  $i_{circ}$ .

2)And in the case of subtracting Equations (1), (2), and replace for Equation (3) obtain:

$$V_t = \frac{V_{low} - V_{up}}{2} + \frac{L_a}{2} \frac{di_t}{dt} + R_a i_t \quad (8)$$

The  $\frac{V_{low} - V_{up}}{2}$  this term is the inner EMF (electromotive force) of phase, and defined by:

$$V_t^* = \frac{V_{low} - V_{up}}{2} \quad (9)$$

$i_t$  is given:

$$L_f \frac{di_t}{dt} + R_f i_t = v_g - V_t \quad (10)$$

Equations (8) and (9) combined could produce the MMC dynamics:

$$V_t = V_t^* + \left( \frac{L_a}{2} + L_f \right) \frac{di_t}{dt} + \left( \frac{R_a}{2} + R_f \right) i_t \quad (11)$$

$R_s$  and  $L_s$  are given as follows:

$$\begin{aligned} L_s &= \frac{L_a}{2} + L_f \\ R_s &= \frac{R_a}{2} + R_f \end{aligned} \quad (12)$$

The voltage reference for controlling the upper and lower SMs of the MMC is defined by Equation (13):

$$\begin{cases} V_{up} = \frac{V_{dc}}{2} - V_t^* - v_{circ} \\ V_{low} = \frac{V_{dc}}{2} + V_t^* - v_{circ} \end{cases} \quad (13)$$

### III. PROPOSED SM VOLTAGE ESTIMATION SCHEME

The Sliding Mode Observer (SMO) is a well-known algorithm extensively used in various fields. It is robust to parameter fluctuations and external disturbances and has precise finite-time convergence characteristics [27], [28].

In this section, the Sliding Mode Observer (SMO) is designed, and the stability analysis of the observer is provided. The SMO uses the arm currents and DC-link voltage to estimate the capacitor voltages. A voltage-sensorless operation utilizing the SMO is developed to replace voltage measurements, as indicated in the following equations [23]:

This paper focuses on the upper arm as an example. The voltage of the upper arm can be represented as follows, noting that  $i$  refers to the  $i$ -th SM ( $i = 1, 2, \dots, 2N$ ):

$$V_{ci} = \frac{1}{C} \int_0^t S_i(t) i_{up}(t) dt + V_{ci}(0) \quad (14)$$

For SMO, the state variables are chosen to be the voltage across the capacitor and the current through the arm. The continuous-time sliding mode function allows for the acquisition of the voltage across the upper arm capacitor and the current flowing through the arm:

$$\begin{aligned} \frac{d\hat{V}_{ci}}{dt} &= \frac{1}{C} S_i \hat{i}_{up} + \\ &k_{uf} \left( \sum_{i=1}^N S_i V_{ci} - \sum_{i=1}^N S_i \hat{V}_{ci} \right) \end{aligned} \quad (15)$$

$$\begin{aligned} \frac{d\hat{i}_{up}}{dt} &= \frac{1}{L_a} \left[ \frac{V_{dc}}{2} - \sum_{i=1}^N S_i \hat{V}_{ci} - R_a \hat{i}_{up} - V_t \right] + \\ &k_{if} \left( \sum_{i=1}^N i_{up} - \sum_{i=1}^N \hat{i}_{up} \right) \end{aligned} \quad (16)$$

A sign function, denoted as  $f(x)$ , is employed:

$$f(x) = \begin{cases} 1, & x > 0 \\ 0, & x = 0 \\ -1, & x < 0 \end{cases} \quad (17)$$

$$\frac{dV_{ci}}{dt} = \frac{1}{C} S_i i_{up} - k_{uf} \left( \sum_{i=1}^N S_i V_{ci} \right) \quad (18)$$

$$\frac{di_{up}}{dt} = \frac{1}{L_a} \left( \sum_{i=1}^N S_i V_{ci} \right) - k_{if} i_{up} \quad (19)$$

Hence, the sliding surfaces are:

$$\sum_{i=1}^N S_i V_{ci} = \left( \sum_{i=1}^N S_i V_{ci} - \sum_{i=1}^N S_i \hat{V}_{ci} \right) \quad (20)$$

$$i_{up} = \left( i_{up} - \hat{i}_{up} \right) \quad (21)$$

Consequently, an equation for a Lyapunov candidate can be formulated:

$$V_e = \frac{1}{2} \left( i_{up}^2 + \sum_{i=1}^N S_i V_{ci}^2 \right) \quad (22)$$

$$V_e = \frac{1}{2} \left( i_{up} \dot{i}_{up} + \sum_{i=1}^N S_i V_{ci} \dot{V}_{ci} \right) \quad (23)$$

$$\begin{aligned} V_e &= \left\{ \frac{1}{L_a} \left( \sum_{i=1}^N S_i V_{ci} \right) i_{up} + k_{if} \left( i_{up} \right) \right\} + \\ &\sum_{i=1}^N S_i \left\{ \frac{1}{C} S_i i_{up} V_{ci} - k_{uf} \left( \sum_{i=1}^N S_i V_{ci} \right) \right\} \end{aligned} \quad (24)$$

To ensure  $V_e \leq 0$  adapts to all conditions, the following inequalities must be met.

$$\frac{1}{L_a} \left( \sum_{i=1}^N S_i V_{ci} \right) i_{up} \leq k_i$$

$$\frac{1}{C} S_i i_{up} V_{ci} \leq k_u \quad (25)$$

#### IV. CONTROL SYSTEM FOR THE MMC

The objective of this part is to design a novel controller for a single-phase grid-connected MMC-based PV system, with the goal of achieving comprehensive control over the system.

Figure 3 presents a detailed control scheme for the considered system. Before delving into the explanation of system control in this section, it is essential to highlight that the primary objective of this paper is not to address the issue of DC-DC converter control. However, it is important to note that the technique used for MPPT is Incremental Conductance (IC).

Thus, the regulator for MMC will be designed by combining 2 primary phases [29]:

- Output power control.
- Internal dynamics control of the MMC.

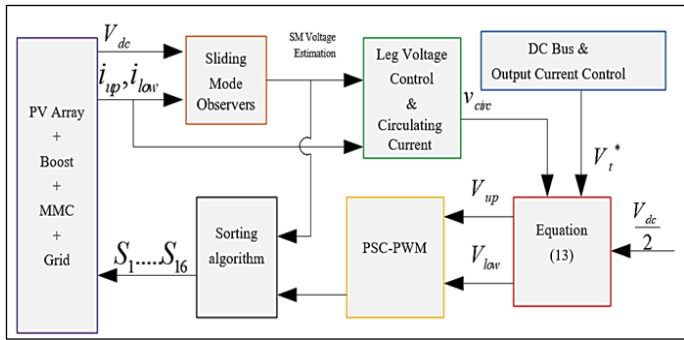


Figure 3: Overall control diagram.  
Source: Authors, (2025).

#### IV.1 OUTPUT POWER CONTROL

The design of the output power control for a grid-connected PV system involves three control loops:

##### IV.1.1 INNER CONTROL LOOP: GRID CURRENT CONTROL

The inner control loop is developed using a Proportional-Resonant (PR) controller. This loop directly acts on the grid current, ensuring precise regulation and stability of the current injected into the grid.

##### IV.1.2 OUTER CONTROL LOOP: CONTROL OF THE DC BUS

A Proportional-Integral (PI) controller is used in the outer control loop to maintain the DC bus voltage at a reference level. The reference of this controller is derived from the output active power.

##### IV.1.3 PHASE-LOCKED LOOP: GRID SYNCHRONIZATION

Grid synchronization is achieved using a Phase-Locked Loop (PLL), which determines the reference current angle. The PLL ensures that the inverter output is in phase with the grid voltage, facilitating proper synchronization and seamless operation.

These three control loops work together to achieve the desired control performance of the output power.

#### IV.2 INTERNAL DYNAMICS CONTROL OF THE MMC

The main aspects of internal dynamics control in MMCs are:

##### IV.2.1 CONTROL OF AVERAGE SM VOLTAGE BALANCING AND CIRCULATING CURRENT

The control loop is designed based on the reference [30]. The Average SM Voltage Balancing Control uses a Proportional-Integral (PI) controller to maintain the average voltage of the SM at a specified level that aligns with the SM capacitor voltage. The PI controller takes input from the average values of the SM capacitor voltages, calculated by dividing the total estimated capacitor voltages (obtained from the SMO) by the number of SMs in the leg (2N). The output of the PI controller adjusts the reference value for the circulating current. A Proportional-Resonant (PR) controller is used for circulating current control [31], [32].

##### IV.2.2 CONTROL OF INDIVIDUAL SM VOLTAGE BALANCING

Individual SM voltage balancing control typically involves a sorting algorithm, which selects the appropriate SMs to be inserted or bypassed based on the direction of the arm currents. This process ensures that the capacitor voltages are balanced, maintaining safe operating limits for the MMC [14].

The voltage commands produced by the two PR controllers, which control the grid current and circulating current, are utilized for the generation of SM voltage references.

#### IV.3 MODULATION TECHNIQUE

PSC-PWM is a widely used modulation strategy for multilevel inverters that employs phase-shifted carrier signals to synthesize the output voltage waveform with reduced harmonics [33], [34]. PSC-PWM generates the switching signals for the power devices. PSC-PWM takes the voltage references for each SM and produces the corresponding switching states to control the power devices within each SM. This integration allows the MMC to synthesize the desired output voltage waveform by accurately managing the switching of the individual SMs.

#### V. SIMULATION ANALYSES

To verify the effectiveness of the control strategy proposed in this paper, simulations were conducted using Matlab/Simulink software. The control system utilizes a SMO to estimate the capacitor voltages of the MMC. This approach was simulated and compared to a sensor-based method. Evaluations included responses under stable operating conditions, dynamic responses to variations in irradiance and switching frequency, and robustness against changes in capacitor values. The parameters of the grid-connected MMC are listed:  $P = 3\text{kW}$ ,  $v_g = 230\text{V}$ ,  $v_{dc} = 800\text{V}$ ,  $N = 4$ ,  $f_c = 4\text{kHz}$ ,  $L_a = 1\text{mH}$ ,  $R_a = 0.1\Omega$ ,  $C = 800\mu\text{F}$ ,  $L_f = 8.4\text{mH}$ ,  $R_f = 1\Omega$ .

### V.1 STEADY-STATE

In this part of the simulation results, the steady-state performance of the system under normal weather conditions is analyzed for both the sensor-based scheme and the proposed estimation scheme.

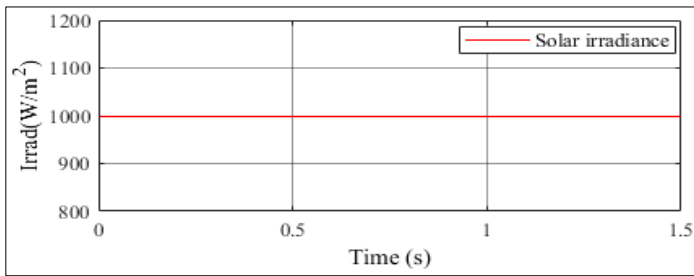
Case 1: In the sensor-based scheme, sensors are used to measure the following: (1) DC-link voltage, (2) grid voltages, (3) grid current, (4) arm currents, and (5) sub-module (SM) capacitor voltages (2N voltage sensors, where N is the number of SMs in each arm), as well as the PV output current and voltage. The simulation results are displayed in Figures 5.

Case 2: In the proposed estimation scheme, a Sliding Mode Observer (SMO) is used to estimate the capacitor voltages, with the simulation results displayed in Figures 6.

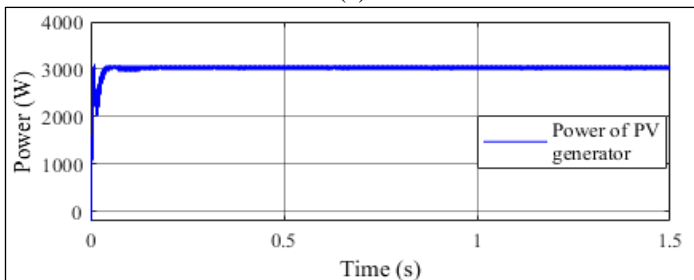
The results of the simulation shown in Figure 4 demonstrate that the MPPT technique performs well, delivering optimum power from the PV array to the grid with excellent performance characteristics under normal weather conditions.

In both schemes, whether it is a Case 1 or Case 2 scheme, the voltage loop controller of the internal dynamics control system effectively regulates the equilibrium of the sub-module capacitors, thereby eliminating circulating currents within the MMC. Consequently, the DC-link voltage is successfully maintained at its nominal value of 800 V. Additionally, the MMC is capable of generating a multilevel output voltage, which helps reduce harmonics and improve the overall power quality of the system. In both cases, the system provides a sinusoidal current with low ripple, closely synchronized with the grid voltage, thereby improving overall power quality. This demonstrates the effectiveness of the proposed observer, as it successfully maintains grid power quality in accordance with power quality standards.

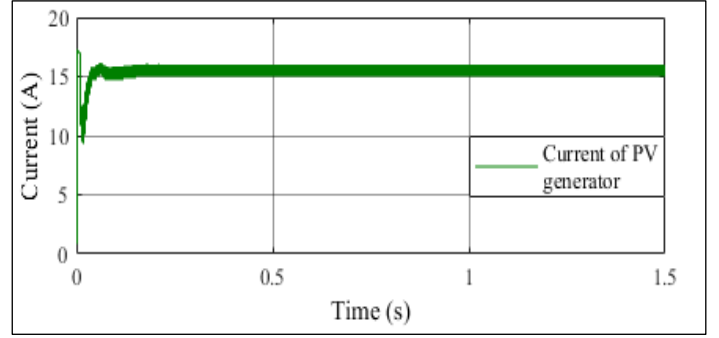
In general, the results demonstrate that both cases exhibit good and satisfactory performance in efficiently transferring energy from photovoltaic sources to the grid. However, the second case is particularly noteworthy for significantly reducing the number of sensors required, specifically by eliminating the eight sensors responsible for measuring capacitor voltages. This enhances control performance, lowers system costs, and increases reliability in grid-connected MMC systems. Reducing the number of sensors simplifies the control system, allowing it to focus on crucial parameters, which improves response times and stability.



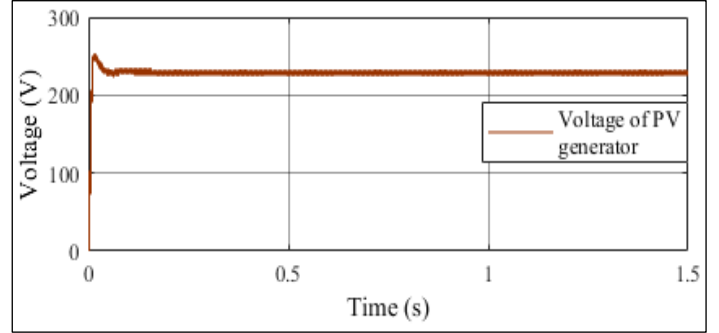
(a)



(b)



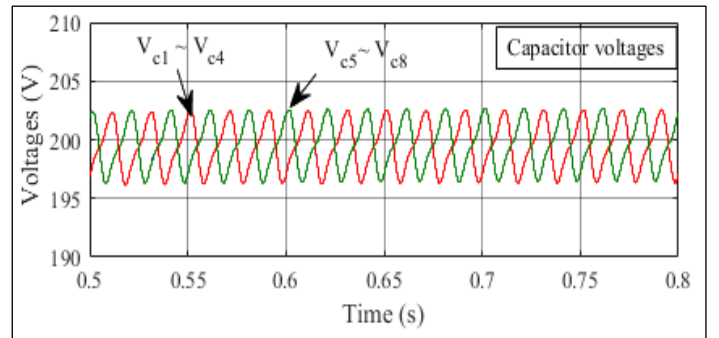
(c)



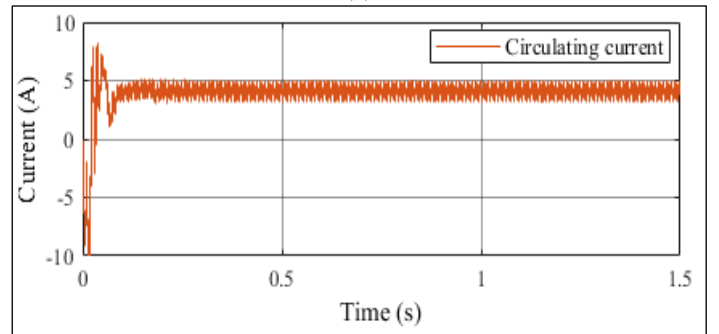
(d)

Figure 4: PV side results: (a) Irradiance profile, (b) PV output power, (c) PV output current, (d) PV output voltage.

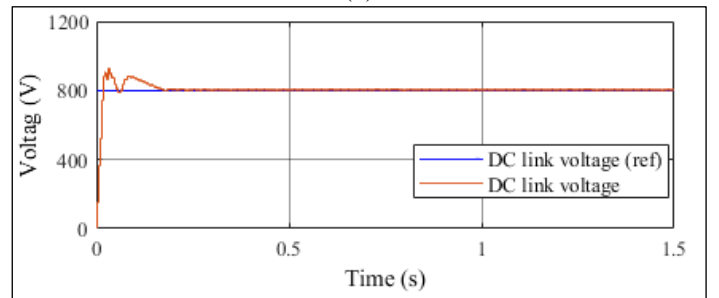
Source: Authors, (2025).



(a)

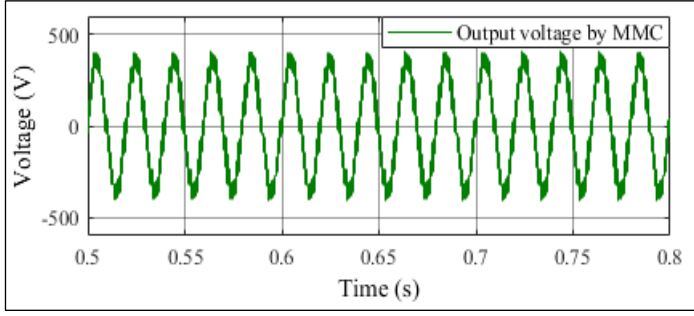


(b)

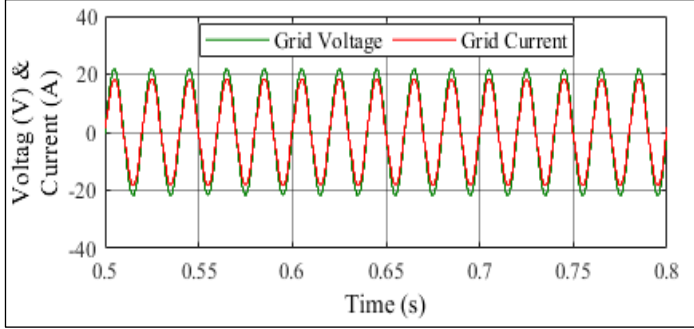


(c)



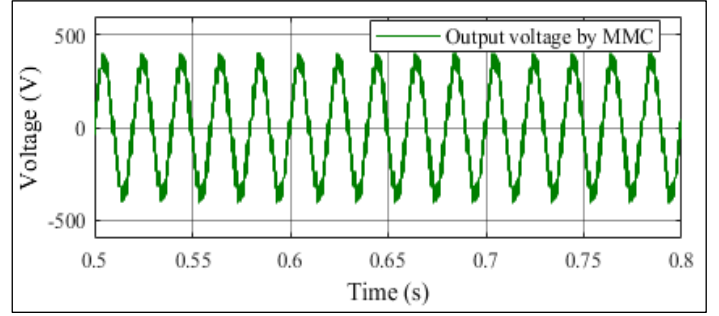


(d)

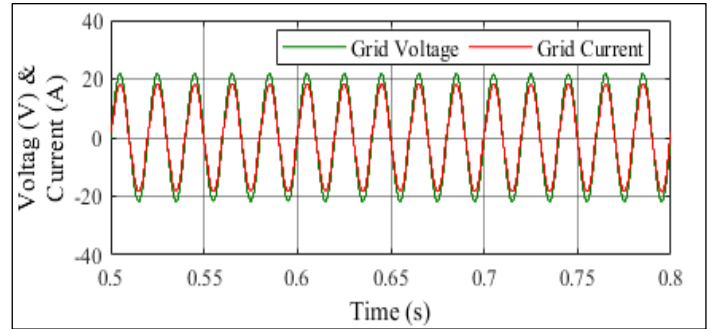


(e)

Figure 5: Case1 simulation results: (a) Capacitor voltages;(b) Circulating current error;(c)DC-link voltage;(d)Output voltage by MMC; (e).Grid phase voltage and current.  
Source: Authors, (2025).



(d)



(e)

Figure 6: Case2 simulation results:(a) Capacitor voltages, (b) Circulating current error, (c) DC-link voltage, (d) Output voltage by MMC, (e). Grid phase voltage and current.  
Source: Authors, (2025).

## V.2 DYNAMIC TEST

The dynamic test in the simulation results for the proposed estimation scheme involves analyzing the performance of the SMO under varying environmental conditions. This includes studying the impact of changes in solar irradiance and switching frequency. The simulations aim to model the dynamic behavior of the SMO for voltage sensor-less control of grid-connected MMCs, which is essential for understanding how the system responds to rapid fluctuations in such conditions.

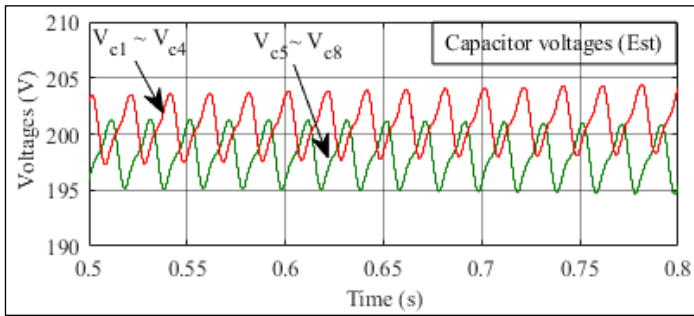
### V.2.1 CHANGES IN IRRADIANCE PROFILE

Figures (7-8) below illustrate the simulation results under various weather conditions, according to the irradiance profile shown in Figure 7a. As shown in Figure 7b, there is a direct correlation between variations in weather conditions and PV power

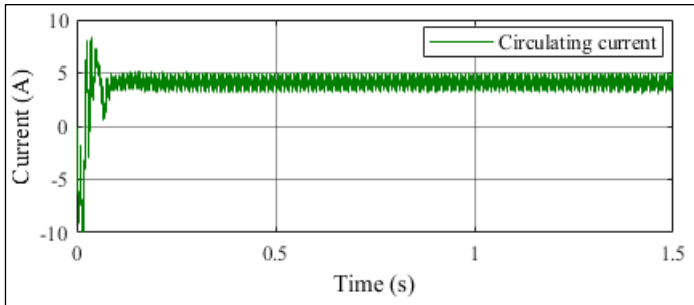
Figure 8.a displays the voltage levels of the upper and lower capacitors as estimated by the SMO. The results underscore that the MMC voltages remain maintained at their directed values. Accurate voltage estimation is essential for optimizing capacitor voltage balance, which significantly impacts the overall performance of the MMC.

The proposed algorithm provides good accuracy in estimating SM voltage. This is evident from the following results. Figure 8b indicates that a constant voltage above the reference value of 800V was maintained. The DC-link voltage is calculated by summing the SM voltages. In addition, Figure 8c demonstrates a direct proportionality between changes in irradiance and output current, indicating a corresponding change in output power.

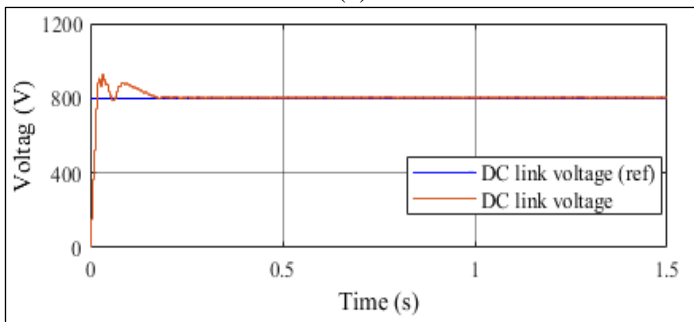
Figure 8d shows that the amplitudes of the circulating current and the capacitor voltage ripples are directly proportional to the active power, demonstrating the robust and reliable stability of the voltage estimation system.



(a)



(b)



(c)

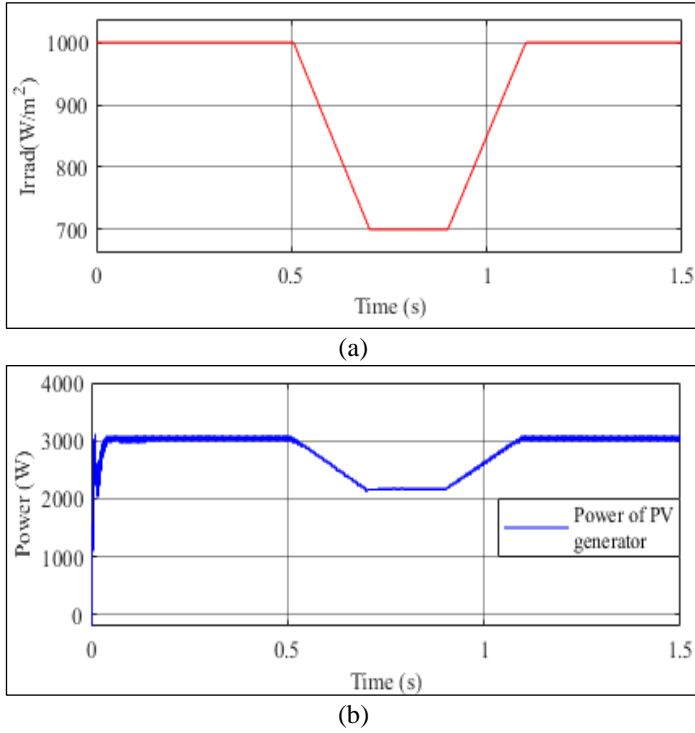


Figure 7: PV side results: (a) Irradiance profile (b), PV output power.

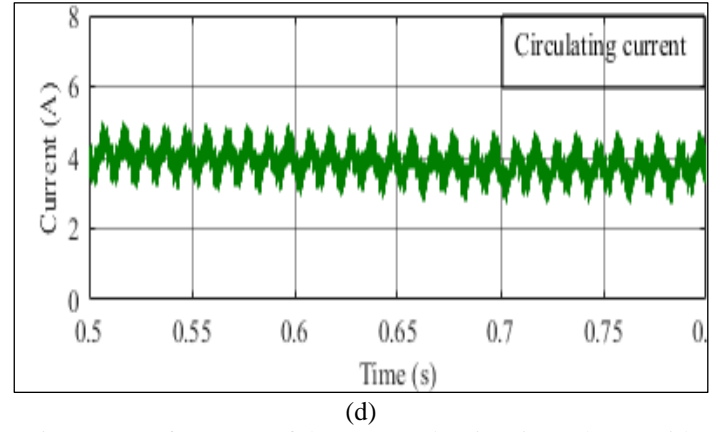
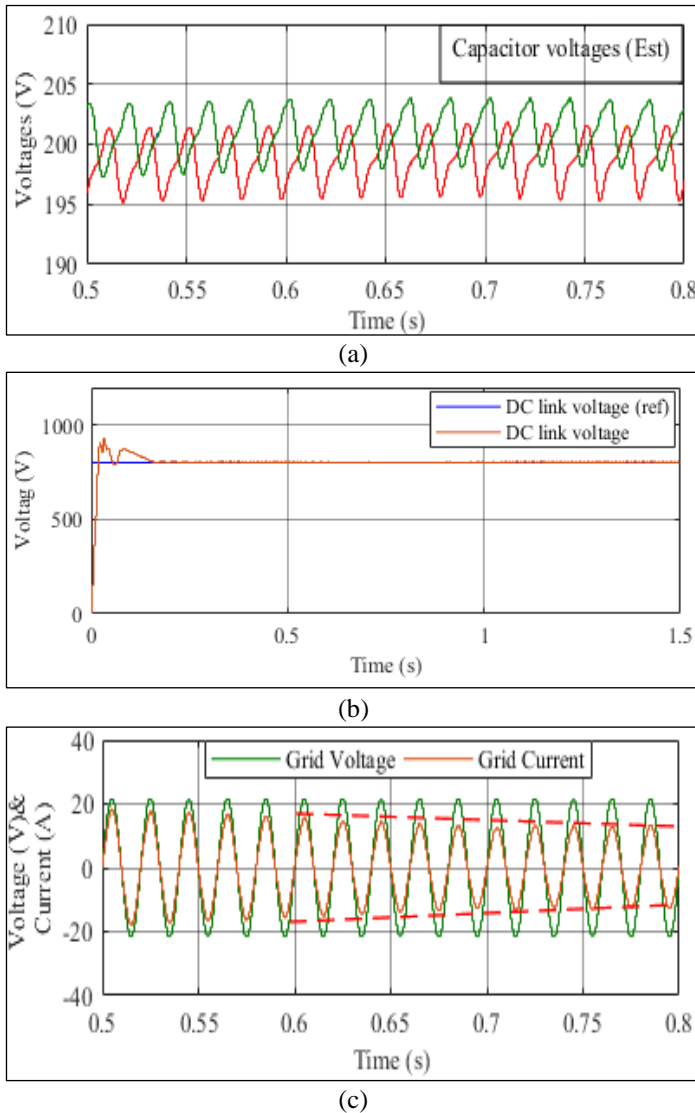
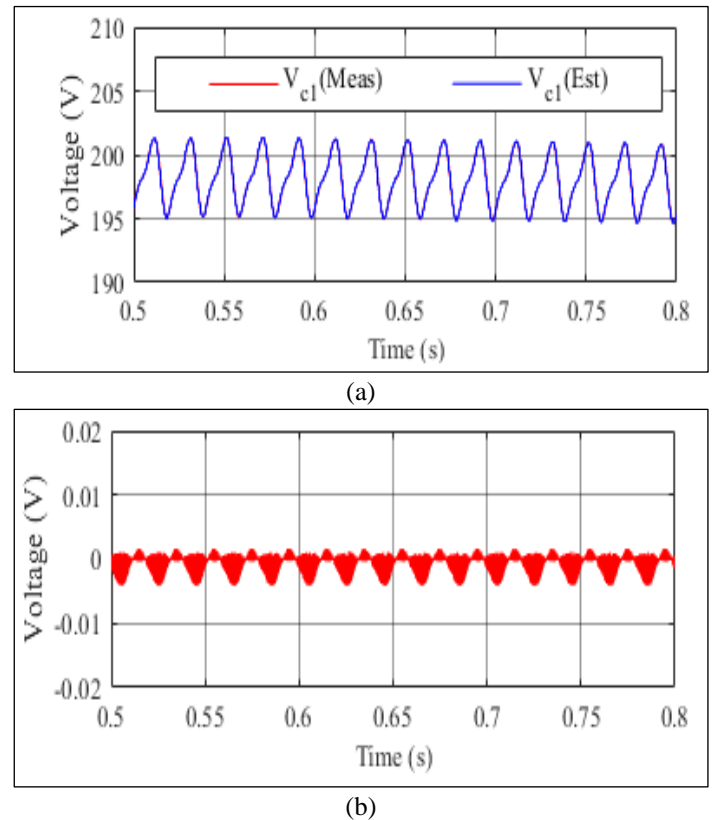


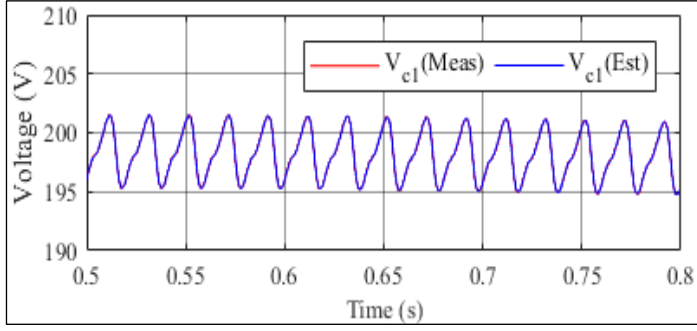
Figure 8: Performance of the proposed estimation scheme with changes in irradiance: (a) Estimated Capacitor voltages by SMO, (b) DC-link voltage, (c) Grid phase voltage and current, (d) Circulating current error .  
Source: Authors, (2025).

## V.2.2 CHANGES IN SWITCHING FREQUENCY

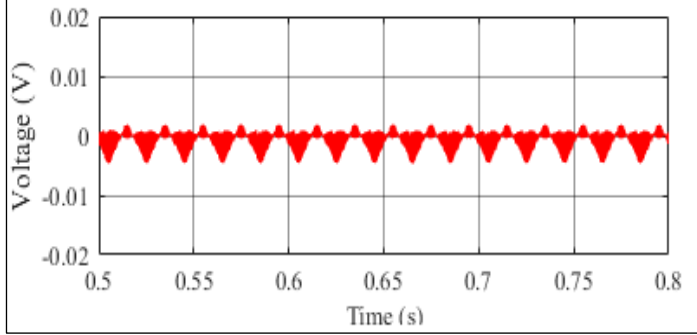
Figure 9 presents various switching frequencies to observe system dynamics and evaluate the effectiveness of the suggested controller. Despite the significant impact of switching frequency on capacitor voltage ripple and switching losses, the stability of capacitor voltage estimation, particularly for  $C_1$ , remains notable. The SMO demonstrates strong robustness, showing no observer error across cases, ensuring reliable voltage estimates despite frequency variations. While lower frequencies affect system dynamics and electrical parameters, their direct influence on output voltage and power transfer is important but beyond the scope of this study. This research emphasizes evaluating controller stability and performance under varying frequencies.



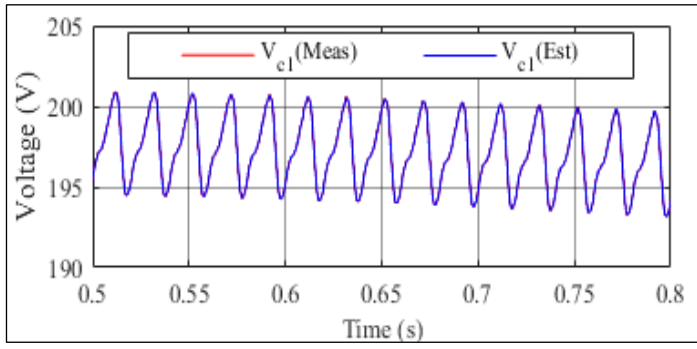
$f_c = 4 \text{ kHz}$



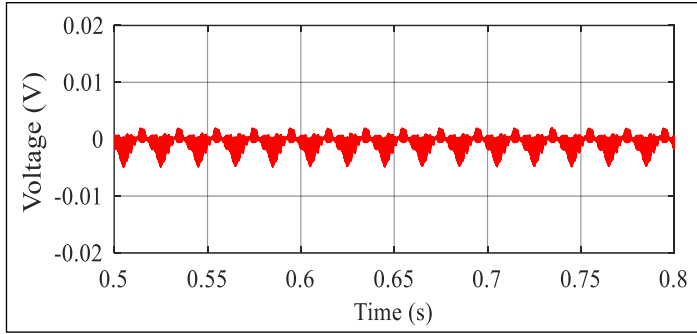
(a)



(b)

 $f_c = 2 \text{ kHz}$ 


(a)



(b)

 $f_c = 750 \text{ Hz}$ 

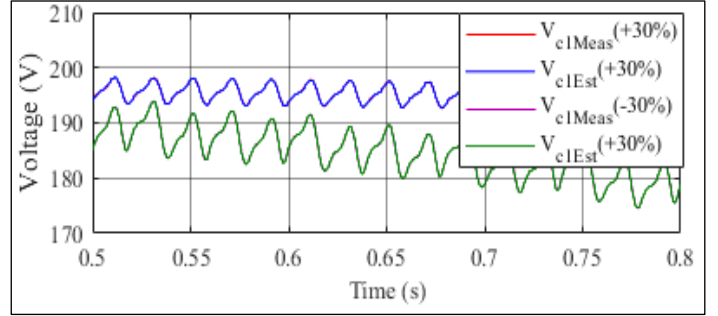
Figure 9: Performance of the proposed estimation scheme with changes in switching frequency for all eight SMs.  
Source: Authors, (2025).

### V.2.3 ROBUSTNESS TEST

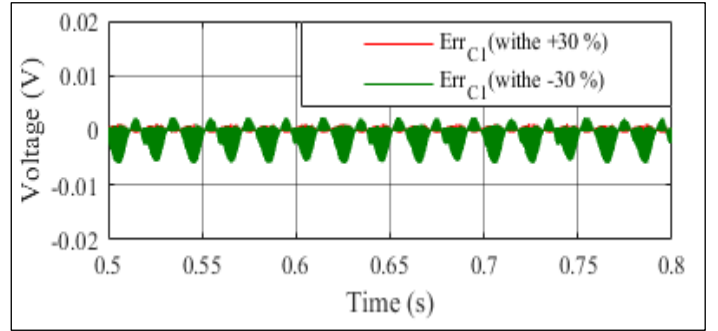
The robustness of the SMO is examined through variations in the capacitance values.

The reliability of the proposed algorithm for estimating SM voltage fluctuations in  $C_{j1}$  is confirmed by comparing the estimated SM capacitor voltage fluctuation with the measured value of when the nominal capacitance of the capacitor is increased or decreased

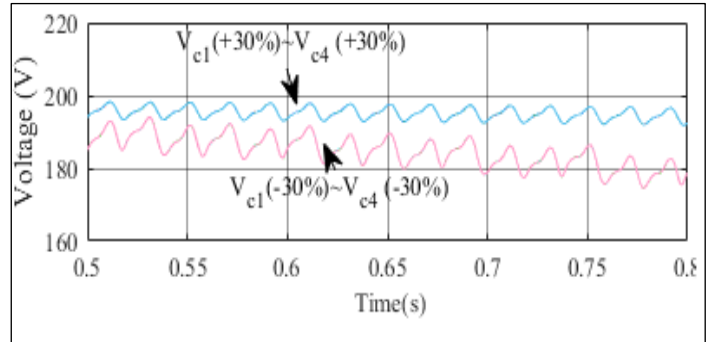
by 30%. This comparison is illustrated in Figure 10a. It is evident that the estimated SM voltage closely tracked the measured value of the individual SM voltages in terms of both shape and with nearly no observer errors, as shown in Figure 10b. The simulation results, which examined the SM voltage variations across the four SMs in the upper arm (Fig. 10c), showed that the SM capacitor voltages were maintained at a balanced level of 200 V (the nominal value limits). This ensured that the voltage fluctuations remained within the acceptable range specified by the system requirements. The proposed algorithm demonstrated high efficiency in estimating SM voltage variations.



(a)



(b)



(c)

Figure 10: Performance of the proposed estimation scheme with variations in all capacitors.  
Source: Authors, (2025).

## VI. CONCLUSIONS

This study presented the development and application of a Sliding Mode Observer (SMO) for sub-module voltage estimation in Modular Multilevel Converters (MMCs) used in photovoltaic (PV) applications. The results demonstrate that the SMO provides a robust and reliable alternative to traditional voltage sensing methods, which are often cost-prohibitive and prone to sensor failures. By accurately estimating sub-module voltages without extensive physical sensors, the SMO enhances system reliability, reduces costs, and simplifies the hardware structure.

Simulation validations confirmed the effectiveness of the SMO in maintaining accurate voltage estimations both in steady-state and during dynamic changes. This improved voltage balancing and overall control of the MMC contributes to the safe and efficient operation of PV systems. Results from the studies show that the proposed method outperforms the sensor-based scheme.

In conclusion, the Sliding Mode Observer is a viable and effective solution for sub-module voltage estimation in MMCs. Its ability to mitigate the drawbacks of traditional voltage sensing methods positions it as a valuable tool for enhancing the performance and reliability of MMCs in PV applications. Future work should explore further optimization of the SMO design and its potential integration into other power electronic systems to fully leverage its benefits. Additionally, plan to implement it in an experimental environment in the future.

## VI. AUTHOR'S CONTRIBUTION

**Conceptualization:** Imane Alia, Imad Merzouk and Mehamed Mounir Rezaoui.

**Methodology:** Imane Alia, Imad Merzouk and Mehamed Mounir Rezaoui.

**Investigation:** Imane Alia, Imad Merzouk and Mehamed Mounir Rezaoui.

**Discussion of results:** Imane Alia, Imad Merzouk and Mehamed Mounir Rezaoui.

**Writing – Original Draft:** Imane Alia, Imad Merzouk and Mehamed Mounir Rezaoui.

**Writing – Review and Editing:** Imane Alia, Imad Merzouk and Mehamed Mounir Rezaoui.

**Resources:** Imane Alia, Imad Merzouk and Mehamed Mounir Rezaoui.

**Supervision:** Imane Alia, Imad Merzouk and Mehamed Mounir Rezaoui.

**Approval of the final text:** Imane Alia, Imad Merzouk and Mehamed Mounir Rezaoui.

## VII. REFERENCES

- [1]Alotaibi, S., & Darwish, A. "Modular Multilevel Converters for Large-Scale Grid-Connected Photovoltaic Systems", A Review. *Energies*, 14(19), 6213, 2021. <https://doi.org/10.3390/en14196213>.
- [2]Pu, H., Bai, Z., Xin, Y., Zhao, J., Bai, R., Luo, J., & Yi, J. "Efficient (2N+1) selective harmonic elimination in modular multilevel converters using an evolutionary many-tasking approach with prior knowledge", *Applied Soft Computing*, 144, 110468, 2023. <https://doi.org/10.1016/j.asoc.2023.110468>.
- [3]Alia, I., Merzouk, I., & Rezaoui, M. M. "Robust line voltage sensor-less control of grid-connected MMC converter in PV Applications", *STUDIES IN ENGINEERING AND EXACT SCIENCES*, 5(1), 2366–2390, 2024. <https://doi.org/10.54021/seesv5n1-117>.
- [4]Tian, Y., Wickramasinghe, H. R., Li, Z., Pou, J., & Konstantinou, G. "Review, Classification and Loss Comparison of Modular Multilevel Converter Submodules for HVDC Applications", *Energies*, 15(6), 1985, 2022. <https://doi.org/10.3390/en15061985>.
- [5]An, Y., Sun, X., Ren, B., Li, H., & Zhang, M. "A data-driven method for IGBT open-circuit fault diagnosis for the modular multilevel converter based on a modified Elman neural network", *Energy Reports*, 8, 80–88, 2022. <https://doi.org/10.1016/j.egy.2022.08.024>.
- [6]Ke, L., Zhang, Y., Yang, B., Luo, Z., & Liu, Z. "Fault diagnosis with synchrosqueezing transform and optimized deep convolutional neural network: An application in modular multilevel converters", *Neurocomputing*, 430, 24–33, 2021. <https://doi.org/10.1016/j.neucom.2020.11.037>.

- [7]Barros, L. A. M., Martins, A. P., & Pinto, J. G. "A Comprehensive Review on Modular Multilevel Converters, Submodule Topologies, and Modulation Techniques", *Energies*, 15(3), 1078, 2022. <https://doi.org/10.3390/en15031078>.
- [8]Luo, Y., Jia, Z., Xu, L., Li, Q., & Song, Y. "A reduced switching frequency capacitor voltage balancing control for modular multilevel converters", *International Journal of Electrical Power & Energy Systems*, 2022. 142, 108272. <https://doi.org/10.1016/j.ijepes.2022.108272>.
- [9]Ramirez, D., Zarei, M. E., Gupta, M., & Serrano, J. "Fast Model-based Predictive Control (FMPC) for grid connected Modular Multilevel Converters (MMC) ", *International Journal of Electrical Power & Energy Systems*, 119, 105951, . 2020. <https://doi.org/10.1016/j.ijepes.2020.105951>.
- [10]Parvari, R., Filizadeh, S., & Muthumuni, D. "An accelerated detailed equivalent model for modular multilevel converters", *Electric Power Systems Research*, 223, 109648, 2023. <https://doi.org/10.1016/j.epr.2023.109648>.
- [11]Zhang, Y., Hu, H., Liu, Z., Zhao, M., & Cheng, L. "Concurrent fault diagnosis of modular multilevel converter with Kalman filter and optimized support vector machine", *Systems Science & Control Engineering*, 7(3), 43–53, 2019. <https://doi.org/10.1080/21642583.2019.165084>.
- [12]Li, Q., Li, B., He, J., Prieto-Araujo, E., Westerman Spier, D., Lyu, H., & Gomis-Bellmunt, O. "A novel design of circulating current control target to minimize SM capacitance in MMC", *International Journal of Electrical Power & Energy Systems*, 143, 108432, 2022. <https://doi.org/10.1016/j.ijepes.2022.108432>.
- [13]Hu, P., Teodorescu, R., & Guerrero, J. M. "State observer based capacitor-voltage-balancing method for modular multilevel converters without arm-current sensors", *International Journal of Electrical Power & Energy Systems*, 113, 188–196, 2019. <https://doi.org/10.1016/j.ijepes.2019.05.025>.
- [14]Zhao, J., Gu, C., Wu, S., Liu, W., Lei, Y., Hang, J., & Ding, S. "Improved power loss balance control for modular multilevel converters based on variable capacitor voltage deviation predefined value under SM malfunction", *International Journal of Electrical Power & Energy Systems*, 156, 109729, 2024. <https://doi.org/10.1016/j.ijepes.2023.109729>.
- [15]Guo, L., Sun, Y., & Jin, N. "A Capacitor Voltage Balancing Control Strategy for Modular Multilevel Converter", *Electric Power Components and Systems*, 48(12–13), 1410–1420, 2020. <https://doi.org/10.1080/15325008.2020.1856230>.
- [16]Konstantinou, G., Wickramasinghe, H. R., Townsend, C. D., Ceballos, S., & Pou, J. " Estimation Methods and Sensor Reduction in Modular Multilevel Converters", A Review. 2018 8th International Conference on Power and Energy Systems (ICPES), 23–28, 2018. <https://doi.org/10.1109/ICPESYS.2018.8626987>.
- [17]Abushafa, O. S. H. M., Dahidah, M. S. A., Gadoue, S. M., & Atkinson, D. J. "Submodule Voltage Estimation Scheme in Modular Multilevel Converters with Reduced Voltage Sensors Based on Kalman Filter Approach", *IEEE Transactions on Industrial Electronics*, 65(9), 7025–7035, 2018. <https://doi.org/10.1109/TIE.2018.2795519>.
- [18]Islam, M. D., Razzaghi, R., & Bahrani, B. "Arm-Sensorless Sub-Module Voltage Estimation and Balancing of Modular Multilevel Converters", *IEEE Transactions on Power Delivery*, 35(2), 957–967, 2020. <https://doi.org/10.1109/TPWRD.2019.2931287>.
- [19]Liu, H., Ma, K., Loh, P. C., & Blaabjerg, F. "A sensorless control method for capacitor voltage balance and circulating current suppression of modular multilevel converter", 2015 IEEE Energy Conversion Congress and Exposition (ECCE), 6376–6384, 2015. <https://doi.org/10.1109/ECCE.2015.7310553>.
- [20]Abdelsalam, M., Marei, M., Tennakoon, S., & Griffiths, A. "Capacitor voltage balancing strategy based on sub-module capacitor voltage estimation for modular multilevel converters", *CSEE Journal of Power and Energy Systems*, 2(1), 65–73, 2016. <https://doi.org/10.17775/CSEEJPES.2016.00010>.
- [21]Trabelsi, M., Ghanes, M., Ellabban, O., Abu-Rub, H., & Ben-Brahim, L. "An interconnected observer for modular multilevel converter", 2016 IEEE Energy Conversion Congress and Exposition (ECCE), 1–7. 2016. <https://doi.org/10.1109/ECCE.2016.7854853>.
- [22]da Silva, G. S., Vieira, R. P., & Rech, C. "Modified sliding-mode observer of capacitor voltages in Modular Multilevel Converter", 2015 IEEE 13th Brazilian Power Electronics Conference and 1st Southern Power Electronics Conference (COBEP/SPEC), 1–6, 2015). <https://doi.org/10.1109/COBEP.2015.7420217>.



- [23] Luo, Y., Wang, F., Bai, T., Guo, H., & Feng, X, "A Sensorless Control Method for MMC Based on Sliding Mode Observer", 2018 IEEE International Power Electronics and Application Conference and Exposition (PEAC), 1–6, 2018. <https://doi.org/10.1109/PEAC.2018.8590231>.
- [24] da Silva, G. S., Vieira, R. P., & Rech, C, "Discrete-Time Sliding-Mode Observer for Capacitor Voltage Control in Modular Multilevel Converters", IEEE Transactions on Industrial Electronics, 65(1), 876–886, 2018. <https://doi.org/10.1109/TIE.2017.2721881>.
- [25] Hafez, A. A., Mahmoud, A. A., & Yousef, A. M, "Robust and Intelligent Control for Single-stage Grid-Connected Modular Multilevel Converter in PV Applications", Journal of Electrical Engineering & Technology, 16(2), 917–931, 2021. <https://doi.org/10.1007/s42835-020-00639-8>.
- [26] Imane, A., Imad, M., & Osama, A, "Robust and Intelligent Control for PV System of Two Converters: DC-DC Converter/ Single-Phase Modular Multilevel Converter to Operate Grid Connected", 2023 International Conference on Decision Aid Sciences and Applications (DASA), 278–283, 2023. <https://doi.org/10.1109/DASA59624.2023.10286773>.
- [27] Guo, L., Li, Y., Jin, N., Dou, Z., & Wu, J, "Sliding mode observer-based AC voltage sensorless model predictive control for grid-connected inverters", IET Power Electronics, 13(10), 2077–2085, 2020. <https://doi.org/10.1049/iet-pel.2019.1075>.
- [28] Guo, B., Su, M., Wang, H., Tang, Z., Liao, Y., Zhang, L., & Shi, S, "Observer-based second-order sliding mode control for grid-connected VSI with LCL-type filter under weak grid", Electric Power Systems Research, 183, 106270, 2020. <https://doi.org/10.1016/j.epsr.2020.106270>.
- [29] Mahmoud, A. A., Hafez, A. A., Yousef, A. M., Gaafar, M. A., Orabi, M., & Ali, A. F. M, "Fault-tolerant modular multilevel converter for a seamless transition between stand-alone and grid-connected microgrid", IET Power Electronics, 16(1), 11–25, 2023. <https://doi.org/10.1049/pel2.12359>.
- [30] Hagiwara, M., & Akagi, H, "Control and Experiment of Pulsewidth-Modulated Modular Multilevel Converters", IEEE Transactions on Power Electronics, 24(7), 1737–1746, 2009. <https://doi.org/10.1109/TPEL.2009.2014236>.
- [31] Nguyen, V.-T., Kim, J.-W., Lee, J.-W., & Park, B.-G, "Optimal Design of a Submodule Capacitor in a Modular Multilevel Converter for Medium Voltage Motor Drives", Energies, 17(2), 471, 2024. <https://doi.org/10.3390/en17020471>.
- [32] Lyu, Y., Zi, Y., & Li, X, "Improved Control of Capacitor Voltage Balancing in Modular Multilevel Converter Submodules", IEEE Access, 12, 19510–19519, 2024. <https://doi.org/10.1109/ACCESS.2024.3350178>.
- [33] Nguyen, M. H., Kwak, S., & Kim, T, "Phase-Shifted Carrier Pulse-Width Modulation Algorithm With Improved Dynamic Performance for Modular Multilevel Converters", IEEE Access, 7, 170949–170960, 2019. <https://doi.org/10.1109/ACCESS.2019.2955714>.
- [34] Luo, D., Lin, D., Zhang, W., & Lian, W, "A novel jittered-carrier phase-shifted sine pulse width modulation for cascaded H-bridge converter", The Journal of Engineering, 2024(6), 2024. <https://doi.org/10.1049/tje2.12391>.



# INCORPORATING ANFIS BASED CURRENT REGULATION INTO A MULTI ACTIVE FULL BRIDGE CONVERTER FOR REDUCING CURRENT RIPPLE

Rathod Rama Krishna<sup>1</sup>, G. Yesuratnam<sup>2</sup> and Dr. Punnaiah Veeraboina<sup>3</sup>

<sup>1</sup>Department of Electrical Engineering, University College of Engineering, Osmania University, Hyderabad, Telangana 500007, India

<sup>2</sup>Senior Professor, Department of Electrical Engineering, University College of Engineering, Osmania University, Hyderabad, Telangana, India

<sup>3</sup>Electrical Engineering Section, Engineering Department, BRIC-CDFD, Minister of Science and Technology, Govt of India

<sup>1</sup><http://orcid.org/0009-0002-4669-3124>, <sup>2</sup><http://orcid.org/0000-0002-4730-4496>, <sup>3</sup><http://orcid.org/0000-0001-9158-4109>

Email: [rathodkrishnaou@osmania.ac.in](mailto:rathodkrishnaou@osmania.ac.in), [ratnamgy@uceou.edu](mailto:ratnamgy@uceou.edu), [drveera33@gmail.com](mailto:drveera33@gmail.com)

## ARTICLE INFO

### Article History

Received: January 11, 2025

Revised: February 20, 2025

Accepted: March 15, 2025

Published: March 31, 2025

### Keywords:

Zero Voltage Switching (ZVS),  
Zero Current Switching (ZCS),  
Electric Vehicle (EV),  
PI (Proportional and Integral),  
Adaptive Neuro Fuzzy Inference  
System (ANFIS)

## ABSTRACT

A multi-active full bridge converter is a type of DC-DC converter typically used in high-power applications like renewable energy systems, electric vehicles, or uninterruptible power supplies. Four switches (often MOSFETs or IGBTs) grouped in an H-bridge configuration make up the full bridge topology. The term "multi-active" implies that the power conversion involves a number of active components, which may indicate complicated switching management for improved efficiency and regulation. Changing the phase shift between two switch pairs is how phase-shifted full-bridge converters are controlled. Without altering the switching frequency, the output voltage can be controlled by adjusting the phase difference between the bridge's two legs (S1-S4 and S2-S3). To lower switching losses, soft switching strategies like ZVS or ZCS might be used. improving overall efficiency. In this approach, the current through the switches is monitored and controlled to improve transient response and stability. Typically implemented in combination with voltage mode control, it ensures better regulation, especially in systems with fast load changes. The secondary side full bridge switches are controlled by current feedback phase delay controller which restricts the battery charge current. Each EV battery has its own charge current limit which is set in the current controller for battery protection. The controlled charge current improves the charge efficiency of the EV battery increasing the reliability of the cells and the overall circuit. The charge control which is a conventional PI controller is further updated with ANFIS for better stability in the EV battery charging current. A comparative analysis with PI and ANFIS controllers is proposed and the results are generated with same rating of EV batteries and system parameters.



Copyright ©2025 by authors and Galileo Institute of Technology and Education of the Amazon (ITEGAM). This work is licensed under the Creative Commons Attribution International License (CC BY 4.0).

## I. INTRODUCTION

As per the present climatic conditions we are at verge of crossing temperature limits due to global warming caused by carbon emissions. The carbon emissions are majorly caused by the industrial manufacturing plants which need to be limited. Another major reason for the emissions is transportation using fossil fuel vehicles for domestic and commercial purposes [1].

The utilization of petrol or diesel engines in the vehicles is leading to extreme climatic conditions causing health issues for all the living beings on the planet. It is very vital to replace these

vehicles with zero carbon emission vehicles which run on complete electrical power. This can be achieved by electrical vehicles (EVs) which operate by electrical motor drive. The electrical motor receives power from mobile battery pack (combination of several battery cells) which need to be charged [2]. Charging the EV battery pack using conventional power generation sources like coal plants or diesel generators is considered to be futile [3]

Therefore, these battery packs need to be charged using renewable sources like solar generation plants, wind farms, bio gas plants, tidal energy etc. The renewable sources are inter

connected to the conventional grid which shares power to the local loads or EV charging stations or to the other grid network as per the demand [4]. Grid interconnection of renewable sources creates stable operation of the network as the renewable sources are unpredictable. However, in remote areas the grid availability cannot be expected as the transmission lines may not reach some localities.

Therefore, backup storage devices need to be installed along with the renewable sources for voltage and power stability [5]. High capacity back up storage devices like battery modules are associated with the renewable source for storing or providing power as per requirement. A local load is connected to this network with an inverter operated by Sin PWM technique to ensure Sinusoidal AC generation from the DC power generated by the PV plant and battery storage module.

The load connected to the inverter is a static load which is operated at fundamental AC frequency of 50Hz [6]. At the DC common link an EV charging station is connected with multiple charging points for charging several EVs. The complete structure with standalone PV plant with battery storage module and EV charging station is presented in figure 1.

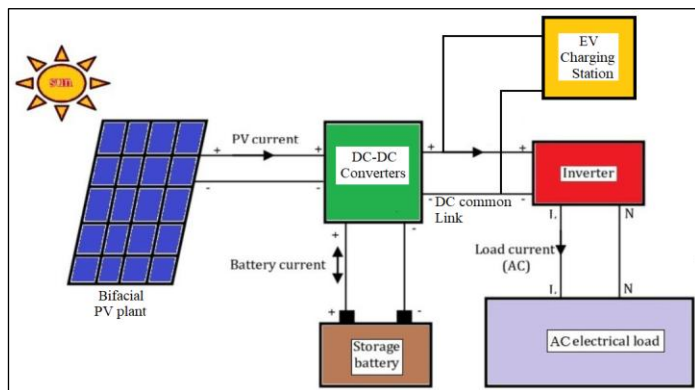


Figure 1: Outline structure of standalone PV plant with EV charging station.

Source: Authors, (2025).

As presented in figure 1 the PV plant and battery storage are connected to DC-DC converters for power delivery and exchange. The PV plant uses 'Bifacial PV module' which has two panels connected back-to-back for more power generation than the conventional PV plant. The back panels have the capability to generate 20% extra PV power by the solar radiation reflection [7]. The Bifacial PV panels are connected to boost converter operated by MPPT controller for maximum power extraction from the panels.

The storage battery module is connected to a bidirectional converter with power exchanging capabilities as per the demand and availability. The AC electrical load is a fixed value static load feeding from the DC common link. The EV charging station connected at the DC common link has Multi Active Full Bridge (MAFB) converter exchanging power between the DC common link and EV batteries [8].

The MAFB has the capability to operate in G2V (Grid to Vehicle) and V2G (Vehicle to Grid) modes as per the requirement. The charging and discharging currents of the MAFB converter circuit is controlled by individual current regulators. The MAFB is operated by phase shift pulse modulation (PS-PM) technique which creates phase delay in the pulses of the active switches of the full bridges [9]. The phase delay value in the PS-PM technique is generated by the current regulator integrated in the controller. Initially the current regulator considered is a PI

regulator which has more damping. Due to the heavy damping in PI regulator, the battery currents have more oscillations and ripple. Therefore, the PI regulator is replaced with ANFIS current regulator with optimal damping creating robust phase shift signal for the switches. This reduces the oscillations and ripple in the battery currents [10].

This paper is organized with introduction to the proposed structure of the PV standalone system with EV charging station in section 1. The section 2 is included with configuration of the complete system with design of the circuits and controllers used for the stabilization of the system. The EV charging module MAFB converter circuit with PI and ANFIS current regulators designs are discussed in section 3. The following section 4 has the results analysis of the simulations designed and modelled operating in different operating conditions. A simulation comparative analysis is presented in this section 4 followed by conclusion in section 5 validating the optimal controller. The references cited in the paper are included at the end of the paper after section 5.

## II. CONFIGURATION PROPOSED SYSTEM

As previously mentioned, charging the EV battery packs by the conventional fossil fuel sources is futile. Therefore, renewable sources need to be installed in the system operating in standalone mode. In the proposed system a standalone PV source is installed for sharing power to the local load and EV charging station for charging the battery pack with renewable power. The PV sources use Bifacial PV panels for extra renewable power generation with the same solar irradiation.

Due to the Bifacial structure of the PV panels a 20% extra power is generated from the PV plant. Bifacial PV arrays are solar panels capable of generating electricity from sunlight on both their front and rear sides [11]. These panels capture sunlight directly on the front while also utilizing reflected or diffused light on the rear. As a result, bifacial PV panels can produce more electricity per panel, particularly in environments with high albedo, such as snowy areas, sandy locations, or on white roofs.

Bifacial solar panels can achieve 10–30% more energy output compared to traditional single-faced panels, depending on installation and the albedo (reflectivity) of the ground surface [12]. This increased energy generation per panel reduces the overall cost of electricity over the system's lifetime, allowing for fewer panels or less land to achieve the same energy output as single-faced systems. Many bifacial panels are constructed with glass on both sides, which makes them more durable and resistant to environmental stressors such as humidity, UV radiation, and mechanical loads.

As a result, they tend to degrade more slowly over time, ensuring consistent performance. Bifacial panels can be effectively used in various applications, including carports, pergolas, or other elevated structures where the rear side can receive significant reflected or diffused light [13]. They also perform well under cloudy conditions or in areas with considerable diffused sunlight, as both sides of the panel can contribute to energy generation.

Standalone photovoltaic (PV) systems, also known as off-grid solar systems, operate independently of the utility grid. While they provide a clean and renewable energy source, they also have some drawbacks and challenges [14]. These systems are typically designed to meet a specific energy demand. If energy consumption exceeds the system's capacity, upgrades will be necessary. Users must manage their energy use carefully to avoid

overloading the system, particularly during peak consumption times.

To ensure reliable performance throughout the year, standalone systems are often oversized, which can lead to higher initial costs and potential energy waste during peak sunlight periods [15]. Additionally, these systems are generally not suitable for powering high-energy equipment or industrial applications without significant scaling. To maintain consistent power availability, standalone systems require batteries to store energy generated during sunny periods and provide power during times of lower generation. The circuit structure of the PV panels standalone system with battery storage backup feeding the local load and EV charging station is presented in figure 2.

As observed in figure 2, Bifacial PV array is connected to single switch boost converter which is operated using P&O MPPT technique [16]. The duty ratio of the switch is changed as per the voltage and current of the Bifacial PV array which is dependent on solar irradiation. The change in duty ratio is given as:

$$\Delta D = \begin{cases} \text{If } P_{pv}(n) > P_{pv}(n-1) \text{ and } V_{pv}(n) > V_{pv}(n-1) \\ \text{If } P_{pv}(n) < P_{pv}(n-1) \text{ and } V_{pv}(n) < V_{pv}(n-1) \end{cases} \quad (1)$$

$$\Delta D = \begin{cases} \text{If } P_{pv}(n) < P_{pv}(n-1) \text{ and } V_{pv}(n) > V_{pv}(n-1) \\ \text{If } P_{pv}(n) > P_{pv}(n-1) \text{ and } V_{pv}(n) < V_{pv}(n-1) \end{cases} \quad (2)$$

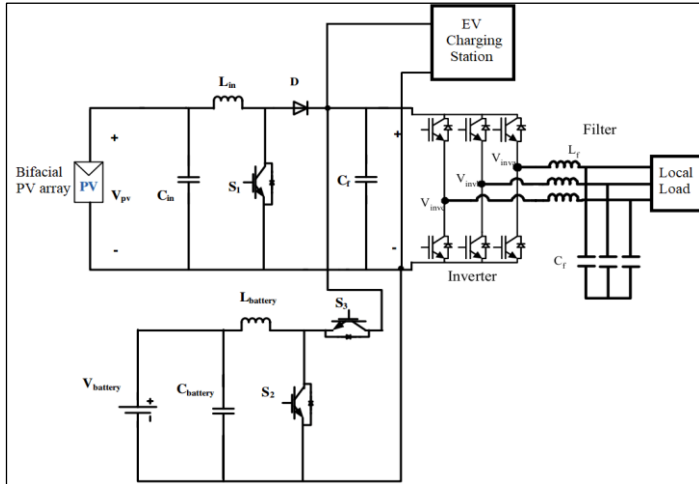


Figure 2: Circuit structure of standalone PV source with battery backup storage.

Source: Authors, (2025).

The previous duty ratio  $D(n-1)$  is updated by an integrated  $\Delta D$  value either adding or subtracting the previous duty ratio. Here,  $P_{pv}(n)$  and  $P_{pv}(n-1)$  are the present and previous values of Bifacial PV array power.  $V_{pv}(n)$  and  $V_{pv}(n-1)$  are the present and previous values of Bifacial PV array voltage.

On the other hand, the battery storage is connected to bidirectional converter with two switches connected in the circuit [17]. These two switches are operated alternatively using voltage regulator controller. This voltage regulator controller maintains the DC common link voltage at specified reference value for stability system voltages [18]. The voltage regulator controller for the battery storage circuit is presented in figure 3.

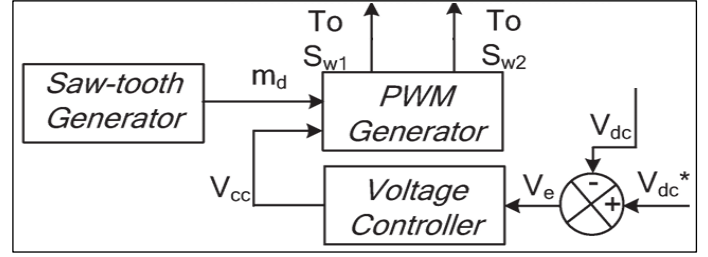


Figure 3: Voltage regulator controller.

Source: Authors, (2025).

As per figure 3, the reference DC common link voltage ( $V_{dc}^*$ ) are compared to measured DC link voltage generating error voltage ( $V_e$ ). The  $V_e$  signal is given to voltage regulator controller to generate duty ratio ( $V_{cc}$ ) of the switch  $S_{w1}$ . The  $V_{cc}$  is compared to sawtooth generator for generating pulses to the  $S_{w1}$  and the NOT gate signal is set to  $S_{w2}$ . Here, the voltage regulator controller is PI controller with tuned  $K_{pdc}$  and  $K_{idc}$  (Proportional and Integral) gains set as per the DC common link voltage stability [19]. The duty ration  $V_{cc}$  is given as:

$$V_{cc} = (V_{dc}^* - V_{dc}) \left( K_{pdc} + \frac{K_{idc}}{s} \right) \quad (3)$$

The stabilized DC common link voltage is fed to three phase inverter converting DC to three phase AC feeding the local load. The three-phase inverter is controlled by Sin PWM technique which generates pulses to the switches by comparing three phase Sinusoidal signals with high frequency triangular waveform.

### III. MAFB CONTROL DESIGN

In the proposed system the EV charging station connected at the DC common link has multiple bidirectional converters [20]. The conventional bidirectional converter with two switches has very high-power loss, high ripple and lesser efficiency. This converter is replaced with dual active full bridge converters for better efficiency, less ripple and reduced power loss.

As the dual active full bridge converter has single input and single output terminals, several converters need to be connected individually to each EV battery for exchanging power. This increases the number of components in the charging station which leads to initial installation cost. Therefore, multiple dual active full bridge circuits are replaced with a single Multi active full bridge (MAFB) topology with single input and multi output terminals [21].

A MAFB topology is a type of DC-DC power converter that is widely used in high-power applications, including renewable energy systems, electric vehicle chargers, uninterruptible power supplies (UPS), and industrial power systems. This design is based on the conventional full-bridge topology but incorporates advanced techniques to enhance efficiency, reduce losses, and facilitate bidirectional power transfer. This makes it particularly useful in systems like battery storage, where energy needs to flow in both directions for charging and discharging.

The basic topology consists of four active switches, typically MOSFETs or IGBTs, arranged in a full-bridge structure. These switches alternate between on and off states to generate a high-frequency AC signal [22]. A High-Frequency Transformer (HFT) is employed to provide galvanic isolation between the input and output, while also allowing for voltage scaling (either stepping up or stepping down) based on the turns ratio.



The converter is capable of operating in both rectification and inversion modes, making it ideal for systems like energy storage, where power must flow in either direction. Techniques such as Zero Voltage Switching (ZVS) and Zero Current Switching (ZCS) are utilized to minimize switching losses and enhance overall efficiency, particularly at high frequencies.

The converter can incorporate advanced control strategies like PS-PM to achieve precise regulation of output voltage and current [23]. The MAFB is a versatile and efficient solution that meets the growing demand for high-performance and reliable power converters in modern applications. Its ability to manage bidirectional power flow and maintain high efficiency makes it a foundational technology in the field of power electronics. The circuit of the MAFB topology connected at the DC common link of the standalone system is shown in figure 4.

The input DC voltage is applied to a full-bridge circuit, which is made up of four active switches (either MOSFETs or IGBTs) arranged in an "H" configuration. By alternately turning these switches on and off in a specific pattern, a high-frequency square-wave AC signal is generated at the output of the bridge. This switching frequency is typically high, ranging from tens to hundreds of kilohertz, which helps reduce the size of the transformer and other passive components [24]. The high-frequency AC produced by the full-bridge circuit is then fed into a HFT.

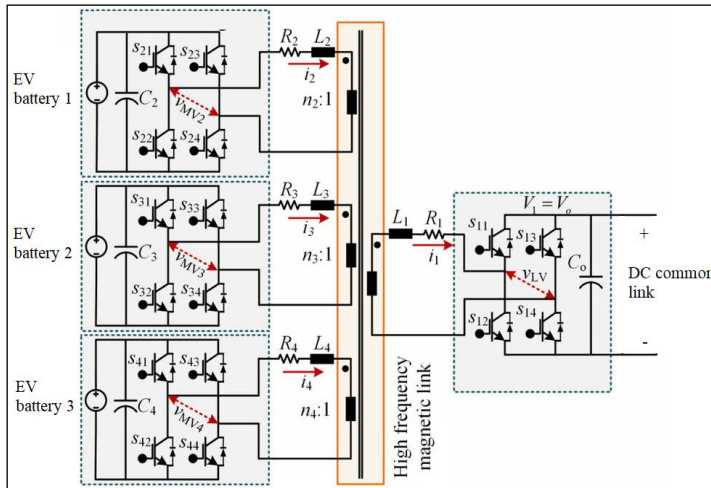


Figure 4: MAFB circuit topology for EV charging station.

Source: Authors, (2025).

Depending on the application and the turns ratio of the transformer, it can step the voltage up or down. The transformer also provides electrical isolation between the input and output, enhancing safety and noise suppression. On the secondary side of the transformer, the high-frequency AC is rectified back into DC using diodes or synchronous rectifiers. The resulting rectified output is then processed through a filtering stage, usually composed of capacitors and inductors, to smooth out any ripples and produce a stable DC output voltage.

The MAFB can be operated in both directions which can charge and discharge the EV batteries as per the requirement. During charging of the EV batteries, the mode is preferred as G2V and during discharging of EV batteries the mode is preferred as V2G. In G2V mode the power from the PV source or the battery storage module charges the EV batteries. And during V2G mode the EV batteries provide power to the local load or charge the storage battery [25].

These modes are controlled by PS-PM technique which creates phase delay in the pulses which receives power. The switching pulses of full bridge which delivers power always lead to the switching pulses of full bridge which receives power. The phase delay in the switching pulses of the receiving full bridge varies the voltage developed at the output terminals.

For higher phase delay, high voltage magnitude is generated at the output of the receiving full bridge. Therefore, by varying the phase delay of the switches, regulates the EV battery charging current [26]. The phase delay signal is generated by a phase delay regulator controller which defines the phase delay angle of the switches. The control structure of the phase delay current regulator is presented in figure 5.

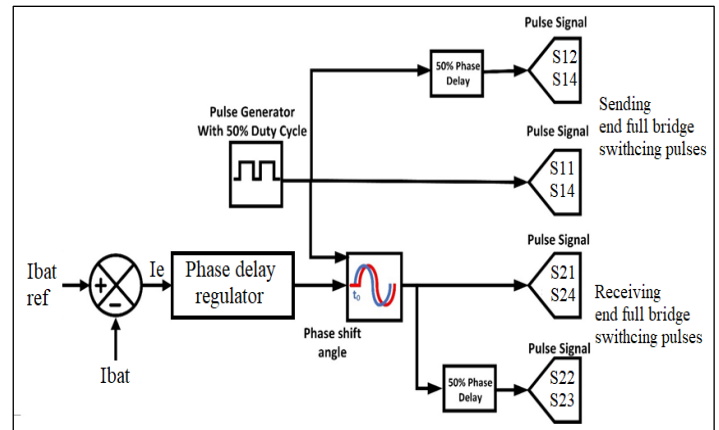


Figure 5: Phase delay regulator controller of MAFB circuit.

Source: Authors, (2025).

The controller presented in figure 5 comprises of a fixed duty ratio (50%) pulse generator producing pulses at high frequency of 20kHz. This pulse is directly fed to the sending end full bridge switches S1 S4 and with 50% phase delay to switches S2 S3. The phase shift angle for the receiving end full bridge switches is generated by the Phase delay regulator with maximum value of 90degrees.

The regulator receives error current signal ( $I_e$ ) by comparison of reference battery current ( $I_{bat\ ref}$ ) and measured battery current ( $I_{bat}$ ) of the EV battery pack. The Phase delay regulator is a PI controller with optimal  $K_{pph}$  and  $K_{iph}$  values which are tuned as per the current response of the EV battery pack. The phase delay signal 'Ph' is given as:

$$Ph = (I_{bat\ ref} - I_{bat}) \left( K_{pph} + \frac{K_{iph}}{s} \right) \quad (4)$$

PI controllers are not ideal for systems with rapidly changing dynamics or significant disturbances. They can experience overshoot or oscillations during transient conditions, especially if the controller gains are not tuned properly. Unlike more advanced controllers, such as PID or model-based controllers, PI controllers cannot predict future errors or anticipate changes in system behaviour.

This lack of predictive capability often results in slower response times in dynamic systems. The integral term in the PI controller accumulates error over time, which may lead to delayed corrective actions in the face of sudden disturbances. Therefore, proper tuning of the proportional (P) and integral (I) gains is essential for optimal performance. If these gains are not tuned correctly, the controller may exhibit problems such as instability, sluggishness, or excessive overshoot. Therefore, the conventional PI controller is replaced with advanced controller ANFIS

regulator for generating the phase delay angle of the receiving end full bridge switches [27].

The ANFIS is a hybrid model that merges the learning capabilities of neural networks with the reasoning abilities of fuzzy logic. It is commonly used in applications that require intelligent, adaptive, and efficient control or prediction systems. ANFIS automatically adjusts membership functions and fuzzy rules based on input-output data, which enhances its performance in dynamic or complex environments.

This system is particularly effective for modelling and controlling highly nonlinear systems, where traditional methods often struggle. During the training process, ANFIS optimizes its parameters, such as membership functions and rule weights, making it self-tuning and reducing the need for manual adjustments [27].

By integrating the interpretability of fuzzy logic with the learning capabilities of neural networks, ANFIS enhances decision-making in uncertain or ambiguous situations. The proposed ANFIS regulator comprises single input and single output variables. The input variable 'E' and output variable 'Ph' are added with seven membership functions (MFs) in each variable.

The input MFs are added with 'triangular' shape and the output MFs are constants. The input variable is set with a range of -100 to 100, considered as per the maximum and minimum error current. The phase delay Ph is set with a range from -0.0001 to 0.0001, set as the per the response of the controller. The MFs of the two variables 'E' and 'Ph' are presented in figure 6.

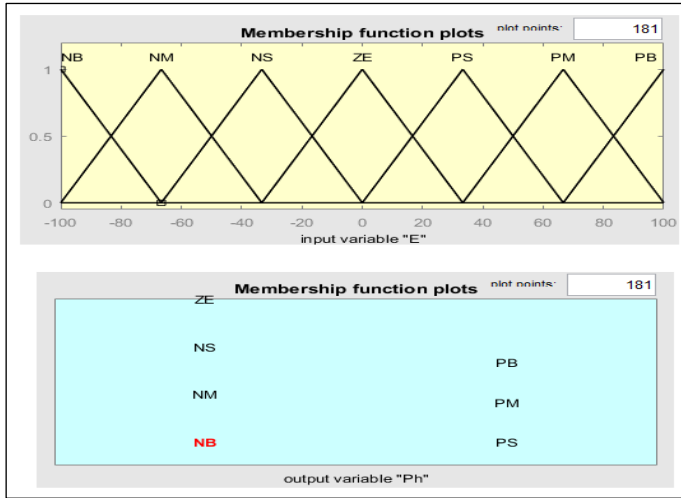


Figure 6: ANFIS variable MFs.

Source: Authors, (2025).

Each MF is defined with specific name given as per the position of the MF in the given range. On the negative side (below zero) MFs are named as NB (Negative Big), NM (Negative Medium) and NS (Negative Small). And on the positive side (above zero) are named as PS (Positive Small), Positive Medium (PM) and PB (Positive Big). However, the MF at the centre is named as ZE (Zero). Each MF covers a specific range which defines the input signals MF.

The output value is generated by rule base of the ANFIS controller given as per the requirement. The rule base used in the ANFIS modelling is 'Linear rule base' with only seven rules set as per the input and output MFs. The ANFIS is then trained using 'back propagation' optimization technique in the tool with the data provided by the input and output of the PI regulator [28]. The new trained data of the ANFIS tool can be observed in figure 7.

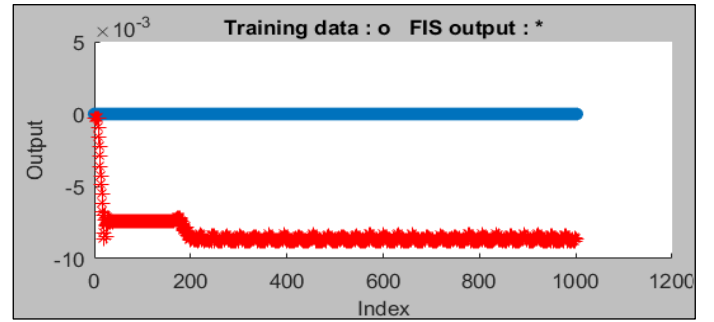


Figure 7: ANFIS trained data.

Source: Authors, (2025).

This trained ANFIS data is exported to the current regulator of the MAFB phase delay controller. The ANFIS phase delay regulator generates a stable, less oscillations phase delay signal controlling the full bridge converter with more stability. This reduces the ripple and response time of the EV battery current for the same reference signal of the controller. A comparative analysis between both the phase delay regulators (PI and ANFIS) is included in following section.

#### IV. SIMULATION ANALYSIS

The simulation modeling of the proposed standalone Bifacial PV array with battery backup storage module connected to local load and EV charging station is done using Simulink blocks of MATLAB software. The main blocks are taken from the Simulink library of 'Electrical' sub category and control blocks are taken from 'Continuous' and 'Signal routing' sub categories. The simulation blocks are updated as per the parameters given in table 1.

Table 1: Simulation parameters.

Name of the module	Parameters
Bifacial solar module	$V_{mp} = 76.7V$ , $I_{mp} = 5.8A$ , $V_{oc} = 90.5V$ , $I_{sc} = 6.21A$ , $N_s = 4$ , $N_p = 40$ , $P_{pv\ front} = 71.2kW$ , $P_{pv\ back} = 71.2kW * 0.2 = 14.2kW$ , Boost converter: $C_{in} = 100\mu F$ , $L_b = 1mH$ , $C_{dc} = 12mF$ , MPPT $\Delta D = 0.05$ , MPPT gain = 5, $D_{int} = 0.5$ , $f_s = 5kHz$ .
Battery storage module	$V_{nom} = 500V$ , Capacity = 200Ah, $SOC_{int} = 90\%$ Bidirectional converter: $L_{bb} = 161.95\mu H$ , $C_{out} = 220\mu F$ , $V_{dcref} = 725V$ , $K_p = 0.02$ , $K_i = 0.0023$ , $f_c = 5kHz$ .
Local load	Three phase Sinusoidal inverter-controlled load = 10kW
Conventional EV charging station	$C_{in} = 220\mu F$ , $L_{bdc} = 161.95\mu H$ , $R_{igbt} = 1m\Omega$ , $C_{out} = 0.52443mF$ , $K_{pi} = 2$ , $K_{ii} = 0.0023$ , $f_{sw} = 5kHz$ .
MAFB EV charging station	$R_{igbt} = 1m\Omega$ , HFTF: $P_n = 100kVA$ , $f_n = 50kHz$ , 1:1, $R_n = 0.1\Omega$ , $L_n = 2\mu H$ , $R_m = 500\Omega$ , $L_m = 1mH$ . $K_{pph} = 0.01e-6$ ; $K_{iph} = 7e-7$
EV batteries	EV <sub>1</sub> - BMW i3 2019: $V_{nom} = 353V$ , Capacity = 120Ah EV <sub>2</sub> - Volkswagen e-golf: $V_{nom} = 323V$ , Capacity = 110Ah EV <sub>3</sub> - Fiat 500e: $V_{nom} = 364V$ , Capacity = 66Ah

Source: Authors, (2025).

With the given simulation parameters the model is updated and the simulation of the model is run with G2V and V2G modes for 1sec simulation time. The graphs of each module are presented in both operating modes of the MAFB showing the versatility of the converter. All the graphs of the voltages, currents and powers are plotted with time as reference.

The figure 8 represents the characteristics of Bifacial PV source with constant solar irradiation of 1000W/m<sup>2</sup>. The voltage of the Bifacial PV array is set at 300V and the combined currents of front and back panels is 280A. The figure 9 represents the characteristics of storage battery pack. Initially the battery storage discharges to stabilize the DC common link voltage which later on charges with the excess PV power generated. The charging of the battery is represented by negative current direction of 40A and raising SOC (State of Charge).

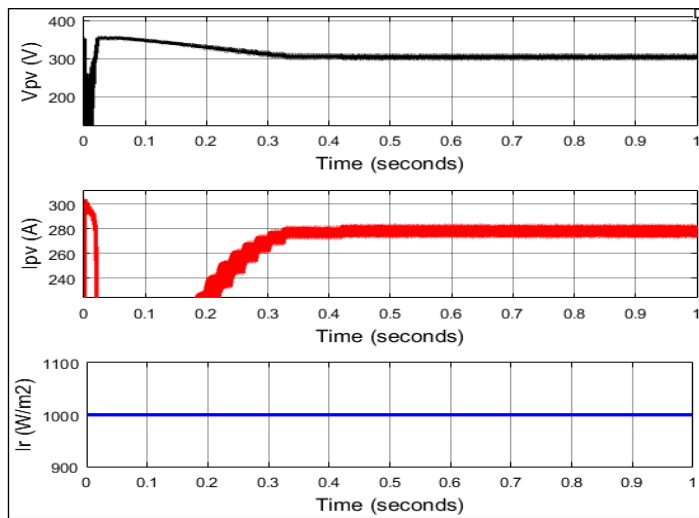


Figure 8: Bifacial PV array characteristics.  
Source: Authors, (2025).

The figure 8 represents the characteristics of Bifacial PV source with constant solar irradiation of 1000W/m<sup>2</sup>. The voltage of the Bifacial PV array is set at 300V and the combined currents of front and back panels is 280A. The figure 9 represents the characteristics of storage battery pack. Initially the battery storage discharges to stabilize the DC common link voltage which later on charges with the excess PV power generated. The charging of the battery is represented by negative current direction of 40A and raising SOC (State of Charge).

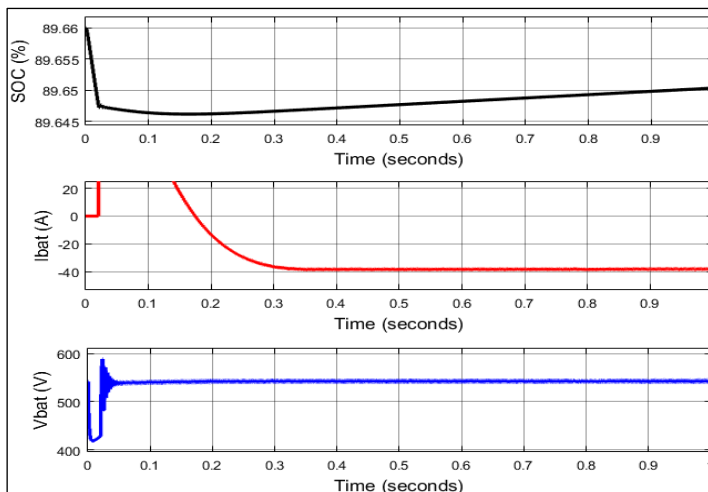


Figure9: Storage battery module characteristics during G2V mode  
Source: Authors, (2025).

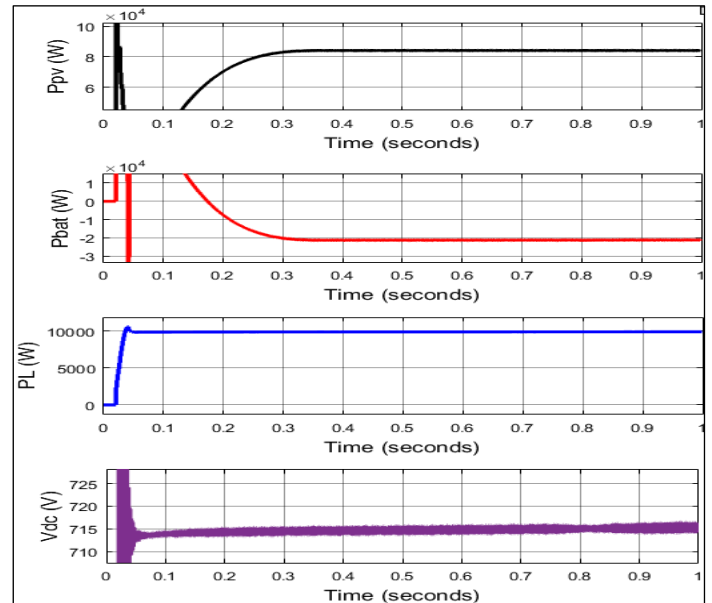


Figure 10: Active powers of Bifacial PV array, battery, load and DC common voltage during G2V

The active powers of all the modules are presented in figure 10 when the MAFB is operated in G2V mode. In this mode the power from the DC common link is transferred to the EV batteries with phase delay controller limiting the charging currents of the batteries. The total power generated by the Bifacial PV array is noted to be 82kW from which 10kW is consumed by local load, 44kW is consumed by EV charging station and the battery storage charges with 21kW.

Here, the missing 7kW is considered to be conversion loss or conduction loss of the components used in the system. The figure 11 represents the charging active powers of each EV battery connected on the secondary side of the MAFB. As per the limiting reference current set at 40A in the current controller the EV1 and EV3 battery takes 15kW, EV2 takes 14kW with a complete consumption of 44kW by the charging station.

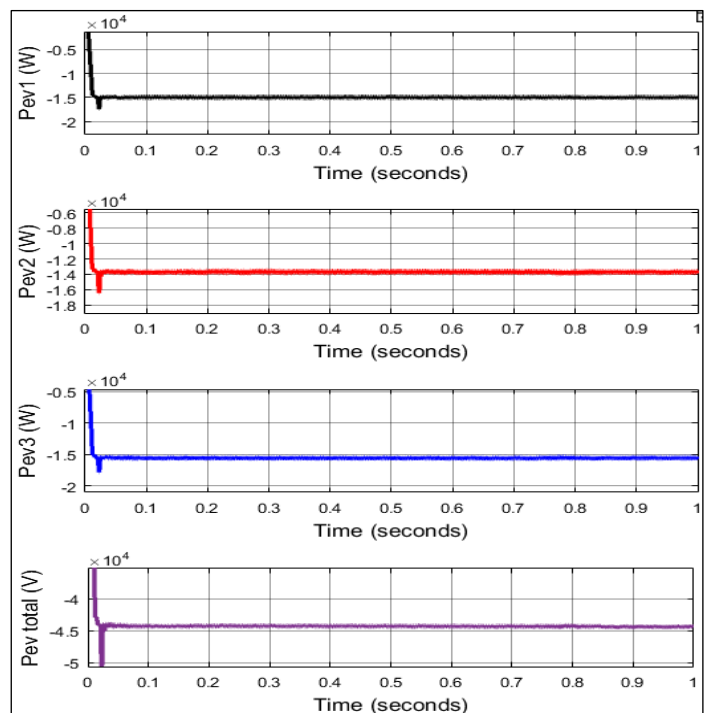


Figure 11: Active powers of EVs during G2V mode  
Source: Authors, (2025).

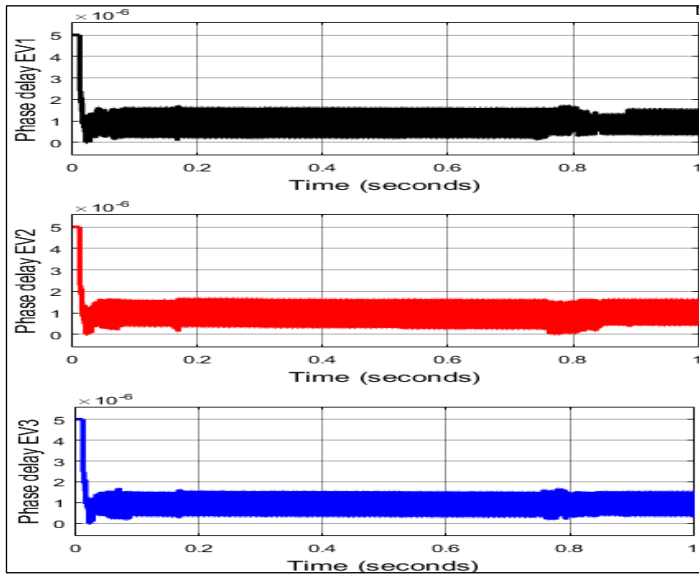


Figure 12: Phase delay time of EV full bridges switches during G2V mode.  
Source: Authors, (2025).

The figure 12 shows the phase delays of each full bridge switches which is generated by the phase delay regulator controller. This time delay is caused in the pulses of the secondary bridges to ensure power consumption from the primary side winding of the HFT. In the next operating mode, the system is now operated in V2G mode where all the EVs are discharged injecting power to the battery storage module connected at the DC common link.

The figure 13 has the graphs of all the modules when operating in V2G mode. The Bifacial PV power and local load power are intact with 82kW and 10kW respectively. The battery power is increased to 140kW negative direction representing charging from PV panels and EV batteries. Adding the both the PV source power of 72kW after local load consumption and total EV charging station power of 80kW charges the battery storage with 140kW. Here, the conversion loss is 12kW in V2G mode.

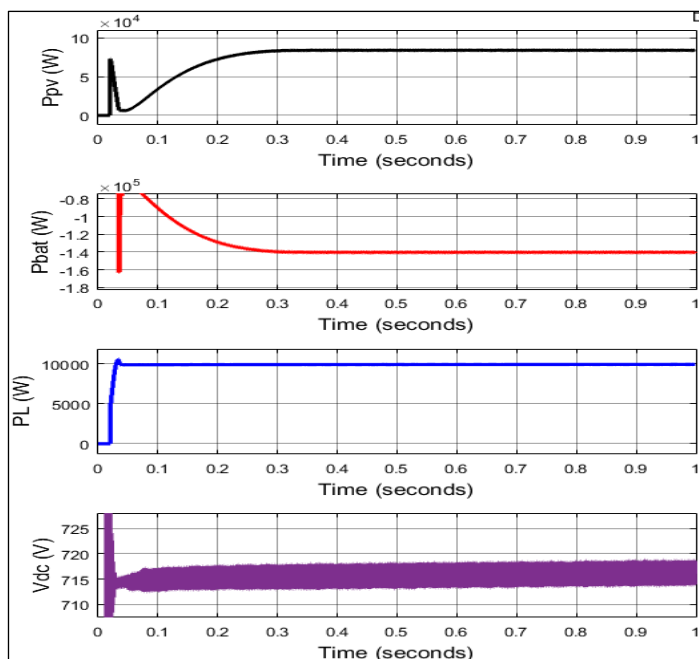


Figure 13: Active powers of Bifacial PV array, battery, load and DC common voltage during V2G.

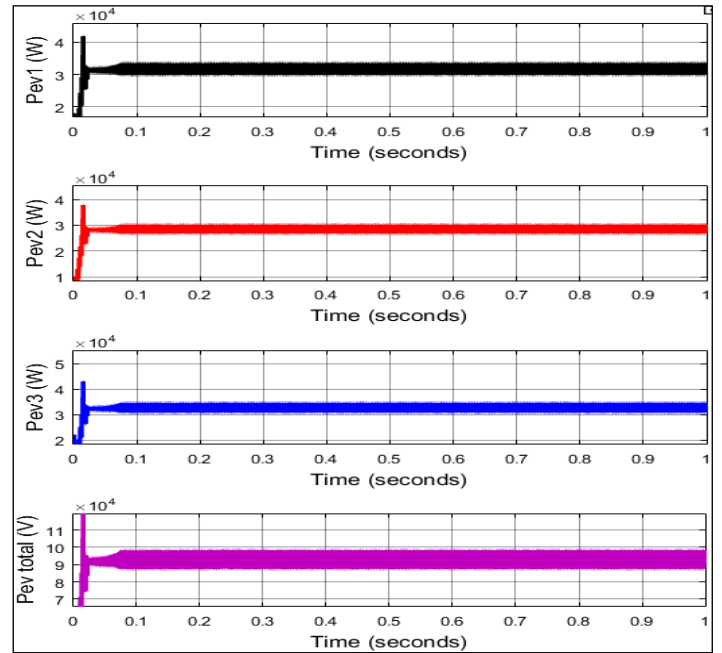


Figure 14: Active powers of EVs during V2G mode.  
Source: Authors, (2025).

As per figure 14 each EV battery is discharged with powers around 30kW with a total discharge power of 90kW injected to the DC common link in V2G mode. The phase delay time generated by the phase delay regulator controller in V2G mode is presented in figure 15

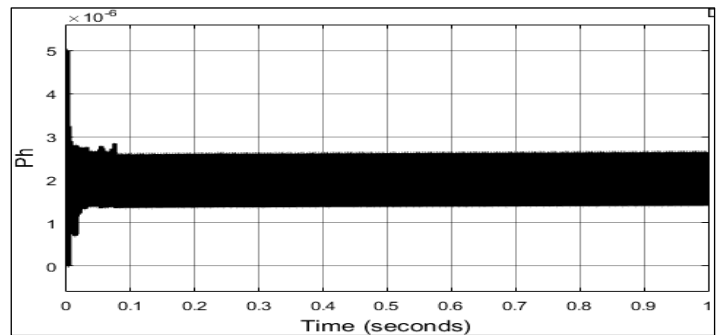


Figure 15: Phase delay time of DC common link connected full bridge during V2G mode.  
Source: Authors, (2025).

The phase delay regulators are now updated with ANFIS replacing the PI controller and the simulation is run for the same ratings of the system and modes. The battery currents comparison with both the controllers can be observed in figure 16 and 17 in G2V and V2G modes respectively.

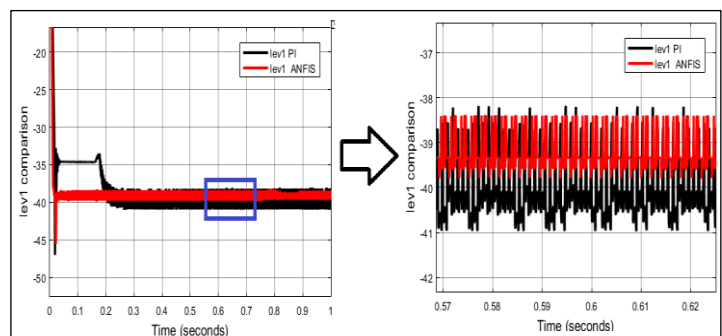


Figure 16: EV battery current comparison during G2V mode  
Source: Authors, (2025).



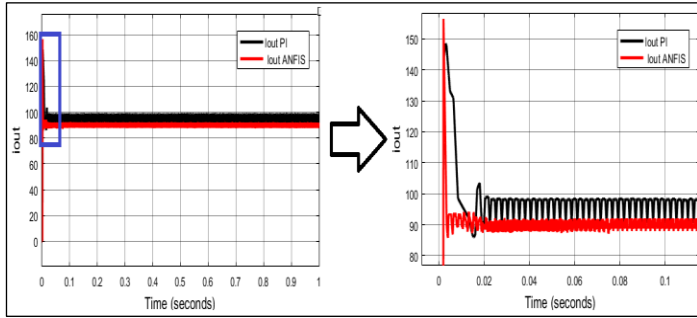


Figure 17: DC common link side full bridge output current comparison during V2G mode.

Source: Authors, (2025).

As observed from the battery current and primary full bridge currents in figure 16 and 17, the ripple and settling time are drastically reduced when the phase delay regulator is operated by ANFIS controller. This creates stability in the battery cells and the voltages of the system making it more robust to the changes occur in the circuits. The table 2 and 3 are the parametric comparison of the battery current characteristics in both operating modes G2V and V2G.

Table 2: Current characteristics comparison in G2V mode.

Name of the parameter	PI	ANFIS
Peak overshoot	47A	45A
Actual value	41A	39.5A
Settling time	0.2sec	0.03sec
Ripple	7.6%	3.8%

Source: Authors, (2025).

Table 3: Current characteristics comparison in V2G mode.

Name of the parameter	PI	ANFIS
Peak overshoot	150A	155A
Actual value	95A	90A
Settling time	0.02sec	0.003sec
Ripple	10.5%	3.2%

Source: Authors, (2025).

## V. CONCLUSIONS

The implementation of standalone Bifacial PV source with battery storage backup connected to local AC load and EV charging station is successfully implemented. The conventional EV charging station with traditional bidirectional converter is replaced with MAFB topology with single input and multi output ports. The primary side full bridge of the MAFB is connected to DC common link where PV source, battery storage and local load are parallelly connected.

The MAFB topology has the capability to operate in both directions charging and discharging the EV batteries as per the requirement. The phase delay regulator controller of the MAFB is designed with PI regulator initially for limiting the charge and discharged currents of the EV batteries. Due to high damping of the controller more oscillations are generated in the phase delay time signal leading to higher ripple and settling time in the battery currents.

The PI controller is later replaced by ANFIS regulator for controlling the phase delay time value improving the EV battery current and full bridge current characteristics. As per the table 2 and 3 operating the MAFB with PI and ANFIS regulators in both G2V and V2G modes it is observed that there is a significant improvement in the current characteristics when operating with ANFIS controller. There is a drastic drop in ripple

and settling time of the EV batteries and output current of the primary bridge when the MAFB is operated with ANFIS regulator. The current regulator can further be updated with adaptive controllers to reduce the peak overshoot and ripple content to lower values to ensure more stability of the EV battery units.

## VI. AUTHOR'S CONTRIBUTION

**Conceptualization:** Author One, Author Two and Author Three.

**Methodology:** Author One and Author Two.

**Investigation:** Author One and Author Two, and Author Three.

**Discussion of results:** Author One, Author Two and Author Three.

**Writing – Original Draft:** Author One.

**Writing – Review and Editing:** Author One and Author Two.

**Resources:** Author Two.

**Supervision:** Author Two and Author Three.

**Approval of the final text:** Author One, Author Two and Author Three.

## VII. REFERENCES

- [1] Mikalai Filonchyk, Michael P. Peterson, Lifeng Zhang, Volha Hurynovich, Yi He, "Greenhouse gases emissions and global climate change: Examining the influence of CO<sub>2</sub>, CH<sub>4</sub>, and N<sub>2</sub>O," *Science of The Total Environment*, Volume 935, 2024, 173359, ISSN 0048-9697, <https://doi.org/10.1016/j.scitotenv.2024.173359>.
- [2] Höök, Mikael & Tang, Xu. (2013). Depletion of fossil fuels and anthropogenic climate change - A review. *Energy Policy*. 53. 797-809. [10.1016/j.enpol.2012.10.046](https://doi.org/10.1016/j.enpol.2012.10.046).
- [3] Tonmoy Choudhury, Umar Nawaz Kayani, Azeem Gul, Syed Arslan Haider, Sareer Ahmad, "Carbon emissions, environmental distortions, and impact on growth," *Energy Economics*, Volume 126, 2023, 107040, ISSN 0140-9883, <https://doi.org/10.1016/j.eneco.2023.107040>.
- [4] Osman, A.I., Chen, L., Yang, M. et al. Cost, environmental impact, and resilience of renewable energy under a changing climate: a review. *Environ Chem Lett* **21**, 741–764 (2023). <https://doi.org/10.1007/s10311-022-01532-8>
- [5] Alanazi, F. Electric Vehicles: Benefits, Challenges, and Potential Solutions for Widespread Adaptation. *Appl. Sci.* **2023**, *13*, 6016. <https://doi.org/10.3390/app13106016>
- [6] U. N. A. Siddiqui and V. A. Kulkarni, "Grid Connected Electric Vehicle Charging Station with Multi Renewable Source," 2022 IEEE 7th International conference for Convergence in Technology (I2CT), Mumbai, India, 2022, pp. 1-5, doi: 10.1109/I2CT54291.2022.9824620.
- [7] P. C. D. Goud, C. S. Nalamati and R. Gupta, "Grid Connected Renewable Energy Based EV Charger with Bidirectional AC/DC Converter," 2018 5th IEEE Uttar Pradesh Section International Conference on Electrical, Electronics and Computer Engineering (UPCON), Gorakhpur, India, 2018, pp. 1-6, doi: 10.1109/UPCON.2018.8596882.
- [8] Sami Jouttijärvi, Gabriele Lobaccaro, Alekski Kamppinen, Kati Miettinen, "Benefits of bifacial solar cells combined with low voltage power grids at high latitudes," *Renewable and Sustainable Energy Reviews*, Volume 161, 2022, 112354, ISSN 1364-0321, <https://doi.org/10.1016/j.rser.2022.112354>.
- [9] Koohi, P.; Watson, A.J.; Clare, J.C.; Soeiro, T.B.; Wheeler, P.W. A Survey on Multi-Active Bridge DC-DC Converters: Power Flow Decoupling Techniques, Applications, and Challenges. *Energies* **2023**, *16*, 5927. <https://doi.org/10.3390/en16165927>
- [10] J. Mukhopadhyay, S. Choudhury and S. Sengupta, "ANFIS Based Speed and Current Controller for Switched Reluctance Motor," 2021 IEEE 4th International Conference on Computing, Power and Communication Technologies (GUCON), Kuala Lumpur, Malaysia, 2021, pp. 1-6, doi: 10.1109/GUCON50781.2021.9573617.
- [11] Eduardo Lorenzo, "On the historical origins of bifacial PV modelling," *Solar Energy*, Volume 218, 2021, Pages 587-595, ISSN 0038-092X, <https://doi.org/10.1016/j.solener.2021.03.006>.

- [12] Chraiga, Hassen Ayed. (2024). MATLAB based modeling to study the performance of bifacial solar PV system under various operating conditions .. 10.13140/RG.2.2.31357.58086.
- [13] Badran, G., Dhimish, M. Comprehensive study on the efficiency of vertical bifacial photovoltaic systems: a UK case study. *Sci Rep* **14**, 18380 (2024). <https://doi.org/10.1038/s41598-024-68018-1>
- [14] Debnath, Dipankar & Chatterjee, Kishore. (2015). Two-Stage Solar Photovoltaic-Based Stand-Alone Scheme Having Battery as Energy Storage Element for Rural Deployment. *Industrial Electronics, IEEE Transactions on*. 62. 4148-4157. 10.1109/TIE.2014.2379584.
- [15] Rekha Chandola, Ashish K. Panchal, "A standalone photovoltaic energy storage application with positive pulse current battery charging," *Journal of Energy Storage*, Volume 85, 2024, 111184, ISSN 2352-152X, <https://doi.org/10.1016/j.est.2024.111184>.
- [16] Javed, K.; Ashfaq, H.; Singh, R.; Hussain, S.M.S.; Ustun, T.S. Design and Performance Analysis of a Stand-alone PV System with Hybrid Energy Storage for Rural India. *Electronics* **2019**, *8*, 952. <https://doi.org/10.3390/electronics8090952>
- [17] Jose, Kiran & Mohammed Sulthan, Sheik & Mansoor, O.. (2022). Performance Study of Solar PV System with Bifacial PV Modules. 10.1007/978-981-19-4971-5\_48.
- [18] Ganesh, D. & Moorthi, Sridivya & Sudheer, H.. (2012). A Voltage Controller in Photo-Voltaic System with Battery Storage for Stand-Alone Applications. *International Journal of Power Electronics and Drive Systems*. 2. 9-18. 10.11591/ijpeds.v2i1.127.
- [19] Jamroen, Chaowanant & Pannawan, Akekachai & Sirisukprasert, Siriroj. (2018). Battery Energy Storage System Control for Voltage Regulation in Microgrid with High Penetration of PV Generation. 1-6. 10.1109/UPEC.2018.8541888.
- [20] A. K. Bhattacharjee, N. Kutkut and I. Batarseh, "Review of multiport converters for solar and energy storage integration", *IEEE Trans. Power Electron.*, vol. 34, no. 2, pp. 1431-1445, Feb. 2019.
- [21] V. Uttam and V. M. Iyer, "A Unified Modeling Approach for a Multi-Active Bridge Converter," 2022 International Power Electronics Conference (IPEC-Himeji 2022- ECCE Asia), Himeji, Japan, 2022, pp. 1614-1620, doi: 10.23919/IPEC-Himeji2022-ECCE53331.2022.9807074.
- [22] S. Bandyopadhyay, P. Purgat, Z. Qin and P. Bauer, "A Multiactive Bridge Converter With Inherently Decoupled Power Flows," in *IEEE Transactions on Power Electronics*, vol. 36, no. 2, pp. 2231-2245, Feb. 2021, doi: 10.1109/TPEL.2020.3006266.
- [23] S. Bandyopadhyay, Z. Qin and P. Bauer, "Decoupling Control of Multiactive Bridge Converters Using Linear Active Disturbance Rejection," in *IEEE Transactions on Industrial Electronics*, vol. 68, no. 11, pp. 10688-10698, Nov. 2021, doi: 10.1109/TIE.2020.3031531.
- [24] H. Chen, Z. Hu, H. Luo, J. Qin, R. Rajagopal and H. Zhang, "Design and planning of a multiple-charger multiple-port charging system for PEV charging station", *IEEE Trans. Smart Grid*, vol. 10, no. 1, pp. 173-183, Jan. 2019.
- [25] J. Schäfer, D. Bortis and J. W. Kolar, "Multi-port multi-cell DC/DC converter topology for electric vehicle's power distribution networks", *Proc. IEEE 18th Workshop Control Model. Power Electron.*, pp. 1-9, 2017.
- [26] Y. Chen, P. Wang, H. Li and M. Chen, "Power flow control in multi-active-bridge converters: Theories and applications", *Proc. IEEE Appl. Power Electron. Conf. Expo.*, pp. 1500-1507, 2019.
- [27] P. Mitra, S. Maulik, S. P. Chowdhury and S. Chowdhury, "ANFIS Based Automatic Voltage Regulator with Hybrid Learning Algorithm," 2007 42nd International Universities Power Engineering Conference, Brighton, UK, 2007, pp. 397-401, doi: 10.1109/UPEC.2007.4468980.
- [28] M. Jamma, M. Akherraz and M. Barar, "ANFIS Based DC-Link Voltage Control of PWM Rectifier-Inverter System with Enhanced Dynamic Performance," *IECON 2018 - 44th Annual Conference of the IEEE Industrial Electronics Society*, Washington, DC, USA, 2018, pp. 2219-2224, doi: 10.1109/IECON.2018.8591620.

# POTENTIAL ADOPTION OF BLOCKCHAIN IN FOOD COLD SUPPLY CHAIN: A BIBLIOMETRIC STUDY AND FUTURE RESEARCH AGENDA

Thabed Tholib Baladraf<sup>1</sup>, Marimin Marimin<sup>1</sup>

<sup>1,2</sup> IPB University, Bogor, Indonesia

<sup>1</sup> <https://orcid.org/0000-0002-4953-1318> , <sup>2</sup> <https://orcid.org/0000-0002-9415-5008> 

Email: [thabedtholib@apps.ipb.ac.id](mailto:thabedtholib@apps.ipb.ac.id), [marimin@apps.ipb.ac.id](mailto:marimin@apps.ipb.ac.id)

## ARTICLE INFO

### Article History

Received: January 11, 2025

Revised: February 20, 2025

Accepted: March 15, 2025

Published: March 31, 2025

### Keywords:

Blockchain,  
Cold chain,  
Digitalization,  
Supply chain.

## ABSTRACT

The food cold chain represents a crucial aspect of the highly sensitive food industry. Insufficient supervision can give rise to a range of adverse consequences, including contamination, fraud, and food waste. In line with technological advancement, the implementation of cold chains is becoming increasingly integrated with digital solutions, with blockchain technology representing a notable example. However, some bibliometric analyses have not focused on the cold supply chain, limiting their scope to the supply chain in general. Consequently, further studies are required to gain a more comprehensive understanding of this complex and evolving field. The objective of this analysis is to provide a bibliometric examination of the potential implementation of blockchain technology in the context of food cold chains. This will facilitate the identification of the most recent developments, prevailing trends, and research gaps that require further investigation. This research uses the combination of PRISMA and bibliometric analysis method through Biblioshiny and Vosviewer using 201 scientific articles. The results show that this topic has an annual growth of 96.77%, and there are 3 interesting research clusters, namely 1) blockchain technology transformation in improving traceability and reducing food waste, 2) blockchain technology in improving the competitiveness of cold supply chain companies, and 3) blockchain that can improve food safety, leading to increased consumer confidence. Based on the major themes obtained and strategic diagram, there are various future research opportunities, including capability freight transportation, deterioration, food contamination, storage and transportation, carbon emissions, competitiveness, delphi analysis, agricultural products and sales.



Copyright ©2025 by authors and Galileo Institute of Technology and Education of the Amazon (ITEGAM). This work is licensed under the Creative Commons Attribution International License (CC BY 4.0).

## I. INTRODUCTION

Agricultural, livestock, and fishery commodities are products that are used to fulfill daily needs by humans. However, agricultural, livestock, and fishery commodities have characteristics that are sensitive, perishable, and have a relatively short shelf life [1]. Some commodities that are sensitive and perishable include milk, fish, meat, fruits, and vegetables, so they need to be distributed in a cold storage called a cold supply chain [2]. Cold supply chain is a supply chain management for commodities, especially agriculture, livestock, and fisheries, which have perishable properties by maintaining their temperature and humidity from the production process to reach consumers to remain

in optimal conditions [3], [4]. The application of cold supply chains is a very good thing because the quality and selling value of these commodities can be well maintained from upstream to downstream [5]. The cold supply chain can also prevent the delivered agricultural commodities from becoming food waste and food loss.

However, in its implementation, there are still various problems faced in the cold supply chain process that occurs. The crucial problem encountered is the poor handling of the cold supply chain which causes a decrease in the quality of commodities during the process to become food waste. Referring to the United Nations Environment Programme, the cold supply chain is the highest contributor to food loss and food waste in the world with a total of 526 million metric tons of waste or 12% of the total food waste in

the world [6]. Poor handling of the cold supply chain is caused by the incompetence of workers, the occurrence of violations or fraud, and the lack of traceability in the cold supply chain implemented [7]–[9]. This certainly has a negative impact on the course of the supply chain and has the potential to cause chain damage [10]. Therefore, research on cold supply chain traceability is very important to be carried out, one of which is through blockchain technology.

Blockchain is decentralized data that involves a credentialed block chain that cannot be changed, deleted, or removed [11]. Blockchain is a system that is chronologically connected to one another [12]. This makes blockchain a technology that can anticipate the occurrence of fraud or falsification of data. In its implementation, blockchain has a very broad application in various fields including government [13], economy [14], health [15], [16], automotive [17], and supply chain [18]–[20]. Based on the characteristics and advantages of blockchain, it has great potential to be applied to the cold supply chain to increase consumer confidence, preserve consumer rights, and maintain quality [21].

Several studies applying blockchain to cold supply chains are currently being favored by researchers as it provides a positive multiplier effect. Research by Ma et al. applied blockchain technology to the cold supply chain to detect contamination in products distributed to consumers [22]. On the other hand, Ali et al. applied blockchain to trace the traceability of the halalness of an agricultural product [23]. Liu et al. also conducted similar research by utilizing blockchain to trace the freshness of an agricultural product from upstream to downstream [24].

The bibliometric study in this research will provide a new perspective on the application of blockchain in the cold supply chain and is different from previous studies that discuss digital supply chains in general.

This study will discuss in depth and specifically the implementation of blockchain in the cold supply chain starting from the latest developments, trends that are in vogue, to potential research opportunities so that the hope is that it can provide new knowledge for agro-industry players to academics. In more detail, this research aims to answer several research questions that are presented as follows:

Q1: What is the current state of research on the application of blockchain to the cold food supply chain?

Q2: What are the most prolific and influential articles, sources, and countries in research on blockchain applications in the cold food supply chain?

Q3: What are the favored research trends on the application of blockchain to the cold food supply chain?

Q4: What are the gaps and potential future research opportunities in the application of blockchain to the cold food supply chain?

## **II. THEORETICAL REFERENCE**

### **II.1 BLOCKCHAIN**

Blockchain can be described as a technology in the form of interconnected blocks of blocks containing transactions with a decentralized system and cannot be modified in the system [25]. In its implementation, blockchain has four main attributes, namely decentralized structure, cryptographic system, consensus mechanism, and smart contract [26].

A decentralized system means that all parties involved have equal access and visibility of data, a cryptographic system is a random code that records or tracks a chain of data over time through a block that contains a hash and cannot be modified, a

consensus mechanism is the principle of retrieving some important information from cryptographic data, while a smart contract is an agreement feature in a transaction that can be recorded in data [27].

In its application in the supply chain system, blockchain has great potential to be applied because there are several factors that support it. According to Wang et al., these supporting factors include the creation of a supply chain based on full trust, simplifying the complexity of a more visible supply chain, product security and authenticity, and finally increasing the fight against fraud and fraud [28].

Some of the broad uses of blockchain include digitizing transactions, improving data security, and implementing smart contracts in the process. Blockchain is also often combined with other technologies to optimize its performance such as sensors and the internet of things [29], [30]

### **II.2 FOOD COLD SUPPLY CHAIN**

The cold supply chain of food commodities is the process of transforming raw products into semi-finished or finished materials but at low temperatures [31]. Cold supply chains aim to maintain the quality of food products during the production, storage or shipping process while reducing the food waste created [32], [33]. In addition, the cold supply chain of food for some time also serves to prevent food products from contamination that threatens food safety [4].

In its implementation, cold supply chains in the food sector often use several modes of transportation such as refrigerated trucks, refrigerated trains, or refrigerated ships [34]. Based on the literature review, food cold supply chains have the main disadvantage of difficult monitoring of temperature, humidity, and traceability. Poor monitoring will lead to various frauds or cooling temperature errors that result in a decrease in the quality of food products and create food waste.

The food cold supply chain is the largest contributor to food waste in the world with a proportion of 20%. It is necessary to combine the cold supply chain with technologies such as the internet of things, machine learning, artificial intelligence, deep learning, RFID, and blockchain to facilitate monitoring activities carried out [35], [36].

## **III. MATERIALS AND METHODS**

This research uses the preferred reporting items systematic review and meta analysis (PRISMA) and combines it with bibliometric analysis to find out the research trends that occur in a sector so that it can be known which research is often done and which research gets less attention.

The combination of PRISMA systematic literature review and bibliometric analysis is often used because it successfully helps researchers find research gaps and potential topics [37], [38]. In the analysis conducted, several software tools were used, including Vosviewer and Biblioshiny through R. Vosviewer and Biblioshiny are useful software for summarizing previous research both qualitatively and quantitatively. In addition, the software helps in the data visualization process so that the data collected is easier to understand.

There are several steps that need to be applied in conducting combination PRISMA method and bibliometric analysis, including conducting literature studies, identification and screening data collection (open acces and english articles), screening data selection through eligibility literature, and conducting bibliometric analysis (qualitative synthesis, quantitative synthesis, research gap,



and further research agenda). As for the details regarding the research framework using PRISMA in this study it is presented in Figure 1.

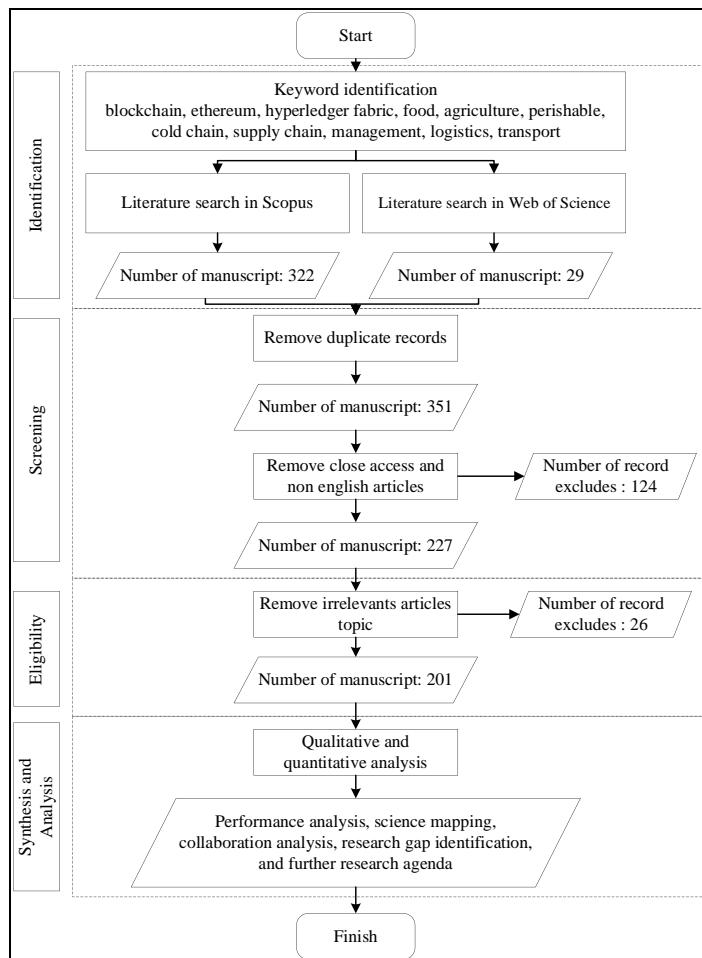


Figure 1: PRISMA research framework.  
Source: Authors (2025).

In the literature study stage, a literature search related to blockchain and cold supply chain was conducted through credible international sources, namely Scopus. In the identification and screening data collection, several rules were used in accordance with the criteria of the topic being analyzed. Some of the criteria set are research publications using English, published in 2019-

2024, publications in the form of experimental articles, publication must open access, and using several keywords combination to obtain accurate analysis using logic gate including “blockchain”, “ethereum”, “hyperledger fabric”, “food”, “agriculture”, “perishable”, “cold chain”, “supply chain”, “management”, “logistics”, “transport”. The results of the literature search through scientific databases that have been carried out managed to get 351 scientific articles related to the application of blockchain technology in the cold supply chain.

The data that has been collected is then screening data to eliminate close access literature and do not meet the criteria so that 201 articles are ready to be analyzed. Bibliometric analysis will provide a comprehensive, coherent, and broad explanation of the application of blockchain and cold supply chains. In more detail, bibliometric analysis will provide information on the distribution of research fields, the distribution of researchers, and the productivity of a research field [39].

This is certainly useful for finding the latest trends and providing knowledge for the industry to develop. In this bibliometric analysis, the results will be presented quantitatively, qualitatively, and visually because there are several things that will be analyzed, including research trend analysis, research distribution, keywords, and research gaps.

## IV. RESULTS AND DISCUSSIONS

### IV.1 PERFORMANCE ANALYSIS

Research performance analysis is the first thing that is done to identify developments and provide an overview of blockchain research in the cold supply chain. The topic of blockchain research on the cold supply chain is an interesting new field and is experiencing very rapid development. In the 2019-2024 period there were 201 research publications produced by 639 researchers and obtained from 113 sources publisher.

Blockchain research on the cold supply chain also has a very good impact and development with an average citation of 22.51 per document and an annual growth rate of 96.77%. This shows that blockchain research on the cold supply chain is something interesting with significant growth year on year, but further identification is needed to find out the current trends and gaps that need to be filled for the future. The summary of research performance in the field of blockchain in the cold supply chain is presented in Table 1 and Figure 2.

Table 1: Descriptive analysis of research performance

Component	Description	Result
Publication	Total number of research publications	201
Publication Period	Active period of research publications	2019-2024
Productivity	Publication/period	33,5
Source	Total number of journal sources in related fields	113
Total Citation	Total number of citations in related fields	4.525
Average Citations per Document	Total citation/publication	22,51
Average Citations per Year	Total citation/period	754
Total Author	Total research authors contributing to the field	639
Single Author Publication	Individual research publications	6
Group Author Publication	Group research publications	195
Collaboration Index	Total author/publication	3,18
Collaboration Coefficiency	(1- (publication /total author)	0,69

Source: Authors (2025)

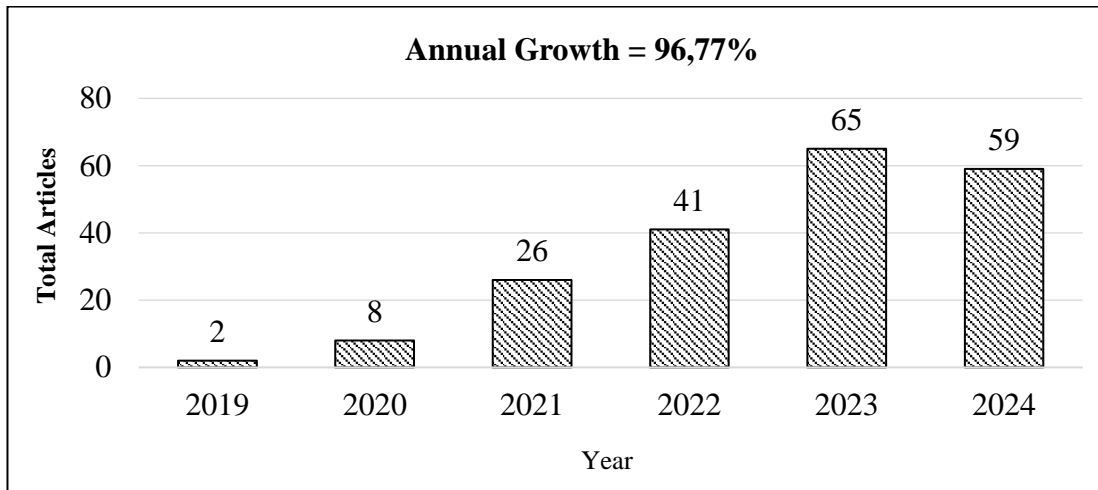


Figure 2: Year on year research trends

Source: Authors (2025)

## IV.2 SCIENCE MAPPING

Research mapping is a section that will explain the distribution of research on the application of blockchain in the cold supply chain in a structured manner by analyzing several things such as the distribution of researchers, the distribution of sources, the distribution of countries, and the distribution of keywords. Some of these things will be analyzed for their impact through the number of publications and citations.

Citation is often used as an indicator in measuring the quality and impact of a study because it shows the usefulness and relationship of one study with another [40]. In more detail, citations are divided into two types in bibliometric analysis, namely global citation and local citation. Global citation is defined as citations obtained from various studies on the internet, while local citation is a citation obtained from 201 studies involved in bibliometric analysis.

Based on the analysis conducted on total global citations, the research on the application of blockchain in the cold supply chain with the title of “A Systematic Literature Review on Machine Learning Applications for Sustainable Agriculture Supply Chain

Performance” by Sharma et al. [41] received the highest total global citations with 427 global citations. Followed by the research of Rejeb et al. [42] titled “Leveraging the Internet of Things and Blockchain Technology in Supply Chain Management” with 280 total global citations. Meanwhile, the research of Tsang et al. [43] titled “Blockchain-Driven IoT for Food Traceability With an Integrated Consensus Mechanism” received the third highest global citations with 216 total global citations.

In total local citations, the study by Tsang et al. [43] titled “Blockchain-Driven IoT for Food Traceability With an Integrated Consensus Mechanism” received the highest total local citations with 15 total local citations. Followed by the research of Aamer et al. [44] with the title “The Internet of Things in The Food Supply Chain: Adoption Challenges,” which received 5 total local citations. Meanwhile, the research of Masudin et al. [45] titled “The

Effect of Traceability System and Managerial Initiative on Indonesian Food Cold Chain Performance: A Covid-19 Pandemic Perspective” is in third place with 4 total local citations. The complete analysis of the top 10 scientific articles on blockchain implementation in the cold supply chain based on global and local citations is presented in Table 2 below.

Table 2: Top 10 best scientific articles based on global and local citations.

Articles	TGC	Articles	TLC
Sharma, 2020, Compt Ops Res	427	Tsang, 2019, IEEE	15
Rejeb, 2019, Future Internet	280	Aamer, 2021, Benchmarking	5
Tsang, 2019, IEEE	216	Masudin, 2021, Global J Flex Sys Man	4
Ali, 2021, Tech Forecast Soc Change	153	Kumar, 2020, Benchmarking	4
Golpîra, 2021, J Ind Infor Integr	120	Kayikci, Int J Log Manag	4
Ali, 2022, J Bus Res	118	Feng, 2020, IEEE	3
Wu, 2023, Int J Prod Res	116	Afreen, 2021, IEEE	2
Liu, 2021, Trans Res Part E Log Trans Rev	88	Kumar, 2022, Ops Manag Res	2
Kumar, 2020, Benchmarking	86	Kashyap, 2023, Benchmarking	1
Mishra, 2022, Int J Logist Manag	83	Gupta, 2024, Benchmarking	1

Note: TGC = Total Global Citation; TLC = Total Local Citation

Source: Authors (2025).

Further analysis to determine the impact of researchers also included co-citation analysis. In simple terms, co-citation can be defined as a shared citation in a third article from other researchers [46]. In the co-citation analysis, the researchers were divided into two clusters based on the similarity of research topics, namely cluster 1 with red color and cluster 2 with green color. In cluster 1, Zhang X is the most dominant researcher, followed by Zhang J, Wang X, Wang Y, Liu Y, and Ruiz-Garcia L. In cluster 1, the topics

discussed are directed towards the application of blockchain that can impact to sustainable aspects especially about the environment, such as the reduction of carbon emissions and the reduction of food waste produced in food cold chain.

Meanwhile, in cluster 2 with the green color, Gunasekaran A is the most influential researcher, followed by Mangla SK, Kumar A, Sarkis J, and Govindan K. In cluster 2, the topics discussed revolve around the adoption of blockchain technology in food cold

supply chain and its impact from others sustainable perspective especially on economic and social aspects such as cost minimization, long-term investment, and social welfare. As for the

visual representation of the co-citation in this study, it is detail presented in Figure 3.

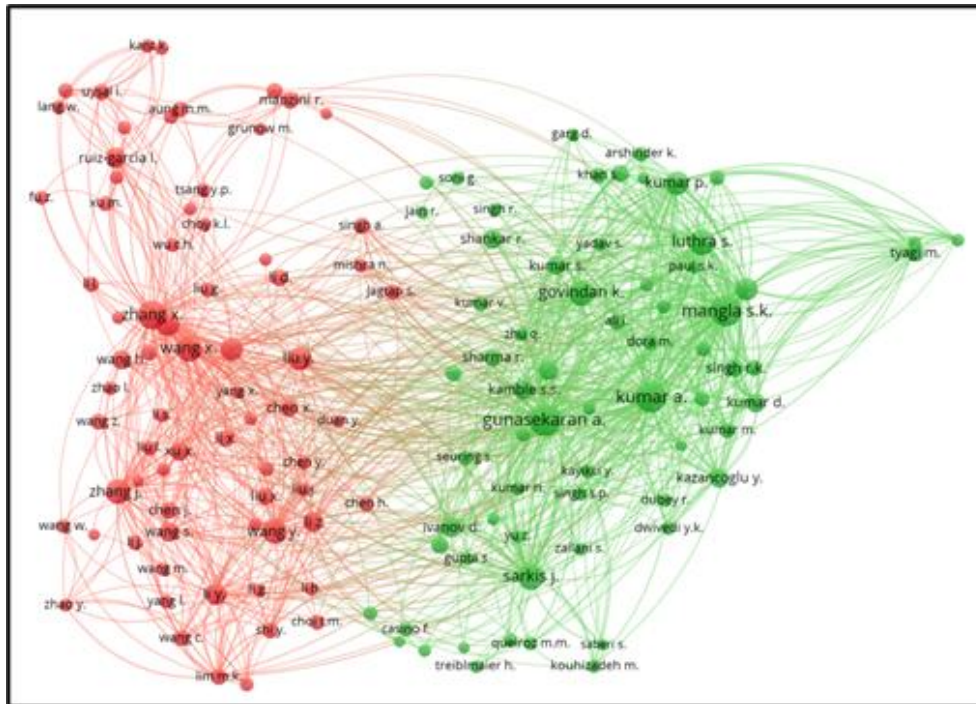


Figure 3: Cocitation analysis.  
Source: Authors (2025).

This research also analyzes the sources that publish studies on the application of blockchain in cold supply chains. Based on the collected data, there are 113 sources that will be analyzed for their impact by measuring several indicators, including H-index, G-index, total citations, and total articles. The H-index is an indicator used to measure the impact of a source based on the total number of articles and total citations it has. Meanwhile, the G-index is an indicator that not only measures the total number of articles and total citations but G-index also measures about the distribution of citations to other research articles, making it considered more accurate in measuring impact.

Analysis of publication sources is conducted to identify potential sources that can be targeted for publishing articles on the

application of blockchain in cold supply chains. Based on publication sources with the topic of blockchain application in cold supply chains. If viewed from the H-index, the Journal of Cleaner Production (6), IEEE Access (6), and Sustainability (5) are the best. If viewed from the G-index, Sustainability (11), Journal of Cleaner Production (9), and IEEE Access (8) are the best. If viewed from total citations, IEEE Access (445), Benchmarking (213), and Computers and Industrial Engineering (189) are the highest. Meanwhile, if viewed from total publications, Sustainability (11), Journal of Cleaner Production (9), and IEEE Access (8) are the most compared to other publication sources. The top 10 publication sources based on the various indicators mentioned above are presented in Table 3.

Table 3: Top 10 best publication sources based on index.

Rank	Sources	H-Index	G-Index	Cite	Articles
1	Sustainability	5	11	160	11
2	Journal of Cleaner Production	6	9	175	9
3	IEEE Access	6	8	445	8
4	Benchmarking	5	6	213	6
5	Annals of Operations Research	4	6	175	6
6	Environment, Development and Sustainability	3	5	68	5
7	Computers and Industrial Engineering	4	4	189	4
8	Foods	4	4	122	4
9	Expert Systems with Applications	3	4	61	4
10	Operations Management Research	2	4	17	4

Source: Authors (2025).

The next analysis conducted is a distribution analysis to determine the spread of blockchain research in the cold supply chain. In total, there are 33 countries that have conducted research on the application of blockchain in cold supply chains, spread across the world. The continents that dominate this field are Asia and Europe. This can happen because both continents that is Asia

and Europe continent have concerns to cold supply chain of food because its have correlation with economic.

Based on the analysis conducted, if we look at the number of publications, it was found that China is the most productive country in producing research with 51 scientific articles, followed by India with 44 scientific articles, and Italy with 12 scientific articles.

Meanwhile, if we look at the number of citations, China ranks highest with 812 citations, followed by India in second place with 745 citations, and the United Kingdom in third place with 664 citations. China has become the dominant country in blockchain application research in the cold supply chain because China is a

leader in blockchain research across various fields, including food and cold supply chains [12]. The 10 most countries based on total publications and the most impactful based on citations are presented in Figures 4 and 5.

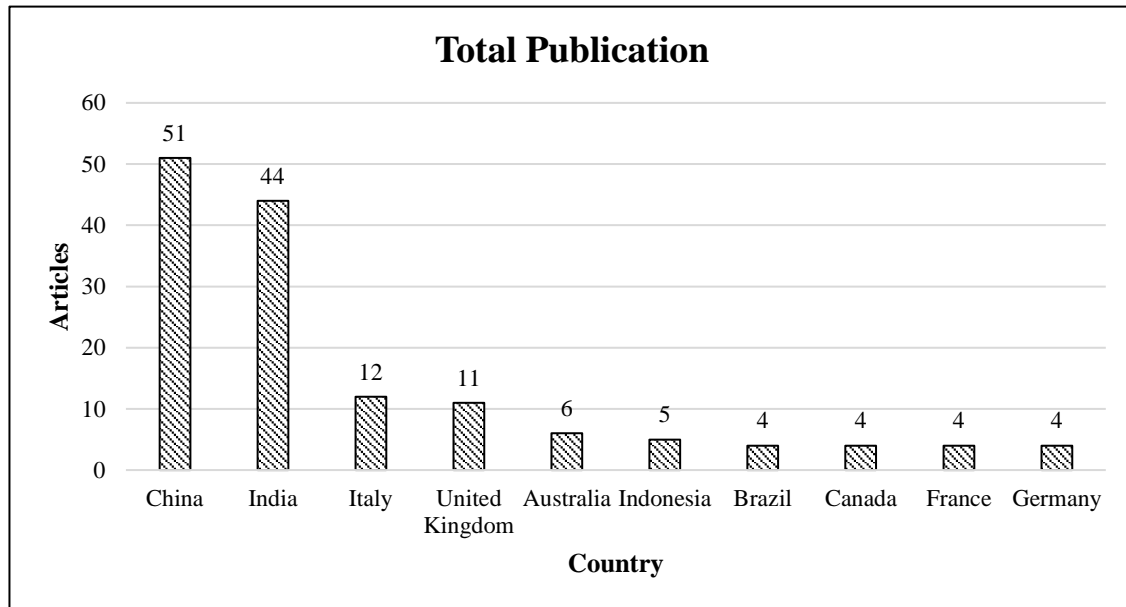


Figure 4: Distribution of the 10 most productive countries based on publications.  
Source: Authors (2025).

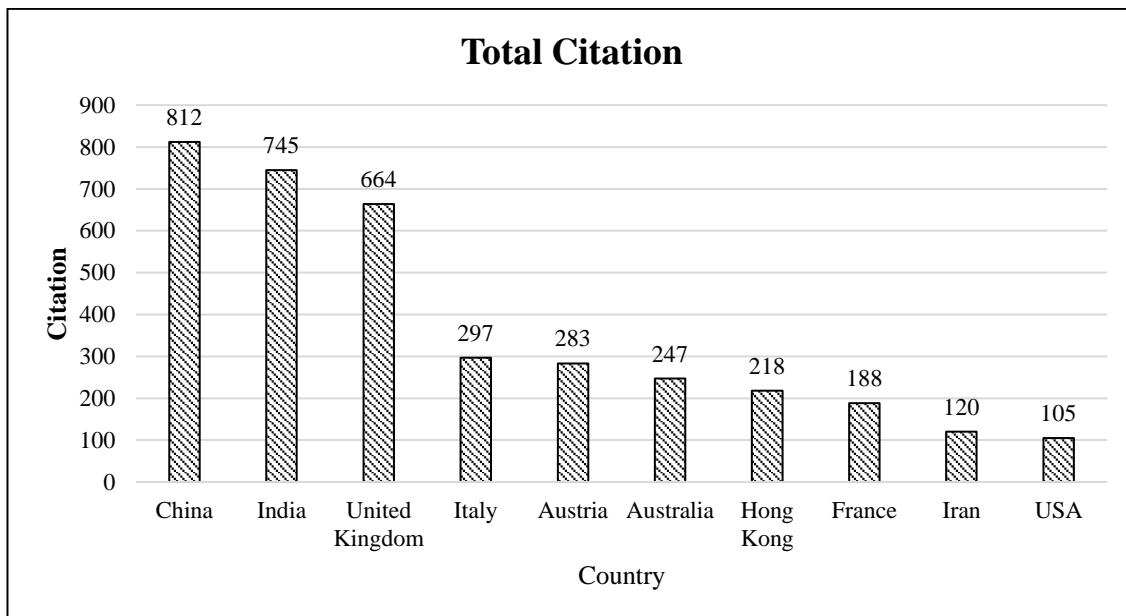


Figure 5: Distribution of the 10 most impactful countries based on total citations.  
Source: Authors (2025).

Keyword analysis was also conducted in this study because it serves the function of understanding the relationships that occur between one keyword and another. Keyword analysis was conducted using the Vosviewer software. Through keyword analysis, research gaps and potential future research can also be identified. The selected keywords must appear 3 times in the chosen scientific articles to obtain accurate and interrelated keywords. Based on the keyword analysis conducted, the results showed that 39% of the keywords are in cluster 1, 37% of the keywords are in cluster 2, and 24% are in cluster 3.

The distribution of keywords in the bibliometric analysis conducted shows something interesting because several frequently

keywords were identified in this part. Some of the most frequently appearing keywords include "supply chains" appearing 57 times, "blockchain" appearing 51 times, "food supply" appearing 48 times, "internet of things" appearing 28 times, "decision making" appearing 26 times, "sustainability" appearing 25 times, "food safety" appearing 21 times, "traceability" appearing 18 times, "food waste" appearing 12 times, and "logistics" appearing 12 times.

Based on word analysis, it can be concluded that blockchain is one of the potential technologies applied in cold supply chain logistics to support the creation of a sustainable cold supply chain. Some benefits that can be obtained from the application of blockchain in the cold supply chain include facilitating decision-



making, enhancing food safety, improving product traceability, increasing consumer trust, boosting product sales, and even in some cases, being implemented to minimize food waste. for more

detailed visual representation of the keyword, it is presented in Figure 6.

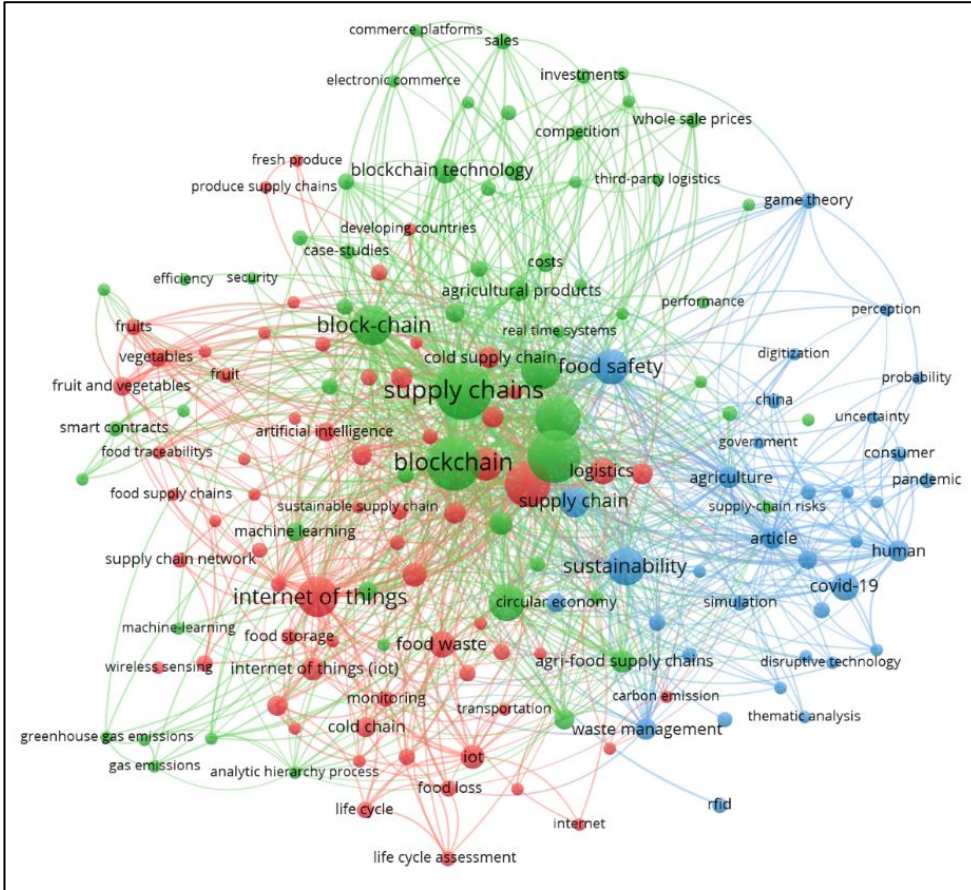


Figure 6: Keyword analysis and its development.  
Source: Authors (2025).

Based on the results obtained above, it can be concluded that the research topic on the application of blockchain in the cold supply chain currently aims to enhance the sustainability of the cold supply chain by optimizing sustainability aspects such as the environment (minimizing food waste and greenhouse gas emissions), economy (increasing competitiveness and sales), and social factors. (minimize uncertainty and increase food safety for consumers). In the keyword analysis, the analysis was conducted by dividing it into three major thematic clusters. Cluster 1, marked in red, discusses the internal agro-industry, specifically the use of blockchain technology transformation in improving traceability and reducing food waste. Cluster 2, marked in green, discusses the impact of blockchain technology on enhancing the competitiveness level of cold supply chain companies. Meanwhile, in cluster 3 with the blue color, it discusses in detail the presence of blockchain that can enhance food safety, thereby impacting the increase in consumer trust.

### IV.3 COLLABORATION ANALYSIS

In this study, the collaboration between researchers and between countries will be analyzed to understand the latest developments in blockchain research in the cold supply chain. The collaboration analysis was conducted with the condition that the document must be written by at least 2 researchers in 1 document. Based on the analysis results, it was found that 97.01% of the research was conducted collaboratively by the researchers, while

the remaining 2.99% was done individually. Based on collaboration and their relationships with each other, the researchers were divided into 4 clusters. The cluster division was based on the collaborations that had been conducted, the documents produced, and the similarity of themes discussed together with other researchers. Cluster 1 in red consists of 9 researchers, cluster 2 in green consists of 7 researchers, cluster 3 in blue consists of 7 researchers, and cluster 4 in yellow consists of 3 researchers. In cluster 1 with the red color, there is Mangla SK as the researcher who has collaborated the most and produced research with 9 collaborations and 5 published documents. In cluster 2 with the green color, there is Kumar A with 12 collaborations and 9 published documents. In cluster 3 with the blue color, there is Kazancoglu Y with 7 collaborations and 3 published documents. Meanwhile, in cluster 4 with the yellow color, there is Singh RK with 3 collaborations and 3 published documents.

The analysis results show that researchers are still mapped based on their countries of origin, and international collaboration has not yet been realized effectively. To gain a more detailed understanding of the collaboration conducted by the researchers, a visualization will be presented in Figure 7. When viewed by country, the majority of researchers who dominate the collaboration are fairly evenly distributed across several continents such as Asia, Europe, and America. To gain further insight into this matter, it will be discussed in detail in the next section.

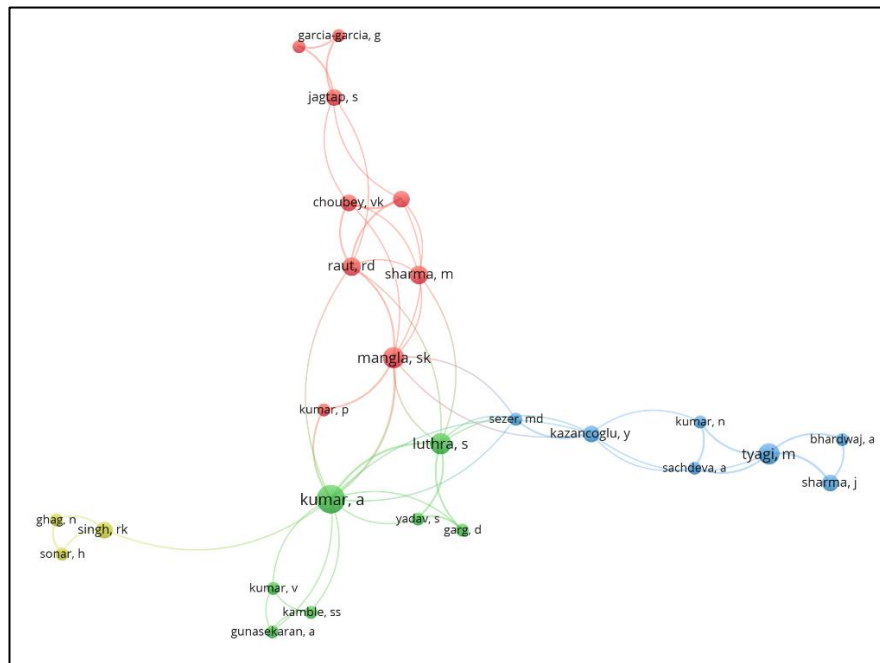


Figure 7. Collaboration among researchers.  
Source: Authors (2025).

After understanding the spread of collaboration among researchers, the next step will be to analyze the spread of collaboration among the countries involved. Interesting findings were obtained in this research, as there are several agrarian countries (China, India, Indonesia) and non-agrarian countries (United Kingdom, Germany, Italy) that significantly dominate the blockchain research in cold supply chains. In the analysis of the spread of collaboration between countries, clustering was also performed, dividing them into 3 clusters. In terms of distribution, cluster 1 consists of 16 countries, cluster 2 consists of 16 countries, and cluster 3 consists of 5 countries.

In cluster 1, marked in red, the United Kingdom is the most dominant country in research on blockchain in cold supply chains, having successfully collaborated with 26 other countries and

produced 32 publication documents. In cluster 2, marked in green, India is more dominant than China, with 19 international collaborations and 61 publication documents produced. Meanwhile, in cluster 3, Finland slightly outperformed Indonesia with 7 international collaborations and 3 published documents. The United Kingdom and India have become the largest because both countries are technology nations that easily adapt to new technologies and implement them in the food sector, which is considered crucial [47]. The collaboration between countries certainly signifies something positive because the issues of blockchain and cold supply chains have become crucial topics to discuss together. The mapping of international collaboration is presented in Figure 8.

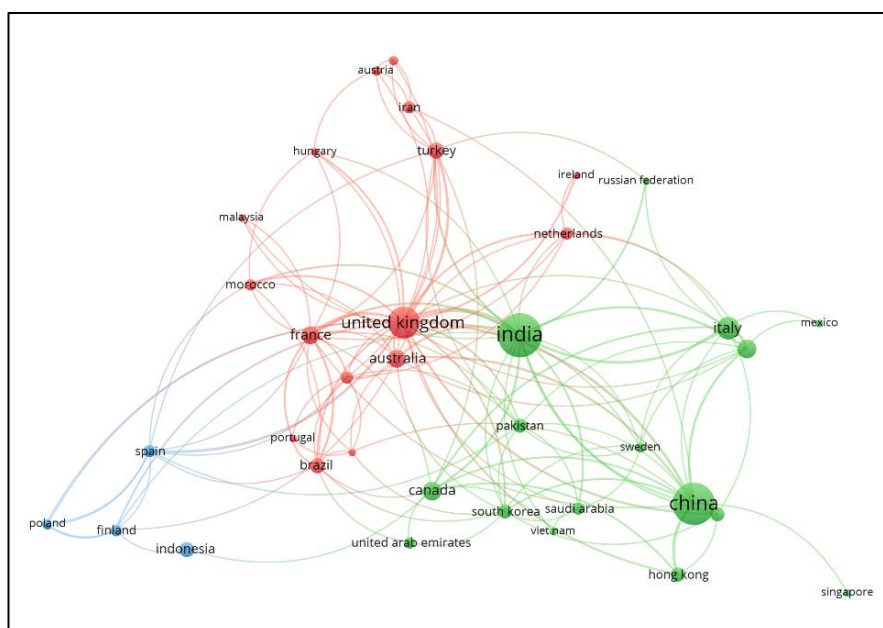


Figure 8: Collaboration between countries.  
Source: Authors (2025).

#### IV.4 REPORT FINDING IMPLEMENTATION BLOCKCHAIN IN COLD SUPPLY CHAIN

The application of blockchain in the cold food supply chain has become a recent trend with its extensive implementation and positive impact on the cold supply chain industry. Based on the conducted study, it was found that the majority of research

discusses conceptual models, influencing factors, and their application in the cold supply chain-based food industry. To provide a clearer picture, an extraction was conducted from several literatures available in the database that focuses on the contribution of blockchain in the cold supply chain-based food industry. As for more detailed information on this matter, it is presented in Table 3.

Table 3: Contribution of literature to application of blockchain in cold supply chains.

No.	Authors	Contribution	Type
1	Munir et al. [48]	Provided recommendations on how to adopt blockchain in the cold supply chain from an environmental, economic, social, perspective.	Journal
2	Li et al. [49]	Created intelligent distribution system based on blockchain to establish operations that are green logistics.	Journal
3	Feng et al. [50]	Created multisensor blockchain-based monitoring system for frozen shellfish quality.	Journal
4	Zhang et al. [51]	Created recording system from upstream to downstream for frozen aquatic products using a combination of blockchain and internet of things.	Journal
5	Gao & Li [52]	Created a high quality data for coordination and pricing system in the cold supply chain to minimize miscoordination using blockchain and neural networks.	Journal
6	Xue & Li [53]	Created a multichain blockchain system for fruit and vegetable with more efficient queries.	Journal
7	Zuo et al. [54]	Created a decentralized system combined with internet of things and neural networks for optimizing the delivery routes of cold agricultural products.	Journal
8	Wu et al. [55]	Analyzed the adoption of blockchain in the cold chain of fresh products and comparing it with several scenarios.	Journal
9	Tsang et al. [43]	Created a more practical food product traceability by combining fuzzy logic, internet of things, and blockchain.	Journal
10	Khanna et al [56]	Created a blockchain based traceability system specifically for the dairy agro-industry.	Journal
11	Patidar et al. [57]	Identified critical factors and finding that blockchain can enhance the fresh supply chain.	Journal
12	Jo et al. [58]	Created a blockchain system for the cold supply chain of meat commodities and measuring environmental impact.	Journal
13	Ma et al. [22]	Identified strategies to anticipate contamination in fresh or chilled food products by utilizing blockchain.	Journal
14	Ahmad et al. [59]	Analyzed the current needs and challenges in the implementation of blockchain in the food industry.	Journal
15	Nayal et al. [60]	Identified mediating factors that influence the adoption of blockchain in the cold food supply chain.	Journal
16	Morales et al. [61]	Analyzed consumer trust in perishable products through a blockchain system.	Journal
17	Ali et al. [23]	Formulate a blockchain framework for halal-based cold supply chains to enhance supply chain integrity.	Journal
18	Wang et al. [62]	Designing a blockchain framework combined with radio frequency identification in food cold chain.	Journal
19	Majdalawieh et al. [63]	Created a combination system blockchain and internet of things in the poultry agroindustry.	Journal
20	Bai et al. [64]	Designing a blockchain system for the cold supply chain of fresh agricultural products and analyzing the tripartite behavioral strategy.	Journal

Source: Authors (2025).

Based on the above contribution study, researchers agree that the presence of blockchain in the cold supply chain can provide a good multiplier effect and can be applied in various sectors and under various conditions. In its implementation, blockchain can also be combined with various other synergistic technologies such as the Internet of Things, digital twin, and radio frequency

identification. The presence of blockchain can facilitate agro-industries with cold supply chains to identify discrepancies, make quick decisions, streamline several operations, and easily determine the root of problems. In the long term, the adoption of blockchain technology can certainly provide various benefits, especially in increasing consumer trust and making the agro-

industry more adaptive. This illustrates that blockchain has a very wide potential to be implemented in to optimize the food cold chain

#### IV.5 TREND ANALYSIS AND IDENTIFIED POTENTIAL FUTURE RESEARCH

A trend analysis and an investigation of prospective topics will furnish readers with new knowledge, thereby facilitating further research in the domain of blockchain applications in cold supply chains. The trend analysis indicates that the field of blockchain in cold supply chains is undergoing rapid development with a multitude of applications. This is substantiated by the annual growth in research, which has consistently increased year on year. The advancement can be attributed to blockchain becoming a transformative technology that generates a positive multiplier effect, particularly in the context of cold supply chains.

In examining the evolution of blockchain applications in the context of cold supply chains, a strategic diagram is employed to discern current trends, dominant themes, unique themes, emerging themes, and fundamental themes. As evidenced by the trend diagram, several topics have recently emerged as subjects of discussion in the context of blockchain applications within the cold supply chain. These include concerns related to contamination of cold supply chain products, the minimization of carbon emissions, the assurance of cold supply chain product freshness, and increased cold chain product sales.

The issue of contamination in cold supply chain products has become a matter of great urgency, as it bears directly on the safety of the products in question, particularly foodstuffs. A number of studies have employed blockchain technology to identify contamination in livestock products and other foodstuffs within the cold supply chain [65]. The utilisation of blockchain within the context of the cold food supply chain offers a number of advantages, including the expedient detection of contamination, the identification of contamination sources, the determination of contamination timing, and the streamlining of product recalls from the market [22], [56], [66]–[68].

The second point pertains to the topic of carbon minimization within the context of blockchain. Given the relative scarcity of research on this subject, it represents an intriguing topic for further investigation. The research by Chen & Yin [69] is noteworthy for its proposal of a blockchain-based supply chain model for fresh food items such as dairy products. Shakhbulatov et al. [70] also developed a carbon tracking system for the distribution of cold chain food products, given that the cold chain is regarded as a significant contributor to carbon emissions. The integration of blockchain technology in carbon minimization can facilitate the assessment and decision-making processes for subsequent stages by stakeholders [7].

In addition to being able to identify contamination and carbon, blockchain in the cold supply chain can indirectly maintain product freshness. This can happen because with a transparent and trustworthy system, all actors involved in the cold supply chain from upstream to downstream will strive to maintain the freshness of the product [49]. Another advantage that consumers will gain is that they will be much more interested and have a much higher inclination to buy if there is a system that shows the transparency of product freshness [71].

From an economic standpoint, the implementation of blockchain technology in cold supply chain management is poised to bolster sales of associated products implemented blockchain technology and subsequently measured the sales levels of the product, demonstrating a notable increase due to the emergence of consumer trust [72]. Conversely, Chen et al. [73] assessed consumer preferences in the Jiangxi province of China. This study evaluated comparable fresh products and contrasted consumers' willingness to pay between fresh products that utilize blockchain technology, fresh products that employ conventional systems, fresh products with rigorous credit monitoring, and fresh products with international certification. The findings indicate that consumers are willing to pay a premium for fresh products that implement blockchain technology due to their perceived assurance of security for buyers. Detailed the trend diagram presented in Figure 9.

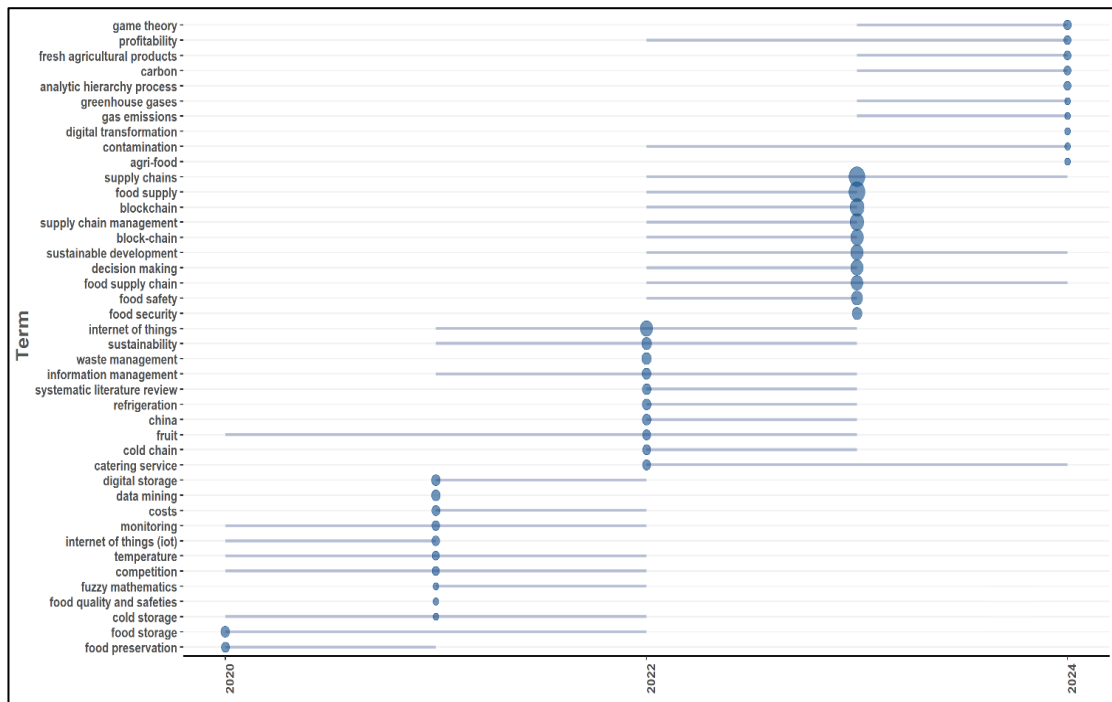


Figure 9: Research trend diagram.  
Source: Authors (2025).



After conducting a research trend analysis, the next step is to analyze potential topics on the application of blockchain in the cold supply chain. Potential topic analysis was conducted using a strategic diagram and dividing potential topics into four quadrants. Topics in quadrant 1 are those that act as drivers due to their large number and high influence. Quadrant 2 is filled with highly developed topics that are specific and isolated. Quadrant 3 contains topics that are either developing or declining with still low numbers and centrality. Quadrant 4 is filled with topics that underpin blockchain research in the cold supply chain [74], [75].

The results of the strategic diagram correlate with the results of the previous research trend diagram. In quadrant 1, there are several keywords including sustainability, commerce, vegetables,

and fruits. In quadrant 2, there are keywords such as capability freight transportation, deterioration, and food contamination. In quadrant 3, it consists of storage and transportation, carbon emissions, competitiveness, delphi analysis, agricultural products, and sales. Meanwhile, quadrant 4, which serves as the basis for research, consists of supply chains, blockchain, digital storage, and the internet of things. Based on the results obtained above, quadrants 2 and 3 can be an interesting focus for further research development considering they still have relatively low density, thus offering significant potential for further exploration. Regarding the strategic diagram on the topic of blockchain in the cold supply chain, it is presented in Figure 10.

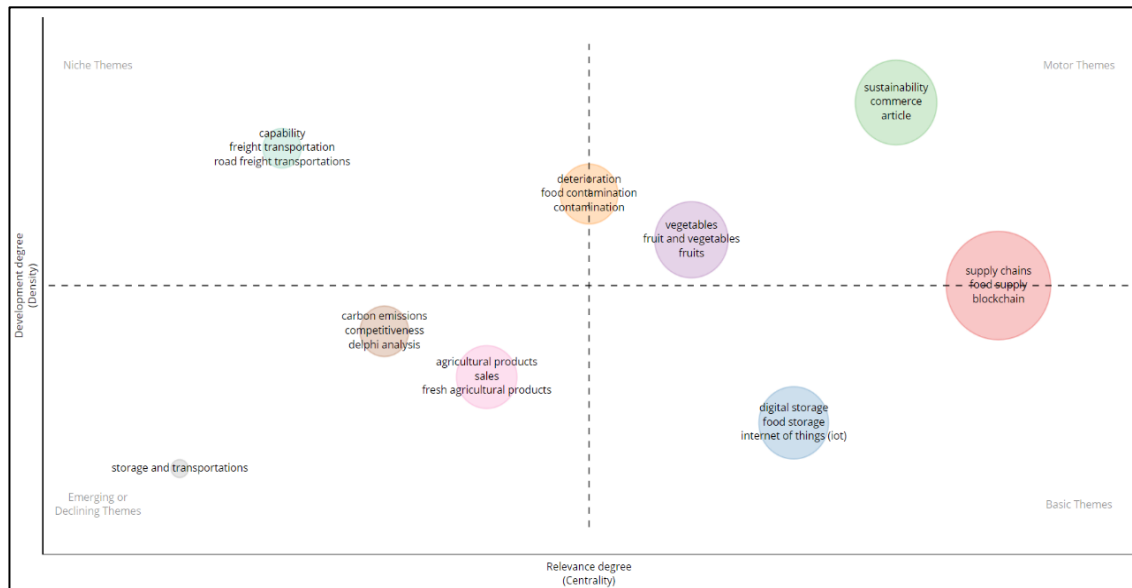


Figure 10: Identify potential future research with a strategic diagram.

Source: Authors (2025).

## V. CONCLUSIONS

Based on the systematic literature review and bibliometric analysis that has been conducted, several conclusions have been drawn, including the following:

1. Research on the application of blockchain in the cold food supply chain has been rapidly developing year by year, evidenced by an annual growth rate of 96.77%.
2. The productivity and impact of blockchain research in the cold food supply chain are measured by articles, sources, and countries. From the perspective of article productivity and impact, the article titled "A Systematic Literature Review on Machine Learning Applications for Sustainable Agriculture Supply Chain Performance" ranks highest in total global citations. Meanwhile, the article titled "Blockchain-Driven IOT for Food Traceability With an Integrated Consensus Mechanism" ranks highest in total local citations. In terms of source productivity and impact, Sustainability, Journal of Cleaner Production, and IEEE Access are the best. Whereas, when viewed from the perspective of productivity and the impact of countries, China, India, and Italy rank highest in total publications, while in terms of total citations, China, India, and the United Kingdom rank highest.
3. The trend analysis results indicate that there are several interesting topics to discuss further regarding blockchain in food cold chain, namely contamination of cold supply chain products,

minimization of carbon emissions, assurance of freshness of cold supply chain products, and increased sales.

4. The results of the gap analysis using strategic diagram indicate that there are several topics filling quadrants 2 and 3, namely capability freight transportation, deterioration, food contamination, storage and transportation, carbon emissions, competitiveness, delphi analysis, agricultural products, and sales.

## VI. AUTHOR'S CONTRIBUTION

**Conceptualization:** Thabed Tholib Baladraf, Marimin

**Methodology:** Thabed Tholib Baladraf, Marimin

**Investigation:** Thabed Tholib Baladraf, Marimin

**Discussion of results:** Thabed Tholib Baladraf, Marimin

**Writing – Original Draft:** Thabed Tholib Baladraf

**Writing – Review and Editing:** Thabed Tholib Baladraf

**Resources:** Marimin

**Supervision:** Marimin

**Approval of the final text:** Marimin

## VII. ACKNOWLEDGMENTS

The authors are grateful for the scholarship support provided by the Ministry of Education, Culture, Research and Technology of Indonesia and IPB University. The authors would also like to thank Prof. Marimin, M.Sc. for his guidance and direction in carrying out the research.

# VIII. REFERENCES

- [1] A. Estes, M. M. E. Alemany, and Á. Ortiz, "Impact of product perishability on agri-food supply chains design," *Appl. Math. Model.*, vol. 96, pp. 20–38, 2021, doi: 10.1016/j.apm.2021.02.027.
- [2] S. Shashi, P. Centobelli, R. Cerchione, and M. Ertz, "Food cold chain management: what we know and what we deserve," *Supply Chain Manag.*, vol. 26, no. 1, pp. 102–135, 2021, doi: 10.1108/SCM-12-2019-0452.
- [3] H. Zhu, C. Liu, G. Wu, and Y. Gao, "Cold Chain Logistics Network Design for Fresh Agricultural Products with Government Subsidy," *Sustain.*, vol. 15, no. 13, 2023, doi: 10.3390/su151310021.
- [4] P. Arriaga-Lorenzo, E. de Jesús Maldonado-Simán, R. Ramírez-Valverde, P. A. Martínez-Hernández, D. N. Tirado-González, and L. A. Saavedra-Jiménez, "Cold chain relevance in the food safety of perishable products," *Foods Raw Mater.*, vol. 11, no. 1, pp. 116–128, 2023, doi: 10.21603/2308-4057-2023-1-559.
- [5] Y. Huaizhi and A. R. Abdullah, "Article on Cold Chain Logistics of Agricultural Products in Shandong, China," *Int. J. Bus. Technol. Manag.*, vol. 6, no. 2, pp. 378–395, 2024, doi: 10.55057/ijbtm.2024.6.2.34.
- [6] United Nations Environment Programme, Sustainable food cold chains: Opportunities, challenges and the way forward. 2022.
- [7] S. Wang, "Causes and Solutions of Cold Chain Logistics Chain Fracture," *Manuf. Serv. Oper. Manag.*, vol. 4, no. 4, pp. 85–90, 2023, doi: 10.23977/msom.2023.040410.
- [8] J. Zhang, W. Cao, and M. Park, "Reliability analysis and optimization of cold chain distribution system for fresh agricultural products," *Sustain.*, vol. 11, no. 13, 2019, doi: 10.3390/su11133618.
- [9] R. D. Raut, B. B. Gardas, V. S. Narwane, and B. E. Narkhede, "Improvement in the food losses in fruits and vegetable supply chain - a perspective of cold third-party logistics approach," *Oper. Res. Perspect.*, vol. 6, no. June, p. 100117, 2019, doi: 10.1016/j.orp.2019.100117.
- [10] J. Loisel et al., "Cold chain break detection and analysis: Can machine learning help?," *Trends Food Sci. Technol.*, vol. 112, no. March, pp. 391–399, 2021, doi: 10.1016/j.tifs.2021.03.052.
- [11] M. M. Chavalala, S. Bag, J. H. C. Pretorius, and M. S. Rahman, "A multi-method study on the barriers of the blockchain technology application in the cold supply chains," *J. Enterp. Inf. Manag.*, vol. 37, no. 2, pp. 745–776, Jan. 2024, doi: 10.1108/JEIM-06-2022-0209.
- [12] Q. Wang, M. Su, and R. Li, "Is China the world's blockchain leader? Evidence, evolution and outlook of China's blockchain research," *J. Clean. Prod.*, vol. 264, p. 121742, 2020, doi: 10.1016/j.jclepro.2020.121742.
- [13] R. Beck, C. Müller-Bloch, and J. L. King, "Governance in the blockchain economy: A framework and research agenda," *J. Assoc. Inf. Syst.*, vol. 19, no. 10, pp. 1020–1034, 2018, doi: 10.17705/1jais.00518.
- [14] T. M. Tan and J. Salo, "Ethical Marketing in the Blockchain-Based Sharing Economy: Theoretical Integration and Guiding Insights," *J. Bus. Ethics*, vol. 183, no. 4, pp. 1113–1140, 2023, doi: 10.1007/s10551-021-05015-8.
- [15] A. Firdaus, N. B. Anuar, M. F. A. Razak, I. A. T. Hashem, S. Bachok, and A. K. Sangaiah, "Root Exploit Detection and Features Optimization: Mobile Device and Blockchain Based Medical Data Management," *J. Med. Syst.*, vol. 42, no. 6, 2018, doi: 10.1007/s10916-018-0966-x.
- [16] K. N. Griggs, O. Ossipova, C. P. Kohlios, A. N. Baccarini, E. A. Howson, and T. Hayajneh, "Healthcare Blockchain System Using Smart Contracts for Secure Automated Remote Patient Monitoring," *J. Med. Syst.*, vol. 42, no. 7, pp. 1–7, 2018, doi: 10.1007/s10916-018-0982-x.
- [17] B. D. Dayana, C. S. Krishnan, C. S. Patrick, and N. Venkateswaran, "Tracking and monitoring of vehicles and a stable and secure tolltax payment methodology based on blockchain enabled cryptocurrency E-wallets," *Int. J. Eng. Adv. Technol.*, vol. 8, no. 4, pp. 685–690, 2019.
- [18] C. Durán, A. K. Yazdi, I. Derpich, and Y. Tan, "Leveraging Blockchain for Maritime Port Supply Chain Management through Multicriteria Decision Making," *Mathematics*, vol. 12, no. 10, pp. 1–23, 2024, doi: 10.3390/math12101511.
- [19] Y. Arkeman, N. J. Hidayah, A. Suharso, F. Adhizima, and T. Kusuma, "Implementation of Artificial Intelligence and Blockchain in Agricultural Supply Chain Management," *J. Int. Soc. Southeast Asian Agric. Sci.*, vol. 29, no. 1, pp. 135–149, 2023.
- [20] D. Novianti, Y. Arkeman, M. N. Almunawar, L. Haditjaroko, and A. Ismayana, "Designing a Transparent Distributed Systems for Halal Supply Chains Using Blockchain Technology," *J. Bus. Econ. Anal.*, vol. 03, no. 02, pp. 151–170, 2020, doi: 10.36924/sbe.2020.3204.
- [21] S. Jagtap, F. Bader, G. Garcia-Garcia, H. Trollman, T. Fadji, and K. Salonitis, "Food Logistics 4.0: Opportunities and Challenges," *Logistics*, vol. 5, no. 1, pp. 1–19, 2021, doi: 10.3390/logistics5010002.
- [22] D. Ma, K. Li, H. Qin, and J. Hu, "Impacts of blockchain technology on food supply chains with potential food contamination," *Electron. Commer. Res. Appl.*, vol. 64, p. 101375, 2024, doi: 10.1016/j.elerap.2024.101375.
- [23] M. H. Ali, L. Chung, A. Kumar, S. Zailani, and K. H. Tan, "A sustainable Blockchain framework for the halal food supply chain: Lessons from Malaysia," *Technol. Forecast. Soc. Change*, vol. 170, no. May, p. 120870, 2021, doi: 10.1016/j.techfore.2021.120870.
- [24] Y. Liu, D. Ma, J. Hu, and Z. Zhang, "Sales mode selection of fresh food supply chain based on blockchain technology under different channel competition," *Comput. Ind. Eng.*, vol. 162, p. 107730, 2021, doi: 10.1016/j.cie.2021.107730.
- [25] W. He and H. Zheng, "Literature Review on Block Chain: Technology, Principle and Development," *J. Phys. Conf. Ser.*, vol. 1848, no. 1, pp. 1–6, 2021, doi: 10.1088/1742-6596/1848/1/012166.
- [26] K. S. Hald and A. Kinra, "How the blockchain enables and constrains supply chain performance," *Int. J. Phys. Distrib. Logist. Manag.*, vol. 49, no. 4, pp. 376–397, Jan. 2019, doi: 10.1108/IJPDLM-02-2019-0063.
- [27] A. Batwa and A. Norrman, "Blockchain technology and trust in supply chain management: A literature review and research agenda," *Oper. Supply Chain Manag.*, vol. 14, no. 2, pp. 203–220, 2021, doi: 10.31387/oscm0450297.
- [28] Y. Wang, J. H. Han, and P. Beynon-Davies, "Understanding blockchain technology for future supply chains: a systematic literature review and research agenda," *Supply Chain Manag. An Int. J.*, vol. 24, no. 1, pp. 62–84, Jan. 2019, doi: 10.1108/SCM-03-2018-0148.
- [29] M. U. A. Gondal, M. A. Khan, A. Haseeb, H. M. Albarakati, and M. Shabaz, "A secure food supply chain solution: blockchain and IoT-enabled container to enhance the efficiency of shipment for strawberry supply chain," *Front. Sustain. Food Syst.*, vol. 7, 2023, doi: 10.3389/fsufs.2023.1294829.
- [30] J. N. V. Rampur, D. Gangodkar, A. M. B. C., and A. K. N., "Improved block chain system for high secured IoT integrated supply chain," *Meas. Sensors*, vol. 25, p. 100633, 2023, doi: 10.1016/j.measen.2022.100633.
- [31] M. F. M. S. Mustafa, N. Navaranjan, and A. Demirovic, "Food cold chain logistics and management: A review of current development and emerging trends," *J. Agric. Food Res.*, vol. 18, no. July, p. 101343, 2024, doi: 10.1016/j.jafr.2024.101343.
- [32] J. Qian et al., "Food traceability system from governmental, corporate, and consumer perspectives in the European Union and China: A comparative review," *Trends Food Sci. Technol.*, vol. 99, no. July 2019, pp. 402–412, 2020, doi: 10.1016/j.tifs.2020.03.025.
- [33] J. Qian, Q. Yu, L. Jiang, H. Yang, and W. Wu, "Food cold chain management improvement: A conjoint analysis on COVID-19 and food cold chain systems," *Food Control*, vol. 137, no. January, pp. 1–12, 2022, doi: 10.1016/j.foodcont.2022.108940.
- [34] S. Liu, "Multimodal Transportation Route Optimization of Cold Chain Container in Time-Varying Network Considering Carbon Emissions," *Sustain.*, vol. 15, no. 5, 2023, doi: 10.3390/su15054435.
- [35] S. S. Turgut, A. Myustedzhebov, and A. H. Feyissa, "Low-cost multispectral sensor reveals cold chain breaks, meat type, and storage time in chicken meat samples," *Food Control*, vol. 167, p. 110816, 2025, doi: 10.1016/j.foodcont.2024.110816.

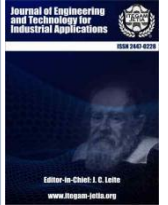
- [36] J. Gillespie et al., "Real-Time Anomaly Detection in Cold Chain Transportation Using IoT Technology," *Sustain.*, vol. 15, no. 3, pp. 1–24, 2023, doi: 10.3390/su15032255.
- [37] W. M. Lim, S. Kumar, and N. Donthu, "How to combine and clean bibliometric data and use bibliometric tools synergistically: Guidelines using metaverse research," *J. Bus. Res.*, vol. 182, no. December 2023, p. 114760, 2024, doi: 10.1016/j.jbusres.2024.114760.
- [38] G. Marzi, M. Balzano, A. Caputo, and M. M. Pellegrini, "Guidelines for Bibliometric-Systematic Literature Reviews: 10 steps to combine analysis, synthesis and theory development," *Int. J. Manag. Rev.*, no. December 2022, pp. 81–103, 2024, doi: 10.1111/ijmr.12381.
- [39] O. Öztürk, R. Kocaman, and D. K. Kanbach, "How to design bibliometric research: an overview and a framework proposal," *Rev. Manag. Sci.*, no. 0123456789, 2024, doi: 10.1007/s11846-024-00738-0.
- [40] P. M. Hasugian and B. Nadeak, "Bibliometric Analysis On Techniques for Data Visualization," *J. Info Sains Inform. dan Sains*, vol. 14, no. 01, pp. 425–433, 2024, doi: 10.58471/JIS.v13i01.
- [41] R. Sharma, S. S. Kamble, A. Gunasekaran, V. Kumar, and A. Kumar, "A systematic literature review on machine learning applications for sustainable agriculture supply chain performance," *Comput. Oper. Res.*, vol. 119, no. May, 2020, doi: 10.1016/j.cor.2020.104926.
- [42] A. Rejeb, J. G. Keogh, and H. Treiblmaier, "Leveraging the Internet of Things and Blockchain in SC.pdf," *Futur. Internet*, vol. 11, no. 161, pp. 1–22, 2019, doi: 10.3390/fi11070161.
- [43] Y. P. Tsang, K. L. Choy, C. H. Wu, G. T. S. Ho, and H. Y. Lam, "Blockchain-Driven IoT for Food Traceability with an Integrated Consensus Mechanism," *IEEE Access*, vol. 7, pp. 129000–129017, 2019, doi: 10.1109/ACCESS.2019.2940227.
- [44] A. M. Aamer, M. A. Al-Awlaqi, I. Affia, S. Arumsari, and N. Mandahawi, "The internet of things in the food supply chain: adoption challenges," *Benchmarking An Int. J.*, vol. 28, no. 8, pp. 2521–2541, Jan. 2021, doi: 10.1108/BIJ-07-2020-0371.
- [45] I. Masudin, A. Ramadhani, D. P. Restuputri, and I. Amallynda, "The Effect of Traceability System and Managerial Initiative on Indonesian Food Cold Chain Performance: A Covid-19 Pandemic Perspective," *Glob. J. Flex. Syst. Manag.*, vol. 22, no. 4, pp. 331–356, 2021, doi: 10.1007/s40171-021-00281-x.
- [46] E. M. M. Ramli, D. Bin Zainudin, and R. Islam, "Explore the Research Trends of Green Supply Chain in the Manufacturing Industry: A Bibliometric Analysis," *Oper. Supply Chain Manag.*, vol. 15, no. 3, pp. 345–358, 2022, doi: 10.31387/oscm0500351.
- [47] R. M. Ellahi, L. C. Wood, and A. E. D. A. Bekhit, "Blockchain-Based Frameworks for Food Traceability: A Systematic Review," *Foods*, vol. 12, no. 16, pp. 1–28, 2023, doi: 10.3390/foods12163026.
- [48] M. A. Munir et al., "Blockchain Adoption for Sustainable Supply Chain Management: Economic, Environmental, and Social Perspectives," *Front. Energy Res.*, vol. 10, no. May, pp. 1–24, 2022, doi: 10.3389/fenrg.2022.899632.
- [49] Y. Li, C. Tan, W. H. Ip, and C. H. Wu, "Dynamic blockchain adoption for freshness-keeping in the fresh agricultural product supply chain," *Expert Syst. Appl.*, vol. 217, p. 119494, 2023, doi: 10.1016/j.eswa.2022.119494.
- [50] H. Feng, W. Wang, B. Chen, and X. Zhang, "Evaluation on Frozen Shellfish Quality by Blockchain Based Multi-Sensors Monitoring and SVM Algorithm during Cold Storage," *IEEE Access*, vol. 8, pp. 54361–54370, 2020, doi: 10.1109/ACCESS.2020.2977723.
- [51] Y. Zhang, Y. Liu, Z. Jiong, X. Zhang, B. Li, and E. Chen, "Development and assessment of blockchain-IoT-based traceability system for frozen aquatic product," *J. Food Process Eng.*, vol. 44, no. 5, pp. 1–14, 2021, doi: 10.1111/jfpe.13669.
- [52] Z. Gao and D. Li, "Blockchain-Based Neural Network Model for Agricultural Product Cold Chain Coordination," *Comput. Intell. Neurosci.*, vol. 2022, 2022, doi: 10.1155/2022/1760937.
- [53] F. Xue and F. Li, "A Quality Traceability System for Fruit and Vegetable Supply Chain Based on Multi-Chain Blockchain," *Int. J. Inf. Syst. Supply Chain Manag.*, vol. 16, no. 1, pp. 1–18, 2023, doi: 10.4018/IJISSCM.330681.
- [54] X. Zuo, Z. Cui, H. Lin, and D. Wang, "Route Optimization of Agricultural Product Distribution Based on Agricultural Iot and Neural Network from the Perspective of Fabric Blockchain," *Wirel. Commun. Mob. Comput.*, vol. 2022, 2022, doi: 10.1155/2022/5106215.
- [55] X. Y. Wu, Z. P. Fan, and B. B. Cao, "An analysis of strategies for adopting blockchain technology in the fresh product supply chain," *Int. J. Prod. Res.*, vol. 61, no. 11, pp. 3717–3734, 2023, doi: 10.1080/00207543.2021.1894497.
- [56] A. Khanna, S. Jain, A. Burgio, V. Bolshev, and V. Panchenko, "Blockchain-Enabled Supply Chain platform for Indian Dairy Industry: Safety and Traceability," *Foods*, vol. 11, no. 17, pp. 1–29, 2022, doi: 10.3390/foods11172716.
- [57] S. Patidar, V. K. Sukhwani, and A. C. Shukla, "Modeling of Critical Food Supply Chain Drivers Using DEMATEL Method and Blockchain Technology," *J. Inst. Eng. Ser. C*, vol. 104, no. 3, pp. 541–552, 2023, doi: 10.1007/s40032-023-00941-0.
- [58] J. Jo, S. Yi, and E. Lee, "Including the reefer chain into genuine beef cold chain architecture based on blockchain technology," *J. Clean. Prod.*, vol. 363, p. 132646, 2022, doi: 10.1016/j.jclepro.2022.132646.
- [59] R. W. Ahmad, K. M. Ko, A. Rashid, and J. J. P. C. Rodrigues, "Blockchain for Food Industry: Opportunities, Requirements, Case Studies, and Research Challenges," *IEEE Access*, vol. 12, no. August, pp. 117363–117378, 2024, doi: 10.1109/ACCESS.2024.3447918.
- [60] K. Naya, R. D. Raut, B. E. Narkhede, P. Priyadarshinee, G. B. Panchal, and V. V. Gedam, "Antecedents for blockchain technology-enabled sustainable agriculture supply chain," *Ann. Oper. Res.*, vol. 327, no. 1, pp. 293–337, 2023, doi: 10.1007/s10479-021-04423-3.
- [61] L. E. Morales, M. D. Ehmke, and A. Sheridan, "Consumer Trust and Purchase of Perishable Fresh Food Online Versus In-Store: The Case of beef," *J. Int. Food Agribus. Mark.*, vol. 36, no. 2, pp. 177–199, Mar. 2024, doi: 10.1080/08974438.2022.2072992.
- [62] L. Wang, Y. He, and Z. Wu, "Design of a Blockchain-Enabled Traceability System Framework for Food Supply Chains," *Foods*, vol. 11, no. 5, pp. 1–18, 2022, doi: 10.3390/foods11050744.
- [63] M. Majdalawieh, N. Nizamuddin, M. Alaraj, S. Khan, and A. Bani-Hani, "Blockchain-based solution for Secure and Transparent Food Supply Chain Network," *Peer-to-Peer Netw. Appl.*, vol. 14, no. 6, pp. 3831–3850, 2021, doi: 10.1007/s12083-021-01196-1.
- [64] Y. Bai, H. Wu, M. Huang, J. Luo, and Z. Yang, "How to build a cold chain supply chain system for fresh agricultural products through blockchain technology-A study of tripartite evolutionary game theory based on prospect theory," *PLoS One*, vol. 18, no. 11 November, pp. 1–27, 2023, doi: 10.1371/journal.pone.0294520.
- [65] A. S. Patel, M. N. Brahmabhatt, A. R. Bariya, J. B. Nayak, and V. K. Singh, "Blockchain technology in food safety and traceability concern to livestock products," *Heliyon*, vol. 9, no. 6, p. e16526, 2023, doi: 10.1016/j.heliyon.2023.e16526.
- [66] V. Sri Vigna Hema and A. Manickavasagan, "Blockchain implementation for food safety in supply chain: A review," *Compr. Rev. Food Sci. Food Saf.*, vol. 23, no. 5, pp. 1–29, 2024, doi: 10.1111/1541-4337.70002.
- [67] B. M. Yakubu, R. Latif, A. Yakubu, M. I. Khan, and A. I. Magashi, "RiceChain: secure and traceable rice supply chain framework using blockchain technology," *PeerJ Comput. Sci.*, vol. 8, pp. 1–24, 2022, doi: 10.7717/PEERJ-CS.801.
- [68] N. Kshetri and J. Defranco, "The Economics behind Food Supply Blockchains," *Computer (Long. Beach. Calif.)*, vol. 53, no. 12, pp. 106–110, 2020, doi: 10.1109/MC.2020.3021549.
- [69] H. Chen and L. Yin, "Research on the Coordination of Fresh Food Supply Chain Based on the Perspective of Blockchain and Low Carbon," *Discret. Dyn. Nat. Soc.*, vol. 2023, 2023, doi: 10.1155/2023/6156039.
- [70] D. Shakhbulatov, A. Arora, Z. Dong, and R. Rojas-Cessa, "Blockchain implementation for analysis of carbon footprint across food supply chain," *Proc. - 2019 2nd IEEE Int. Conf. Blockchain, Blockchain 2019*, pp. 546–551, 2019, doi: 10.1109/Blockchain.2019.00079.

- [71] P. Hou, T. Feng, Y. Li, and S. Peng, "Blockchain adoption for product freshness traceability under platform competition," *Int. J. Prod. Res.*, pp. 1–14, doi: 10.1080/00207543.2024.2377694.
- [72] X. Brusset, A. Kinra, H. Naseraldin, and R. Alkhudary, "Increasing willingness to pay in the food supply chain: a blockchain-oriented trust approach," *Int. J. Prod. Res.*, pp. 1–22, doi: 10.1080/00207543.2024.2352763.
- [73] X. Chen et al., "Health is wealth: Study on consumer preferences and the willingness to pay for ecological agricultural product traceability technology: Evidence from jiangxi province China," *Int. J. Environ. Res. Public Health*, vol. 18, no. 22, 2021, doi: 10.3390/ijerph182211761.
- [74] J. R. López-Robles, J. R. Otegi-Olaso, R. Arcos, N. K. G.- Rosales, and H. Gamboa-Rosales, "Mapping the structure and evolution of JISIB: A bibliometric analysis of articles published in the Journal of Intelligence Studies in Business between 2011 and 2017," *J. Intell. Stud. Bus.*, vol. 8, no. 3, pp. 9–21, 2018, doi: 10.37380/jisib.v8i3.362.
- [75] A. S. Jafari Roodbandi, A. Choobineh, N. Barahmand, and M. Sadeghi, "Research outputs in ergonomics and human factors engineering: a bibliometric and co-word analysis of content and contributions," *Int. J. Occup. Saf. Ergon.*, vol. 28, no. 4, pp. 2010–2021, Oct. 2022, doi: 10.1080/10803548.2021.1955495.





ISSN ONLINE: 2447-0228



## RESEARCH ARTICLE

## OPEN ACCESS

# LONG - TERM ASSESSMENT OF THE SPATIAL TEMPORAL TRENDS IN SELECTED CLOUD RADIATIVE PROPERTIES OVER THE THREE DISTINCT SITES IN KENYA

Sostine N. Makokha<sup>1</sup>, John W. Makokha<sup>2</sup> and Festus B. Kelonye<sup>3</sup>

<sup>1,2</sup> Department of Science, Technology and Engineering, Kibabii University, P.O BOX 1699-50200, Bungoma, Kenya.

<sup>3</sup> Department of Biological and Environmental science, Kibabii University, P.O BOX 1699-50200, Bungoma, Kenya..

<sup>1</sup><http://orcid.org/0000-0003-3416-5818> , <sup>2</sup><http://orcid.org/0000-0003-3267-4512> , <sup>3</sup><http://orcid.org/0000-0002-5880-3493>

Email: [makokhasostine@gmail.com](mailto:makokhasostine@gmail.com), [makokhajw@kibu.ac.ke](mailto:makokhajw@kibu.ac.ke), [fberu@kibu.ac.ke](mailto:fberu@kibu.ac.ke)

## ARTICLE INFO

## Article History

Received: May 11, 2024

Revised: July 20, 2025

Accepted: March 15, 2025

Published: April 31, 2025

## Keywords:

MODIS,

MERRA-2,

TRMM,

Seasons

Clouds radiative properties

## ABSTRACT

The presence of clouds in the Earth's atmosphere plays an important role in regulating the Earth's energy budget. Increased anthropogenic activities and emissions can significantly lead to changes in cloud composition and cloud structure affecting the cloud properties causing alterations in climatic conditions over Kenya. Given this, the present study examined the spatial temporal radiative properties of clouds over Nairobi, Malindi and Mbita by paying a special consideration on cloud parameters such as; Cloud Effective Radius (CER), Cloud Optical Thickness (COT), Water Vapor (WV), Precipitation Rate (PR) and Cloud Albedo (CA). These cloud parameters were retrieved from MODerate resolution Imaging Spectroradiometer (MODIS) sensor, the Modern Era Retrospective analysis for Research and Applications, version2 (MERRA-2) model and Tropical Rainfall Measurement Mission (TRMM) between January 2005 and December 2020. Data retrieved on clouds radiative properties was utilized to estimate the trends and spatial variations and assess their statistical significance on climate over the study domain. The Spatial patterns of seasonal mean of cloud parameters from the sensors and the model were generally characterized with positive and negative trends over Kenya observed during the four seasons. Spatial trends in the selected cloud properties were determined and observed to vary both seasonally and regionally, the study revealed patterns of trends in cloud radiative properties and forms a basis for further research on clouds over Kenya.



Copyright ©2025 by authors and Galileo Institute of Technology and Education of the Amazon (ITEGAM). This work is licensed under the Creative Commons Attribution International License (CC BY 4.0).

## I. INTRODUCTION

Clouds form a very crucial component of the atmosphere and play a pivotal role in regulating the Earth's energy budget (Zhang et al., 2018). Apart from other important modulators of climate, Clouds strongly modulate the radiation budget by absorbing and scattering solar and thermal radiation (Roebeling et al., 2006). In particular, they play a key role in determining the solar radiation reaching the Earth's surface by generally reducing it (by up to nearly 80%) depending mainly on the cloud type, its optical thickness and distribution in the sky (Calbo et al., 2005). They also interact with the solar radiation causing direct effect such as absorption or scattering (Ichoku et al., 2004).

The interactions of the clouds and other components in the atmosphere cause both predictable and unpredictable weather patterns affecting the climate of the study domain. These simple processes that takes place in the atmosphere may affect the daily weather patterns over any region and any slightest change in these properties would perturb cloud radiative forcing and modulate the radiative balance of the Earth system (George and Wood, 2010). Moreover, temporal trends of the changes in intensity, frequency, and duration of temperature and precipitation events are indicators of a changing climate (Audu et al., 2021) caused as a result in variations in cloud characteristics. Cloud radiative properties can be assessed through determining the variations in some major cloud parameters such as the Cloud effective radius (CER), Cloud

Optical Thickness (COT), Water Vapor (WV), Precipitation Rate (PR) and Cloud Albedo (CA).

Various recent studies have been done on assessing and determining the radiative properties of clouds both regionally and globally with the aim of providing knowledge on cloud properties over those study regions. These studies have provided the necessary knowledge on both methods of data acquisition, processing and analysis of the data obtained with an aim of giving it a statistical significance.

A study was done on the radiative cloud properties in USA by Liou and Wittman (1979). This study was aimed at studying parameterization of the radiative properties of clouds. Reflection, transmission, and absorption of solar radiation by four cloud types (low, middle, high and stratus clouds) were computed as functions of the solar zenith angle and cloud liquid water/ice content.

The reflection, transmission and emission of the infra-red radiation by cirrus clouds are calculated as functions of the cloud ice content. The plane-parallel radiative transfer program employed is based on the discrete-ordinate method with applications to inhomogeneous absorption in scattering atmospheres covering the entire solar and infrared spectra taking into consideration the gaseous absorption in scattering atmospheres (Li *et al.*, 2020).

The resulting values of the solar radiative properties of clouds were fitted with known mathematical functions involving the solar zenith angle and cloud liquid water/ice content as variables. The effects of the atmospheric profile were discussed and the effects of surface reflectivity on the solar radiative properties of clouds were parameterized in terms of the water vapor absorptivity below the cloud ground reflection and average cloud reflection.

The parameterized equations for the infrared flux reflectivity of cirrus clouds were also presented as functions of the cloud ice content. Computations were made for various cloud thicknesses, holding the cloud base at a constant height for each case. The vertical liquid water content  $W$  of which cloud thickness is given by  $W = w\Delta z$ , where  $w$  is the mean water/ice content and  $\Delta z$  the geometrical cloud thickness.

The ranges of cloud thicknesses used in the radiative transfer calculations of this study for Cu, As, St and Ci were 0.15-2.25, 0.1-1.5, 0.05-0.75 and 0.1-2.9 km respectively. the corresponding ranges of vertical liquid water/ice content are 49.5-742.5, 24.0-360.0, 39.0-585.0 and 5.2-150.4  $\text{gm}^{-2}$  respectively. The findings from this study illuminates our understanding on parameterization of clouds radiative properties and the effect of the variation on climatic variables.

Further studies were carried out by (Boiyo *et al.*, 2018) on assessment of optical, microphysical and radiative properties of aerosol over a rural site in Kenya. Ground based remote sensing method was used in data collection by taking direct measurements of direct sun and diffuse sky radiances in 15-30minutes interval between spectral ranges of 340-1640nm and 440-1040nm respectively.

The daily average values were used to derive a long term (2007-2015) climatology of each of the variables over the study area (MBITA) (Boiyo *et al.*, 2018). The data retrieved showed a strong variation with the season of the year (Boiyo *et al.*, 2018), this is a clear indicator that the cloud properties (cloud being an aerosol) varies from one region to the other also affects the amount of heat reaching and leaving the surface of the earth.

Also, Y.X. Hu and K. Stamnes (1993), carried out a study on parameterization of the radiative properties of water clouds suitable for use in climate models over Alaska in the United States

of America (USA). It was found out that cloud optical properties depended mainly on the equivalent radius throughout the solar and terrestrial spectrum and they were insensitive to the details of the droplet size distribution such as shape, skewness, width and modality.

This implied that measurements of cloud liquid water content and the extinction coefficient are sufficient to determine cloud optical properties experimentally. The cloud optical properties are then parameterized as a function of cloud liquid water path and equivalent cloud droplet radius by using a nonlinear least – square fitting leading to computations of cloud heating and cooling rates. The findings of this study were then used to infer on the effect of the cloud properties on the climatic patterns over the study domain.

Ali *et al.*, (2019).), carried out a study over Bangladesh in South Asia. The study was aimed at investigating Spatiotemporal characteristics of aerosol optical depth (AOD), Cloud properties and Top of Atmosphere (TOA) Net Cloud Radiative Effect (Net CRE) using MODIS, with CERES sensor and a NOAA HYSPLIT model over Bangladesh for the period 2001-2016. The study investigated the relationship of AOD against cloud parameters and Net CRE over the study domain. Linear regression analysis showed increasing trends for AOD, CF, WV, COT, CTP and CTT. Such studies provide very crucial information on instrumentation and dataset for the study of radiative cloud properties over other regions of the world.

A study was carried out on the relationship between clouds radiative forcing, cloud fraction and cloud albedo in the USA (Liu *et al.*, 2011). The study was done for the period 1997-2009 mainly putting emphasis on three interconnected topics; quantitative relationship between surface shortwave cloud radiative forcing, cloud fraction, and cloud albedo, also, surface based approach for measuring cloud albedo and multiscale variations and covariations were carried out in order to assess the variations in short wave cloud radiative forcing, cloud fraction and cloud albedo (Mueller *et al.*, 2011).

The study collected hourly datasets on cloud radiative forcing, cloud fraction and cloud albedo over the study domain during the specified study period to explore the expected multiscale variations as per the study objectives. The observations from the study were very pivotal for diagnosing and analyzing deficiencies of cloud – radiation parameterizations in climate models (Liu *et al.*, 2011), which in turn assisted in learning and understanding the effects of those variations on climate change.

In (Haywood *et al.*, 2021), a study was done on the Cloud - Aerosol - Radiation interaction over South - East Atlantic. This study region was selected for study since it had high atmospheric aerosol loadings and semi-permanent stratocumulus clouds are co-located providing an optimum region for studying the full range of aerosol – radiation and aerosol – cloud interactions and their perturbations of Earth's radiation budget.

One of the main objectives of the study was to improve the knowledge and representation of the processes determining stratocumulus cloud microphysical and radiative properties and their transitions to cumulus regimes. Satellite measurements were used in this study in order to obtain the relationships of the interactions. The observations of the above study lacked the spatial and temporal resolutions, nor the required level of precision to come up with deeper assessment of the interactions as per the objectives of the study.

From the above cited earlier researches and studies done on radiative properties of clouds, it is evident that Kenya still lags behind in terms of data and knowledge on the radiative properties

of clouds and the effect of those variations in clouds properties on the Earth's radiation budget. This study seeks to address the knowledge gap over the study sites by assessing the spatial temporal radiative properties of clouds over Nairobi, Malindi and Mbita study sites for a period of 16 years from 2005-2020. The cloud parameters assessed by this study were; CER, COT, WV, PR and CA (Zhao *et al.*, 2019). Data from MODIS was retrieved for the entire study period and spatial trends and seasonal variations were obtained through a system of algorithms to provide a comprehensive assessment of the clouds radiative properties.

## II. MATERIALS AND METHODS

### II.1 STUDY AREA

The study was conducted over Kenya, a region that is bounded by Latitudes 5° S - 5° N and Longitudes, 34° E - 42° E. Kenya is an East African country bordered by Ethiopia to the North, Tanzania to the South, South Sudan to the North-west, Uganda to the West and lastly Somalia to the East. The proposed study was done over the Republic of Kenya over three main environmentally distinct regions. The regions of focus were; Nairobi (1° S, 36° E), Mbita (0° S, 34° E) and Malindi (4° S, 40° E).

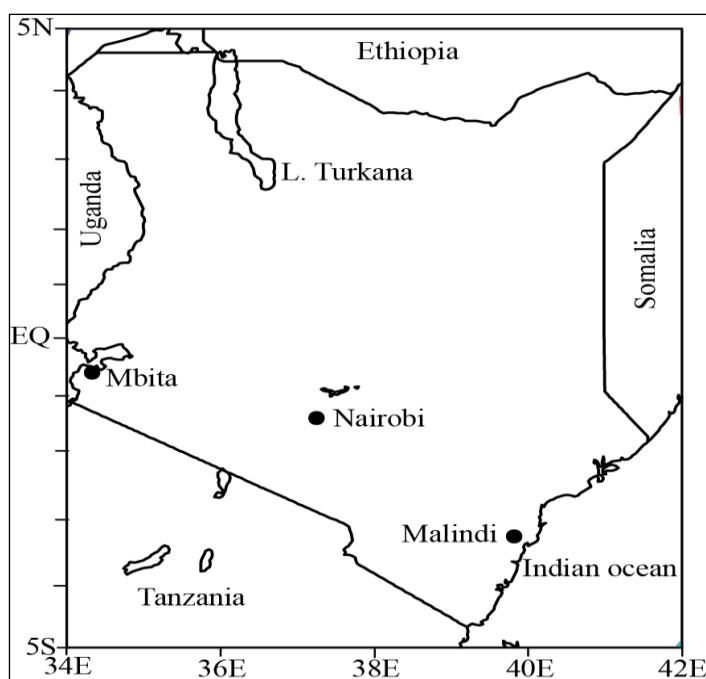


Figure 1: map of Kenya showing the three study sites in Kenya. Source: Authors, (2025).

Nairobi is 1669 m high above the sea level (Mideva, E. M. 2021). The Nairobi region represents the urban climate. The main contributors to the cloud content and characteristics are anthropogenic as a result of industrial-vehicular emissions (Makokha *et al.*, 2013) in the Nairobi area.

The climate here is warm and temperate, and a significant amount of rainfall is received throughout including in the driest month of the year. The annual rainfall is 674mm while the average temperature is 18.8°C. Nairobi has the highest population about 4.397 million people according to the Kenya National Bureau of Statistics (KNBS, 2019).

Malindi is a town in Kilifi County on Malindi bay at the mouth of Sabaki River lying on the Indian Ocean coast of Kenya. It is 120 km north-east of Mombasa with a population of 119,859 (KNBS Census 2019) with an elevation of 118m above the sea

level. According to Koppen-Geiger climate classification of climate, Malindi has a hot tropical type of climate with a winter dry season with an average temperature of about 26.2°C. Malindi receives much rain during summer than winter according to the Koppen – Geiger and an annual rainfall of 755mm. Malindi borders the Indian Ocean and as a result, it experiences the maritime atmosphere which is its largest contributors of the cloud content and properties.

Mbita region is in Homabay county on the shores of Lake Victoria, 1125m above the sea level (Boiyo *et al.*, 2018), with a population of approximately 14,916 (KNBS, 2019). Mbita in this present study represents the Kenyan rural atmosphere. Mbita experiences tropical type of climate and receives an average annual rainfall of approximately 1259.3mm (Bakayoko *et al.*, 2021) even the driest month still has a lot of rainfall. The annual average temperatures for Mbita are about 23.7°C.

Based on the prevailing meteorological conditions, a year was then divided into four seasons. December-January-February (DJF), March- April-May (MAM), June-July-August (JJA) and lastly, the September-October-November (SON) seasons. The DJF and JJA represents the local dry seasons characterized by reduced rainfall (Khamala *et al.*, 2022) while the MAM and SON seasons representing the local wet seasons characterized by enhanced rainfall (Khamala *et al.*, 2022; Boiyo *et al.*, 2018).

### II.2 MODIS SATELLITE SENSOR

MODerate Imaging Spectroradiometer (MODIS) is a Polar-orbiting satellite sensor launched into the Earth orbit by National Aeronautics and Space Administration (NASA) (Barnes *et al.*, 2003) Goddard Space Flight Center on board the Terra (morning orbit) on 18<sup>th</sup> December 1999 and Aqua (afternoon orbit) satellite launched on 4<sup>th</sup> May 2002 (Khamala *et al.*, 2022; Mito *et al.*, 2012; Remer *et al.*, 2005).

With a band of ~2330 km and time-based (Temporal) resolution of 1-2 days (King *et al.*, 2013), and acquires data globally over 36 spectral bands ranging in wavelengths from 0.415 to 14.235µm at three spatial resolutions (2 bands at 250 m, 5 bands at 500 m, and 29 bands at 1 km). MODIS is a 36-band Spectroradiometer that provides several cloud properties using the spectral bands from visible to thermal infrared (Cao *et al.*, 2013).

MOD08-D3 product is also used, which includes daily measurements of optical thickness, cloud top pressure and effective particle radius (Platnick *et al.*, 2003) gridded at a latitude and longitude resolution of 1° × 1° (roughly 100 km×100 km at mid-latitudes). The clouds and Earth's Radiant energy system (CERES) is also a radiometer also on board the Terra and Aqua platforms.

CERES measures the radiation on top of the atmosphere in three channels; the first channel is a shortwave channel for the solar reflected radiation in 0.3-5 µm, the second channel measures the Earth's surface emitted radiation in the atmospheric window of 8-12 µm and lastly, the third channel measures the whole spectrum.

MODIS datasets are very important for collecting various statistics on cloud microphysical properties as a result of aerosols (Platnick *et al.*, 2016). For water vapor, the retrieval for the near infrared region is used. MODIS uses an infrared band to determine the physical properties of clouds in relation to CTT and CTP. Visible and near infrared bands are used to determine the optical and microphysical cloud properties. (Alam *et al.*, 2010).

Daily global level 2 data are provided whereby the cloud particle, phase effective cloud, particle radius and cloud optical thickness are derived using the near infrared channel radiances. Also, the cloud top height, effective emissivity, phases and cloud fraction are produced by the infrared retrieval methods day and



night at 5×5 1-km pixel resolution. In summary, MODIS measures the cloud top properties (temperature, pressure and effective emissivity), cloud thermodynamic phase and cloud optical and microphysical parameters (optical thickness, effective particle radius and water path). The MODIS resolution ranges between 0.25 to 1km (Platnick *et al.*, 2003).

The present study utilized the level 3 monthly data on cloud parameters retrieved from MODIS Terra at a spatial resolution of  $1^\circ \times 1^\circ$  for a period of 16 years (January 2005 to December 2020) to study trends and their significance levels over Kenya.

These data products were sourced from <http://giovanni.gsfc.nasa.gov/giovanni/>. The MODIS datasets are preferred because they are open to the public and more precise to spatial and temporal distribution. The dataset can also enable one to find an empirical relationship between the reflectivity and the microphysical cloud properties which in turn can derive a conclusion of variations of cloud physical properties on climatic variables.

### II.3 MERRA-2 Model

The Modern-Era Retrospective Analysis and Research and Application, version 2 (MERRA-2) atmospheric reanalysis product was newly released and launched by NASA Global Modeling and Assimilation Office (GMAO) to provide data since 1980 (Randles *et al.*, 2017). MERRA-2 replaced the original MERRA dataset (Bosilovich *et al.*, 2015) because of the advances made in the assimilation system that enable assimilation of modern hyper spectral radiances and microwave observations.

Also uses NASA's Ozone profile observations that began in the late 2004. The model is based on the version of the GEOS-5 atmospheric data from 1980 to 2016 at  $0.5^\circ \times 0.625^\circ$  resolution with 72 layers and spanning the satellite observing era from 1980 to the present (Khamala *et al.*, 2022).

Along with the enhancements in the meteorological assimilation, MERRA-2 takes some significant steps towards GMAO's targets of an earth system reanalysis. In the present study, MERRA-2 M2TMNXAER v5.12.4 level-3 monthly time-averaged data on cloud parameters were retrieved at a spatial resolution of  $0.5^\circ \times 0.625^\circ$  from January 2005 to December 2020. These data products were sourced from <http://giovanni.gsfc.nasa.gov/giovanni/>.

### II.4 TROPICAL RAINFALL MEASUREMENT MISSION (TRMM) - SATELLITE

The Tropical Rainfall Measurement Mission (TRMM) is a research satellite that has been actively in operation between 1997 – 2015 mainly designed to improve the understanding of the distribution and variability of precipitation within the Tropics as part of the water cycle in the current climate system. TRMM provides the necessary information needed on rainfall and its associated heat release that helps to power the global atmospheric circulation which shapes both weather and climate (Xie, P., and Arkin, P.A., 1997).

TRMM uses space-borne instruments to increase our understanding of the interactions between water vapor, clouds and precipitation which are core in regulating the Earth's climate. The satellite has a precipitation Radar that provides information on Tropical storm structure and intensification and the TRMM Microwave Imager (TMI) that measures microwave energy emitted by the Earth and its atmosphere in order to quantify the

amount of water vapor, cloud water and the rainfall intensity in the atmosphere.

This study has used TRMM in retrieving data on the precipitation rate over the study domains for the various seasons from January 2005 up to December 2020. The variations in the precipitation rate averages are then used to infer on the variation of the cloud properties on climate. This is so important since precipitation and the hydrological cycle controls the weather and climate of any particular region.

### II.5 METHODS

This section highlights the suitable methods used during the analysis of the data retrieved from MODIS and MERRA-2 in order to obtain any significant statistical interpretation of the data obtained.

#### II.6 LINEAR REGRESSION ANALYSIS

Determination of the combined effect of cloud physical and radiative properties on the climatic parameters such as precipitation rate makes use of the linear regression analysis. Linear regression provides very crucial information and direction on how well a set of variables can predict a particular outcome. It focuses on the conditional probability distribution of the response given the values of the predictors, rather than on the joint probability distribution of all of these variables.

The Linear Regression makes use of the following derivation; let  $Y$  denote the “dependent” variable whose values you wish to predict and let  $X_1 \dots X_k$  denote the “independent” variable from which you wish to predict it, with the value of variable  $X$  in the period  $t$  (or in row  $t$  of the dataset) denoted by  $X_{1t}$ . Then the equation for computing the predicted value of  $Y_t$  is given by;

$$Y_t = b_0 + b_1X_{1t} + b_2X_{2t} + \dots + b_kX_{kt} \quad (1)$$

Where  $Y$  – is a straight-line function of each of the  $X$ -variable holding others constant, the contributions of different  $X$  variables to the predictions are additive.

$b_1, b_2 \dots b_k$  are the slopes of their individual straight-line relationships with  $Y$ , the coefficients of the variables,  $b_0$  – the intercept is the prediction that the model would make if the  $X$ 's were zero. The coefficients and intercept are estimated by least squares i.e., setting them equal to the unique values that minimize the sum of squared errors within the sample of data to which the model is fitted. And the model's prediction errors are typically assumed to be independently and identically normally distributed.

#### II.7 TREND ANALYSIS

The study has determined the spatial and temporal variation of clouds radiative properties through assessing the variations in cloud parameters using trend analysis to determine the variability of the trends in Kenya. Numerous statistical methods exist to quantify trends in the time series of a geophysical variable,

Mann Kendall test has been used by this present study to evaluate annual, seasonal and monthly trends of climatic variables (Audu *et al.*, 2021) for the selected regions in Kenya over a 16-year period (2005-2020) (Syed *et al.*, 2021). The test has been found to be the most appropriate for analysis of climatic changes in climatological time series for detection of a climatic discontinuity (Wanjuhi, 2016).



The method is applied to the long-term data in this study to detect statistically significant trends and the method is preferred when various stations are tested in a single study (Mondal *et al.*, 2012), and for this study, Nairobi, Malindi and Mbita clouds can be studied at the same time using this Mann Kendall test. In this test the null hypothesis ( $H_0$ ) is that there has been no trend in precipitation over time the alternative hypothesis ( $H_1$ ) is that there has been a trend (increasing or decreasing) over time.

The mathematical equations for calculating Mann-Kendall statistics  $S$ ,  $V(s)$  and standardized test statistics  $Z$  are as follows;

$$S = \sum_{i=1}^{n-1} \sum_{j=i+1}^n \text{sig}(X_j - X_i) \quad (2)$$

The application of trend test is done to a time series  $X_i$  that is ranked  $i=1, 2, \dots, n-1$  and  $X_j$ , which is ranked from  $j= i+1, 2, \dots, n$  (Mondal *et al.*, 2012); (Yadav *et al.*, 2014). Each of the data products  $X_i$  is taken as the reference point which is compared with the rest of the data points  $X_j$  so that;

$$\text{Sgn}(X_j - X_i) = \{H(X_j - X_i)\} = 0 \quad (3)$$

$$\text{Sgn}(X_j - X_i) = \begin{cases} +1 & \text{if } (X_j - X_i) > 0 \\ 0 & \text{if } (X_j - X_i) = 0 \\ -1 & \text{if } (X_j - X_i) < 0 \end{cases} \quad (4)$$

$$V(s) = \frac{1}{18} \left[ n(n-1)(2n+5) - \sum_{p=1}^q t_p \right] \quad (5)$$

Equation (3) and (4) yields a standard normal distribution factor  $Z$  given by;

$$Z = \begin{cases} \frac{s-1}{\sqrt{VAR(s)}} & \text{if } s > 0 \\ 0 & \text{if } s = 0 \\ \frac{s+1}{\sqrt{VAR(s)}} & \text{if } s < 0 \end{cases} \quad (6)$$

A positive value of  $Z$  i.e. ( $\text{Sgn}(X_j - X_i)$ ) signifies an upward trend while a negative value of  $Z$  signifies a downward trend in the time series observations in chronological order (Mondal *et al.*, 2012).

In these equations,

$X_i$  and  $X_j$  = are the time series observations in chronological order

$n$  is the length of time series

$t_p$  is the number of ties for  $p^{\text{th}}$  value

$q$  is the number of tied values

Positive  $Z$  – values indicate an upward trend in the hydrologic time series;

Negative  $Z$  -values indicate a negative trend. If  $|Z| > Z_{1-\alpha/2}$ , ( $H_0$ ) is rejected and a statistically significant trend exist in the hydrologic time series.

The critical value of  $Z_{1-\alpha/2}$  for a p value of 0.05 from the standardized normal table is 1.96 (Ahmad *et al.*, 2015). In the present work, linear regression analysis was used to estimate monthly trends in key cloud parameters (CA, WV, COT and CER). The method has been discussed widely by Weatherhead *et al.*, (1998). This test also assists in determining the variations of the climatic variables with time for the period between the year 2005 and 2020.

### III. RESULTS AND DISCUSSIONS

#### III.1 TRENDS IN CLOUD EFFECTIVE RADIUS

Cloud effective radius (CER) refers to the weighted mean of the size distribution of cloud droplets. A ratio of the third to the second moment of droplet size distribution. The trends in Cloud effective radius retrieved from MODIS data were observed to vary both seasonally and spatially ranging from positive to negative trends as obtained during the whole study period.

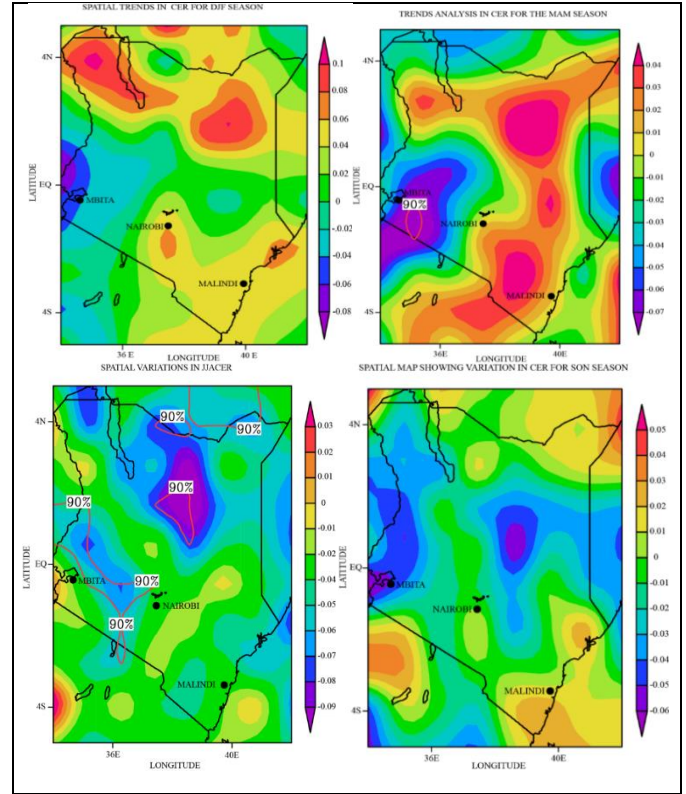


Figure 2: spatial map of Kenya showing the variations of the CER  
Source: Authors, (2025).

Positive seasonal trends in CER are observed in all seasons for the Malindi clouds. Positive trends in DJF season over Nairobi with negative trends in both JJA and SON seasons over Nairobi clouds. And lastly negative trends over Mbita clouds except during the JJA season. It is observed that cloud over Malindi has the highest average CER in all the four seasons as compared to Nairobi and Mbita clouds over the whole study period.

CER is higher over oceans than over the ground (King *et al.*, 2013). Furthermore, it is noted that the effective radius of the polluted cloud will decrease when compared to the pristine cloud (Saponaro, G. 2020) and for this reason, clouds over Nairobi region have the smallest effective radius due to the net industrial emissions of gases and other pollutants from the industries, biomass burning and vehicular emissions.

#### III.2 TRENDS IN CLOUD OPTICAL THICKNESS

COT is a measure of the attenuation of solar radiation passing through the atmosphere; this attenuation is caused by the scattering and absorbing of light by the cloud droplets (<https://svs.gsfc.nasa.gov/30007>). The cloud optical thickness together with effective particle radius are the key parameters which determines radiative properties of clouds such as reflectance, transmission and absorption of solar radiation (Kikuchi, N., *et al.*, 2003).

COT has a number of applications in radiative transfer and climate change as well as in computing the Earth's radiation budget. This study made use of the MODIS terra satellite to retrieve data on COT over the study sites for the 16 years' period. Data obtained was analyzed through linear regression analysis to produce average trends in COT for every season during the study period.

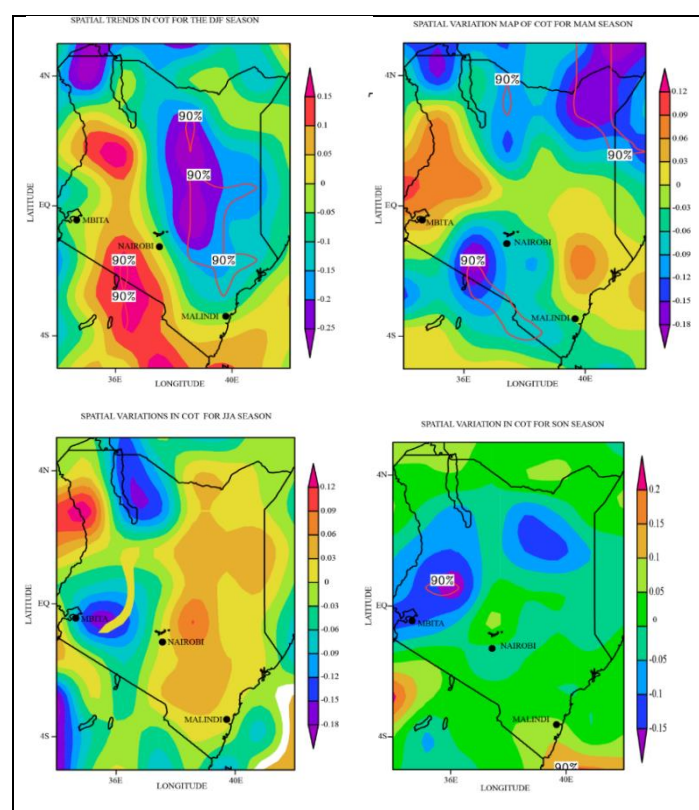


Figure 3: spatial analysis for COT over Kenya.

Source: Authors, (2025).

Using the above displayed spatial maps for the four seasons, COT variation over Kenya can still be analyzed by the use of the different colors displayed in the maps and the color bar shown besides every map, however, this study is only interested in studying the radiative clouds properties over Nairobi, Malindi and Mbita.

Clouds in colder, higher latitudes are optically thicker than clouds in warmer, lower latitudes. Malindi has maritime conditions and aerosols coupled with long range transport of monsoon winds (Makokha, J.W., and Angeyo, H.K. 2013), while Nairobi experiences heavy vehicular and industrial emissions dominance.

These explains the higher COT and hence higher reflectance over Malindi and Nairobi (Makokha, J.W., and Angeyo, H.K. 2013). Clouds in Mbita have the lowest COT and hence lowest reflectance as compared to these other two study regions due to biomass burning and lower latitude in Mbita.

These findings clearly state how the clouds radiative properties vary from one region to the other as a result of the shown variations in the clouds optical thickness over the study regions. The variations in COT affects directly the radiative properties of clouds such as extent of reflectivity of clouds on the incoming solar radiation.

The variations in the cloud reflectance on the incoming solar radiations causes significant effect on the prevailing weather patterns, higher reflection cools the atmosphere as a result of a larger percentage of the solar radiations are reflected back in space,

this leads to a lower temperature being recorded. Lower cloud reflectivity results to heating of the atmosphere leading to higher atmospheric temperatures. The variations in temperature determines the weather and climate of the study sites.

### III.3 TRENDS IN PRECIPITATION RATE

Variations in precipitation rate from one region to another can clearly demonstrate the difference in cloud properties. The precipitation rate depends on several factors such as the prevailing winds, presence of mountains and seasonal winds and the aerosol concentration in those Clouds (Li *et al.*, 2011). Presence of aerosols affects the vertical development of clouds and the precipitation (Li *et al.*, 2011).

This study used the TRMM to retrieve data on daily precipitation rate over Kenya, data obtained was merged into monthly and then seasonally using the software MATLAB which then applied the knowledge of linear regression and trend analysis applications, together with the Illustrator and then GRADS, which then assisted in coming up with the trends and the spatial maps showing the variations in PR over the entire Kenya for all the 16 years of study.

Nairobi and Malindi posted negative trends in PR in all the seasons for all the 16 years of study with no significant trend during the JJA season over Nairobi. Positive trends over Mbita during the DJF, MAM and the SON season, no significant trend in PR during the JJA season over Mbita. It is also evident that spatial variations occur in PR when trend analysis was done over the three study sites in every season.

High precipitation rate is experienced near the equator (Tandon *et al.*, 2018) that is why Mbita receives the highest precipitation rate (0.005mm/day) in almost all the seasons of the year except for JJA season of above 0 when compared with the two other study regions. Heavy precipitation is normally experienced near the equator and decreases with increase in the latitude (Hopkins, L.C., and Holland, G. J. 1997). This clearly indicates the higher moisture content in the Mbita clouds than over Nairobi and Malindi.

Low precipitation rate is experienced over Malindi. This is attributed to the presence of dry monsoon winds which drive away the moisture reducing the moisture content in clouds over Malindi and causing Atmosphere - ocean mechanisms of rainfall anomalies at the coastal regions (Hastenrath *et al.*, 1993).

High precipitation rate over Mbita clearly indicates higher moisture supply/content over Mbita clouds. Emission of aerosols into the atmosphere from vehicles, industries, burning of fuels and all other anthropogenic emissions in Nairobi affects the cloud characteristics, cloud lifetime and vertical cloud development and hence the low precipitation rate (Li *et al.*, 2011).

The variations in the rate of precipitation depicts its dependency on clouds physical and radiative properties which explains the correlation ship between clouds properties and climate change. Figure 3.3 shows the spatial maps of Kenya representing the trends in the precipitation rates over the study sites.



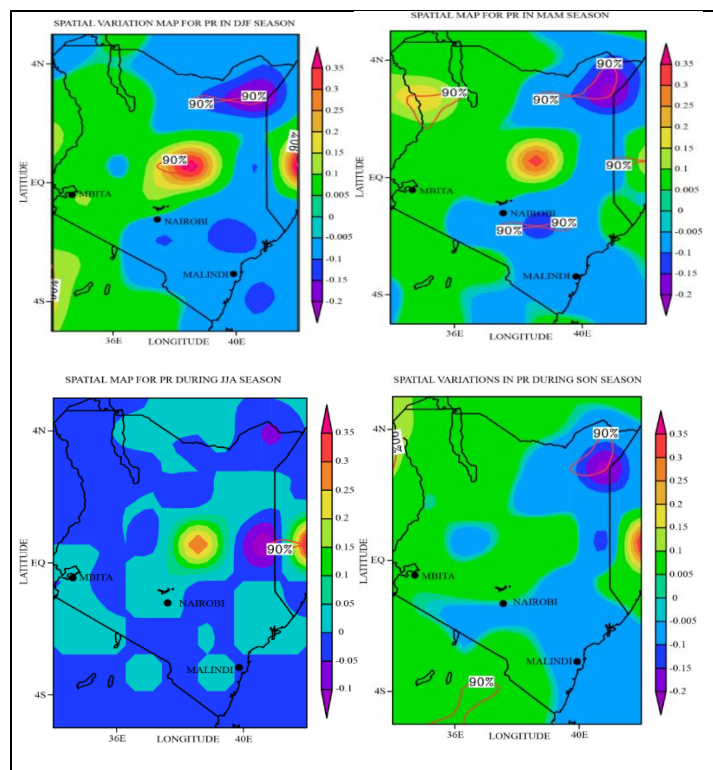


Figure 4: spatial distribution maps for PR over Kenya  
Source: Authors, (2025).

### III.4 TRENDS IN WATER VAPOR

Water vapor is the absolute amount of water dissolved in air. It is measured in millimeters (mm). Water vapor in the atmosphere is a parameter of great importance in climate models because it plays a role as a greenhouse gas (Nilsson, T., and Elgered, G. 2008). In fact, studies show that only an increase of water vapor in the atmosphere by only 20 percent would cause a larger impact than doubling of carbon (iv) oxide concentration (Buehler *et al.*, 2006). The study made use of the MODIS data during the study period to investigate the variation of the cloud water vapor content and the net effect of the WV on the prevailing climatic conditions.

This cloud parameter is also important in the study of clouds and climate since the amount of water vapor in the atmosphere normally affects the formation of secondary aerosols such as nitrates and sulfates which in response affects the cloud characteristics and the climate (Ding *et al.*, 2021). Values of the cloud water vapor content were obtained from the models and satellites described in the chapter three of this study, monthly averages for all the study period were merged into seasons so that the average values and spatial variation maps are drawn for the study domains.

Positive trends in water vapor across all the seasons apart from the DJF season over Nairobi where negative trends were observed. Malindi and Mbita experiences almost similar trends most of the seasons as a result of both being closer to the large water bodies that is the Indian ocean and the Lake Victoria respectively. The amount of water vapor contained in the clouds and the hydrological cycle cannot be separated this is due to the fact that the hydrological cycle transports the water vapor present in the clouds (Quan *et al.*, 2022), this indicates the high dependence of climate on the clouds and the hydrological cycle. MODIS – Terra retrieval separately reveals the outcomes for WV in the clouds over Nairobi, Malindi and Mbita. Clouds over Mbita has the highest average water vapor content in the atmosphere (between 0

and 0.015) as compared Malindi and Nairobi clouds with the least averages for all the four seasons of the study duration. It is also observed that Malindi and Mbita produced the highest averages of the amount of water vapor during the DJF season.

The difference in the amount of WV content is attributed to the variations in the temperature of these study regions. This is because the temperature of the surrounding atmosphere limits the maximum amount of water vapor the atmosphere can contain ([https://www.acs.org/climate science](https://www.acs.org/climate-science)). WV accounts for about 60% of the Earth's greenhouse warming effect and the amount of water vapor is controlled by the temperature of that particular region ([https://www.acs.org/climate science](https://www.acs.org/climate-science)).

The two study regions Mbita and Malindi experiences relatively higher amounts of temperature that causes the higher rate of both surface water evaporation and the evaporation of the waters from both Lake Victoria and the Indian ocean respectively, this higher rate of water evaporations leads to higher WV content in the clouds over those two regions as compared to the clouds over Nairobi. Figure 5 shows the spatial map showing the variation in water vapor content in clouds over the three study regions for the period 2005-2020.

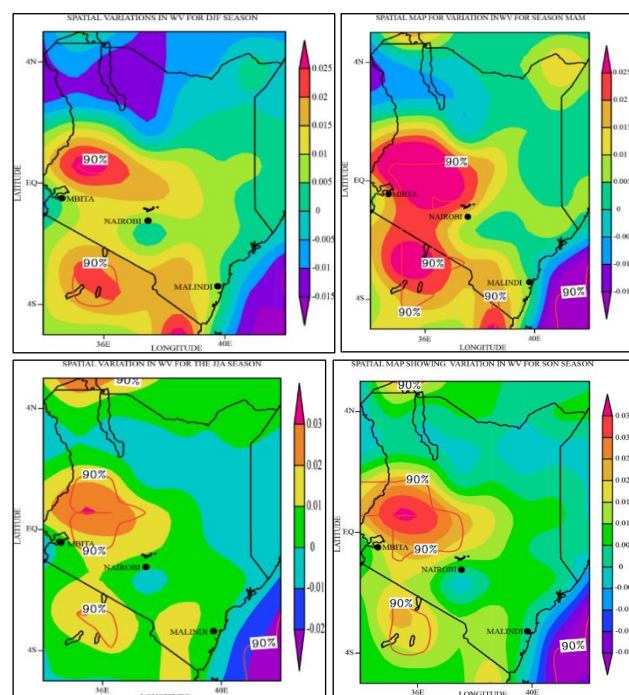


Figure 5: showing the spatial variation map for water vapor content.

Source: Authors, (2025).

Looking at the spatial distribution maps, the values of water vapor content varies periodically and seasonally throughout the study period which in turn indicates the changes in the atmospheric content and hence change in climate.

There is a possibility that adding more WV to the atmosphere could produce a negative feedback effect (Sherwood *et al.*, 2010). This could happen if more WV leads to formation of clouds.

Water vapor equably lies at the heart of all key terrestrial atmospheric processes (Sherwood *et al.*, 2010), presence of water vapor in the atmosphere is essential for development of disturbed weather influences both directly and indirectly through formation of clouds, affecting the planetary radiative balance and influences surface fluxes (Sherwood *et al.*, 2010). Clouds reflect sunlight and reduce the amount of energy that reaches the Earth's surface to

warm it. If the amount of solar warming decreases, then the temperature of that particular region also decreases. In that case, the effect of adding more water vapor would be cooling rather than warming. These indicates the high dependency of both regional and global climates on the cloud characteristics.

Since the amount of water vapor in the atmosphere acts as the greenhouse gases, variations in its content great influences the climate of any regions just like other greenhouse gases which causes global warming, higher precipitation rates, melting of ice, increase in sea, ocean and lake water levels as a result of melting of ice and high precipitation levels. All these effects result into adverse weather patterns.

Water vapor content in the clouds becomes one of the major parameters that can indicate and also be used to assess clouds physical characteristics and hence its study and findings can enable scholars to clearly explain the concepts of climate change since water vapor has a strong positive feedback on climate changes driven by other influences (Sherwood *et al.*, 2010).

### III.5 CLOUD ALBEDO

Cloud albedo is a measure of the albedo or reflectivity of cloud. Higher albedo implies higher cloud cover and lower absorption of solar energy. This parameter strongly influences the Earth's energy budget (Feinberg, A. 2022).

Cloud albedo depends on several factors which includes the total mass of water, size and shape of the cloud droplets and the distribution of the particles in space (Schulze *et al.*, 2020). The major causes of the variation in cloud albedo are the liquid water path, aerosol indirect effect and the Zenith angle (Gryspeerdt *et al.*, 2019). Seasonal values of Cloud Albedo were retrieved from MERRA-2 model for the years 2005 -2020 the spatial maps showing the variations in trends were done in order to assess the significance of the trends using trend analysis.

Negative trends in MAM and JJA seasons for all the study sites, negative trends in CA over Nairobi and Malindi during the SON season with positive trends over Mbita during the same season. And lastly, positive trends in spatial variations during the DJF season over the three study sites. These variations in CA are key in assessing the general characteristics of clouds and their effect on climatic variables.

It is evident that variations in the cloud albedo has an effect on the regional climate, when Cloud Albedo increases, reduction in the absorbed solar radiation takes place leading to cooling of the atmosphere (Bala *et al.*, 2011), it is also taken into account that variations in air pollutions leads to variations in cloud condensation nuclei, creating a feedback loop that influences the atmospheric temperature, relative humidity and cloud formation (Wiedensohler *et al.*, 2009) depending on cloud and regional characteristics eg; aerosols reduces the precipitation efficiency resulting in positive feedback loop in which decreased precipitation efficiency increase aerosol atmospheric longevity.

High cloud albedo represents thick clouds such as stratocumulus, reflect a large amount of incoming solar radiation (Liou, K.N. 1976), low solar radiation represents cooling of the atmosphere. Low cloud albedo represents thin clouds such as cirrus clouds, transmit more solar radiation, heating up the atmosphere causing warming of the atmosphere. The variations in cloud

Albedo over Kenya can be represented in spatial maps. See Figure 6;

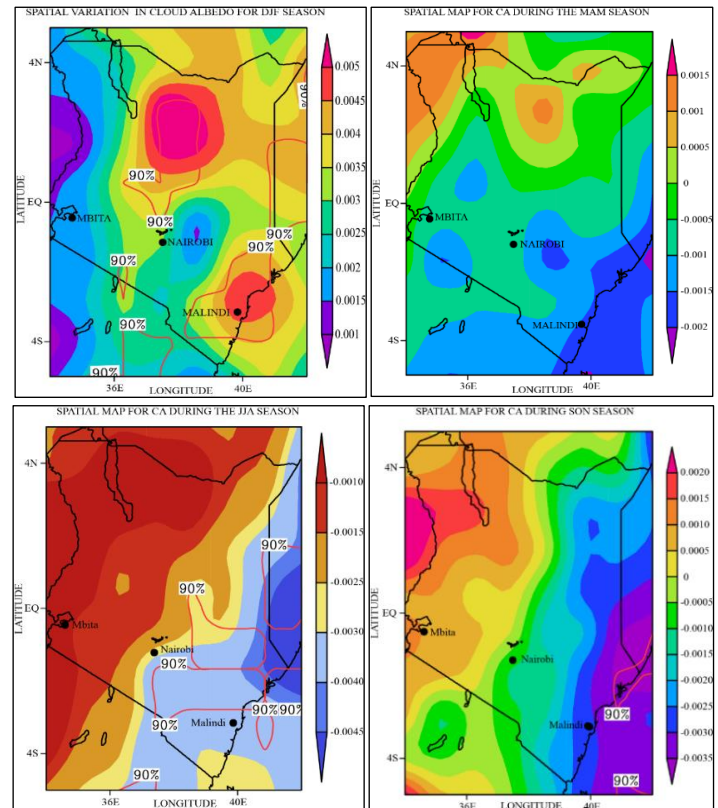


Figure 6: showing the spatial variation map for Cloud Albedo.

Source: Authors, (2025).

### IV. CONCLUSIONS

Using the data sets retrieved from MODIS sensor, MERRA-2 model and the TRMM, the present study revealed an in depth understanding of trends in CER, COT, WV, PR and CA as well as the spatial distribution in the above parameters over Kenya for the period 2005-2020. The spatial variations in cloud parameters from MODIS- sensor, the MERRA-2 model and the TRMM were used to infer on the general radiative properties of clouds over the three study sites and their effect on the climate.

The study domains were dominated by positive trends in most of the cloud parameters, with a significance of 90% in most of the seasons. The variation in trends in clouds radiative properties is attributed to biomass burning, vehicular and industrial emissions that contributes to foreign materials into the atmosphere over the study domain.

The study domain was dominated by negative trends in CER, CA and COT except for CER over Malindi in all seasons and Nairobi during the DJF and MAM seasons. Seasonally, positive trends in Water vapor (WV) were observed in all the season over the study domain due to changes in climatic condition and anthropogenic activities such as biomass burning and both vehicular and industrial emissions which increases the cloud lifetime and aerosols acting as the condensation nuclei in the atmosphere increasing the cloud formation and hence increasing the amount of water in the atmosphere.

The study domain significantly exhibited decreasing and increasing trends in all the cloud parameters over the study period clearly indicating variations in clouds physical properties caused as a result of different clouds contributors and modulators of cloud characteristics. The knowledge on spatial trends and spatial



distribution maps is very important. Both seasonal and regional variations in clouds parameters would mean variations in climatic variables which then form a basis of understanding the concepts of climatic variations and climate change. This important information and data is lacking over Kenya hence opening a link and a need for further investigation and research on clouds radiative properties.

## V. AUTHOR'S CONTRIBUTION

**Conceptualization:** Sostine N. Makokha<sup>1</sup>, John W. Makokha<sup>2</sup> and Festus B. Kelonye<sup>3</sup>.

**Methodology:** Sostine N. Makokha<sup>1</sup> and John W. Makokha<sup>2</sup>.

**Investigation:** Sostine N. Makokha<sup>1</sup> and John W. Makokha<sup>2</sup>.

**Discussion of results:** Sostine N. Makokha<sup>1</sup>, John W. Makokha<sup>2</sup> and Festus B. Kelonye<sup>3</sup>.

**Writing – Original Draft:** Sostine N. Makokha<sup>1</sup>.

**Writing – Review and Editing:** Sostine N. Makokha<sup>1</sup> and John W. Makokha<sup>2</sup>.

**Resources:** John W. Makokha<sup>2</sup>.

**Supervision:** John W. Makokha<sup>2</sup> and Festus B. Kelonye<sup>3</sup>.

Approval of the final text: Sostine N. Makokha<sup>1</sup>, John W. Makokha<sup>2</sup> and Festus B. Kelonye<sup>3</sup>.

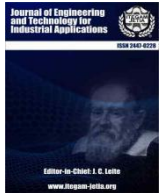
## VI. ACKNOWLEDGMENTS

The authors wish to pass their sincere gratitude to the NASA and Giovanni online analysis and visualization system for providing and processing MODIS, MERRA-2 data used in this study. The lead author (Mr. Sostine N. Makokha) extends sincere gratitude to the Ministry of Higher Education, Science and Technology of Kenya and Kibabii University, Kenya, for providing an opportunity to undertake Masters of Science (physics) studies.

## VII. REFERENCES

- [1] Alam, K., Iqbal, M. J., Blaschke, T., Qureshi, S., & Khan, G. (2010). Monitoring spatio-temporal variations in aerosols and aerosol–cloud interactions over Pakistan using MODIS data. *Advances in Space Research*, 46(9), 1162-1176.
- [2] Ali, M. A., Islam, M. M., Islam, M. N., and Almazroui, M. (2019). Investigations of MODIS AOD and cloud properties with CERES sensor based net cloud radiative effect and a NOAA HYSPLIT Model over Bangladesh for the period 2001–2016. *Atmospheric Research*, 215, 268-283.
- [3] Audu, M. O., Ejembi, E., and Igbawua, T. (2021). Assessment of Spatial Distribution and Temporal Trends of Precipitation and Its Extremes over Nigeria. *American Journal of Climate Change*, 10(3), 331-352.
- [4] Bakayoko, A., Galy-Lacaux, C., Yoboué, V., Hickman, J. E., Roux, F., Gardrat, E., ... and Delon, C. (2021). Dominant contribution of nitrogen compounds in precipitation chemistry in the Lake Victoria catchment (East Africa). *Environmental Research Letters*, 16(4), 045013.
- [5] Bala, G., Caldeira, K., Nemani, R., Cao, L., Ban-Weiss, G., and Shin, H. J. (2011). Albedo enhancement of marine clouds to counteract global warming: impacts on the hydrological cycle. *Climate dynamics*, 37(5), 915-931.
- [6] Barnes, W. L., Xiong, X., Guenther, B. W., and Salomonson, V. (2003). Development, characterization, and performance of the EOS MODIS sensors. *Earth Observing Systems VIII*, 5151, 337-345.
- [7] Boiyo, R.K., Kumar, R. and Zhao, T. (2018) Optical, Microphysical and Radiative properties of Aerosols over a tropical Rural site in Kenya, East Africa: source Identification, Modification and Aerosols Type Discrimination. *Journal Atmospheric Environment*, 177, 234-252.
- [8] Boiyo, R., Kumar, K. R., Zhao, T., and Bao, Y. (2017). Climatological analysis of aerosol optical properties over East Africa observed from space-borne sensors during 2001–2015. *Atmospheric environment*, 152, 298-313.
- [9] Bosilovich, M. G., Lucchesi, R., and Suarez, M. (2015). *MERRA-2: File specification*. Global Modeling and Assimilation Office, Maryland.
- [10] Buehler, S. A., Von Engel, A., Brocard, E., John, V. O., Kuhn, T., and Eriksson, P. (2006). Recent developments in the line-by-line modeling of outgoing longwave radiation. *Journal of Quantitative Spectroscopy and Radiative Transfer*, 98(3), 446-457.
- [11] Calbo, J., Pages, D., and Gonzale, J., (2005): Empirical studies of cloud effects on UV radiation; a review, *Review Geophysics*, 43, 1-28.
- [12] Cao, C., De Luccia, F. J., Xiong, X., Wolfe, R., and Weng, F. (2013). Early on-orbit performance of the visible infrared imaging radiometer suite onboard the Suomi National Polar-Orbiting Partnership (S-NPP) satellite. *IEEE Transactions on Geoscience and Remote Sensing*, 52(2), 1142-1156.
- [13] Ding, J., Dai, Q., Zhang, Y., Xu, J., Huangfu, Y., and Feng, Y. (2021). Air humidity affects secondary aerosol formation in different pathways. *Science of The Total Environment*, 759, 143540.
- [14] en.wikipedia.org/wiki/cloud.date accessed on 25/09/2021.
- [15] Feinberg, A. (2022). A re-radiation model for the earth's energy budget and the albedo advantage in global warming mitigation. *Dynamics of Atmospheres and Oceans*, 97, 101267.
- [16] George, R. C., and Wood, R. (2010). Subseasonal variability of low cloud radiative properties over the southeast Pacific Ocean. *Atmospheric Chemistry and Physics*, 10(8), 4047-4063.
- [17] Gryspeerdt, E., Goren, T., Sourdeval, O., Quaas, J., Mülmenstädt, J., Dipu, S., and Christensen, M. (2019). Constraining the aerosol influence on cloud liquid water path. *Atmospheric Chemistry and Physics*, 19(8), 5331-5347.
- [18] Hastenrath, S., Nicklis, A., and Greischar, L. (1993). Atmospheric-hydrospheric mechanisms of climate anomalies in the western equatorial Indian Ocean. *Journal of Geophysical Research: Oceans*, 98(C11), 20219-20235.
- [19] Haywood, J. M., Abel, S. J., Barrett, P. A., Bellouin, N., Blyth, A., Bower, K. N., and Zuidema, P. (2021). The CLOUD–Aerosol–Radiation interaction and forcing: Year 2017 (CLARIFY-2017) measurement campaign. *Atmospheric Chemistry and Physics*, 21(2), 1049-1084.
- [20] Hopkins, L. C., and Holland, G. J. (1997). Australian heavy-rain days and associated east coast cyclones: 1958–92. *Journal of Climate*, 10(4), 621-635.
- [21] <https://svs.gsfc.nasa.gov/30007>. 04/10/2022
- [22] Hu, Y. X., and Stamnes, K. (1993). An accurate parameterization of the radiative properties of water clouds suitable for use in climate models. *Journal of climate*, 6(4), 728-742.
- [23] Ichoku C., Kaufman, Y.J, Remor, L. A. and Levy R. (2004). Global aerosol remote sensing from MODIS. *Advances in Space Research* 34: 820-827.
- [24] KNBS and Republic of Kenya (2019a), 2019 Kenya Population and Housing Census: Vol 1: Population by County and Sub-County,
- [25] Khamala, G. W., Makokha, J. W., Boiyo, R., and Kumar, K. R. (2022). Long-term climatology and spatial trends of absorption, scattering, and total aerosol optical depths over East Africa during 2001–2019. *Environmental Science and Pollution Research*, 1-15.
- [26] Kikuchi, N., Nakajima, T., Kumagai, H., Kuroiwa, H., Kamei, A., Nakamura, R., and Nakajima, T. Y. (2006). Cloud optical thickness and effective particle radius derived from transmitted solar radiation measurements: Comparison with cloud radar observations. *Journal of Geophysical Research: Atmospheres*, 111(D7).
- [27] King, M. D., Platnick, S., Menzel, W. P., Ackerman, S. A., and Hubanks, P. A. (2013). Spatial and temporal distribution of clouds observed by MODIS onboard the Terra and Aqua satellites. *IEEE transactions on geoscience and remote sensing*, 51(7), 3826-3852.
- [28] Li, Z., Niu, F., Fan, J., Liu, Y., Rosenfeld, D., and Ding, Y. (2011). Long-term impacts of aerosols on the vertical development of clouds and precipitation. *Nature Geoscience*, 4(12), 888-894.

- [29] Lin, W., Zhang, M., and Loeb, N. G. (2009). Seasonal variation of the physical properties of marine boundary layer clouds off the California coast. *Journal of climate*, 22(10), 2624-2638.
- [30] Li, W., Zhang, F., Shi, Y. N., Iwabuchi, H., Zhu, M., Li, J., and Ishimoto, H. (2020). Efficient radiative transfer model for thermal infrared brightness temperature simulation in cloudy atmospheres. *Optics Express*, 28(18), 25730-25749.
- [31] Liou, K. N. (1986). Influence of cirrus clouds on weather and climate processes: A global perspective. *Monthly Weather Review*, 114(6), 1167-1199.
- [32] Liou, K. N., and Wittman, G. D. (1979). Parameterization of the radiative properties of clouds. *Journal of Atmospheric Sciences*, 36(7), 1261-1273.
- [33] Liou, K. N. (1976). On the absorption, reflection and transmission of solar radiation in cloudy atmospheres. *Journal of Atmospheric sciences*, 33(5), 798-805.
- [34] Liu, Y., Wu, W., Jensen, M. P., and Toto, T. (2011). Relationship between cloud radiative forcing, cloud fraction and cloud albedo, and new surface-based approach for determining cloud albedo. *Atmospheric Chemistry and Physics*, 11(14), 7155-7170.
- [35] Makokha, J. W., and Angeyo, H. K. (2013). Investigation of radiative characteristics of the Kenyan atmosphere due to aerosols using sun spectrophotometry measurements and the COART model.
- [36] Makokha, J.W., Kimani, J.N. and Angeyo, H.K. (2013) Estimation of Radiative Forcing Due to Aerosols over selected sites in Kenya. *Journal of meteorological Research*, 6, 3-13.
- [37] Matuszko, D. (2012). Influence of the extent and genera of cloud cover on solar radiation intensity. *International Journal of climatology*, 32(15), 2403-2414.
- [38] Mideva, E. M. (2021). *Atrium Daylight Penetration in Dense Apartment Blocks. a Case of Roysambu Nairobi, Kenya*. University of Nairobi School of the Environment Department of Architecture NS Building Science, Nairobi.
- [39] Mondal, A., Kundu, S., and Mukhopadhyay, A. (2012). Rainfall trend analysis by Mann-Kendall test: A case study of north-eastern part of Cuttack district, Orissa. *International Journal of Geology, Earth and Environmental Sciences*, 2(1), 70-78.
- [40] Mueller, Richard; Trentmann, Jörg; Träger-Chatterjee, Christine; Posselt, Rebekka; Stöckli, Reto (2011). "The Role of the Effective Cloud Albedo for Climate Monitoring and Analysis". *Remote Sensing*. 3 (11): 23052320. Bibcode:2011RemS3.2305M. doi:10.3390/rs3112305. ISSN 2072-4292.
- [41] National Aeronautics and Space Administration, Science Mission Directorate. (2010). The Earth's Radiation Budget. Retrieved [ october 21, 2022], from NASA Science website: [http://science.nasa.gov/ems/13\\_radiationbudget](http://science.nasa.gov/ems/13_radiationbudget)
- [42] Nilsson, T., and Elgered, G. (2008). Long-term trends in the atmospheric water vapor content estimated from ground-based GPS data. *Journal of Geophysical Research: Atmospheres*, 113(D19).
- [43] Platnick, S., King, M., Ackerman, S., Menzel, W., Baum, B., Riedi, J., and Frey, R.,(2003): The MODIS cloud products;algorithms and examples from Terra, *IEEE Transactions on Geoscience and Remote sensing*, 41, 459-473.
- [44] Platnick, S., Meyer, K. G., King, M. D., Wind, G., Amarasinghe, N., Marchant, B., ... and Riedi, J. (2016). The MODIS cloud optical and microphysical products: Collection 6 updates and examples from Terra and Aqua. *IEEE Transactions on Geoscience and Remote Sensing*, 55(1), 502-525
- [45] Quan, Q., Liang, W., Yan, D., and Lei, J. (2022). Influences of joint action of natural and social factors on atmospheric process of hydrological cycle in Inner Mongolia, China. *Urban Climate*, 41, 101043.
- [46] Rana, P., and Sathiyamoorthy, V. (2018). INVESTIGATION OF CLOUDS AND CLOUD RADIATIVE FORCING ON THE WINDWARD SIDE OF THE MADAGASCAR MOUNTAIN CHAINS. *The International Archives of Photogrammetry, Remote Sensing and Spatial Information Sciences*, 42, 901-906.
- [47] Randles, C. A., Da Silva, A. M., Buchard, V., Colarco, P. R., Darmenov, A., Govindaraju, R., and Flynn, C. J. (2017). The MERRA-2 aerosol reanalysis, 1980 onward. Part I: System description and data assimilation evaluation. *Journal of climate*, 30(17), 6823-6850.
- [47] Remer, L. A., Kaufman, Y. J., Tanré, D., Mattoo, S., Chu, D. A., Martins, J. V., and Holben, B. N. (2005). The MODIS aerosol algorithm, products, and validation. *Journal of the atmospheric sciences*, 62(4), 947-973.
- [48] Roebeling, R. A., Feijt, A. J., and Stammes, P. (2006). Cloud property retrievals for climate monitoring: Implications of differences between Spinning Enhanced Visible and Infrared Imager (SEVIRI) on METEOSAT-8 and Advanced Very High Resolution Radiometer (AVHRR) on NOAA-17. *Journal of Geophysical Research: Atmospheres*, 111(D20).
- [49] Saponaro, G. (2020). *Application of remotely-sensed cloud properties for climate studies*. *Journal of Geophysical Research: Atmospheres*, 185, 1-5. <http://hdl.handle.net/10138/308930>.
- [50] Schulze, B. C., Charan, S. M., Kenseth, C. M., Kong, W., Bates, K. H., Williams, W., and Seinfeld, J. H. (2020). Characterization of aerosol hygroscopicity over the Northeast Pacific Ocean: Impacts on prediction of CCN and stratocumulus cloud droplet number concentrations. *Earth and Space Science*, 7(7), e2020EA001098.
- [51] Sherwood, S. C., Roca, R., Weckwerth, T. M., and Andronova, N. G. (2010). Tropospheric water vapor, convection, and climate. *Reviews of Geophysics*, 48(2).
- [52] Tandon, N. F., Zhang, X., and Sobel, A. H. (2018). Understanding the dynamics of future changes in extreme precipitation intensity. *Geophysical Research Letters*, 45(6), 2870-2878.
- [53] Wanjuhi, D. M. (2016). *Assessment of Meteorological Drought Characteristics in North Eastern Counties of Kenya* (Doctoral dissertation, University of Nairobi).
- [54] Wiedensohler, A., Cheng, Y. F., Nowak, A., Wehner, B., Achtert, P., Berghof, M., ... and Pöschl, U. (2009). Rapid aerosol particle growth and increase of cloud condensation nucleus activity by secondary aerosol formation and condensation: A case study for regional air pollution in northeastern China. *Journal of Geophysical Research: Atmospheres*, 114(D2).
- [55] Xie, P., and Arkin, P. A. (1997). Global precipitation: A 17-year monthly analysis based on gauge observations, satellite estimates, and numerical model outputs. *Bulletin of the american meteorological society*, 78(11), 2539-2558.
- [56] Zhang, J., Liu, P., Zhang, F., and Song, Q. (2018). Cloud Net: Ground-based cloud classification with deep convolutional neural network. *Geophysical Research Letters*, 45(16), 8665-8672.
- [57] Zhao, C., Chen, Y., Li, J., Letu, H., Su, Y., Chen, T., and Wu, X. (2019). Fifteen-year statistical analysis of cloud characteristics over China using Terra and Aqua Moderate Resolution Imaging Spectroradiometer observations. *International Journal of Climatology*, 39(5), 2612-2629.



RESEARCH ARTICLE

OPEN ACCESS

## A NOVEL HYBRID STEGANOGRAPHY APPROACH FOR SECURING TEXT, IMAGES, AND AUDIO WITH ROBUST ENCRYPTION IN AUDIO STEGANOGRAPHY

T Srinivasa Padmaja<sup>1</sup> and Shaik Mahaboob Basha<sup>2</sup>

<sup>1</sup> Dept of E.C.E, Research Scholar, Jawaharlal Nehru Technological, Anantapur, India.

<sup>2</sup> Dept of E.C.E Professor, N.B.K.R. Institute of Science & Technology, Vidyannagar, India.

<sup>1</sup><http://orcid.org/0000-0001-6218-910x>, <sup>2</sup><http://orcid.org/0000-0002-5843-4472>

Email: [padmajats@gmail.com](mailto:padmajats@gmail.com), [mohisin7@yahoo.co.in](mailto:mohisin7@yahoo.co.in)

### ARTICLE INFO

#### Article History

Received: August 11, 2024

Revised: October 20, 2025

Accepted: March 15, 2025

Published: April 31, 2025

#### Keywords:

Hybrid Steganography,  
Audio Steganography,  
Data Encryption,  
Secure Communication,  
Data Security.

### ABSTRACT

This research proposes an imaginative hybrid steganography technique meant to strengthen the protection of text, pictures, and audio in response to the critical problem of information security. The incorporation of strong encryption in audio steganography adds to the innovation. In response to rising dangers in digital communication, the study investigates the vulnerabilities of text, picture, and audio mediums. The inquiry looks into White Space and Least Significant Bit (LSB) approaches for text steganography, while Quantization Index Modulation (QIM) is combined with LSB for image steganography. A revolutionary hybrid solution for audio steganography develops, combining Adaptive QIM and LSB. Python implementations are provided to demonstrate the use and effectiveness of these strategies in maintaining data integrity and secrecy. The study broadens its reach by presenting a novel data security paradigm in audio files that combines AES encryption, Rubik's Cube-like scrambling, and adaptive steganography. The method begins with strong AES encryption, which is then followed by a clever scrambling algorithm inspired by the Rubik's Cube. The distinguishing characteristic is seen in the last stage, when adaptive QIM embeds scrambled data into audio files, thereby disguising encrypted material. This innovative solution not only strengthens data security through the complexities of AES and Rubik's Cube-like scrambling, but it also provides a full framework for safe data transfer, exemplifying the synergy of classical encryption and current steganography techniques. The results reveal a considerable improvement in information security across various digital forms, indicating a big step forward in reinforcing sensitive data transfer.



Copyright ©2025 by authors and Galileo Institute of Technology and Education of the Amazon (ITEGAM). This work is licensed under the Creative Commons Attribution International License (CC BY 4.0).

### 1. INTRODUCTION

The current explosion in web technology has resulted in increasing social networking and online media sharing. Images, music, and video are exchanged in massive amounts via the internet. Obviously, data and privacy must be protected. To overcome this barrier, employ chaotic systems for picture encryption to improve security in the field of Steganography [1] (Aruna et al., 2023). Steganography and steganalysis are key tools for

information concealing and extraction. Steganography is concerned with strategies for concealing information, whereas steganalysis finds the concealed information with little or no knowledge of the steganography algorithm or its parameters [2](Kumar al., 2023). The fast evolution of digital communication technology has ushered in an era where information security and privacy are of the utmost significance. This research study digs into the intricate world of steganography, a critical component of current cybersecurity, and investigates novel strategies for hiding information inside various digital mediums [3] (Nasr et al., 2023). The study



presents and investigates cutting-edge techniques such as whitespace manipulation, Quantization Index Modulation (QIM), and Least Significant Bit (LSB) embedding, with a focus on text, image, and audio steganography [4](Monika et al., 2023).

Text Steganography is at the forefront of this investigation, demonstrating how messages may be surreptitiously buried within the whitespace of text documents using the intricacy of binary encoding to preserve stealth. Image Steganography expertly complements this, using QIM and LSB methods to encode binary messages into an image's pixel structure, quietly modifying its composition without detectable alterations [5](Adhanadi et al., 2020). The research then delves into Audio Steganography, which involves embedding messages in audio recordings using a combination of LSB and Adaptive QIM. This technology assures that the encoded data is imperceptible to the human ear, demonstrating the intricacy of modern steganographic technologies [6](Subhi et al., 2020).

Furthermore, the study integrates Advanced Encryption Standard (AES) encryption with Rubik's Cube-like scrambling as well as audio steganography, a ground-breaking method in digital security [7](Sultani et al., 2023). This approach not only encrypts but also obfuscates data, making pattern detection in encrypted data much more difficult. The integration of these sophisticated approaches, each with its own set of obstacles and weaknesses, is systematically examined to get a thorough grasp of their potential and limits [8](Zhuo et al., 2023). Aside from technical research, the paper examines the ethical and legal issues that emerge with the deployment of such advanced data protection mechanisms, notably in the areas of privacy and digital rights. Looking ahead, the possible influence of upcoming technologies such as quantum computing and artificial intelligence on the fields of cryptography and steganography is also examined [9] (Joshi et al., 2022). The research study intends to make a substantial contribution to the field of secure digital communication by using a multidimensional approach. It emphasizes the rising relevance and promise of steganography in information security, emphasizing its important role in an increasingly linked digital world [10] (Abikoye et al., 2022).

## II. THEORETICAL REFERENCE

The literature research included here analyses important advancements in steganography techniques over a wide range of domains, including text, image, audio, and video. Notable contributions include the use of bit cycling to increase the security of encrypted text, the use of LSB methods in audio steganography for enhanced concealment, and the invention of unique picture and video steganography algorithms. Maintaining data integrity, optimizing embedding procedures for real-time applications, and resolving the trade-off between data capacity and security are among the challenges mentioned. Future research directions include improving algorithms, improving encryption methods, and doing comprehensive testing to increase the overall efficacy, security, and practicality of steganographic systems in secure data transfer and concealment.

The unique use of bit cycling in the area of secure communication is highlighted by the work of [11] (W. Abood et al., 2022) who use this approach to improve the security of encrypted text through the refining of the Least Significant

Bit (LSB) method. This is an important contribution to audio steganography methods, presenting a unique methodology that has shown excellent results in improving the concealment of encrypted data within audio recordings. The protocol's effectiveness is based on its ability to improve security and effectively avoid discovery. Nonetheless, issues such as sensitivity to sophisticated steganalysis methods, probable loss of audio quality while embedding, and embedding capacity constraints have emerged. Addressing these issues in future research will need a concentrated effort to preserve audio quality, investigate complex algorithms to improve detection resistance, and increase embedding capacity while keeping a high degree of confidentiality. In the context of India, [12] (Kumar, et al., 2023) created a technique for hiding sensitive information in text, image, video, and audio files by applying the Least Significant

Bit (LSB) algorithm (MH). Their study showed that secret data could be successfully concealed; however, issues persisted with the LSB algorithm's ability to embed bigger data volumes without appreciably degrading the quality of the host media and the method's resilience against sophisticated detection techniques. By strengthening the algorithm's resistance to steganalysis techniques and investigating cutting-edge data embedding techniques to reduce quality loss in host media, these challenges may be overcome and the steganographic approach's overall efficacy increased. In order to improve data hiding capabilities and fortify security, [13] (Tasnim, et al., 2023) introduced an audio steganography technique.

The developed technique demonstrated improved security measures and a greater ability to conceal information in audio files, which led to encouraging findings from the study. The authors did, however, face some challenges, including the need to maintain audio quality when embedding data and potential issues with the method's computational complexity, which could have an impact on real-time applications. Subsequent studies could tackle these problems by optimizing the algorithm's performance to reduce computational overhead and simplifying the embedding process to reduce the loss of audio quality.

This would make the suggested audio steganography method more beneficial and effective. A novel text steganography method was introduced by [14] (Singh et al., 2023) in their study. Although the uniqueness of their research held promise, more research is necessary to address issues like the method's security and resilience to steganalysis techniques. Future research should concentrate on conducting thorough security evaluations and strengthening the method's resistance to detection techniques in order to overcome these obstacles and ultimately improve the efficacy and dependability of this cutting-edge text steganography technique. Arabic letters' diacritical marks and picture layers were used by [15] (Alqahtany et al., 2023) in their study to present a dynamic multi-layer steganography technique.

The study demonstrated the method's efficacy in hiding data in images, but issues like possible deterioration of image quality and security risks related to detection techniques must be resolved. In order to address these issues and improve the practicality and dependability of this novel steganography method, further research can concentrate on optimizing the embedding procedure to reduce the impact on image quality, investigating sophisticated encryption and authentication methods for increased security, and carrying out extensive testing to guarantee resilience against steganalysis techniques.



In the investigation conducted by [16] (Naik, et al., 2022) looked into audio steganography. The specific methods the authors used were not made explicit, even though their study illuminated the field. Yet, the study most likely yielded conclusions regarding audio steganography, its applications, or upcoming advancements in the industry. Common issues in audio steganography include data hiding while maintaining audio quality, security and resilience against detection, and optimizing the embedding process for real-time applications.

To address these challenges, further research may involve refining embedding algorithms, employing advanced encryption techniques, and conducting extensive testing to enhance the security and viability of audio steganography approaches. [14] (Singh et al., 2023) did not specifically develop their own methods; instead, they performed a thorough review of the methods that are currently in use in audio steganography as part of their survey. The survey probably provided a summary of different approaches and findings in the field, illuminating the development and variety of audio steganography techniques.

The survey may have covered challenges pertaining to data capacity, imperceptibility, and resilience to steganalysis. Future research may focus on creating sophisticated audio steganography methods that balance high data hiding capacity, low perceptual distortion, and resistance to contemporary detection techniques in order to overcome these difficulties. Furthermore, the security of audio steganography may be further improved by adding encryption and authentication methods, guaranteeing its efficacy in safe data transmission and storage. [17] (Firman Ashari, 2022) assessed audio steganography as an image file embedding technique in his study, using Snappy compression and encryption. It's possible that the study included results about how well this method works to safely hide picture data inside audio files.

Typical problems with audio steganography include embedded capacity constraints, possible loss of audio quality, and robustness against detection. Future studies may look into ways to reduce quality loss in the compression and encryption processes, maximize embedding capacity, and strengthen the method's resilience against contemporary steganalysis techniques in order to address these issues. By doing this, audio steganography for image file embedding can become more viable and reliable, increasing its usefulness for safe data transfer and storage. In order to assess the advantages and disadvantages of different audio steganography techniques, [18] (Aslantaş, et al., 2022) carried out a comparative analysis of these methods in their study.

Most likely, the study offered a thorough analysis of the various audio steganography techniques currently in use and how well they work in comparison. Creating uniform evaluation criteria and figuring out the best methods for various application scenarios are two common problems in these kinds of comparative research. Future work may focus on improving evaluation metrics, creating uniform benchmarks, and offering guidance for choosing the best audio steganography technique based on particular use cases in order to address these issues and help make well-informed decisions regarding secure data protection and communication.

(Bilal et al., 2022) created an image steganography technique using a Matlab-implemented graphical user interface (GUI). It's possible that their research involved developing an easy-to-use tool for embedding and extracting hidden data from image files. While specific outcomes and difficulties were

not covered in detail in the reference, maintaining a balance between security and usability as well as maximizing the steganographic method's robustness are frequent problems in image steganography with GUI implementations. The practicality and dependability of this image steganography tool in secure data communication and concealment may be advanced by further research focusing on improving the GUI design for a better user experience, implementing robust encryption and authentication mechanisms to increase security, and conducting extensive testing to evaluate the method's performance and resilience against steganalysis.

A novel coverless audio steganography technique based on Generative Adversarial Networks (GANs) was presented by [19] (Li, et al., 2023) in their research. Although the reference did not include all of their findings, it is likely that this method showed improvements in safe data embedding in audio files. A common challenge in coverless audio steganography is maintaining data integrity and resilience to detection methods. Future research may focus on developing more sophisticated steganalysis-resistant mechanisms, optimizing the steganographic process for better data integrity, and further refining GAN-based techniques in order to address these issues.

Through these efforts, coverless audio steganography for safe data transmission and protection would become more reliable and practical. A hybrid encryption algorithm and the Least Significant Bit (LSB) technique were combined to create an image steganography method by [20] (Alanzy et al., 2023). Although the reference did not provide specific findings and challenges, their approach probably involved data concealment within images, integrating LSB for data embedding, and using hybrid encryption algorithms to increase security.

The trade-off between data capacity and security, as well as the requirement to guarantee robustness against detection, are common challenges in image steganography. Future research may focus on improving the hybrid encryption algorithms, enhancing data embedding for increased security and data integrity, and creating defences against sophisticated steganalysis techniques in order to address these issues.

These initiatives would help to improve the usefulness and dependability of this image steganography technique for safe data transmission and archiving. To hide images within audio data, [21] (Ros, et al., 2023) set out to develop a deep steganography technique. Although the source did not specify the precise outcomes and difficulties they faced, their work probably contributed to the development of image-in-audio steganography. Optimizing the embedding process for data capacity and minimizing perceptual distortions while maintaining robustness against steganalysis techniques are common challenges in deep steganography.

Future research may concentrate on improving deep steganography algorithms, investigating cutting-edge neural network architectures, and carrying out extensive testing to evaluate the efficacy and security of the technique in order to address these issues. This would make image-in-audio deep steganography more useful and dependable, increasing its efficacy for secure data transmission and concealment. A coverless video steganography method based on the combination of audio and frame features was created in [22] (Zhang et al., 2022).

This approach probably involved innovations in secure data embedding within video files through the fusion of audio and frame characteristics, though specific results and challenges were not specified in the reference. Problems with data capacity,

preserving video quality, and guaranteeing robustness against steganalysis are frequently linked to coverless video steganography. Future research may focus on improving the steganographic procedure to strike a balance between data capacity and video quality, streamlining the integration of frame and audio features, and putting in place sophisticated steganalysis-resistant techniques in order to overcome these difficulties. These initiatives would help to improve coverless video steganography's usefulness and dependability for secure data communication and protection. An innovative JPEG steganography technique with high capacity and robustness was created via adversarial training in the study done by [23] (Shang, et al., 2023).

This technique probably represented advancements in safely embedding data within JPEG images, with an emphasis on data capacity and resilience against detection, even though specific results and challenges were not mentioned in the reference. Keeping data capacity and image quality in check while also addressing flaws in current steganalysis methods are common problems in JPEG steganography.

Future work may focus on improving adversarial training strategies, streamlining the embedding procedure to minimize visual distortion and increase data capacity, and creating defences against sophisticated detection techniques in order to address these issues. These initiatives would help to improve the usefulness and dependability of robust and high-capacity JPEG steganography for safe data transfer and security.

Previous steganography research encountered issues such as steganalysis sensitivity, probable audio quality loss, limited embedding capacity, and detection method flaws. Future research will try to tackle these challenges by optimizing algorithms for audio quality preservation, boosting resistance to steganalysis, investigating advanced data embedding methods, and increasing confidentiality capacity.

GAN-based algorithms improve coverless audio steganography, hybrid encryption improves picture steganography, and deep steganography is optimized for image-in-audio applications. Coverless video steganography is enhanced by improved frame-audio integration and steganalysis-resistant methods. Improved adversarial training and reduced embedding techniques in JPEG steganography provide increased capacity and robustness. By addressing these issues, steganographic systems for secure data transport and protection become more reliable.

### III. METHODOLOGY

#### III.1 TEXT STEGANOGRAPHY(STEGOTEXT)

The message is translated to binary form and then carefully inserted among the whitespaces of the original text. Each character of the binary message corresponds to the least important bits of the characters in the text; this strategy depends on changing inconsequential components of the carrier (text) to hide the message without visible changes to the human eye [24] (Rashmi et al., 2023).

The key approach used includes manipulating whitespace characters; the script finds existing whitespace in the text and adds extra spaces that encode the binary message. The whitespace works as a carrier for the concealed information, successfully disguising it within the seemingly benign spaces between words and lines. This delimiter helps the extraction procedure by specifying when the encoded

binary message ends, assuring correct and ambiguous recovery [25] (Rani et al., 2022).

#### III.2 IMAGE STEGANOGRAPHY(PIXEL QUANTA)

Our proposed work demonstrates a technique called Quantization Index Modulation (QIM) combined with the Least Significant Bit (LSB) method for steganography, embedding secret messages into images and extracting them without perceptible visual changes [26] (Khodher et al., 2020).

The suggested work represents transforming a text message to binary and hiding it in a picture using LSB substitution in the least significant bits of the RGB channels. Retrieves the concealed binary message from the stego picture by analyzing the LSBs of the RGB channels, and finds any pixel-wise discrepancies between the original and stego images to ensure the steganographic process's integrity [27] (Ramdoss et al., 2022).

Finally, compare the original and stego photos to visually analyze any variations between the two photographs. The QIM method provides detection resistance, but the LSB method allows for minimum visual distortion, making it suited for hidden communication.

#### III.3 AUDIO STEGANOGRAPHY (QUANTUMAUDIO)

The amalgamation of Adaptive Quantization Index Modulation (QIM) and Least Significant Bit (LSB) methods forms the foundation for our proposed work, enabling the concealment of both audio and textual information within audio files.

The technique includes calculating frame energies to allow adaptive embedding inside the audio stream, guaranteeing an optimum concealment strategy. The Adaptive QIM embedding technology smoothly embeds pieces of information by modifying audio samples based on a predetermined delta value. In addition, the Least Significant Bit (LSB) approach conceals textual information within audio samples, resulting in a hybrid model for strong and thorough data concealment [28] (Jain et al., 2022).

#### III.4 ADAPTIVE QUANTIZATION INDEX MODULATION (QIM)

**Adaptive QIM Embedding:** This technique modifies audio samples by embedding information in their quantized representations based on a predefined delta value, using a QIM scheme.

The Adaptive QIM technique is a sophisticated approach geared towards embedding an audio message into a host audio file. This method hinges on the principle of selectively modifying certain parts of the audio based on their energy levels – a strategy that brings adaptiveness into play. Audio steganography system marries the robustness and perceptual transparency of Adaptive QIM with the simplicity and subtlety of LSB. Adaptive QIM is adept at embedding messages in parts of the audio that are less likely to reveal alterations, while LSB offers a straightforward way of hiding text messages with negligible impact on the audio quality.

**Adaptive QIM Extraction:** It reverses the embedding process to extract the hidden information from the modified samples [29] (Hao et al., 2023).

### Steganography Embedding (QIM)

Given:

Audio frame  $F$ .

Binary bit to embed  $b$ . Delta value  $\Delta$ .

The embedding function for QIM can be defined as:

$$\begin{cases} \left\lfloor \frac{F}{\Delta} \right\rfloor \cdot \Delta + \frac{\Delta}{4}, & \text{if } b = 1 \\ \left\lfloor \frac{F}{\Delta} \right\rfloor \cdot \Delta - \frac{\Delta}{4}, & \text{if } b = 0 \end{cases} \quad (1)$$

### Steganography Extraction (QIM)

Given:

$$\begin{cases} 1, & \text{if } F > \left\lfloor \frac{F}{\Delta} \right\rfloor \cdot \Delta \\ 0, & \text{otherwise} \end{cases} \quad (2)$$

Modified audio frame  $F'$ .

Delta value  $\Delta$ .

### III.5 LEAST SIGNIFICANT BIT (LSB) EMBEDDING

This method embeds text information by manipulating the least significant bits of the audio samples.

The proposed steganographic model combines QIM and LSB approaches, proving its effectiveness through actual application. The encoded information is unnoticeable to aural examination, and the original audio quality is effectively preserved. The QIM-based embedding's adaptive nature, directed by energy thresholds, enables optimal concealing capacity without compromising audio fidelity [30] (Guan et al., 2022).

Finally, the presented research adds a unique way to audio steganography by combining QIM and LSB approaches. The hybrid architecture proposed provides a stable and extensible framework for hidden data transfer within audio recordings. The imperceptibility of embedded information, together with message extraction efficacy, highlights the potential for real-world applications needing secure and covert communication routes (Jiang et al., 2023).

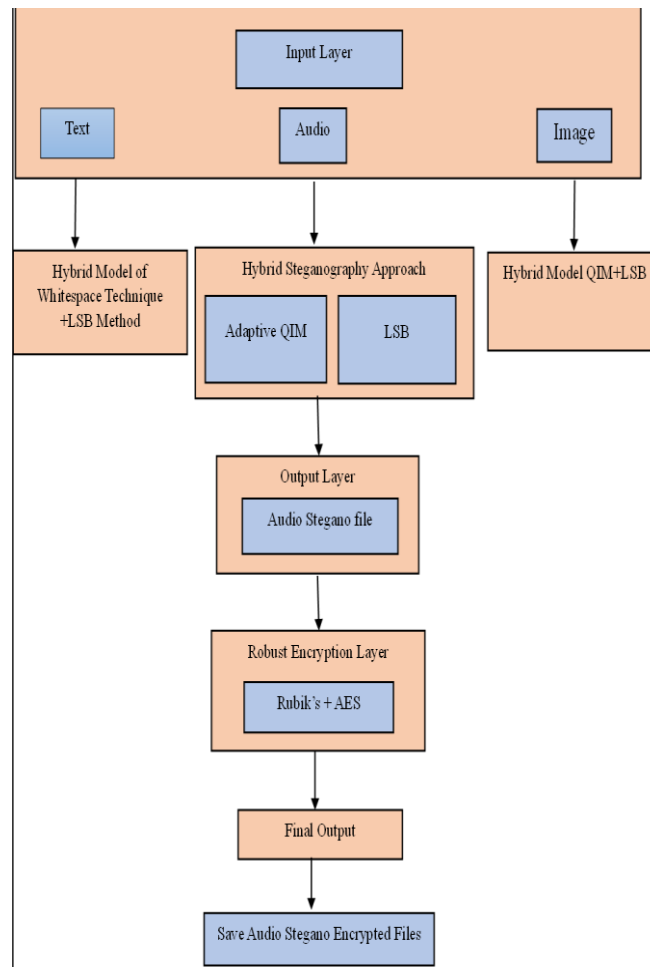


Figure 1: Hybrid Audio Security Process Flow Diagram.

Source: Authors, (2025).

The diagram shows how to safeguard audio recordings using a multi-layered security approach that combines encryption and steganography. At first, the Input Layer supports a number of media formats, such as text, audio, and photos. The data is then processed using a Hybrid Steganography Approach, which hides the data from view by embedding it into an audio file using methods like LSB and Adaptive QIM [6] (Mohammed et al., 2022). At the Output Layer, the resultant file is called an Audio Stegano file,

signifying that the data has been hidden inside the audio. This steganographically enhanced file is then subjected to an additional layer of security called a Robust Encryption Layer, which uses a combination of the Advanced Encryption Standard (AES) and Rubik's Cube algorithmic strategies in addition to Quantum Key Encryption, which proposes the use of quantum-resistant encryption techniques. At the Final

Output, the procedure is complete. The Audio Stegano files are now encrypted, offering a high degree of

confidentiality and privacy, and are prepared for safe transmission or storage (Chen et al., 2021).

### III.6 RUBIK CIPHER AUDIO

Embedding data within an audio file using a technique called Quantization Index Modulation (QIM), allowing to modify audio samples to encode hidden information our proposed work implements Advanced Encryption Standard (AES) encryption, a symmetric key algorithm renowned for its security and efficiency in data encryption [31] (Thabit et al., 2021). Our proposed work implements Advanced Encryption Standard (AES) encryption, a symmetric key algorithm renowned for its security and efficiency in data encryption.

AES operates in Cipher Block Chaining (CBC) mode, providing confidentiality through block-level encryption. After that we initialize the AES cipher in CBC mode with a specific key finally, we perform encryption and decryption using AES with padding to ensure the input data is of the correct block size (Nuur Alifah Roslan et al., 2022).

#### AES Encryption:

Given:

Plaintext P.

Key K.

Initial Vector IV generated randomly.

The AES encryption process can be represented as:

$$C = \text{AES}_{K,IV}(P) \quad (3)$$

Where C is the ciphertext  $\text{AES}_{K,IV}(P)$  is the AES encryption of plaintext P using key K

And initial vector IV .

#### AES Decryption:

Given:

Ciphertext C.

Key K.

Initial Vector IV.

The AES decryption process is represented as:

$$P = \text{AES}_{K,IV}^{-1}(C) \quad (4)$$

Where P is the decrypted plaintext, and  $\text{AES}_{K,IV}^{-1}(C)$  is the AES decryption of ciphertext C

Using key K and initial vector IV.

Steganography conceals information within other data (here, an audio file) without arousing suspicion. Our proposed work uses Quantization Index Modulation (QIM) for embedding bits into audio samples [32] (J. Sharafi et al., 2021). It embeds a binary message into an audio file by slightly modifying audio samples based on a delta value, extracts the hidden binary message from the modified audio file using the same delta value employs custom algorithms for data manipulation, including reversible scrambling inspired by the

Rubik's Cube and binary representation conversion, scrambles and unscrambles data using a key, implementing a custom reversible algorithm inspired by the Rubik's Cube, and

applying text messages into binary representations for embedding within the audio file and reverses the process for message extraction [33] (k et al., 2022).

#### III.6.1 RUBIK'S CUBE-LIKE SCRAMBLING:

Given:

Scrambled data D.

Key K represented as a sequence of integers  $K = [k_1, k_2, \dots, k_n]$ .

The unscrambling process for each byte  $D_i$  in D can be described as:

$$D_i = \text{Unscramble}(D_i, K) \quad (5)$$

where  $D_i$  is the unscrambled byte. The unscrambling process involves reversing the scrambling steps applied previously.

The struct module facilitates the conversion between Python values and binary data, Audio frames are manipulated at the sample level to embed and extract hidden bits, ensuring minimal perceptual impact [34] (Rui Wu et al., 2022)

#### 3.6.2 Mean Squared Error (MSE):

The difference in squares between the original and stego audio signals' equivalent values is measured by the Mean Squared Error.

$$\text{MSE} = \frac{1}{N} \sum_{i=1}^N (x_i - y_i)^2 \quad (6)$$

Where N is the number of samples and  $x_i$  and  $y_i$  are the corresponding sample the original and stego.

#### 3.6.3 Peak Signal-to-Noise Ratio (PSNR):

PSNR is a measure of the quality of the stego audio signal compare to the original audio signal. Its express in decibels(dB)

$$\text{PSNR} = 10 \cdot \log_{10} \left( \frac{\text{MAX}^2}{\text{MSE}} \right) \quad (7)$$

Where MAX is the maximum possible pixel value (usually 1 for normalized audio) and MSE is the Mean Squared Error.

#### 3.6.4 Signal-to-Noise Ratio (SNR):

SNR is measure of the quality of the stego audio compared to the original audio signal. It is also expressed in decibels (dB).

$$\text{SNR} = 10 \cdot \log_{10} \left( \frac{\text{signalpower}}{\text{Noisepower}} \right) \quad (8)$$

When it comes to audio processing, the signal power (signal power) can be thought of as the original. The energy difference between the original and stego signals is known as the noise power, and it is represented by the audio signal.

### IV. RESULTS AND DISCUSSIONS

The steganography techniques demonstrated in the text, picture, and audio domains are successful in concealing



information. Binary messages are discretely encoded in text whitespace, and picture pixels are subtly altered by Quantization Index Modulation (QIM). The audio steganography uses adaptive QIM embedding, and a strong encryption method assures safe connection. Evaluation measures like as MSE, PSNR, and SNR indicate the success of these technologies, which provide a complete and secure way of covert communication across several media.

#### IV.1. TEXT.

Figure 2 shows contain some original message which we are going to use to apply steganography techniques. The message is converted into binary form and then strategically embedded within the whitespace of the original text. Each character of the binary message corresponds to the least significant bits of the characters in the text, this technique relies on altering insignificant components of the carrier (text) to hide the message without perceptible changes to the naked eye.

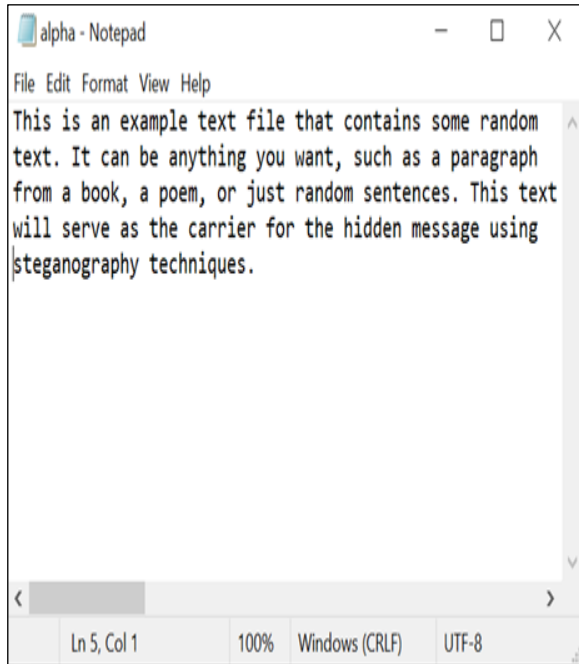


Figure 2: Original Text.  
Source: Authors, (2025).

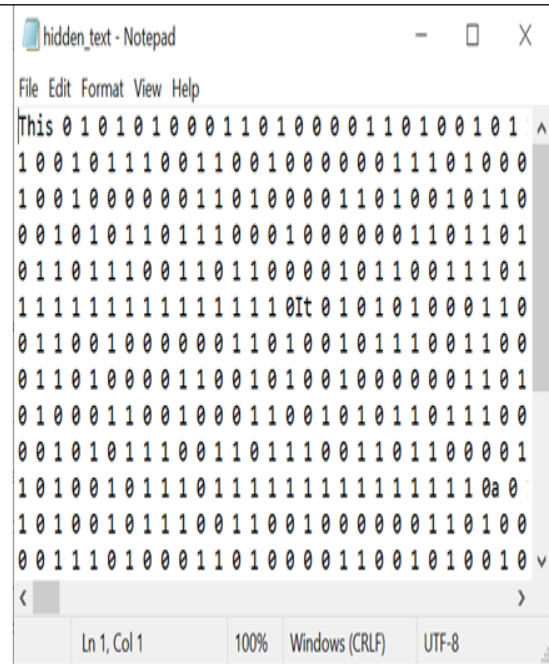


Figure 3: Hidden text.  
Source; Authors, (2025).

This is an example text file that contains some random text. It can be anything you want, such as a paragraph from a book, a poem, or just random sentences. This text will serve as the carrier for the hidden message using steganography techniques.

Figure 4: Screenshot of Output text.  
Source: Authors, (2025).

Figure 3 shows the primary technique employed in this code involves manipulating whitespace characters, the script identifies existing whitespace in the text and inserts additional spaces that encode the binary message.

The whitespace acts as a carrier for the hidden message, effectively concealing it within the seemingly innocuous gaps between words and lines. This delimiter helps the extraction process by indicating where the embedded binary message concludes, ensuring accurate retrieval without ambiguity.

Figure 4 shows Our final step is performed to showcase the final appearance of the text after the steganography process, emphasizing the effectiveness of concealing information within seemingly innocuous text through subtle whitespace alterations.

#### IV.2. IMAGE



Figure 4: Original Image. Figure 5: Steganographic image.  
Source; Authors, (2025). Source; Authors, (2025).

Figure 4 shows the original image (lena\_std.tif) most likely represents the well-known "Lena" image, a typical test image often used in image processing. Figure 5 shows the `embed\_message` function takes an image and a textual message as inputs. Initially, it converts the message into a binary representation and appends a delimiter to mark the end of the message. Subsequently, the function traverses each pixel of the input image. During this iteration, it embeds the binary message into the least significant bits (LSBs) of the red, green, and blue channels of each pixel. The process involves bitwise

operations to modify the LSBs while preserving the overall color information. This embedding ensures that the alterations are subtle and often imperceptible to the human eye. Finally, the function saves the modified image, known as the stego image, preserving the original appearance but concealing the

binary message within its pixel values. This steganographic technique, Quantization Index Modulation (QIM), enables hidden communication within the visual content of the image, providing a means of covert information transfer.

### IV.3 AUDIO

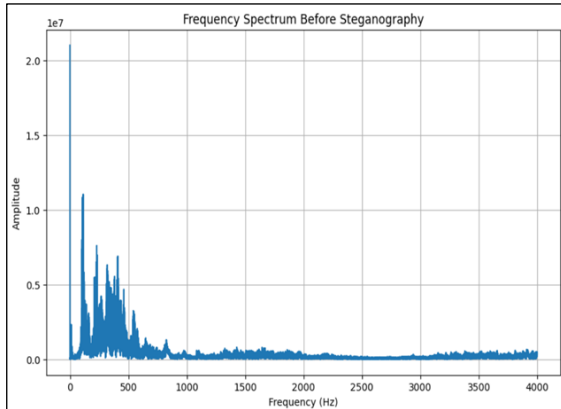


Figure 6: Frequency Spectrum Before Steganography.  
Source; Authors, (2025).

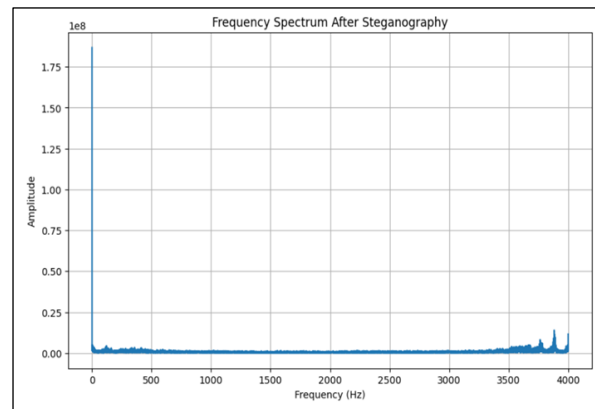


Figure 7: Frequency Spectrum After Steganography.  
Source; Authors, (2025).

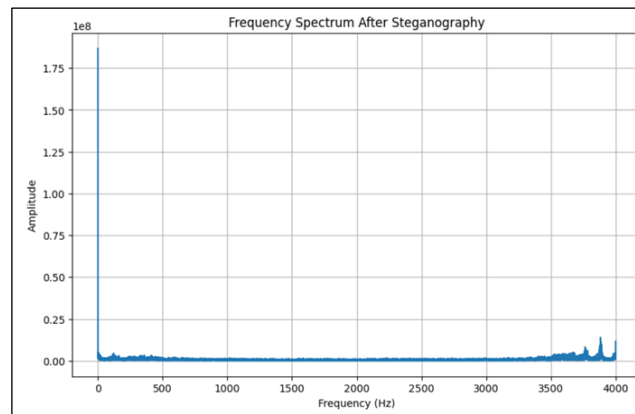


Figure 7: Frequency Spectrum After Steganography.  
Source; Authors, (2025).

The provided parameters detail the components and settings for an audio steganography process. The "Input audio file" serves as the original audio source for message embedding, and the "Output audio file" designates where the steganographic audio will be saved. Users have the option to embed either a "Secret audio message" or a "Text message" within the input audio file.

The "Delta" value is specified for the Adaptive QIM embedding technique, influencing the degree of message concealment. Additionally, an "Energy threshold" is established for adaptive steganography, determining the level of energy required for effective concealment. These parameters collectively define the configuration and goals of the audio steganography operation, allowing for customization based on the user's preferences and requirements.

The resulting visualizations depict the amplitude distribution across frequencies, allowing for a comparative analysis of the spectral characteristics before and after the steganographic process. These plots serve as valuable insights into the alterations introduced by the steganography method, aiding in the assessment of its impact on the audio signal. By comparing the plots before and after steganography, one can

observe any changes introduced during the embedding process, aiding in the assessment of how steganography affects the frequency characteristics of the audio signal in Figure 6 and 7.

#### IV.3.1 Steganography Audio Encryption.

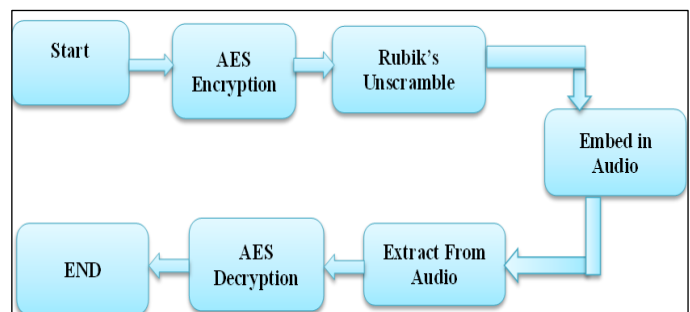


Figure 8: Robust Encryption Approach.  
Source: Authors, (2025).

Figure 8 illustrates the study begins with AES encryption in CBC mode, a commonly used approach for assuring plaintext security by mixing a random initialization vector (IV) with a predetermined key. The succeeding Rubik's Unscramble method takes a novel approach to reversing data scrambling by rearranging pieces depending on byte values inside a certain key, with the goal of restoring data to its pre-scrambling condition. Quantization Index Modulation (QIM) is an audio embedding technique that surreptitiously encodes binary signals into audio files, gently modifying audio samples that are unnoticeable to the human ear. This entails translating

a textual message to binary for embedding and recovering embedded binary messages via audio extraction. Furthermore, the explanation of AES decryption emphasizes the significance of safe key generation, as demonstrated by the development of a random 16-byte AES key. Finally, the research shows generic data encryption and decryption using AES-CBC mode, emphasizing the symmetric aspect of AES by utilizing the same key for both encryption and decryption. These strategies, when combined, demonstrate the flexibility of cryptographic methods in safeguarding information and enabling clandestine communication.

Table 1: Audio Files with after Steganography Analysis of MSE, PSNR and SNR.

Audio Name	Stego Name	Audio Size	Stego Size	MSE	PSNR	SNR
Audio1.wav	stego_audio1.wav	1.51 mb	1.50 mb	0.09282929450273514	10.323149501470688 dB	-2.794678807258606 dB
Audio2.wav	stego_audio2.wav	3.33 mb	3.29 mb	0.07753556221723557	11.104990596574197 dB	-2.8700366616249084 dB
Audio3.wav	stego_audio3.wav	3.36 mb	3.27 mb	0.030982017517089844	15.088903048463372 dB	-12.872124910354614 dB

Source: Authors, (2025).

The table presents information on original audio files and their stego versions, including file names, sizes, and quality metrics. The "MSE" (Mean Squared Error) indicates the difference between original and stego signals, with lower values indicating better quality. "PSNR" (Peak Signal-to-Noise Ratio)

measures stego audio quality, higher values suggesting better fidelity. "SNR" (Signal-to-Noise Ratio) reflects the overall quality of stego audio. The table provides a concise assessment of steganography effectiveness for each audio pair.

#### IV.4 COMPARATIVE ANALYSIS.

Table 2: Comparison Analysis (A), (B), (C) with the Existing System for our Proposed System.

A. Comparative Analysis for Proposed System with Existing System (Text)		
Aspects	Stegotext Steganography	Traditional Text Steganography
Security and Detectability	High security owing to obscurity; modifications are less detected.	Lower security; modifications may be more obvious and detected.
Resistance to Automated Detection	Less likely to be detected by automated tools due to subtle changes.	More likely to be detected by tools designed to analyze text patterns.
Adaptability to Text Formats and Inspection Resistance	Adaptable to a broad range of text types and difficult to recognize through casual inspection.	May be confined to certain formats or need specific text circumstances. Possibility of discovery by close reading or text analysis.
Integrity of Original Text	Maintains the original content and structure of the text.	May require altering the actual text content or structure.
Ease of Implementation	Relatively simple to implement using standard text editing tools.	Might require more complex manipulations or specific software.
Capacity for Hidden Information	Limited capacity due to dependency on whitespace and LSB only.	It may have greater capacity since it can employ more text features for hiding.
B. Comparative Analysis for Proposed System with Existing System (Image)		
Aspects	PixelQuanta	Traditional Image Steganography
Robustness Against Compression	Higher robustness against lossy compression like JPEG.	Lower robustness; often susceptible to quality loss during compression.
Capacity for Hidden Information	The combination of QIM and LSB methods results in a high capacity.	Variable, but often lower when compared to QIM + LSB.
Image Quality Preservation	Preserves image quality better making changes less detectable.	Image quality may degrade, making steganography more detectable.
Security and Detectability	Enhanced security due to less detectability of hidden data.	Less secure, as alteration can be more evident.
Resistance to Image Manipulation	More resistance to picture alteration such as cropping and scaling.	Less resistant; tampering has the potential to erase the secret data.
Complexity and Computational Load	Higher complexity and computational requirements.	Simpler and less computationally intensive.
Flexibility and Adaptability	Highly flexible and adaptable to various image formats and condition.	May have limitation in adaptability to different image types.
C. Comparative Analysis for Proposed System with Existing System (Audio)		
Aspects	Quantum audio	Traditional Audio Steganography
Robustness Against Compression	Offers robust resistance to lossy audio compression due to the resilience of Adaptive QIM; LSB also contributes but is less robust.	Typically, more susceptible to degradation from compression.
Capacity for Hidden Information	High capacity achieved through the efficient use of Adaptive QIM for audio messages and LSB for text, utilizing different aspects of the audio.	Lower capacity; limitations based on the audio format and method used.

Audio Quality Preservation	Superior preservation of audio quality; adaptive nature of QIM ensures less perceptible alterations, complemented by the subtlety of LSB.	This might result in obvious quality decrease or artefacts.
Security and Detectability	Enhanced security with challenging detectability due to the adaptive embedding of QIM and the subtleness of LSB alterations.	Less secure, as modifications can be more evident or predictable.
Resistance to Audio Manipulation	Higher resistance to audio processing like filtering and equalization, particularly due to Adaptive QIM's selective embedding.	Decrease resistance; processing has the ability to disrupt or erase concealed information.
Complexity and Computational Load	Higher, reflecting the sophisticated nature of Adaptive QIM combined with LSB, requiring more computational resources.	Generally simpler and less computationally demanding.
Flexibility and Adaptability	Highly adaptable to varying audio contents and conditions, benefiting from the selective embedding of Adaptive QIM and the universality of LSB.	May have limited adaptability depending on the technique used.
Suitability for High-Security Needs	More suitable for high-security applications due to enhanced stealth and difficulty in detecting embedded messages.	Due to increased detectability, it is less suitable for high-security applications.

Source: Authors, (2025).

Table 2 shows the comparative analysis demonstrates that when compared to the suggested systems, typical steganographic approaches, whether in the context of text, picture, or audio, frequently have major shortcomings. One significant disadvantage is their lack of security and detectability. Traditional text steganography makes modifications more visible and identifiable, making it less appropriate for high-security applications. Similarly, traditional picture steganography techniques are frequently subject to quality loss during compression, making them less resilient, while traditional audio steganography may result in

apparent quality deterioration or artefacts, reducing their capacity to successfully conceal secret information.

The flexibility and resilience to manipulation of classic steganography technologies is another major drawback. Traditional text and picture steganography may be confined to certain forms or need specific circumstances, making them less adaptable and practical for a wide range of applications. In contrast, the suggested systems in each domain provide improved flexibility, compression resistance, and manipulation resistance. These benefits make them more suitable for high-security applications and scenarios requiring the preservation of original content quality.

Table 3: Comparison of Traditional and Hybrid Audio Steganography with Robust Encryption.

Aspects	Rubik Cipher Audio	Traditional Encryption Methods
Encryption Strength	Extremely high due to AES's strong encryption algorithm combined with additional scrambling.	Varies, but often lower, especially in older or simpler algorithms.
Computational Complexity	Higher, due to the two-step process involving both AES encryption and Rubik's Cube-like Scrambling.	Generally lower, involving straightforward encryption processes.
Resistance to Cryptanalysis	Enhanced resistance; the scrambling adds an extra layer of complexity for attackers.	Depends on the algorithm; some older methods are more vulnerable.
Data Pattern Obfuscation	Superior, as the Rubik's Cube-like method disrupts data patterns, making analysis more difficult.	Less effective, especially if the encryption doesn't include additional obfuscation techniques.
Key Management Complexity	Increased complexity due to the need for managing both AES and scrambling keys.	Simpler, usually involving a single key or key pair.
Decryption Process	Requires precise reverse steps, adding to the complexity and time for decryption.	Typically, straightforward and faster.
Suitability for Sensitive Data	Highly suitable for highly sensitive data due to the robustness of the combined methods.	Suitability varies; some methods may not be recommended for highly sensitive data.
Implementation Difficulty	More challenging due to the integration of two distinct methods.	Generally easier to implement with standard libraries and tools.
Flexibility and Adaptability	Highly adaptable to different types of data and security requirements.	Varies; some methods are less adaptable to new or varied requirements.

Source: Authors, (2025).

Table 3 shows the comparison of Rubik Cipher Audio and traditional encryption methods for audio steganography reveals that the Rubik Cypher Audio method combines AES encryption with Rubik's Cube-like scrambling to achieve exceptionally high encryption strength and enhanced resistance to cryptanalysis, making it highly suitable for safeguarding highly sensitive data. It does, however, come with increasing computational complexity and implementation difficulties. Traditional encryption methods, on the other hand, while typically simpler to apply, vary in encryption strength and may provide less protection, with limited flexibility to diverse data

types and security needs. As a result, the decision between both ways is determined by the application's individual security requirements and complexity, with the Rubik Cypher Audio method providing a strong solution for maximal data protection.

## V. CONCLUSIONS

This study presents a ground-breaking hybrid steganography technique that combines strong encryption methods like the Advanced Encryption Standard (AES) and Rubik's Cube-like scrambling with advanced steganographic techniques like White Space, Least Significant Bit (LSB), Quantization Index



Modulation (QIM), and Adaptive Modulation. The study demonstrates the feasibility and efficacy of these strategies in real-world circumstances, emphasizing their potential to improve data integrity and confidentiality across text, picture, and audio data in digital communication.

In comparison to previous systems, this hybrid method provides improved security, increased resistance to detection, and better flexibility to multiple formats, placing it as a flexible option for secure digital communication. The study not only represents a huge advancement in information security, but it also sets the path for future research, notably in the fields of quantum computing and artificial intelligence, to further develop these strategies and solve increasing cybersecurity concerns.

## VI. AUTHOR'S CONTRIBUTION

**Conceptualization:** T.Srinivasa Padmaja, Shaik Mohammad Basha.

**Methodology:** T.Srinivasa Padmaja, Shaik Mohammad Basha.

**Investigation:** T.Srinivasa Padmaja, Shaik Mohammad Basha.

**Discussion of results:** T.Srinivasa Padmaja. Shaik Mohammad Basha.

**Writing – Original Draft:** T Srinivasa Padmaja.

**Writing – Review and Editing:** T.Srinivasa Padmaja. Shaik Mohammad Basha.

**Resources:** T.Srinivasa Padmaja, Shaik Mohammad Basha.

**Supervision:** Shaik Mohammad Basha.

**Approval of the final text:** T.Srinivasa Padmaja. Shaik Mohammad Basha.

## VII. REFERENCES

- [1] Aruna, Ms& Nandika, L & Sneha, C & Xavier, imothy& George, Treesa. (2023). Text, Image and Audio Steganography. International Journal for Research in Applied Science and Engineering Technology. 11. 4435-4439. 10.22214/ijraset.2023.51091.
- [2] Kumar, A.V. & G., Rahul & Musirin, I. & Irawati, Indrarini& Amine, Abdelmalek & Bri, Seddik. (2023). A Study of Steganography Approach for Securing Data in a Confidential Communication Using Encryption. 10.4018/978-1-6684-6581-3.ch005.
- [3] Nasr, Marwa & El-Shafai, Walid & El-Rabaie, El-Sayed & El-Fishawy, Adel & Dessouky, M.I. & Abdelsalam, Naiman & Abd El-Samie, Fathi. (2023). A Robust Technique for Steganography of Enhanced Audio Signals. 1-6. 10.1109/ICEEM58740.2023.10319573.
- [4] Monika, A. & Rajagopal, Eswari & Singh, Swastik. (2023). Detection of Location of Audio-Stegware in LSB Audio Steganography. 10.1007/978-981-99-0609-3\_31.
- [5] Adhanadi, Fikri & Novamizanti, Ledy & Budiman, Gelar. (2020). DWT-SMM-based audio steganography with RSA encryption and compressive sampling. TELKOMNIKA (Telecommunication Computing Electronics and Control). 18. 1095. 10.12928/telkomnika.v18i2.14833.
- [6] Subhi, Nooruldeen& Salih Mahdi, Mohammed. (2023). Using Special Letters And Diacritics In Steganography In Holy Quran. Iraqi Journal for Computers and Informatics. 49.
- [7] Sultani, Zainab & Dhannoon, Ban. (2021). Image and audio steganography based on indirect LSB. Kuwait Journal of Science. 48. 10.48129/kjs.v48i4.8992.
- [8] Zhuo, Peiwen & Yan, Diqun& Ying, Kaiyu & Wang, Rangding& Dong, Li. (2023). Audio steganography cover enhancement via reinforcement learning. Signal, Image and Video Processing. 10.1007/s11760-023-02819-1.
- [9] Joshi, Ranjana & Trivedi, (Dr.) Munesh & Goyal, Vishal & Bhati, Deepshikha. (2022). Recent Trends for Practicing Steganography Using Audio as Carrier: A Study. 10.1007/978-981-19-5292-0\_52.
- [10] Abikoye, Oluwakemi & Ogundokun, Roseline & Misra, Sanjay & Agrawal, Akasht. (2022). Analytical Study on LSB-Based Image Steganography Approach. 10.1007/978-981-16-8484-5\_43.
- [11] W.Abood, Enas& Abdullah, Abdulhussein & Al Sibahee, Mustafa & Abduljabbar, Zaid & Nyangaresi, Vincent & Ahmad, Saad & Kalafy, Ali & Jalil, Mudhafar&Ghrabta, Jassim & Wahab, Enas. (2022). Audio steganography with enhanced LSB method for securing encrypted text with bit cycling. Bulletin of Electrical Engineering and Informatics. 11. 185-194. 10.11591/eei.v11i1.3279.
- [12] Kumar, Madhurendra& Kumari, Muskan & Patil, Tushar & Pradhan, Rahul & Giri, Manish. (2023). Hiding secret data in audio,video,image,text steganography using least significant bit algorithm(MH)India. 9. 874-877.
- [13] Tasnim, Orora& Hossain, Md & Rahman, Mahfujur. (2023). Audio Steganography with Intensified Security and Hiding Capacity. European Chemical Bulletin. 12. 162-173. 10.48047/ecb/2023.12.10.013.
- [14] Singh, Mr& Diwakar, Anirudra & Upadhyaya, Ms. (2023). A Novel Approach to Text Steganography. 10.7763/IPCST.2014.V59.2.
- [15] Alqahtany, Saad & Alkhodre, Ahmad & Al Abdulwahid, Abdulwahid & Alohal, Manar. (2023). A Dynamic Multi-Layer Steganography Approach Based on Arabic Letters' Diacritics and Image Layers. Applied Sciences. 13. 7294. 10.3390/app13127294.
- [16] Naik, Vaibhavi & Fernandes, Dr. (2022). Audio Steganography. International Journal of Scientific Research in Computer Science, Engineering and Information Technology. 196-201. 10.32628/CSEIT5228368.
- [17] Firman Ashari, Ilham. (2022). The Evaluation of Audio Steganography to Embed Image Files Using Encryption and Snappy Compression. Indonesian Journal of Computer Science. 11. 318-336. 10.33022/ijcs.v11i2.3050.
- [18] ASLANTAŞ, Funda & HANILÇİ, Cemal. (2022). Comparative Analysis Of Audio Steganography Methods. Journal of Innovative Science and Engineering (JISE). 6. 10.38088/jise.932549.
- [19] Li, Jing & Wang, Kaixi& Jia, Xiaozhu. (2023). A Coverless Audio Steganography Based on Generative Adversarial Networks. Electronics. 12. 1253. 10.3390/electronics12051253.
- [20] Alanzy, May & Alomrani, Razan & Alqarni, Bashayer& Almutairi, Saad. (2023). Image Steganography Using LSB and Hybrid Encryption Algorithms. Applied Sciences. 13. 11771. 10.3390/app132111771.
- [21] Ros, Jaume & Geleta, Margarita & Pons, Jordi & Giró-i-Nieto, Xavier. (2023). Towards Robust Image-in-Audio Deep Steganography. 10.48550/arXiv.2303.05007.
- [22] Zhang, Chunhu (2022). Coverless Video Steganography Based on Audio and Frame Features. Security and Communication Networks 10.1155/2022/1154098.
- [23] Shang, Fei (2023). Toward High Capacity and Robust JPEG Steganography Based on Adversarial Training. Security and Communication Networks.10.1155/2023/3813977.
- [24] Rashmi, S.. (2023). Implementation of Image Steganography and Combination of Cryptography and Steganography. 10.4018/978-1-6684-9317-5.ch014.
- [25] Rani, Rajneesh & Singh, Samayveer. (2022). A survey of recent advances in image steganography. Security and Privacy. 6. 10.1002/spy2.281.
- [26] Khodher, Maisa'A& Khairi, Teaba. (2020). Review: A comparison Steganography Between Texts and Images. Journal of Physics: Conference Series. 1591. 012024. 10.1088/1742-6596/1591/1/012024.
- [27] Ramadoss, Janarthanan (2022). A Three-Dimensional Autonomous System with a Parabolic Equilibrium: Dynamical Analysis, Adaptive Synchronization via

Relay Coupling, and Applications to Steganography and Chaos Encryption. Complexity 10.1155/2022/8362836.

[28] Jain, Jaishree (2022). Securing E-Healthcare Images Using an Efficient Image Encryption Model. Scientific Programming 10.1155/2022/6438331.

[29] Hao, Chaolong& Yang, Xukui& Ma, Quangong& Qu, Dan & Wang, Ran & Zhang, Tao. (2023). Quantum Audio LSB Steganography with Entanglement-assisted Modulation. 10.21203/rs.3.rs-3366077/v1.

[30] Guan, Bo (2022). A Novel Coverless Text Steganographic Algorithm Based on Polynomial Encryption. Security and Communication Networks 10.1155/2022/1153704.

[31] Thabit, R.; Udzir, N.I.; Yasin, S.M.; Asmawi, A.; Roslan, N.A.; Din, R. A Comparative Analysis of Arabic Text Steganography. Appl. Sci. 2021, 11, 6851. <https://doi.org/10.3390/app11156851>

[32] J. Sharafi, Y. Khedmati, M.M. Shabani, Image steganography based on a new hybrid chaos map and discrete transforms, Optik, Volume 226, Part 2, 2021, 165492, ISSN 0030-4026, <https://doi.org/10.1016/j.ijleo.2020.165492>.

[33] K. Manjunath, G.N. Kodanda Ramaiah, M.N. GiriPrasad, Backward movement oriented shark smell optimization-based audio steganography using encryption and compression strategies, Digital Signal Processing, Volume 122, 2022, 103335, ISSN 1051-2004, <https://doi.org/10.1016/j.dsp.2021.103335>.

[34] Rui Wu, Suo Gao, Xingyuan Wang, Songbo Liu, Qi Li, Uğur Erkan, Xianglong Tang, AEA-NCS: An audio encryption algorithm based on a nested chaotic system, Chaos, Solitons & Fractals, Volume 165, Part 1, 2022, 112770, ISSN 0960-0779, <https://doi.org/10.1016/j.chaos.2022.112770>. [1

## RESEARCH ARTICLE

## OPEN ACCESS

# A TAILORED COMPLIANCE SOLUTION FOR SECURING PERSONAL DATA PRIVACY UNDER LAW 18-07 IN ALGERIA

Redouane Guettal <sup>1</sup>, Mohammed Kamel Benkaddour <sup>2</sup>

<sup>1</sup> Department of Computer Science and Information Technology, Kasdi Merbah University, Ouargla, Algeria.

<sup>2</sup> Department of Computer Science and Information Technology, Laboratory of Artificial Intelligence and Information Technologies (LINATI), Kasdi Merbah University, Ouargla, Algeria.

<sup>1</sup> <http://orcid.org/0009-0006-2471-3242>, <sup>2</sup> <http://orcid.org/0009-0006-2471-3242>

Email: [Guetta.redou1@gmail.com](mailto:Guetta.redou1@gmail.com), [Benkaddour.kamel@univ-ouargla.dz](mailto:Benkaddour.kamel@univ-ouargla.dz)

## ARTICLE INFO

*Article History*

Received: January 12, 2025

Revised: January 20, 2025

Accepted: March 15, 2025

Published: April 31, 2025

*Keywords:*

Data security,  
Personal data privacy,  
Processing of personal data,  
Law 18-07,  
ANPDP.

## ABSTRACT

In an increasingly digitalized world, the management and protection of personal data has become a crucial issue for companies and governments. The rapid flow of information and the ubiquity of technology pose significant challenges to data security and privacy. In response to these concerns, the Algerian state enacted Law 18-07 on June 10, 2018, aimed at protecting individuals concerning the processing of their data. This law led to the creation of the National Authority for the Protection of Personal Data (ANPDP), responsible for supervising its application. This article proposes the design and implementation of a computer application dedicated to compliance with Law 18-07 for the protection of personal data. We first collected and analyzed the legal requirements for data protection and then modeled them using UML diagrams following the UP methodology. We have set up a database management system to ensure data protection and optimized management, incorporating cryptography techniques to enhance the security of the information. The development of this application was carried out with the Microsoft Visual FoxPro V.9 language, thus allowing the creation of a database and interfaces adapted to the needs of Algerian companies to comply with Law 18-07 and guarantee the security of personal data.



Copyright ©2025 by authors and Galileo Institute of Technology and Education of the Amazon (ITEGAM). This work is licensed under the Creative Commons Attribution International License (CC BY 4.0).

## I. INTRODUCTION

With the increasing spread of personal data around the world, growing concerns emerge regarding the protection of individuals' privacy and trust in computer systems. The ubiquity of personal data and its rapid flow across borders, in a world where technology pervades all domains, raises major concerns about preserving individual privacy and trust in IT systems. Compliance with data protection laws thus becomes an imperative necessity to ensure assurance and security in technological environments, where personal data is collected, stored, and shared at an unprecedented rate [1].

Algeria's adoption of Law 18-07 in 2018 marks a significant step forward in the protection of personal data. This law, inspired by international standards, regulates the collection, processing, and use of personal data by organizations. It plays a crucial role in building trust between consumers and service providers, which is essential for boosting digital economies. However, compliance

with this law presents technical and organizational challenges that companies face [1], [2].

Algerian companies face many obstacles in applying Law 18-07, including the understanding the legal requirements, which are often complex, making compliance difficult. Implementing technical and organizational measures to protect personal data, which requires significant resources. Managing individuals' rights, such as access, rectification, or opposition to the processing of their data. Identifying and correcting flaws in existing IT systems, which are not always adapted to current legislation and the risks related to non-compliance, which may result in legal sanctions or reputational damage [2].

This article proposes the design and implementation of a computer application dedicated to compliance with Law 18-07. Its aim is to provide companies with a practical and accessible tool for complying with legal data protection requirements while

strengthening the security and efficient management of their IT systems.

## II. RESEARCH BACKGROUND

### II.1 PRIVACY AND PERSONAL DATA

Privacy is the right of an individual to determine when, how, and to what extent that information is shared with others, as defined by Alain F. Westin [3]. According to Ibrahim Coulibaly [4], the concept of personal data is based on four main elements, namely: "any information", "concerning", "natural person", and "identified or identifiable". According to the CNIL [5], it is any information relating to a natural person who can be identified, directly or indirectly; for instance, a name, photo, fingerprint, postal address, email address, telephone number, social security number, internal identification number, IP address, computer login ID, voice recording, etc.

The processing of personal data, and handling of personal data, includes various actions such as collection, recording, organization, storage, modification, association with other data, transmission, etc. Analyses of the legal and regulatory texts as well as the charters for the use of computer systems have highlighted the six axes on which the protection of personal data is based on the following points [6]:

1. Information: the obligation to inform the user about the processing,
2. Consent: the consent expressed by the data owner to the collection and processing of his/her personal information,
3. Modification: includes several rights of the data owner, among others: access, update, and deletion of the data collected and processed,
4. Justification: Justify the purpose of the data processing by answering the question: "Is it justified to collect such data and use it in the context of such and such processing?"
5. Storage: the period of storage of personal data is limited in time and determined according to the context of the processing,
6. Transmission: The transmission of data to third parties must be limited and subject to authorization, in special cases, it is prohibited altogether.

In information systems, these axes are translated into guidelines, such as data protection by design, privacy impact assessment and data breach notification [7]. Jaap-Henk Hoepman in [8] has defined the following eight strategies that IT architects should apply to embed privacy by design, as illustrated in Figure 1.

1. Minimize: Reduce the impact of a system on privacy as much as possible by collecting only the data strictly necessary for processing.
2. Hide: Hide personal data and its interrelationships to prevent abuse, for example, by using encryption.
3. Separate: Process personal data in a distributed manner, in separate compartments as soon as possible (K-anonymity, I-diversity).
4. Aggregate: Processing personal data at the most aggregated level possible, limiting the details.
5. Inform: Ensure transparency by adequately informing data owners about the processing of their information.
6. Control: Give data subjects full right and control over their personal data.
7. Impose: Implement a privacy policy that complies with legal requirements and ensure it's applied.
8. Demonstrate: Enable the Data Controller to prove compliance with the Privacy Policy and applicable legal requirements.

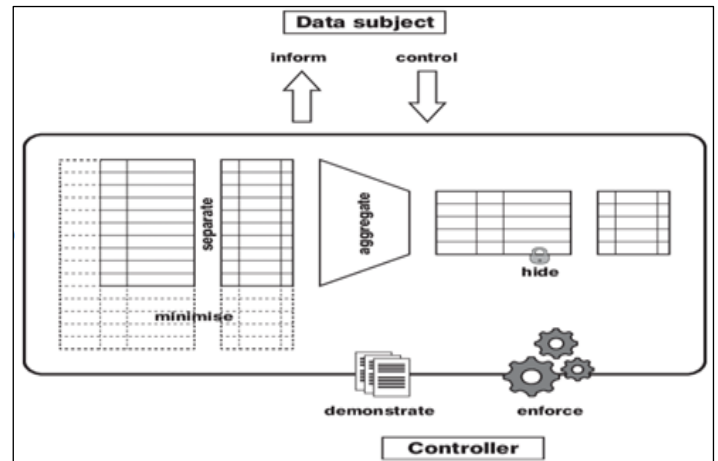


Figure 1: Strategies for personal data privacy.

Source: Authors, (2025).

### II.2 THE NATIONAL AUTHORITY FOR THE PROTECTION OF PERSONAL DATA

The National Authority for the Protection of Personal Data translated in French as 'Autorité Nationale de Protection des Données à caractère Personnel' (ANPDP) is an independent administrative institution functionally attached to the Presidency of the Republic, created by Law 18-07 of 10 June 2018 [7] to protect natural persons in the processing of personal data. The headquarters of the ANPDP are located in Algiers (commune of Hydra) [8]. The ANPDP is responsible for ensuring that the processing of personal data is carried out in accordance with the provisions of this law and for ensuring that the use of information and communication technologies does not involve threats to the rights of individuals, public freedoms, and privacy [9].

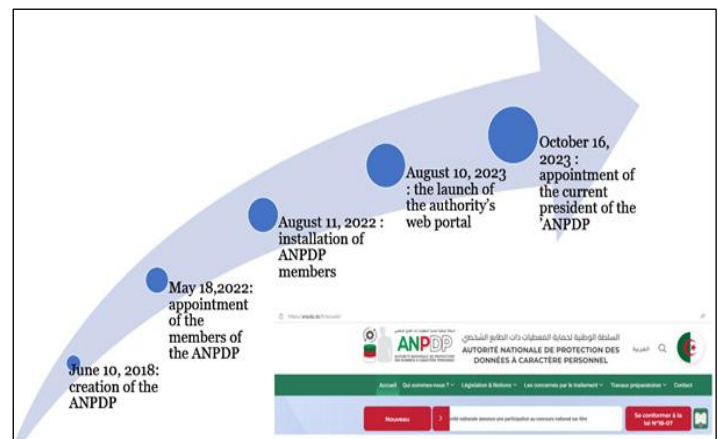


Figure 2: Timeline of the ANPDP

Source: Authors, (2025)

The ANPDP's missions [9]:

1. To issue authorizations and receive declarations relating to the processing of personal data;
2. To inform data subjects and data controllers of their rights and obligations;
3. To advise persons and entities who use the processing of personal data or who carry out tests or experiments likely to lead to such processing;
4. To receive complaints, appeals, and complaints relating to the implementation of the processing of personal data and to inform their authors of the action taken on them;



5. To authorize, under the conditions provided for in this law, cross-border transfers of personal data;
6. To order the necessary changes to the protection of the personal data processed;
7. To order the closure of data, its removal or destruction;
8. To present any suggestions likely to simplify and improve the legislative and regulatory framework relating to the processing of personal data;
9. To publish the authorizations granted and the opinions issued in the national register referred to in Article 28 of Law 18-07;
10. To develop relations of cooperation with similar foreign authorities, subject to reciprocity;
11. To impose administrative sanctions under the conditions defined by Article 46 of this Law 18-07;
12. To develop standards in the field of personal data protection;
13. To draw up rules of good conduct and ethics applicable to processing personal data.

Law No. 18-07 of 10 June 2018 on the protection of natural persons in the processing of personal data is an important step forward in terms of the protection of individual freedoms, but also in the accountability of companies for the data they collect and the preservation of the privacy of natural persons who interact in both the production and consumption processes [10], [11]. It is structured in seven headings, as illustrated in the following Table 1.

Table 1: Structure of Law 18-07.

Titles	Chapters	Articles
General Provisions		1 - 6
Fundamental principles of personal data protection	Prior approval and data quality	7 - 11
	Pre-treatment procedures	12 - 21
The National Authority for the Protection of Personal Data		22 - 31
Rights of the data subject	Right to be informed	32 - 33
	Right of access	34
	Right to rectification	35
	Right to object	36
	Prohibition of Direct Marketing	37
Obligations of the Data Controller	Confidentiality and security of processing	38 - 41
	The processing of personal data related to certification and electronic signature	42
	Processing of personal data in the context of electronic communication	43
	Transfer of data to a foreign country	44 - 45
Administrative and penal provisions	Administrative procedures	46 - 48
	Rules of procedure	49 - 53
	Criminal provisions	54 - 74
Transitional and final provisions		75 - 76

Source: Authors, (2025).

## II.3 THE UP PROCESS

For a better control of our project, the UP process has been integrated, which describes a two-pronged approach [12-14] (Figure 3).

A) A horizontal axis divided into four phases:

1. Inception: corresponds to the initialization of the project where a feasibility study of the system to be built is carried out.
2. Development: corresponds to the validation of the use cases resulting from the previous phase, the risk assessment and the study of the profitability of the project as well as the planning of the construction phase.
3. Construction: corresponds to the production of a first version of the product; it is focused on the phases of design, implementation and testing activities.
4. Transition: corresponds to the delivery of the product for a real operation where “beta tests” are carried out to validate the new system with users.
5. Iterations: an iteration is a complete development circuit that results in the delivery of an executable product.

B) A vertical axis that present the sequence of activities in the UP process:

1. Expression of needs: UP distinguishes between two types of needs. The functional needs that lead to the development of use cases, and Non-functional needs that result in the drafting of a requirements matrix.
2. Analysis: the analysis takes the form of the elaboration of all the diagrams giving a representation of the system, both static (mainly class diagram) and dynamic (diagram of use cases, sequences, activities, state-transitions, etc.).
3. Design: the design takes into account the technical architecture choices made for the development and operation of the system. The design extends the representation of the diagrams at the analysis level by integrating the technical aspects that are closest to the physical concerns.
4. Implementation: This phase corresponds to the production of the software in the form of components, libraries, or files.
5. Test: Tests verify the proper implementation of all requirements (functional and technical), the correct functioning of interactions between objects and the proper integration of all components into the software.

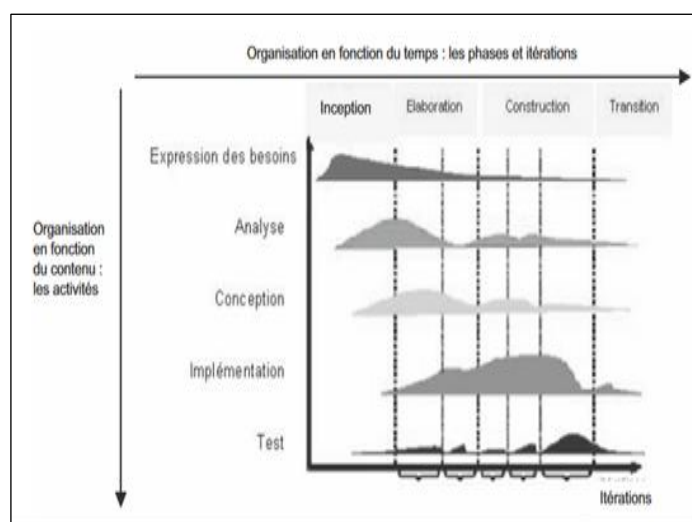


Figure 3: Overall diagram of the UP process.

Source: Authors, (2025).

### III. MATERIALS AND METHODS

The main objectives of the preliminary study are to establish and initial collection of functional and operational requirements and to model the system context. Functional needs represent the main functionalities of the system [15-16]. Non-functional requirements are indicators of the quality of the execution of functional requirements [17].

In this work, Microsoft Visual FoxPro V.9 (VFP) was used as the development environment for our application. The latter is a relational database management system (RDBMS) and an object-oriented programming environment designed to create database applications. Among the features of VFP, we can mention [18]:

- Rapid Application Development (RAD)
- Interactive Development Environment (IDE)
- Table and Database Management
- Data Connectivity

The functional needs are represented in table 1.

Table 2: System functional requirements.

Needs	Features
Management of the register of personal data processing	The Data Controller (DC) monitors the application's processing. The Authorized Representative (AR) verifies the validity of the processing with Law 18-07 and ensures the follow-up of the declaration submitted to the ANPDP.
Management of the register of data subjects' rights	The AR follows the data subject's entitlement request and notifies third parties of the results. The DC processes the request for this right.
Management of the register of personal data breaches	The AR tracks the personal data breach in the app, develops the action plan preventive measures, notifies third parties, and closes the case. The Chief Information Security Officer (CISO) handles the breach.
Database Administration	The administrator : - Controls access to all features, - Manage the Database, - Saves and restores the Database, - Creates and modifies user profiles.
Authentication and access	The user must enter a password to access the app.

Source: Authors, (2025).

In our case, the non-functional requirements are translated into three points:

1. Security: The system administrator is responsible for defining the user profiler and storing passwords securely.
2. Educational: To provide an informative bridge between the operations of the system, on the one hand, and the legal essence of Law 18-07, on the other hand.
3. Usability: Integrate tooltips into the app to help users navigate and interact effectively with the app.

The dynamic context diagram of our application "Conform1807" is illustrated in Figure 4, we emerge with the identified actors of the system:

1. Main actors:
  - The DC,
  - The AR,
  - The CISO,
  - The administrator.
2. Secondary actor :
  - The Data Subject (DS),
  - The ANPDP

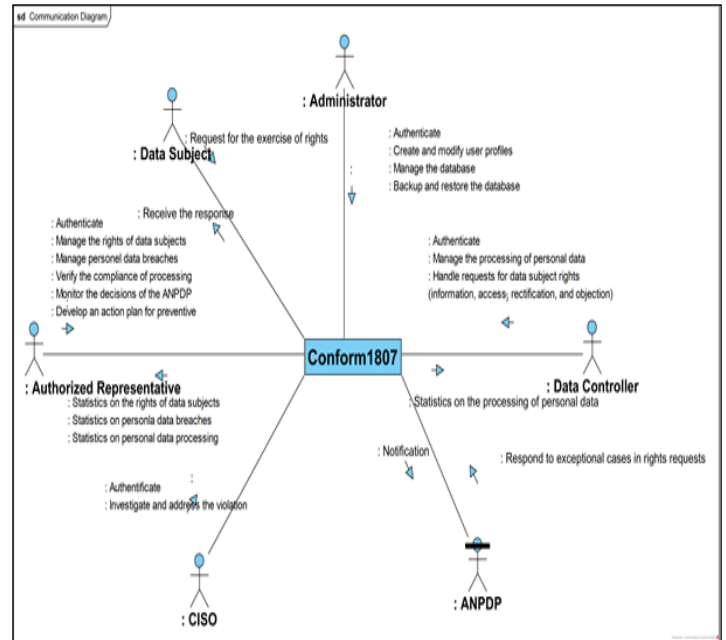


Figure 4: Dynamic context diagram of "Conform1807".

Source: Authors, (2025).

Table 3: Distribution of use cases and actors package.

Use cases	Actors	Package
Tracking the processing of personal data	DC	Management of the processing of personal data
Verify the compliance of personal data processing	AR	
Follow the decisions of the ANPDP	AR ANPDP	
Follow up on the right request of the data subjects	AR DS	Management of data subject rights requests
To process the data subjects' request for rights	DC ANPDP	
Track the personal data breach	AR ANPDP DS	Management of personal data breaches
Handling the breach of personal data	CISO	
Manage users	Administrator	Support service
Manage the Database		

Source: Authors, (2025).

The Use Case Diagram (UCD) identifies four main and two secondary actors:

- Main actors: the data controller, the AR, the CISO and the administrator.
- Secondary actors: the ANPDP and the data subject

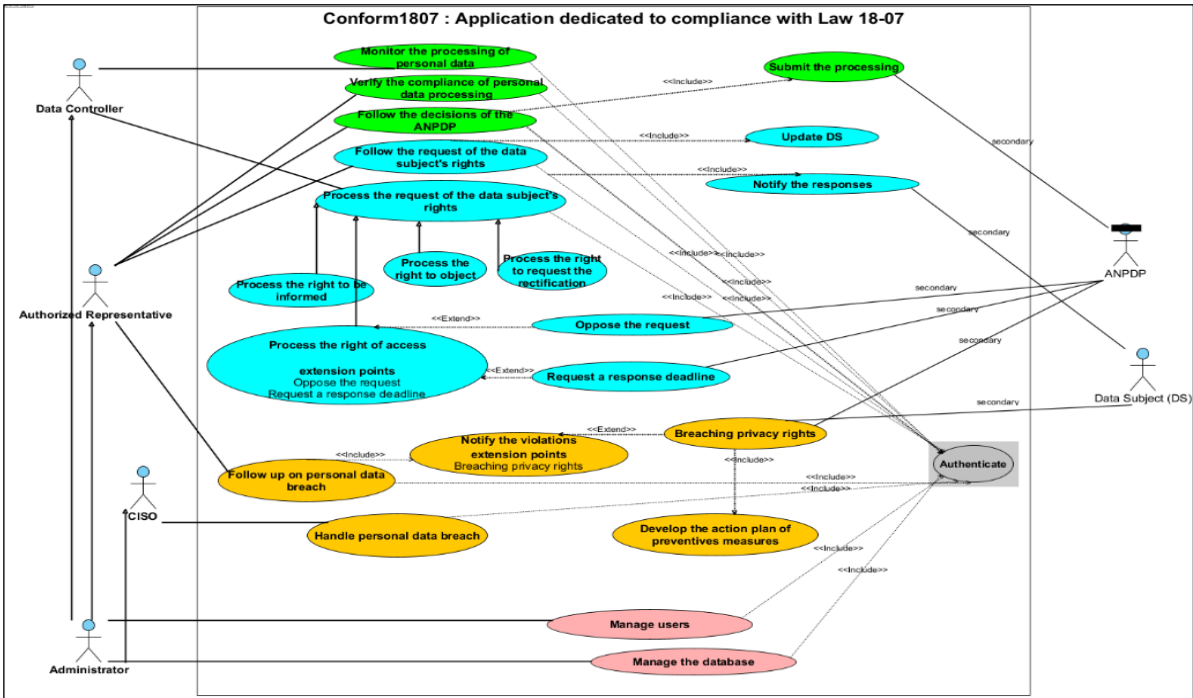


Figure 5: Use case diagram  
Source: Authors, (2025).

In the activity diagram of the “management of personal data processing”, there are two main actors and one secondary actor, as illustrated in figure 6.

1. The data controller, the main actor, monitors the processing of personal data.
2. The Authorized Representative, the main actor, verifies the compliance of the processing with respect to Low 18-07 and prints the processing declaration to be submitted to the ANPDP through the Web portal.
3. The ANPDP, a secondary actor, receives the treatment declaration.

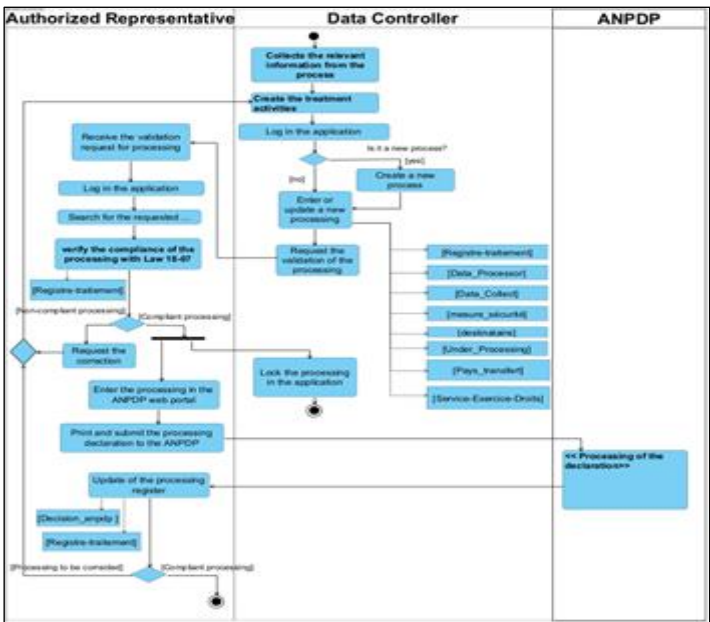


Figure 6: Activity diagram of the Management of Personal Data Processing package.  
Source: Authors. (2025).

In the activity diagram of the "Management of Data Subjects' Rights Requests", there are two main actors and two secondary actors, as illustrated in figure 7.

1. The AR, receives the request for rights from the concerned person and follows up on the rights request. He documents the results and notifies third parties.
2. The data controller, as the main actor, processes the request for the rights of the data subjects.
3. The data subject, who is a secondary actor, requests the exercise of these rights.
4. The ANPDP, a secondary actor, responds to requests for response time.

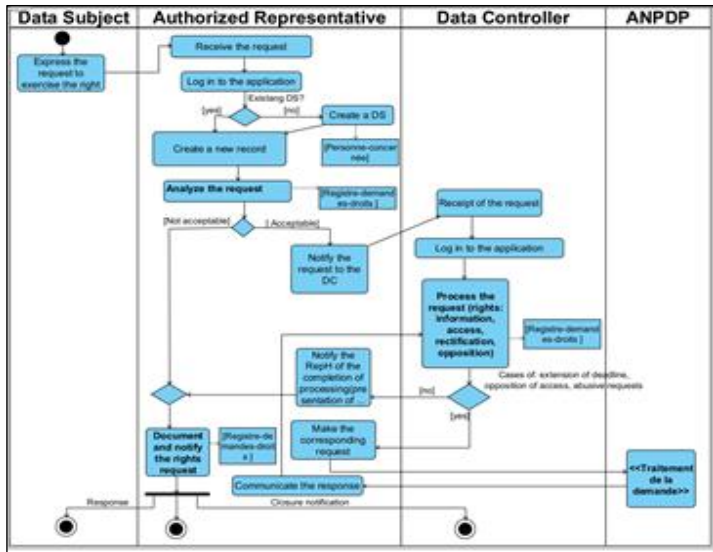


Figure 7: Activity diagram of the Management of Data Subjects Rights Requests package.  
Source: Authors. (2025).



In the activity diagram of the Personal Data Breach Management, there are two main actors and one secondary actor, as illustrated in figure 8.

4. The AR, the main actor, monitors the violation of personal data. He notifies third parties of the breach.

5. The CISO, the main actor, send the report of detection of the personal data breach to the AR, addresses the breach, and develops the action plan for preventive measures.

6. The ANPDP and the concerned person, secondary actors, receive notifications of violations.

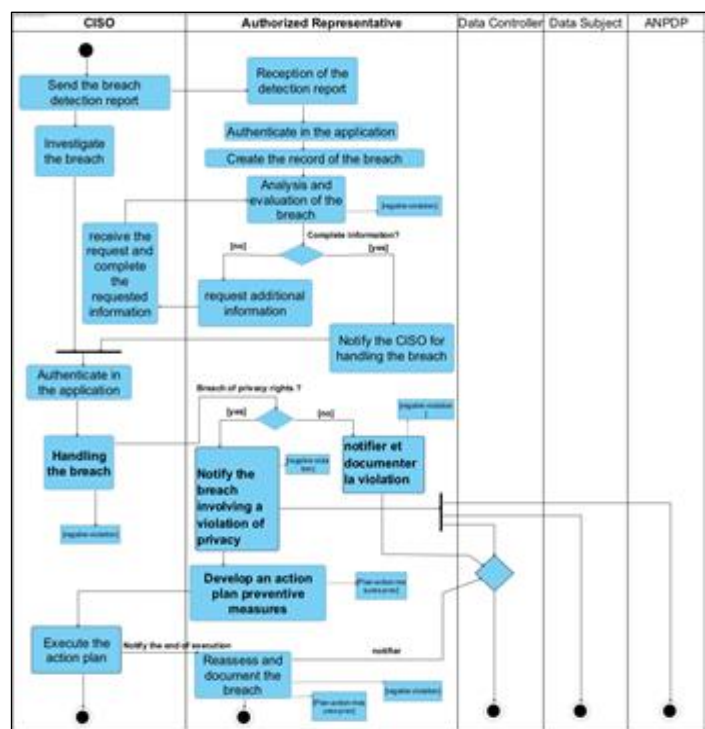


Figure 8: Activity diagram of the “Personal Data Breach Management” package.  
Source: Authors. (2025).

The class diagram of our application is shown in figure 9.

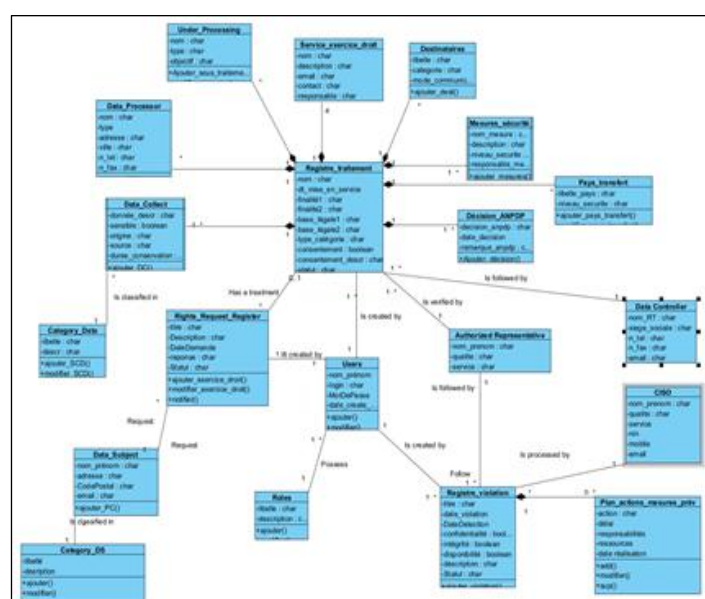


Figure 9: Class diagram.  
Source: Authors, (2025).

In our application, we implemented the SHA-256 hashing algorithm to secure user passwords, as shown in figure 10.

Users					
	ID user	Login	Id_role	E-mail	Pwd_sha
1		Riquelme	1	Riquelme@c70a20092df39a4d21d43db8e1d0e9a5ce9015e39adb33a12a777e033972f9a	
2	7	Abenunci	3	Abenunci@2ada56e837e28493a69318a4912a28b741507d63b0e2c0e363eb3b1a279a7f	

Figure 10: User table with hashed password field (Pwd\_sha).  
Source: Authors, (2025).

## IV. RESULTS AND DISCUSSIONS

To access the application named Conform1807, the user must authenticate with username and password (figure 11).

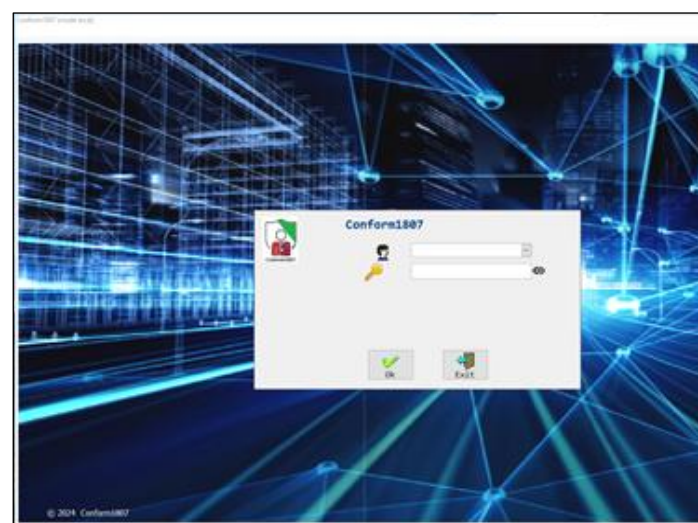


Figure 11 : The “Authentication” interface.  
Source: Authors. (2025).

The Roles interface (figure 12) , allows configuring system access permissions, thus ensuring system protection.

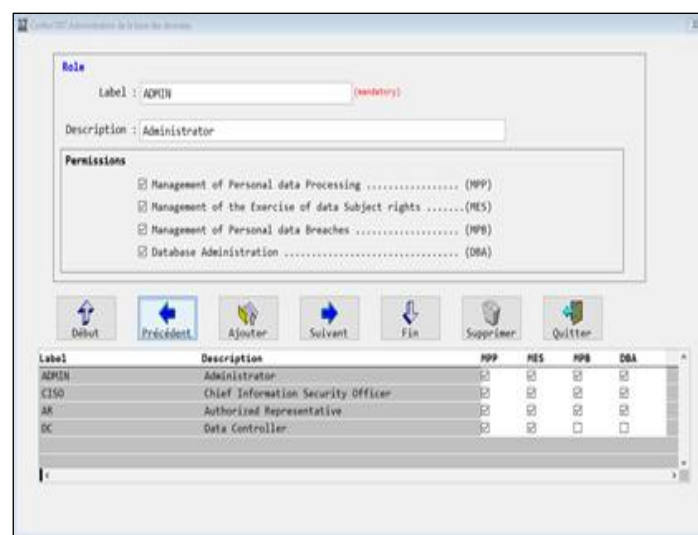


Figure 12 : The “Roles” interface.  
Source: Authors, (2025).

In order to manage users, the “User Management” interface is implemented, as shown in figure 13.



**User management**

**Identification**

First name : GUETTAL (mandatory)

Last name : Boudouane (mandatory)

Email : Boudouane@btp.dz (mandatory)

Login : Boudouane (mandatory)

Role : ADMIN (mandatory)

**Password**

Text : c67ba20002d39e42144b8b1d5edac0c9079e39a833a12e

Creation date : 27/09/2024

Buttons: Search, Previous, New, Next, Save, Delete, Exit

First name	Last name	Login	Email	Role	Password
GUETTAL	Boudouane	Boudouane	Boudouane@btp.dz	ADMIN	c67ba20002d39e42144b8b1d5edac0c9079e39a833a12e
BENSACI	Abdelkader	Abdelkader	Abdelkader@btp.dz	AN	82adab617a28669a093

Figure 13 : The "User Management" interface.

Source: Authors, (2025).

In the Conform1807 application, the management of the personal data processing register is carried out through the interface shown in figure 14.

**Processing Identification**

Name : Selection of recruitment (mandatory)

Type : Manual

Date of commissioning : 01/09/2023

Purpose 1 : Organization and supervision of tests

Purpose 2 : Installation of candidates

Category : Selection of candidates

Legal base 1 : The sixth case of Article 2 of law 18-07 - the pursuit of a legitimate interest by the data controller

Legal base 2 :

Buttons: Search, Previous, New, Next, Save, Delete, Exit

Name	Date of commissioning	Purpose 1	Purpose 2	Category	Legal base 1	Legal base 2	Status
Selection of recruitment	01/09/2023	Manual	Organization and supervision of tests	Selection of candidates	The sixth case of Article 2 of law 18-07 - the pursuit of a legitimate interest by the data controller		Open
Validation of the recruitment process	01/09/2023	Automatic	Installation of candidates	Selection of candidates	The sixth case of Article 2 of law 18-07 - the pursuit of a legitimate interest by the data controller		Validated

Figure 14 : The interface of the "Personal data processing management" module.

Source: Authors, (2025).

Managing data subject rights requests begins with identifying the concerned person, as illustrated in figure 15.

**Identification of the data subject**

First name : All (mandatory)

Last name : Ben Mohamed (mandatory)

Phone number :

Address : Boudouane City, Ouargla, Algeria

Reference :

**Category of the data subject**

Label : Candidates (mandatory)

Buttons: Start, Previous, Add, Next, End, Delete, Exit

First name	Last name	Email	Address	Phone number	Reference	Category
All	Ben Mohamed		Boudouane City, Ouargla,			Candidates

Figure 15: "Data Subjects Update" interface.

Source: Authors, (2025).

Once the data subject is identified, the request is tracked and recorded in the associated registry, as illustrated in figure 16.

**Management of Data Subject Rights Requests**

Request Identification

Number : 123/2023

Title : Request for recruitment test grading (mandatory)

Source : Postal mail

Type : ☒ Right to be informed (OK) ☐ Right of Access (OK) ☐ Right to request the Rectification (OK) ☐ Right to Object (OK)

Date : 15/09/2023 12:00:00 AM

Response Deadline : / /

Additional Information : Recruitment of maintenance operators carried out on 12/09/2023.

Buttons: Cancel, Validate the current step

Number	Title	Date	Source	OK	RA	RO
123/2023	Request for recruitment test grading	15/09/2023 12:00:00 AM	Postal mail			

Figure 16 : The interface of the "Management of requests for rights of data subjects".

Source: Authors, (2025).

The CISO and AR handle the personal data breach register, as explained in figure 17.

**Identification of Personal Data Breach**

Violation Number : 1/2024

Entry Date : 09/09/2024 09:03

Violation Title : Disclosure of the candidate's personal data during recruitment

Violation Types : ☒ Breach of Confidentiality (mandatory) ☐ Breach of Integrity ☐ Breach of Availability

Detection Date/Time : 05/09/2024 12:00:00 AM

Violation Description : (the candidate All Ben Mohamed's personal data subject to the selection & recruitment process).

Buttons: Search, Previous, New, Next, Save, Delete, Exit

Entry Date	Status	Violation Title	Violation Date/Conf.	Integ.	Breaching pri.	Action Plan
09/09/2024 09:03	In Progress	Disclosure of the candidate's personal data during recruitment	05/09/2024 12:00:00 AM			

Figure 17: The interface of the "Personal Data Breach Management" module.

Source: Authors, (2025).

Our application "Conform1807" stands out for its ability to provide companies with an effective tool to comply with the requirements of Law 18-07; it incorporates the principles of personal data protection such as individuals' rights, notification of personal data breaches as an example, and not exhaustively. By offering a user-friendly interface, automated compliance assessments, and personalized advice, it meets a critical need in the local market.

## V. CONCLUSIONS

Law 18-07 marks a significant step forward in Algeria's legal framework for personal data protection, aiming to regulate data processing comprehensively while ensuring the rights of individuals. However, compliance presents technical and organizational challenges, with risks of legal sanctions and reputational harm.

Addressing these issues, our application offers a local, accessible solution tailored to Algerian companies, filling a critical

gap by providing a user-friendly tool that facilitates data processing management, respects individuals' rights, and handles data breaches effectively, all while considering the specificities of algerian legislation and avoiding the high costs and complexity of international alternatives.

## VI. AUTHOR'S CONTRIBUTION

**Conceptualization:** Redouane Guettal, Mohammed Kamel Benkaddour.

**Methodology:** Redouane Guettal, Mohammed Kamel Benkaddour.

**Investigation:** Redouane Guettal, Mohammed Kamel Benkaddour.

**Discussion of results:** Redouane Guettal, Mohammed Kamel Benkaddour.

**Writing – Original Draft:** Redouane Guettal.

**Writing – Review and Editing:** Mohammed Kamel Benkaddour.

**Resources:** Redouane Guettal, Mohammed Kamel Benkaddour.

**Supervision:** Mohammed Kamel Benkaddour.

**Approval of the final text:** Redouane Guettal, Mohammed Kamel Benkaddour.

## VII. REFERENCES

- [1] A. Elguerri, "Protection Of Audiovisual Personal Data in the Digital Environment: Analytical study of Algerian law No. 18-07 on the Protection of Natural Persons with regard to the processing of personal data," Arab International Journal for Information Technology & Data, vol. 3, no. 1, pp. 117–132, 2023.
- [2] Z. Sipos, "CYBERSECURITY IN ALGERIA," Journal of Security & Sustainability Issues, vol. 13, no. 1, 2023.
- [3] A. F. Westin, Privacy and Freedom. Issues and Proposals for the 1970's. Part II, Balancing the Conflicting demands of Privacy, Disclosure, and Surveillance. Columbia Law Review 66, 1205–1253, 1966.
- [4] I. Coulibaly. The protection of personal data in scientific research. Ph.D dissertation, Grenoble Univ., Grenoble, France, 2011.
- [5] CNIL, "Commission Nationale de l'Informatique et des Liberté.", <https://www.cnil.fr>.
- [6] C. De Terwangne, "Council of Europe convention 108+: A modernised international treaty for the protection of personal data," Computer Law & Security Review, vol. 40, p. 105497, 2021.
- [7] W. B. Chik, "Generative Artificial Intelligence: The Protection of Personal Data and Countering False Narratives about the Person," SAclJ, vol. 36, p. 307, 2024.
- [8] J. H. Hoepman, "Privacy Design Strategies", 2013, *arXiv:1210.6621v2*.
- [9] Law No. 18-07, June 10, 2018, Official Journal of the Algerian Republic (JORA), no. 34, June 10, 2018.
- [10] ANPDP, "The National Authority for the Protection of Personal Data," 2024.
- [11] Z. YACoub, "On the protection of personal data in light of law n° 18-07: a new responsibility for companies", Academic Review of Legal Research (RARJ), Jun. 2021.
- [12] Y. Kovalenko, "The Right to Privacy and Protection of Personal Data: Emerging Trends and Implications for Development in Jurisprudence of European Court of Human Rights," Masaryk University Journal of Law and Technology, vol. 16, no. 1, pp. 37–57, 2022.
- [13] E. Gefenas, J. Lekstutiene, V. Lukaseviciene, M. Hartlev, M. Mourby, and K. Ó. Cathaoir, "Controversies between regulations of research ethics and protection of personal data: informed consent at a cross-road," Medicine, Health Care and Philosophy, pp. 1–8, 2022.
- [14] E. Gefenas, J. Lekstutiene, V. Lukaseviciene, M. Hartlev, M. Mourby, and K. Ó. Cathaoir, "Controversies between regulations of research ethics and protection of personal data: informed consent at a cross-road," Medicine, Health Care and Philosophy, pp. 1–8, 2022.
- [15] S. C. Salim and J. Neltje, "Analysis of Legal Protection Towards Personal Data in E-Commerce," in 3rd Tarumanagara International Conference on the Applications of Social Sciences and Humanities (TICASH 2021), Apr. 2022.

[16] N. S. Haliwela, "The Essence of Legal Protection of Personal Data of Customers In Banking Transactions," SASI, vol. 29, no. 3, pp. 548–556, 2023.

[17] M. Durovic and T. Corno, "The privacy of emotions: From the GDPR to the AI Act, an overview of emotional AI regulation and the protection of privacy and personal data," Privacy, Data Protection and Data-driven Technologies, pp. 368–404, 2024.

[18] Inter Soft Associates, "Visual FoxPro's Advanced Technical Features Included Complex Data Processing," 2024.



ISSN ONLINE: 2447-0228

ITEGAM-JETIA

Manaus, v.11 n.52, p. 161-169. March./April., 2025.

DOI: <https://doi.org/10.5935/jetia.v11i52.1565>

## RESEARCH ARTICLE

## OPEN ACCESS

# ASSESSMENT OF THE EFFECT OF SERIES PASSIVE FILTER ON HARMONIC DISTORTION-POWER LOSSES RELATIONSHIP IN AN ELECTRICITY DISTRIBUTION NETWORK

Okuo Michael Ozaveshe<sup>1</sup>, Adebisi Oluseun Ibrahim<sup>2</sup>, Akinola Olubunmi Adewale<sup>3</sup><sup>1,2,3</sup> Department of Electrical engineering, Federal university of agriculture, Abeokuta, Nigeria<sup>1</sup><http://orcid.org/0009-0001-3373-0494>, <sup>2</sup><http://orcid.org/0000-0001-8958-4951>, <sup>3</sup><http://orcid.org/0000-0001-6532-1698>Email: [okuomichael5@gmail.com](mailto:okuomichael5@gmail.com), [adebisioluwaseun@funaab.edu.ng](mailto:adebisioluwaseun@funaab.edu.ng), [akinolaoa@funaab.edu.ng](mailto:akinolaoa@funaab.edu.ng)

## ARTICLE INFO

**Article History**

Received: January 16, 2025

Revised: February 20, 2025

Accepted: March 15, 2025

Published: April 31, 2025

**Keywords:**Non-linear load,  
Power loss,  
Power Quality,  
Series passive filter,  
Total Harmonic Distortion.

## ABSTRACT

Technological innovations in recent times have led to widespread use of non-linear loads in power networks. These loads generate harmonics which result in the distortion of the system's voltage and current signals and consequently, leads to power loss. This research assessed the total harmonic distortion (THD) mitigation capability of series passive filters (SePF) in an electricity distribution network (EDN) with a high penetration level of non-linear loads and the resulting effect on power loss (PL). The EDN for 250-seater computer laboratory facility in Federal University of Agriculture, Abeokuta (FUNAAB), Nigeria was considered as a case study. The network modelled and simulated without and with SePF in MATLAB/Simulink environment (R2023a version). The system's voltage-current THD (THDV-I) and PL were evaluated to determine the relationship between the two parameters. The obtained results showed that when no filter was applied, the THDV-I and PL were 37.38% and 9,703 W, respectively. However, when SePF was used on the network, the THDV-I reduced to 4.90% and the PL minimised to 146 W. These results indicated that PL reduces with decrease in THDV-I. The series passive filter application on the considered facility in this research appropriately mitigated the observed THD and the associated PL.



Copyright ©2025 by authors and Galileo Institute of Technology and Education of the Amazon (ITEGAM). This work is licensed under the Creative Commons Attribution International License (CC BY 4.0).

## I. INTRODUCTION

Power quality problems, especially harmonic distortion and power losses, have grown to be major issues in the current electrical distribution network because non-linear loads are used so frequently. These non-linear loads, which include things like computers, variable speed drives, and fluorescent lights, absorb current in a way that isn't sinusoidal, which adds harmonic currents to the power system. [1-3]. The presence of these harmonic currents distorts the ideal sinusoidal waveform of the voltage and current, leading to various adverse effects, including increased power losses, malfunctioning of sensitive equipment, and overheating of transformers and cables [1], [4-6]. Harmonic distortion in electricity distribution systems, if left unmitigated, can lead to severe reliability and efficiency issues, thereby affecting the overall performance of the system [7-10].

The relationship between power losses and harmonic distortion is essential to comprehending the overall effectiveness of the electrical distribution network. Due to the components with

higher frequency in the current waveform of the system, electrical systems' losses which are mostly caused by resistive losses in conductors and transformers increase when harmonic currents are present. Additional losses are caused by the conductors' increased eddy current losses, core losses, and skin effects as a result of these higher-frequency currents. Also, harmonic distortion can increase system losses by causing voltage instability and interfering with protective device functionality. [1], [8], [11], [12]. Therefore, an effective harmonic mitigation strategy must not only reduce distortion but also minimize the resultant power losses.

Different solutions techniques have been proposed to mitigate harmonic distortion in power networks. To begin with, authors [6], [13-16] explored how to lower harmonic emission from non-linear loads by modifying power network topologies, isolating, and using harmonic reduction transformers. More so, authors [6], [17], [18] discussed the use of power filters as mitigating techniques for harmonic reduction in power networks, encompassing both passive and active filters as well as their

hybrids. Installing passive power filters is one of the commonest ways to reduce harmonic distortion. By creating low-impedance pathways for certain harmonic frequencies to avoid the load, passive filters that consist of resistors, inductors, and capacitors which are intended to lessen particular harmonic frequencies from the electrical network. [19], [13], [18], [17]. Since each strategy has its advantages and disadvantages, it is impossible to definitively identify which is optimal. To choose the optimal solution and avoid wasting financial resources on inappropriate ones, a preliminary analysis of the problem must be carried out. [9], [13], [20]. On the overall, it has been shown that when these mitigation measures are applied, harmonic distortion reduces drastically, thereby reducing power losses in the system [19], [21], [22].

In this context, the assessment of the effect of series passive filters on the harmonic distortion-power loss relationship is essential for improving the efficiency and reliability of electricity distribution networks [20], [23]. The main goal of such assessments is to determine how the installation of these filters influences both the level of harmonic distortion and the associated power losses in the system.

It must define the problem and importance of the research carried out, it presents a (not very extensive) review of the literature on the subject of the article, including the authors' contributions to the state of the art. If you use abbreviations or acronyms, first write the words that identify them and then, in parentheses, the acronym. This set also establishes the research question, the objectives of the work and hypothesis, if necessary, the importance and limitations of the study. Establishes the method used at work. It is written in the present tense.

## II. THEORETICAL REFERENCE

A number of investigations have been conducted on mitigating harmonic distortion and establishing its relationship with power loss without and with filter application.

An assessment of how harmonics affect the distribution of power in the system. Author [4] conducted research on the influence of harmonic effects on energy distribution in a medium voltage network (20kV). The study suggested formulas for calculating energy loss assessments resulting from THDI and power factor noncompliance within the limits imposed by standards. Comparative analysis of ShPF and SAF (shunt active filter) for electrical distribution network harmonic mitigation was presented by author [18]. The study considered a typical bottling company in Nigeria as a test network. Evidence from the results showed that ShPF and SAF minimised the network's THDV and THDI with an indication that ShPF demonstrated better performance than SAF, making it more suitable for mitigating harmonics on the bottling company. Author [19] investigated the effectiveness of harmonic filters in improving power quality under industrial load. Shunt passive filters and hybrid combinations of series active filter and shunt passive filter and shunt active filter and shunt passive filter were shown to be effective harmonic distortion reduction techniques for the test network taken into consideration in this work.

By simultaneously determining the maximum voltage and current harmonic contribution in interconnected networks, Author [22] created a novel technique for reducing harmonic magnitude. According to simulation results, the suggested approach yields more concrete outcomes for accurately identifying the harmonic source that produces the most reduction in harmonic voltage or current in the designated network bus or line. Author [24] presented harmonic analysis in power distribution networks. The research

focused on the improvement of the accuracy and reliability of harmonic analysis in the power distribution network. Author [25] looked at how harmonics affected a distribution transformer's temperature rise and power loss. This study examined the elevated losses and temperature rise under well-defined harmonics in a 25kVA oil-filled distribution transformer. The theoretical and practical data were directly correlated, demonstrating the detrimental harmonics' impact on power losses and the accompanying increase in distribution transformer's temperature.

Previous studies reviewed have shown that passive filters are capable of significantly reducing harmonic distortion, but their impact on power losses has been varied depending on the system configuration, filter design, and the level of harmonics present. The objective of this research is to fill this gap by providing a detailed analysis of how series passive filters influence both harmonic distortion levels and power losses in an electricity distribution network.

## III. MATERIALS AND METHODS

### III.1. HARMONIC INDICES

Harmonic indices are key parameters used to quantify the level of harmonic distortion in power systems, enabling the evaluation of power quality and the identification of potential issues caused by harmonic currents. These indices help in assessing the impact of harmonics on system performance and guide in the design of mitigation strategies like passive filters [11].

### III.2. TOTAL HARMONIC DISTORTION (THD)

One of the most widely used indexes for figuring out a waveform's harmonic content is total harmonic distortion (THD). It can be used to measure the total distortion level of both voltage and current, making it an indicator of a waveform's effective value [14],[26]. Put another way, it is the harmonics' potential heating value in relation to the fundamental. It is possible to compute this index for voltage or current using equation (1)[18],[24]:

$$THD = \frac{\sqrt{\sum_{h>1}^{h_{max}} M_h^2}}{M_1} \quad (1)$$

where  $M_h$  is the M quantity of the RMS value of harmonic component h.

The square root of the sum of the squares is the distorted waveform's RMS value. The THD and the waveform's RMS value are connected by equation (2):

$$RMS = \sqrt{\sum_{h>1}^{h_{max}} M_h^2} = M_1 \sqrt{1+THD^2} \quad (2)$$

When a distorted voltage is placed across a resistive load, the THD can give a fairly accurate estimate of the additional heat generated, but for many applications, one must be mindful of its limitations[14], [26]. The most common usage of the Voltage harmonic distortion is characterized by the THD index. The waveform's fundamental value at the time of the sample is nearly always used as a reference for harmonic voltages.  $THD_v$  is virtually always a substantial figure as the underlying voltage only changes by a few percent. Relating to this work we first have to



determine the total harmonic distortion for both current and voltage. A harmonic affected waveform's current and voltage THD can be written respectively as equations (3) and (4) as:

$$THD_I = \frac{\sqrt{\sum_{h=2}^{\infty} I_h^2}}{I_1} \quad (3)$$

$$THD_V = \frac{\sqrt{\sum_{h=2}^{\infty} V_h^2}}{V_1} \quad (4)$$

Equations (5) and (6) are alternate form of equations (3) and (4) respectively while equation (7) gives the combined expression relating both current and voltage.

$$I^2 = I_1^2 (1 + THD_I^2) \quad (5)$$

$$V^2 = V_1^2 (1 + THD_V^2) \quad (6)$$

$$THD_{V-I} = \sqrt{THD_V^2 + THD_I^2} \quad (7)$$

Where the fundamental current and voltage values are  $I_1$  and  $V_1$ , and the RMS current and voltage values are  $I$  and  $V$ .

The equation (7) is primarily used in power systems research to assess the cumulative effect of voltage and current harmonics on system performance. This combination provides a holistic measure of distortion in systems with complex harmonic interactions, especially when studying the impacts of harmonic pollution on power quality and reliability [27], [28].

### II.3. HARMONIC DISTORTION-POWER LOSS RELATIONSHIP IN DISTRIBUTION NETWORK

Harmonic active power, a product of the same order of harmonic voltage and current, is injected into the distribution system by non-linear loads. Even though It is substantially lesser than the underlying active power, the power due to harmonic distortion will raise the utility supply system's losses.. Power loss and harmonic distortion are related via equations (8) to (21) [29],[30]:

$$\text{Power loss due to harmonics (PL)} = RI^2 \quad (8)$$

where  $R$  is the resistance of the system and  $I$  is the RMS current values and  $I_h$  is harmonic current at individual harmonic  $h$

From equation (3) above we have:

$$THD_I = \frac{\sqrt{\sum_{h=2}^{\infty} I_h^2}}{I_1} \quad (9)$$

Equation (14) can be modified into equations (10) and (11)

$$THD_I \cdot I_1 = \sqrt{\sum_{h=2}^{\infty} I_h^2} \quad (10)$$

$$THD_I^2 \cdot I_1^2 = \sum_{h=2}^{\infty} I_h^2 \quad (11)$$

where RMS current is

$$I^2 = \sum_{h=2}^{\infty} I_h^2 + I_1^2 \quad (12)$$

Making  $\sum_{h=2}^{\infty} I_h^2$  the subject, equation (13) is obtained.

$$\sum_{h=2}^{\infty} I_h^2 = I^2 - I_1^2 \quad (13)$$

Putting equation (13) in equation (11), equations (14) to (16) are obtained.

$$I^2 - I_1^2 = (I_1^2 \cdot THD_I^2) \quad (14)$$

$$I^2 = I_1^2 + (I_1^2 \cdot THD_I^2) \quad (15)$$

$$I^2 = I_1^2 (1 + THD_I^2) \quad (16)$$

Putting Equation (16) into equation (8), equation (17) was obtained

$$P_L = RI_1^2 (1 + THD_I^2) \quad (17)$$

Putting equation (12) in equation (8), equation (18) was obtained

$$P_L = R(I^2 + \sum_{h=2}^{\infty} I_h^2) \quad (18)$$

where  $R$  is resistance of the conductor,  $n$  is the harmonic order,  $I_n$  is the current in harmonic order  $n$ .

For a three-phase three-wire utility, the total losses are expressed in equations (19) and (21)

$$\text{loss due to harmonics} = 3R_p I_p^2 + R_n I_n^2 \quad (19)$$

$$\text{where } I_n^2 = \sum_{h=1}^{\infty} I_{nh}^2$$

RMS phase current is expressed in equation (20)

$$I_p^2 = \sum_{h=1}^{\infty} (I_{ah}^2 + I_{bh}^2 + I_{ch}^2) \quad (20)$$

$$\text{loss due to harmonics} = 3R_p \sum_{h=1}^{\infty} (I_{ah}^2 + I_{bh}^2 + I_{ch}^2) + R_n \sum_{h=1}^{\infty} I_{nh}^2 \quad (21)$$

where the neutral line current is  $I_n$ , while the balanced network's phase current is  $I_p$ . The  $h$ th harmonic of the neutral current is  $I_{nh}$ , the phase and neutral resistances are  $R_p$  and  $R_n$ , and the harmonic  $h$  currents in phases A, B, and C are  $I_{ah}$ ,  $I_{bh}$ , and  $I_{ch}$  respectively [29, 30]. Currents that are zero-sequence and unbalanced can cause overloading due to the neutral wire's significant loss

## II.4. DESIGN OF SERIES PASSIVE FILTER

A filter connected in series with a system is called a series passive filter. Harmonics are blocked before they may enter the system using high impedance passive filters in series. Passive filters are typically connected in series with main switchboards, motor control systems, switch gears, busbars, etc.[3], [13], [17], [31] Designs of single or double-tuned passive filters are very good options for applications that need the suppression of particular harmonics. For this research, SePF with special attention on single tuned filter. The basic configuration of a tuned filter is represented in Figure 1 while the schematic diagrams of SePF is shown in figure 2.

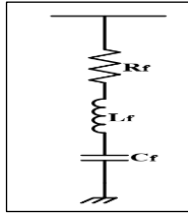


Figure 1: Schematic diagram of a single tuned passive filter  
Source: Authors, (2025).

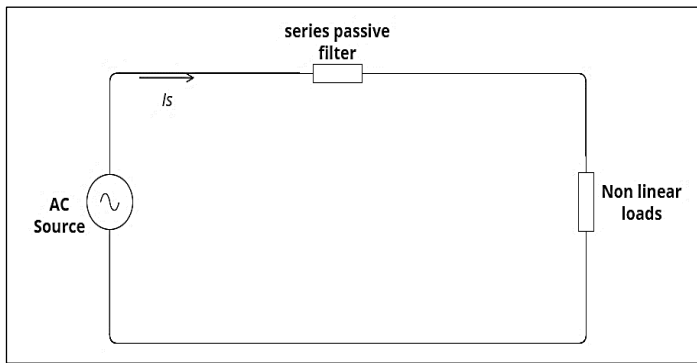


Figure 2: Schematic diagram of SePF  
Source: Authors, (2025).

From a power factor standpoint, selecting the appropriate capacitor size is crucial when designing tuned passive filters. According to author [32] The filter capacitor  $C_f$  is usually sized for a known reactive power compensation  $Q_c$  in order to boost power factor. Consequently,  $C_f$  and  $Q_c$  are related by equation (22):

$$C_f = \frac{Q_c}{2 \pi f V^2} \left( 1 - \frac{1}{n^2} \right) \quad (22)$$

where  $n$  is the harmonic order and  $f$  is the fundamental frequency, and  $V$  is the supply voltage.

Equation (28) governs the series resonance provided by the filter reactor  $L_f$  at the harmonic frequency  $f_n = nf$ :

$$X_L = X_c \quad (23)$$

where the capacitive reactance is denoted by  $X_c$  and the inductive reactance by  $X_L$ .

The values for  $X_L$  and  $X_c$  are provided by equations (24) and (25) as:

$$X_L = 2\pi f_n L_f \quad (24)$$

$$X_c = \frac{1}{2 \pi f_n C_f} \quad (25)$$

In equations (29) and (30) make  $L_f$  and  $C_f$  the subjects, respectively. equations (26) and (27) are obtained as:

$$L_f = \frac{X_L}{2 \pi f_n} \quad (26)$$

$$C_f = \frac{1}{2 \pi f_n X_c} \quad (27)$$

The use of equations (24) and (25) in equation (23) yields equation (28) providing the filter's inductive value..

$$L_f = \frac{1}{4 \pi^2 f_n^2 C_f} \quad (28)$$

The filter's quality factor  $Q$ , which determines how sharp the tuning is, determines the resistance  $R_f$  of a tuned filter [32, 33]. Equation (34), from which  $R_f$  is mathematically derived, is further adjusted in equations (30) and (31) using equation (28) in (29).

$$R_f = \frac{2 \pi f_n L_f}{Q} \quad (29)$$

$$R_f = \frac{\sqrt{L_f}}{\sqrt{C_f}} \quad (30)$$

$$R_f = \sqrt{\frac{L_f}{Q^2 C_f}} \quad (31)$$

The value of  $Q$  ranges from 20 to 100; a higher value of  $Q$  results in better harmonic distortion mitigation. [32, 33]

## II.5. CASE NETWORK

250 seater's computer laboratory electrical network is going to be used as the test system in this study. 250 seater's computer laboratory is a facility in Federal university of Agriculture Abeokuta (FUNAAB) in Ogun state, Nigeria. The facility was fed from a dedicated 33 kV feeder which was stepped down to 11/0.415 kV through a 33 MVA rating power transformer. The facility has a back-up consisting of a generator of 300 kVA rating. The layout of the facility's electrical distribution network is shown in Figure 3 Tables 3 and 4 displays the power requirements of the primary loads.

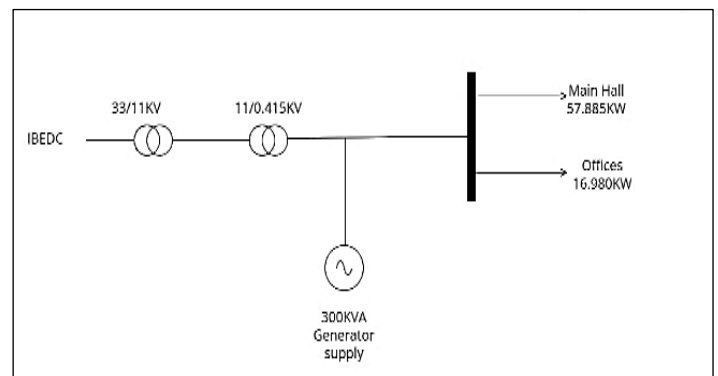


Figure 3: The power network layout of the 250 seater's computer lab.  
Source: Authors, (2025).

Table 3: Power requirements of the main hall loads in 250 seater's computer laboratory.

Loads	Type	Unit	S(VA)	P(W)	Q(Var)
Computers	N	291	23643.75	18915	14186.23
fans	N	30	1312.5	1050	787.2
Compact fluorescent	N	116	4350	3480	2610
Split Air conditioner	N	6	42750	34200	25650
CCTV cameras	N	16	300	240	180
<b>Total</b>			<b>72356.3</b>	<b>57885</b>	<b>43413.6</b>

Source: Authors, (2025).

Table 4: Power requirements of the office loads in 250 seater's computer laboratory.

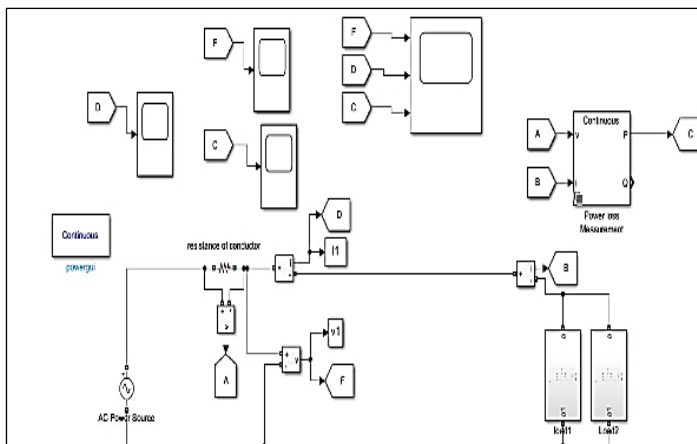
Loads	Type	Unit	S(VA)	P(W)	Q(Var)
Computers	N	12	975	780	585
fans	N	12	525	420	315
Compact fluorescent	N	12	450	360	270
Air conditioner	N	12	18750	15000	11250
printer	N	12	525	420	315
<b>Total</b>			<b>21225</b>	<b>16980</b>	<b>12735</b>

Source: Authors, (2025).

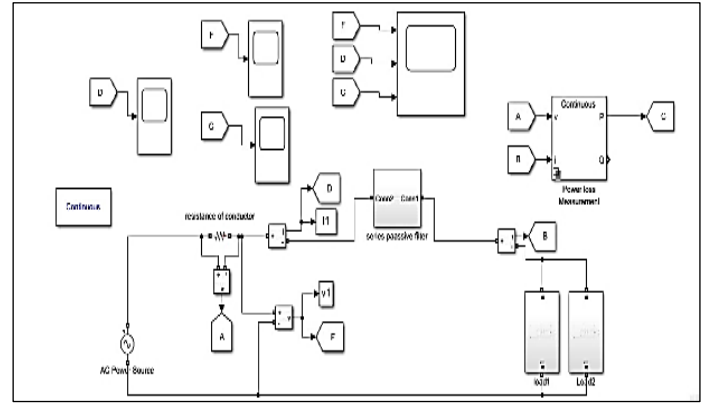
Where N is nonlinear load

## II.6. CHOICE OF SIMULATION SOFTWARE

In order to be able to investigate properly the harmonic distortion's effects on power losses, a virtual environment of the distribution network will be simulated using Matlab/Simulink software. Simulink is a graphical programming environment for modelling and analysing dynamical systems. It is interactive and provides an enabling environment to explore design concept to model non-linear system at any level of complexity. The Simulink model of the considered 250 seater's computer laboratory distribution network. Apart from being interactive, Simulink allows the systematic construction of the distribution network and harmonic mitigation device using basic function blocks [34]. Among its other benefits are the provision of solvers, customized libraries and graphical editors for non-linear systems design and analysis. Hence, the choice of MATLAB/Simulink software for this study. The fast Fourier transform application will be used in deriving the THD of the system as it is very useful in transforming time series signal to frequency axis signal. The Simulink model for the different configuration of filters is depicted in figure 4.



(a)



(b)

Figure 4: Simulink model (a) without filter (b) SePF for 250 seater computer laboratory power distribution network

Source: Authors, (2025).

## IV. RESULTS AND DISCUSSION

### III.1. SIMULATION RESULTS OF TEST NETWORK WITH NO FILTER

The obtained results from simulating the Simulink model of 250 Seater's Computer Laboratory facility network layout without any use of filter are displayed in Figures 5 to 8. Figure 5 and 6 are the three phase waveforms of the network's voltage and current respectively. Figure 7 is the power loss three phase wave form and Figures 8a and 8b is the spectrum for both voltage and current

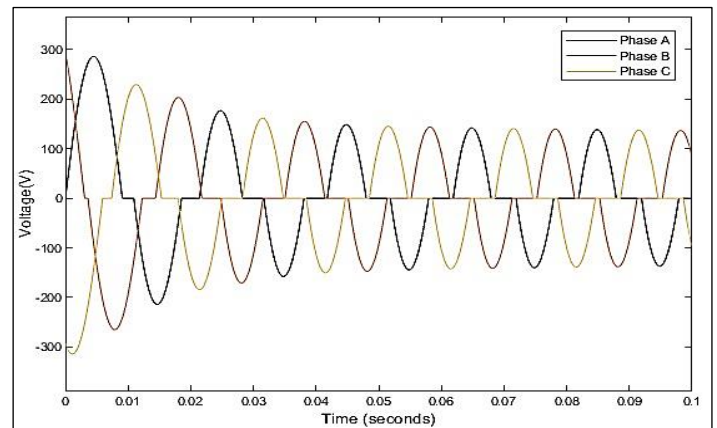


Figure 5: Three phase voltage waveform of the case network without filter

Source: Authors, (2025).

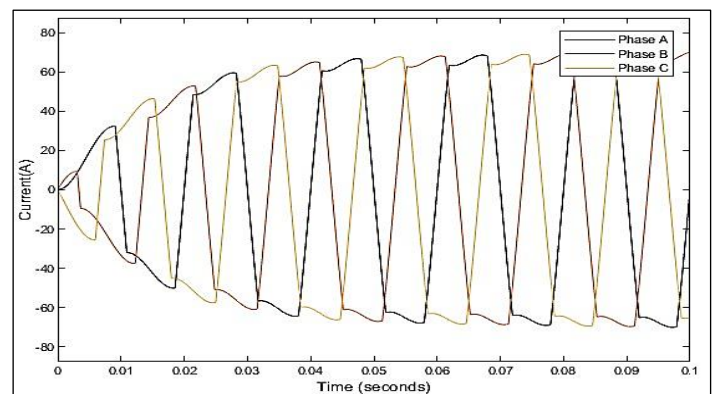


Figure 6: Three phase Current waveform the case network without filter

Source: Authors, (2025).

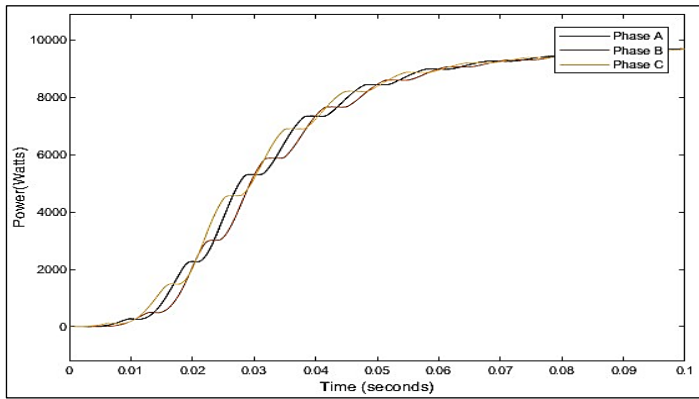
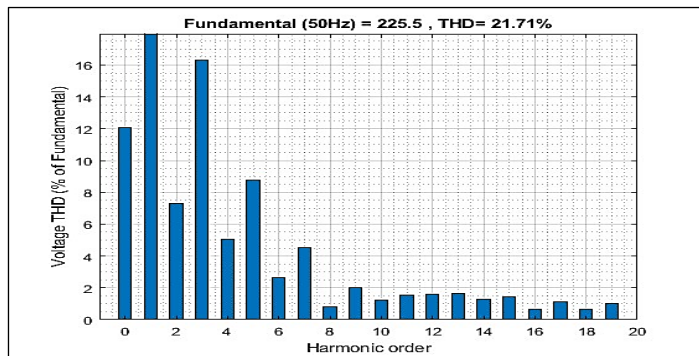
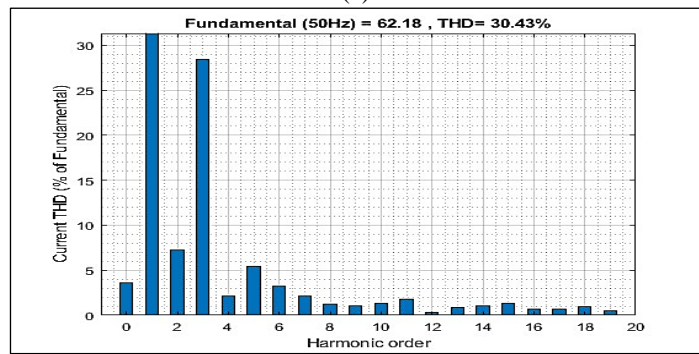


Figure 7: Three phase Power loss waveform the case network without filter  
Source: Authors, (2025).



(a)



(b)

Figure 8: The spectrums of case network without filter (a) voltage  
(b) Current  
Source: Authors, (2025).

The  $THD_V$  and  $THD_I$  in Figure 8a was evaluated as 21.71% and 30.43% respectively. From figure 6 and 7 we can see the distortions in the system's voltage and current signal in their spectrums respectively without filter. According to Figure 7 the maximum power loss in the system was measured as 9703 W. The  $THD_{V-I}$  is calculated using Equation (7) and the value was 37.38% which is very high without filter applied.

### III.2. SIMULATION RESULT OF TEST NETWORK WITH SePF

The results obtained from the simulation of the Simulink model of 250 Seater's Computer Laboratory facility network layout with Series passive filter applied are presented in Figure 9 to 12. Figures 9 and 10 shows the three phase wave form for the system's voltage and current respectively. Figure 11 shows the power loss three phase wave form of the case network and Figures

12a and 12b shows the spectrum for voltage and current respectively.

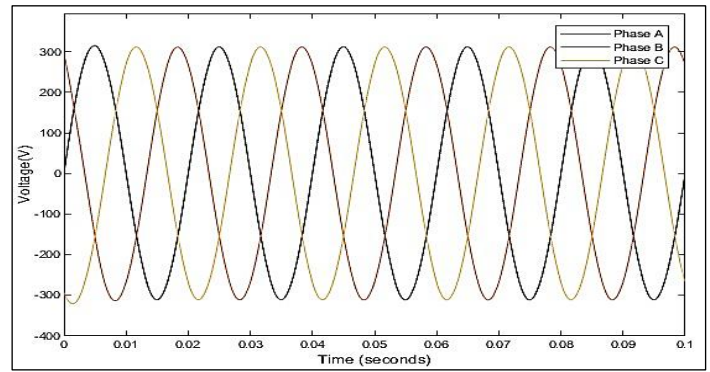


Figure 9: Three phase voltage waveform of the case network with the use of SePF  
Source: Authors, (2025).

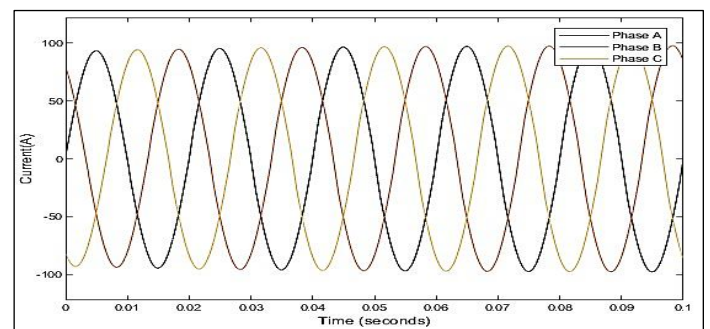


Figure 10: Three phase current waveform of the case network with the use of SePF  
Source: Authors, (2025).

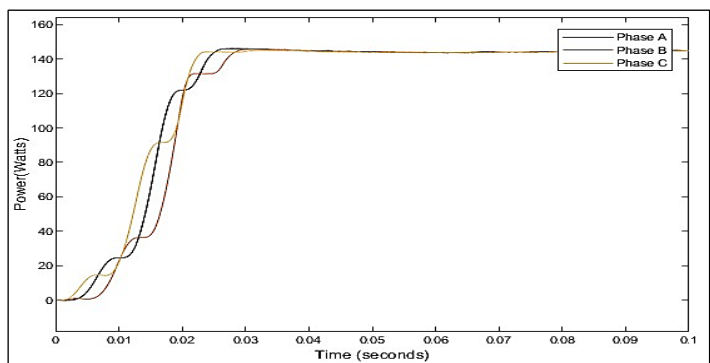
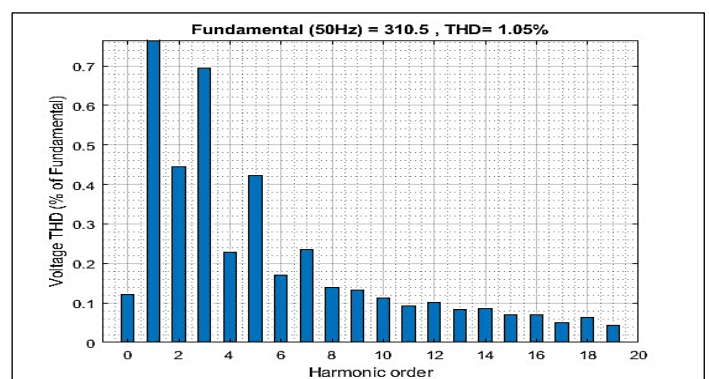


Figure 11: Three phase power loss waveform of the case network with the use of series passive filter  
Source: Authors, (2025).



(a)



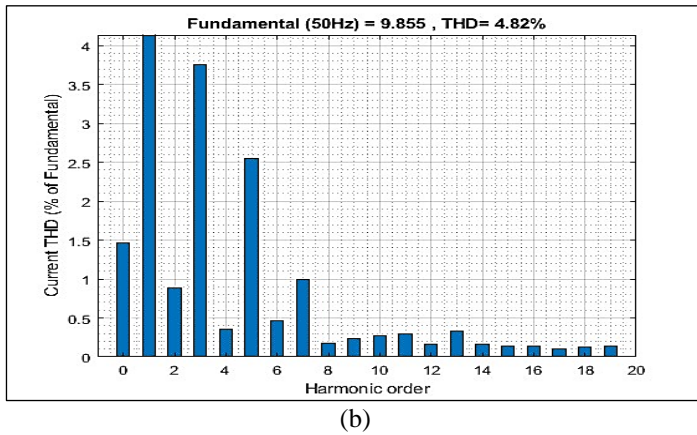


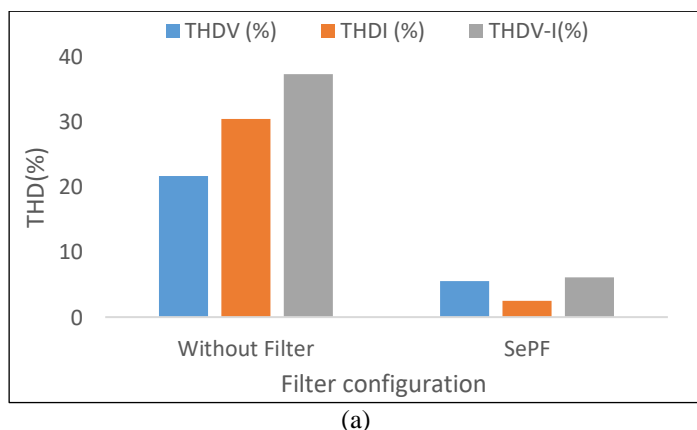
Figure 12: The spectrums of the case network with the use of SePF (a) voltage (b) Current  
Source: Authors, (2025).

Figure 13 and 14 shows the minimized distortion in the voltage and current signals respectively when SePF was applied to the network.  $THD_V$  in Figure 16(a) was evaluated as 0.90% given a reduction of 20.81% when compared with Figure 8(a), while  $THD_I$  in Figure 16(b) was evaluated as 4.82% given a reduction of 25.61% when compared with Figure 8(b). According to Figure 15 the maximum power loss in the system was measured as 146 W given a reduction of 9557 W as when compared with Figure 7. The  $THD_{V-I}$  is calculated using Equation (7) and the value was 4.90% with SePF applied.

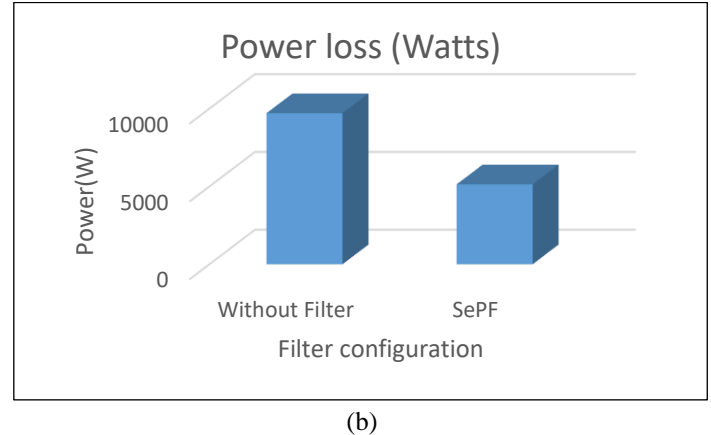
The values of  $THD_V$  and  $THD_I$  gotten from the results of the simulation where inputted in equation (7) to calculate the  $THD_{V-I}$  which is the combination of both  $THD_V$  and  $THD_I$ . Figure 13a shows the comparison of  $THD_V$ ,  $THD_I$ , and  $THD_{V-I}$  and Figure 13b shows the power loss comparison without filter and with SePF applied in the 250 Seater's Computer Laboratory facility distribution network.

### II.3. COMPARISON OF THD ON PL WITHOUT AND WITH THE APPLICATION OF FILTER TO 250 SEATER'S COMPUTER LABORATORY FACILITY DISTRIBUTION NETWORK

The values  $THD_V$  and  $THD_I$  gotten from the results of the simulation where inputted in equation (12) to calculate the  $THD_{V-I}$  which is the combination of both  $THD_V$  and  $THD_I$ . Figure 13 shows the comparison between HD and PL in the 250 Seater's Computer Laboratory facility distribution network. from Figure 21 it can be established that total harmonic distortion is directly proportional to power loss.



(a)



(b)

Figure 13: (a) Bar chart of  $THD_V$ ,  $THD_I$  and  $THD_{V-I}$  (b) Bar chart of Power loss of the simulated results of the 250 Seater's Computer Laboratory facility distribution network without and with application of SePF.  
Source: Authors, (2025).

### III.4. DISCUSSION OF THE FINDINGS

The harmonics present causes the basic system parameters such as voltage and current to deviate from the statutory or tolerance limit, leading to poor operation of the distribution system and consequently, causing power quality problems and high system losses. From the results obtained, it was observed that the  $THD_V$  and  $THD_I$  of the system when no filter was applied were above the recommended harmonic distortion limits of 5 and 16% respectively [2, 35, 36]. However, when SePF were applied respectively, the  $THD_V$  and  $THD_I$  obtained in each filter state reduced drastically to values within the recommended harmonic distortion limit [2, 35, 36]. Assessing from Figure 13, it was found out that power loss increases with increase in THD which indicated that there was a positive correlation between THD and power loss.

The results of the harmonic distortion in the test network in this study aligned with the findings of authors [18, 21, 13, 19] that the application of passive filters has the capabilities of reducing harmonic distortion level within a power network. Authors [25, 37, 38] also asserted that harmonic distortion effects power quality negatively with resulting increase in power loss. This assertion was in tandem with the findings of this research. Hence, this study established that power quality improvement could be achieved with the application of the passive filters to reduce the harmonic distortion levels and by extension reducing power loss within power distribution network.

Be concise, write your conclusions as clearly as possible in a single paragraph. It must be consistent with the objectives of the research and the scientific issues described in it.

### V. CONCLUSIONS

The harmonics present in any power network can cause serious efficiency problems in such system, hence, threatens power quality. The study assessed the THD-PL relationship on a test facility electrical distribution network of 250 Seater's Computer Laboratory in FUNAAB, Nigeria and the mitigation capabilities of SePF on the system. The study noticed high penetration level of harmonics which caused high distortion level and PL in the case network without application of filters. The THD and consequently, the PL reduced appreciably with the use of SePF on the system. The study demonstrates a clear correlation between harmonic distortion and power losses in electricity distribution networks. By

examining the role of series passive filters, the study confirms their effectiveness in reducing harmonic distortion, thereby minimizing associated power losses.

## VI. AUTHOR'S CONTRIBUTION

**Conceptualization:** Okuo Michael Ozaveshe, Adebisi Oluseun Ibrahim, Akinola Olubunmi Adewale.

**Methodology:** Okuo Michael Ozaveshe, Adebisi Oluseun Ibrahim, Akinola Olubunmi Adewale.

**Investigation:** Okuo Michael Ozaveshe, Adebisi Oluseun Ibrahim, Akinola Olubunmi Adewale.

**Discussion of results:** Okuo Michael Ozaveshe, Adebisi Oluseun Ibrahim, Akinola Olubunmi Adewale.

**Writing – Original Draft:** Okuo Michael Ozaveshe, Adebisi Oluseun Ibrahim, Akinola Olubunmi Adewale.

**Writing – Review and Editing:** Okuo Michael Ozaveshe, Adebisi Oluseun Ibrahim, Akinola Olubunmi Adewale.

**Resources:** Okuo Michael Ozaveshe, Adebisi Oluseun Ibrahim, Akinola Olubunmi Adewale.

**Supervision:** Okuo Michael Ozaveshe, Adebisi Oluseun Ibrahim, Akinola Olubunmi Adewale.

**Approval of the final text:** Okuo Michael Ozaveshe, Adebisi Oluseun Ibrahim, Akinola Olubunmi Adewale.

## VIII. REFERENCES

- [1] U. Agus and M. S. Eka, "The influence of harmonic distortion on losses and efficiency of three-phase distribution transformer," *Journal of Physics: Conference Series* 1858 012084, pp. 1-10, 2021.
- [2] R. M. Mohd, M. Azizan and B. Ismail, "Observatory case study on total harmonic distortion in current at laboratory and office building," *Journal of Physics: Conference series*, vol. 1432, no. 1, pp. 1-9, 2020.
- [3] A. A. Hussein, M. El-Metwally and F. M. Osama, "Harmonic Distortion Effects and Mitigation in Distribution Systems," *Journal of American Science*, vol. 6, no. 10, pp. 173-183, 2010.
- [4] B. Nicolae and S. Valentin, "Evaluation of Harmonic Effects on the Power System," *The Annals of "Dunarea de Jos" University of Galati Fascicle III Electrotechnics Electronics Automatic Control and Informatics*, vol. 43, no. 1, pp. 10-18, 2020.
- [5] P. Jong-il, L. Hangsang, Y. Minhan and P. Chang-Hyun, "A Novel Method for Assessing the Contribution of Harmonic Sources to Voltage Distortion in Power System," *IEEE Access*, 2017.
- [6] E. K. Mehdi, "Causes, Effect and Practical Methods of Harmonic Reduction In Iranian Cement Factories with Focus on Plant Development," *JETIA*, vol. 10, no. 50, pp. 61-75, 2024.
- [7] M. Bamigbola, M. Ali and K. Awodele, "Predictive Models of Current, Voltage, and Power Losses on Electric Transmission Lines," *Journal of Applied Mathematics*, vol. 2014, no. 3, pp. 1-5, 2014.
- [8] N. C. Bogdan, G. Gheorghe and S. Florina, "The Influence of Harmonics on Power Losses in Urban Distribution networks," *International symposium on fundamentals of electrical engineering*, pp. 1-4, 2016.
- [9] I. A. Adejumo, O. I. Adebisi and J. Amatu, "Harmonics mitigation on industrial loads using series and parallel resonant filters," *Nigerian Journal of Technology*, vol. 36, no. 2, pp. 611-620, 2017.
- [10] T. R. Muhammad, M. A. Muhammad and M. A. Sheikh, "Analysis and Evaluating the Effect of Harmonic Distortion Levels in Industry," in *4th International Conference on Energy Conservation and Efficiency*, 2021.
- [11] E. Benedict, D. Collins, D. Gotham, S. Hoffman, D. Karipides, S. Pekarek and R. Ramabhadran, "Losses In Electric Power Systems," *ECE Technical Reports*, 1992.
- [12] Y. Gu, "Power quality in distribution networks: estimation and measurement of harmonic distortion and voltage dips," *Technische Universiteit Eindhoven, geboren te Xining*, 2017.
- [13] Z. F. Ahmed, A.-A. H. Shady and B. E. Murat, "Power System Harmonics - Analysis, Effects and Mitigation Power System Harmonics - Analysis, Effects and Mitigation," *InTech*, 2019.
- [14] B. Angelo and H. Zbigniew, *Voltage and Current Harmonics*, Sussex: John Wiley & Sons Ltd, 2008.
- [15] S. Meera and S. Deepa, "A Review of Hybrid Filter Topologies for Power Quality Compensation," *International Research Journal of Engineering and technology*, 2, vol. 2, no. 4, pp. 613-621, 2015.
- [16] A. A. Mohamad, J. Alireza and M. R. P. Behbahani, "A new method for evaluation of harmonic distortion in reconfiguration of distribution network," *Wiley*, vol. 30, no. 12, pp. 2-13, 2020.
- [17] C. A. Eric, "Causes, effects and mitigation of harmonics on distribution transformers," 2021.
- [18] O. Ogundele, O. Adebisi, I. Adejumo and A. Alabi, "Comparative Evaluation of Shunt Passive and Shunt Active Power Filters for Harmonic Mitigation in an Electrical Distribution Network," *Nigerian Research Journal of Engineering and Environmental Sciences*, vol. 8, no. 2, pp. 383-396, 2023.
- [19] O. Adebisi, I. Adejumo, R. Jokojeje and O. Adekoya, "Assessing the Performance of Harmonic Filters for Power Quality Improvement on Industrial Load: 7-Up Industry Plc Power Network as a Case Study," *ABUAD Journal of Engineering Research and Development (AJERD)*, vol. 1, no. 1, pp. 32-48, 2017.
- [20] R. Soares, M. Oliveira, M. Freitas, G. Viajante and E. Chaves, "Loss Analysis Due to Influence of Harmonics in a Distribution System," *International Conference on Renewable Energies and Power Quality*, vol. 19, no. 3, pp. 402-406, 2021.
- [21] H. A. A. Muhamad, M. A. Muhammad, S. Zaliman and W. Y. Mohd, "A review on harmonic mitigation method for non-linear load in electrical power system," 2021.
- [22] M. A. Javad, T. E. Mehdi and V. Behrooz, "A New Method to Reduce Harmonic Magnitude Based on Simultaneous Determination of Maximum Voltage and Current Harmonic Contribution in Interconnected Networks," *Electric Power Components and Systems*, vol. 47, no. 8, pp. 1-13, 2019.
- [23] S. Rosalia, A.-A.-E. M. Khaled and K. T. Mohamed, "Efficiency in Distribution Networks with Harmonic Distortion," *Cape Town*, 2020.
- [24] Y. Wang, "Harmonic analysis in distribution network," *Manchester*, 2020.
- [25] T. Soumya, M. B. Nipun and H. Joachim, "Effects of harmonics on temperature rise and power loss of a distribution transformer," in *CMD*, 2022.
- [26] S. Santoso, M. F. Mark, D. C. Roger and B. H. Wayne, *Electrical Power Systems Quality*, 3rd ed., McGraw-Hill, 2012.
- [27] F. Alasali, N. Khaled, F. Husam, H. William, V. Arangarajan and A. Asma, "Modern Optimal Controllers for Hybrid Active Power Filter to Minimize Harmonic Distortion," *MDPI Journals*, vol. 11, no. 9, pp. 1-17, 2022.
- [28] F. Peng, A. Hirofumi and N. Akira, "A new approach to harmonic compensation in power systems-a combined system of shunt," *IEEE Transaction on Industry Applications*, vol. 20, no. 6, pp. 983-990, 1990.
- [29] G. M. Jawad and H. Mokhtari, "Impact of Harmonics on Power Quality and Losses in Power Distribution Systems," *International Journal of Electrical and Computer Engineering*, vol. 5, no. 1, pp. 166-174, 2015.
- [30] L. Johan, "harmonic distortion in power system," *Goteborg*, 2001.
- [31] Candence, 28 June 2024. [Online]. Available: <https://resources.pcb.cadence.com/blog/2023-passive-electronic-components-building-blocks-of-electronic-circuits>.
- [32] M. Tali, A. Obbadi, A. Elfajri and Y. Errami, "Passive Filter for Harmonic Mitigation in Standalone PV System for Non Linear Load," *IEEE*, pp. 499-504, 2014.

- [33] Z. Memon, M. Uquaili and M. Una, "Harmonics Mitigation of Industrial Power System Using Passive Filters," Mehran University Research Journal of Engineering and Technology, vol. 31, no. 2, 2016.
- [34] O. Ejiofor, N. Benneth, O. Uche and C. Nnabugwu, "Dynamic modelling and simulation of an induction motor with completely reduced stator transients," Journal of Asian scientific Research,, vol. 9, no. 7, pp. 56-64, 2019.
- [35] S. Daniel, N. Mathew, K. Kevin and J. Steven, "IEEE Power Quality Standards," in 20th International Conference on Harmonics & Quality of Power (ICHQP), Naples, 2022.
- [36] IEEE, "IEEE Standard for Harmonic Control in Electric Power Systems," IEEE Std 519-2022 (Revision of IEEE Std 519-2014), pp. 1-31, 5 August 2022.
- [37] F. A. A. Basholli, "Monitoring and assessment of the quality of electricity in a building.," Engineering Applications, vol. 2, no. 1, pp. 32-48, 2023.
- [38] Y. Wenqian, Y. Xiang, X. Longwei, Z. Chao and M. Xinsheng, "Harmonic Loss Analysis of Low-Voltage Distribution Network Integrated with Distributed Photovoltaic," MDPI Sustainability, vol. 15, no. 4334, pp. 1-23, 2023.



## RESEARCH ARTICLE

## OPEN ACCESS

# COMBINATION OF MINIMUM ENTROPY DECONVOLUTION METHOD AND VAN CITTERT ALGORITHM FOR FEATURES EXTRACTION OF BEARINGS

Nesrine Gouri<sup>1</sup>, Hocine Bendjama<sup>2</sup>, Mohamed Larbi Mihoub<sup>3</sup>

<sup>1,3</sup>Mathematical Modeling and Numerical Simulation Research Laboratory, Badji Mokhtar University, Po. Box 12, Annaba 23000, Algeria

<sup>2</sup>Research Center in Industrial Technologies CRTI, P.O.Box 64, Cheraga Algiers, Algeria

<sup>1</sup><https://orcid.org/0009-0007-4344-8920> , <sup>2</sup><https://orcid.org/0000-0001-6221-028X> , <sup>3</sup><https://orcid.org/0000-0001-7230-7165> 

Email: [gou.nesrine@gmail.com](mailto:gou.nesrine@gmail.com), [nesrine.gouri@univ-annaba.org](mailto:nesrine.gouri@univ-annaba.org), [h.bendjama@crti.dz](mailto:h.bendjama@crti.dz), [mihoubmedlarbi@yahoo.fr](mailto:mihoubmedlarbi@yahoo.fr)

## ARTICLE INFO

**Article History**

Received: January 17, 2025

Revised: February 20, 2025

Accepted: March 15, 2025

Published: April 31, 2025

**Keywords:**

Fault diagnosis,  
Rotating machine,  
Bearing vibration signal,  
Deconvolution,  
Iterative algorithm.

## ABSTRACT

Rolling bearings functionality has a primary importance for the correct operation of the rotating machines. In this paper, a monitoring technique based on deconvolution approach is proposed to restore the impulsive shape from the measured vibration signal. This latter is obtained from a convolution of real impulse signal and transmission function. The proposed procedure consists of two major steps; firstly, using the minimum entropy deconvolution (MED) to obtain the inverse filter, secondly introducing the iterative deconvolution algorithm to go back to the initial problem that is mathematically described by the convolution process to reconstitute the impulsive signal. The proposed procedure is applied to bearing diagnosis, and its effectiveness is validated by simulated and experimental data acquired from operational bearings. Moreover, the monitoring obtained results are satisfactory.



Copyright ©2025 by authors and Galileo Institute of Technology and Education of the Amazon (ITEGAM). This work is licensed under the Creative Commons Attribution International License (CC BY 4.0).

## I. INTRODUCTION

Due to the complexity of mechanical system, multiple faults may co-exist in rotating machinery, especially in one of their most important component rolling element bearings. Therefore, the requirement for fault diagnosis has grown and proves that it is extremely essential task in process monitoring; it provides operators with the process operation information. Early diagnosis of process faults like rolling bearing faults can help to avoid abnormal event progression, and to reduce productivity loss in order to ensure the safe running of machines. Several monitoring methods for this purpose have been developed, including dynamics, tribology, nondestructive methods and vibration [1-3].

The vibration signal analysis has been widely used over the past decade, as it provides valuable information about the health condition of mechanical equipment. Vibration signals from rolling bearings are particularly important for fault diagnosis due to their critical role as mechanical components. However, these signals often contain significant noise because of their sensitivity to various faults. In the presence of background noise, the useful

information can be obscured. Therefore, to extract the effective information, various feasible and effective techniques need to be applied. Numerous researches for this goal are available in the literature.

From a mathematical perspective, the bearing vibration signal is viewed as the result of a convolution process involving periodic impacts caused by faults and the response of mechanical components. This work builds on this concept, aiming to restore the original impulsive signal from the measured one. There has been a considerable amount of research into the creation of different restoration techniques during the last decades. Among the many proposals found in the scientific literature, there are: wavelet transform [4], [5], Variational Mode Decomposition (VMD) [6], [7], Empirical Mode Decomposition (EMD) [8], [9], Blind Separation Sources (BSS) [10], [11] and the Minimum Entropy deconvolution (MED) [12- 15] etc.

MED has been shown to be a successful deconvolution method, it was proposed by Wiggins [16] to enhance the excitation component in the fault vibration signal. This technique is based on the maximization of the kurtosis by finding an inverse



filter while considering that the initial excitation was impulsive. After that, Endo and Randall [17] applied MED to detect faults in rotating machines diagnosis, more precisely in gears. Then, Sawalhi et al. [18], [19] adopted this technique to enhance the detection of bearings faults. Li et al. [20] combined a monostable stochastic resonance with minimum entropy deconvolution based on time-delay feedback for fault diagnosis of rolling bearings. Jiang et al. [21] suggested rolling bearing condition monitoring technique based on the envelope spectrum and MED. Recently, many researchers such as: A. Had and k. Sabri [22], Cheng et al [23], J. Zhang et al [24], B. Chen et al. [25]... etc. employed different deconvolution methods as an important step in an effective strategy in order to reconstitute the informative impulse. Unfortunately, unless the development of those different researches, the results are limited.

As mentioned previously, the vibration signal of rolling bearings is often contaminated by significant noise due to their sensitivity to various faults, leading to many difficulties in extracting useful information. Although different studies have been conducted to isolate the impulse signal and eliminate unwanted sources. Unfortunately, the results remain insufficient to overcome these difficulties. For this purpose, we propose a novel strategy in this paper, combining MED with iterative algorithms to restore the impulsive components present in the bearing signal.

Firstly, an investigation by applying the deconvolution techniques and adopting the MED method to optimize the finite impulse response (FIR) filter that eliminates the effect of the transmission path through inverse filtration to get a signal closer to the original impulse, this useful information corresponds to the convolution process of the generated impulses and the transmission path of the mechanical component. Although the MED filter has been estimated as a first step, this latest leads a solution of an appropriate ill-posed problem and it requires the result to be regularized, hence this typically referred to operates it in combination with other signal processing techniques in order to overcome these limitations. For this reason, we present in the second step of this procedure, an estimation of the original impulses by applying iterative algorithms regularized by Tikhonov-Miller (TM) based on integrated a priori model of solution.

The rest of this paper is structured as follows: section 2 describes in detail the proposed method. Section 3 contains the theoretical background of MED, iterative algorithm and TM Regularization. In section 4, verification of the suggested procedure's efficacy utilising simulated bearing signal and the experimental data collected from bearing test rig. Section 5 discussed the obtained results. Finally, the conclusions are drawn in Section 6.

## II. THEORETICAL BACKGROUND:

### II.1 MINIMUM ENTROPY DECONVOLUTION (MED)

Deconvolution is defined as the opposite process of convolution. In fact, the measured signal may be seen as result of a convolution operation of the original signal and the transmission path. Figure (1) illustrates the convolution/deconvolution process in which the signals  $g(k)$  and  $x(k)$  represent respectively the original impulse and the measured output,  $h(k)$  represents the effect of the transmission path,  $f(k)$  is the finite impulse response (FIR) filter,  $n(k)$  represents the noise and  $*$  denotes the convolution.

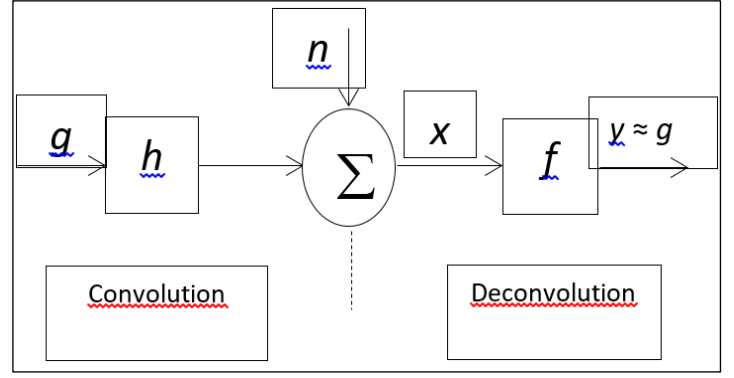


Figure 1: Convolution/deconvolution basic process.  
Source: Authors, (2025).

As mentioned previously different deconvolution techniques are employed to restore the original impulses. In this work we present the MED method, which has been recently introduced to the machine monitoring domain. Wiggins [16] was the first to suggest it in the area of blind convolution, and it was effectively used in seismic treatment.

The fundamental idea of applying the MED technique is to construct an inverse filter in order to eliminate the effect of the transmission path from the measured signal. Thus, the filtered output signal  $y_k$  produced by the input signal (measured signal)  $x_k$  ( $k=1, 2 \dots N$ ) and the building inverse filter  $f=[f_1, f_2, \dots, f_L]$  with  $L$  coefficients, as follows:

$$y(k) = f(k) * x(k) = \sum_{i=1}^L f(i)x(k-i) + n_k \quad (1)$$

Such that:

$$x(k) = g(k) * h(k) + n_k \quad (2)$$

The figure (2) illustrates the basically process of MED, this process is implemented for calculating the optimal set of filter coefficients by maximizing the kurtosis of  $y(k)$ .]

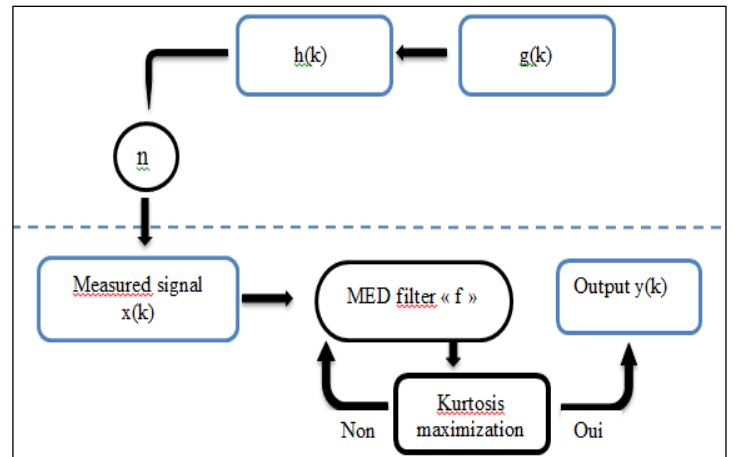


Figure 2: MED process.  
Source: Authors, (2025).

Hence, the kurtosis of an output signal  $y$  is given by:

$$k = \frac{E(y^4)}{(E(y^2))^2} - 3 \quad (3)$$

$$y = fx + b \quad (4)$$

Unfortunately, the challenge of reconstructing  $x$  from equation (4) leads to an ill-posed problem; in other words, the solution  $x$  of equation (4) may not be unique, may not exist, or may not depend continuously on the data. It is clear that these limitations must be overcome by introducing stability criteria; more precisely regularizing this ill-posed problem, and through adopting a deconvolution algorithm.

## II.2 ITERATIVE ALGORITHM AND TIKHONOV-MILLER REGULARIZATION

### II.2.1 VAN CITTERT ALGORITHM

Iterative algorithms are used to inspect the solution more precisely than when calculating in a single operation, in other words they generally have the advantage of not imposing the direct calculation of inverse operators.

Van Cittert algorithm [26] serves as a foundational tool for many iterative deconvolution methods. This approach is a fixed-point [27], its iterative formula is given by:

$$\begin{cases} x_{n+1} = x_n + (y - f x_n) \\ x_0 = y \end{cases} \quad (5)$$

The vector  $x_n$  represents an intermediate solution that lies between the initial estimate  $x_0$  and the final solution  $x_\infty$ . It can be demonstrated that the Van Cittert algorithm converges to a solution  $x_\infty$  that is equivalent to that derived from direct inversion (Eq. 6).

$$x_\infty \rightarrow f^{-1}y \quad (6)$$

This property underlines the effectiveness of the algorithm in reconstructing signals. But unfortunately the Van Cittert algorithm does not consider the presence of noise in the measured signal. This leads from a mathematical point of view to an unstable solution if the problem is ill-posed. Therefore, it is essential to incorporate an effective regularization in order to achieve a reliable solution.

### II.2.2 TIKHONOV-MILLER REGULARIZATION

When the problem is poorly conditioned, it can lead to an unstable solution. Therefore, it is necessary to use a regularization method to obtain a desirable solution. Different regularization methods have been proposed and discussed [28-30].

Tikhonov regularization is regarded as one of the most widely used methods for addressing ill-posed problems and solving inverse problems. It is accomplished by choosing a solution that does not only reconstructs a signal close to the measured one but also aligns with prior knowledge of the original signal [31-34]. From mathematical perspective, this method consists of redefining the concepts of inversion and solution such that the regularized solution depends continuously on the data and remains close to the exact solution. In other words, it reduces the sensitivity of the solution to errors in the data.

This regularization method is based on a quadratic criterion (least squares between the measured data and the reconstructed signal), so this quadratic quantity is required to be lower than the noise energy  $\|y - f\hat{x}\|^2 \leq \|b\|^2$ . According this method, the stabilization of the estimated solution is achieved generally by differentiating a functional to be minimized:

$$\Delta = \|y - f\hat{x}\|^2 + \alpha \|D\hat{x}\|^2 \quad (7)$$

Where  $\alpha > 0$  and  $D$  is a stabilizing operator;  $D$  measures the degree of regularity of the solution such that  $\|D\hat{x}\|^2 \leq r^2$ . It is chosen according to the treatment context and some previous information about the original signal.  $D$  is typically used to smooth the estimated signal, followed by the selection of a gradient or discrete Laplacian. Its spectrum functions as a high-pass filter, for more details, refer to [32], [35] and [36]. The minimization of  $D$  proposed by Tikhonov is given as follow:

$$\hat{x} = \operatorname{argmin}(\|y - f\hat{x}\|^2 + \alpha(\|D\hat{x}\|^2 - r^2)) \quad (8)$$

Such that,  $\operatorname{argmin}$  represents the argument that minimizes the expression between brackets, and  $\alpha$  is the regularization parameter. This latest controls the trade-off between data-fidelity and regularization term. It is a challenging task to find the regularization parameter  $\alpha$  that provides the best balance between signal smoothing and feature preservation, see [28], [37]. The previous minimization problem can be solved by the system below:

$$(f^T f + \alpha D^T D)\hat{x} = f^T y \quad (9)$$

The regularized solution has the following form:

$$\hat{x} = (f^T f + \alpha D^T D)^{-1} f^T y \quad (10)$$

Where

$$f^+ = \hat{x} = f^T f + \alpha D^T D \quad (11)$$

The generalized matrix  $f^+$  is more conditioned that is why it replaces the matrix  $H$ , which described the deconvolution process before regularization. The system becomes more stable by the modification of the eigenvalues of  $H$ .

The regularization operator  $D$  selection should not present any issues as long as the eigenvalue modification criterion is followed, and the regularization value  $\alpha$  must be chosen optimally in order to achieve reconstruction quality. In fact, the matrix  $H$  is not as well-conditioned when this parameter is estimated poorly, thus, the solution is degenerated. By replacing the iterative resolution of  $y = f y$  by that of

$$f^T y = (f^T f + \alpha D^T D)x \quad (12)$$

The Van Cittert algorithm with Tikhonov-Miller regularization is written as follows:

$$\begin{cases} x_{n+1} = x_n + [f^T y - (f^T f + \alpha D^T D)x_n] \\ x_0 = f^T y \end{cases} \quad (13)$$

## III. THE PROPOSED PROCEDURE

This paper proposes a novel deconvolution procedure in order to effectively restore the original periodic impulses from faulty bearing vibration signals. The bearing vibration signal acquired from an accelerometer sensor is considered as measured signal, this later is a convolution between periodical impulses signal and a transmission path.

A suitable combination between MED and iterative algorithm based on a priori model of solution is adopted as a deconvolution procedure to extract the original signal from the measured signal.

In the first step, MED is employed to determine a deconvolution filter by maximizing the kurtosis of the output. This involves finding the optimal inverse filter to counteract the

effects of the transmission path. The filter coefficients can be computed using a second-order iterative Kurtosis algorithm based on the Hessian matrix. With the known source, the coefficients of the mixing matrix  $f$  can be estimated. The filter coefficients  $f_{m,n}(l)$  are estimated using the following formula:

$$f_{k,l}(l) = \frac{E(x(k)y(k-l))}{E(y(k)^2)}, \quad k = 1, 2, \dots, N, \\ l = 1, 2, \dots, M \quad (14)$$

Unfortunately, the obtained inverse filter cannot directly reflect the convolution relationship between source features and the transmission path. In other words, restoring the original impulses using the resulting inverse filter involves solving an ill-posed problem, where noise prevents the solution from being unique or stable. Therefore, in the second step, we propose to solve this ill-posed problem by introducing the Van Cittert algorithm, based on Tikhonov-Miller regularization, using an a priori model of the solution. The detailed strategy of this method is summarized in Figure 3.

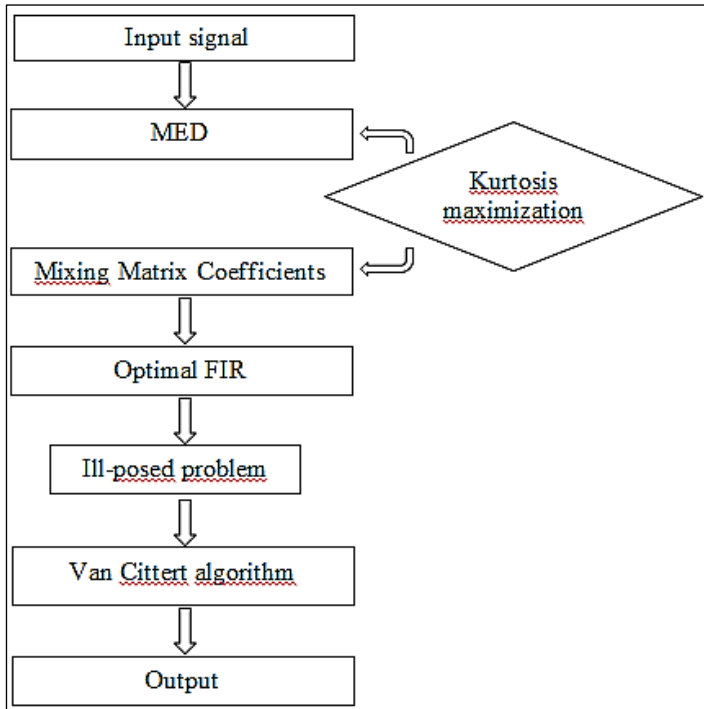


Figure 3: The flowchart of the proposed strategy.  
Source: Authors, (2025).

## IV. NUMERICAL SIMULATION AND EXPERIMENTAL VALIDATION

### IV.1 NUMERICAL SIMULATION

In this part, a numerical simulation is presented to evaluate the effectiveness of the proposed procedure. This investigation demonstrates the importance of the two steps in the proposed strategy. We have chosen a model that simulates the impulse response derived from a pulse train. The model modulates each pulse with two harmonic frequencies, with exponential decay occurring. Hence, the impulse response could serve to model the modulated signal of a bearing system, and is presented as follows:

$$x(t) = e^{-\varepsilon t} (\sin(2\pi f_1 t) + 3 \times \sin(2\pi f_2 t)) \quad (15)$$

With

$$\tau = \text{mod}\left(t, \frac{1}{f_d}\right) \quad (16)$$

Where  $\varepsilon$ ,  $f_1$ ,  $f_2$ , and  $f_d$  represent, respectively, the frequencies of decay, resonance, and defect (modulation).

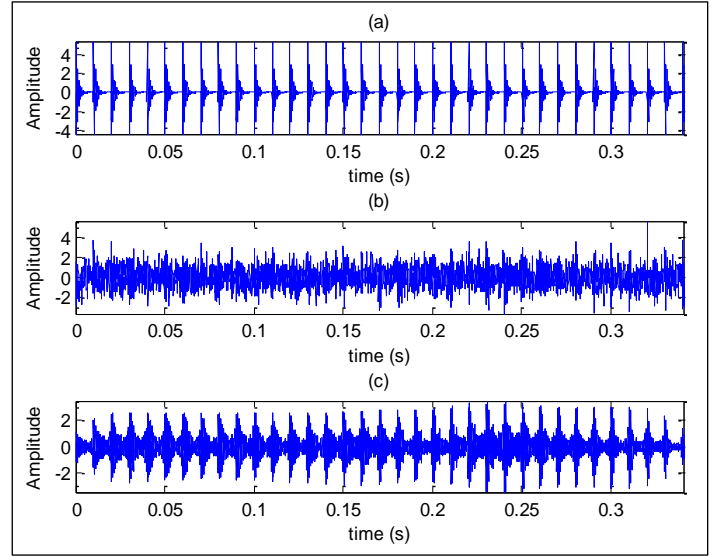


Figure 4: **a)** Simulated signal without noise, **b)** Signal with noise and **c)** Filtered signal.  
Source: Authors, (2025).

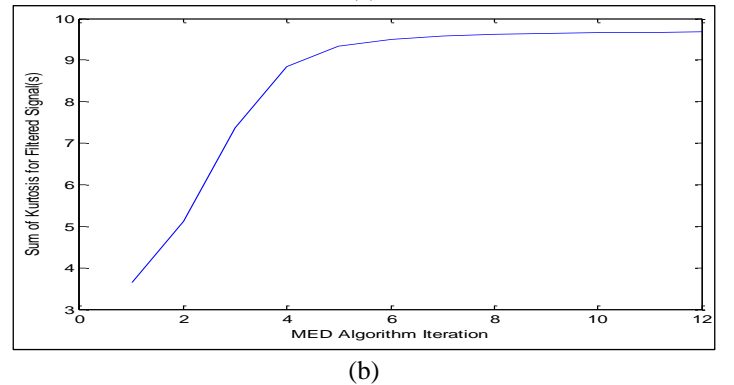
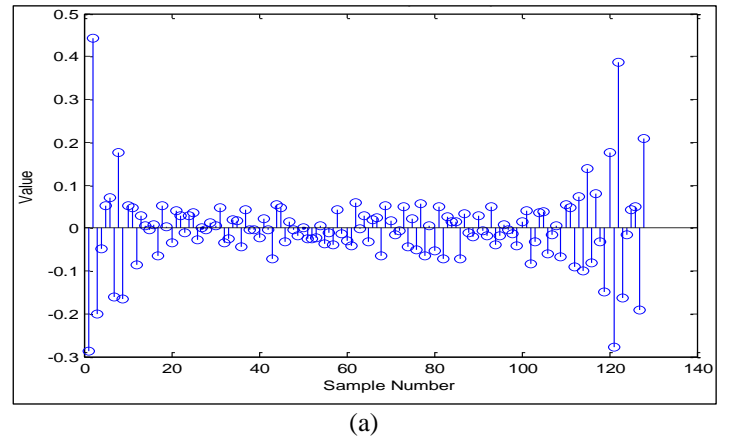


Figure 5: **a)** Final Filter, Finite Impulse Response, **b)** Kurtosis maximization during MED Algorithm iteration.  
Source: Authors, (2025).

The simulated vibration signal obtained from Eq. 15 is displayed in Figure 4a with Gaussian noise and in Figure 4b without it. A comparison of Figures 4a and 4b shows that the periodic impulses in Figure 4b are not clearly visible in the time

domain. It is important to note that the main advantage of the proposed procedure is its ability to detect periodic effects, enabling the extraction of useful information. The inverse filter constructed using the MED technique is shown in Figure 5a, while the kurtosis maximization during MED Algorithm iteration is illustrated in Figure 5b. After applying the Van Cittert algorithm as a second step, the filtered signal is obtained by maximizing kurtosis to extract the impulsive signal from bearing vibration.

Figure 4c illustrates the resulting signal from the proposed procedure. The impulsive shape of the signal is more clearly visible, with a kurtosis value of 3.96 compared to the input signal's value of 3.67, indicating effective noise reduction while preserving key impulsive features. Although the improvement in the kurtosis value is slight, it is clearly visible in Figure 2, reflecting the enhancement in the clarity of the impulsive features after processing.

#### IV.2 EXPERIMENTAL VALIDATION

Vibration measurement used for defect diagnosis and condition monitoring imposes various kinds and degrees of equipment and methods selected according to the available resources, skills and knowledge.

In this study, we present the experimental measurements utilized entirely from the vibration data acquired at the Case Western Reserve University Bearing Data Center [38]. As illustrated in Figure 6, the vibration data were obtained using accelerometers mounted on the housing with magnetic bases. The measurement unit is mm/s<sup>2</sup> (gravity).

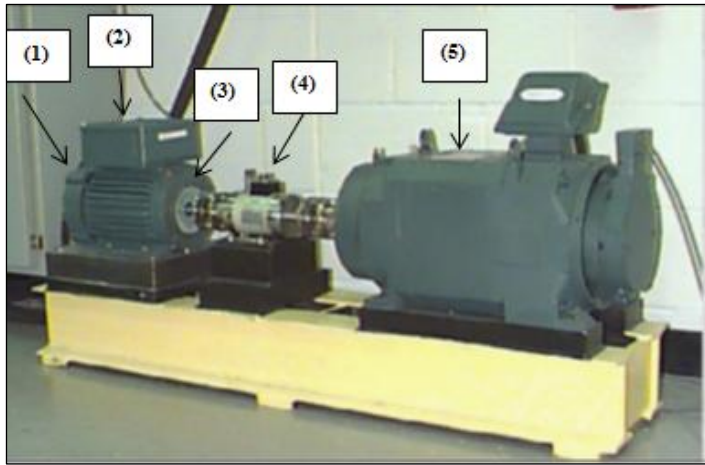


Figure 6: Bearing test rig.

1- Fan end bearing, 2-induction motor, 3-Drive end bearing, 4-Torque transducer, 5-Load Motor

Source: Authors, (2025).

The vibration signals were obtained from four various bearing conditions: (1) Bearing without fault i.e. Normal state (NS); (2) Bearing with Outer Race Fault (OrF); (3) Bearing with Ball Fault (BF) and (4) Bearing with Inner Race Fault (IrF). The vibration signals were sampled at a rate of 12000 Hz.

Deep groove ball bearings were used in the experiments, with the following specifications: ball diameter = 7.94 mm; pitch diameter = 39.04 mm; number of balls = 9; and contact angle = 0. The electro-discharge machining (EDM) technique created faults in the test bearings, using varying diameters: 0.1778 mm, 0.28 mm and 0.5334 mm. The bearings were tested at four rotational speeds (ranging from 1797 to 1730 rpm) and under four different

loads (ranging from 0 to 4 horsepower (hp)) using a dynamometer.

In this study, the motor speeds considered are 1797 rpm and 1750 rpm, corresponding to 0 hp and 2 hp, respectively. The defect sizes in both the inner and outer races are recorded at 0.1778 mm and 0.5334 mm. Since there are many samples in every signal, choosing sample numbers that spans a sufficient amount of full rotations is necessary to reduce computing time. For the two rotation speeds considered in this study, selecting 4096 samples provides approximately 12 full rotations that is enough for analysis. While preserving the essential system information.

Vibration signals collected from defective bearings, with IrF, BF and OrF, at speeds of 1797 and 1750 rpm, are plotted in Figure 8. From these plots, Impulse responses are not directly identifiable, aside from OrF cases, in which they are noticed along with background noise. Overall, the signals obtained from the experiments are contaminated by noise, which introduces various frequency components and can lead to inaccurate conclusions during interpretation.

The proposed procedure processes the measured signals to extract periodic impulses, thereby revealing the fault information. Because there were so many findings, we have chosen to display just a few. The filtered signals are displayed in Figures. 9b, 10b, and 11b. Compared with the input (measured) signal, it is clear that the bearing impulses show periodically over time to evaluate the quality of the signals produced by the proposed procedure, Table (1) presents the calculated kurtosis values. The optimal filter size, determined as 64, was selected based on kurtosis maximization, as illustrated in Fig. 7 this analysis was performed using the vibration signal of a bearing with IrF of diameter 0.5334 mm.

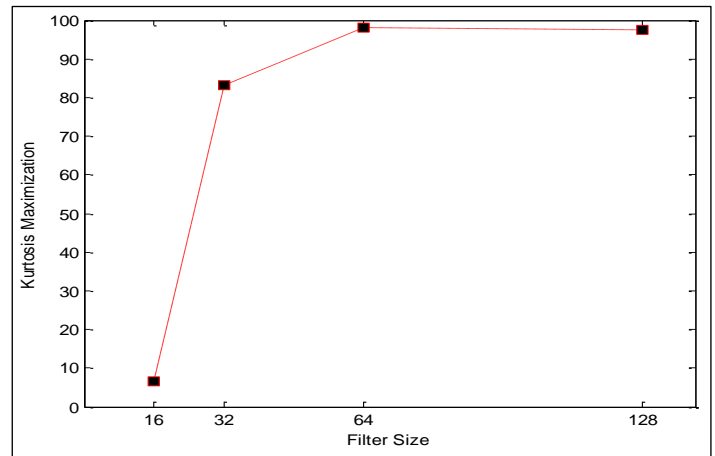


Figure 7: Effect of filter size on Kurtosis maximization.

Source: Authors, (2025).

The results demonstrate that the extracted signal, which exclusively represents the rolling bearing fault characteristics, is accurately reconstructed.

Table 1: Comparison of Input and Filtered Signals for Bearing Faults with different Fault Sizes.

Bearing faults	IrF	OrF	BF
Fault size	0.5334 mm		0.1778 mm
Input signal	6.8718	4.4488	2.6767
Filtered signal	98.1651	5.5134	102.9748

Source: Authors, (2025).



The results in the table confirm a significant difference between the input signal and the resulting one for the two rotational speeds examined (1797 and 1750 rpm), suggesting that the extracted signals include more defect-related information. The chosen characteristics are then rebuilt for every rotation speed (Figure 9, 10 and 11), especially in Figure 9 and 11, which show the bearing signals with an IrF and BF measured at different rotational speeds of 1797 rpm and 1750 rpm. In these figures, periodic impulses are seen in the time domain. These impulses occur when the balls make contact with the defect, clearly showing peaks associated with the fault.

The combined approach shows better results regarding residual noise removal and fault identification effectiveness. The achieved outcomes demonstrate that the suggested method might be successfully utilized to extract utility characteristics from bearing vibration signals, as evidenced by a comparison with previous studies. However, accurately identifying fault features in both the time and frequency domains remains challenging due to interference from rotating components. To address this issue, the suggested procedure first constructs the inverse filter using the MED technique, followed by the application of the Van Cittert algorithm to recover the most relevant features that contain the key fault information.

The results indicate that our strategy successfully identifies the fault characteristic frequencies of damaged bearings, outperforming methods from previous research, such as those cited in [10], [37], [39-41]. While these studies applied different methods to extract useful information directly from the measured signal through filtering, our approach introduces a crucial step before filtration: the extraction of the inverse filter. The results presented here validate the effectiveness of this additional step in improving fault detection and feature extraction.

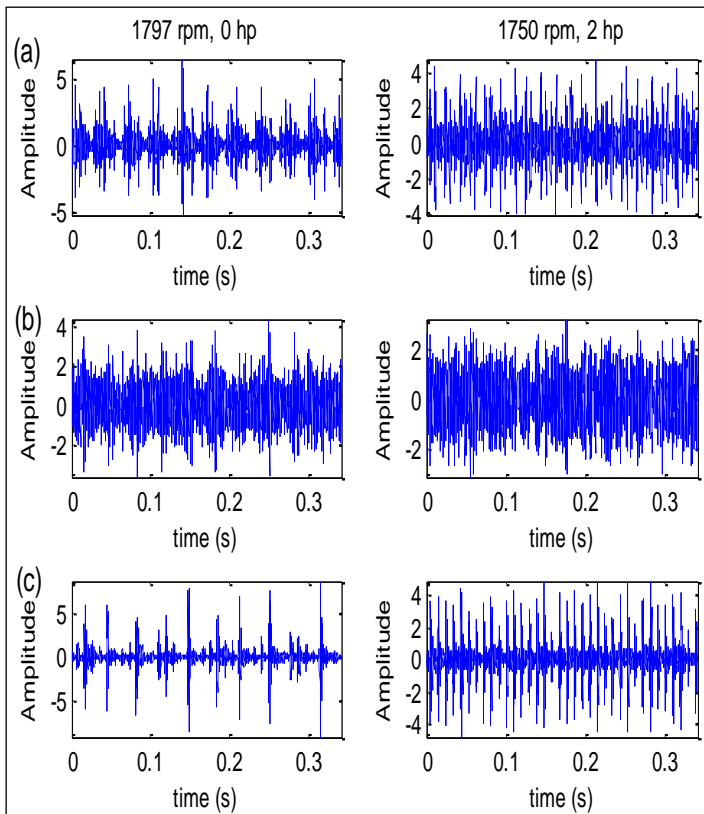


Figure 8: Vibration signals in time domain of bearing with:

a) IrF, b) BF and c) OrF.

Source: Authors, (2025).

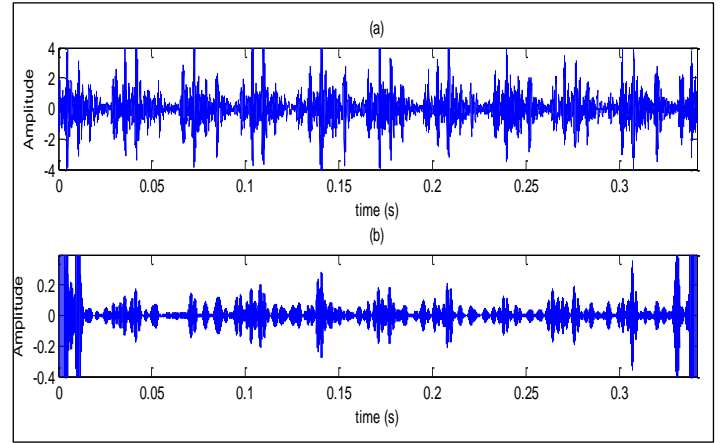


Figure 9: Bearing with IrF of diameter 0.5334 mm:

a) Measured signal, b) filtered signal.

Source: Authors, (2025).

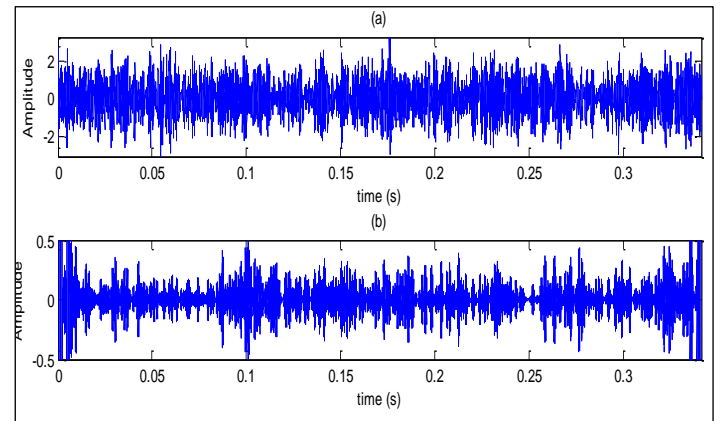


Figure 10: Bearing with BF of diameter of 0.1778 mm:

a) Measured signal, b) filtered signal.

Source: Authors, (2025).

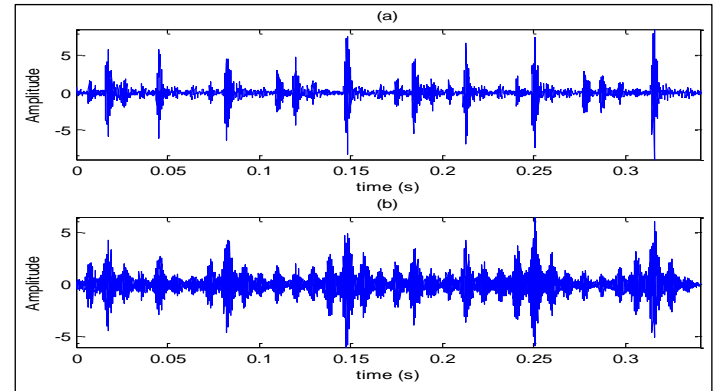


Figure 11: Bearing with OrF of diameter 0.5334 mm:

a) Measured signal, b) filtered signal.

Source: Authors, (2025).

## V. CONCLUSIONS

This work presents an effective method for diagnosing bearing faults by reconstructing a signal that closely approximates the original one. First, the measured signal was processed using the Maximum Entropy Deconvolution (MED) technique to design an optimal inverse filter, effectively offsetting the influence of the transmission path. The restoration of the original impulses through this inverse filter corresponds to solving an inherently ill-posed problem.

To address this challenge, the Van Cittert algorithm was employed as a second step, working in tandem with MED to iteratively refine the reconstructed signal. This combination ensures a stable solution by suppressing noise while retaining crucial diagnostic information embedded in the fault-induced impulses. The iterative nature of the Van Cittert algorithm enables the process to progressively approximate the original signal, achieving a balance between noise reductions and preserving the true signal characteristics.

The proposed approach has proven effective in enhancing the visibility of fault-related impulse components, even in the presence of significant noise. This methodology highlights the significance of integrating advanced deconvolution techniques with regularization algorithms for reliable signal restoration in fault diagnosis, offering a competitive alternative to existing methods in the field.

## VI. AUTHOR'S CONTRIBUTION

**Conceptualization:** Nesrine Gouri, Hocine Bendjama.

**Methodology:** Nesrine Gouri, Hocine Bendjama and Mohamed Larbi Mihoub.

**Investigation:** Nesrine Gouri, Hocine Bendjama and Mohamed Larbi Mihoub.

**Discussion of results:** Nesrine Gouri, Hocine Bendjama and Mohamed Larbi Mihoub.

**Writing – Original Draft:** Nesrine Gouri, Hocine Bendjama.

**Writing – Review and Editing:** Nesrine Gouri, Hocine Bendjama.

**Resources:** Hocine Bendjama.

**Supervision:** Hocine Bendjama and Mohamed Larbi Mihoub.

**Approval of the final text:** Nesrine Gouri, Hocine Bendjama and Mohamed Larbi Mihoub.

## VIII. REFERENCES

- [1] X. Zhu, C. Zhong, J. Zhe, "Lubricating oil conditioning sensors for online machine health monitoring—a review", *Tribol. Int.*, vol. 109, pp. 473-484, 2017, doi: 10.1016/j.triboint.2017.01.015.
- [2] A. Choudhary, T. Mian, and S. Fatima, "Convolutional neural network based bearing fault diagnosis of rotating machine using thermal images", *Measurement*, vol. 176, 2021, doi: 10.1016/j.measurement.2021.109196.
- [3] H. Bendjama, "Bearing fault diagnosis based on optimal morlet wavelet filter and teager Kaiser Energy operator", *J. Braz. Soc. Mech. Sci. Eng.*, vol. 44, no. 9, pp. 392, 2022, doi: 10.1007/s40430-022-03688-4.
- [4] J. Chebil, G. Noel, M. Mesbah, and M. Deriche, "Wavelet decomposition for the detection and diagnosis of faults in rolling element bearings", *Jordan j. mech. ind. eng.*, vol. 3, no. 4, pp. 260-267, 2009.
- [5] H. Bendjama, and M. S. Boucherit, "Wavelets and Principal Component Analysis Method for Vibration Monitoring of Rotating Machinery," *J. theor. appl. mech.*, vol. 54, no. 2, pp. 659-670, 2016, doi: 10.15632/jtam-pl.54.2.659.
- [6] X. An, L. Pan, and F. Zhang, "Analysis of hydropower unit vibration signals based on variational mode decomposition," *JVC*, vol. 3, no. 12, pp. 1938–1953, 2015, doi: 10.1177/1077546315605240.
- [7] J. Zhang, J. Wu, B. Hu, J. Tang, "Intelligent fault diagnosis of rolling bearings using variational mode decomposition and self-organizing feature map", *JVC*, vol. 26, no. 21-22, pp. 1886-1897, 2020, doi: 10.1177/1077546320911484.
- [8] Y. Damine, N. Bessous, R. Pusca, A. C. Megherbi, R. Romary, and S. Sbaa, "A new bearing fault detection strategy based on combined modes ensemble empirical mode decomposition, kmad, and an enhanced deconvolution process", *Energies*, vol. 16, no. 6, 2023, doi: 10.3390/en16062604.
- [9] H. Bendjama, "Feature extraction based on vibration signal decomposition for fault diagnosis of rolling bearings", *Int. J. Adv. Manuf. Technol.*, vol. 130, no. 1, pp. 821-836, 2024, doi: 10.1007/s00170-023-12710-5
- [10] A. Had, and K. Sabri, "A two-stage blind deconvolution strategy for bearing fault vibration signals", *Mech. Syst. Signal Process.*, vol. 134, 2019, doi: 10.1016/j.ymssp.2019.106307
- [11] M. L. Cherrad, H. Bendjama, and T. Fortaki, "Combination of single channel blind source separation method and normal distribution for diagnosis of bearing faults", *Jordan j. mech. ind. eng.*, vol. 16, no. 4, pp. 493-502, 2022.
- [12] B. Peng, Y. Bi, B. Xue, M. Zhang, and S. Wan, "A survey on fault diagnosis of rolling bearings", *Algorithms*, vol. 15, no 10, p. 347, 2022, doi: 10.3390/a15100347.
- [13] Y. Cheng, N. Zhou, Z. Weihua, Z. Wang, "Application of an improved minimum entropy deconvolution method for railway rolling element bearing fault diagnosis", *J. Sound Vib.*, vol. 425, pp. 53-69, 2018, doi: 10.1016/j.jsv.2018.01.023.
- [14] Z. Zhang, M. Entezami, E. Stewart, C. Roberts, "Enhanced fault diagnosis of roller bearing elements using a combination of empirical mode decomposition and minimum entropy deconvolution", *Proc. Inst. Mech. Eng., Part C*, vol. 231, no. 4, pp. 655-671, doi: 10.1177/0954406215623575.
- [15] Z. Liao, J. Xu, M. Jin, Y. Cao, D. Hou, and P. Huang, "An improved adaptive minimum entropy deconvolution method in bearing fault detection", *Fourth International Conference on Mechanical, Electronics, and Electrical and Automation Control (METMS 2024)*, SPIE, pp. 1841-1848, 2024.
- [16] R. A. Wiggins, "Minimum entropy deconvolution", *Geoexploration*, vol. 16, no. 1–2, pp. 21–35, 1978, doi: 10.1016/0016-7142(78)90005-4.
- [17] H. Endo, R. B. Randall, "Enhancement of autoregressive model based gear tooth fault detection technique by the use of minimum entropy deconvolution filter", *Mech. Syst. Signal Process.*, vol. 21, no. 2, pp. 906-919, 2007, doi: 10.1016/j.ymssp.2006.02.005.
- [18] N. Sawalhi, R. B. Randall, H. Endo, "The Enhancement of Fault Detection and Diagnosis in Rolling Element Bearings Using Minimum Entropy Deconvolution Combined with Spectral Kurtosis", *Mech. Syst. Signal Process.*, vol. 21, no. 2, pp. 2616-2633, 2007, doi: 10.1016/j.ymssp.2006.12.002.
- [19] T. Barszcz, and N. Sawalhi, "Fault detection enhancement in rolling element bearings using the minimum entropy deconvolution", *Arch. Acoust.*, vol. 37, no. 2, pp. 131-141, 2012, doi: 10.2478/v10168-012-0019-2.
- [20] J. Li, M. Li and J. Zhang, "Rolling bearing fault diagnosis based on time-delayed feedback monostable stochastic resonance and adaptive minimum entropy deconvolution", *J. Sound Vib.*, vol. 401, pp. 139-151, 2017, doi: 10.1016/j.jsv.2017.04.036.
- [21] R. Jiang, J. Chen, G. Dong, T. Liu, and W. Xiao, "The weak fault diagnosis and condition monitoring of rolling element bearing using minimum entropy deconvolution and envelop spectrum", *Proc. Inst. Mech. Eng., Part C*, vol. 227, no. 5, pp. 1116–1129, 2013, doi: 10.1177/0954406212457892.
- [22] A. Had, K. Sabri, "A two-stage blind deconvolution strategy for bearing fault vibration signals", *Mech. Syst. Signal Process.*, vol. 134, 2019, doi: 10.1016/j.ymssp.2019.
- [23] Y. Cheng, B. Chen, and W. Zhang, "Adaptive multipoint optimal minimum entropy deconvolution adjusted and application to fault diagnosis of rolling element bearings", *IEEE sensors journal*, 2019, vol. 19, no. 24, pp. 12153-12164, doi: 10.1109/JSEN.2019.2937140
- [24] J. Zhang, M. Zhong, J. Zhang, "Detection for weak fault in planetary gear trains based on an improved maximum correlation kurtosis deconvolution", *Meas. Sci. Technol.*, vol. 31, no. 2, 2019, doi: 10.1088/1361-6501/ab43ed.
- [25] B. Chen, W. Zhang, D. Song, and Y. Cheng, "Blind deconvolution assisted with periodicity detection techniques and its application to bearing fault feature enhancement", *Measurement*, vol. 159, 2020, doi: 10.1016/j.measurement.2020.107804.
- [26] P. H. Van Cittert, "Zum einfluss der spaltbreite auf die intensitätsverteilung in spektrallinien. II", *Z. Physik*, vol. 69, no. 5, pp. 298-308, 1931, 10.1007/BF01391351.

- [27] G. Speranza, "Application of the Van Cittert Algorithm for Deconvolving Loss Features in X-ray Photoelectron Spectroscopy Spectra", *Materials*, vol. 17, no. 3, p. 763, 2024, doi: 10.3390/ma17030763.
- [28] C. R. Vogel, "Computational methods for inverse problems". Society for Industrial and Applied Mathematics, 2002.
- [29] X. Xiong, X. Xue, and Z. Qian, "A modified iterative regularization method for ill-posed problems", *Appl. Numer. Math.*, vol. 122, pp. 108-128, 2017, doi: 10.1016/j.apnum.2017.08.004
- [30] M. Singhal, M. Goyal, and R. K. Singla, "A review of regularization strategies and solution techniques for ill-posed inverse problems, with application to inverse heat transfer problems", *Rev. Math. Phys.*, vol. 36, no. 01, 2024, doi: 10.1142/S0129055X23300078.
- [31] Y. Teng, Y. Zhang, H. Li, and Y. Kang, "A convergent non-negative deconvolution algorithm with Tikhonov regularization ", *Inverse Problems*, vol. 31, no. 3, 2015, doi: 10.1088/0266-5611/31/3/035002.
- [32] E. Pantin, J. L. STARCK, and F. MURTAGH, "Deconvolution and blind deconvolution in astronomy", *Blind Image Deconvolution*, 2017, pp. 301-340, doi: 10.1201/9781420007299
- [33] X. Xiong, J. Li, and J. Wen, "Some novel linear regularization methods for a deblurring problem", *Inverse problems and imaging*, vol. 11, no. 2, pp. 403-426, 2017, doi: 10.3934/ipi.2017019.
- [34] H. Pan, Y. W. Wen, and H. M. Zhu, "A regularization parameter selection model for total variation based image noise removal", *App. Math. Model.*, vol. 68, pp. 353-367, 2019, doi: 10.1016/j.apm.2018.11.032.
- [35] M. Boulakroune and D. Benatia, "Multi-Scale Deconvolution of Mass Spectrometry Signals", *Advances in Wavelet Theory and Their Applications in Engineering, Physics and Technology*, pp. 125-152, 2012, doi: 10.5772/37772.
- [36] M. Boulakroune, "Reliability of multiresolution deconvolution for improving depth resolution in SIMS analysis". *Appl. Surf. Sci.*, vol. 386, pp. 24-32. 2016, doi.org/10.1016/j.apsusc.2016.05.164
- [37] O. San, and P. Vedula, "Generalized deconvolution procedure for structural modeling of turbulence", *J. Sci. Comput.*, vol. 75, pp. 1187-1206, 2018, doi: 10.1007/s10915-017-0583-8.
- [38] K. A. Loparo. Bearing vibration dataset, Case Western Reserve University, 2016 Available at: [www.eecs.case.edu/laboratory/bearing](http://www.eecs.case.edu/laboratory/bearing).
- [39] F. B. Abid, and A. Braham, "Advanced signal processing techniques for bearing fault detection in induction motors", 15th International Multi-Conference on Systems, Signals & Devices (SSD), IEEE, pp. 882-887, 2018, doi: 10.1109/SSD.2018.8570403.
- [40] G. Manjunatha, H. C. Chittappa and D. Kumar, "Fault Detection of Bearing using Signal Processing Technique and Machine Learning Approach", *J. Mines Met. Fuels*, vol. 70, no. 10a, pp. 380-388, 2022, doi: 10.18311/jmmf/2022/32937.
- [41] P. Yu, J. Zhang, B. Zhang, J. Cao, Y. Peng, "Research on small sample rolling bearing fault diagnosis method based on mixed signal processing technology". *Symmetry*, vol. 16, no 9, p. 1178, 2024, doi.org/10.3390/sym16091178.



## RESEARCH ARTICLE

## OPEN ACCESS

## Solder Lead Waste Reduction of a Selected Mobile Phone Factory: A Six Sigma DMAIC Approach

Md. Mehedi Hassan Munna<sup>1</sup>, Jonayed Abdullah<sup>2</sup>, Tarequl Islam<sup>3</sup>, Most. Anika Tabassum Little<sup>4</sup>

<sup>1,2</sup>Department of Industrial and Production Engineering Shahjalal University of Science and Technology, Sylhet, Bangladesh

<sup>3</sup>Department of Logistics Systems Engineering Bowling Green State University, Ohio, USA.

<sup>4</sup>Department of Electrical and Electronic Engineering. Khulna University of Engineering & Technology, Khulna, Bangladesh.

<sup>1</sup><http://orcid.org/0009-0000-6480-0048>, <sup>2</sup><http://orcid.org/0009-0006-7130-7597>, <sup>3</sup><http://orcid.org/0009-0002-8313-3150>,

<sup>4</sup><http://orcid.org/0009-0002-1330-7784>

Email: [\\_mehedi.ipe.sust@gmail.com](mailto:_mehedi.ipe.sust@gmail.com), [jonayedabdullah.ipe@gmail.com](mailto:jonayedabdullah.ipe@gmail.com), [tareq.ipe.sust@gmail.com](mailto:tareq.ipe.sust@gmail.com), [anika.kuet.eee@gmail.com](mailto:anika.kuet.eee@gmail.com)

## ARTICLE INFO

### Article History

Received: January 21, 2025

Revised: February 20, 2025

Accepted: March 15, 2025

Published: April 31, 2025

### Keywords:

Quality,  
Six Sigma,  
DMAIC,  
VOC,  
Wastage.

## ABSTRACT

Six Sigma is an explicit statistical method of reducing variability and improving processes. Our research works with internal customers within the assembly lines. This study aims to identify and analyze the VOC of internal customers and show improvement based on the VOC. The Six Sigma DMAIC method was followed to conduct this research. Six mobile phone assembly lines were selected to collect wastage data for two months after identifying the problem. Collected data were analyzed in MS Excel and this analysis showed that the wastage rates were 91.38% in July 2024 and 80.67% in August 2024. The average waste rate was 0.44 g/unit and 0.41 g/unit in July 2024 and August 2024. The root cause analysis, and cause and effect diagram illustrated that most of the reasons behind wastages were related to soldering operators. An awareness and training session was conducted. We collected data for the next month and found the wastage was reduced to 69.27% in September 2024 which is a 24.5% reduction considering August 2024 as the base. The average waste rate was reduced to 0.28 g/unit. The effectiveness of following the Six Sigma method to solve quality or wastage issues is evident hereafter accomplishing this research.



Copyright ©2025 by authors and Galileo Institute of Technology and Education of the Amazon (ITEGAM). This work is licensed under the Creative Commons Attribution International License (CC BY 4.0).

## I. INTRODUCTION

Manufacturing firms are concerned with reducing wastage from the production process. Some wastages can be identified and eliminated, and some cannot. This wastage has a great impact on the pricing of any product. Increased wastage also increases the cost of making products[1]. Customers always want good products at a reasonable price[2].

Companies invest significant amounts of money to provide the best product to the customer at a minimum price. Thus, the market has become price and quality-competitive [3]. If any organization fails to give the products with higher products and lower prices, that organization is said to be out of the competition [4]. Process improvements play a vital role here that reducing the waste in the process by eliminating process variability. This reduction leads to a decrease in the cost of product making.

Six Sigma is one of the most effective approaches that deals with process variability. The integration of Six Sigma and Lean can reduce process variability and process waste. The purpose of this research is,

- to observe the process and define the problem
- to measure the extent of the problem and find root causes
- to take required actions for improvement
- 

This study explored a real problem and observed the difference between before and after improvement scenarios. A mobile phone company was selected for this study. The scenario was observed and then a problem statement was generated. Following this, five steps of Six Sigma were deployed to get effective outcomes.



## II. THEORETICAL REFERENCE

### II.1 SIX SIGMA

Six Sigma is not a reactive or detection-based approach; rather, it is proactive and prevention-based. A top-quality process gives fewer than 3.4 defective parts per million and is considered as Sigma level six. Sigma ( $\sigma$ ) is a Greek letter that stands for standard deviation, a measurement of variance[5].

Six Sigma is a methodical approach that lets businesses analyze their current state of operations and enhance their procedures to cut down on variances[6]. Both the industrial and service sectors use Six Sigma[7]. Manufacturing companies deploy hundreds of Six Sigma projects annually, which need a significant financial commitment and careful research to guarantee that the benefits outweigh the initial expenditure [8]. Six Sigma offers academics and practitioners new challenges even though it has more benefits than traditional quality management techniques[9]. The total quality management (TQM) procedures include Six Sigma practices[10].

Six Sigma is a process, system, or product improvement methodology emphasizing scientific and statistical techniques to lower the rejection or waste [11], [12]. This approach can lower the quantity of faulty goods the business produces. DMAIC stands for Define, Measure, Analyze, Improve, and Control, and it is one approach to the Six Sigma methodology. The Plan-Do-Check-Act and Juran and Gryna's Seven-Step Method are two popular manufacturing techniques that are comparable to the DMAIC methodology in that they both seek to enhance [13]. It has been successfully applied to many procedures and needs in the healthcare industry. Certain articles in the literature discuss the use of SS, frequently in conjunction with the Lean methodology, to enhance surgical procedures by decreasing hospital stays and wait times or increasing the effectiveness of operating rooms[14], [15]. Another approach is named DMADV, which stands for Define, Measure, Analyze, Design, and Verify. This approach is very well-liked for creating new processes or products.[16].

### II.2 DMAIC

DMAIC is a six-sigma method that is based on the PDCA or plan, do, act, and check developed by Deming. Define, measure, analyze, improve, and control are the five specified stages.

**Define:** During the Define phase, the team is formed, the project's goals are defined, the process is mapped, customers are identified, and the high impact qualities, or CTQs (Critical to Quality), are identified.

**Measure:** The Measure phase entails creating and carrying out a methodical plan for gathering data for the targeted process's critical metrics (CTQs).

**Analysis:** By identifying the primary types of wastes embedded in the production processes and their underlying causes, the Analyze phase analyzes the data gathered in the Measure phase to determine the underlying causes of the discrepancy between the current performance and the goals established in the first phase.

**Improve:** Identifying expected solutions, proposing a range of alternative solutions to improve performance, and putting some of these solutions into practice under the available budget and the

anticipated cost of each alternative are the main goals of the improvement phase.

**Control:** The control phase focuses on developing and monitoring response strategies to maintain improvements, disseminate the results and methods throughout the organization, and ensure the development of a new organizational culture. Additionally, the Control phase documents and publishes operating standards and procedures.[9], [12]

### II.3 LEAN MANUFACTURING

Delivering the best quality product to customers at the lowest cost while reducing waste from the value-adding process is known as lean manufacturing. Here, customer needs are given priority. To properly implement lean services, key principles must be followed, such as ensuring that all services operate and, in particular, collaborate to solve customers' problems; preventing time waste; and giving customers exactly what they want, exactly where they want it, and at the exact moment they want it.[17], [18].

### II.4 SEVEN QC TOOLS

Quality control management uses some tools within any organization to monitor the ongoing processes and check the process parameters whether they match the defined standards.

**Check Sheet:** Since data collection and measurement serve as the foundation for any analysis, this activity must be organized to ensure that the information gathered is thorough and pertinent. Check sheets are instruments for collecting information. They are made especially for the kind of data that would be collected. Check sheets facilitate the methodical collection of data. Daily maintenance check sheets, attendance logs, production logbooks, and so forth are a few examples of check sheets. The collected data must be appropriately categorized. To plan for more analysis and provide a relevant result, this classification aids in obtaining a preliminary knowledge of the data's relevance and dispersion. Stratification is the process of meaningfully classifying data. Group, location, kind, origin, symptom, etc. are some examples of stratification[19]. Researchers used check sheets in pharmaceutical quality control to monitor input variabilities [20].

**Histogram:** A histogram is an effective tool to identify the distribution of any dataset. This bar chart helps users illustrate the distribution of recorded data and the degree of deviation in a process by visualizing both variable data and attributes of a product or process. It shows the mean, mode, and average of the three different measurements of central tendency. It should be appropriately constructed so that those working on the operational process may use and comprehend it without any problem. Additionally, a histogram can examine and determine the variable's distribution.[21]

**Pareto Analysis:** A Pareto diagram is a tool that shows which elements have the most influence by ranking them according to the size of their contributions. In SPC and quality improvement, this tool is used to prioritize projects for improvement, prioritize the formation of corrective action teams to address issues, identify the products that receive the most complaints, determine the type of complaints that occur most frequently, determine the most common reasons for rejections, and for other related purposes. An Italian economist, Vilfredo Pareto, noticed that a significant amount of wealth was owned by a small number of individuals. He

saw that most fields shared this distribution trend. The 80/20 rule, sometimes referred to as the Pareto principle, is applied in materials management for ABC analysis. 80% of the value is accounted for by 20% of the things that a corporation purchases. These are the things that receive the most attention. To separate the "vital few" issues from the "trivial many," or what is now known as the "useful many," Dr. Juran proposed using this theory for quality control[21]. Pareto charts were used in grinding unit research[22] to determine the major reasons for downtime, which improved maintenance plans.

**Fishbone Diagram:** Kaoru Ishikawa is credited for creating and popularizing the 'Fishbone' diagram, also known as the Cause-and-Effect Diagram. In 1943, Dr. Kaoru Ishikawa introduced the cause-and-effect diagram. The diagram is also known as the Ishikawa diagram or fishbone because of its design, which resembles a fish's skeleton and is used to rank quality issues according to their significance. One method for solving problems is the cause-and-effect diagram, which methodically examines and evaluates every possible or actual cause that contributes to a certain outcome. However, it is a useful tool that gives the ability to investigate potential problem reasons [23]. By "gathering and organizing the possible causes, reaching a common understanding of the problem, exposing gaps in existing knowledge, ranking the most probable causes, and studying each cause" this diagram may aid in finding solutions. Six elements or causes typically comprise categories: environment, materials, machine, measurement, man, and method.[19].

**Scatter Diagram:** This diagram identifies and analyzes a pattern relationship between two variables, as well as determines whether a relationship exists at all and what type of relationship it is such as weak, strong, positive, or negative. A scatter diagram is a useful tool for drawing the distribution of information in two dimensions. The correlation may indicate the root causes of an issue, and the scatter diagram's form frequently illustrates the strength and direction of a connection between two variables. When it comes to regression modeling, scatter diagrams are quite helpful. [24], [25]. The following correlations between two variables can be shown by the scatter diagram: a) positive, b) negative, or c) no correlation.

**Flowchart:** A flowchart is a diagrammatic representation of a sequence of steps in an activity or process that shows several symbols. In contrast, a flowchart shows the inputs, actions, control points, and outputs in an image that is easy to use and comprehend concerning the process's overall goal[19]. This chart is an invaluable tool for finding and improving process quality. It is used methodically to identify and analyze parts or points of the process that may have had potential difficulties by documenting and interpreting an operation. Flowcharts were used [26] to document production workflows in a quality management system for mining operations, streamlining processes and reducing delays.

**Control Chart:** Walter A. Shewhart created the control chart, also known as the Shewhart control chart, at Bell Telephone Laboratories in the 1920s. It is arguably the most technically sophisticated tool for quality control. [24]. A specific type of run chart that illustrates the amount and nature of variation in the process over time is a control chart. Additionally, it illustrates and explains the process. Applying a control chart is crucial because it allows for the observation and monitoring of methods that are in statistical control following sampling that fall between the upper

control limit (UCL) and the lower control limit (LCL). Since there is no statistical control between UCL and LCL, the process is out of control; therefore, a control chart can be used to identify the root causes of any quality issues. The primary goal is to stop process flaws. Because poor products or services are more expensive than preventing them with tools like control charts, it is crucial for a variety of enterprises and industries[27]. A food sector case study[28] illustrated how control charts can minimize deviations and guarantee consistent meat quality.

### III. CASE STUDY

This case study was conducted in a renowned mobile phone and accessories manufacturer in Bangladesh. This organization manufactures mobile phones: Feature phones, Smartphones, mobile accessories: battery, charger, USB cable. The capacity of production is around 17,300 phones/day and 28,000 accessories/day. Around 500 employees work in a single shift to produce the targeted products. The management found a huge amount of waste from solder lead in the soldering of mobile phones in different parts. After that, this study was initiated. The study was focused on mobile assembly lines. This study is divided into five stages based on DMAIC and discussed in the following subsections.

#### III.1 DEFINE

Before defining our problems, we have selected our team as an internal customer so that we can represent our problem as VOC and identify CTQs. After observing the total processes of 6 assembly lines, we noticed a significant amount of solder lead wastage in the assembly lines. Some of the photographs have been given.



Figure 1: Solder Lead Wastages.  
Source: Authors, (2025).

Some points we raised as VOC are,

- Solder lead wastage is higher
- Unnecessary rework
- Violation of SOP

Some points for CTQs are,

- Wastage results in lower productivity
- Recycling or reusing this waste solder lead might lower the joint quality

Therefore, the major focus of this study is to reduce the waste of solder lead by taking necessary actions.

### III.2 MEASURE

After identifying the problem, we collected necessary data from the floor for two months. The data have been presented in the following tables.

Table 1: Wastage Data for July 2024.

Line	S. Lead Provided (Kg)	Actual Wastage (Kg)	Actual Wastage (%)	Output Qty	Avg. Wastage (g/pc)
A-1	22	15.36	69.82%	63,052	0.24
A-2	57	52.679	92.42%	115,221	0.46
A-3	46	44.89	97.59%	95,586	0.47
A-4	42	39.527	94.11%	81,474	0.49
A-5	37	40.51	109.49%	88,667	0.46
A-6	66	53.766	81.46%	112,889	0.48
<b>July</b>	<b>270</b>	<b>246.732</b>	<b>91.38%</b>	<b>556,889</b>	<b>0.44</b>

Source: Authors, (2025).

Table 2: Wastage Data for August 2024.

Line	S. Lead Provided (Kg)	Actual Wastage (Kg)	Actual Wastage (%)	Output Qty	Avg. Wastage (g/pc)
A-1	52	44.501	85.58%	98,747	0.45
A-2	42	33.391	79.50%	102,478	0.33
A-3	57	46.367	81.35%	115,836	0.40
A-4	54	42.327	78.38%	78,324	0.54
A-5	19	13.8	72.63%	41,964	0.33
A-6	49	39.84	81.31%	102,436	0.39
<b>August</b>	<b>273</b>	<b>220.226</b>	<b>80.67%</b>	<b>539,785</b>	<b>0.41</b>

Source: Authors, (2025).

Table 3: Summarized Wastage Data for Two Months.

Month	S. Lead Provided (Kg)	Actual Wastage (Kg)	Used (%)	Actual Wastage (%)	Output Qty	Avg. Wastage (g/unit)
July	270.00	246.73	8.62%	91.38	556,889	0.44
August	273.00	220.23	19.33%	80.67	539,785	0.41

Source: Authors, (2025).

### III.3 ANALYZE

In this phase, we worked to identify the underlying reasons for the wastage of solder lead. We performed root cause analysis and illustrated a cause-and-effect diagram to analyze the reasons.

After analyzing the scenario on the production floor, we found the following root causes,

- The direct reason is that the solder withdrawal is too late. Another reason is inserting extra lead while soldering.
- Operators are maintaining proper SOP while soldering. Operators often don't use jigs while soldering which results in mismatches and misalignment and increases soldering wastages because those need to be re-soldered.
- Soldering iron excessive heat. According to SOP, the soldering iron temperature is  $350 \pm 10$  °C.

- The excessive heat of soldering iron results in wastage and reduces the soldering bit life cycle.
- Operators do not maintain proper working method soldering. They didn't clean the soldering bit when it was needed. That results in longer soldering time and excess Lead for soldering.

A cause-and-effect diagram is illustrated in Figure 2 to find the sources of the causes.

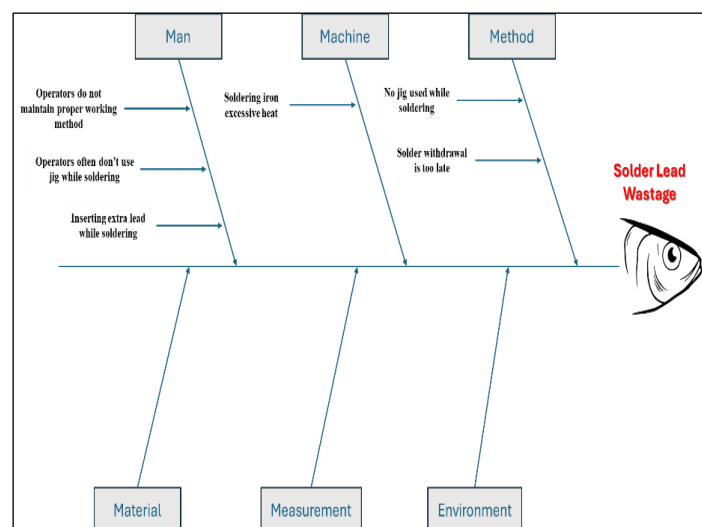


Figure 2: Cause and Effect Diagram of Reasons for Wastages.

Source: Authors, (2025)

This figure shows that the most responsible reasons are from the sources man and method. We have identified the sources for improvements.

### III.4 IMPROVE

Based on the analysis phase, some measures had been taken as follows,

A session has been taken with all the soldering people and educated about the SOP and proper handling method while soldering to solve the problems associated with operators.

A check sheet has been maintained to ensure that every soldering operator has appropriate jigs to maintain the optimum temperature of a soldering iron.

Strongly follow up on all the issues related to lead wastage by all the assembly lines concerned.

There is a problem with the machine because of the excessive soldering iron heating issue. A temperature controller must be mounted on the soldering iron to eliminate this problem.

After implementing the improvement techniques, we collected data for another month. The collected data are represented in the following table,

Table 4: Summarized Wastage Data for September 2024.

Line	S. Lead Provided (Kg)	Actual Wastage (Kg)	Actual Wastage (%)	Output Qty	Avg. Wastage (g/pc)
A-1	43	35.091	81.61%	130,528	0.27
A-2	44	30.984	70.42%	124,175	0.25
A-3	50	38.067	76.13%	131,261	0.29
A-4	43	29.967	69.69%	95,193	0.31
A-5	17	0	0.00%	-	-
A-6	43	32.143	74.75%	119,245	0.27



September	240	166.252	69.27%	600,402	0.28
-----------	-----	---------	--------	---------	------

Source: Authors, (2025).

Table 5: Summarized Wastage Data for Three Months.

Month	S. Lead Provided (Kg)	Actual Wastage (Kg)	Used (%)	Actual Wastage (%)	Output Qty	Avg. Wastage (g/unit)	Wastage Reduced (%)
July	270.00	246.73	8.62%	91.38%	556,889	0.44	-
August	273.00	220.23	19.33%	80.67%	539,785	0.41	10.74%
September	240.00	166.25	30.73%	69.27%	600,402	0.28	24.51%

Source: Authors, (2025).

### III.5 CONTROL

We observed remarkable improvements in reducing waste. To keep an eye on the sustainability of this improvement some controlling instructions must be followed,

- Follow the standard operating procedure or SOP strictly
- Training of the operators regularly
- New operators should not be engaged in soldering operations
- Proper documentation of daily wastage must be ensured

### IV. RESULTS AND DISCUSSIONS

The improvement phase showed that there is a significant change in the wastage of solder lead. Figure 4 and Figure 5 show the gradual decrease in the wastage of solder lead in soldering. The waste rate was 91.38% in July 2024 and was reduced to 80.67% in August 2024 by consulting the operators. After focusing on wastage and implementing improvement strategies, the waste rate was reduced to 69.27% in September 2024 as shown in Figure 3. In addition, solder waste per unit was 0.44 g/unit in July 2024 and was reduced to 0.28 g/unit in September 2024 as shown in Figure 4.

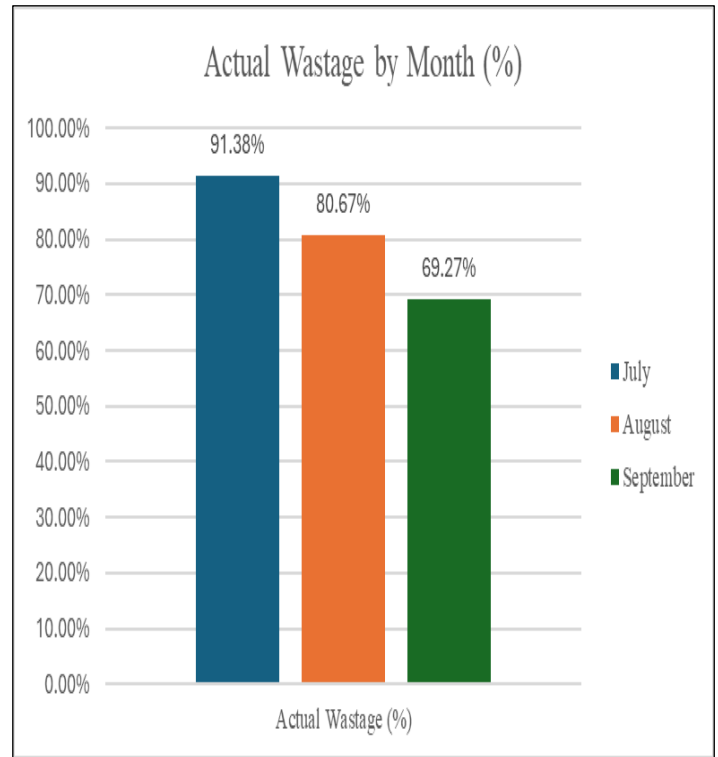


Figure 3: Monthly Comparison by Waste (%).  
Source: Authors, (2025).

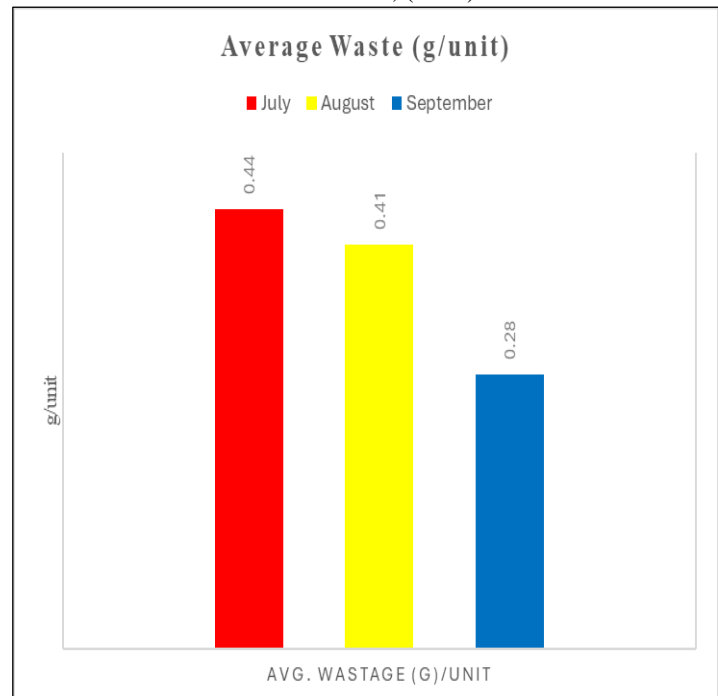


Figure 4: Monthly Comparison by Average Waste (g/unit).  
Source: Authors, (2025).

### V. CONCLUSIONS

This study has reflected the effectiveness of Six Sigma in solving practical problems on the production floor. This study aimed to identify the variability within the processes and take necessary actions to eliminate or reduce the variability. After recognizing the problem, we found that the total solder lead wastage was 91.38% and 80.67% in July and August respectively and the average solder waste per unit was 0.44 g/unit and 0.41 g/unit. The waste rate was way higher than our expectations. We reduced the waste rate by 10.74% after this finding in August 2024.



As a part of continuous improvement, we continued analyzing the root causes for this unusual finding, we found that the workers' skills and some methodological problems aroused this wastage rate. We arranged a training session for the soldering operators and instructed them on the proper use of solder iron and adjusted the solder iron temperature issue.

Then we collected data for another month and found that in September 2024 the wastage rate was dramatically reduced to 69.27%. It is still a bit high, but the change is noticeable. The waste rate was reduced by 24.51% as compared to the waste rate in August 2024. Per unit, average solder waste was also reduced to 0.28 g/unit. To sustain the improvement, we developed some controlling strategies to keep the operators and lower management alert.

We have some limitations to this study,

- We could not find the sigma level of the process as the unit of solder lead wastages is not pieces.
- We could not show the exact value of recycling the solder lead waste.

## VI. AUTHOR'S CONTRIBUTION

**Conceptualization:** Md. Mehedi Hassan Munna, and Jonayed Abdullah.

**Methodology:** Jonayed Abdullah, and Tarequl Islam.

**Investigation:** Md. Mehedi Hassan Munna, and Most. Anika Tabassum Little.

**Discussion of results:** Jonayed Abdullah, Md. Mehedi Hassan Munna, and Tarequl Islam.

**Writing – Original Draft:** Jonayed Abdullah.

**Writing – Review and Editing:** Jonayed Abdullah, Tarequl Islam, and Md. Mehedi Hassan Munna.

**Resources:** Md. Mehedi Hassan Munna, and Most. Anika Tabassum Little.

**Supervision:** Jonayed Abdullah, and Md. Mehedi Hassan Munna.

**Approval of the final text:** Md. Mehedi Hassan Munna, Jonayed Abdullah, Tarequl Islam, and Most. Anika Tabassum Little

## VII. ACKNOWLEDGMENTS

The author would like to express his gratitude to all parties, starting from data collection and data processing so that this article can be compiled. Hopefully this article is useful and useful as learning material.

## VIII. REFERENCES

[1] A. H. Ibrahim, X. Lyu, H. E. Sharafeldin, and A. B. ElDeeb, "Eco-Friendly and Complex Processing of Vanadium-Bearing Waste for Effective Extraction of Valuable Metals and Other By-Products: A Critical Review," *Recycling*, vol. 10, no. 1, p. 6, Jan. 2025, doi: 10.3390/recycling10010006.

[2] A. Palange and P. Dhattrak, "Lean manufacturing a vital tool to enhance productivity in manufacturing," *Materials Today: Proceedings*, vol. 46, pp. 729–736, 2021, doi: 10.1016/j.matpr.2020.12.193.

[3] C. Bai, A. Satir, and J. Sarkis, "Investing in lean manufacturing practices: an environmental and operational perspective," *International Journal of Production Research*, vol. 57, no. 4, pp. 1037–1051, Feb. 2019, doi: 10.1080/00207543.2018.1498986.

[4] T. M. Khalil, *Management of technology: the key to competitiveness and wealth creation*. Boston, Mass.: McGraw-Hill, 2000.

[5] Arunesh Patel, Chintan Chudgar, and ITM Universe, Vadodara, "Understanding basics of Six Sigma," *IJERT*, vol. V9, no. 05, p. IJERTV9IS050866, Jun. 2020, doi: 10.17577/IJERTV9IS050866.

[6] H. Erbiyik and M. Saru, "Six Sigma Implementations in Supply Chain: An Application for an Automotive Subsidiary Industry in Bursa in Turkey.," *Procedia - Social and Behavioral Sciences*, vol. 195, pp. 2556–2565, Jul. 2015, doi: 10.1016/j.sbspro.2015.06.447.

[7] A. C.R. and J. J. Thakkar, "Application of Six Sigma DMAIC methodology to reduce the defects in a telecommunication cabinet door manufacturing process: A case study," *IJQRM*, vol. 36, no. 9, pp. 1540–1555, Oct. 2019, doi: 10.1108/IJQRM-12-2018-0344.

[8] J. Singh, H. Singh, A. Singh, and J. Singh, "Managing industrial operations by lean thinking using value stream mapping and six sigma in manufacturing unit: Case studies," *MD*, vol. 58, no. 6, pp. 1118–1148, May 2019, doi: 10.1108/MD-04-2017-0332.

[9] A. Mittal, P. Gupta, V. Kumar, A. Al Owad, S. Mahlawat, and S. Singh, "The performance improvement analysis using Six Sigma DMAIC methodology: A case study on Indian manufacturing company," *Heliyon*, vol. 9, no. 3, Mar. 2023, doi: 10.1016/j.heliyon.2023.e14625.

[10] S. Salah and A. Rahim, "Integrated Company-Wide Management System (ICWMS)," in *An Integrated Company-Wide Management System*, Cham: Springer International Publishing, 2019, pp. 127–163. doi: 10.1007/978-3-319-99034-7\_8.

[11] A. Baptista, F. J. G. Silva, R. D. S. G. Campilho, S. Ferreira, and G. Pinto, "Applying DMADV on the industrialization of updated components in the automotive sector: a case study," *Procedia Manufacturing*, vol. 51, pp. 1332–1339, 2020, doi: 10.1016/j.promfg.2020.10.186.

[12] S. Hakimi, S. M. Zahraee, and J. Mohd Rohani, "Application of Six Sigma DMAIC methodology in plain yogurt production process," *International Journal of Lean Six Sigma*, vol. 9, no. 4, pp. 562–578, Jan. 2018, doi: 10.1108/IJLSS-11-2016-0069.

[13] Y.-T. Jou, R. M. Silitonga, M.-C. Lin, R. Sukwadi, and J. Rivaldo, "Application of Six Sigma Methodology in an Automotive Manufacturing Company: A Case Study," *Sustainability*, vol. 14, no. 21, p. 14497, Nov. 2022, doi: 10.3390/su142114497.

[14] G. Improta *et al.*, "Agile Six Sigma in Healthcare: Case Study at Santobono Pediatric Hospital," *IJERPH*, vol. 17, no. 3, p. 1052, Feb. 2020, doi: 10.3390/ijerph17031052.

[15] A. M. Ponsiglione *et al.*, "A Six Sigma DMAIC methodology as a support tool for Health Technology Assessment of two antibiotics," *MBE*, vol. 18, no. 4, pp. 3469–3490, 2021, doi: 10.3934/mbe.2021174.

[16] M. T. Pereira, M. I. Bento, L. P. Ferreira, J. C. Sá, F. J. G. Silva, and A. Baptista, "Using Six Sigma to analyse Customer Satisfaction at the product design and development stage," *Procedia Manufacturing*, vol. 38, pp. 1608–1614, 2019, doi: 10.1016/j.promfg.2020.01.124.

[17] N. Kumar, S. Shahzeb Hasan, K. Srivastava, R. Akhtar, R. Kumar Yadav, and V. K. Choubey, "Lean manufacturing techniques and its implementation: A review," *Materials Today: Proceedings*, vol. 64, pp. 1188–1192, 2022, doi: 10.1016/j.matpr.2022.03.481.

[18] M. A. Samad, J. Abdullah, and Md. A. H. Rifat, "Reduction of Manufacturing Lead Time by Value Stream Mapping of a Selected RMG Factory in Bangladesh," *AJEAT*, vol. 12, no. 1, pp. 10–17, May 2023, doi: 10.51983/ajeat-2023.12.1.3578.

[19] N. A. Parmar and S. Awasthi, "Review on Quality Management using 7 QC Tools," *International Journal of Trend in Research and Development*, vol. 5, no. 2, pp. 355–358, 2018.

[20] A. Silva, P. Miranda, D. D'Aiuto, and G. Conceição, "Implementation of the Lead Time methodology for managing the analysis of pharmaceutical inputs in Quality Control," in *Annals of the Symposium: building pathways to accelerate the development of the national technological innovation ecosystem*, Instituto de Tecnologia em Imunobiológicos, 2024, pp. 112–112. doi: 10.35259/isi.biomang.2024\_63725.

[21] J. George, A. Singh, and A. K. Bhaisare, "A Study of Basic 7 Quality Control Tools and Techniques for Continuous Improvement," in *A Study of Basic 7 Quality Control Tools and Techniques for Continuous Improvement*, Bhopal: Journal of Engineering & Technology, Mar. 2018.

- [22] Y. Sadraoui, M. Er-Ratby, M. S. Kadiri, and A. Kobi, "Quality Process Control and Preventive Maintenance Optimization of a Grinding Unit: A Case Study," in *2024 10th International Conference on Optimization and Applications (ICOA)*, Almeria, Spain: IEEE, Oct. 2024, pp. 1–6. doi: 10.1109/ICOA62581.2024.10753891.
- [23] J. M. Juran and A. B. Godfrey, *Juran's quality handbook*, 5th ed. New York San Francisco Washington [etc.]: McGraw Hill, 1999.
- [24] D. C. Montgomery and W. H. Woodall, "An Overview of Six Sigma," *Int Statistical Rev*, vol. 76, no. 3, pp. 329–346, Dec. 2008, doi: 10.1111/j.1751-5823.2008.00061.x.
- [25] J. S. Oakland, *Total quality management: text with cases*, 3. ed., Reprint. Oxford: Butterworth Heinemann, 2007.
- [26] A. A. S. Elmahdi, "SYSTEMATIC REVIEW: THE IMPACT OF TOTAL QUALITY MANAGEMENT ON GOLDMINING INDUSTRY PERFORMANCE IN SUDAN," *Geostrategy*, 2023, doi: 10.30546/3006-0346.2023.6.78.109.
- [27] D. C. Montgomery, *Introduction to statistical quality control*, 8th ed. Hoboken, NJ: J. Wiley & Sons, 2019.
- [28] N. Trisno, B. Arnawisuda Ningsi, and I. Arofah, "ANALISIS PENGENDALIAN KUALITAS DAGING DENGAN MENGGUNAKAN SEVEN TOOLS DI THE FOODHALL PLAZA INDONESIA," *SCI TECH ED MATH*, vol. 5, no. 3, pp. 2109–2130, Dec. 2024, doi: 10.46306/lb.v5i3.785.



## RESEARCH ARTICLE

## OPEN ACCESS

# ENHANCING OVERALL EQUIPMENT EFFECTIVENESS (OEE) OF A SELECTED MACHINE IN A LIGHT MANUFACTURING FACTORY IN BANGLADESH

<sup>1</sup>Jonayed Abdullah, <sup>2</sup>Md. Al Hossain Rifat, <sup>3</sup>Avirup Deb Ray

<sup>1,2,3</sup>Department of Industrial and Production Engineering, Shahjalal University of Science and Technology, Sylhet, Bangladesh.

<sup>1</sup><https://orcid.org/0009-0006-7130-7597>, <sup>2</sup><https://orcid.org/0009-0002-1839-6472>, <sup>3</sup><https://orcid.org/0009-0005-6675-8345>

Email: [jonayedabdullah.ipe@gmail.com](mailto:jonayedabdullah.ipe@gmail.com), [rifatsustipe@gmail.com](mailto:rifatsustipe@gmail.com), [avirup11@student.sust.edu](mailto:avirup11@student.sust.edu)

## ARTICLE INFO

**Article History**

Received: January 22, 2025

Revised: February 20, 2025

Accepted: March 15, 2025

Published: April 31, 2025

**Keywords:**

OEE,  
Availability,  
Performance,  
Quality,  
Lean Manufacturing.

## ABSTRACT

Overall equipment effectiveness provides reliable and considerable performance indicators for machinery performance. This research aimed to measure the OEE of the selected machine, identify the reasons behind its poor performance, and take action to improve the machine's overall performance. A tire-curing machine was chosen for the research as the target machine for OEE analysis. After collecting data for a month, we did our calculation using Microsoft Excel and found OEE of just 63%, which is far below the industry standards. We investigated the causes of the low OEE and found that most affected the availability and performance metrics while quality was good. For the following month, several performance improvement activities were taken including maintenance improvements, process optimizations, and operator training. The new data collection and analysis phase was carried out after the implementation phase to measure the impact results of the interventions. The OEE of the machine improved from 63% to 73%, showcasing a significant increase in efficiency; that is, availability increased by 79% to 85%, while performance improved from 82% to 88%. This research also highlights the importance of OEE as it gives a comprehensive view of how machines and equipment may be tracked and improved.



Copyright ©2025 by authors and Galileo Institute of Technology and Education of the Amazon (ITEGAM). This work is licensed under the Creative Commons Attribution International License (CC BY 4.0).

## 1. INTRODUCTION

In the fast-pacing competition, leading manufacturing firms must closely monitor the performance of all functions, including production and maintenance, to gain a benefit over competitors. As worldwide competition intensifies, executives are shifting from merely enhancing efficiency through economies of scale and internal specialization to meeting market demands for flexibility, timely delivery, and quality. Increasing productivity is essential for businesses looking to succeed in their ventures. [1]

Production costs are considerable, and manufacturing systems frequently run at poor productivity and below capacity. Factory maintenance accounts for 25–30% of the overall cost of production [2]. The profitability of a firm is greatly impacted by the quality of maintenance. Since maintenance expenses make up a sizable portion of manufacturing companies' operational budgets, the significance of maintenance functions has grown because of their

involvement in maintaining and enhancing product quantity, availability, and safety regulations [3]. The Japanese created and presented the idea of Total Productive Maintenance (TPM) in 1971 in response to maintenance issues that arose in manufacturing environments. TPM is a Japanese maintenance system that was developed by Nakajima and encompasses all aspects of equipment life, including planning, manufacture, and maintenance [4]. To continuously improve product quality, operational efficiency, capacity assurance, and safety, it outlines a synergistic link between all organizational functions, but especially between production and maintenance. [5]

A tire vulcanization machine has been selected for this research. Then we collected data for a month and then worked based on the collected data. The objectives of this research are,

- to assess the current OEE of the chosen machine
- to investigate the root cause
- to suggest improvement strategies.

This research explores the effectiveness of using OEE as a performance indicator of the machines in the manufacturing and how to improve where the performance is lower than the standards.

## II. REVIEW OF LITERATURE

### II.1 LEAN MANUFACTURING

Lean manufacturing can be termed as continuous improvement nowadays [6]. It is used in industries to maximize the production and minimize the cost of production [7]. The foundation of Taiichi Ohno's widely promoted lean manufacturing methodology is lean thinking which is guided by certain principles. Value specification, value stream mapping, flow optimization, pull production system, and perfection or continuous improvement are the five pillars of lean manufacturing [6].

Lean service prioritizes the consumer in addition to the individuals involved in the transformation process. In contrast to production, the client is the initial point of contact when selling services. Unlike most industries, the service firm works directly with the consumer on the front line.[8] While raw materials and equipment are expensive and a major emphasis in manufacturing operations, labor is one of the most important aspects in service operations when it comes to work expenses [9]. Lean manufacturing divides the times into value added time, non-value added time, and unavoidable non value added time and finally works on eliminating or reducing non value added times [10]. Some of the frequently used lean tools are mentioned below.

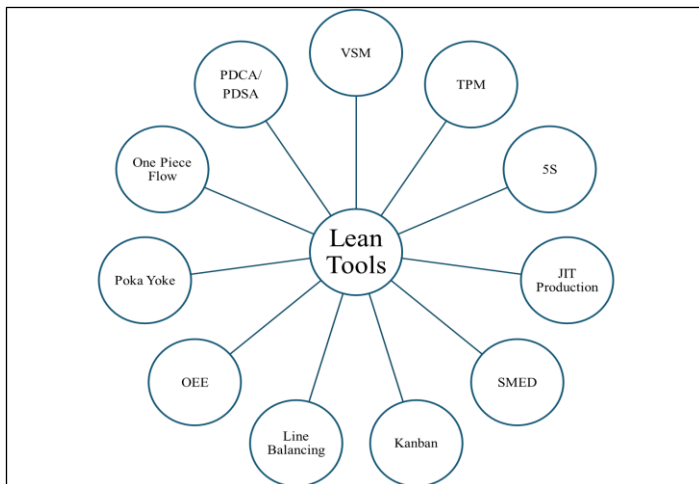


Figure 1: Lean Tools.

Source: [11].

### II.2 OVERALL EQUIPMENT EFFECTIVENESS (OEE)

OEE is the ratio of the amount of a product or part that is created without defects to the amount that might be produced based on the design of the equipment. An OEE of 100% indicates that a machine or process is operating at maximum capacity with no problems [12]. Three crucial factors are Availability (A), Performance Rate (PR), and Quality Rate (QR) combined to generate Overall Equipment Effectiveness (OEE). The machine tool that transforms the product from its raw condition into finished items must be dependable when increased production is anticipated [13]. Machine availability with minimal downtime is a component of reliability. The availability of machines for the intended performance is shown by a higher meantime between failures (MTBF). It is necessary to try to increase MTBF and decrease the mean time to repair (MTTR). Root cause analysis and failure data

analysis are necessary. OEE is a machine capability metric. It indicates where the scope of improvements is. Statistical data collected from the tire manufacturing process results in useful information for improvement areas. [14], [15]

Six big losses- One of the primary goals of OEE and TPM projects is to address the Six Big Losses, which are the most common reasons of industrial efficiency loss. The connections between the Six Big Losses and the OEE Loss categories are shown in the following.

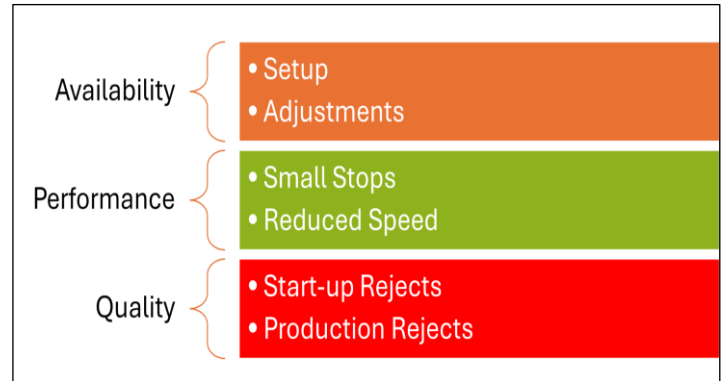


Figure 2: Six big losses.

Source: [12], [14].

### II.3 TOTAL PRODUCTIVE MAINTENANCE (TPM)

A complete productive maintenance delivery system encompassing the whole life of the equipment and including all personnel from production and maintenance divisions to top management is how TPM describes its program for equipment maintenance [4]. Through daily operations involving the whole workforce, TPM is described as a new approach to maintenance that maximizes equipment effectiveness, reduces failures, and encourages autonomous maintenance by operators that also integrates 5S in the floor [16]. TPM can also be implemented in service sector to provide error free services [17]. TPM essentially aims to integrate the organization to identify, unleash, and make use of its abilities and potential. Bringing managers, supervisors, and other stakeholders together to take corrective action when necessary is the goal of TPM [18]. One productive maintenance program that emphasizes the following is called Total Productive Maintenance (TPM):

- maximizing the overall efficiency of the device.
- putting in place a planned Preventive Maintenance (PM) scheme for the machine's lifetime.
- involving every worker, from the production floor to upper management.
- giving workers the freedom to start remedial actions. [19], [20]

The word 'total' in TPM has 3 meanings:

- Total effectiveness denotes TPM's efforts to increase profitability and economic efficiency.
- Total maintenance system includes Maintenance Prevention (MP) and Maintainability Improvement (MI), as well as PM. Incorporating dependability, maintainability, and supportability features into the equipment design, essentially refers to a maintenance-free design.
- Total engagement of all operators involves Autonomous Maintenance (AM) by operators by small group activities. In essence, a team effort is used to complete maintenance,



and the operator is ultimately in charge of taking care of his or her equipment. (Nakajima and Nakajima, 1988)

Pillars of TPM: Eight pillars of TPM have a great impact on the manufacturing of any product. The below figure illustrates the pillars,

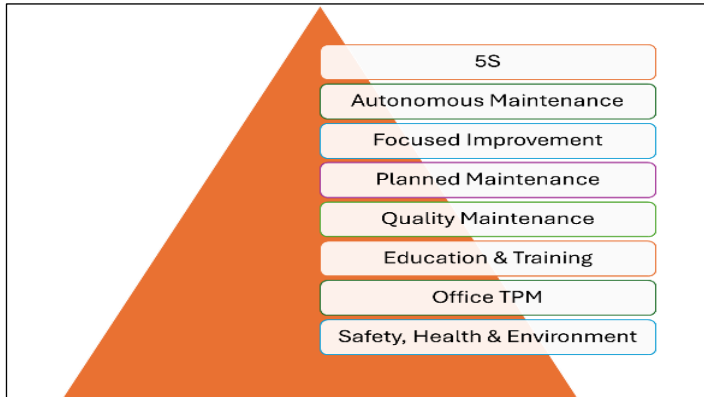


Figure 3: Pillars of TPM.  
Source: [21], [22].

#### II.4 SINGLE MINUTE EXCHANGE OF DIE (SMED)

Shingo created SMED, or quick changeover of tools, and described it as a scientific method to cut set-up times that any machine and industrial facility may use. The time should be less than 9 minutes.[23] Setup time is the preparation period between the end of the last product generated and the first product manufactured in the next process [24]. The shortest length of time required to switch the kind of manufacturing operation, taking consideration of the moment when the final unit of a prior lot was created and the first unit produced by the succeeding lot, was known as SMED [25].

There are four steps involved in reducing the set-up in the SMED: preliminary steps, internal and external set-up separation, internal to external set-up conversion, and simplifying every part of preparation [26]. Two significant activities are involved in Single Minutes Exchange of Die (SMED).

They are the internal and external setups:

- Internal time: may only be performed once the device or operation has finished
- External time: maybe while the device or operation is still running

The SMED concepts were applied accordingly to specific pre-defined conventional processes, Plan, Do, Check, and Act (PDCA) cycle is a four-step checklist that must be followed to get from problem-faced to problem-solved. [11], [26]

#### II.5 CONCEPT OF QUALITY

Quality is the degree of excellence of a procedure, service, or product that your business provides and that satisfies the standards set by ISO and, of course, by your clients [27], [28]. To understand a little more about quality, this post will cover three fundamental concepts of quality:

- Quality Assurance: Ensuring that the operational quality standards and criteria, which have previously been set, are applied in all subsequent development stages, whether for a product or service, is known as quality assurance.
- Quality Control: This idea, which is mostly implemented through inspections, aims to satisfy the quality criterion. The

process of analyzing and evaluating whether a product or service's qualities meet predetermined standards to ascertain whether a nonconformity has occurred is known as quality inspection.

- Quality Management: Coordination of manufacturing process and service operations to ensure high-quality performance is known as quality management. [29]

Keeping in mind that the dimensions of quality may be interpreted as performance, dependability, perception, durability, characteristics, conformance, and service, this management strives for perfection in the execution of all activities and operations. One of the phases in Quality Management, which we discussed in the previous post, is the establishment of a Quality Management System (QMS). However, for a QMS to provide outstanding outcomes for a company, the team must practice and adhere to the seven quality principles:



Figure 4: Principles of Quality.  
Source: [29].

For the betterment of quality, there are seven QC tools introduced by the researchers,

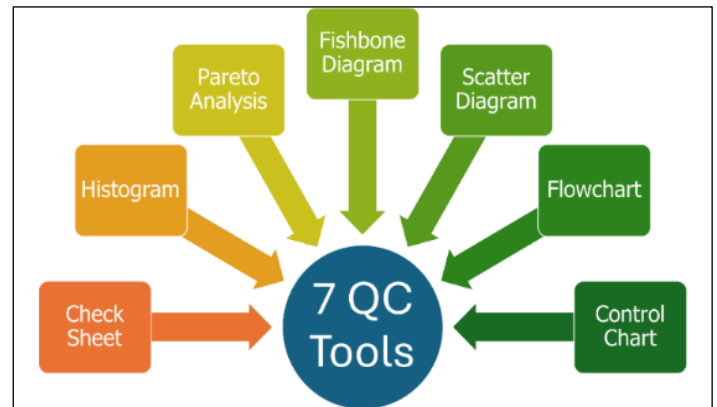


Figure 5: Seven QC Tools.  
Source: [27], [30].

#### II.6 ROOT CAUSE ANALYSIS

Root Cause Analysis (RCA), a key component of quality management systems, helps identify and address the underlying issues that improve quality and productivity in more significant ways. RCA is frequently used as a receptive approach to identify the source of an occurrence or event, uncover problems, and determine their nature [31]. Since the root cause of an undesirable state or issue is the most fundamental factor, root cause analysis (RCA) is too important for a production engineer. RCA is a methodical approach to identifying the basic flaws or underlying

causes. The first stage in the RCA is to define and describe the issue. RCA was founded in 1958 when Toyota's production procedures were being developed. The researchers have employed a variety of tools to apply RCA in industrial settings, and the comparative analysis of those tools has been predicated on their suitable applications. Experimental research in the multistage manufacturing sector was carried out to increase product quality and productivity. It was discovered that after implementing countermeasures on the underlying reasons, the defect decreased from 11.87% to 1.92%. [32]

### III. METHOD AND ANALYSIS

The below flow chart shows the steps we have followed to complete this research.

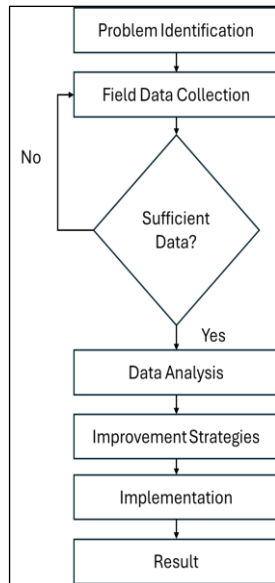


Figure 6: Steps Followed.  
Source: Authors, (2025).

For our research, we have selected a vulcanizing machine. The required field data are presented in the Appendices.

As we know,

$$OEE = Availability \times Performance \times Quality \quad (1)$$

We can find the OEE from our collected data. We need to find availability, performance, and quality from our field data to do this.

Equation for availability.

$$Availability = \frac{Net\ Operating\ Time}{Operating\ Time} = \frac{Operating\ Time - Breakdown\ Time}{Operating\ Time} \quad (2)$$

Equation for performance.

$$Performance = \frac{Production}{Production\ Target} = \frac{Production}{(Cycle\ Time)/(Operating\ Time)} \quad (3)$$

Equation for quality.

$$Quality = \frac{Good\ Qty}{Total\ Production} = \frac{Total\ Production - Rejection\ Qty}{Total\ Production} \quad (4)$$

Finding the values from equation 2, 3, and 4, we found the current OEE of the selected machine by substituting the values in equation 1 that is shown in table 1.

Table 1: Average OEE.

Availability	Performance	Quality	OEE
79%	82%	98%	63%

Source: Authors, (2025).

From the data analysis, it is visible that the machine can provide a good quality product that is 98%. This value is good enough. Availability is also fair enough, that is 79% and the performance is 82%. Worldwide OEE standard is 85% where 90% availability, 95% performance, and 99% quality [33]. As current availability and performance is lower than the standards, we will work to improve here. So, we will investigate the reasons for lower availability and performance by using some lean techniques. After diving into the reasons for lower availability we found the following reasons presented in table 2.

Table 2: Unplanned Downtime Reason.

Reason	Duration (min)	%
Manpower Short	1,152	36.25%
Air Problem	936	29.45%
Mold Problem	523	16.46%
Material Shortage	203	6.39%
Electrical Problem	178	5.60%
Color Problem	125	3.93%
Air Pressure Low	31	0.98%
Machine Transfer	30	0.94%

Source: Authors, (2025).

Plotting this duration of unplanned break down in pareto chart we identified the three reasons that are illustrated in Figure 7.

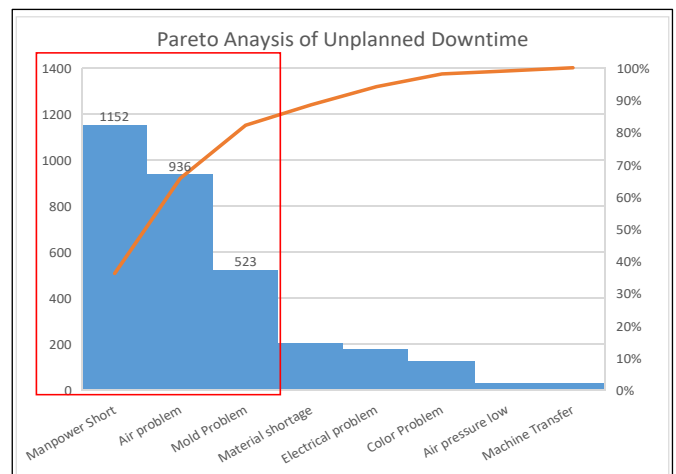


Figure 7: Pareto Chart for Unplanned Downtime.  
Source: Authors, (2025).

After studying the total system, we have found some root causes that affected the machine's performance. Those reasons have been shown below by illustrating cause and effect diagram,

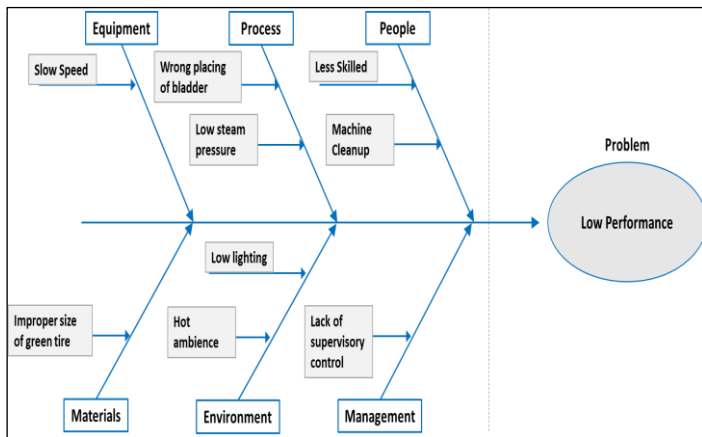


Figure 8: Cause and Effect Diagram for Low Performance.  
Source: Authors, (2025).

#### IV. IMPROVEMENT STRATEGY

From our data analysis, it is clear that we have a good opportunity to improve in the availability and performance aspects. Table 7 & Figure 7 show that Manpower shortage, air problems, and mold problems incur 36.2%, 29.5%, and 16.5% of the total downtime respectively. These reasons are 82.2% of total downtime. We may take the following steps to overcome these problems and increase the availability of the selected machine,

- To overcome the manpower shortage, we worked with the human resource department to find the manpower so that the machine does not have to stay idle. Following this we provided manpower requisition to the HR department.
- To overcome the air problem, we assigned one person to keep an eye on the compressor room. There might be some power shutdown and for that reason, the compressor takes a short too long time to increase the air pressure. In addition, we installed an air reservoir tank that would reserve a minimum amount of air with the desired pressure to give backup support to production immediately after the power shutdown is over.
- To overcome the mold problem, molds were properly cleaned by the operators at regular intervals. There should not be any rust or any type of dent on the mold body.

Figure 8 shows the root causes of the low performance of the machine. The following strategies could be effective to increase the performance of the selected machine,

- As the machine speed was slow, operators strictly followed the regular machine maintenance. Lubricating the moving parts was done as a practice to remove the rust and allow the machine to work at maximum speed.
- The slow performance of the operator also affected the performance of the machine. Operators were given proper training before working on this machine.
- Low steam pressure leads to longer cycle time for the selected machine. Steam pressure was controlled by installing a steam regulating valve. Pressure Regulating Valves (PRV) were installed to see the outcome of the machine. The maintenance team was given instructions to implement TPM to reduce breakdown of air compressors.

- Proper lighting on the production floor is inevitable for the performance of operators. The maintenance team must ensure proper light.
- An optimum level of airflow is necessary to work properly. Thus, a proper air ventilation system was installed on the production floor.
- Process control was followed strictly to avoid the mistakes in green tire making.
- Operators might become lazy sometimes or they might not understand the process. In that case, a supervisor was there to ensure the hourly output from the operators or the machines.

#### V. RESULTS AND DISCUSSIONS

We have worked on the total system implementing the improvement strategies and we have found the following outcomes for that selected machine shown in Table 3.

The result assures that there is a visible improvement in availability, performance, and OEE of that machine.

Table 3: OEE after Improvement.

Month	Availability	Performance	Quality	OEE
January	79%	82%	98%	63%
March	85%	88%	98%	73%

Source: Authors, (2025).

The final output showed significant improvements in the machine's performance after implementing the strategies. Though the installation of some mechanical parts and air ventilation took time, we waited for a month and then recorded the data.

#### VI. CONCLUSIONS

We conducted a detailed study to improve the Overall Equipment Effectiveness of a selected machine. First, we measured the current performance of the machine and recorded an OEE of 63%, which suggested ample scope for improvement. We then conducted a root cause analysis in detail to identify the main causes of the poor OEE. The availability and performance issues were found to be the major problems.

Accordingly, targeted improvement strategies were formulated and implemented. We then waited a month to monitor the machine's performance and determine how the interventions affected performance. For instance, there was an increase in average OEE in March by up to 73%, which constitutes a 10% increase. In addition, there was an increase in availability from 79% to 85%, and its performance went up from 82% to 88%. These improvements show that our methodology is effective.

Even with this improvement, the machine performance has been well below industrial standards, which are 90% availability, 95% performance, and 95% quality. The improvement has reached a very high value, with the potential still open for further optimization to fill the gap between industrial standards. Our study has some limitations,

- We could not show the cost of some systems installed for the improvements
- Showing a comparison between the productivity growth would make this research more complex. Thus, we could not mention it.

## VII. AUTHOR'S CONTRIBUTION

**Idea Generation:** Jonayed Abdullah, Md. Al Hossain Rifat, and Avirup Deb Ray.

**Methodology:** Jonayed Abdullah, and Md. Al Hossain Rifat.

**Analysis:** Jonayed Abdullah.

**Discussion of results:** Jonayed Abdullah, and Avirup Deb Ray

**Writing – Original Draft:** Jonayed Abdullah, and Md. Al Hossain Rifat.

**Writing – Review and Editing:** Jonayed Abdullah, and Md. Al Hossain Rifat.

**Resources:** Jonayed Abdullah.

**Supervision:** Md. Al Hossain Rifat, and Avirup Deb Ray.

**Approval of the final text:** Jonayed Abdullah, Md. Al Hossain Rifat, and Avirup Deb Ray.

## VIII. ACKNOWLEDGMENTS

The author would like to express his gratitude to all parties, starting from data collection and data processing so that this article can be compiled. Hopefully this article is useful and useful as learning material.

## IX. REFERENCES

- [1] M. Sayuti, Juliananda, Syarifuddin, and Fatimah, "Analysis of the Overall Equipment Effectiveness (OEE) to Minimize Six Big Losses of Pulp machine: A Case Study in Pulp and Paper Industries," *IOP Conf. Ser.: Mater. Sci. Eng.*, vol. 536, no. 1, p. 012136, Jun. 2019, doi: 10.1088/1757-899X/536/1/012136.
- [2] D. S. Thomas, "The costs and benefits of advanced maintenance in manufacturing," National Institute of Standards and Technology, Gaithersburg, MD, NIST AMS 100-18, Apr. 2018. doi: 10.6028/NIST.AMS.100-18.
- [3] O. A. Oluwatoyin, S. A. Afolalu, and S. I. Monye, "Maintenance Impact on Production Profitability in Industry - An Overview," in *2024 International Conference on Science, Engineering and Business for Driving Sustainable Development Goals (SEB4SDG)*, Omu-Aran, Nigeria: IEEE, Apr. 2024, pp. 1–8. doi: 10.1109/SEB4SDG60871.2024.10630377.
- [4] G. L. Tortorella, F. S. Fogliatto, P. A. Cauchick-Miguel, S. Kurnia, and D. Jurburg, "Integration of Industry 4.0 technologies into Total Productive Maintenance practices," *International Journal of Production Economics*, vol. 240, p. 108224, Oct. 2021, doi: 10.1016/j.ijpe.2021.108224.
- [5] A. Hallioui *et al.*, "A Review of Sustainable Total Productive Maintenance (STPM)," *Sustainability*, vol. 15, no. 16, p. 12362, Aug. 2023, doi: 10.3390/su151612362.
- [6] N. Kumar, S. Shahzeb Hasan, K. Srivastava, R. Akhtar, R. Kumar Yadav, and V. K. Choubey, "Lean manufacturing techniques and its implementation: A review," *Materials Today: Proceedings*, vol. 64, pp. 1188–1192, 2022, doi: 10.1016/j.matpr.2022.03.481.
- [7] M. Deshmukh, A. Gangele, D. K. Gope, and S. Dewangan, "Study and implementation of lean manufacturing strategies: A literature review," *Materials Today: Proceedings*, vol. 62, pp. 1489–1495, 2022, doi: 10.1016/j.matpr.2022.02.155.
- [8] G. Yadav, S. Luthra, D. Huisin, S. K. Mangla, B. E. Narkhede, and Y. Liu, "Development of a lean manufacturing framework to enhance its adoption within manufacturing companies in developing economies," *Journal of Cleaner Production*, vol. 245, p. 118726, Feb. 2020, doi: 10.1016/j.jclepro.2019.118726.
- [9] M. Mohan Prasad, J. M. Dhiyaneswari, J. Ridzwanul Jamaan, S. Mythreyan, and S. M. Sutharsan, "A framework for lean manufacturing implementation in Indian textile industry," *Materials Today: Proceedings*, vol. 33, pp. 2986–2995, 2020, doi: 10.1016/j.matpr.2020.02.979.
- [10] V. Agostinho and C. R. Baldo, "Assessment of the impact of Industry 4.0 on the skills of Lean professionals," *Procedia CIRP*, vol. 96, pp. 225–229, 2021, doi: 10.1016/j.procir.2021.01.079.
- [11] M. A. Samad, J. Abdullah, and Md. A. H. Rifat, "Reduction of Manufacturing Lead Time by Value Stream Mapping of a Selected RMG Factory in Bangladesh," *AJEAT*, vol. 12, no. 1, pp. 10–17, May 2023, doi: 10.51983/ajeat-2023.12.1.3578.
- [12] E. J. Clements, V. Sonwaney, and R. K. Singh, "Measurement of overall equipment effectiveness to improve operational efficiency," *IJPMB*, vol. 8, no. 2, p. 246, 2018, doi: 10.1504/IJPMB.2018.10010267.
- [13] S. Di Luo, G. R. Pop, and M. M. Schiraldi, "The Human Performance Impact on OEE in the Adoption of New Production Technologies," *Applied Sciences*, vol. 11, no. 18, p. 8620, Sep. 2021, doi: 10.3390/app11188620.
- [14] C. K. Cheah, J. Prakash, and K. S. Ong, "An integrated OEE framework for structured productivity improvement in a semiconductor manufacturing facility," *IJPPM*, vol. 69, no. 5, pp. 1081–1105, Feb. 2020, doi: 10.1108/IJPPM-04-2019-0176.
- [15] P. Tsarouhas, "Improving operation of the croissant production line through overall equipment effectiveness (OEE): A case study," *IJPPM*, vol. 68, no. 1, pp. 88–108, Jan. 2019, doi: 10.1108/IJPPM-02-2018-0060.
- [16] I. M. Ribeiro, R. Godina, C. Pimentel, F. J. G. Silva, and J. C. O. Matias, "Implementing TPM supported by 5S to improve the availability of an automotive production line," *Procedia Manufacturing*, vol. 38, pp. 1574–1581, 2019, doi: 10.1016/j.promfg.2020.01.128.
- [17] A. Ali, "Application of total productive maintenance in service organization," *Int. J. Res. Ind. Eng.*, no. Online First, Mar. 2019, doi: 10.22105/riej.2019.170507.1076.
- [18] T. K. Agustiady and E. A. Cudney, "Total productive maintenance," *Total Quality Management & Business Excellence*, pp. 1–8, Feb. 2018, doi: 10.1080/14783363.2018.1438843.
- [19] A. Ceruti, P. Marzocca, A. Liverani, and C. Bil, "Maintenance in aeronautics in an Industry 4.0 context: The role of Augmented Reality and Additive Manufacturing," *Journal of Computational Design and Engineering*, vol. 6, no. 4, pp. 516–526, Oct. 2019, doi: 10.1016/j.jcde.2019.02.001.
- [20] Z. Tian Xiang and C. Jeng Feng, "Implementing total productive maintenance in a manufacturing small or medium-sized enterprise," *JIEM*, vol. 14, no. 2, p. 152, Feb. 2021, doi: 10.3926/jiem.3286.
- [21] E. Y. T. Adesta, H. A. Prabowo, and D. Agusman, "Evaluating 8 pillars of Total Productive Maintenance (TPM) implementation and their contribution to manufacturing performance," *IOP Conf. Ser.: Mater. Sci. Eng.*, vol. 290, p. 012024, Jan. 2018, doi: 10.1088/1757-899X/290/1/012024.
- [22] S. San, "A Systematic Literature Review of Total Productive Maintenance On Industries," *Performa*, vol. 20, no. 2, p. 97, Nov. 2021, doi: 10.20961/performa.20.2.50087.
- [23] R. G. P. Junior, R. H. Inácio, I. B. Da Silva, A. Hassui, and G. F. Barbosa, "A novel framework for single-minute exchange of die (SMED) assisted by lean tools," *Int J Adv Manuf Technol*, vol. 119, no. 9–10, pp. 6469–6487, Apr. 2022, doi: 10.1007/s00170-021-08534-w.
- [24] I. B. Da Silva and M. Godinho Filho, "Single-minute exchange of die (SMED): a state-of-the-art literature review," *Int J Adv Manuf Technol*, vol. 102, no. 9–12, pp. 4289–4307, Jun. 2019, doi: 10.1007/s00170-019-03484-w.
- [25] O. Celis-Gracia, J. L. García Alcaraz, F. J. Estrada-Orantes, and F. Hermosillo Villalobos, "Single-Minute Exchange of Die (SMED)," in *Lean Manufacturing in Latin America*, J. L. García Alcaraz, G. C. Robles, and A. Realvásquez Vargas, Eds., Cham: Springer Nature Switzerland, 2025, pp. 285–308. doi: 10.1007/978-3-031-70984-5\_13.
- [26] P. Burawat, "Productivity Improvement of Carton Manufacturing Industry by Implementation of Lean Six Sigma , ECRS , Work Study , and 5 S : A Case Study of the ABC Co . , Ltd," 2019. [Online]. Available: <https://api.semanticscholar.org/CorpusID:244771009>
- [27] Dr. M. A. A. Hasin, *Quality Control and Management*, 1st ed. Bangladesh Business Solutions, 2007.
- [28] P. Rogala and S. Wawak, "Quality of the ISO 9000 series of standards-perceptions of quality management experts," *IJQSS*, vol. 13, no. 4, pp. 509–525, Nov. 2021, doi: 10.1108/IJQSS-04-2020-0065.



[29] S. Barbosa, "Quality concepts: everything you need to know," *paripassu*. Nov. 11, 2021. Accessed: Apr. 14, 2024. [Online]. Available: <https://www.paripassu.com.br/en/blog/quality-concepts>

[30] B. Neyestani, "Seven Basic Tools of Quality Control: The Appropriate Techniques for Solving Quality Problems in the Organizations," Apr. 09, 2017, *Open Science Framework*. doi: 10.31219/osf.io/jkbtz.

[31] D. Pietsch, M. Matthes, U. Wieland, S. Ihlenfeldt, and T. Munkelt, "Root Cause Analysis in Industrial Manufacturing: A Scoping Review of Current Research, Challenges and the Promises of AI-Driven Approaches," *JMMP*, vol. 8, no. 6, p. 277, Dec. 2024, doi: 10.3390/jmmp8060277.

[32] M. Rahman, M. Rabbi, and S. Banik, "INVESTIGATION OF PRODUCTION LINE DEFECTS USING ROOT CAUSE ANALYSIS: A CASE STUDY ON AN AUTOMOBILE INDUSTRY IN BANGLADESH," *INTERNATIONAL JOURNAL OF INDUSTRIAL ENGINEERING RESEARCH AND DEVELOPMENT*, vol. 12, no. 1, Mar. 2021, doi: 10.34218/IJIERD.12.1.2021.003.

[33] C. Jaqin, A. Rozak, and H. H. Purba, "Case Study in Increasing Overall Equipment Effectiveness on Progressive Press Machine Using Plan-do-check-act Cycle," *IJE*, vol. 33, no. 11, Nov. 2020, doi: 10.5829/ije.2020.33.11b.16.



ISSN ONLINE: 2447-0228



## RESEARCH ARTICLE OPEN ACCESS

## COMPARATIVE STUDY OF 2D DESIGNS OF 12/8 AND 10/8 SWITCHED RELUCTANCE MOTORS USING ANSYS MAXWELL

Layachi Chebabhi<sup>1</sup>, Toufik tayeb Naas<sup>2</sup>, Mohamed Zitouni<sup>3</sup><sup>1</sup> Laboratory of Applied Automation and Industrial Diagnostics (LAADI), Department of Mechanical Engineering in the Faculty of Science and Technology, Ziane Achour University of Djelfa, PO Box 3117, Djelfa 17000, Algeria.<sup>2</sup> Laboratory of Renewable Energy Systems Applications (LASER), Department of Mechanical Engineering in the Faculty of Science and Technology, Ziane Achour University of Djelfa, PO Box 3117, Djelfa 17000, Algeria.<sup>3</sup> Laboratory of Electrotechnical Research L.R.E, National Polytechnic School (ENP), Department of Electrical Engineering in the Faculty of Science and Technology, Ziane Achour University of Djelfa, PO Box 3117, Djelfa 17000, Algeria.<sup>1</sup><https://orcid.org/0009-0002-4451-8533>, <sup>2</sup><http://orcid.org/0000-0002-5539-6415>, <sup>3</sup><https://orcid.org/0009-0003-3088-7431>Email: [layachi.chebabhi@univ-djelfa.dz](mailto:layachi.chebabhi@univ-djelfa.dz), [t.naas@univ-djelfa.dz](mailto:t.naas@univ-djelfa.dz), [med.zitouni@univ-djelfa.dz](mailto:med.zitouni@univ-djelfa.dz)

## ARTICLE INFO

*Article History*

Received: February 02, 2025

Revised: March 20, 2025

Accepted: March 15, 2025

Published: April 31, 2025

*Keywords:*Switched Reluctance Motor,  
ANSYS Maxwell,  
Operating Conditions,  
Electromagnetic Analysis,  
Losses.

## ABSTRACT

The switched reluctance motor (SRM) is one of the common industrial applications where many fields of different models are used, but they differ in performance, thus the selection of the appropriate prototype must be determined according to the application's requirements. In this study, a comparative analysis was conducted between 12/8 and 10/8 switched reluctance motors (SRMs) using ANSYS Maxwell where the same dimensions, parameters, and operating conditions were adopted in the designs and only the number of stator poles were changed to evaluate the magnetic, mechanical, and electrical characteristics. Then we study their effect on the SRMs performance focusing on several aspects of torque, speed, various losses, electromagnetic analysis of intensity, and magnetic flux density. Electrical losses were reviewed, and the study revealed significant differences between the SRMs' electromagnetic performance, highlighting the importance of the SRM design to reduce losses and improve efficiency. The results show that the importance of choosing between the two SRMs depends on the application requirements, whether it requires high speed and efficiency or high torque. This study provides a comprehensive insight into the SRM designs deep analysis, supporting the drive for more efficient and sustainable technology in optimizing the electric motors' overall performance.



Copyright ©2025 by authors and Galileo Institute of Technology and Education of the Amazon (ITEGAM). This work is licensed under the Creative Commons Attribution International License (CC BY 4.0).

## I. INTRODUCTION

During recent years, researchers have focused on enhancing and improving various electric motor prototype models and control techniques [1-3], such as Switched Reluctance Motors (SRMs). SRMs have emerged as a suitable choice for industrial power applications in electric transportation and renewable energy due to their simple structure [4],[5], low cost because of the absence of permanent magnets, high reliability, ability to operate in extreme conditions, and durability. The SRMs function on the principle of magnetic pole excitation, which produces varying torque, which makes the focus on the geometry and the pole design of the rotor and stator crucial in establishing the characteristics and performance of this type of motor.

Despite the features of the SRMs, they have drawbacks that affect their behavior in operation, such as the cogging torque and ripples [6],[7]. The difficulty in controlling speed and torque accurately [8-10]. High noise and vibration due to direct magnetic force variations during operation [11],[12]. Complexity in the design of magnetic coils [13]. Power loss due to eddy currents and thermal losses [14]. Performance fluctuates with variations in speed and sensitivity to changes in load and voltage [15]. Several researchers have been developing prototypes of SRMs for various application requirements of solar water pumping systems [16],[17], electric vehicle EV [18-20], elevator applications [21], and cooling fan applications [22]. Recent research has focused on optimizing the SRMs through Artificial Intelligence and machine learning [23-25]. The selection of the material applied to the

stator and rotor in the SRMs contributes to minimizing losses and significantly increasing efficiency [26].

The direct torque control (DTC) method for the 5-phase 10/8 SRMs was introduced, focusing on achieving rapid response torque and precise stator flux control [27], while the same method was proposed based on the Fuzzy method to reduce torque ripples [28]. Multilevel inverters have been investigated by using space vector modulation (SVM) in controlling SRM applications with a focus on 10/8, 8/6 and 6/4 geometric types [29]. A validated analytical model for 10/8 and 8/6 SRM was presented. To prove the accuracy, the results were compared with experimental measurements. [30]. A novel SRM that has a permanent magnet between the pole tips of the stator is proposed to enhance efficiency and improve torque compared to traditional SRMs [31].

Various control strategies of the 12/8 switched reluctance motor were compared [32]. A design of 12/8 SRM with a segmental rotor type is proposed for cooling fan applications. The structure rotor consists of a series of discrete segments, and the stator consists of two types of poles: auxiliary and exciting poles [33]. A comparative analysis of winding arrangement types for a 12/8 SRM is presented, focusing on the reduction of flux reversal and analysis of torque performance [34].

The analysis and optimization of a 12/8 SRM using the Grey Wolf Optimization (GWO) algorithm for electric vehicle applications is proposed with a focus on enhancing the torque density through geometric optimizations [35]. The torque performance of 12/8 SRM is enhanced by checking the embrace of rotor poles and focusing on the rotor and stator pole arc to obtain minimum ripple torque and maximum average torque [36]. A study of the magnetic characteristics of three-phase 12/8 SRM is presented to improve the starting torque by focusing on the effect of important geometric parameters on enhancing efficiency and torque [37].

Although previous research has provided many 12/8 and 10/8 SRM designs for electric vehicles and various industrial applications, and while they differ in the number of stator poles only, they are significantly different in behavior in many aspects, therefore it is critical to select the SRM accurately according to the application requirements.

This paper aims to conduct an analytical study to compare the behavior of two SRMs with similar parameters, dimensions and operating conditions, focusing on changing only the number of stator poles to investigate their effect on the SRM's performance in terms of efficiency, losses and electromagnetic behavior. This comparison is based on data from detailed simulation results using ANSYS Maxwell that includes electromagnetic analysis of the magnetic field. As well as analysis

of performance curves for efficiency, torque, speed, stranded losses, current, voltage, and flux linkages.

Finally, this research contributes to the field of SRM design optimization by focusing on factors that affect the performance such as pole and core design, magnetic flux distribution, coil resistance improvement, and loss reduction, thereby enhancing the sustainability, operational flexibility, and the performance efficiency of the SRMs in various industrial applications. The results of this detailed analysis provide practical data and indicators to enable the selection of the most suitable 12/8 and 10/8 SRMs based on specific operating conditions. This contributes to the improvement of these motors and their ability to be adapted to different application requirements. The finite element method offers many advantages in simplifying complex geometry models in a fast time, making it a common choice in many fields of electrical engineering.

This paper is structured as follows: in section 2, the proposed designs with their basic dimensions of the 12/8 and 10/8 SRMs. Section 3 presents the finite element method in electrical machines. Section 4 incorporates mathematical modeling of the basic equations for the SRMs. In Section 5, the simulation results and comparison of the SRMs are discussed. Finally, section 6 provides a conclusion and summary of this work.

## II. APPROACHED DESIGN OF THE SWITCHED RELUCTANCE MOTORS

This paper provides modeling and designing of 12/8 and 10/8 switched reluctance motors based on similar proportions and parameters in both motors, as illustrated in Table 1. The stator poles were changed only to examine the effect of increasing stator poles on the performance of the machines. Steel 1008 was applied in addition to copper in the stator and rotor parts because the selected materials contribute to reducing total losses and increasing efficiency [26]. The motors were designed under a voltage of 220 V, speed of 3000 RPM, and power of 5000 W. At first, the basic dimensions and appropriate operating conditions were specified according to various mathematical equations and basic computations. The prototype was created and tested using the ANSYS RMxprt tool to evaluate the essential parameters and verify the initial designs. The efficiency of the obtained machines is estimated to be more than 95 %. After that, two-dimensional models were established using the Maxwell2D tool to compare the performance of the SRMs in terms of efficiency, torque, speed, total losses and various other machine data and performance curves. The ANSYS Maxwell approach is adopted by the finite element method, which is accurate and fast in simplifying complex models.

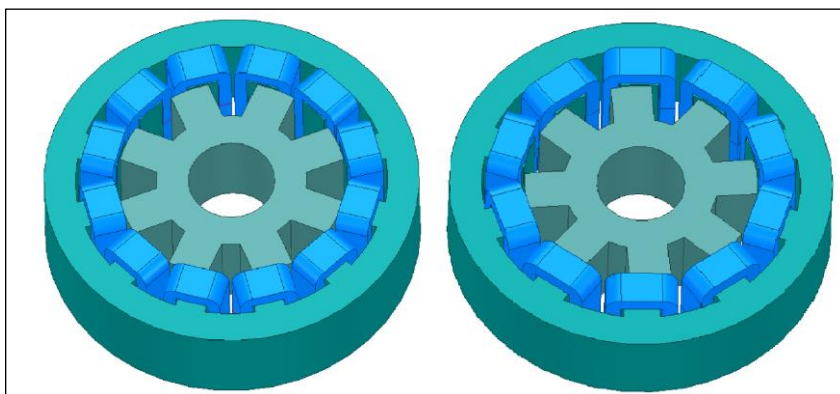


Figure 1: 3D models of the 12/8 and 10/8 SRMs.

Source: Authors, (2025).

Table 1: Parameters of the presented 12/8 and 10/8 SRMs.

Parameters	12/8 SRM	10/8 SRM
Outer Diameter of Stator (mm):	150	150
Inner Diameter of Stator (mm):	95	95
Number of Stator Poles:	12	10
Pole Embrace:	0.6	0.6
Outer Diameter of Rotor (mm):	94	94
Inner Diameter of Rotor (mm):	50	50
Length of Stator Core (mm):	70	70
Type of Steel:	steel_1008	steel_1008
Number of Rotor Poles:	8	8
Pole Embrace:	0.5	0.5
Yoke Thickness (mm):	12	12
Rated Output Power (kW):	5	5
Rated Voltage (V):	220	220
Given Rated Speed (rpm):	3000	3000
Operating Temperature (C):	75	75

Source: Authors, (2025).

Table 2 indicates the copper and steel material consumption in the switched reluctance motors for the rotor and stator parts. The material consumption is similar for both machines in the rotor part, with a slight difference in the weight of copper and steel in the stator core.

Table 2: Materials consumption in the SRMs.

MATERIALS	12/8 SRM	10/8 SRM
Stator Copper Density (kg/m <sup>3</sup> ):	8900	8900
Stator Core Steel Density (kg/m <sup>3</sup> ):	7872	7872
Rotor Core Steel Density (kg/m <sup>3</sup> ):	7872	7872
Stator Copper Weight (kg):	1.25071	1.36846
Stator Core Steel Weight (kg):	4.30679	4.30611
Rotor Core Steel Weight (kg):	2.06099	2.06099
Total Net Weight (kg):	7.61849	7.73556
Stator Core Steel Consumption (kg):	8.42751	8.42751
Rotor Core Steel Consumption (kg):	3.77157	3.77157

Source: Authors, (2025).

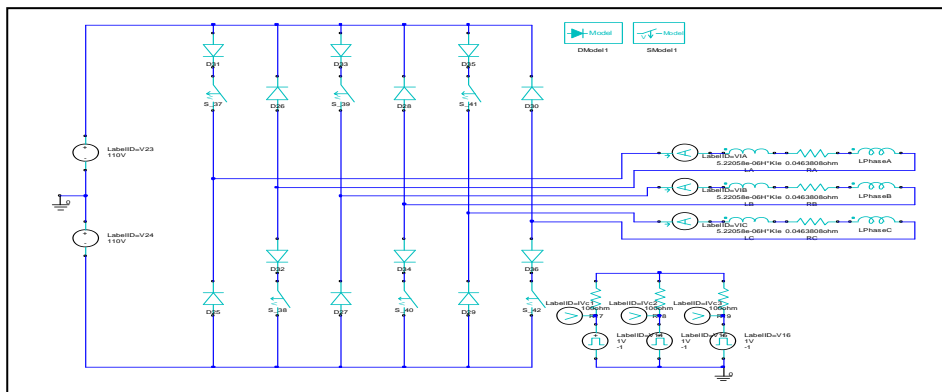


Figure 2: Drive circuit of the 12/8 and 10/8 switched reluctance motors.

Source: Authors, (2025).

### III. FINITE ELEMENT METHOD

The finite element method (FEM) is a numerical technique based on dividing a complex geometric field into many small elements to simplify and facilitate its mathematical handling. It is used in solving partial differential equations relating to various physical systems approximately within each element separately after the solutions for all elements are combined to obtain a comprehensive overview of the system's performance. The electromagnetic field distribution of the flux, the vectorial distribution of magnetic flux, and the magnetic intensity in a switched reluctance motor can be solved using the FEM. The electromagnetic analysis of the interaction between the stator and rotor is crucial to ensuring optimal functioning. Both SRMs were designed with the same dimensions and conditions applied except for the number of stator poles changed, as shown in Figure 1 and Table 1.

The Finite Element Method (FEM) is a powerful, accurate and speedy design tool used to enhance many industrial applications designs such as electrical machines and transformers, which contributes to increasing efficiency and reliability, improving overall system performance, and reducing magnetic losses. Electromagnetic analysis based on the ANSYS and FEM allows to specify the parts that are exposed to the magnetic saturation that must be focused on to reduce electrical losses. It permits the evaluation of the interactions between electric currents and magnetic fields in complex components and systems, focusing on the non-linear properties of magnetic materials, the

effects of eddy currents and magnetic flux distribution on the performance.

### IV. MATHEMATICAL MODELING OF THE SWITCHED RELUCTANCE MOTOR

For a thorough comprehension of the dynamic behavior and determination of the main impacts on a switched reluctance motor's performance, mathematical equations are considered that contribute to illustrating the interrelation between various components such as torque, power, and efficiency. These equations reflect the theoretical underpinnings of electromagnetic analysis and the analysis of experimental data. These later are crucial to explain the transformation of energy, the effect of external load on the motor, and the interactions between magnetic fields and mechanical motion, which contribute to a detailed examination of the complex behavior of the machines under various operating conditions.

From the equivalent circuit given in Figure 3, the phase voltage equation of the SRMs is given in Equation 1:

$$V = iR_s + \frac{d\lambda}{dt}(\theta, i) \quad (1)$$

Where  $i$  is the phase current,  $R_s$  the phase resistance,  $\theta$  the rotor position, and  $\lambda$  the flux linkage for each phase that is expressed by:

$$\lambda = L(\theta, i)i \quad (2)$$



Where  $L$  is the dynamical winding inductance that depends on the rotor position and the current per phase excitation, the equation of voltage for a phase can be defined as:

$$V = iRs + \frac{L(\theta,i)di}{dt} + i \frac{dL}{dt}(\theta, i) \quad (3)$$

$$V = iRs + L(\theta, i) \frac{di}{dt} + i \frac{d\theta}{dt} \frac{dL}{d\theta}(\theta, i) \quad (4)$$

The derivative of the rotor's angular position  $\theta$  relative to the time is the angular speed of the machine  $\omega_m$ , then:

$$V = iRs + L(\theta, i) \frac{di}{dt} + i\omega_m \frac{dL}{d\theta}(\theta, i) \quad (5)$$

Where  $\omega_m$  is the angular speed.

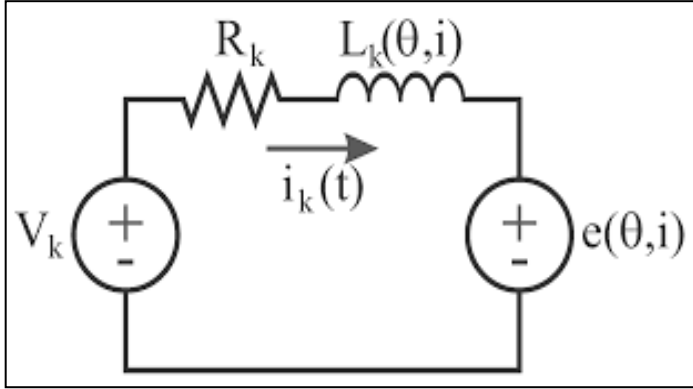


Figure 3: The SRM per phase equivalent circuit.

Soucer: [38].

$$e = -d\varphi(i, \theta)/dt \quad (6)$$

Where  $\varphi(i, \theta)$  is the flux linkage that represents a function of the current and the angle of the rotor. Then:

$$\frac{d\varphi(i, \theta)}{dt} = \frac{Ldi}{dt} + \frac{idL}{d\theta} \frac{d\theta}{dt} + \omega_m i \frac{dL}{d\theta} \quad (7)$$

The switched reluctance motor's amount of power  $P$  developed is expressed by Equation 8:

$$P = \frac{Lidi}{dt} + \omega_m i^2 \frac{dL}{dt} \quad (8)$$

The SRM energy stored in the magnetic field  $W_e$  can be obtained as:

$$W_e = \frac{1}{2} Li^2 \quad (9)$$

The power generated by the change in the magnetic field is expressed by Equations 10 and 11:

$$\frac{dW_e}{dt} = \frac{1}{2} L 2i \frac{di}{dt} + \frac{1}{2} i^2 \frac{dL}{dt} \quad (10)$$

$$\frac{dW_e}{dt} = Li \frac{di}{dt} + \frac{1}{2} i^2 \frac{dL}{d\theta} \omega_m \quad (11)$$

Where  $P_m$  is the difference between the received power from the supply and the power due to the magnetic field variation and is expressed in Equation 12:

$$P_m = \omega_m T_m \quad (12)$$

$$P_m = \frac{1}{2} \omega_m i^2 \frac{dL}{d\theta} \quad (13)$$

The switched reluctance motor air gap power  $P_{ag}$  is given as follows in Equations 14 and 15:

$$P_{ag} = \frac{1}{2} i^2 \frac{dL(\theta, i)}{dt} = \frac{1}{2} i^2 \frac{dL(\theta, i)}{d\theta} \frac{d\theta}{dt} \quad (14)$$

$$P_{ag} = \frac{1}{2} i^2 \frac{dL(\theta, i)}{d\theta} \omega_m \quad (15)$$

The main contribution to the developing mechanical power in the rotor is the contribution from the air gap power. The equation for the developed mechanical power of the rotor is provided in Equation 12.

The SRM electromagnetic torque for phases can be calculated by summing the torque of the phases  $T_{ph}$ :

$$\begin{aligned} T_{ph} &= \frac{1}{2} i^2 \frac{dL(i, \theta)}{d\theta} \\ T_e &= \sum_m T_{ph} \end{aligned} \quad (16)$$

The average torque  $T_{avg}$  equation is given as follow:

$$\begin{aligned} T_{avg} &= \frac{1}{\tau} \int_0^\tau T_e(t) dt \\ \text{with, } \tau &= \frac{60}{nN_r} \end{aligned} \quad (17)$$

Where  $n$  is the speed in the rotor (rpm),  $N_r$  is the number of poles in the rotor.

The torque ripple of the switched reluctance motor is expressed in Equation 18.

$$T_{ripple} = \frac{T_{max} - T_{min}}{T_{avg}} = \frac{\Delta T}{T_{avg}} \quad (18)$$

Where  $T_{max}$  is the maximum torque in the SRM;  $T_{min}$  is the minimum torque in the SRM.

The motion equation of the machine can be described by the Equation 19:

$$T_e - T_l = B\omega + j \frac{d\omega}{dt} \quad (19)$$

Where  $T_l$  is the load torque,  $B$  is the friction coefficient, and  $j$  is the inertia moment.

The Equation of the SRM efficiency is given as:

$$\eta = \frac{P_o}{P_{in}} = \frac{P_{in} - P_{cu} - P_{core}}{P_{in}} \quad (20)$$

Where  $P_o$  is the output power,  $P_{in}$  is the input power,  $P_{cu}$  is the copper loss  $P_{core}$  is the core loss.

## V. RESULTS AND DISCUSSIONS

To evaluate the provided 12/8 and 10/8 SRMs and compare their performance, as shown in the first section include Tables 3 and 4 to compare the basic parameters and comparing the various losses through the bar charts illustrated in Figure 4. The results of the second section highlights a comparison of the electromagnetic analysis of the magnetic flux density, the vectorial distribution of magnetic flux density, and the magnetic intensity in Figures 5, 6 and 7, which contributes to a more

precise analysis of the mechanical performance and an understanding of the electromagnetic behavior between the stator and rotor. The results in the last section present the various performance curves for both SRMs that include efficiency curves, torque, speed, Stranded losses, currents, voltages, and flux linkages.

Table 3: Evaluation of the 12/8 and 10/8 SRMs performance.

Parameters	12/8 SRM	10/8 SRM
Input DC Current (A):	23.7302	23.5383
Phase RMS Current (A):	36.7278	29.2256
Phase Current Density (A/mm <sup>2</sup> ):	11.095	7.00377
Iron-Core Loss (W):	0.0414556	0.207566
Output Power (W):	4962	4973.91
Input Power (W):	5220.63	5178.42
Efficiency (%):	95.0459	96.0508
Rated Speed (rpm):	9361.01	20904.7
Rated Torque (N.m):	5.0618	2.27209
Flux Linkage (Wb):	0.0559623	0.0255368
Maximum Output Power (W):	19203.7	22969.8

Source: Authors, (2025).

Both of the SRMs have roughly similar input DC current indicating comparable current consumption. The phase RMS current of the 12/8 SRM reaches 36.7278 versus 29.2256 A in the 10/8 SRM. The phase current density of the 12/8 SRM reaches 11.095 A/mm<sup>2</sup>, while the 10/8 SRM reaches 7.00377 A/mm<sup>2</sup>. This difference indicates that the 12/8 SRM consumes more power compared to the 10/8 SRM, which may affect the overall losses and increase the thermal and magnetic stress in the coils while contributing to significantly increasing the output torque.

The output power in the 12/8 SRM has 4962 W versus 4973.91 W in the 10/8 SRM. The input power in 12/8 SRM is 5220.63 W, and in 10/8 SRM is 5178.42 W. This data shows that 10/8 SRM has higher output power with lower input power and excels in producing the maximum power, which increases its efficiency as the 12/8 SRM efficiency reaches 95.0459%, while the 10/8 SRM efficiency reaches 96.0508%. The flux linkage data reveals that the 12/8 SRM has a higher flux of 0.0559623 Wb while the 10/8 SRM has 0.0255368 Wb.

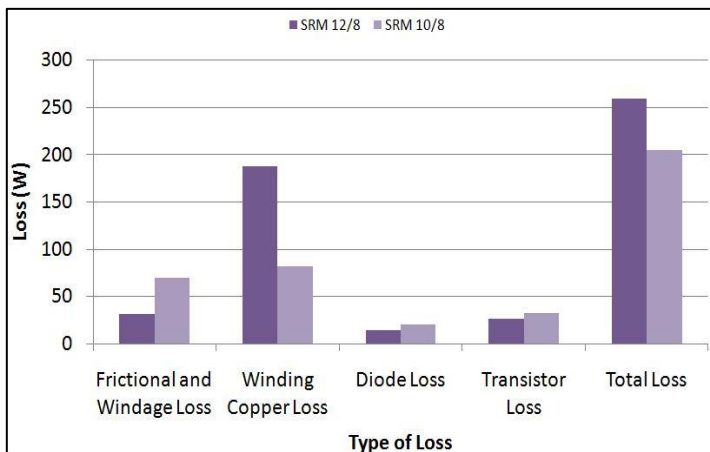


Figure 4: Comparison of losses in the 12/8 and 10/8 SRMs.

Source: Authors, (2025).

The frictional and windage loss in the 12/8 SRM is 31.2034 W, which is 55.2% less than the 10/8 SRM's 69.6824 W.

This means that the 10/8 SRM has significantly higher frictional and windage loss, which reduces its dynamic efficiency. The 12/8 SRM significantly reduces iron core loss by about 80% to estimated 0.0414556 W, while in the 10/8 SRM it reaches 0.207566 W, which improves the behavior in magnetic conditions. The 12/8 SRM exhibits more winding copper loss of 187.693 W compared to the 10/8 SRM's 81.8344 W due to the increased number of stator poles, which may lead to overheating. The data illustrates that the 10/8 SRM has higher diode and transistor losses compared to the 12/8 SRM. This analysis shows that the 12/8 SRM is more efficient in terms of electronic components with a 32.5% improvement in diode loss compared to the 10/8 SRM. The 10/8 SRM has a total loss of 204.509 W, 20.9% less than the 12/8 SRM with 258.635 W, indicating a more power efficient functioning due to the consistency in the distribution of the number of poles.

Table 4: Estimation of the stator and rotor poles flux density and the winding of the 12/8 and 10/8 SRMs.

Parameters	12/8 SRM	10/8 SRM
Stator-Pole Flux Density (Tesla):	1.37232	1.04559
Stator-Yoke Flux Density (Tesla):	0.849767	0.775533
Rotor-Pole Flux Density (Tesla):	1.11211	1.01496
Rotor-Yoke Flux Density (Tesla):	0.2756	0.251524
Winding Resistance in Phase (ohm):	0.0463808	0.0191619
Winding Resistance at 20C (ohm):	0.038152	0.0157622
Winding Leakage Inductance (mH):	0.0275105	0.00980801

Source: Authors, (2025).

The flux density in the stator poles of the 12/8 SRM motor has 1.37232 Tesla, while in the 10/8 SRM it has 1.04559 Tesla. This difference shows that the 12/8 SRM achieves 31.1% higher magnetic density, which enhances its ability to generate greater torque and more efficient operation but also increases the possibility of magnetic saturation at high loads. As for the stator yoke flux density, it is 0.849767 Tesla in the 12/8 SRM compared to about 0.775533 Tesla in the 10/8 SRM. This difference indicates that the 12/8 SRM exhibits 9.5% higher density, which enhances the efficiency of magnetic usage and reduces magnetic losses.

For the rotor pole flux density, the 12/8 SRM has a 1.11211 Tesla, while the 10/8 SRM has a 1.01496 Tesla. This disparity reflects the preference of the 12/8 SRM, which enhances the motor's ability to produce torque and response to loads. The rotor yoke flux density reaches 0.2756 Tesla in the 12/8 SRM versus 0.251524 Tesla in the 10/8 SRM. This indicates that the 12/8 SRM has 9.6% greater density, which enhances behavior stabilization under various loads.

The winding resistance in phase of the 12/8 SRM has 0.0463808 ohms, while the 10/8 SRM has a lower resistance of 0.0191619 ohms. This indicates that the 12/8 SRM exhibits higher resistance in the windings leading to higher losses due to overheating. The 12/8 SRM exhibits higher resistance even when measuring the windings' resistance at 20°C. This difference reflects the 10/8 SRM's ability to reduce heating losses significantly, indicating its higher operational efficiency.

The 12/8 SRM has a higher winding leakage inductance value of 0.0275105 mH, which leads to power loss and response delay, while the 10/8 SRM shows a lower inductance of 0.00980801 mH. This enhances the motor response and minimizes losses due to the winding leakage inductance.

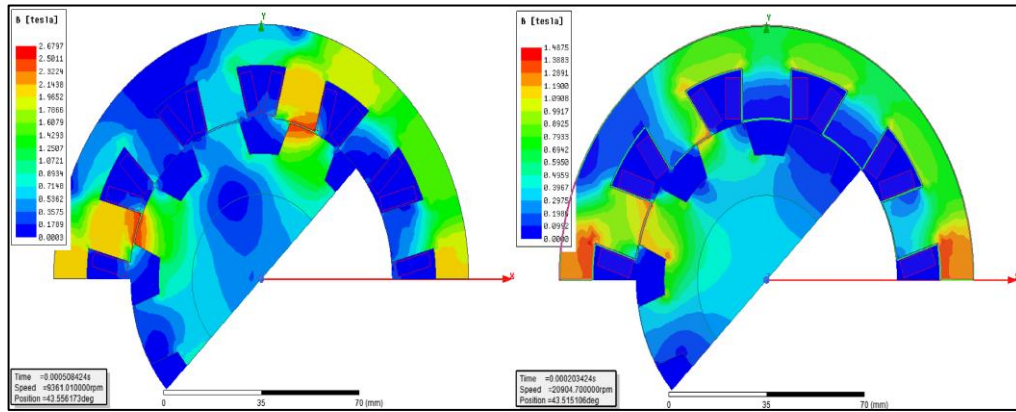


Figure 5: Variation of the SRMs Magnetic Flux Density.

Source: Authors, (2025).

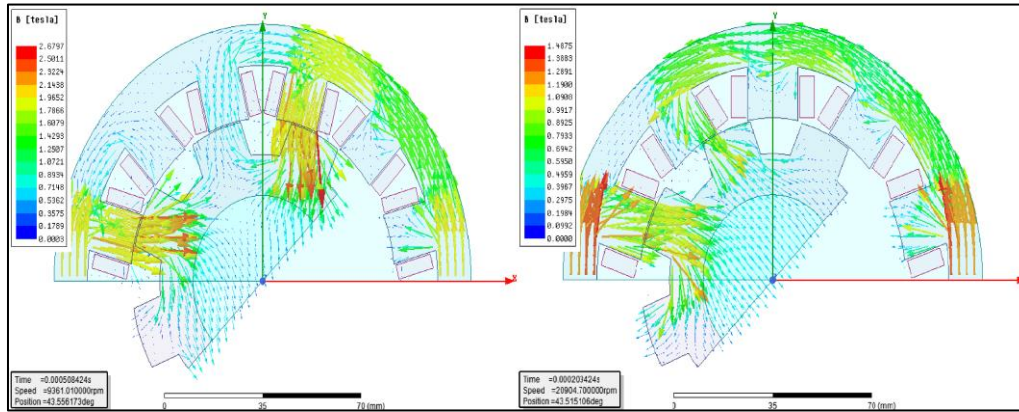


Figure 6: The SRMs vectorial distribution of magnetic flux density.

Source: Authors, (2025).

In Figures 5 and 6, the comparative analysis of the magnetic flux density at the same 43.5 degrees position indicates that the 12/8 SRM significantly outperforms the 10/8 SRM in terms of magnetic flux density and distribution, showing that the 12/8 SRM can generate a more powerful magnetic flux of 2.6797 T by about 35% comparing to the 10/8 SRM's 1.4875 T. This

indicates a higher performance in applications that require effective power conversion, efficient magnetization, and high torque, particularly at high loads. In contrast, the 10/8 SRM exhibits a lower performance due to the variability and irregularity of the flux distribution and its relatively low values.

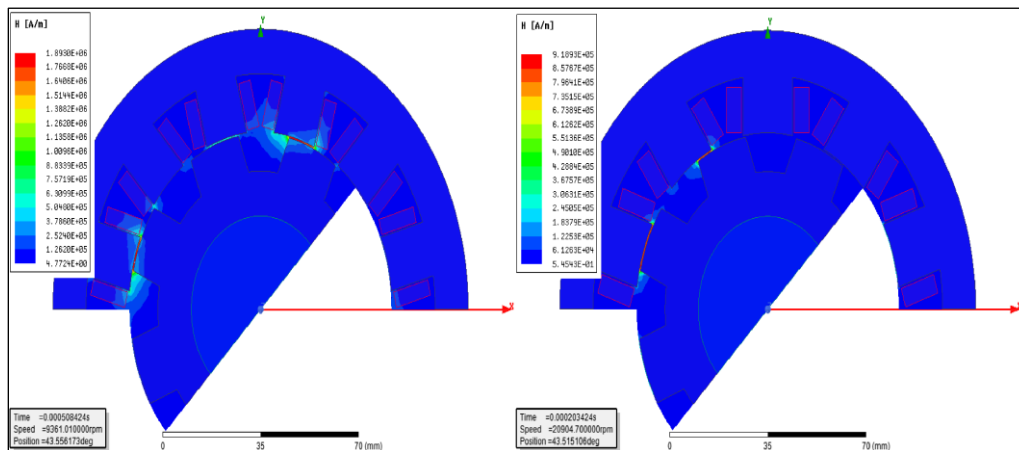


Figure 7: Variation of the SRMs Magnetic Intensity.

Source: Authors, (2025).

Figure 7 indicates the magnetic intensity distribution, showing that the 12/8 SRM is more balanced and uniform than the 10/8 SRM, with similar effective regions of maximum magnetic intensity. This reflects the stability of behavior and more efficient conversion of magnetic energy into mechanical

energy. In contrast, the 10/8 SRM exhibits unbalanced and non-uniform magnetic intensity distribution, which can lead to reduced electromagnetic conversion efficiency and fluctuations in output torque.

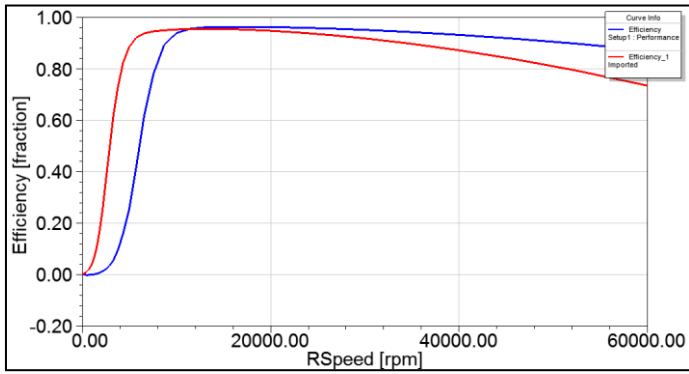


Figure 8: Variation of the SRMs Efficiency.  
Source: Authors, (2025).

Figure 8 shows the variations in efficiency curves versus the speed for the 10/8 SRM shown in blue and the 12/8 SRM shown in red. The results indicate that the 12/8 SRM quickly reaches higher efficiency values initially at speeds below 12000 rpm compared to the 10/8 SRM. At speeds above 20000 rpm, the efficiency curve of the 12/8 SRM decreases gradually compared to the 10/8 SRM.

This decrease is due to the increasing dynamic losses and the losses due to eddy currents and electromagnetic interference which are affected by the design and number of stator poles while the 10/8 SRM retains its efficiency even as the speed increases making it more suitable for applications that require stable behavior at high rotational speeds.

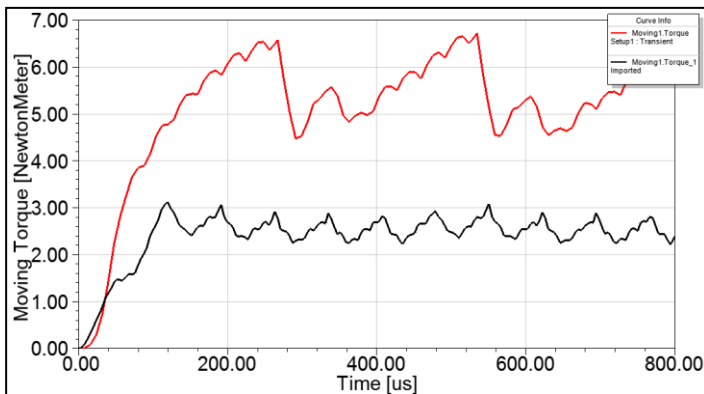


Figure 9: Variation of the SRMs Moving Torque.  
Source: Authors, (2025).

The torque curves for both machines are shown in Figure 9. After increasing the number of stator poles of the SRMs, there is a 55.1% increase in average torque from 2.27 Nm to 5.06 Nm, indicating that the 12/8 SRM has improved dynamic behavior, increased power, and enhanced response to heavier loads, making it suitable for applications that require high torque and greater thrust.

However, the 12/8 SRM torque curve illustrated in blue exhibits a higher torque fluctuation compared to the 10/8 SRM, which is a result of increasing the number of stator poles, which leads to more complicated magnetic interactions and affects the performance stability. Note that in this case, the increase in stator poles was considered only without adjusting the other factors, but the fluctuation and ripple in torque of the 12/8 SRM can be reduced by improving the different aspects.

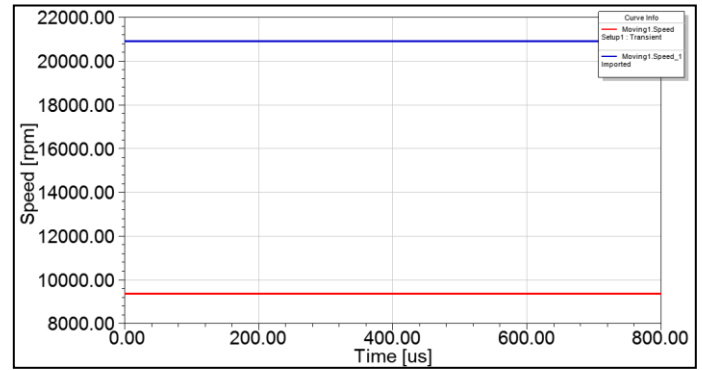


Figure 10: Variation of the SRMs Speed.  
Source: Authors, (2025).

Based on the analysis of the speed curves as shown in Figure 10, the 10/8 SRM is more suitable for applications requiring high speeds and lower torque, with an estimated speed of 20904 rpm, which is 55.2% greater than the 12/8 SRM, which is suitable for applications requiring lower speeds and higher torque while maintaining control and stability, with an estimated speed of 9361 rpm. Although the 12/8 SRM provides higher torque, the emphasis on speed is a critical factor in many applications.

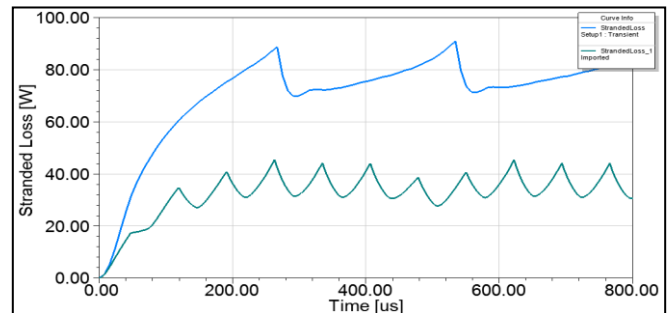


Figure 11: Variation of the SRMs Stranded Losses.  
Source: Authors, (2025).

Figure 11 represents stranded loss curves where the 12/8 SRM shown in red exhibits a significantly higher stranded loss, up to 87.5 watts at extreme values. This indicates that more power is consumed to obtain a higher torque, which affects the overall efficiency. The stranded losses in the 10/8 SRM are noticeably lower with extreme values ranging around 37.5 watts. This illustrates the efficiency of the machine in terms of minimizing losses. This makes it a more suitable choice in applications that require low power consumption due to the consistency in the distribution of the poles as the stator poles are proportional to the rotor.

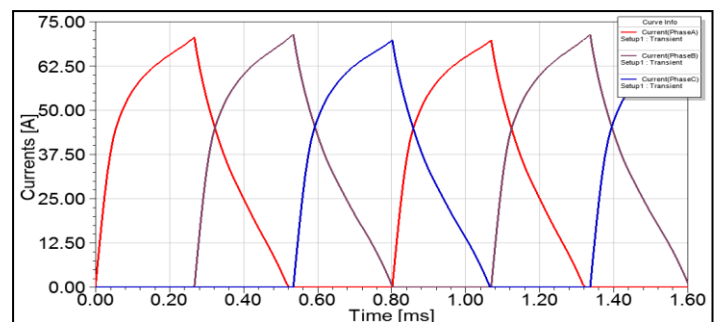


Figure 12: Variation of 12/8 the SRM Currents.  
Source: Authors, (2025).



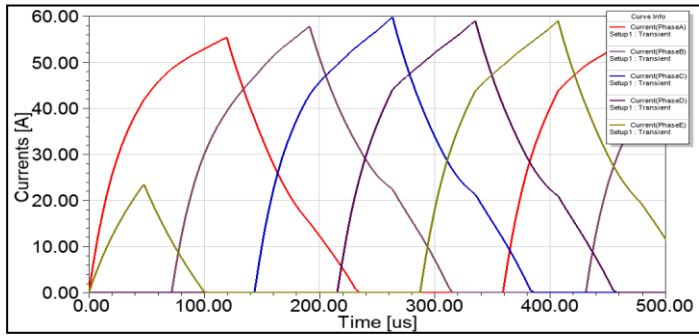


Figure 13: Variation of the 10/8 SRM Currents.  
Source: Authors, (2025).

From Figures 12 and 13, the maximum current values in the 12/8 SRM reach about 75 A. While in the 10/8 SRM it reaches about 60 A. The maximum current in the 12/8 SRM appears to be about 25% more compared to the 10/8 SRM, reflecting the ability to produce greater torque and higher electrical power capacity in the phases. This means that the 12/8 SRM functions at lower speeds but provides a more steady current with distinct peaks and little overlap with other phases, indicating improved current distribution. Reducing the number of poles in the 10/8 SRM leads to interference between phases, which decreases the efficiency of the electromagnetic conversion and makes controlling the currents and power distribution between phases difficult and more complicated.

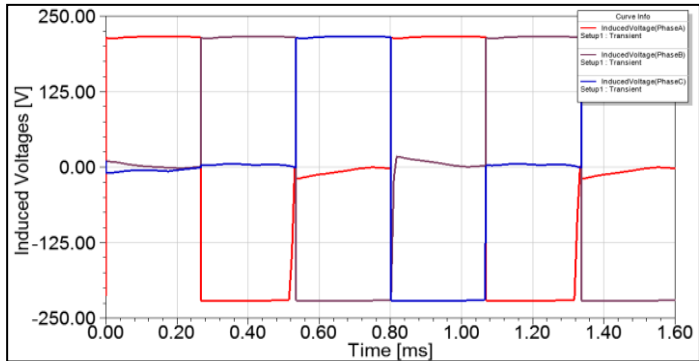


Figure 14: Variation of the 12/8 SRM Induced Voltages.  
Source: Authors, (2025).

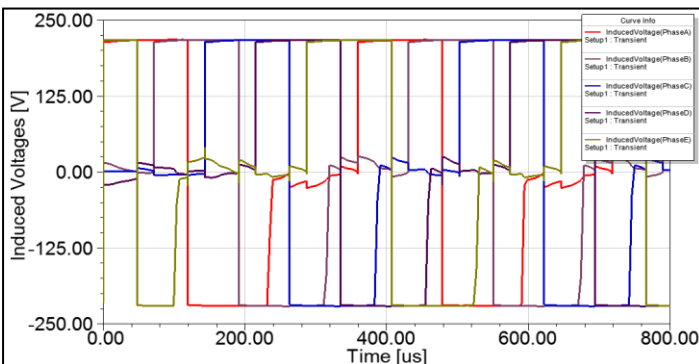


Figure 15: Variation of the 10/8 SRM Induced Voltages.  
Source: Authors, (2025).

Figures 14 and 15, represent the variation of the induced voltage vs the time. Both of the SRMs show an identical range of induced voltage values between 220V. Although the maximum values of the induced voltage are similar in both machines, the method of voltage generation and usage are significantly different between the two SRMs. The results show that the 12/8 SRM

provides an easier and more stabilized control system due to the longer periods between voltage variations and the synchronization between the phases thus it is more appropriate in applications that require accuracy and stability in torque. On the other side, the 10/8 SRM requires advanced and complicated control techniques to handle the frequent interference and rapid variations in the induced voltage between the phases. Increasing the number of poles in the 12/8 SRM improves the synchronization and stabilization of the induced voltage across the phases, which facilitates torque control and aids in maintaining consistent dynamic behavior.

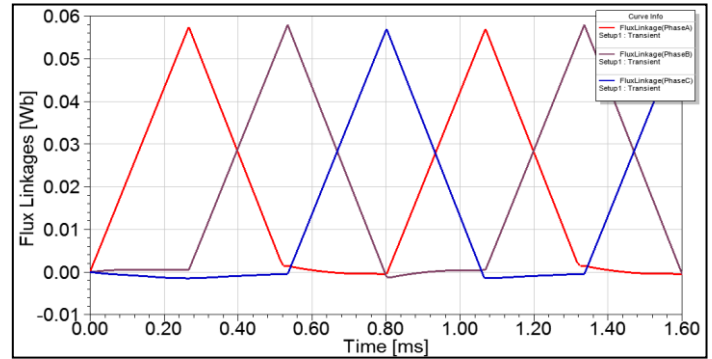


Figure 16: Variation of the 12/8 SRM Flux Linkages.  
Source: Authors, (2025).

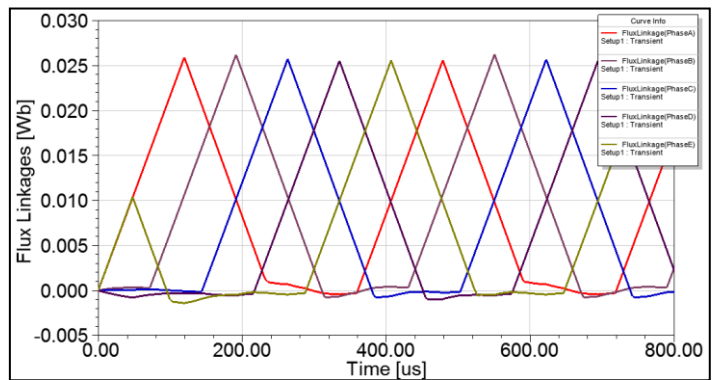


Figure 17: Variation of the 10/8 SRM Flux Linkages.  
Source: Authors, (2025).

In Figures 16 and 17, it is shown that the flux linkage curves for both SRMs have a regular and repetitive form, reaching specific peaks of 0.057Wb at the 12/8 SRM and 0.026Wb at the 10/8 SRM and decreasing rapidly when the phase current is eliminated. It is clear from these results that the distribution of flux linkages is highly dependent on the number of poles and their design. In the 10/8 SRM, the peaks of the flux linkages are lower compared to the 12/8 SRM, with a greater overlap between the peaks. The response time is faster, indicating that the 12/8 SRM provides a more stabilized distribution of flux linkages with higher peaks and less overlap between the phases.

## VI. CONCLUSIONS

This paper presents a comparative study of the designs of 12/8 and 10/8 SRMs featuring an effective design based on similar dimensions and operating conditions. Only the stator poles were changed to study its impact on efficiency, performance, and losses. The results show that increasing the number of poles in the stator varies the behavior of the current and its distribution between the phases and allows an increase in the maximum

current values, leading to improved dynamic performance and torque stabilization. Reducing the number of poles in the 10/8 SRM leads to interference between phases, which leads to difficulty in maintaining torque stability and reduces the efficiency of the electromagnetic conversion. The 12/8 SRM has higher total losses, especially in copper losses, while the 10/8 SRM has higher of frictional and windage losses.

Electromagnetic analysis data shows that the 12/8 SRM has higher magnetic flux density and magnetic field strength, which enhances its ability to generate high torque, while the 10/8 SRM has higher efficiency in magnetic resistance and magnetic leakage, which makes it an appropriate choice in applications where high power efficiency is required. Both SRMs have distinct characteristics that make them suitable for different applications.

The choice between them depends on the specific application requirements in terms of speed, torque, efficiency, noise, and vibration. The 12/8 SRM can be used in applications that require high torque at low speeds and the 10/8 SRM in applications that require high speeds and low losses.

## VII. AUTHOR'S CONTRIBUTION

**Conceptualization:** Layachi Chebabhi, Toufik tayeb Naas, Mohamed Zitouni.

**Methodology:** Layachi Chebabhi, Toufik tayeb Naas, Mohamed Zitouni.

**Investigation:** Layachi Chebabhi, Toufik tayeb Naas, Mohamed Zitouni.

**Discussion of results:** Layachi Chebabhi, Toufik tayeb Naas, Mohamed Zitouni.

**Writing – Original Draft:** Layachi Chebabhi, Toufik tayeb Naas, Mohamed Zitouni.

**Writing – Review and Editing:** Layachi Chebabhi, Toufik tayeb Naas, Mohamed Zitouni.

**Resources:** Layachi Chebabhi, Toufik tayeb Naas, Mohamed Zitouni.

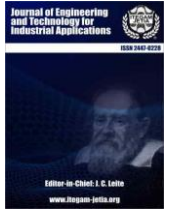
**Supervision:** Author Two and Author Layachi Chebabhi, Toufik tayeb Naas, Mohamed Zitouni.

**Approval of the final text:** Author Layachi Chebabhi, Toufik tayeb Naas, Mohamed Zitouni.

## VIII. REFERENCES

- [1] Djaloul Karboua, Toufik Mebkhouta, Youcef Chouiha, Abdelkader Azzeddine Bengharbi, B. ouadeh Douara, and Belgacem Toulal, "Enhancing Performance of Permanent Magnet Synchronous Motor Drives Through Hybrid Feedback Linearization and Sliding Mode Control," ITEGAM- Journal of Engineering and Technology for Industrial Applications (ITEGAM-JETIA), vol. 10, no. 49, pp. 178–186, Jan. 2024, doi: <https://doi.org/10.5935/jetia.v10i49.1222>.
- [2] G. Challa and M. D. Reddy, "Acoustical Noise Mitigation in Slip Angle Controlled DTC of Open-End Winding Induction Motor Drive Using AISPWM Based Triple Randomization Scheme for EV Application," ITEGAM- Journal of Engineering and Technology for Industrial Applications (ITEGAM-JETIA), vol. 10, no. 49, pp. 202–210, Jan. 2024, doi: <https://doi.org/10.5935/jetia.v10i49.1275>.
- [3] Sriramulu Naik Mudhavath, Kesana Gopikrishna, and A. Kumar, "DTC OF A 5 LEVEL MMC FED 3- $\Phi$  INDUCTION MOTOR WITH PI AND FLC USING CBAPOD PWM TECHNIQUE," ITEGAM- Journal of Engineering and Technology for Industrial Applications (ITEGAM-JETIA), vol. 10, no. 50, Jan. 2024, doi: <https://doi.org/10.5935/jetia.v10i50.1295>.
- [4] S. Mafrici, V. Madonna, C. Maria Meano, K. Friis Hansen, and A. Tenconi, "Switched Reluctance Machine for Transportation and Eco-Design: A Life Cycle Assessment," IEEE Access, vol. 12, pp. 68334–68344, 2024, doi: <https://doi.org/10.1109/access.2024.3400324>.
- [5] I. Mahmoud and Adel Khedher, "RETRACTED: Geometric Parameter Optimization of Switched Reluctance Machines for Renewable Energy Applications using Finite Element Analysis," Periodica Polytechnica Electrical Engineering and Computer Science, vol. 68, no. 2, pp. 178–192, Jan. 2024, doi: <https://doi.org/10.3311/ppee.21747>.
- [6] A. Abdel-Aziz, M. Elgenedy, and B. Williams, "Review of Switched Reluctance Motor Converters and Torque Ripple Minimisation Techniques for Electric Vehicle Applications," Energies, vol. 17, no. 13, p. 3263, Jul. 2024, doi: <https://doi.org/10.3390/en17133263>.
- [7] M. Omar, M. H. Bakr, and A. Emadi, "Advanced Design Optimization of Switched Reluctance Motors for Torque Improvement Using Supervised Learning Algorithm," IEEE Access, vol. 11, pp. 122057–122068, 2023, doi: <https://doi.org/10.1109/access.2023.3328143>.
- [8] M. N. Kumar and R. Chidanandappa, "Particle swarm optimization technique for speed control and torque ripple minimization of switched reluctance motor using PID and FOPID controllers," International Journal of Information Technology, vol. 16, no. 2, pp. 1185–1201, Jan. 2024, doi: <https://doi.org/10.1007/s41870-023-01656-2>.
- [9] D. M. Ismael and Thamir Hassan Atyia, "Comparative Evaluation of Speed Control Techniques for Switched Reluctance Motors in Industrial Applications," Engineering Research Express, Sep. 2024, doi: <https://doi.org/10.1088/2631-8695/ad7d6b>.
- [10] P. Ren, J. Zhu, Y. Liu, Y. Zhao, and Z. Jing, "An Improved Model-Predictive Torque Control of Switched Reluctance Motor Based on Sector Adaptive Allocation Technology," IEEE Transactions on Power Electronics, vol. 39, no. 4, pp. 4567–4577, Jan. 2024, doi: <https://doi.org/10.1109/tpe.2023.3349283>.
- [11] P. Saiteja and B. Ashok, "Experimental investigation of vibro-acoustic noise analysis in the switched reluctance motor through transient model-based multiphysics analysis for electric vehicles applications," Applied Acoustics, vol. 220, p. 109957, Mar. 2024, doi: <https://doi.org/10.1016/j.apacoust.2024.109957>.
- [12] F. S. El-Faouri, Y. Cai, and A. Chiba, "Refinement of Analytical Current Waveform for Acoustic Noise Reduction in Switched Reluctance Motor," IEEE Open Journal of Industry Applications, vol. 5, pp. 325–337, 2024, doi: <https://doi.org/10.1109/ojia.2024.3434668>.
- [13] Mouli Thirumalasetty and G. Narayanan, "Influence of Stator Winding Reconnection and Bipolar Excitation on the Performance Characteristics of Solid-Rotor Switched Reluctance Machine," IEEE Transactions on Industry Applications, vol. 60, no. 3, pp. 3773–3789, Jan. 2024, doi: <https://doi.org/10.1109/tia.2024.3354225>.
- [14] H. Chen, F. Yu, W. Yan, and M. Orabi, "Calculation and Analysis of Eddy-Current Loss in Switched Reluctance Motor," IEEE Transactions on Applied Superconductivity, vol. 31, no. 8, pp. 1–4, Jun. 2021, doi: <https://doi.org/10.1109/tasc.2021.3091068>.
- [15] Agus Adhi Nugroho, Muhammad Khosyi'in, Bustanul Arifin, Bhakti Yudho Suprpto, Muhamad Haddin, and Zainuddin Nawawi, "Load Effect on Switched Reluctance Motor Using Hysteresis Current and Voltage Control," pp. 59–63, Oct. 2021, doi: <https://doi.org/10.23919/eecsi53397.2021.9624267>.
- [16] G. Sundari, R. Muniraj, and J. Shanmugapriyan, "Switched reluctance motor based water pumping system powered by solar using hybrid approach," Applied Energy, vol. 365, p. 123188, Jul. 2024, doi: <https://doi.org/10.1016/j.apenergy.2024.123188>.
- [17] N. Priyadarshi, M. S. Bhaskar, Dhafer Almakhlis, and F. Azam, "A New PV Fed High Gain Boost-Ćuk Converter Employed SRM Driven Water Pumping Scheme with IDEPSO MPPT," IEEE Transactions on Power Electronics, pp. 1–13, Jan. 2024, doi: <https://doi.org/10.1109/tpe.2024.3459810>.
- [18] N. R. Patel, K. L. Mokariya, J. K. Chavda, and S. Patil, "A Novel Approach to the Design and Development of a C-Core Sandwich-Type Radial Field Switched Reluctance Motor with On-Shaft Implementation in EV Application," SAE International Journal of Electrified Vehicles, vol. 14, no. 1, Nov. 2024, doi: <https://doi.org/10.4271/14-14-01-0007>.

- [19] Y. Zhu, W. Wei, J. Wang, and C. Xing, "Multi-objective optimization of switched reluctance motor driving electric vehicles based on vehicle operating condition," *Proceedings of the Institution of Mechanical Engineers Part D Journal of Automobile Engineering*, Oct. 2024, doi: <https://doi.org/10.1177/09544070241290073>.
- [20] M. A. Abdel, Hamdy Shatla, and M. Bahy, "Analysis of Slotted Tooth Switched Reluctance Motors for Electric Vehicle Applications," *Journal of Electrical and Computer Engineering*, vol. 2024, no. 1, Jan. 2024, doi: <https://doi.org/10.1155/2024/4493590>.
- [21] S. B. Shah, M. Khalid, and Berker Bilgin, "Design of a Switched Reluctance Motor for an Elevator Application," pp. 1–6, Jun. 2024, doi: <https://doi.org/10.1109/itec60657.2024.10598892>.
- [22] Augustine Mathu Gnaniah, E. Sehar, Appadurai Mangalaraj, and B. Mahadevan, "Thermal analysis of modified segmented switched reluctance motor with aluminium metal matrix composite fins used in cooling fan applications," *Matéria (Rio de Janeiro)*, vol. 29, no. 2, Jan. 2024, doi: <https://doi.org/10.1590/1517-7076-rmat-2024-0075>.
- [23] M. Omar, M. Bakr, and A. Emadi, "Switched Reluctance Motor Design Optimization: A Framework for Effective Machine Learning Algorithm Selection and Evaluation," 2024 IEEE Transportation Electrification Conference and Expo (ITEC), pp. 1–6, Jun. 2024, doi: <https://doi.org/10.1109/itec60657.2024.10598839>.
- [24] A. L. Saleh and László Számel, "Improved Direct Instantaneous Torque Control Strategy of Switched Reluctance Motor based on Artificial Neural Network," pp. 166–172, Jun. 2024, doi: <https://doi.org/10.1109/gpecom61896.2024.10582580>.
- [25] W. Qiu, X. Zhao, A. Tyrrell, Suresh Perinpanayagam, S. Niu, and G. Wen, "Application of Artificial Intelligence-Based Technique in Electric Motors: A Review," *IEEE Transactions on Power Electronics*, vol. 39, no. 10, pp. 13543–13568, Jun. 2024, doi: <https://doi.org/10.1109/tpe.2024.3410958>.
- [26] L. Chebabhi, T. T. Naas, M. Zitouni, I. Ghibeche, and T. Benmessaoud, "Influence of choosing materials on 6/4 switched reluctance motor performance," *STUDIES IN ENGINEERING AND EXACT SCIENCES*, vol. 5, no. 1, pp. 2391–2406, May 2024, doi: <https://doi.org/10.54021/seesv5n1-118>.
- [27] M. R. Feyzi and Y. Ebrahimi, "Direct torque control of 5-Phase 10/8 switched reluctance motors," *DOAJ (DOAJ: Directory of Open Access Journals)*, Sep. 2009, [Online]. Available: <https://doaj.org/article/d3442ec0953545e6abc67347a1d443f0>
- [28] M. R. Feyzi, Y. Ebrahimi, and M. Zeinali, "Direct torque control of 5-phase 10/8 switched reluctance motor by using fuzzy method," *International Journal of Engineering and Technology*, vol. 1, no. 3, pp. 256–263, Jan. 2009, doi: [10.7763/ijet.2009.v1.48](https://doi.org/10.7763/ijet.2009.v1.48).
- [29] N. Farah, M. H. N. Talib, J. Lazi, M. A. Ali, and Z. Ibrahim, "Multilevel Inverter Fed Switched Reluctance Motors (SRMs): 6/4, 8/6 and 10/8 SRM Geometric Types," *International Journal of Power Electronics and Drive Systems/International Journal of Electrical and Computer Engineering*, vol. 8, no. 2, p. 584, Jun. 2017, doi: [10.11591/ijpeds.v8.i2.pp584-592](https://doi.org/10.11591/ijpeds.v8.i2.pp584-592).
- [30] Krzysztof Bienkowski et al., "Validated Analytical Model of 8/6 and 10/8 Switched Reluctance Motors," *Energies*, vol. 15, no. 2, pp. 630–630, Jan. 2022, doi: <https://doi.org/10.3390/en15020630>.
- [31] S. S. Chaware, M. F. A. R. Satarkar, and P. Kotwal, "10/8 Conventional Switched Reluctance Motor for Electric Vehicles," *Journal of Emerging Technologies and Innovative Research (JETIR)*, vol. 11, no. 1, pp. 1–X, Jan. 2024.
- [32] M. Chouitek, A. Chaouch, and B. Bekkouche, "COMPARISON OF THE VARIOUS CONTROLS OF THE SWITCHED RELUCTANCE MOTOR 12/8," *REVUE ROUMAINE DES SCIENCES TECHNIQUES — SÉRIE ÉLECTROTECHNIQUE ET ÉNERGÉTIQUE*, vol. 68, no. 1, pp. 52–57, Apr. 2023, doi: [10.59277/rst-ee.2023.68.1.9](https://doi.org/10.59277/rst-ee.2023.68.1.9).
- [33] H. Zhang, D.-H. Lee, C.-W. Lee, and J.-W. Ahn, "Design and analysis of a segmental rotor type 12/8 switched reluctance motor," *Journal of Power Electronics*, vol. 14, no. 5, pp. 866–873, Sep. 2014, doi: [10.6113/jpe.2014.14.5.866](https://doi.org/10.6113/jpe.2014.14.5.866).
- [34] Ruchao Pupadubsin, Seubsuang Kachapornkul, Prapon Jitkreeyarn, Pakasit Somsiri, and Kanokvate Tungpimolrut, "Investigation of Torque Performance and Flux Reversal Reduction of a Three-Phase 12/8 Switched Reluctance Motor Based on Winding Arrangement," *Energies*, vol. 15, no. 1, pp. 284–284, Jan. 2022, doi: <https://doi.org/10.3390/en15010284>.
- [35] M. S. Rahman, G. F. Lukman, Pham Trung Hieu, K.-I. Jeong, and J.-W. Ahn, "Optimization and Characteristics Analysis of High Torque Density 12/8 Switched Reluctance Motor Using Metaheuristic Gray Wolf Optimization Algorithm," *Energies*, vol. 14, no. 7, pp. 2013–2013, Apr. 2021, doi: <https://doi.org/10.3390/en14072013>.
- [36] B. M. Dinh and D. H. Linh, "Torque Performances of Switched Reluctance Motor 12/8 By Rotor Pole Embrace Verification," Mar. 2021, doi: <https://doi.org/10.46254/an11.20210768>.
- [37] E. C. Abunike, G. D. Umoh, I. E. Nkan, and O. I. Okoro, "Investigating the Magnetic Characteristics of 12/8 Switched Reluctance Motor for Enhanced Starting Torque," *Nigerian Journal of Technological Development*, vol. 18, no. 1, pp. 70–75, Jun. 2021, doi: <https://doi.org/10.4314/njtd.v18i1.10>.
- [38] Sandeep Vuddanti, Vinod Karknalli, and Surender Reddy Salkuti, "Design and comparative analysis of three phase, four phase and six phase switched reluctance motor topologies for electrical vehicle propulsion," *Bulletin of Electrical Engineering and Informatics*, vol. 10, no. 3, pp. 1495–1504, Jun. 2021, doi: <https://doi.org/10.11591/eei.v10i3.3054>.



## RESEARCH ARTICLE

## OPEN ACCESS

# MONITORING AND EVALUATION OF WATER QUALITY IN RURAL ANDEAN AREAS OF PERU USING WIRELESS SENSORS WITH LORA

Wohler Gonzales Saenz<sup>1</sup>, Luz Marina Acharte Lume<sup>2</sup>, Javier Camilo Poma Palacios<sup>3</sup>  
Alejandro Filimón Quispe Coica<sup>4</sup>, Agustí Pérez Foguet<sup>5</sup>

<sup>1, 2, 3, 4, 5</sup> Universidad Nacional de Huancavelica Peru.

<sup>1</sup><https://orcid.org/0000-0003-0728-9479> , <sup>2</sup><https://orcid.org/0000-0001-7717-6408> , <sup>3</sup><https://orcid.org/0000-0002-8527-809X>

<sup>4</sup><https://orcid.org/0000-0001-6396-0218>

Email: [wohler.gonzales@unh.edu.pe](mailto:wohler.gonzales@unh.edu.pe), [luz.acharte@unh.edu.pe](mailto:luz.acharte@unh.edu.pe), [javier.poma@unh.edu.pe](mailto:javier.poma@unh.edu.pe), [fquispec@gmail.com](mailto:fquispec@gmail.com)

## ARTICLE INFO

**Article History**

Received: February 03, 2025

Revised: March 20, 2025

Accepted: March 15, 2025

Published: April 31, 2025

**Keywords:**

Water quality,  
Wireless sensors,  
Monitoring,  
Internet of things.

## ABSTRACT

The objective of this research was to implement wireless sensors for remote monitoring and evaluation of water quality in five reservoirs in rural Andean communities in the district of Huancavelica-Peru, given the scarcity of information on water quality and its poor monitoring. It is important to monitor water quality for its safe management according to the sustainable development goals of the 2030 agenda, against natural or anthropogenic contaminants. The remote monitoring evaluated the performance of wireless sensors and water quality (temperature, pH and turbidity) for 10 days. The wireless sensors were calibrated with Hanna Instruments brand equipment achieving an R<sup>2</sup> of 98.98%, 96.81% and 89.82% for temperature, pH and turbidity respectively. The average amount of data received was 456/462, 8.73 km maximum communication distance, received signal strength RSSI (-93 to -122 dBm), signal to noise ratio SNR (9 to 13 dB), water temperature (-2.90 to 14.4 °C), pH (6.60 to 8.24) and turbidity (0.34 to 4.98 NTU). The wireless sensors are highly effective in remote monitoring; the quality of the monitored water complies with Peruvian and World Health Organization regulations.



Copyright ©2025 by authors and Galileo Institute of Technology and Education of the Amazon (ITEGAM). This work is licensed under the Creative Commons Attribution International License (CC BY 4.0).

## I. INTRODUCTION

Water is a fundamental resource for life and human health that is found in various sources such as rivers, springs, lagoons, dams, etc., whose accessibility and quality are important to monitor for an adequate sustainable management within the scope of the "Sustainable Development Goals" SDG 6 of the United Nations 2030 agenda [1]. Monitoring must be able to analyze water quality systematically for adequate and timely decision-making in the face of anomalies that arise; since, water is changing in space and time due to its own dynamics or due to anthropogenic activities in its environment that can ultimately affect the health and welfare of people [2]–[5].

Currently, water quality monitoring is commonly performed manually on site or by transferring samples to a laboratory; where, the execution of the procedure requires a long time according to the characteristics of its geographical area of

study that make it impossible to develop continuous and real-time monitoring considering unforeseen situations in water change [6], [7]. In this regard, when reviewing the state of the art on water quality monitoring in rural areas of the Andes mountain range of

Peru in the province and district of Huancavelica, [8] identified that monitoring is precarious and that there is little information available on water quality due to various factors such as the manual procedure that takes a long time, the lack of nearby

laboratories, the high costs of monitoring and especially the geographical remoteness and difficult accessibility to the places where the sample that evaluates the water is taken, making it impossible to implement frequent monitoring programs recommended by [9]; also, due to the irregular way in which it is carried out, being temporarily limited to monitoring between one time or twice a year [10].

In response to poor water quality monitoring in different scenarios; different authors have proposed remote monitoring as an



alternative for which different wireless prototypes have been developed such as [11]–[14] that have monitored water quality reaching distances up to 120 m; others such as [15]–[18] have improved monitoring reaching distances up to 2.0 km, with the particularity that these investigations have been developed and are limited to flat and low altitude geography less than 200 m above sea level.

However, the achievements are not sufficient for monitoring water quality in spaces with a greater range of distance and complex geography, such as the case of the rural Andean area of Huancavelica, where water sources are located between rugged mountain ranges and steep areas between 3,800 m and 4,000 m above sea level [19], which require continuous and real-time monitoring.

In response to this, this research work has proposed the implementation of wireless sensors for remote monitoring of water quality and its evaluation as an alternative to poor manual monitoring in the complex geographic conditions of the rural Andean area of the Huancavelica department; wireless sensors that monitor water quality continuously and in real-time.

In this regard, the contribution of this article is to present the results of remote monitoring of water quality based on wireless sensors with Long Range (LoRa) technology for its application in data management and quick decision-making on water quality in distant and complex geographic areas similar to the rural Andean area of Huancavelica among others; directly benefiting with information to the rural communities population, environmentalists, ecologists, among others who are interested in monitoring water quality for informed decision making.

## II. MATERIALS AND METHODS

### II.1 DESCRIPTION OF THE STUDY AREA

The research was carried out in five water reservoirs for human consumption in the high Andean rural communities of the province and district of Huancavelica-Peru ( $-12^{\circ} 47.237$ ,  $-74^{\circ} 58.389$ ) located in mountainous geographic areas of difficult access with altitudes of around 4000 m and located at distances of up to 16.9 km from the urban area of Huancavelica of difficult access by road and rough rural roads. The reservoirs belong to the communities of Sachapite, Antacocha, Pampachaca, Huaylacucho, and San Gerónimo as detailed in Table 1.

Table 1: Location of reservoirs in rural communities for remote monitoring.

Community	Latitude	Length	Altitude (masl)	Distance km
S1 Sachapite	$-12^{\circ} 44.069$	$-74^{\circ} 54.590$	4196	16.9
S2 Antacocha	$-12^{\circ} 44.697$	$-74^{\circ} 54.948$	4084	12.3
S3 Pampachaca	$-12^{\circ} 48.643$	$-74^{\circ} 55.271$	4072	10.2
S4 Huaylacucho	$-12^{\circ} 47.521$	$-74^{\circ} 56.905$	3823	4.7
S5 San Gerónimo	$-12^{\circ} 47.045$	$-74^{\circ} 59.931$	3885	1.2

Source: Authors, (2025).

Figure 1 presents the location map of the wireless sensors in the five identified communities (S1, S2, S3, S4, and S5), with which remote monitoring was carried out.

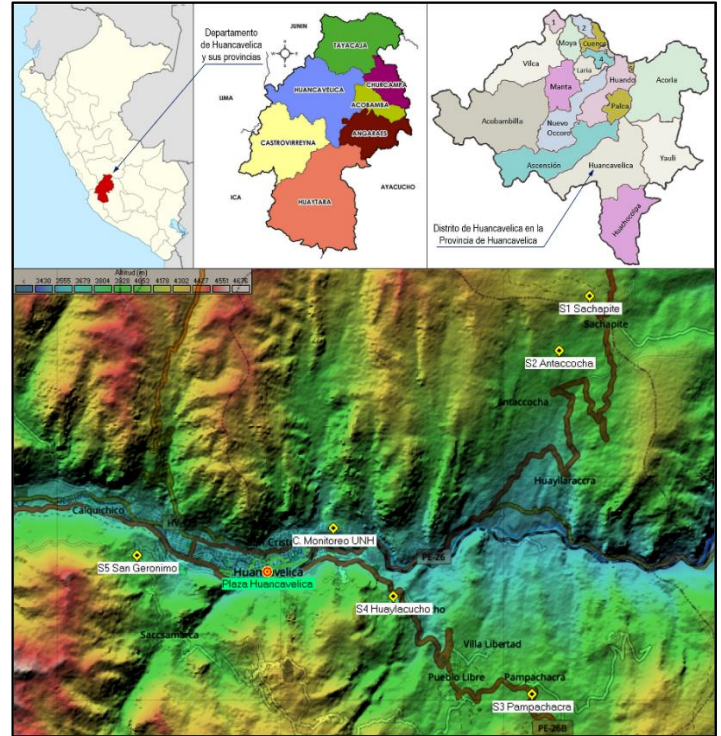


Figure 1: Location map of remote monitoring with wireless sensors.

Source: Authors, (2025).

### II.2 SCOPE

The scope of the research was to evaluate water quality monitoring through wireless sensors with LoRa technology in the five communities that involved the implementation of the wireless sensors, the evaluation of the amount of data received from remote monitoring, the transmission distance, the intensity of the received signal RSSI and the signal-to-noise ratio SNR, according to the parameters indicated in Table 2.

Table 2: Remote monitoring data transmission/reception capability variables.

Variable	Unit	Range	Reference
Amount of data received	unit	$\leq 462$	ThingSpeak
Transmission distance	km	$< 10$	[20] (Heltec Automation, 2023) [21] (Semtech, 2020)
RSSI, Received Signal Strength	dBm	$> -135$	
SNR, signal-to-noise ratio	dB	$> -20$	

Source: Authors, (2025).

Likewise, the results of remote monitoring corresponding to water temperature, pH, and turbidity corresponded to the ranges indicated in Table 3.

Table 3: Water quality parameters according to WHO and DIGESA-Peru.

Variable	Unit	Range	Reference
Temperature	$^{\circ} \text{C}$	$< 20$	[22](WHO, 2011)
Hydrogen potential	pH	6.5 to 8.5	[23] (WHO, 1971)
Turbidity	NTU	0 to 5	[24](DIGESA, 2010)

Source: Authors, (2025).

### II.3 SAMPLE COLLECTION AND DATA ANALYSIS

The sample size was directed with non-probabilistic sampling in a total of 462 daily samples of remote monitoring. Samples were collected digitally automated by the wireless sensors in time intervals of approximately three minutes in which the five sensors perform the process of acquiring, processing, transmitting and storing the information. The field tests were carried out between July and August 2024 for ten days of 24 hours each.

Data were grouped and tabulated according to the type of variable to be analyzed (transmission distance, received signal characteristics RSSI, SNR, and water quality measurements such as temperature, pH, and turbidity). Central tendency and dispersion statistics were used to describe the capacity of remote monitoring, and box plots were used to represent the distribution of the acquired data.

Calibration of the wireless sensors was performed in the laboratory during prototyping through comparisons between sensor measurements and Hanna Instruments contrast equipment, whose level of accuracy was verified with metrics such as coefficient of determination ( $R^2$ ), root mean square error (MSE) and standard error of estimation (SEE).

### II.4 REMOTE MONITORING MODEL ARCHITECTURE

The architecture is made up of three stages as shown in Figure 2. The first stage corresponds to the data acquisition and processing section of the physical phenomenon (water quality), the second corresponds to the stage of wireless data transmission within the Low Power Wide Area Network (LPWAN) and Wireless Fidelity (WIFI), and finally, the third stage of remote storage and dissemination of information.

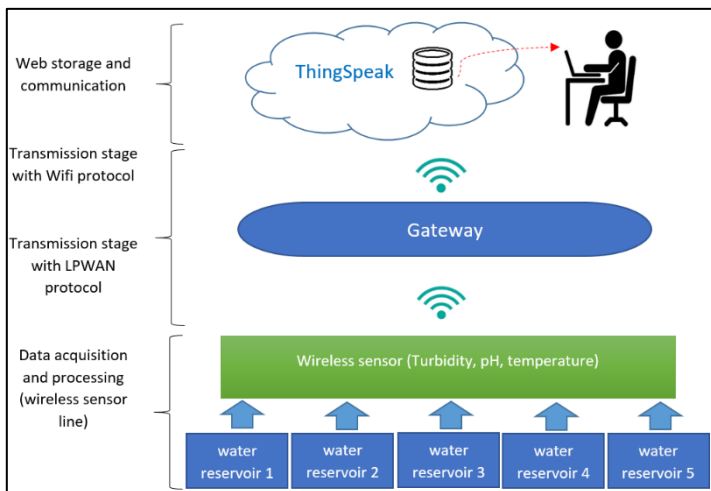


Figure 2: Architecture of remote water quality monitoring.  
Source: Authors, (2025).

### II.5 IMPLEMENTATION OF WIRELESS SENSORS

Wireless sensors have four electronic circuit blocks (see Figure 3). The first consists of the physical sensors, the second by data acquisition and processing block, the third by data transmission block, and finally the power supply block.

The sensor block consists of the DS18B20 temperature sensor that measures the temperature change with a probe-type electrode with a 12-bit resolution; the PH-4502C sensor that measures the acidity or alkalinity of the water through a potential difference between a glass electrode that is sensitive to  $H^+$  ions and another metal one that measures the electric potential that translates

into pH; also, the LGZD V1.1 turbidity sensor that is an infrared light optoelectronic device with which the amount of turbidity is determined from the variability of the voltage of the receiving photodiode.

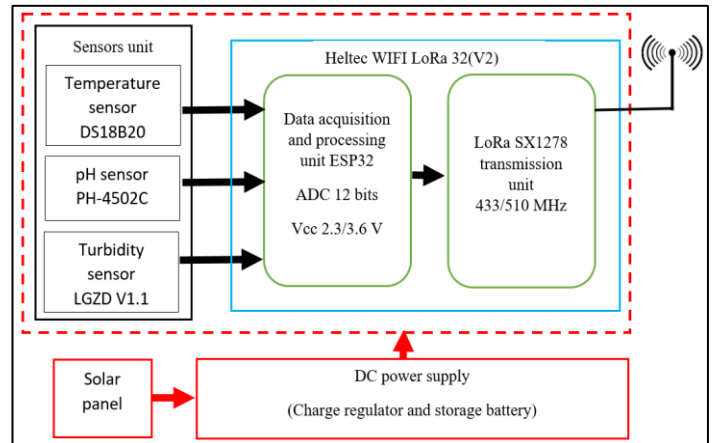


Figure 3: Structure of wireless sensors.  
Source: Authors, (2025).

Table 4 presents the technical characteristics of each sensor.

Table 4: Characteristics of physical sensors and calibration instruments.

Variable	Unit	Model	Characteristics	Calibration instrument
Temperature	° C	DS18B20	Range: -10 to 85 °C Accuracy: ± 0.5 °C	Hanna HI98121 0 - 60 °C
Hydrogen potential	pH	PH-4502C	Range: 0 to 14 pH	Hanna HI98121 0 - 14 pH
Turbidity	NTU	LGZD V1.1	Voltage: 0V to 4.50V	Hanna HI93703 0 to 50 NTU

Source: Authors, (2025).

The data acquisition and processing block consists of the ESP32 microcontroller incorporated in the Heltec WIFI Lora 32(V2), to which the physical sensors are connected for sampling and 12-bit digital analog conversion of the water temperature, pH and turbidity variables. Figure 4. illustrates the calibration activity of the Hanna sensors and instruments.

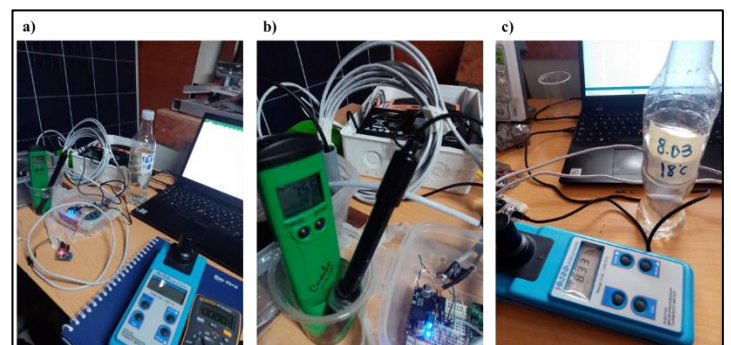


Figure 4: Calibration of, a) Wireless sensors with the multimeter, b) Temperature and pH with the Hanna multi-parameter HI98121, and c) Turbidity with the Hanna turbidimeter HI93703.

Source: Authors, (2025).



The DS18B20 temperature sensor and the PH-4502C hydrogen potential sensor were calibrated with the Hanna Instruments HI98121 multiparameter equipment under room temperature conditions of 15 °C; the temperature was calibrated through the simultaneous immersion in water of the electrodes and the contrasting equipment at temperatures between 8.8 to 24.2 °C, the sensor is of the 12-bit direct digital type whose precision oscillates in  $\pm 0.5$  °C in the range of -10°C to +85°C [25]. From the correlation of measurements, a coefficient of determination  $R^2$  of 98.98% ( $p < 0.001$ ) and averages of  $8.36 \pm 0.12$ ,  $13.84 \pm 0.17$ ,  $14.76 \pm 0.51$ ,  $17.04 \pm 0.04$ ,  $20.25 \pm 0.06$  and  $24.25 \pm 0.13$  were obtained for temperatures of 8.80, 13.90, 14.50, 16.90, 20.10 and 24.20 °C respectively.

The pH calibration was also performed by simultaneous immersion of the electrodes in calibration solutions of Hanna HI7004L (4.01 pH), HI7007L (7.01 pH) and drinking water of 7.6 and 7.9 pH. The coefficient of determination of the calibration of the sensors was  $R^2 = 96.81\%$  ( $p < 0.001$ ) and average values of  $4.19 \pm 0.06$ ,  $7.09 \pm 0.08$ ,  $7.77 \pm 0.21$ ,  $7.98 \pm 0.18$  for the 4.01, 7.01, 7.6 and 7.9 pH solutions, respectively. The PH-4502C sensor incorporates in its electronic design a temperature sensor for pH correction against temperature changes which has been considered in the implementation of the prototype taking as reference equation (1) [26] [27] where the variation of pH(end) ranges between 0 and 0.17 for temperatures of 15 and 0 °C respectively.

$$pH_{(end)} = pH_{T_1} + 0.0114 (T_1 - T_2) \quad (1)$$

Where,  $pH_{(end)}$  is the temperature-corrected pH,  $pH_{T_1}$  is the pH value at the measurement temperature  $T_1$ ,  $T_2$  is the reference temperature (15 °C).

The LGZD V1.1 turbidity sensor was calibrated with the Hanna Instruments HI93703 turbidity meter by simultaneously measuring different water solutions in the range of 1 NTU to 12 NTU and temperature of 10 °C. The sensor measures turbidity based on the transmittance of infrared light from the transmitter to the receiver at an angle of 180° generating an output voltage of 4.40V (10 °C) for turbidity less than 0.5 NTU; the output voltage rises for low temperatures or low turbidity, and decreases with increasing water temperature or turbidity [28][29]. Experimentally, equation (2) was obtained for the calculation of water turbidity from the correlation of the measurements of the contrast equipment and the turbidity sensor with a coefficient of determination of  $R^2$  of 89.82% and NTU averages of  $1.17 \pm 1.38$ ,  $1.22 \pm 0.38$ ,  $3.42 \pm 0.34$ ,  $6.18 \pm 0.37$ ,  $6.79 \pm 0.57$  and  $8.99 \pm 0.68$  for turbidity references of 1, 2, 5, 6, 9 and 12 NTU respectively with output voltages of between 4.397 V and 4.364 V. The accuracy obtained was accepted in the investigation because the sensor had a positive response and provided an acceptable reference approximation of turbidity despite being a low-cost device compared to the HI93703 contrast equipment, where the differences in measurements ranged around 1 NTU for values lower than 5 NTU, which we consider favorable in contrast to the non-existent monitoring of water turbidity in rural areas.

$$NTU = \frac{V_{T_b} - V_{T_a} + 0.0069(T_b - T_a)}{-0.003} \quad (2)$$

Where,  $V_{T_b}$  is the sensor voltage at  $T_b$  (temperature of the water turbidity reading),  $V_{T_a}$  is the sensor voltage at  $T_a$  (reference temperature 10 °C of the turbidity reading).

Table 5 describes the accuracy level metrics of the calibrated sensors concerning the coefficient of determination  $R^2$ ,

the root mean square error (MSE), and the standard error of estimation (SEE).

Table 5: Evaluating the accuracy level of wireless sensors.

Sensor	Calibration range	Accuracy Level Metrics		
		$R^2$	MSE	SEE
Temperature (DS18B20)	8.8 °C to 24.2 °C	0.9898	0.222	0.419
pH (PH-4502C)	4.01 pH, 7.01 pH, 7.6 pH, 7.9 pH,	0.9681	0.026	0.205
Turbidity (LGZD V1.1)	1 NTU to 12 NTU	0.8982	3.023	0.905

Source: Authors, (2025).

In Figure 5, the linear models of the calibration of the temperature, pH and turbidity sensors are presented.

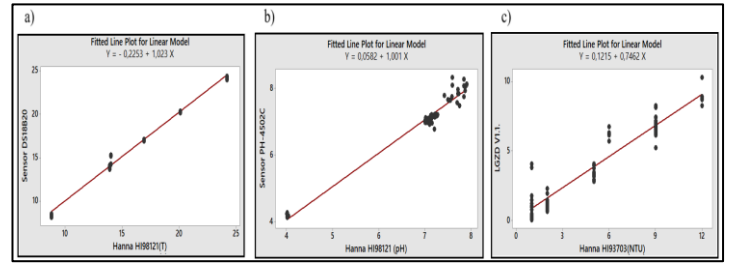


Figure 5: The linear model of the calibration level of wireless sensors, a) temperature b) hydrogen potential pH, and c) turbidity. Source: Authors, (2025).

The data transmission unit is made up of two wireless communication systems. The first one is made up of the wireless sensors through Semtech LoRa SX1278 devices embedded in the Heltec Automation LoRa 32(V2) WiFi card and configured in an LPWAN network with a spreading factor (SF=12), transmission power of 13 dBm, in the frequency band for the industrial, scientific and medical (ISM) area of 433 MHz. The second communication system is made up of the Gateway that retransmits the signal from the wireless sensors to the Internet through the IEEE 802.11 b/g/n and TCP/IP WiFi protocol. The wireless sensors and the Gateway have an algorithm coded in C language and compiled in the LoRa32(V2) WiFi development boards through the Arduino IDE using the libraries "heltec.h", "OneWire.h" and "DallasTemperature.h" and the routines in Figure 6.

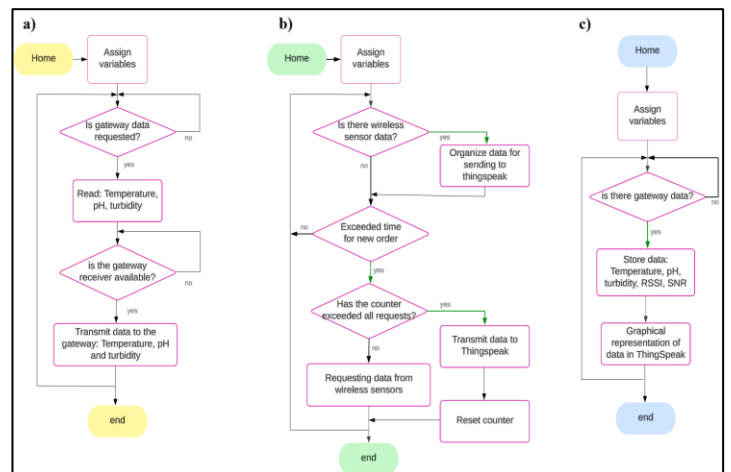


Figure 6: Flow diagrams of data transmission and reception routine, a) Wireless sensor with LPWAN protocol, b) Gateway with LPWAN/Wifi protocols, and c) ThingSpeak. Source: Authors, (2025).

The Gateway starts the process by requesting data from the wireless sensors within the LPWAN network with their respective identifier code; on the wireless sensor network side, the requests are iteratively verified and data acquisition and processing are carried out to then transmit them to the Gateway; the Gateway receives and organizes all the data and sends it to ThingSpeak; finally, the data from the wireless sensors is stored and graphically represented on the ThingSpeak platform. The process is repeated iteratively from start to finish approximately every 3 minutes.

All sensor devices, the ESP32 microcontroller, and the SX1278 transmitters of the WiFi LoRa 32(V2) from Heltec Automation are connected to the power supply provided by a 12V/7Ah battery through a 12V/5V charge regulator.

## II.6 INSTALLATION AND REMOTE MONITORING WITH WIRELESS SENSORS

The wireless sensors installed in the communities' reservoirs were identified as S1 Sachapite, S2 Antacocha, S3 Pampachacra, S4 Huaylacucho, and S5 San Gerónimo; on the other hand, the Gateway is identified as "Monitoring Center (UNH) Huancavelica". Figure 7 illustrates the installation of the wireless sensors.

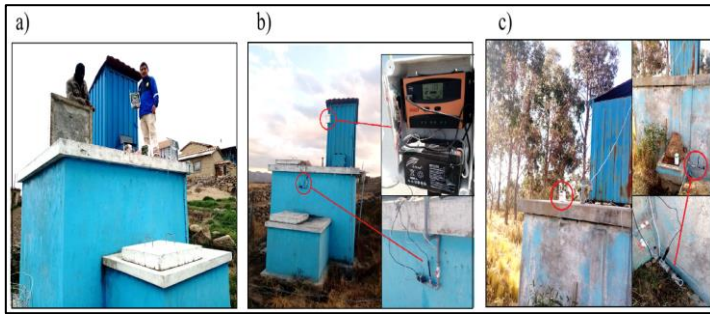


Figure 7: Water reservoirs in rural communities, a) prior to the installation of the wireless sensor, b) and c) with wireless sensors.

Source: Authors, (2025).

Table 6 describes the transmission paths of wireless sensors in remote monitoring.

Table 6: Transmission paths of wireless sensors in remote monitoring

Routes	Origin: Transmission	Location	Destination: Reception	Location
1	S1 Sachapite	-12° 44.069 -74° 54.590	S3 Pampachacra	-12° 48.643 -74° 55.271
2	S4 Huaylacucho	-12° 47.521 -74° 56.905	S2 Antacocha	-12° 44.697 -74° 54.948
3	S2 Antacocha	-12° 44.697 -74° 54.948	S3 Pampachacra	-12° 48.643 -74° 55.271
4	S3 Pampachacra	-12° 48.643 -74° 55.271	Monitoring Center (UNH) Huancavelica	-12° 46.733 -74° 57.617
5	S5 San Gerónimo	-12° 47.045 -74° 59.931		

Source: Authors, (2025).

Figure 8 graphically illustrates the transmission routes of wireless sensors within the mountainous rural Andean geography of Huancavelica.

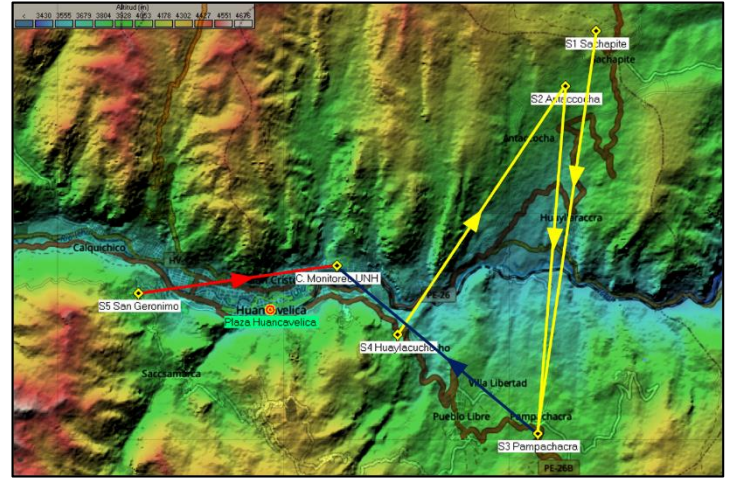


Figure 8: Transmission paths of wireless sensors in remote monitoring.

Source: Authors, (2025).

Figure 9 presents the data display panel for remote monitoring with wireless sensors.

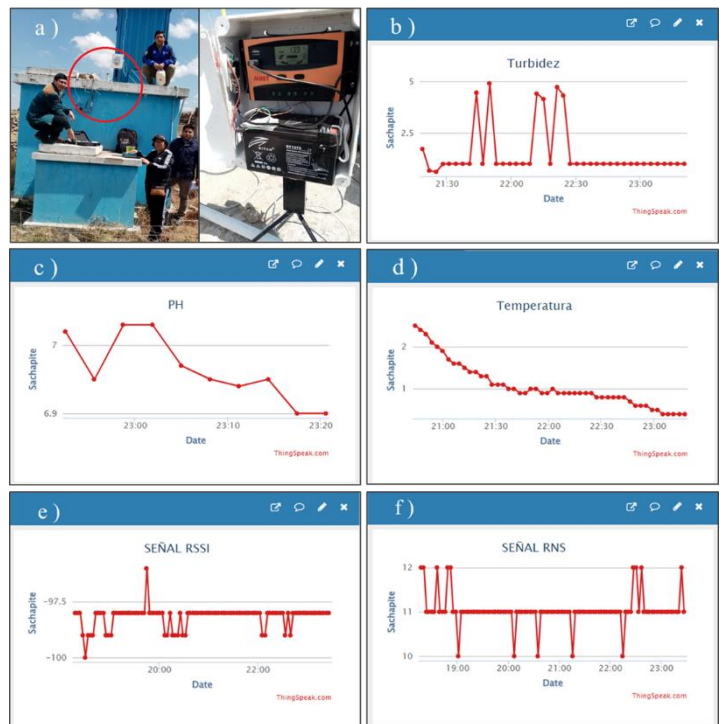


Figure 9: Remote monitoring of water quality; a) wireless sensor in the reservoir, b) turbidity monitoring, c) pH, d) temperature, e) RSSI, and f) RNS.

Source: Authors, (2025).

## III. RESULTS AND DISCUSSIONS

Five wireless sensors have been implemented to facilitate real-time remote monitoring of water quality using wireless transceivers and temperature (DS18B20), pH (PH-4502C), and turbidity (LGZD V1.1) sensors, with an approximate accuracy of 98.98%, 96.81% and 89.82% respectively; the installation of the sensors makes up a low-power wide area network (LPWAN) distributed in five communities and a Gateway in charge of recording the information on the ThingSpeak Internet platform. LPWAN communication is carried out using the spread spectrum modulation technique through the LoRa 32 (V2) WiFi card with SX1278 transceiver, spreading factor (SF) of 12, and transmission



power of 13 dBm in the 433 MHz ISM frequency band; the Gateway also uses the Wifi 802.11 b/g/n protocol.

In this regard, various studies state that monitoring water quality in rural areas is complex due to various factors such as geography, logistics, and manual procedures that make it difficult and impossible to develop frequent monitoring in favor of rural populations and the availability of information [8], [10], [30].

The results demonstrate the feasibility of monitoring water quality in rural, extensive, and mountainous geographic areas such as Huancavelica-Peru, based on the use of technologies such as LoRa [30], [31] with which the difficulties of monitoring are minimized; on the contrary, it enables remote monitoring of water quality, expanding the availability of information in favor of rural communities for water security and control actions according to the standard [32].

Table 7 shows the results of the data received during the transmission of the wireless sensors within the LPWAN network, where the overall average of the 5 reservoirs was 456 out of a total of 462 expected data, representing 98.7% effectiveness in the transmission and reception of data; a result similar to that recorded by [17] corresponding to 95.5% during the transmission of 600 data and much better than the 80% reported by [33] for a homogeneous LoRaWAN network. The research shows that wireless sensors ensure high effectiveness of data transmission and reception with LoRa transceivers in rural geographic spaces.

Table 7: Data received from the wireless sensors (S1 Sachapite, S2 Antacocha, S3 Pampachacra, S4 Huaylacucho, S5 San Gerónimo)

Day	S1	S2	S3	S4	S5
1	459.00	459.00	456.00	456.00	455.00
2	458.00	457.00	456.00	455.00	454.00
3	458.00	455.00	460.00	456.00	457.00
4	458.00	460.00	458.00	458.00	456.00
5	456.00	458.00	458.00	458.00	454.00
6	458.00	457.00	457.00	457.00	455.00
7	457.00	456.00	456.00	454.00	457.00
8	457.00	456.00	458.00	457.00	453.00
9	454.00	456.00	458.00	455.00	455.00
10	456.00	451.00	457.00	456.00	457.00
General Average	457.10	456.50	457.40	456.20	455.30

Source: Authors, (2025).

On the other hand, Table 8 shows the distances and altitudes of signal transmission, as well as the maximum and minimum values of RSSI and SNR during data reception from the wireless sensors.

The maximum distance reached was 8.73 km between the S1 Sachapite and S3 Pampachacra positions located between 4196 and 4072 m of altitude respectively.

The results exceed the remote monitoring distances of research such as [11], [12], [14], [34], which reported monitoring at distances up to 120 m with Wifi systems and others up to 2.0 km with LoRa communication systems [15], [18], [35], [36] in flat and coastal geography.

However, despite the achievement, the challenge of improving the communication distance over 10 km recorded with technologies such as LoRa SX1272 or RN2483 still arises [37] [38].

Table 8: Results for RSSI and SNR considering transmission distances and altitudes.

Origin of transmission Location, altitude	Transmission destination Location, altitude	Distance (km)	RSSI dBm	SNR dB
S1 Sachapite 4196	S3 Pampachacra 4072	8.73	-95 to -104	10 to 12
S2 Antacocha 4084	S3 Pampachacra 4072	6.43	-93 to -102	10 to 12
S4 Huaylacucho 3823	S2 Antacocha 4084	5.45	-103 to -111	10 to 13
S3 Pampachacra 4072	Monitoring Center (UNH)	3723	-96 to -115	10 to 13
S5 San Gerónimo 3885		3723	-110 to -122	09 to 12

Source: Authors, (2025).

On the other hand, the RSSI received signal strength measurements were recorded in the range of -122 dBm to -93 dBm for different distances between 4.29 km to 8.73 km. These RSSI results are similar to the measurements of [39] and [40] whose achieved range was -120 dBm to -100 dBm for distances of 1560 m and 500 m respectively. It is evident that wireless sensors with the WiFi LoRa 32(V2) still have an adequate RSSI sensitivity at long distances, also having an approximate 9% tolerance margin with respect to the minimum limit of -135 dBm indicated by the manufacturer [20].

Regarding the results of the signal-to-noise ratio (SNR) of the communication, these were found in the range of 9 dB to 13 dB and according to [41], SNR values greater than 0 dB represent signals of good transmission quality with a minimum packet loss error rate. Therefore, the remarkable thing about the measured results of RSSI and SNR, is that they guarantee good communication of wireless sensors in far rural and mountainous scenarios where the quality of data transmission remains similar to those of short distances.

Table 9 presents the results of remote monitoring of water temperature, pH and turbidity for the five reservoirs.

Table 9. Results of remote monitoring of temperature, pH and turbidity in the rural Andean area of Huancavelica.

Ubication	Min	Quartile 1	Quartile 2	Quartile 3	Max
<b>a) Temperature ( °C )</b>					
S1 Sachapite	-2.90	1.60	5.00	10.50	12.20
S2 Antacocha	-1.30	3.00	5.20	9.70	14.40
S3 Pampachacra	-1.90	1.10	3.80	9.00	13.50
S4 Huaylacucho	0.60	4.10	7.00	10.20	13.00
S5 San Gerónimo	0.50	1.90	4.50	10.50	13.70
(WHO, 2011)	< 20	< 20	< 20	< 20	< 20
<b>b) Hydrogen potential (pH)</b>					
S1 Sachapite	6.76	7.13	7.52	7.60	7.80
S2 Antacocha	6.86	7.35	7.50	7.68	7.98
S3 Pampachacra	6.60	6.99	7.14	7.35	7.87
S4 Huaylacucho	6.88	7.14	7.32	7.44	7.89
S5 San Gerónimo	6.80	7.19	7.67	7.76	8.24
(DIGESA, 2010) (WHO, 1971)	6.5 - 8.5	6.5 - 8.5	6.5 - 8.5	6.5 - 8.5	6.5 - 8.5
<b>c) Turbidity (NTU)</b>					
S1 Sachapite	0.50	1.43	2.20	2.90	4.94

S2 Antacocha	0.34	2.09	2.85	3.45	4.51
S3 Pampachacra	1.00	1.42	2.10	3.20	4.98
S4 Huaylacucho	0.50	1.23	2.07	2.70	4.90
S5 San Gerónimo	0.80	1.57	2.20	3.47	4.91
(DIGESA, 2010) (WHO, 1971)	< 5	< 5	< 5	< 5	< 5

Source: Authors, (2025).

Figure 10 illustrates through a box plot the distribution of the data collected from the ten days of remote monitoring experimentation.

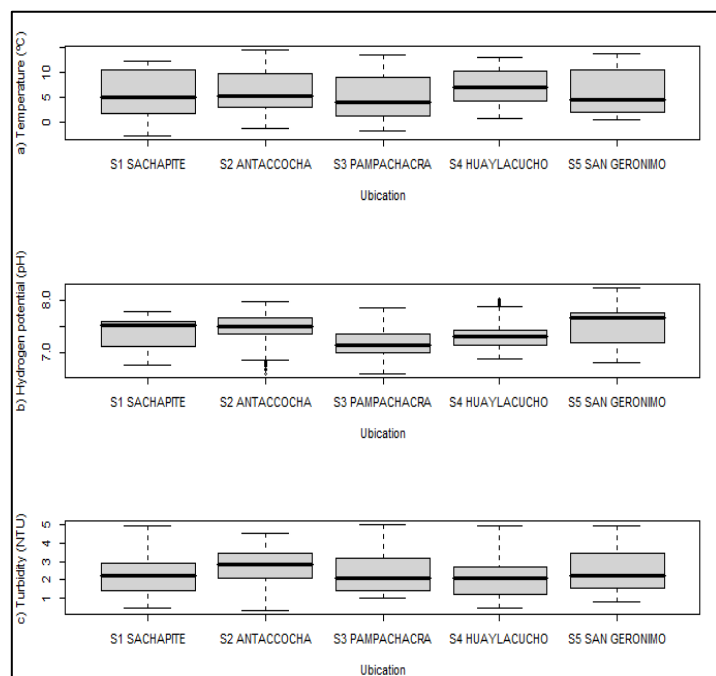


Figure 10. Remote monitoring of water quality in the reservoirs.

a) Temperature, b) pH and c) Turbidity

Source: Authors, (2025).

The results for temperature, pH and turbidity reveal significant variations in water quality among the five rural communities. Temperature measurements ranged from a minimum of -2.90 °C in S1 Sachapite to a maximum of 14.40 °C in S2 Antacocha between night and day respectively, with intermediate values ranging between 3.8 °C and 7.0 °C, which highlights the cold climate of the region with which naturally ensures low water temperature (< 20 °C), fulfilling the recommendation of the WHO [22] so that the various microorganisms such as *V. Cholerae*, *Legionella* spp among others do not have high growth rates and propagation.

The pH levels were within the acceptable range of 6.5 to 8.5 of the Peruvian standard [42] and WHO [23] with a minimum value of 6.60 recorded in S3 Pampachacra and a maximum value of 8.24 in S5 San Gerónimo, which indicates the adequate neutrality of the monitored waters, evidencing a natural pH balance and the safety it represents for consumption within the monitored communities.

As for turbidity levels, all were found to be below the WHO threshold of 5 NTU with a variation ranging from a minimum of 0.34 NTU identified in S2 Antacocha to a maximum value of 4.98 NTU in S3 Pampachacra, results that suggest good water clarity and quality with respect to suspended particles or sediments from soil erosion of the rural springs from which the water is obtained.

Therefore, the results indicate that the remotely monitored water sources have favorable physicochemical characteristics (°C,

pH, NTU) and meet the drinking water quality guidelines of Peruvian and WHO regulations. Likewise, they temporarily reflect the adequate preservation of water quality conditions in relation to previous physicochemical evaluations [43]; preservation that is probably due to the rural geographic location of the waters where anthropogenic intervention is minimal and moderate hydrological cycles that however are susceptible to alteration due to climate change effects which should be taken into consideration [44]–[46].

Finally, it highlights the importance of monitoring water in order to ensure its quality [32], [47], which, remote monitoring with wireless sensors is a feasible tool that facilitates continuous water monitoring minimizing the geographical gaps and limitations of the rural environment.

#### IV. CONCLUSIONS

In the research, wireless sensors have been implemented that allowed remote and real-time monitoring of water quality in complex rural geographic spaces with an accuracy of 98.98%, 96.81%, and 89.82% for temperature, pH, and turbidity respectively. A high effectiveness of around 98.7% has been achieved in the transmission and reception of data covering distances of up to 8.73 km in mountainous rural geography with altitudes between 4072 m and 4196 m, demonstrating the feasibility of using LoRa wireless technology in minimizing geographic distances during remote monitoring of water quality. Similarly, it has been verified that the received signal strength RSSI and signal to noise ratio SNR in long distance communications have a tolerance margin of up to 9% for the RSSI with respect to the limit value of -135 dBm indicated by the manufacturer of the Wifi LoRa 32(V2) and that the SNR is in the range of 9 dB to 13 dB, showing that the transmitted signals are of good quality with a minimum packet loss error rate.

Remote monitoring of water quality in the five rural communities involved confirmed that the temperature, pH, and turbidity meet Peruvian and World Health Organization standards, with temperatures below 20 °C (minimum -2.90 °C in S1 Sachapite and maximum 14.40 °C in S2 Antacocha); pH within the range of 6.5 and 8.5 (minimum 6.60 pH in S3 Pampachacra and maximum 8.24 pH in S5 San Gerónimo) and turbidity below 5 NTU (minimum 0.34 NTU in S2 Antacocha and maximum 4.98 NTU in S3 Pampachacra).

#### V. AUTHOR'S CONTRIBUTION

**Conceptualization:** Wohler Gonzales Saenz, Luz Marina Acharte Lume, Javier Camilo Poma Palacios, Alejandro Filimón Quispe Coica, Agustí Pérez Foguet.

**Methodology:** Wohler Gonzales Saenz, Luz Marina Acharte Lume, Javier Camilo Poma Palacios, Alejandro Filimón Quispe Coica, Agustí Pérez Foguet.

**Investigation:** Wohler Gonzales Saenz, Luz Marina Acharte Lume, Javier Camilo Poma Palacios, Alejandro Filimón Quispe Coica, Agustí Pérez Foguet.

**Discussion of results:** Wohler Gonzales Saenz, Luz Marina Acharte Lume, Javier Camilo Poma Palacios, Alejandro Filimón Quispe Coica, Agustí Pérez Foguet. **Writing – Original Draft:** Author One.

**Writing – Review and Editing:** Wohler Gonzales Saenz, Luz Marina Acharte Lume, Javier Camilo Poma Palacios, Alejandro Filimón Quispe Coica, Agustí Pérez Foguet.

**Resources:** Wohler Gonzales Saenz, Luz Marina Acharte Lume, Javier Camilo Poma Palacios, Alejandro Filimón Quispe Coica, Agustí Pérez Foguet.

**Supervision:** Wohler Gonzales Saenz, Luz Marina Acharte Lume, Javier Camilo Poma Palacios, Alejandro Filimón Quispe Coica, Agustí Pérez Foguet.

**Approval of the final text:** Wohler Gonzales Saenz, Luz Marina Acharte Lume, Javier Camilo Poma Palacios, Alejandro Filimón Quispe Coica, Agustí Pérez Foguet.

## VI. ACKNOWLEDGMENTS

This research was made possible due to funding from the Universidad Nacional de Huancavelica through the Camisea socioeconomic development fund (FOCAM). We also are very thankful to the communities of Sachapite, Antacocha, Pampachacra, Huaylacucho and San Gerónimo for providing us access to the water reservoirs in their jurisdiction.

## VII. REFERENCES

- [1] UNESCO, "El valor del agua. Informe mundial sobre el Desarrollo de los Recursos Hídricos 2021," 2021.
- [2] D. Choque-Quispe et al., "Proposal of a Water-Quality Index for High Andean Basins" *Water*, vol. 14, no. 654, p. 19, 2022.
- [3] A. J. Ramadhan, "Smart water-quality monitoring system based on enabled real-time internet of things," *J. Eng. Sci. Technol.*, vol. 15, no. 6, pp. 3514–3527, 2020.
- [4] S. N. S. Taha@Tahir et al., "Implementation of LoRa in River Water Quality Monitoring," *Proc. Int. Conf. Artif. Life Robot.*, pp. 153–161, 2022, doi: 10.5954/icarob.2022.os22-2.
- [5] O. Toyin and O. Ibitoye, "Catchment Scale Assessment of Pollution Threats To Water Quality in Relation To Prevalence of Water-Borne Diseases in Some Communities in Omu-Aran, Nigeria," *J. Eng. Technol. Ind. Appl.*, vol. 7, no. 30, pp. 69–74, 2021, doi: 10.5935/jetia.v7i30.760.
- [6] G. A. Lopez-Ramirez and A. Aragon-Zavala, "Wireless Sensor Networks for Water Quality Monitoring: A Comprehensive Review," *IEEE Access*, vol. 11, no. August, pp. 95120–95142, 2023, doi: 10.1109/ACCESS.2023.3308905.
- [7] ANA-Perú, "Protocolo nacional para el monitoreo de la calidad de los recursos hídricos superficiales," Ministerio de Agricultura y Riego. p. 92, 2016, [Online]. Available: <http://repositorio.ana.gob.pe/handle/20.500.12543/209>.
- [8] A. Quispe-Coica, S. Fernández, L. Acharte Lume, and A. Pérez-Foguet, "Status of Water Quality for Human Consumption in High-Andean Rural Communities: Discrepancies between Techniques for Identifying Trace Metals," *J. — Multidiscip. Sci. J.*, vol. 3, no. 2, pp. 162–180, 2020, doi: 10.3390/j3020014.
- [9] D. Choque-Quispe et al., "Insights from water quality of high andean springs for human consumption in Peru," *Water (Switzerland)*, vol. 13, no. 19, 2021, doi: 10.3390/w13192650.
- [10] M. Custodio, R. Peñaloza, F. Chanamé, J. L. Hinostroza-martínez, and H. De Cruz, "Water quality dynamics of the Cunas River in rural and urban areas in the central region of Peru," *Egypt. J. Aquat. Res.*, vol. 47, no. 3, pp. 253–259, 2021, doi: 10.1016/j.ejar.2021.05.006.
- [11] T. Santos, "Monitor Water: A Monitoring System Using NodeMCU ESP8266," pp. 3–6, 2020.
- [12] M. H. Amin, A. A. B. Sajak, J. Jaafar, H. S. Husin, and S. Mohamad, "Real Time Water Quality Monitoring System for Smart City in Malaysia," *ASEAN J. Sci. Eng.*, vol. 2, no. 1, pp. 47–64, 2022, doi: 10.17509/ajse.v2i1.37515.
- [13] X. Wang, Y. Feng, J. Sun, D. Li, and H. Yang, "Research on Fishery Water Quality Monitoring System Based on 6LoWPAN Research on Fishery Water Quality Monitoring System Based on 6LoWPAN," 2020, doi: 10.1088/1742-6596/1624/4/042057.
- [14] B. U. Adarsh et al., "Design of 6LoWPAN enabled Real Time Water Quality Monitoring System using CoAP," *Proc. Asia-Pacific Adv. Netw.*, vol. 38, no. 0, p. 42, 2014, doi: 10.7125/apan.38.7.
- [15] D. Pikulins, R. Gotlaufs, T. Solovjova, A. Aboltins, J. Grizāns, and S. Migla, "On the Development of Long-Range Water Quality Monitoring System for Outdoor Aquaculture Objects," *Electr. Control Commun. Eng.*, vol. 18, no. 1, pp. 37–42, 2022, doi: 10.2478/ecce-2022-0005.
- [16] H. Y. Miao, C. T. Yang, E. Kristiani, H. Fathoni, Y. S. Lin, and C. Y. Chen, "On Construction of a Campus Outdoor Air and Water Quality Monitoring System Using LoRaWAN," *Appl. Sci.*, vol. 12, no. 10, 2022, doi: 10.3390/app12105018.
- [17] S. Prompt, S. Maithomklang, and C. Panya-isara, "Design and Analysis Performance of IoT-Based Water Quality Monitoring System using LoRa Technology," *TEM J.*, vol. 12, no. 1, pp. 29–35, 2023, doi: 10.18421/TEM121-04.
- [18] W. M. Sanya, M. A. Alawi, and I. Eugenio, "Design and development of Smart Water Quality Monitoring System Using IoT," *Int. J. Adv. Sci. Res. Eng.*, vol. 08, no. 03, pp. 01–13, 2022, doi: 10.31695/ijasre.2022.8.3.1.
- [19] C. A. Borda, "Características de las zonas altoandinas en el Perú," no. 511, 2015.
- [20] Heltec Automation, "Specifications WiFi LoRa 32(V2)," vol. 32. 2023, [Online]. Available: <https://heltec.org/project/wifi-lora-32v2/>.
- [21] Semtech, "Wireless & sensing products Datasheet Sx1276/77/78/79," Semtech Corp., no. Rev. 7 May 2020, pp. 1–132, 2020, [Online]. Available: <http://www.semtech.com>.
- [22] WHO, "Guidelines for Drinking-water Quality," *Guidel. Drink. Qual.* - 4th ed., 2011.
- [23] WHO, "International standards for colour," in *International standards for drinking-water*, Elsevier, 1971, pp. 1–70.
- [24] DIGESA, "Reglamento de la calidad del Agua para consume humano," Dirección General de Salud Ambiental-Perú, no. 9. pp. 1689–1699, 2010, [Online]. Available: <https://cdn.www.gob.pe/uploads/document/file/273650/reglamento-de-la-calidad-del-agua-para-consumo-humano.pdf>.
- [25] Maximintegrated, "DS18B20 Programmable Resolution 1," vol. 92, pp. 1–20, 2019.
- [26] J. M. Gieskes, "Effect on the pH of seawater," *Inst. fur Meereskunde, Kiel, Ger.*, p. 679–685, 1969.
- [27] Mohammad et al., "Temperature Compensation in pH meter-A Survey," *SUST J. Eng. Comput. Sci.*, vol. 16, no. October, pp. 16(2): 1–9, 2015.
- [28] DFRobot, "Turbidity Sensor," Datasheet Turbid. Sens. SEN0189, no. 19, pp. 1–18, 2022, [Online]. Available: [https://wiki.dfrobot.com/Turbidity\\_sensor\\_SKU\\_SEN0189](https://wiki.dfrobot.com/Turbidity_sensor_SKU_SEN0189).
- [29] L. D. Silva, C. M. Schweitzer, and E. G. J. Júnior, "Water Quality Monitoring through Arduino Robotic Sensors," *J. Eng. Res.*, vol. 1, no. 1, pp. 2–24, 2021, doi: 10.22533/at.ed.3172115109.
- [30] M. Pule, A. Yahya, and J. Chuma, "Wireless sensor networks: A survey on monitoring water quality," *J. Appl. Res. Technol.*, vol. 15, no. 6, pp. 562–570, Dec. 2017, doi: 10.1016/j.jart.2017.07.004.
- [31] M. Bor and U. Roedig, "LoRa transmission parameter selection," in *Proceedings - 2017 13th International Conference on Distributed Computing in Sensor Systems, DCOSS 2017*, Jul. 2017, vol. 2018-Janua, pp. 27–34, doi: 10.1109/DCOSS.2017.10.
- [32] Bordallo et al., "Water Quality of Igarapé Pau-Cheiroso and the Process of Urbanization of the Municipality Igarapé-Açu," *ITEGAM- J. Eng. Technol. Ind. Appl.*, vol. 3, no. 9, 2017, doi: 10.5935/2447-0228.20170008.
- [33] O. A. Agbolade, F. M. Dahunsi, and S. A. Oyetunji, "Heterogeneous Lorawan Deployment for Application Dependent Iot Networks," *J. Eng. Technol. Ind. Appl.*, vol. 8, no. 34, pp. 4–11, 2022, doi: 10.5935/jetia.v8i34.798.
- [34] X. Wang, Y. Feng, J. Sun, D. Li, and H. Yang, "Research on Fishery Water Quality Monitoring System Based on 6LoWPAN," in *Journal of Physics: Conference Series*, Nov. 2020, vol. 1624, no. 4, doi: 10.1088/1742-6596/1624/4/042057.

- [35] S. Sağır, İ. Kaya, C. Şişman, Y. Baltacı, and S. Ünal, "Evaluation of Low-Power Long Distance Radio Communication in Urban Areas: LoRa and Impact of Spreading Factor," IEEE, 2019, doi: 10.1109/ICDIPC.2019.8723666.
- [36] W. Chen et al., "Research and Design of Distributed IoT Water Environment Monitoring System Based on LoRa," Wirel. Commun. Mob. Comput., vol. 2021, 2021, doi: 10.1155/2021/9403963.
- [37] J. Petäjäjärvi, K. Mikhaylov, and T. Hänninen, "2015 14th International Conference on ITS Telecommunications, ITST 2015," 2015 14th Int. Conf. ITS Telecommun. ITST 2015, pp. 55–59, 2016.
- [38] R. Sanchez-Iborra, J. Sanchez-Gomez, J. Ballesta-Viñas, M. D. Cano, and A. F. Skarmeta, "Performance evaluation of lora considering scenario conditions," Sensors (Switzerland), vol. 18, no. 3, 2018, doi: 10.3390/s18030772.
- [39] S. N. Syed Taha, M. S. Abu Talip, M. Mohamad, Z. H. Azizul Hasan, and T. F. Tengku Mohmed Noor Izam, "Evaluation of LoRa Network Performance for Water Quality Monitoring Systems," Appl. Sci., vol. 14, no. 16, 2024, doi: 10.3390/app14167136.
- [40] J. P. Tovar-Soto, C. F. Pareja-Figueroa, O. L. García-Navarrete, and L. C. Gutiérrez-Martínez, "Performance evaluation of lora technology for implementation in rural areas," DYNA, vol. 88, no. 216, pp. 69–78, Jan. 2021, doi: 10.15446/dyna.v88n216.88258.
- [41] E. Bonilla Cadena, "Análisis de comunicaciones punto a punto con simulaciones open-source de LoRa," Rev. Investig. en Tecnol. la Inf., vol. 10, no. 21, pp. 14–23, 2022, doi: 10.36825/riti.10.21.003.
- [42] DIGESA, "Reglamento de la calidad del agua para consumo humano," vol. 19, no. 5, pp. 1–23, 2011.
- [43] W. Gonzales, L. M. Acharte, J. C. Poma Palacios, V. G. Sánchez Araujo, F. A. Quispe Coica, and R. Meseguer Pallares, "Evaluación fisicoquímica y microbiológica del agua de consumo humano en seis comunidades rurales altoandinas de Huancavelica-Perú," Rev. Investig. Altoandinas - J. High Andean Res., vol. 25, no. 1, pp. 23–31, 2023, doi: 10.18271/ria.2023.486.
- [44] T. Ahmed, M. Zounemat-Kermani, and M. Scholz, "Climate change, water quality and water-related challenges: A review with focus on Pakistan," Int. J. Environ. Res. Public Health, vol. 17, no. 22, pp. 1–22, 2020, doi: 10.3390/ijerph17228518.
- [45] Silva et al, "Analysis of Historical Series of Mamirauá Lake Level (Preliminary Study)," J. Eng. Technol. Ind. Appl., vol. 5, no. 20, pp. 157–159, 2019, doi: 10.5935/2447-0228.20190101.
- [46] W. de A. Moraes, C. A. Nahum, J. D. da G. Melo, and I. S. de Oliveira, "Analysis of physico-chemical parameters of waters of the micro basin of the igarapé of the forty in the city of Manaus," ITEGAM- J. Eng. Technol. Ind. Appl., vol. 4, no. 14, 2018, doi: 10.5935/2447-0228.20180039.
- [47] T. Omotoso and J. N. Falana, "Catchment Scale Assessment of River-Water Quality in an Ungauged Environment," J. Eng. Technol. Ind. Appl., vol. 7, no. 32, pp. 4–11, 2021, doi: 10.5935/jetia.v7i32.780.





ISSN ONLINE: 2447-0228



## RESEARCH ARTICLE

## OPEN ACCESS

# A FAST ENHANCED MEDICAL IMAGE ENCRYPTION SCHEME BASED ON 2D-CHAOTIC MAP AND IMPROVED ZIGZAG CONFUSION

Ammar Bouchemel<sup>1</sup> and Elhadi Mehallel<sup>2</sup>, Abdelaziz Rebahi<sup>3</sup>

<sup>1,2</sup> LABCAV advanced control laboratory, Faculty of Science and Technology, Université 8 mai 1945, BP 401, Guelma 24000, Algeria.

<sup>3</sup> Laboratory of Telecommunication and Smart Systems (LTSS), Faculty of Science and Technology University of Djelfa, PO Box 3117, Djelfa 17000 Algeria.

<sup>1</sup><https://orcid.org/0000-0002-2861-4819> , <sup>2</sup><https://orcid.org/0000-0001-7488-162X> , <sup>3</sup><http://orcid.org/0000-0001-8684-4754>

Email: [bouchemel.ammam@univ-guelma.dz](mailto:bouchemel.ammam@univ-guelma.dz), [e.mehallel@univ-djelfa.dz](mailto:e.mehallel@univ-djelfa.dz), [abdelaziz.rabehi@univ-djelfa.dz](mailto:abdelaziz.rabehi@univ-djelfa.dz)

## ARTICLE INFO

**Article History**

Received: February 09, 2025

Revised: March 20, 2025

Accepted: March 15, 2025

Published: April 31, 2025

**Keywords:**

Chaotic maps,  
Medical image encryption,  
Magic diffusion,  
2D-LSCM,  
Data security.

## ABSTRACT

The rapid growth of telecommunication systems has increased the need for the secure transmission of data images in the telemedicine context, ensuring confidentiality and reliability. Chaotic image cryptography, known for its ergodicity and sensitivity to initial conditions, is a robust solution against attacks on medical data in unsecured networks. This paper introduces a chaotic image encryption scheme utilizing the 2D-logistic sine-coupling map (2D-LSCM) to enhance the reliability and security level of medical encrypted images. 2D-LSCM has been used to generate chaotic matrices for achieving confusion and diffusion processes. In the confusion step, a variety of permutation operations are utilized, such as improved 2D zigzag transform, magic confusion, pixel confusion, and image rotation. We use also a pixel diffusion based on modulo arithmetic. Several simulations were carried out to prove the reliability and robustness of the proposed algorithm in protecting medical images. Additionally, we evaluate the system's performance and security, comparing it to other well-known chaos-based encryption schemes. The results obtained in the simulation demonstrated the high security of the cryptosystem, therefore our system can effectively secure multiple medical image formats and resist different security attacks.



Copyright ©2025 by authors and Galileo Institute of Technology and Education of the Amazon (ITEGAM). This work is licensed under the Creative Commons Attribution International License (CC BY 4.0).

## 1. INTRODUCTION

In the digital age, medical images, including X-rays, MRIs, CT scans, and ultrasounds, are crucial in diagnosis, treatment planning, and patient monitoring [1]. These images contain sensitive patient information, and their confidentiality is of paramount importance. The rise in cyber threats and unauthorized access to medical data has necessitated the development of robust encryption techniques to protect these images [2-4]. Traditional encryption techniques, such as Advanced Encryption-Standard (AES) [5] and Data encryption-standard (DES) [6] are not suitable for encrypting image data and unable to ensure data privacy and security [7] due to the images' dimensions, high redundancy and pixel correlation [8, 9]. There have been many approaches for encrypting image data over the last two decades, but chaos-based encryption has proven to be the most successful [10-15].

Chaotic systems are ideal candidates for encryption due to their deterministic randomness, meaning they can generate unpredictable sequences that are highly sensitive to initial conditions. Small changes in the initial state of the system result in dramatically different outcomes. This property of chaos [16] is used to scramble the image data in such a way that unauthorized decryption becomes infeasible without the correct parameters and initial conditions. Currently, chaotic systems are widely used for encrypting medical images because of their simplicity, efficiency, and ability to create high-security encryption [17, 18]. Existing chaotic maps are generally classified into two types: one-dimensional (1D) [19, 20] and high-dimensional (HD) [21, 22] maps.

1D chaotic maps have fewer parameters and variables, resulting in a smaller secret key space and lower security [23]. The most commonly used 1D chaotic maps in image encryption is the

logistic, sine, and tent map [24-25]. In contrast, high-dimensional chaotic maps feature more variables and parameters, offer a more complex structure, better chaotic performance, and higher complexity in the transformation process, which makes it more secure compared to 1D chaotic maps.

However, given their performance and implementation costs, 2D chaotic maps are regarded as excellent options for image encryption. In order to generate a chaotic matrix using initial values and parameters as secret keys, several 2D chaotic maps have been recently introduced for image encryption. For example, the 2D sine logistic modulation map (2D-SLMM) [26], 2D logistic-adjusted-sine map (2D-LASM) [27], the two-dimensional Sine infinite collapse modulation map (2D-SIMM) [28], 2D logistic-sine-coupling map (2D-LSCM) [29], Logistic Iterative Chaotic Map modulation map (2D-SLIM), and the 2D logistic-modulated-sine-coupling-logistic map (2D-LSMCL) [30].

However, these chaotic maps share a common limitation: their chaotic trajectories are narrow, unevenly distributed, and lack good ergodicity, making them vulnerable to unauthorized attacks and image information theft. While chaotic image encryption schemes provide greater security than conventional methods, their security depends heavily on the chaotic behavior of the maps used and the algorithm's structure. Researchers have shown that if the chaotic performance is inadequate or the algorithm's structure is not robust, these schemes become vulnerable to security issues and attacks.

Many chaos-based image encryption algorithms have drawbacks related to the chaotic systems used and their encryption structures. To overcome these limitations, this paper introduces a novel chaotic image encryption scheme for medical images, designed to enhance chaotic performance and increase the randomness of encrypted data, providing protection against various statistical attacks and cryptanalysis. This is achieved by utilizing the 2D-Logistic Sine-Coupling Map (2D-LSCM) in the algorithm to generate chaotic sequences, which are the used in confusion and diffusion operations. The 2D-LSCM map is a two-dimensional chaos map that offers a wider chaotic range, improved ergodicity, and greater unpredictability compared to several existing 2D maps [29]. The main contributions of this paper are outlined below.

- A novel fast chaotic image encryption algorithm that uses the 2D-LSCM map to enhance chaotic performance and provide greater security for the encrypted medical image.
- The proposed 2D-LSCM medical image encryption algorithm based on improved 2D zigzag confusion and two-level of magic confusion and pixel diffusion.
- Security analysis tests such as key sensitivity analysis, differential analysis, Shannon's entropy, local Shannon's entropy and contrast tests are conducted to validate the proposed scheme's resistance to various attacks.
- The Experimental results of these tests are compared with other prominent chaotic encryption schemes to highlight the improvements achieved by the proposed scheme.

The remainder of the paper is structured as follows: In Section 2, we present a review of existing research on medical image encryption algorithms based on chaotic systems. The 2D-LSCM and its chaotic performance evolution are presented in Section 3. Section 4 develops a new medical image encryption scheme based on 2D-LSCM. The simulation results and security performance of our scheme and its comparisons with several other image

encryption algorithms are presented in Section 5. Section 6 provides the conclusion of this paper.

## II. RELATED WORKS

Medical image encryption is a critical area of research, given the sensitive nature of medical data and the increasing reliance on digital imaging in healthcare. Chaotic maps are widely used for encryption due to their inherent properties of sensitivity to initial conditions, randomness, and low computational overhead. Currently, various technologies have been implemented in the field of medical image encryption. Below is an overview of the current state of the art with references from recent works.

Kumar and Dua [31] developed a novel chaos-based medical image encryption scheme using a sine-cosine chaotic map. Their method involves generating a pseudorandom key and constructing a cipher image through a three-phase process. Its proposed chaotic map exhibited a wider chaotic range and more complex behavior compared to existing maps, enhancing encryption robustness.

Yang et al. [32] introduced a medical image encryption scheme-based on Josephus traversing and a hyperchaotic Lorenz system. The algorithm employs a hyperchaotic sequence in both scrambling and diffusion stages, utilizing Josephus and Arnold maps for confusion. Experimental results indicated effective hiding of plaintext image information and resistance to common attack types. Another medical image encryption algorithm that utilizes a variable dimensional chaotic map was proposed by Zhang et al. in 2023 [33]. Their method features full and semi-full encryption modes, utilizing a confusion-diffusion structure with image integrity verification to balance security and time efficiency.

Dua et al., [34] proposed a medical image encryption scheme-based on an improved cosine fractional chaotic map combined with DNA operations. The scheme involves generating intermediate keys and chaotic sequences, followed by DNA encoding and diffusion. Security performances such as NPCR, UACI, and information entropy indicated the scheme's robustness.

In the same context, Demla and Anand [35] presented an encryption method that integrates wavelet transform with multiple chaotic maps. Utilizing Lorenz and logistic maps for chaotic key generation, the scheme demonstrated high security, low time complexity, and resistance against crop attacks. Zhuang et al., [36] developed a medical image encryption algorithm based on a new five-dimensional multi-band multi-wing chaotic system and QR decomposition. The method utilizes QR decomposition and chaotic sequences for encryption, demonstrating a large key space, strong key sensitivity, and effective resistance to statistical analysis attacks.

Koppu et al. [37] developed a fast image encryption system-based on chaotic cryptography. Their approach utilized a hybrid chaotic magic transform (HCMT) to generate the encrypted image from a secret key. By employing the HCMT, which combines the Lanczos algorithm with the chaotic magic transform (CMT), they achieved a correlation coefficient of 0.0012. This result surpassed the performance of the CMT method by Hua et al. [26], which had a correlation coefficient of 0.042. Jain et al. [38] present a novel chaotic encryption scheme for medical images that combines Arnold's Cat Map with 2D-LSCM, offering improved security level and time complexity over other existing methods.

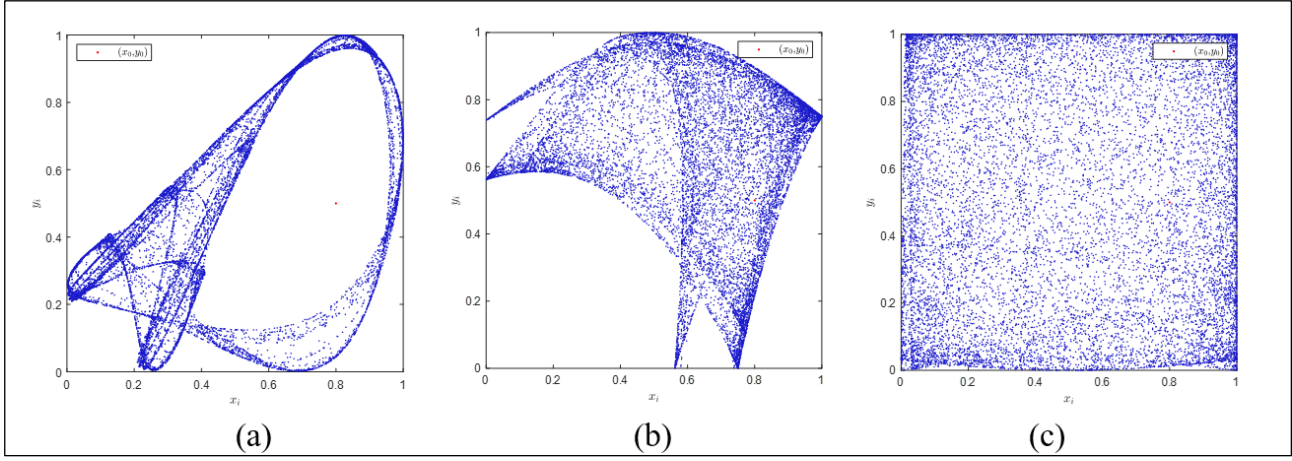


Figure 1: Trajectories of three 2D chaotic maps: (a) the 2D Logistic map with  $r = 1.19$ ; (b) the 2D-LSCM with  $\alpha = 1$ ; (c) the 2D-LSCM with  $\theta = 0.99$ .

Source: Authors, (2025).

### III. CHAOTIC MAPS

#### III.1 LOGISTIC MAP

The Logistic map is a simple yet well-known chaotic system [39], described by the iterative equation (1)

$$x_{i+1} = r(1 - x_i) \quad (1)$$

where  $x_i$  is the state variable at the  $i$ -th iteration, while  $x_i \in [0,1]$ , and  $r \in [1,4]$  is a parameter that controls the dynamic system.

#### III.2 LOGISTIC MAP

The Sine map is another 1D chaotic map defined as [40]

$$x_{i+1} = \alpha \sin(\pi x_i) \quad (2)$$

where  $x_i \in [0,1]$  is the state variable at the  $i$ -th iteration, and  $\alpha \in [0,1]$  is a parameter that controls the dynamic map.

#### III.3 SINE MAP

The two-dimensional logistic-sine-coupling map (2D-LSCM) represents a significant advancement in chaotic systems, especially in the context of image encryption [29]. This discrete chaotic map is created by combining features from both the Logistic map and the Sine map, which enhances its chaotic properties and randomness.

The traditional one-dimensional Logistic and Sine maps have certain limitations, including simplistic dynamics and low chaotic ranges, which can negatively impact some chaos-based applications [26]. However, by combining the Logistic and Sine maps, a new chaotic map with significantly more complex behavior and large chaotic range, known as the 2D-LSCM, can be created. This map is defined as [29].

$$\begin{cases} x_{i+1} = \sin(\pi(4\theta x_i(1 - x_i) + (1 - \theta)\sin(\pi y_i))) \\ y_{i+1} = \sin(\pi(4\theta y_i(1 - y_i) + (1 - \theta)\sin(\pi x_{i+1}))) \end{cases} \quad (3)$$

Where the control parameter  $\theta$  is within the range of  $[0,1]$ .

Its definition makes clear that this combination allows to extend the dimension from 1D to 2D. As a result, this approach allows for the effective integration of the complexities of the

Logistic and Sine maps, resulting in highly intricate chaotic behavior.

Figure 1 illustrates the trajectories of the 2D-logistic map (2D-LM) [41], 2D-sine logistic modulation map (2D-SLMM) [26], and the 2D-LSCM. To generate the trajectories of this three 2D maps, the initial conditions were set as  $(0.8, 0.5)$  and the control parameters are chosen as the settings that enable the corresponding chaotic maps to achieve their optimal chaotic performance. In particular, the control parameters for the 2D Logistic map, 2D-SLMM, and 2D-LSCM are set to 1.19, 1, and 0.99, respectively. As shown in the figure, the phase space covered by the 2D-LSCM trajectory is significantly larger compared to the Logistic map and 2D-LSCM. This demonstrates that the randomness exhibited by the 2D-LSCM map is high, making them suitable for secure cryptographic applications.

### IV. 2D-LSCM-BASED MEDICAL IMAGE ENCRYPTION ALGORITHM

In this section, we design the 2D-LSCM-based medical image encryption algorithm using 2D-LSCM, and its structure is illustrated in Figure 2. First, the plaintext image  $P$  is the original image and the cipher image  $C$  is the encrypted image. The secret key is used to generate initial values and control parameters for 2D-LSCM map. In the proposed scheme, we used a 2D-LSCM map to generate the chaotic matrices for confusion and diffusion operations. The confusion and diffusion operations are used to randomly shuffle pixel positions, and change pixel values of the plaintext image, respectively.

Zigzag confusion and magic confusion are used to achieve the confusion property by randomly shuffling all pixel positions. The image rotation operation involves rotating the image clockwise by  $90^\circ$  for a high-efficiency scrambling. The pixel diffusion operation is used to achieve the diffusion property by randomly changing all pixel values. To obtain random-like encryption results while avoiding the cases that 2D-LSCM may lose its chaotic behaviors in some parameter settings the proposed image encryption algorithm uses two steps of magic confusion and pixel diffusion operations. The decryption process simply reverses the encryption operations of image encryption algorithm, as shown in Figure 2.

The proposed algorithm for medical image encryption is detailed as follows:



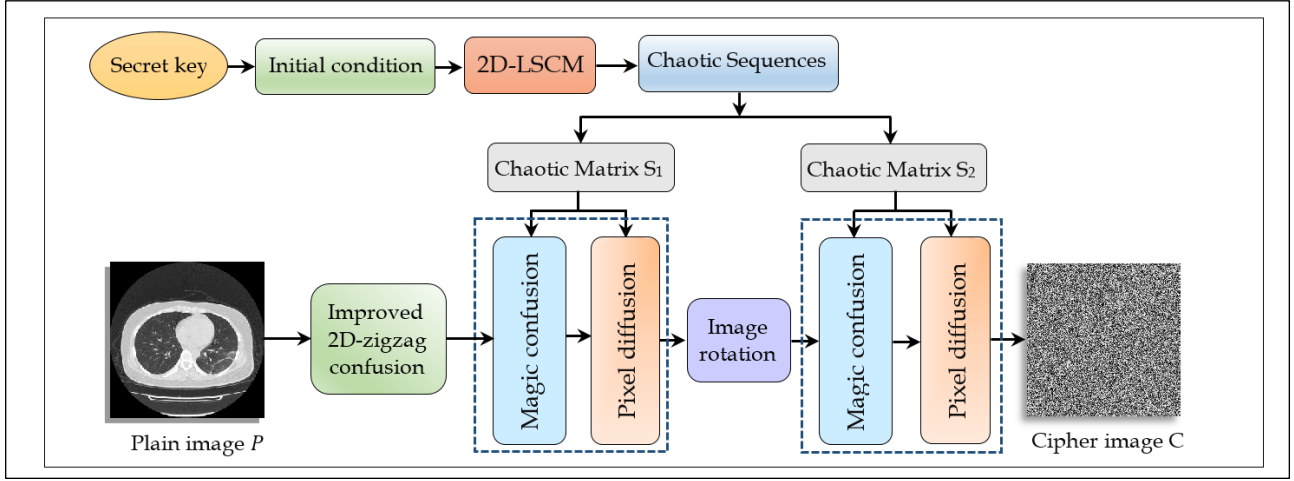


Figure 2: Block diagram of the proposed image encryption Method.

Source: Authors, (2025).

**Algorithm 1: The proposed medical image encryption scheme**

**Input:** The secret key  $K = (x_0, y_0, \theta, H, G_1, G_2)$  and the original image  $P$  with dimensions  $M \times N$ .

- 1-Transform the binary sequences  $x_0, y_0, \alpha, H$  into decimal numbers, and  $G_1, G_2$  into integers ;
- 2-Obtain two groups of initial conditions  $(x_0^1, y_0^1, \theta_1)$  and  $(x_0^2, y_0^2, \theta_2)$ ;
- 3-Generate two chaotic matrices  $S_1$  and  $S_2$  with the same size of  $P$  using 2D-LSCM with two groups of initial conditions in Step 2;
- 4-Apply zigzag confusion to the plaintext image  $P$ ;
- 5-Apply magic confusion using the chaotic matrix  $S_1$ ;
- 6-Apply pixel diffusion using the chaotic matrix  $S_1$ ;
- 7-Image rotation;
- 8-Apply magic confusion using the chaotic matrix  $S_2$ ;
- 9-Apply pixel diffusion using the chaotic matrix  $S_2$ ;

**Output:** The encrypted image  $C$

**IV.1 INITIAL CONDITION GENERATION**

The secret key  $K$  a binary sequence with a length of 256 bits which is used to generate the chaotic matrix. Its structure is shown in Figure 3. It contains information of initial values and control parameters of 2D-LSCM and can be divided into 6 parts:  $x_0, y_0, \theta, H, G_1$  and  $G_2$  are initial values and  $\theta$  is control parameter.  $H, G_1$  and  $G_2$  are designed to change the initial values and parameters to enlarge the security key space.  $x_0, y_0, \alpha$ , and  $H$  are decimal numbers which are generated by a 52-bit string  $\{b_0, b_1, \dots, b_{52}\}$  using the IEEE 754 format [41],[42], as shown in Equation 4.

$$x = \frac{1}{2^{52}} \sum_{i=1}^{52} b_i 2^{52-i} \quad (4)$$

$G_1$  and  $G_2$  are two integer coefficients generated by a 24-bit string  $\{b_0, b_1, \dots, b_{24}\}$ .

$x_0$	$y_0$	$\theta$	$H$	$G_1$	$G_2$
52bits	52 bits	52bits	52 bits	24bits	24 bits

Figure 3: The security key structure.

Source: Authors, (2025).

The equation 5 defines the initial values and control parameters of 2D-LSCM chaotic map for generating two chaotic matrices, which can be effectively employed in our algorithms to perform confusion and diffusion operations.

$$\begin{cases} x_0^{(i)} = (x_0 + G_i H) \bmod 1 \\ y_0^{(i)} = (y_0 + G_i H) \bmod 1 \\ \theta_i = (\theta + G_i H) \bmod 0.1 \end{cases} \quad (5)$$

Where the phase number  $i$  is equal to 1 or 2. In Equation 5, the two generated initial values will fall into the range of  $[0, 1]$ , and the control parameter  $\theta$  will be limited within  $[0, 1]$ . As a result, we can use the initial value  $(x_0^i, y_0^i, \text{ and } \theta_i)$  to generate a sufficiently long chaotic matrices, whose length equals the size of the original image  $P$  using the Equation 3.

In such a way, we make encryption key  $K$  to generate two initial states and control the two pseudo-random matrices produced from the 2D-LSCM for pixel confusion, magic confusion, and pixel diffusion in each phase. Therefore, the 2D-LSCM demonstrates strong chaotic performance with these settings. In our medical image encryption algorithm, users can either manually choose a 256-bit binary sequence or randomly generate a binary stream to create the security key. In our simulations and comparisons, we generate random 256-bit binary streams as the security keys, which are provided along with the encrypted results for image decryption.

In our medical image encryption algorithm, the users have the flexibility of manually selecting a binary sequence with 256 bits or randomly generating a binary stream to produce the security key. In our simulations and comparisons, we randomly generate binary streams with a length of 256 bits as the security keys that will be returned along with the encrypted results for image decryption.

**IV.2 IMPROVED 2D ZIGZAG CONFUSION**

The 2D zigzag scan [43] was generally employed to scramble the pixel positions of medical images. This operation can effectively disrupt the high correlation between adjacent pixels. The process began with the first pixel of the medical image matrix, and subsequent pixels were traversed in a 2D zigzag pattern [44]. This traversal transformed the two-dimensional matrix into a one-dimensional sequence, as illustrated in Figure 4.

In this section, we present a new scrambling algorithm inspired by the zigzag transform. The concept of the improved 2D



zigzag confusion is detailed in algorithm 3, with a numerical example provided in Figure. 4. The detailed zigzag confusion procedure is as follows:

For the pixel located in the  $i$ -th row and  $j$ -th column of the original image, its value is represented by  $P(i, j)$ . The corresponding index for this pixel is calculated as  $(M - j) \times N + i$ , denoted as  $I(i, j)$ . The typical zigzag transformation technique involves starting from one corner of the matrix array  $I(i, j)$ , moving along the diagonal to its end, scanning all elements parallel to the diagonal to form a one-dimensional vector, and then reconstructing the vector based on predetermined rules.

#### Algorithm 3: Improved 2D zigzag confusion

**Input:** the original image  $P$  with dimensions  $M \times N$ .

1-Applz zigzag transform to the plaintext image  $P$ , obtain two-dimensional array  $I$  and corresponding one-dimensional index array  $I_V$ ;

2-Reshape the matrix  $P$  into a vector array  $P_V$ ;

3-for  $i = 1$  to  $M \times N$  do

4-  $P_{1V} = P_V(I_V(i))$ ;

5-end for

6-Reshape the vector  $P_{1V}$  into a matrix array  $P_2$

**Output:** Zigzag confusion result  $P_2$ .

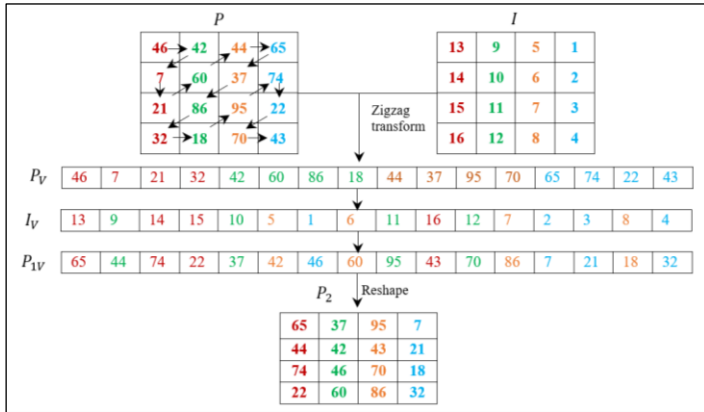


Figure 4: A numerical example of the improved 2D zigzag confusion.

Source: Authors, (2025).

### IV.3 MAGIC CONFUSION

Digital images typically exhibit high information redundancy due to the strong correlations between neighboring pixels. To disrupt these correlations, this section proposes employing a magic confusion method based on a chaotic matrix to randomly alter the positions of image pixels.

The shuffling procedure using magic confusion based chaotic magic confusion can be detailed as follows [26]:

•**Step 1:** the original image  $P$  and chaotic matrix  $S$  with the same size of  $M \times N$ , which is generated using the 2D-LSCM with the initial state;

•**Step 2:** Sort each column of  $S$  in ascending order to obtain the sorted matrix  $\hat{S}$  and its corresponding index matrix  $O$ . The generation of the index matrix  $O$  from a chaotic matrix  $S$  is then defined as follows

$$O(i, j) = k \quad \text{for } \hat{S}(i, j) = S(i, j) \quad (6)$$

where  $i, j$ , and  $k$  are integers,  $1 \leq i, k \leq M$  and  $1 \leq j \leq N$

•**Step 3:** Set row index  $i = 1$ ;

•**Step 4:** Connect the pixels in  $P$  with positions  $\{(P_{i,1}, 1), (P_{i,2}, 2), (P_{i,3}, 3), \dots, (P_{i,N}, N)\}$  using the locations  $\{(O_{i,1}, 1), (O_{i,2}, 2), (O_{i,3}, 3), \dots, (O_{i,N}, N)\}$  into a circle;

•**Step 5:** Shift these pixels  $i$  positions to the left;

•**Step 6:** Iterate Step 3 to Step 6 up to  $i = M$ , we can obtain the magic confusion result  $T$ .

To clarify the process of magic confusion using 2D-LSCM, an illustrative numerical example with an image size of  $4 \times 4$  is provided, as illustrated in Figure 5.

The magic confusion procedure have the ability to modify the pixel positions in the original image  $P$  based on the chaotic matrices  $S_1$  et  $S_2$  produced by 2D-LSCM. It randomly links pixels from different rows and columns into circular groups and then shifts their positions within these circles.

### IV.4 IMAGE ROTATION

As mentioned in the previous section, the scrambling process only rearranges the  $L^2 \times L^2$  portion of the image, leaving the remaining pixels with strong correlations between them. To ensure that all the pixels in the image are shuffled during encryption, image rotation is introduced as another operation of scrambling. This is achieved by rotating the image by  $90^\circ$  in the anticlockwise direction. The rotation angle of the image does not significantly affect the final encryption parameter values, so the image can be rotated by any random angle. The primary purpose of rotation is to displace the image pixels from their original positions. In the decryption step, the scrambled image is rotated clockwise to reverse these changes and restore the pixels to their original positions. Therefore, this operation not only shifts the pixel positions but also changes their spatial arrangement, making it more difficult to reverse-engineer the image.

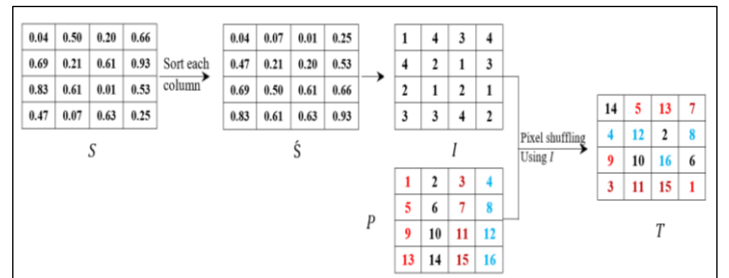


Figure 5: An example of the pixel shuffling processes using magic confusion.

Source: Authors, (2025).

### IV.5 PIXEL DIFFUSION

An encryption algorithm with good diffusion properties can effectively resist chosen plaintext attacks. Diffusion property ensures that even a minor difference between two plaintexts, when encrypted with the same key, produces completely different cipher images. This process spreads small changes in the plain image across all pixels in the cipher image. It involves altering the current pixel based on the previous pixel and a randomly generated value. To perform the diffusion operation, Let the scrambling result matrix  $T$  and the generated chaotic matrix  $S$  both have dimensions of  $M \times N$ . Then, the pixel diffusion result is defined by the mathematical eq. (7) [45].

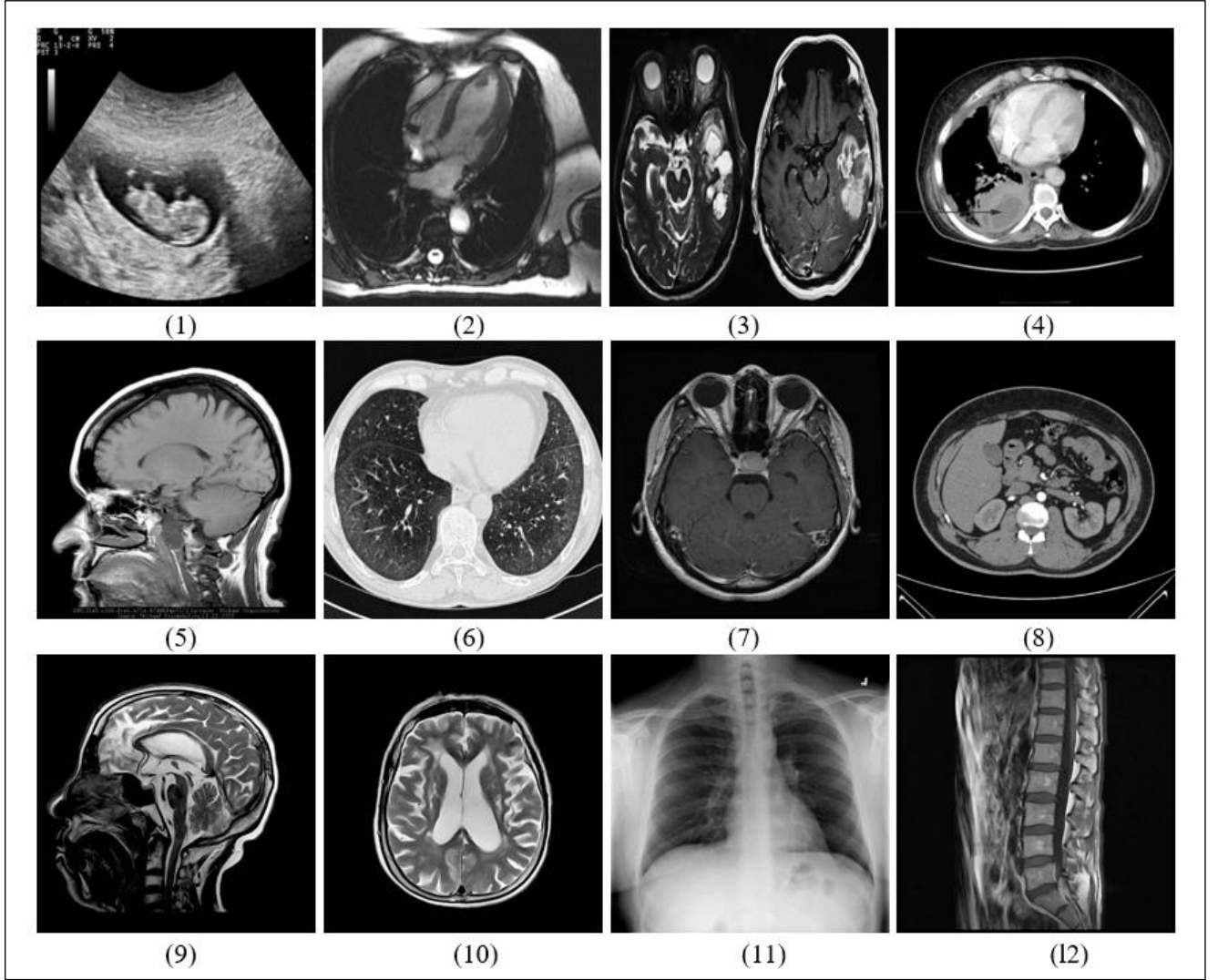


Figure 6: Examples of medical images used to test the proposed algorithm.

Source: Authors, (2025).

$$C_{i,j} = \begin{cases} (T_{i,j} + T_{M,N} + S_{i,j}) \bmod F, & \text{if } i = 1, j = 1 \\ (T_{i,j} + T_{M,j-1} + S_{i,j}) \bmod F, & \text{if } i = 1, j = 1 \sim N \\ (T_{i,j} + T_{i-1,j} + S_{i,j}) \bmod F, & \text{if } i = 1 \sim M \end{cases} \quad (7)$$

where  $F$  denotes the number of intensity levels, e.g.  $F = 256$  if a pixel is represented by 8 bits.  $S$  is a chaotic matrix generated by 2D-LSCM with the initial state  $(x_0^i, y_0^i, \theta_i)$  ( $i = 1$  in the first phase and  $i = 2$  in the second phase). It has the same size and its elements are represented as the same data format as the pixels in  $T$ . In the decryption process, the inverse operation of Eq. (7) is defined as

$$T_{i,j} = \begin{cases} (C_{i,j} - T_{M,N} - S_{i,j}) \bmod F, & \text{if } i = 1, j = 1 \\ (C_{i,j} - C_{M,j-1} - S_{i,j}) \bmod F, & \text{if } i = 1, j = 1 \sim N \\ (C_{i,j} - C_{i-1,j} - S_{i,j}) \bmod F, & \text{if } i = 1 \sim M \end{cases} \quad (8)$$

## V. SIMULATION RESULTS AND SECURITY ANALYSIS

This section simulates the proposed medical image encryption algorithm based on 2D-LSCM map and evaluates its performance under the MATLAB implementation. A variety of medical images, including MRI, X-ray, CT, and ultrasound images, successfully encrypted using our algorithm. The majority of test

medical images used in our experiments are chosen from the Open Access Open-I images dataset (<https://openi.nlm.nih.gov>). For simplicity, we use twelve images, displayed in Figure 6, as examples for our experiments and security analysis. In Figure 6, the images in (1)-(4) have dimensions of  $256 \times 256$ , the images in (5)-(8) have dimensions of  $512 \times 512$ , but the size of the last four images is  $1024 \times 1024$ .

### V.1 COMPUTATION TIME ANALYSIS

In this section, we assess the encryption and decryption times of the developed image encryption algorithm and compare its execution times with those of four recent schemes. All the algorithms, including the developed one, are implemented in the MATLAB environment (R2021b), and the experiments are conducted on a computer with an Intel i5-7300U CPU @ 2.60GHz, 8 GB of RAM, and the Windows 10 operating system. Table 1 presents a comparison of the encryption and decryption times of various image encryption algorithms for different image sizes. The simulation results indicate that our proposed algorithm outperforms the others in terms of total computation time. Furthermore, our encryption algorithm not only offers better security but also executes faster than the other advanced image encryption schemes.

Table 1: Comparison of encryption and decryption times for different encryption algorithms.

Test image	Size of the image	Computation Time (second)				
		Ref. [26]	Ref. [23]	Ref. [29]	Ref. [38]	Our
Image 3	256 × 256	2.12	4.21	1.75	1.38	1.66
Image 5	512 × 512	3.97	13.73	2.71	2.30	2.23
Image 9	1024×1024	8.24	102.64	4.76	5.91	4.35

Source: Authors, (2025).

## V.2 SECURITY KEY ANALYSIS

Evaluating performance metrics is essential for assessing the effectiveness and security of medical image encryption techniques. Various key indicators are typically used to evaluate these algorithms, such as the key space and key sensitivity. However, the users are flexible to choose any other settings by considering the tradeoff between the security level and computation cost.

### V.2.1 SECURITY KEY SPACE

One of the typical fundamental elements used to evaluate encryption algorithms is key space, which refers to the total number of possible keys that can be generated for an encryption algorithm. A substantial key space is crucial for protection against brute-force attacks, making it a cornerstone of effective encryption systems. Generally, a key space exceeding  $2^{100}$  is required to ensure sufficient defense against such threats [46]. In theory, a larger key space enhances the algorithm's security. The proposed medical image encryption algorithm uses a security key of 256 bits, resulting in a key space of  $2^{256}$ . This key space is large enough to withstand brute-force attacks, given the computational power of current computers.

### V.2.2 KEY SENSITIVITY ANALYSIS

Another important metric that is used to evaluate encryption algorithms is key sensitivity, which measures how responsive the encryption algorithm is to changes in initial conditions or keys. In chaotic systems, even minor variations can lead to dramatically different results, ensuring that each encrypted image remains unique and secure. This characteristic helps to undermine potential attacks that rely on predictability. However, the secret key should exhibit sensitivity during both the encryption and decryption processes. This means that a single-bit difference between two secret keys will lead to completely different cipher-images during encryption and result in totally different decrypted images during the decryption process.

Figures 7 display the key sensitivity analysis for the encryption and decryption processes, respectively.  $K_2$  and  $K_3$  are two secret keys derived from  $K_1$  with one bit difference. As shown in Figure 7, when the plain-image is encrypted using  $K_2$ , and  $K_3$ , the resulting cipher-images are completely different as shown in Figure 7(b) and 7(c). Figure 7(e) illustrates that the cipher-image can only be fully reconstructed with the correct secret key, and even a small difference in the secret keys produces entirely different decrypted images, as seen in Figure 7(f) and 7(g). Therefore, our medical image encryption algorithm is highly sensitive to changes in its secret key in both the encryption and decryption processes.

## V.3 STATISTICAL ANALYSIS

In this section, we evaluate the resistance of our medical image encryption scheme to statistical attacks by examining four aspects: histogram, correlation, information entropy, and local Shannon entropy. This section presents several experiments to demonstrate the reliability of our proposed algorithm.

### V.3.1 HISTOGRAM ANALYSIS

Histogram analysis is used to evaluate how effectively the algorithm randomizes pixel values within encrypted images. An ideal histogram should display a uniform distribution across pixel intensity values, indicating successful scrambling of the image data while preventing any leakage of information about the original content. The histograms of the original images and their corresponding encrypted images are shown in Figure 8. The results clearly indicate that the encrypted images exhibit a much more uniform distribution compared to the original images, indicating a high resistance to statistical attacks.

### V.3.2 INFORMATION ENTROPY ANALYSIS

The randomness of the pixels in the encrypted image is a crucial factor in ensuring the security of the encryption scheme. This randomness can be effectively measured using Local Shannon Entropy [47], calculated using the formula provided in Eq. (9).

$$H(x) = - \sum_{i=0}^{2^n-1} Pr(x_i) \log_2 Pr(x_i) \quad (9)$$

Here,  $Pr(x_i)$  is the probability of a specific symbol  $x$ , and  $n$  denotes the number of bits in a pixel.

For an encrypted image to be secure against attacks, its pixel distribution must be completely uniform. When the pixel distribution of an  $n$ -bit image is fully uniform, the entropy of the image equals  $n$ . In this study, as we are working with 8-bit images, the objective is to achieve entropy values close to 8, ensuring a uniform pixel distribution and maximizing security [47].

Table 2. shows the information entropy values of twelve medical images with different sizes encrypted by several image encryption algorithms. As shown in Table 4, our encryption scheme achieves a mean entropy value of 7.998884, which is closer to 8 compared to other schemes used in comparison, indicating superior performance. These result indicates that the proposed scheme can encrypt images into cipher-images with good randomness.

### V.3.3 LOCAL SHANNON ENTROPY

Global Shannon entropy, discussed in the previous subsection as information entropy, has certain limitations such as inaccuracy, inconsistency, and low efficiency [47]. To address these issues, the local Shannon entropy (LSE) has been introduced, which can provide a precise characterization of the randomness in image pixels. For a data image  $I$ , we divide the image  $I$  into  $k$  non-overlapping sub-image blocks  $S_1, S_2, \dots, S_k$ , each sub-image block containing  $T_B$  pixels. Then, the LSE is defined as:

$$H_{k,T_B}(I) = - \sum_{i=0}^k \frac{H(S_i)}{k} \quad (10)$$

Here  $H(S_i)$  represents the Shannon entropy of image block  $S_i$ .



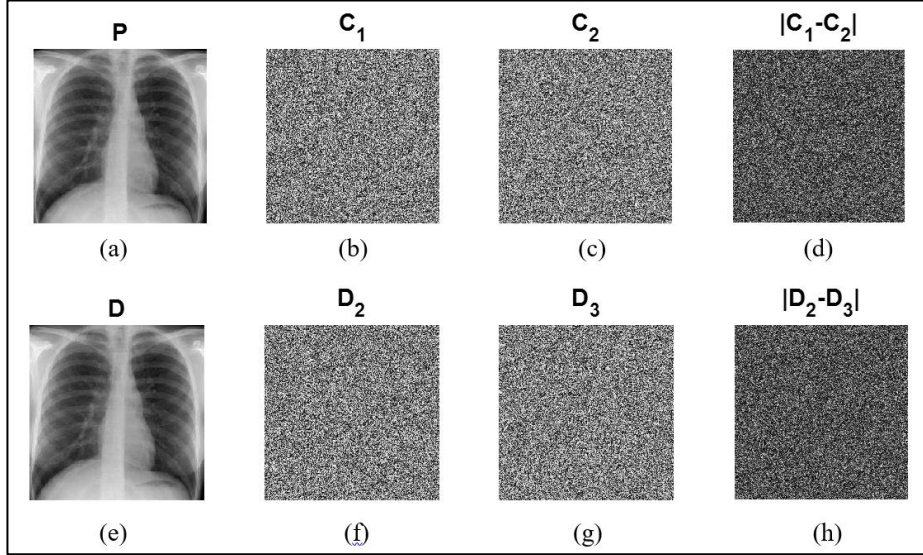


Figure 7: Key sensitivity analysis. (a) Plaintext image  $P$ ; (b) ciphertext image  $C_1$ , (c) ciphertext image  $C_2$ ; (d) difference of ciphertext images:  $|C_1 - C_2|$ ; (e) decrypted image  $D_1$ , (f) decrypted image  $D_2$ , (g) decrypted image  $D_3$  and (h) difference of decrypted images:  $|D_2 - D_3|$ .

Source: Authors, (2025).

In our experiment, we certain medical images from the OPEN-I image dataset for simulation to validate the robustness of our scheme. To enable comparisons with other encryption algorithms and following the recommendation in [47], we set the parameters  $k = 30$ , and  $T_B = 1936$  with a significance level of  $\alpha = 0.05$  [48-50]. Under these settings, the ideal LSE value is 7.902469317, and LSE test is considered successful if the score for a ciphered image falls between 7.901901305 and 7.903037329 [47].

Table 3 presents the LSE results, showing that the pass rate of our algorithm is 12/12, which is notably higher compared to 8/12 [26], 7/12 [23], and 8/12 [29], and 10/12 [38]. Additionally, the average LSE value for ciphered images generated by our algorithm is 7.902467, with a standard deviation of 0.000349. These results indicate that the average LSE value from our proposed scheme is very close to the theoretical value of 7.902469317, with the smallest standard deviation among the compared methods. Therefore, our scheme demonstrates superior security. This means that the encrypted images by our scheme have better random distributions. This suggests increased unpredictability in pixel values, enhancing security against statistical attacks.

### V.3.4 PIXEL CORRELATION ANALYSIS

Correlation reflects the linear relationship between two random variables and is used to measure the relationship between adjacent pixels in image processing. In plain-images, the pixels tend to have a high correlation with their neighboring pixels in all direction. Therefore, it is important to ensure that the correlation between adjacent pixels is low enough to prevent recognition in horizontal, vertical, or diagonal directions. Therefore, the image encryption algorithm aims at breaking these pixel correlations in the original images and transforming them into noise-like encrypted images with little or no correlations. Generally, having a correlation coefficient close to 0 is one of the important performance indicators of an excellent encryption scheme. The values of the correlation coefficient can be calculated by

$$C_{xy} = \frac{cov(x, y)}{\sqrt{D(x)} \times \sqrt{D(y)}} \quad (11)$$

where

$$cov(x, y) = \frac{1}{N} \sum_{i=0}^N (x_i - E(x))(y_i - E(y)) \quad (12)$$

and

$$D(x) = \frac{1}{N} \sum_{i=0}^N (x_i - E(x))^2, \quad E(x) = \frac{1}{N} \sum_{i=0}^N x_i \quad (13)$$

where  $x_i$  and  $y_i$  present the adjacent pixels,  $D(\cdot)$  is variance of corresponding pixels,  $E[\cdot]$  is the expectation value. If two sequences  $x$  and  $y$  have high correlations, their correlation value is close to 1. Otherwise, it is close to 0.

In our test, we randomly select 2000 pairs of neighbor pixels from original and encrypted images and we analyses correlation from adjacent pixels along with the horizontal, vertical and diagonal directions. Figure 9 plots the distributions of the pixel sequence pairs,  $X$  and  $Y$  of the original image and its encrypted version generated by the proposed algorithm. As shown in Figure 9, the horizontal axis represents the concentration of randomly selected pixels, while the vertical axis shows the intensity of their corresponding neighboring pixels. In the original image, the neighboring pixel pairs are distributed or near the diagonal line, indicating that the pixels are similar or nearly identical, reflecting a strong correlation between adjacent pixels. In contrast, the neighboring pixel pairs of the encrypted image are distributed randomly across the entire data range, demonstrating an extremely low correlation in the encrypted image.

Table 5 compares correlations of the original images with its encrypted versions generated by the proposed medical image encryption algorithm. The results of the original image are close to 1 while the ciphertext image's results are close to 0. These further verify that the encrypted image by the medical image encryption algorithm has an extremely low correlation. The results indicate that this can effectively eliminate the correlation between neighboring pixels in an input image.



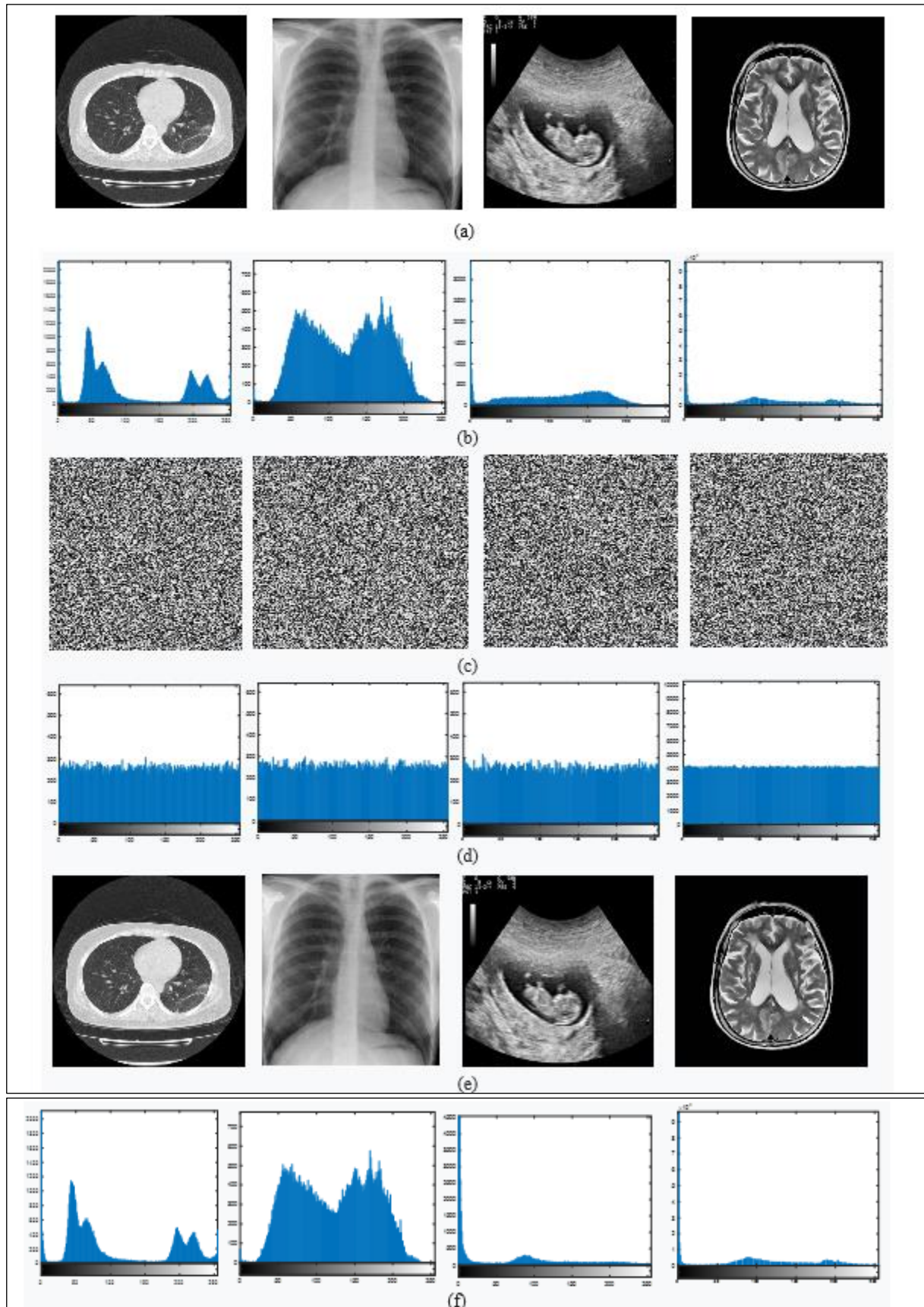


Figure 8: Simulation result of histogram analysis of some images. (a) The original images; (b) the histogram of (a); (c) the encrypted images; (d) the histogram of (c); (e) the decrypted images; (f) the histogram of (e).

Source: Authors, (2025).

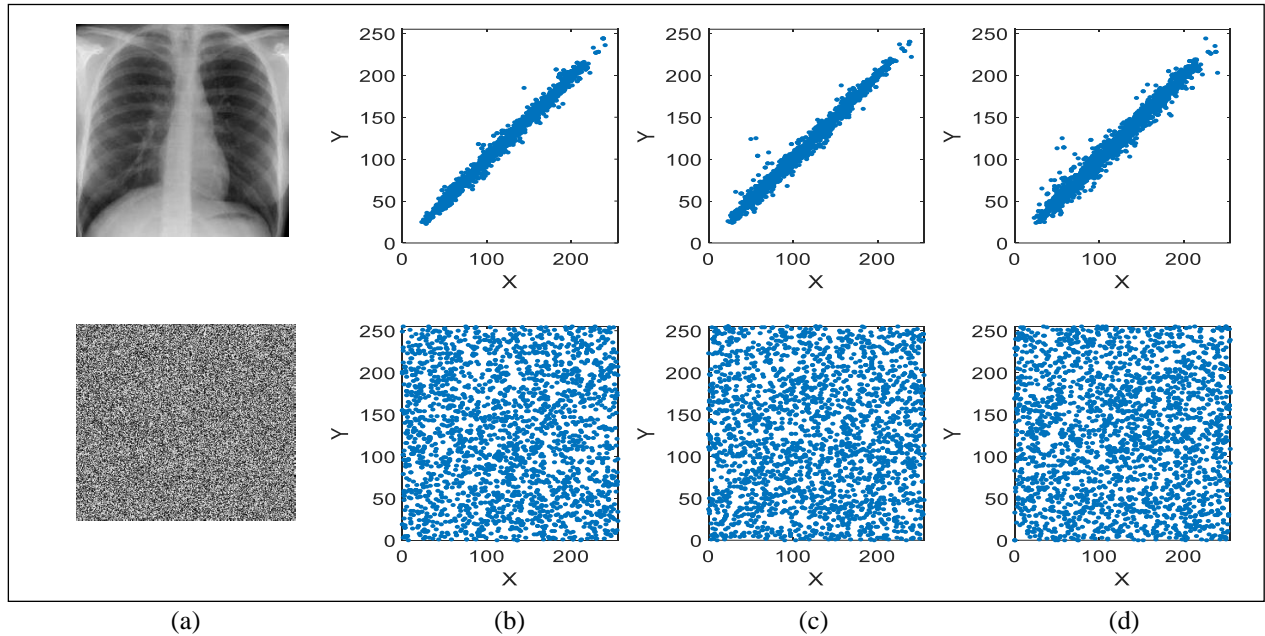


Figure 9: Distributions of adjacent pixel sequence pairs of (a) the plain-image and its cipher-image along with the (b) horizontal, (c) vertical, and (d) diagonal directions, respectively.

Source: Authors, (2025).

Table 2: Comparison of information entropy values for various encrypted images.

Test image	Size of the image	Original image	Encrypted image				
			Ref. [26]	Ref. [23]	Ref. [29]	Ref. [38]	Our algorithm
Image 1	256 × 256	6.018538	7.997298	7.997468	7.997207	7.997504	7.997500
Image 2		6.670125	7.997163	7.997241	7.997547	7.997385	7.997445
Image 3		6.864571	7.997214	7.997274	7.997055	7.997355	7.997390
Image 4		4.867913	7.997508	7.997061	7.997466	7.997128	7.997567
Image 5	512 × 512	5.529474	7.999429	7.999382	7.999297	7.999220	7.999316
Image 6		7.249175	7.999301	7.999299	7.999320	7.999284	7.999372
Image 7		6.033099	7.999357	7.999328	7.999305	7.999392	7.999304
Image 8		4.467764	7.999296	7.999407	7.999296	7.999300	7.999325
Image 9	1024 × 1024	4.613337	7.999819	7.999796	7.999843	7.999821	7.999849
Image 10		4.046626	7.999826	7.999820	7.999806	7.999846	7.999854
Image 11		7.677182	7.999846	7.999824	7.999815	7.999841	7.999849
Image 12		6.342696	7.999819	7.999815	7.999858	7.999817	7.999845
<b>Mean</b>		5.86504167	7.998823	7.9988091	7.9988179	7.9988244	7.9988846
<b>Std</b>		1.17006255	0.0011497	0.0011639	0.001136	0.001121	0.001064

Source: Authors, (2025).

Table 3: The LSE scores of cipher-images encrypted by different image encryption schemes.

Test image	Size of the image	LSE values of encrypted images				
		Ref. [26]	Ref. [23]	Ref. [29]	Ref. [39]	Our algorithm
Image 1	256 × 256	7.902104	7.903087	7.902114	7.902997	7.902732
Image 2		7.902343	7.900276	7.901377	7.902443	7.902637
Image 3		7.901306	7.900218	7.902113	7.902936	7.902304
Image 4		7.904267	7.900625	7.902801	7.901417	7.901921
Image 5	512 × 512	7.902099	7.902357	7.905825	7.899788	7.902898
Image 6		7.902596	7.901037	7.901908	7.902434	7.902831
Image 7		7.902716	7.902308	7.905475	7.901833	7.902070
Image 8		7.899989	7.901197	7.902024	7.902961	7.902322
Image 9	1024 × 1024	7.903846	7.901467	7.900868	7.902690	7.902111
Image 10		7.902185	7.902204	7.901187	7.902942	7.902432
Image 11		7.901439	7.903602	7.902529	7.903084	7.902351
Image 12		7.902638	7.902749	7.903081	7.902112	7.902998
<b>Mean</b>		7.902294	7.901760	7.902608	7.902303	7.902467
<b>Std</b>		0.0011199	0.0011192	0.001558	0.000948	0.0003495
<b>Pass/All</b>		8/12	7/12	8/12	10/12	12/12

Source: Authors, (2025).

Table 4: Correlation coefficients for various encrypted images.

Test image	Size of the image	Original image			Encrypted image		
		Horizontal	Vertical	Diagonal	Horizontal	Vertical	Diagonal
Image 1	256 × 256	0.979429	0.978050	0.961882	-0.022281	0.015536	0.035114
Image 2		0.980633	0.974735	0.957295	0.000035	0.007166	-0.037567
Image 3		0.885755	0.953481	0.853835	-0.003321	0.004171	-0.003195
Image 4		0.971358	0.966191	0.934692	-0.000554	0.000274	0.005378
Image 5	512 × 512	0.986619	0.985892	0.973654	-0.009633	0.001169	-0.001427
Image 6		0.987208	0.986487	0.974914	-0.009005	0.009597	0.007787
Image 7		0.987514	0.984080	0.970312	0.004144	0.021803	-0.001043
Image 8		0.968627	0.948725	0.940331	0.005555	0.004621	0.007703
Image 9	1024 × 1024	0.992121	0.993768	0.983130	-0.024726	0.028376	-0.009513
Image 10		0.992848	0.996047	0.989666	0.040142	-0.012564	0.013787
Image 11		0.998847	0.999121	0.998515	-0.001969	0.004487	-0.001418
Image 12		0.995155	0.998722	0.994371	-0.006361	0.009663	0.004471
Mean		0.97717617	0.98044158	0.9610498	-0.002331	0.0078583	0.0016731

Source: Authors, (2025).

Table 5: Comparison of correlation values of encrypted images for various algorithms.

Test image	Size of the image	Direction	Encrypted image				
			Ref. [26]	Ref. [23]	Ref. [29]	Ref. [38]	Our algorithm
Image 3	256 × 256	Horizontal	-0.005232	-0.021848	0.025001	-0.038534	0.000035
		Vertical	0.003435	-0.002923	-0.028009	0.005827	0.007494
		Diagonal	-0.030729	0.014174	-0.001203	0.003749	-0.003195
Image 5	512 × 512	Horizontal	-0.000637	0.028980	0.006032	-0.004001	-0.009661
		Vertical	0.011822	-0.015811	0.004157	-0.013116	-0.045108
		Diagonal	-0.016458	0.013305	0.012856	0.033941	-0.008454
Image 9	1024 × 1024	Horizontal	0.020733	0.027330	0.021507	-0.003379	0.000213
		Vertical	0.009093	0.006693	-0.024616	0.009539	-0.000159
		Diagonal	-0.031264	0.017534	-0.009884	0.036621	-0.009210
Mean			-0.00436	0.0074927	0.000649	0.0034052	0.000276

Source: Authors, (2025).

#### V.4 RESISTANCE TO DIFFERENTIAL ATTACK

The differential attacks analyze how variations in plaintexts influence the corresponding ciphertexts. For an image encryption algorithm, its resistance to such attacks can be evaluated quantitatively using the Number of Pixel Change Rate (NPCR) and the Unified Average Change Intensity (UACI) metrics. NPCR quantifies the number of differing pixels between two images, while UACI measures the intensity of pixel value differences between the two images. Let  $C_1$  and  $C_2$  represent two cipher-images encrypted from plain-images that differ by only one bit. The NPCR and UACI are defined as follows:

$$\text{NPCR} = \frac{1}{M \times N} \sum_{i=0}^M \sum_{j=0}^N D(i, j) \times 100(\%) \quad (14)$$

and

$$\text{UACI} = \frac{1}{M \times N} \sum_{i=1}^M \sum_{j=1}^N \frac{C_1(i, j) - C_2(i, j)}{2^l - 1} \times 100(\%) \quad (15)$$

Here,  $M$  and  $N$  denote the width and height of the image, respectively, while  $l$  represents the number of binary bits per pixel.  $D$  represents the difference between  $C_1$  and  $C_2$ , defined as

$$D(i, j) = \begin{cases} 0, & \text{if } C_1(i, j) = C_2(i, j) \\ 1, & \text{if } C_1(i, j) \neq C_2(i, j) \end{cases} \quad (17)$$

The theoretical values of NPCR and UACI is recorded as 99.6094% and 33.4635%, respectively [51].

The NPCR and UACI test results of various medical images for different encryption algorithms are shown in Table 6. It can see from the Table 6 that our scheme achieves high performance by having NPCR values no less than 99.5810 % and UACI values no less than 33.461%. Moreover, we can see that our medical image encryption scheme achieves excellent NPCR and UACI results with a mean score of 99.6085% for NPCR and 33.5665% for UACI, which are close to ideal values. Thus, we can conclude that the proposed scheme is well resistant to differential attacks.

#### V.5 ROBUSTNESS TO RESIST DATA LOSS AND NOISE ATTACKS

When a digital image is transmitted through networks or stored in the physical media, it is easily contaminated by noise or may have the data loss. An image encryption algorithm should have the robustness to resist noise and the data loss. In the proposed algorithm, the encryption and decryption processes are asymmetric. In the encryption process, one pixel change in the plaintext image will spread over all pixels in the ciphertext image. However, in the decryption procedure, the change of one pixel in the ciphertext image can affect only a few pixels in the recovered result. Thus, the proposed medical image algorithm can decrypt the ciphertext image with noise or data loss.

In the first experiment, we simulate a scenario where medical images are illegally intercepted during transmission and subjected to varying degrees of data loss. Specifically, we examine four cases where 1/16, 1/8, 1/4, and 1/2 of the encrypted medical image 5 are obscured. Figure 10(a) illustrates the encrypted medical images and its corresponding decrypted images, while Figures 10(b)-(d) the encrypted images with 1/16 loss, 1/8 loss, 1/4 loss, and the corresponding restored images using the correct keys.



It is evident that even with minor data loss, useful information about the original image cannot be reconstructed from the decrypted output. This indicates that even if the correct key is compromised and an intruder intercepts most of the encrypted data, the details of the original image remain unrecoverable.

In the second experiment, it is assumed a scenario where images are subjected to varying kinds of noises during transmission. Salt-and-pepper noise with a value of density equal

0.01, Gaussian, and speckle noises with a value of variance equal 0.01 are added to the encrypted medical image no 5. The noisy encrypted images are then decrypted, and the resulting outputs are displayed in Figures 11. It is observed that for encrypted images affected by noise, the decrypted output remains unrecognizable, even when the correct decryption key is used.

Table 6: The NPCR and UACI results of various images for different encryption algorithms.

Test image	Ref. [26]		Ref. [23]		Ref. [29]		Ref. [38]		Proposed algorithm	
	NPCR	UACI	NPCR	UACI	NPCR	NPCR	NPCR	UACI	NPCR	UACI
Image 1	99.6749	33.6001	99.5971	33.5059	99.6093	99.6093	99.5907	33.2772	99.6093	33.4908
Image 2	99.6139	33.5385	99.6475	33.4780	99.6078	99.6078	99.6134	33.5133	99.6078	33.4949
Image 3	99.6215	33.6963	99.6109	33.5487	99.6368	99.6368	99.6310	33.8715	99.6109	33.4151
Image 4	99.5788	33.5234	99.6475	33.3194	99.6139	99.6139	99.5884	33.6033	99.6032	33.4612
Image 5	99.5006	32.4290	99.6101	33.4249	99.6147	99.6147	99.6190	33.4522	99.6147	33.4802
Image 6	99.6181	33.5518	99.6150	33.4572	99.6177	99.6177	99.6252	33.4834	99.6177	33.4744
Image 7	99.6089	33.4472	99.6208	33.4043	99.6143	99.6143	99.5950	33.5015	99.6017	33.4655
Image 8	99.3354	31.6879	99.5895	33.4856	99.6231	99.6231	99.6081	33.5255	99.6059	33.5032
Image 9	99.6091	33.5007	99.6216	33.4638	99.6109	99.6109	99.5800	33.4434	99.6093	33.4654
Image 10	99.6100	33.4661	99.6106	33.4939	99.6061	99.6061	99.6108	33.4589	99.6057	33.4757
Image 11	99.5988	33.4693	99.6031	33.4310	99.6090	99.6090	99.6045	33.4361	99.6090	33.4676
Image 12	99.6081	33.4562	99.6169	33.4510	99.6210	99.6210	99.5180	33.3290	99.5810	33.4838
Mean	99.5815	33.2805	99.6158	33.4553	99.6150	33.5086	99.5986	33.4912	99.6063	33.4731
Std	0.08694	0.59641	0.01746	0.05790	0.01293	0.06059	0.02967	0.14740	0.00914	0.02240

Source: Authors, (2025).

Table 7: Comparison of PSNR values for various schemes under different noise conditions

Schemes	Variance	PSNR [dB]		
		Gaussian noise	Salt and pepper noise	Speckle noise
Ref. [26]	0.001	29.5764	54.1853	30.7218
Ref. [29]		29.2577	29.0399	28.6587
Our scheme		31.4438	54.1853	29.0134
Ref. [26]	0.005	29.2858	40.3832	31.8049
Ref. [29]		29.0933	29.2161	29.0665
Our scheme		31.6086	48.1647	30.9632

Source: Authors, (2025).

Table 7 presents a comparison of PSNR values for different image encryption schemes under different noise conditions when the grayscale medical image 4 of size 512 x 512 is used as a test image. Despite the image after encryption being affected by various kinds of noise with a variance value equal to 0.001, the decrypted images manage to retain much of the original image information. Experimental results validate the efficacy of the encryption algorithm, demonstrating its resilience against various kinds of attacks while providing robust encryption. This indicates that our proposed scheme is effective against noise attacks. Therefore, our method not only demonstrates strong resistance to data loss and noise attacks but also exhibits robust performance overall.

## VI. CONCLUSIONS

Telemedicine facilitates remote monitoring, diagnosis, and first-aid administration, offering cost-effective healthcare solutions, but the transmission of high-resolution medical images through public networks raises concerns about data security. Traditional encryption methods like DES and AES are insufficient for digital image encryption, leading to the development of chaos-based encryption schemes as a promising alternative to secure image transmission and storage. This paper utilizes the 2D-LSCM chaotic map, derived from Sine and Logistic maps, to generate security keys for encryption and decryption. The 2D-LSCM is chosen for its wider chaotic range, better ergodicity, hyperchaotic properties, and superior chaotic performance compared to existing maps. To demonstrate the performance of 2D-LSCM in medical data security applications, a new fast medical image encryption algorithm is designed. This algorithm is essentially based on improved 2D zigzag confusion, magic confusion, and pixel diffusion. The confusion operations can rapidly shuffle adjacent pixels in an image in both the row and column directions, and the latter can achieve the diffusion property by spreading a few original image changes over the entire encrypted image. Simulation results confirm that our scheme efficiently encrypts various medical images into unrecognizable encrypted images with high security and low run time, outperforming some advanced encryption algorithms. Given its high efficiency and security level, future research will explore its application in other media data such as video encryption.



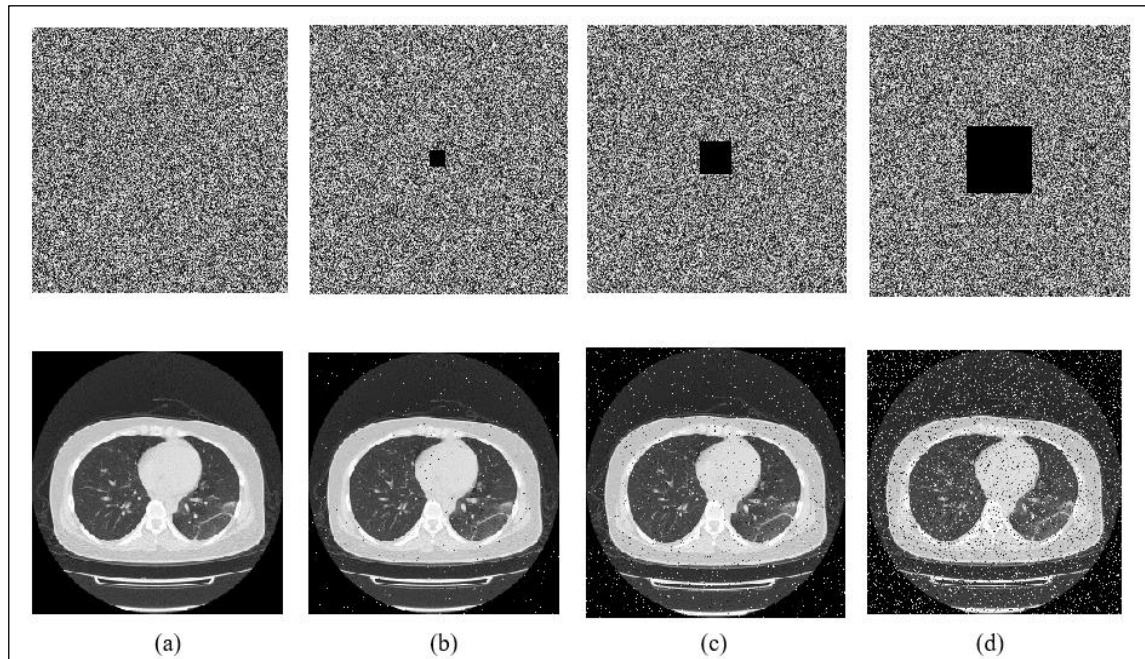


Figure 10: Robustness results to loss data attack. (a) The encrypted original image and its decrypted image; (b)-(d) the encrypted images with 1/16 loss, 1/8 loss, 1/4 loss, and the corresponding restored images.

Source: Authors, (2025).

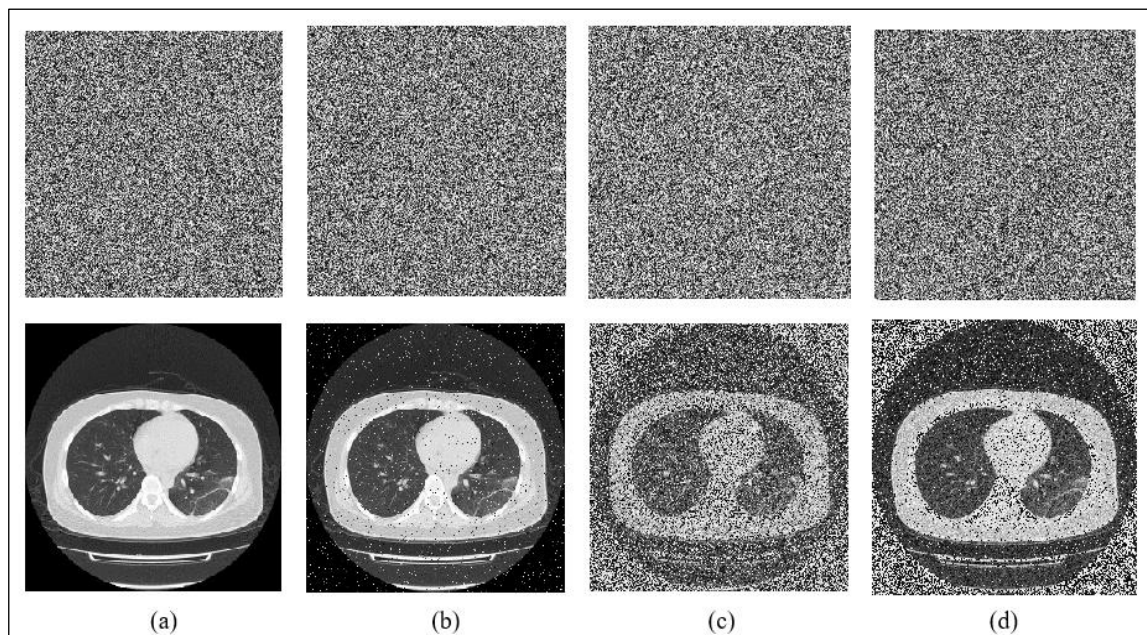


Figure 11: Robustness results to noise attack. (a) The encrypted original image and its decrypted image; (b)-(d) the encrypted images with 1% salt and pepper, 1% Gaussian noise, 1% speckle noise, and the corresponding restored images.

Source: Authors, (2025).

## VII. AUTHOR'S CONTRIBUTION

**Conceptualization:** Author One, Author Two and Author Three.

**Methodology:** Author One and Author Two.

**Investigation:** Author One and Author Two.

**Discussion of results:** Author One, Author Two and Author Three.

**Writing – Original Draft:** Author One.

**Writing – Review and Editing:** Author One and Author Two.

**Resources:** Author Two.

**Supervision:** Author Two and Author Three.

**Approval of the final text:** Author One, Author Two and Author Three.

## VIII. REFERENCES

- [1]. Kiran, Parameshachari B D, Panduranga H T, Naveenkumar S K. "Partial encryption of medical images by dual DNA addition using DNA encoding", Recent Innovations in Signal processing and Embedded Systems, pp.310–314, 2017.
- [2]. J., Ali, M.K., Jamil, R. Ali, et al. "Extended fractional transformation-based S-box and applications in medical image encryption", Multimed Tools Appl, pp.1-17, (2025). <https://doi.org/10.1007/s11042-024-20575-3>.
- [3]. A. Roy, D. R. Mahanta, and L. B. Mahanta, "A Semi-Synchronous Federated Learning Framework with Chaos-Based Encryption for Enhanced Security in Medical Image Sharing", Results in Engineering, 103886, 2025

- [4]. X. Wang, and Y. Wang, "Multiple medical image encryption algorithm based on scrambling of region of interest and diffusion of odd-even interleaved points", *Expert Systems with Applications*, vol.213, Article 118924, 2023.
- [5]. F. Pub, Data encryption standard (des), FIPS PUB (1999) 43–46.
- [6]. V. Rijmen, J. Daemen, Advanced encryption standard, in: *Proceedings of Federal Information Pro*
- [7]. Shannon CE (1949) Communication theory of secrecy systems. *Bell Syst Tech J* 28(4):656–715
- [8]. A., Jolfaei, and A. Mirghadri, "An image encryption approach using chaos and stream cipher", *Journal of Theoretical and Applied Information Technology*, vol.19, no.2, pp.117-125, 2010.
- [9]. X. Wang, L. Teng, X. Qin, "A novel colour image encryption algorithm based on chaos", *Signal Processing*, vol.92, no.4, pp.1101-1108, 2012.
- [10]. Coppersmith Don. "The Data Encryption Standard (DES) and its strength against attacks", *IBM Journal of Research and Development*, 1994.
- [11]. S. Das, "Medical Image Encryption Using 3D Unified Chaotic System and Dynamic DNA Coding", 2022.
- [12]. M. Zia, B. McCartney, J. Scotney, Martinez, M. AbuTair, J. Memon and A. Sajjad. "Survey on image encryption techniques using chaotic maps in spatial, transform and spatiotemporal domains", *Aug* 2022.
- [13]. S. Sun. "A Novel Hyperchaotic Image Encryption Scheme Based on DNA Encoding, Pixel-Level Scrambling and Bit-Level Scrambling", (accessed Dec 24, 2024). [Online]. Available: <https://ieeexplore.ieee.org/document/8320365/>
- [14]. S. Inam, S. Kanwal, R. Firdous and F. Hajje. "Blockchain based medical image encryption using Arnold's cat map in a cloud environment", *Mar* 2024. [Online]. Available: <https://www.nature.com/articles/s41598-024-56364-z>
- [15]. C. İnce, K. İnce and D. Hanbay. "Novel image pixel scrambling technique for efficient color image encryption in resource-constrained IoT devices". *Sep* 2024. [Online].
- [16]. hang, B.; Liu, L. "Chaos-Based Image Encryption: Review, Application, and Challenges", *Mathematics* 2023, vol.11, pp.2585, 2023.
- [17]. H. Li, S. Yu, W. Feng, Y. Chen, J. Zhang, Z. Qin, Z. Zhu and M. Wozniak. "Exploiting Dynamic Vector-Level Operations and a 2D-Enhanced Logistic Modular Map for Efficient Chaotic Image Encryption", *Jul* 2023.
- [18]. R., Tamayo-Pérez, U. J., ... & E. Inzunza-González, "Real-time medical image encryption for H-IoT applications using improved sequences from chaotic maps", *Integration*, vol.90, pp.131-145, 2023.
- [19]. Z. Hua, Y. Zhou, and H. Huang, "Cosine-transform-based chaotic system for image encryption," *Information Sciences*, vol. 480, pp. 403–419, 2019.
- [20]. J. Tang, F. Zhang, and H. Ni, "A novel fast image encryption scheme based on a new one-dimensional compound sine chaotic system", *The Visual Computer*, vol.39, no.10, pp.4955-4983, 2023.
- [21]. B. Zhang, B. Rahmatullah, S. L. Wang, and Z.Liu, "A plain-image correlative semi-selective medical image encryption algorithm using enhanced 2D-logistic map", *Multimedia Tools and Applications*, vol.82, no.10, pp.15735–15762, 2023.
- [22]. Z. Hua, Z. Wu, Y. Zhang, H. Bao and Y. Zhou, "Two-Dimensional Cyclic Chaotic System for Noise-Reduced OFDM-DCSK Communication," in *IEEE Transactions on Circuits and Systems I: Regular Papers*, vol. 72, no. 1, pp. 323-336, Jan. 2025.
- [23]. L. Xu, et al., "A novel bit-level image encryption algorithm based on chaotic maps", *Optics and Lasers in Engineering* vol.78, pp.17–25, 2016.
- [24]. Fang, P., Liu, H., Wu, C., Liu, M.: "A survey of image encryption algorithms based on chaotic system", *Vis. Comput.* (2022). <https://doi.org/10.1007/s00371-022-02459-5>
- [25]. M. Alawida, A. Samsudin, J.S. Teh, R.S. Alkhalwaldeh, "A new hybrid digital chaotic system with applications in image encryption", *Signal Process.* vol.160, pp.45–58 (2019). <https://doi.org/10.1016/j.sigpro.2019.02.016>.
- [26]. Z. Hua, Y. Zhou, C.M. Pun, C.L.P. Chen, "2D Sine Logistic modulation map for image encryption", *Inf. Sci.* Vol.297, pp.80–94, 2015.
- [27]. Z. Hua, Y. Zhou, "Image encryption using 2D Logistic-adjusted-Sine map, *Inf. Sci.* vol.339, pp.237–253, 2016.
- [28]. W. Liu, K. Sun, and C. Zhu, "A fast image encryption algorithm based on chaotic map," *Optics and Lasers in Engineering*, vol. 84, pp. 26–36, 2016.
- [29]. Z. Hua, F. Jin, B. Xu, H. Huang, "2D Logistic-Sine-coupling map for image encryption, *Signal Processing*", vol.149, pp.148–161, 2018.
- [30]. H. Zhu, Y. Zhao, Y. Song, "2D logistic-modulated-sine-coupling-logistic chaotic map for image encryption", *IEEE Access*, vol.7, pp.14081–14098, 2019.
- [31]. A. Kumar, and M. Dua, "A novel chaos map based medical image encryption scheme", *The Imaging Science Journal*, vol.69, no.(5–8), pp:219–238, 2021.
- [32]. N. Yang, S. Zhang, M. Bai, et al. "Medical Image Encryption Based on Josephus Traversing and Hyperchaotic Lorenz System", *J. Shanghai Jiaotong Univ. (Sci.)* vol.29, pp.91–108, 2024. <https://doi.org/10.1007/s12204-022-2555-x>.
- [33]. B. Zhang, B. Rahmatullah, S.L. Wang, et al. "A variable dimensional chaotic map-based medical image encryption algorithm with multi-mode", *Med Biol Eng Comput* vol.61, pp. 2971–3002, 2023. <https://doi.org/10.1007/s11517-023-02874-3>
- [34]. K. Demla, and A. Anand, "MieWC: Medical image encryption using wavelet transform and multiple chaotic maps", *Security and Privacy*, vol.7, no.3, e369, 2024
- [35]. S. Dua, A. Kumar, M. Dua, et al. ICFCM-MIE: "Improved Cosine Fractional Chaotic Map based Medical Image Encryption", *Multimed Tools Appl.* Vol.83, pp. 52035–52060, 2024. <https://doi.org/10.1007/s11042-023-17438-8>
- [36]. Z. Zhuang, Z. Zhuang, and T. Wang, "Medical image encryption algorithm based on a new five-dimensional multi-band multi-wing chaotic system and QR decomposition", *Sci Rep* vol.14, pp. 402, 2024.
- [37]. S. Koppu, V. M. Viswanatham, "A fast enhanced secure image chaotic cryptosystem based on hybrid chaotic magic transform", *Modell Simul Eng.* Vol.1, pp. 7470204, 2017. <https://doi.org/10.1155/2017/7470204>.
- [38]. K. Jain, A. Aji, and P. Krishnan, "Medical image encryption scheme using multiple chaotic maps", *Pattern Recognition Letters*, vol.152, pp. 356-364, 2021.
- [39]. R.M. May, "Simple mathematical models with very complicated dynamics", *Nature*, vol. 261, no. 5560, pp. 261–5560, 1976.
- [40]. Y. Zhou, L. Bao, C.L.P. Chen, "A new 1D chaotic system for image encryption", *Signal Process.* vol.97, pp. 172–182, 2014.
- [41]. Y. Wu, G. Yang, H. Jin, J.P. Noonan, "Image encryption using the two-dimensional logistic chaotic map", *J. Electron. Imaging*, vol.21, no.1, pp. 013014-013014-15, 2012.
- [42]. Wikipedia, "Double-precision Floating-point Format", *Wikipedia, the Free Encyclopedia*, 2013 (online; accessed 10.12.13).
- [43]. X. Wang, J. Zhang, G. Cao, "An image encryption algorithm based on Zigzag transform and LL compound chaotic system", *Opt. Laser Technol.* Vol.119, pp. 105581, 2019. <https://doi.org/10.1016/j.optlastec.2019.105581>
- [44]. K. Prabhavathi, M. B. Anandaraju, and V. Ravi, "Region based medical image encryption using advanced zigzag transform and 2D logistic sine map (2DLSM)", *International Journal of Cognitive Computing in Engineering*, vol.4, pp:349-362, 2023.
- [45]. Z., Hua, S., Yi, and Y. Zhou, "Medical image encryption using high-speed scrambling and pixel adaptive diffusion", *Signal Processing*, vol.144, pp.134-144, 2018.
- [46]. G. Alvarez, S. Li, "Some basic cryptographic requirements for chaos-based cryptosystems", *Int. J. Bifurcation Chaos*, vol.16, no.08, pp.2129–2151, 2006.
- [47]. Y. Wu, Y. Zhou, G. Saveriades, S. Agaian, J.P. Noonan, P. Natarajan, "Local Shannon entropy measure with statistical tests for image randomness", *Inf. Sci.* vol.222, pp.323–342, 2013. <https://doi.org/10.1016/j.ins.2012.07.049>
- [48]. Y. Xian, X. Wang, "Fractal sorting matrix and its application on chaotic image encryption", *Inf. Sci.* vol.547, pp. 1154–1169, 2021.

- [49]. R.M. Haralick, et al., "Textural features for image classification", IEEE Transactions on systems, man, and cybernetics, vol.6, pp.610–621, 1973.
- [50]. T. Li, et al., "Image encryption algorithm based on logistic and two-dimensional lorenz", IEEE Access, vol.8, pp.13792–13805, 2020.
- [51]. Cao, C., Sun, K., Liu, W.: "A novel bit-level image encryption algorithm based on 2D-LICM hyperchaotic map", Signal Process, vol.143, pp.122–133 (2018). <https://doi.org/10.1016/j.sigpro.2017.08.020>.





# SIMULATION OF THE ELASTIC FIELD OF AN INTERFACIAL DISLOCATION IN AN ANISOTROPIC MEDIUM: FOURIER SERIES APPROACH

Allaoua Kherraf<sup>1</sup>, Rachid Benbouda<sup>2</sup> and Mourad Brioua<sup>3</sup>

<sup>1</sup> Laboratory LRP, Department of Mechanical Engineering, University of BATNA 2, Algeria.

<sup>2,3</sup> Laboratory LICEGS, Department of Mechanical Engineering, University of BATNA 2, Algeria.

<sup>1</sup><https://orcid.org/0000-0002-5858-6222> , <sup>2</sup><https://orcid.org/0000-0002-8215-0680> , <sup>3</sup><https://orcid.org/0000-0002-5330-3000> 

Email: [all\\_kherraf@outlook.fr](mailto:all_kherraf@outlook.fr), [r\\_benbouda@yahoo.fr](mailto:r_benbouda@yahoo.fr), [mm\\_brioua@yahoo.fr](mailto:mm_brioua@yahoo.fr)

## ARTICLE INFO

### Article History

Received: February 09, 2025

Revised: March 20, 2025

Accepted: March 15, 2025

Published: April 31, 2025

### Keywords:

Interfacial dislocation networks,  
Anisotropic elasticity,  
Elastic field simulation,  
Stress distribution,  
Crystalline materials/

## ABSTRACT

Interfacial dislocation networks, located at the interface between two crystals, significantly influence the mechanical, thermal and electrical behaviors of materials. Despite their importance, these phenomena have received relatively little attention in the scientific literature. This gap can be mainly explained by the difficulty of analyzing these complex systems under realistic experimental conditions, particularly using advanced techniques, which take into account the anisotropy of materials. This study focuses on the simulation of the elastic field (stresses and displacements) of a dislocation located at the interface of two infinite anisotropic media. Based on previous work in anisotropic elasticity, an analytical formulation based on Fourier series was used to numerically solve a system of 12 equations with 12 unknowns. The results obtained show the equistress curves for different crystalline systems (Al/Al, Cu/Cu and Al/Cu) considering both anisotropic and quasi-isotropic cases. The study highlights more pronounced stress dispersion in copper due to its hardness, as well as notable differences between isotropic and anisotropic cases, especially for heterogeneous materials such as Al/Cu. The conclusions highlight the importance of material heterogeneity in stress distribution and the relevance of the results for modeling crystal interfaces. This work offers promising perspectives for the optimization of materials in industrial fields such as aeronautics, electronics and renewable energies. It also provides a robust methodological framework for the study of complex crystalline materials.



Copyright ©2025 by authors and Galileo Institute of Technology and Education of the Amazon (ITEGAM). This work is licensed under the Creative Commons Attribution International License (CC BY 4.0).

## 1. INTRODUCTION

The fundamental problem of a rectilinear dislocation in an anisotropic medium was solved by Eshelby et al. [1] and Stroh [2]. Tucker [3] was the first to express, within the framework of anisotropic elasticity, the field of displacements of a rectilinear dislocation on a plane joint. Subsequently, Humble and Forwood [4] correct certain typographical errors in formula (27) of Tucker [3] and verify the validity of their expressions by simulating the contrast of such a dislocation.

To solve the problem of a rectilinear dislocation at the interface of two anisotropic media of different nature, Dupeux and Bonnet [5], and starting from an analysis different from that

of Tucker [3], manage to obtain an equivalent analytical expression to that of Humble and Forwood [4].

Richeton and Berbenni [6] used static Field Dislocation Mechanics theory to obtain clear closed-form solutions for the misorientation and network stress fields in the broad framework of heterogeneous anisotropic elasticity.

For a nanometric three-layer material, Makhloufi et al. [7] assessed the effects of elastic fields at the crystalline interface level when bidirectional networks of unidirectional dislocations were present.

Chen et al. [8] used a numerical method similar to that of Wagoner to calculate the equilibrium positions and stress fields of dislocation stacks in an anisotropic heterogeneous medium.



Under uniaxial pressure Liu and Sluiter [9] investigated the stress condition at a grain boundary perpendicular to a maximum incompatibility stress in an infinitely stretched elastic bicrystal.

The purpose of this article is to simulate the elastic field (stress and displacement) in the scenario of anisotropic elasticity for a dislocation situated at the interface of two infinite media, in accordance with the previously mentioned work. The analytical method used is a Fourier series formulation in which the analytical expressions of its coefficients have been determined numerically with a precision that has been verified against the convergence of the series.

For this, a program has been created that allows a system of 12 equations with 12 unknowns to be numerically inverted. The equistress curves  $\pm 0.30$  GPa and  $\pm 0.15$  GPa for the infinite Al/Al and Cu/Cu single crystals as well as for the infinite Al/Cu bicrystal in the anisotropic and quasi-isotropic cases are presented. These systems are representative of materials of interest in various industrial and technological contexts, where interfaces play a determining role in material performance.

Ultimately, this study makes a significant contribution to the modeling of the elastic properties of crystalline interfaces, taking into account the anisotropy of materials. It also opens the way to further investigations on the role of interfacial dislocations in other crystallographic configurations and under various experimental conditions.

## II. PROBLEM STATEMENT

Figure 1 illustrates the geometric configuration of a dislocation positioned within the interface plane between two infinite media, denoted as (+) and (-). The dislocation, characterized as a corner dislocation, has a Burgers vector  $b = (1/2) \langle 110 \rangle$  in aluminum (Al). For visualization purposes, the representation is confined to a finite thickness  $h$ . The dislocation core is located at  $x_1 = -2h/3$ . These two media are distinct in nature and exhibit elastic anisotropy.

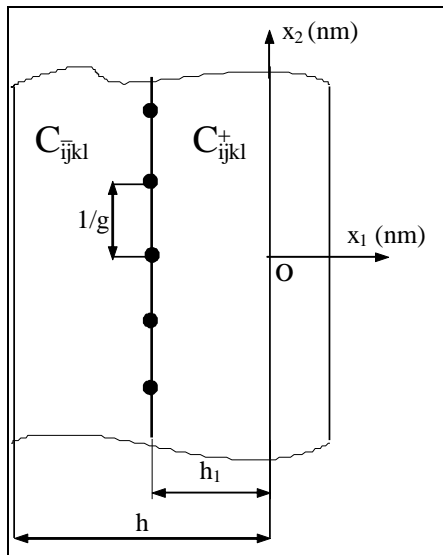


Figure 1: Infinite medium +/-, with an interface unidirectional network of dislocations, the two media's elastic constants are

$$C^+_{ijkl} \text{ and } C^-_{ijkl}.$$

Source: Authors, (2025).

They are distinguished by the period  $\Lambda = 1/g$  and the constants  $C^+_{ijkl}$  and  $C^-_{ijkl}$ , respectively

## III. THE DISPLACEMENT AND STRESS FIELD'S GENERAL FORM

### III.1 DISPLACEMENT FIELD

The deformation can be developed in Fourier series at any point in the two media outside of the discontinuity zones, since it is considered to be periodic along the  $Ox_2$  axis [10]:

$$\varepsilon_{ij}(x_1, x_2) = \sum_G \varepsilon_{ij}^{(G)}(x_1) \cdot \exp\left(\frac{2i\pi n}{\Lambda} x_2\right) \quad (1)$$

The integration of (1) gives the displacement field:

$$u_k = u_k^0 + v_{k1}^0 x_1 + v_{k2}^0 x_2 + \sum_{n \neq 0} u_k^{(n)}(x_1) \cdot \exp(2i\pi g n x_2) \quad k=1,2,3 \quad (2)$$

With  $1/g = \Lambda$

Therefore the expression for the displacement field is also written [11]:

$$u_k = \sum_{n \neq 0} u_k^{(n)}(x_1) \cdot \exp(2i\pi g n x_2) \quad k=1,2,3 \quad (3)$$

This field of displacements  $u_k$  must satisfy generalized Hooke's law, linking stresses and deformations:

$$\sigma_{ij} = C_{ijkl} u_{k,l} \quad (4)$$

The state of equilibrium of the stresses in the distortion region is written:

$$\frac{\partial \sigma_{ij}}{\partial x_j} = 0 \Rightarrow C_{ijkl} \frac{\partial^2 u_k}{\partial x_j \partial x_l} = 0 \quad (5)$$

By replacing (3) in (5), three differential equations that can be expressed as follows are obtained:

$$C_{j1k1} (-4\pi^2 g^2 n^2) u_k^n + (C_{j1k2} + C_{j2k1}) (2i\pi n g) u_{k,2}^n + C_{j2k2} u_{k,22}^n = 0 \quad (6)$$

This equation's general solution is expressed as follows:

$$u_k^{(n)}(x_1) = \lambda'_{\alpha k} \cdot \exp(2i\pi g n p_{\alpha} x_1) \quad (7)$$

Where  $\lambda'_{\alpha k}$  and  $p_{\alpha}$  are complex constants that must be found using the three linear equation system that results from substituting (7) in (6):

$$\left[ C_{j1k1} + (C_{j1k2} + C_{j2k1}) \cdot p_{\alpha} + C_{j2k2} \cdot p_{\alpha}^2 \right] \lambda'_{\alpha k} = 0 \quad (8)$$

This is written:

$$A_{jk} \lambda'_{\alpha k} = 0 \quad (9)$$

$$\text{Or } A_{jk} = \left[ C_{j1k1} + (C_{j1k2} + C_{j2k1}) \cdot p_{\alpha} + C_{j2k2} \cdot p_{\alpha}^2 \right]$$

In the case of a rectilinear dislocation situated within a homogeneous medium exhibiting anisotropic elasticity, the system is analogous to that described by [1]. It admits for each  $p_{\alpha}$  non-trivial solution  $\lambda'_{\alpha k}$  if the determinant of  $A_{jk}$  is equal to zero:

$$\begin{aligned} \det(A_{jk}) &= \left| C_{j1k1} + (C_{j1k2} + C_{j2k1}) p_{\alpha} + C_{j2k2} p_{\alpha}^2 \right| \\ \det(A_{jk}) &= 0 \end{aligned} \quad (10)$$

We thus obtain a sixth degree equation in  $p_{\alpha}$  ( $\alpha=1, \dots, 6$ ) in order to facilitate problem solving and improve numerical efficiency, the displacement field's final expression can be expressed as follows: ( $u_k^0 = 0$ ):

$$\begin{aligned} u_k &= \sum_{n>0} \left( \frac{1}{\pi \cdot n} \right) \sum_{\alpha=1}^3 [\cos[n \cdot \omega (x_2 + r_{\alpha} \cdot x_1)] \\ &\times \text{Re}[( -i \cdot X_{\alpha}^{(n)} ) \cdot L_{\alpha k}] \cdot \exp(-n \cdot \omega \cdot s_{\alpha} \cdot x_1) \\ &+ ( -i \cdot Y_{\alpha}^{(n)} ) \cdot \bar{L}_{\alpha k}] \cdot \exp(n \cdot \omega \cdot s_{\alpha} \cdot x_1)] \\ &+ \{ \sin[n \cdot \omega (x_2 + r_{\alpha} \cdot x_1)] \times \text{Re}[(X_{\alpha}^{(n)} ) \cdot \bar{L}_{\alpha k}] \cdot \exp(-n \cdot \omega \cdot s_{\alpha} \cdot x_1) \\ &+ (Y_{\alpha}^{(n)} ) \cdot \bar{L}_{\alpha k}] \cdot \exp(n \cdot \omega \cdot s_{\alpha} \cdot x_1)] \} \\ &\quad (k=1,2,3) \end{aligned} \quad (11)$$

With  $\omega = 2 \cdot \pi \cdot g$

### III.2 STRESS FIELD

By replacing (11) in Hooke's law, we can obtain the expression for the stress field.

$$\begin{aligned} \sigma_{ij} &= 2 \cdot g \sum_{n>0} \sum_{\alpha=1}^3 [\cos[n \cdot \omega (x_2 + r_{\alpha} \cdot x_1)] \\ &\times \text{Re}[X_{\alpha}^{(n)} \cdot L_{\alpha ij}] \cdot \exp(-n \cdot \omega \cdot s_{\alpha} \cdot x_1) \\ &+ Y_{\alpha}^{(n)} \cdot \bar{L}_{\alpha ij}] \cdot \exp(n \cdot \omega \cdot s_{\alpha} \cdot x_1) + \{ \sin[n \cdot \omega (x_2 + r_{\alpha} \cdot x_1)] \\ &\times \text{Re}[i \cdot X_{\alpha}^{(n)} \cdot L_{\alpha ij}] \cdot \exp(-n \cdot \omega \cdot s_{\alpha} \cdot x_1) + i \cdot Y_{\alpha}^{(n)} \cdot \bar{L}_{\alpha ij}] \cdot \exp(n \cdot \omega \cdot s_{\alpha} \cdot x_1) \} \end{aligned} \quad (12)$$

$$\begin{aligned} \text{With } L_{\alpha kl} &= \lambda_{\alpha j} [C_{klj1} + p_{\alpha} C_{klj2}] \\ i, j &= 1, 2, 3, \quad l = 1, 2 \end{aligned}$$

The complex constants  $X_{\alpha} Y_{\alpha}$  ( $\alpha = 1, 3$ ) depend on the boundary conditions.

## IV. BOUNDARY CONDITIONS OF THE PROBLEM

### IV.1 DISPLACEMENT CONDITIONS

It is possible to express the displacement's linearity with respect to the interface using equations (10a, 10c) [11]:

$$\left[ u_k^+ - u_k^- \right]_{x_1 = -\frac{2}{3}h} = -\frac{b_k}{\pi} \sum_{n=1}^{\infty} (1/n) \sin(n \omega x_2) \quad (13)$$

Where the upper and bottom crystals are denoted by (+) and (-), respectively.

### IV.2 STRESS CONDITIONS

The relationship imposed by the continuity of constraints at the interface is given by:

$$\left[ \sigma_{2k}^+ \right]_{x_1 = -\frac{2}{3}h} = \left[ \sigma_{2k}^- \right]_{x_1 = -\frac{2}{3}h} \quad (14)$$

At the interface, this condition represents equilibrium.

In the limiting case of two infinite media, the complex constants  $X_{\alpha}^-, Y_{\alpha}^+$  ( $\alpha=1, 3$ ) are chosen to be zero to ensure the convergence of the strain field far from the interface.

The boundary conditions result in the numerical inversion of a system of 12 equations with 12 real unknowns, enabling the calculation of both the stress field and the displacement field within the two crystals.

## V. APPLICATION

The equistress curves presented in Figures 2-7 illustrate the evolution of  $\sigma_{22}$  stresses at  $\pm 0.15$  GPa and  $\pm 0.30$  GPa around a corner dislocation, for two orientations of the Burgers vector  $b$  ( $b//Ox_1$  and  $b//Ox_2$ ), in Al/Al, Cu/Cu, and Al/Cu crystals. The study considers two scenarios: anisotropic and quasi-isotropic. These curves highlight the stress distribution around the dislocation at the interface of two infinite media. Many studies based on the isotropic elasticity approximation have studied this model, including those of [12], [13]. In each scenario, the core of the dislocation is positioned at  $x_1 = -2h/3$ .

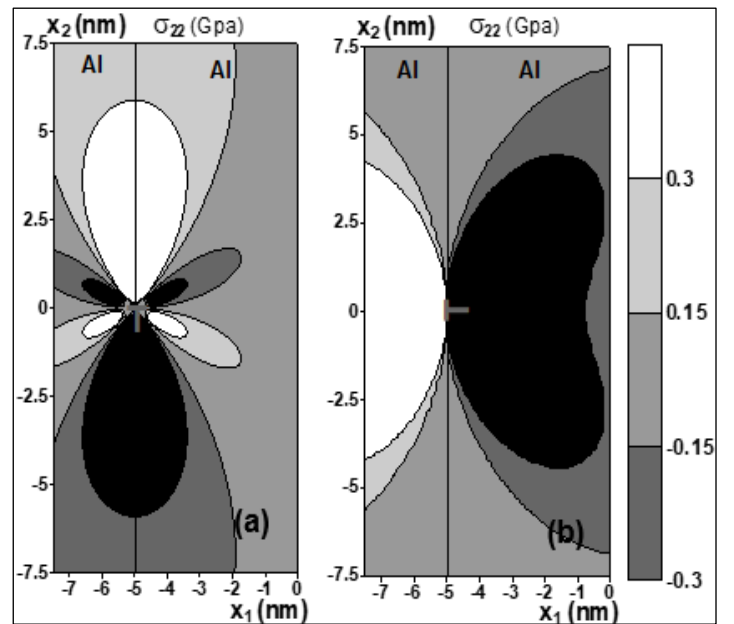


Figure 2: Normal equistress curves  $\sigma_{22} = \pm 0.15$  GPa and  $\pm 0.3$  GPa for a dislocation placed at the interface of an infinite medium Al/Al,  $C_{ij}$  anisotropics, (a)  $b//Ox_1$ , (b)  $b//Ox_2$ .

Source: Authors, (2025).

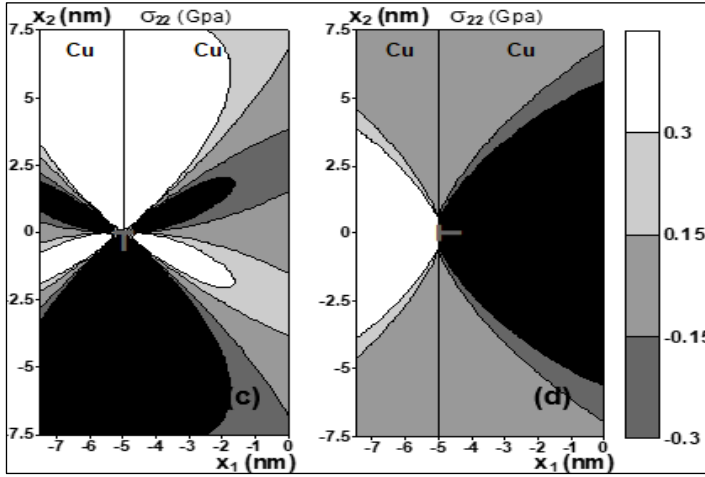


Figure 3: Normal equistresses curves  $\sigma_{22} = \pm 0.15$  GPa and  $\pm 0.3$  GPa for a dislocation placed at the interface of an infinite medium Cu/Cu,  $C_{ij}$  anisotropics, (c)  $b//Ox_1$ , (d)  $b//Ox_2$ . Source: Authors, (2025).

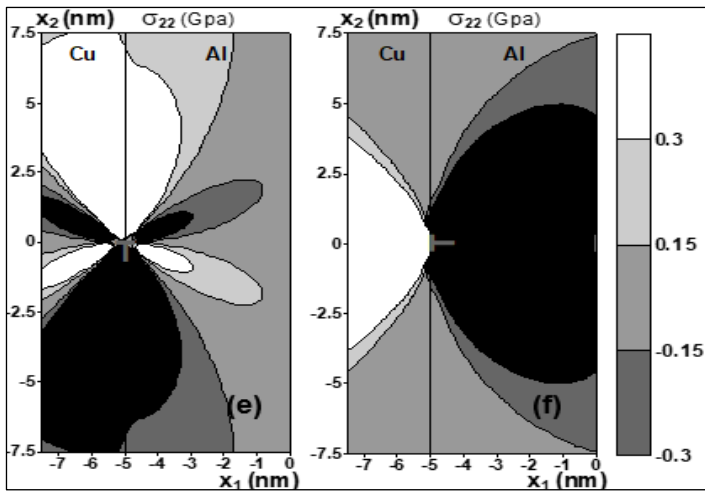


Figure 4: Normal equistresses curves  $\sigma_{22} = \pm 0.15$  GPa and  $\pm 0.3$  GPa for a dislocation placed at the interface of an infinite medium Al/Cu,  $C_{ij}$  anisotropics, (e)  $b//Ox_1$ , (f)  $b//Ox_2$ . Source: Authors, (2025).

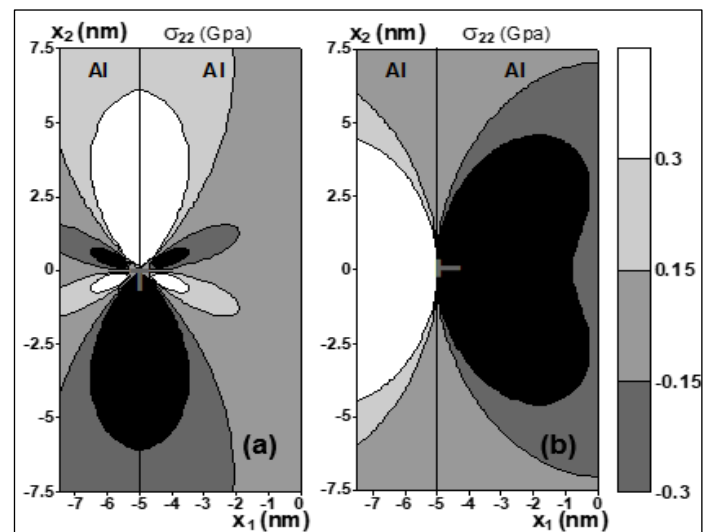


Figure 5: Normal equistresses curves  $\sigma_{22} = \pm 0.15$  GPa and  $\pm 0.3$  GPa for a dislocation placed at the interface of an infinite medium Al/Al,  $C_{ij}$  quasi-isotropics, (a)  $b//Ox_1$ , (b)  $b//Ox_2$ . Source: Authors, (2025).

Table 1 presents the crystal parameters, elastic moduli, and isotropic and anisotropic elastic constants for Al and Cu utilized in our computations [14]. The values of the constants for aluminum and copper show that these materials differ not only in their isotropic properties (with lower  $C_{11}$ ,  $C_{12}$ , and  $C_{44}$  constants for Al) but also in their anisotropic versions, where the constants are adjusted to account for the directionality of the mechanical properties.

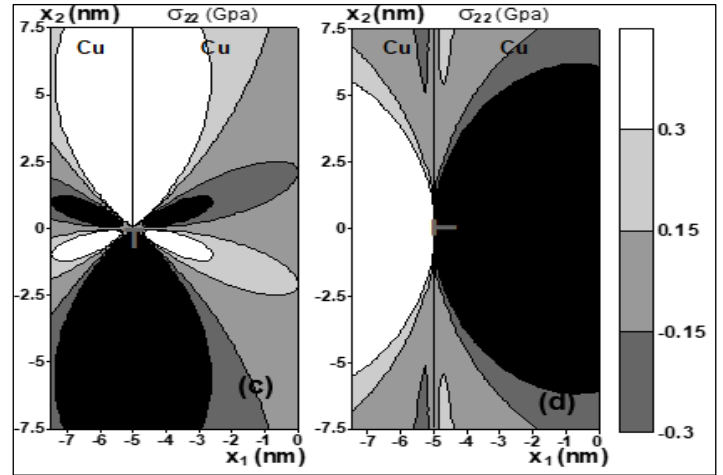


Figure 6: Normal equistresses curves  $\sigma_{22} = \pm 0.15$  GPa and  $\pm 0.3$  GPa for a dislocation placed at the interface of an infinite medium Cu/Cu,  $C_{ij}$  quasi-isotropics, (c)  $b//Ox_1$ , (d)  $b//Ox_2$ . Source: Authors, (2025).

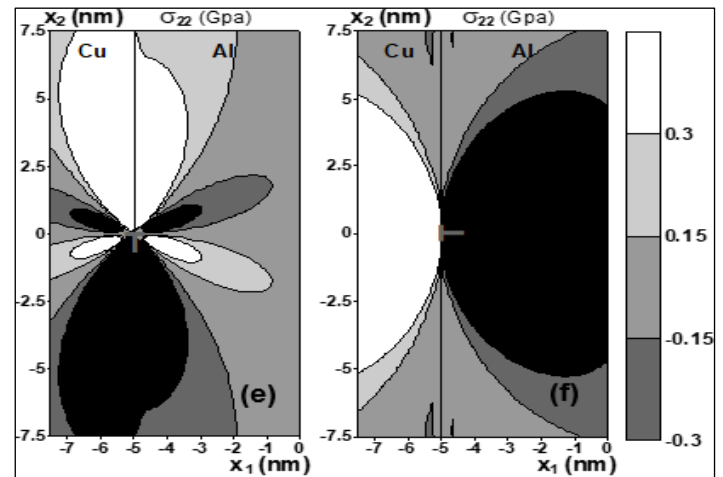


Figure 7: Normal equistresses curves  $\sigma_{22} = \pm 0.15$  GPa and  $\pm 0.3$  GPa for a dislocation placed at the interface of an infinite medium Al/Cu,  $C_{ij}$  quasi-isotropics, (e)  $b//Ox_1$ , (f)  $b//Ox_2$ . Source: Authors, (2025).

Table 1: Crystal parameters, elastic moduli, elastic constants for Al and Cu.

	Parameters	Al	Cu
Isotropic elastic constants	$a$ (nm)	0.405	0.405
	$\mu$ (GPa)	26.50	46.32
	$\nu$	0.347	0.360
	$C_{11}$ (GPa)	113.1	211.748
	$C_{12}$ (GPa)	60.10	119.1
Anisotropic elastic constants	$C_{44}$ (GPa)	26.50	46.32
	$C_{11}$ (GPa)	108.2	168.4
	$C_{12}$ (GPa)	61.30	121.4
	$C_{44}$ (GPa)	28.50	75.4

Source:[15].

To validate our approach, we conducted convergence tests to ensure the reliability of our program, particularly its ability to function in a quasi-isotropic regime. By replacing the anisotropic elastic constants  $C_{ij}$  with their quasi-isotropic counterparts, we obtained results for roots close to the purely imaginary number  $iG$  that are consistent with those reported in isotropic elasticity by [12], [13].

The conventional elasticity formulas are used to get the isotropic elastic constants [15].

$$C_{11} = \lambda + 2\mu; \quad C_{12} = \lambda; \quad C_{44} = \mu \quad \text{and} \quad \lambda = \frac{2\nu\mu}{1-2\nu} \quad (15)$$

Where  $\nu$  is Poisson's ratio and  $\lambda$  and  $\mu$  are the Lamé coefficients.

In the quasi-isotropic case, the constants  $C_{11}$  and  $C_{12}$  are set to their isotropic counterparts derived from equation (15), while  $C_{44}$  is defined as  $(\mu - \mu/1000)$ .

## VI. CONCLUSIONS

This work investigates the behavior of a dislocation at the interface of two elastically anisotropic infinite media. It describes the geometric configuration in which a dislocation, with Burgers vector  $b = 1/2\langle 110 \rangle$  in aluminum (Al), is positioned at the interface between two media denoted by (+) and (-). The study focuses on the displacement and stress fields associated with this dislocation, which are modulated by the elastic properties of the materials involved.

Key results show how the displacement and stress fields are governed by differential equations derived from generalized Hooke's law and equilibrium conditions. Boundary conditions at the interface, including displacement and stress continuity, are used to solve for the stress and displacement fields in both media. The system of equations is numerically inverted to calculate these fields, leading to a model for stress distribution and deformation near the dislocation.

The stress curves in the anisotropic case (Figures 2-4) show the stress distribution in materials with directional properties, which differs from isotropic materials where the properties are uniform in all directions. Al and Cu materials are characterized by different elastic constants that affect the shape and intensity of the stresses.

The results obtained for the quasi-isotropic case (Figures 5-7) show that the curves are practically superimposable to those from the analytical expression of Hirth et al. [15], obtained by Benbouda [16] in the case of an infinite bicrystal. Moreover, the results obtained in the quasi-isotropic case closely match those of the isotropic examples derived by Bonnet [17] using the analytical formulations of Lee and Dundurs [18]. This agreement is particularly notable for aluminum, whose characteristics are close to isotropy. This similarity confirms the reliability of our program in anisotropic elasticity. For this same crystal, the differences between the anisotropic and isotropic cases remain negligible.

Regarding the effect of anisotropy, copper exhibits a greater stress dispersion, which can be attributed to its higher hardness compared to aluminum. This characteristic results in steeper stress gradients near the dislocation interface. In contrast, aluminum, being more isotropic, exhibits less complex and more regular stress curves, with limited differences between the anisotropic and isotropic cases.

The study of equilibrium stress curves shows the impact of the interface between the materials, in particular for the Al/Cu bicrystal, where the stress lobes are located between those of the

two homogeneous crystals (Al/Al and Cu/Cu). The stress transition between the two materials is influenced by the heterogeneity of the materials and the specific anisotropic properties of each phase.

This modeling is useful to understand and predict the behaviors of heterogeneous materials, such as alloys or interfaces in electronic devices, where anisotropic elastic properties play a key role in the mechanical and thermal performance of the materials.

## VII. AUTHOR'S CONTRIBUTION

**Conceptualization:** Allaoua Kherraf, Rachid Benbouda and Mourad Brioua.

**Methodology:** Rachid Benbouda and Mourad Brioua.

**Investigation:** Allaoua Kherraf and Mourad Brioua.

**Discussion of results:** Allaoua Kherraf, Rachid Benbouda and Mourad Brioua.

**Writing – Original Draft:** Rachid Benbouda.

**Writing – Review and Editing:** Allaoua Kherraf, Rachid Benbouda and Mourad Brioua.

**Resources:** Allaoua Kherraf, Rachid Benbouda.

**Supervision:** Rachid Benbouda.

**Approval of the final text:** Allaoua Kherraf, Rachid Benbouda and Mourad Brioua.

## VIII. REFERENCES

- [1] J. D. Eshelby, W.T. Read and W. Shockley, "Anisotropic elasticity with applications to dislocation theory," *Acta Materialia*, vol. 1, pp. 251-259, 1953, doi: 10.1016/0001-6160(53)90099-6.
- [2] A. N. Stroh, "Steady State Problems in Anisotropic Elasticity," *Journal of Mathematics and Physics*, vol. 41, pp. 77-103, 1962, doi: 10.1002/sapm196241177.
- [3] M. O. Tucker, "Plane boundaries and straight dislocations in elastically anisotropic materials," *Philosophical Magazine*, vol. 19, no.162, pp. 1141-1159, 1969, doi: 10.1007/978-3-662-30257-6\_34.
- [4] P. Humble and C. T. Forwood, "Identification of grain boundary dislocations," *Philosophical Magazine*, vol. 31, no. 5, pp. 1025-1048, 1975, doi: 10.1080/0031-8087508226827.
- [5] M. Dupeux and R. Bonnet, "Stresses, displacements and energy calculations for interfacial dislocations in anisotropic two-phase media," *Acta Metallurgica*, vol. 28, pp. 721– 728, 1980, doi: 10.1016/00016160(80)-90150-9.
- [6] T. Richeton and S. Berbenni, "Effects of heterogeneous elasticity coupled to plasticity on stresses and lattice rotations in bicrystals: a Field Dislocation Mechanics viewpoint," *European Journal of Mechanics A/Solids*, vol. 37, pp. 231-247, 2013, doi: 10.1016/j.euromechsol.2012.06.010.
- [7] R. Makhloufi, M. Brioua, R. Benbouda, "The effect of the elastic fields caused by a networks of dislocations placed at interfaces of a three-layer material Cu/Cu/(001) Fe in the case of anisotropic elasticity," *Arabian Journal for Science and Engineering*, vol. 41, no. 5, pp. 1955-1960, 2016, doi: 10.1007/s13369-016-2054-1.
- [8] X. Chen, T. Richeton, C. Motz and S. Berbenni, "Elastic fields due to dislocations in anisotropic bi-and tri-materials: applications to discrete dislocation pile-ups at grain boundaries," *International Journal of Solids and Structures*, Elsevier, vol. 164, pp.141-156, 2019, doi: 10.1016/j.ijsolstr.2019.01.020.
- [9] K. Liu and M. H. F. Sluiter, "Stresses at grain boundaries: The maximum incompatibility stress in an infinitely extended elastic bicrystal under uniaxial loading," *Scripta Materialia*, vol. 234, pp. 1-5, 2023, doi: 10.1016/j.scriptamat.2023.115570.
- [10] R. Bonnet, "Elasticity theory of a thin bicrystal distorted by an interfacial dislocation array parallel to the free surfaces," *Philosophical Magazine A*, vol. 51, no.1, pp. 51-58, 1985, doi:10.1080/01418618508245268.



- [11] R. Bonnet and J. L. Verger-Gaugry, "Couche épitaxiale mince sur un substrat semi-infini: rôle du désaccord paramétrique et de l'épaisseur sur les distortions élastiques," *Philosophical Magazine A*, Vol. 66, no. 5, pp. 849-871, 1992, doi: 10.1080/01418619208201594.
- [12] R. Bonnet, "Une lame mince biphasée déformée par une dislocation interfaciale," *C.R. Acad. Sci. Paris*, t.318, serie II, pp. 289-295, 1994.
- [13] R. Bonnet and R. Zenati, "Une dislocation interfaciale dans un matériau tri-couche," *C.R. Acad. Sci. Paris*, t.318, serie II, pp. 31-36, 1994.
- [15] N. Fribourg-Blanc, M. Dupeux, G. Guenin and R. Bonnet, "Détermination par extensométrie et mesures ultrasonores des six constantes élastiques du cristal  $Al_2Cu(\pi)$ . Discussion de l'anisotropie," *Journal of Applied Crystallography*, vol. 12, 151-155, 1979, doi: 10.1107/S0021889879012103.
- [14] J. P. Hirth and J. Lothe, "Theory of dislocations," 2nd. Ed., Wiley. New York, 1982, pp. 837.
- [16] R. Benbouda, Ph.D Thesis, University of Batna, Algeria, 2006.
- [17] R. Bonnet, "Misfit dislocations in limited inhomogeneous media: A review," *Interface Science*, vol. 4, 169-179, 1997, doi: 10.1007/BF00240239.
- [18] M. S. Lee, J. Dundurs, "Edge dislocation in a surface layer," *International Journal of Engineering Science*, vol. 11, 87-94, 1973, doi: 10.1016/0020-7225(73)90071-2



## RESEARCH ARTICLE

## OPEN ACCESS

# ENHANCING INCENTIVE SCHEMES IN EDGE COMPUTING THROUGH HIERARCHICAL REINFORCEMENT LEARNING

Gowtham R<sup>1</sup>, Vatsala Anand<sup>2</sup>, Yadati Vijaya Suresh<sup>3</sup>, Kasetty Lakshmi Narasimha<sup>4</sup>, R. Anil Kumar<sup>5</sup>, V.Saraswathi<sup>6</sup>

<sup>1</sup>Computing and Information Technology, REVA University, Bangalore, Karnataka, India.

<sup>2</sup>Chitkara University Institute of Engineering and Technology, Chitkara University, Rajpura, Punjab, India.

<sup>3</sup>Rajeev Gandhi Memorial College of Engineering and Technology, Nandyal-518501, Andhra Pradesh, India.

<sup>4</sup>SVR Engineering College, Nandyal, Andhra Pradesh, India.

<sup>5</sup>Aditya University, Surampalem, India.

<sup>6</sup>Rajeev Gandhi Memorial College of Engineering and Technology, Nandyal, Andhra Pradesh, India

<sup>1</sup><http://orcid.org/0009-0006-6556-1089> , <sup>2</sup><http://orcid.org/0000-0001-6143-250X> , <sup>3</sup><http://orcid.org/0009-0005-5490-4990> 

<sup>4</sup><http://orcid.org/0000-0003-0569-3769> , <sup>5</sup><http://orcid.org/0000-0003-0032-2555> , <sup>6</sup><http://orcid.org/0009-0007-3374-8858> 

Email: [gowthamramakrishna19@gmail.com](mailto:gowthamramakrishna19@gmail.com), [vatsala.anand@chitkara.edu.in](mailto:vatsala.anand@chitkara.edu.in), [suri.yvs@gmail.com](mailto:suri.yvs@gmail.com), [kasetty.narsi@gmail.com](mailto:kasetty.narsi@gmail.com), [anidecs@gmail.com](mailto:anidecs@gmail.com), [saraswathiece89@gmail.com](mailto:saraswathiece89@gmail.com).

## ARTICLE INFO

**Article History**

Received: February 13, 2025

Revised: March 20, 2025

Accepted: March 15, 2025

Published: April 31, 2025

**Keywords:**

Machine learning

Hierarchical reinforcement

Edge computing

Server utility

Greedy algorithm.

## ABSTRACT

Edge learning is a distributed approach for training machine learning models using data from edge devices. It preserves privacy by avoiding direct data sharing. However, existing systems struggle with resource inefficiency, malicious node participation and lack of long-term sustainability. These challenges reduce performance and discourage participation in edge learning. This paper proposes Chiron, a robustness-aware incentive mechanism designed to address these issues. Chiron employs a hierarchical reinforcement learning (HRL) framework to optimize resource allocation and ensure fair participation. The framework focuses on three key components: pricing strategy, resource distribution and malicious node detection. Chiron integrates system-level performance and model accuracy into its optimization goals, ensuring a balance between efficiency and effectiveness. The hierarchical structure includes three layers. The top layer determines the total incentive budget to achieve long-term sustainability. The middle layer allocates resources to minimize idle time and enhance efficiency. The bottom layer identifies and excludes malicious or lazy nodes that negatively impact the education process. By tackle both short-term and long-term objectives Chiron ensures fairness and performance stability. Extensive experiments validate Chiron's capabilities using real-world datasets like MNIST and CIFAR-10. Chiron demonstrates robust byzantine resistance and supports sustainable edge learning by addressing critical gaps in current approaches. This work contributes to the advancement of edge learning by presenting a reliable and efficient solution for real-world applications. By integrating security, sustainability and performance, Chiron enables edge learning to be both practical and impactful in various domains.



Copyright ©2025 by authors and Galileo Institute of Technology and Education of the Amazon (ITEGAM). This work is licensed under the Creative Commons Attribution International License (CC BY 4.0).

## I. INTRODUCTION

It A new paradigm of machine learning called edge learning updates a global model across a set of data sources in a collaborative manner, where the data sources do not share their raw data[1]. This paradigm of data management solves two primary difficulties of ordinary machine learning with local data, namely the protection of data, as well as the excessive communication

cost. This is done by having the training done on-device and only sharing model updates. Edge learning of this nature enables us to build quite intelligent systems, especially in privacy-sensitive areas. Important challenges coming up with edge learning! On the one hand, due to resource constraints in edge devices such as computational power, energy and bandwidth, it may be inefficient. While, Sybil or unreliable nodes in the network, may reduce the

performance of the global model. These nodes may report false or malicious updates unintentionally due to resource exhaustion[2] or intentionally. The third one is that it is pretty hard to maintain the contribution of the edge devices in the learning process for a long time. (2) Without proper and strong incentive mechanisms, devices even do not join in the cooperation or only cost very little, and meaningless resources where no device can be ready to contribute reasonable and necessary resource, which would risk the success of the whole cooperative process. Drawing on these challenges this study introduces Chiron. Chiron operates through a HRL framework that guarantees equitable and optimal consumption of resources (for the learning process), detection and eviction of malicious or lethargic nodes, and the long-term resilience of the learning process[3]. Firmly, this introduction defines the programs around edge learning and calls a broad rollout of Chiron in a system level manner. Edge devices usually entail low computational capabilities and resource constraint in terms of energy and bandwidth. Training complex models can tax these resources, causing delays and inefficiencies. Moreover, the variability of devices in an edge network may lead to some devices working much faster than others. If not ruled, the rich devices will take over, the poor devices will be unable to come together. Edge learning has the same decentralized characteristic, making it vulnerable to attack from malicious user[4]. An adversarial node can purposely provide false updates to cripple the learning algorithm. Lazy nodes, on the other hand, may minimize their computational effort by submitting low-quality or randomly generated updates. Both behaviours can compromise the integrity and performance of the global model. Edge learning relies on the voluntary participation of devices[5]. However, active devices incur costs in terms of energy, computation and communication. Without adequate incentives, devices may choose to opt out or reduce their contributions, leading to a decline in the quality and robustness of the global model. Chiron addresses these challenges by integrating robustness, efficiency and sustainability into its design.

It involves a three-layer HRL framework implemented in Chiron, which provides the required mechanisms at different levels of the incentive mechanism: The first layer involves the long-term bucketing where Chiron decides how much bucketing should be allocated towards the learning process in total. This budget is what is available to use in multiple training round to reward active devices. the objective is to allocate incentives in an optimal way to keep the system alive and functional for a long time. With the help of this layer, short-term needs and long-term needs are balanced, preventing resource depletion, thus retaining device engagement [6]. Layer 2 focuses on short-term optimization. It shares resource across participating devices in each training round. The goal of the allocation strategy is to reduce voids time, improve the efficiency of resources and balance the fairness of devices. This layer must assess the computational power, energy availability and communication bandwidth of each device. Through distributed balance resource allocation, it increases the diversity and speed of the learning process [7]. The third layer focuses on ensuring the reliability and integrity of the global model. It identifies and excludes malicious or lazy nodes that negatively impact the learning process. This is achieved by analysing the quality of updates submitted by each node. Nodes that consistently submit low-quality or harmful updates are penalized or excluded from future rounds. This layer ensures that only trustworthy nodes participate, enhancing the overall robustness of the system [8].

Chiron incorporates system performance metrics and model accuracy into its optimization objectives. By participating at a

governance level, the economic structures that dictate behaviours can be tuned towards the wants of both the system and its future. But short-term efficiency cannot come at long-term sustainability or model performance. Chiron is modeled after Recursive Chaining, used to solve complex optimization problems in a hierarchical manner by breaking down to simple ones as sub-problems [9]. Using these layers, we design the incentivization mechanism for Chiron, where each layer has its own kind of target, such that both short term and long-term goals can be enforced against each other. Chiron can also be adapted to serve many edge learning scenarios due to its modular design. Chiron is an effective system to detect malicious or lazy nodes. It also ensures that the accuracy and integrity of the global model are maintained by examining the quality of updates proposed by individual nodes. This property is fundamental in decentralized systems where trust cannot be assumed [10].

Chiron has been empirically validated through large-scale experiments on real-world datasets such as MNIST and CIFAR-10. These datasets are standard benchmarks with broad use in machine learning research, thus ensuring robustness of the results for EDGE learning systems. Chiron shows superior accuracy, efficiency and robustness compared to state-of-the-art methods, as demonstrated by experiments. Chiron is a breakthrough in edge learning technology. For real-world applications, it offers a powerful and efficient solution by tackling key challenges like resource constraints, malicious behaviour and sustainability. Key contributions of this research include:

- A novel HRL-based framework for optimizing incentives in edge learning.
- An integrated approach that balances performance, efficiency and security.
- A scalable solution that can adapt to different edge learning scenarios and datasets.

Chiron offers a comprehensive solution to the challenges of edge learning. Its hierarchical design, integration of performance metrics and robustness against malicious behaviour make it a practical and impactful tool for advancing the field. By enabling efficient, secure and sustainable edge learning. Chiron paves the way for the widespread adoption of this innovative paradigm.

## II. RELATED WORK

Edge learning is a widespread paradigm for decentralized machine learning to collaboratively learn models while preserving privacy among devices. This reviewing work focuses on the fundamental challenges as well as existing solutions in terms of incentive mechanisms, resource optimization, robustness and HRL within the edge learning domain. Chiron serves within the context of these studies according to the review, emphasizing its innovations in robustness, efficiency and sustainability. Edge learning is sustained through incentive mechanisms. There has been a fair number of studies being done around the incentive mechanisms for encouraging the edge devices to make use of its resources. Wang et al. Edge devices are rewarded based on their energy consumption and contributions in the game-theoretic model proposed in [11]. Although good for balancing interactions with minimal resources spent and guests rewarded, this approach fails to prevent bad behaviour or encourage long-term engagement. Zhang et al. [12] developed upon this notion by modeling incentive schemes in contract theory. Their approach links rewards with the quality of contributions, thus enhancing the model performance. Tang et al. [13] introduced an auction-based model to optimize resource contributions dynamically. Their mechanism

prioritizes high-quality contributions but does not integrate model performance into its design. Chiron overcomes these limitations by combining model accuracy and fairness into its incentive decisions. Li et al. [14] proposed a federated learning framework that includes trust-based incentives to mitigate malicious contributions. However, this approach requires extensive monitoring, which increases overhead.

Chiron reduces such overhead by using lightweight reinforcement learning to detect and exclude harmful nodes. Resource allocation is crucial in edge learning due to the limited computational, energy and bandwidth resources of edge devices. Various studies have addressed these constraints. Huang et al. [15] introduced a scheduling algorithm to minimize latency by optimizing resource allocation among edge devices. This approach showed improved efficiency but struggled with fairness across heterogeneous devices. Chen et al. [16] proposed a decentralized resource optimization framework that reduces communication overhead. While effective, the framework does not include mechanisms to identify and address malicious behavior. Liu et al. [17] developed a reinforcement learning-based solution for dynamic resource allocation. This method demonstrated significant improvements in efficiency. However, it lacked robustness mechanisms to handle malicious nodes or low-quality contributions. Tang et al. [18] combined resource optimization with device reputation, ensuring fair allocation based on past performance. While this method improved fairness, it failed to incorporate dynamic adaptability, which Chiron achieves through its multi-layer HRL design. Chiron integrates resource optimization into its incentive mechanism, dynamically adapting to device performance and addressing heterogeneity across devices.

Maintaining robustness is critical in edge learning to ensure the integrity of the global model. Malicious nodes can introduce incorrect updates, significantly degrading model performance. Blanchard et al. [19] introduced byzantine-robust aggregation methods that filter outliers based on statistical analysis. While effective, these methods require significant computational resources, making them unsuitable for real-time edge learning.

Xie et al. [20] proposed a reputation-based system where devices are scored based on their contributions over time. High-reputation devices are prioritized in model aggregation. This approach adds robustness but requires extensive data storage and monitoring. Kang et al. [21] introduced a blockchain-based framework to secure model updates. While blockchain provides transparency and trust, its computational overhead limits scalability in resource-constrained environments. Fung et al. [22] explored federated learning with adaptive aggregation, where the system adjusts weights based on contribution quality. This approach is computationally efficient but does not address long-term sustainability. Chiron advances robustness by integrating byzantine resilience into its hierarchical framework.

HRL is highly applicable for such complex optimization problems at the Edge learning. HRL breaks down tasks, allowing focused and effective solutions. Vezhnevets et al. [23] proved HRL works well in multi-agent systems, encouraging its deployment in edge learning. Their triple layer philosophy inspired Chiron's three-layer design, each of which has a particular optimization goal. Tang et al. HRL was used in a task allocation problem for distributed systems by [24]. The proposed method improved resource utilization at the expense of malicious contributions. Chen et al. [25] HRL with federated learning where both resource allocation and model aggregation were optimized. However, their approach did not include incentive mechanisms from the ground level, while Chiron does it smoothly. Within the HRL framework

that extends to Chiron from previous work, Chiron is able to tackle long-term sustainability (as an aggregate of time) with real-time efficiency and robustness within the same framework.

## II.1 BACKGROUND WORK

This section provides an overview of two key concepts Edge Learning and Deep Reinforcement Learning (DRL). These frameworks support the proposed incentive-driven, Byzantine-resistant approach to edge learning. Edge learning addresses the privacy concerns inherent in distributed training scenarios by enabling collaborative model training without exposing raw data. Before introducing the decentralized scenario, we first describe the traditional centralized training approach for deep learning models. Given a deep learning model, let  $\omega$  denote its parameters. The model's loss function is defined as  $f(\omega, x_j, y_j)$ , here  $x_j$  and  $y_j$  represent the data and label of a given sample  $j$ . For simplicity, we abbreviate  $f(\omega, x_j, y_j)$  as  $f_j(\omega)$ . The objective of training is to update  $\omega$  such that the average loss across all samples is minimized. Mathematically, this is expressed as:

$$\omega^* = \operatorname{argmin}_{\omega} \frac{1}{|D|} \sum_{j \in D} f_j(\omega) \quad (1)$$

Here,  $D$  is the dataset. In decentralized edge learning, data is distributed among several edge nodes, each with its private dataset  $D_i$ . For edge node  $i$ , the loss function over its dataset is:

$$F_i(\omega) = \frac{1}{|D_i|} \sum_{j \in D_i} f_j(\omega) \quad (2)$$

The global loss function across all edge nodes is weighted by their dataset sizes and given as:

$$F(\omega) = \frac{\sum_{i=1}^N \delta_i |D_i| F_i(\omega)}{\sum_{i=1}^N \delta_i |D_i|} \quad (3)$$

Here,  $\delta_i \in \{0,1\}$  is an indicator of whether edge node  $i$  participates in the training round. The goal of edge learning is to collaboratively train the global model by solving:

$$\omega^* = \operatorname{argmin}_{\omega} F(\omega) \quad (4)$$

This optimization is achieved through distributed gradient descent. During each round, edge nodes perform  $\sigma$  epochs of local training on their private datasets. The local update for edge node  $i$  is:

$$\omega_{i,k} \leftarrow \omega_{i,k} - \eta \nabla_{\omega_{i,k}} F_i(\omega_{i,k}, x_j, y_j) \quad (5)$$

Here,  $\eta$  is the learning rate and  $k$  represents the current training round. After local training, edge nodes send their updated parameters  $\omega_{i,k}^{\sigma}$  to the central server, which aggregates them to form the new global model:



$$\omega_{g,k+1} = \frac{\sum_{i=1}^N \delta_{i,k} |D_i| \omega_{i,k}^\sigma}{\sum_{i=1}^N \delta_{i,k} |D_i|} \quad (6)$$

This iterative process allows edge nodes to collaboratively train a global model without compromising data privacy. DRL combines RL with deep neural networks to optimize an agent's decision-making policy through interaction with an environment. The agent observes the current state  $s_t$  of the environment, selects an action  $a_t$  according to its policy  $\pi(s_t)$  and receives a reward  $r_t$ . This interaction evolves the environment to the next state  $s_{t+1}$ . The goal of DRL is to maximize the expected cumulative reward:

$$R = \sum_{t=0}^T \gamma^t r(s_t, a_t) \quad (7)$$

Here,  $\gamma \in [0,1]$  is a discount factor for future rewards. A well-known DRL algorithm is Proximal Policy Optimization (PPO), which operates within the Actor-Critic framework. This framework consists of two networks first is the Actor Network which generates actions based on the current policy and second is the Critic Network used to estimate the value of a state  $V_\pi(s)$ , representing the expected future rewards. The value function  $V_\pi(s_1)$  is defined as:

$$V_\pi(s_1) = E \left[ \sum_{t=1}^{\infty} \gamma^t r(s_t, a_t) | s_1, \pi \right] \quad (8)$$

Using the state value, the advantage of an action can be calculated as:

$$A_t(s_t, a_t) = r(s_t, a_t) + \gamma V(s_{t+1}) - V(s_t) \quad (9)$$

PPO modifies the traditional policy gradient loss function by introducing a clipping factor  $\delta$  to stabilize updates:

$$L_{\text{PPO}}(\theta) = E \left[ \min \left( r(\theta) A_t, \text{clip}(r(\theta), 1 - \delta, 1 + \delta) A_t \right) \right] \quad (10)$$

Here,  $r(\theta)$  is the probability ratio between the new and old policies. DRL's ability to handle high-dimensional states and learn optimal policies through experience makes it a suitable choice for addressing complex problems like incentive-driven edge learning.

## II.2 SYSTEM MODEL

The system model in this study is based on a parameter server architecture, incorporating multiple edge nodes. The model facilitates collaborative learning while it addresses computational and communication challenges. The architecture consists of Parameter Server which manages the global model and aggregates updates from edge nodes. Edge Nodes are used to perform local training using their data and contribute updates to the global model. The training occurs in rounds where edge nodes receive the global model, perform local updates and send results back to the server for aggregation. The next round begins only after all nodes finish

their computations, introducing potential idle times. Each edge node's computation time depends on its local data size, CPU cycles per bit, and frequency:

$$T_{\text{cmp},i,k} = \frac{\sigma c_i d_i}{\zeta_{i,k}} \quad (11)$$

Here,  $\sigma$  is the Number of local epochs,  $c_i$  is the CPU cycles per bit,  $d_i$  is the Local data size and  $\zeta_{i,k}$  is the CPU frequency in round  $k$ . Communication time is determined by the global model size  $\xi$  and the uplink rate  $R_{i,k}$ :

$$T_{\text{com},i,k} = \frac{\xi}{R_{i,k}} \quad (12)$$

The total time for edge node  $i$  is the sum of computation and communication times:

$$T_{i,k} = T_{\text{cmp},i,k} + T_{\text{com},i,k} \quad (13)$$

The overall round time is dictated by the slowest node:

$$T_{\text{round}} = \max_{i \in N} T_{i,k} \quad (14)$$

Faster nodes experience idle times as:

$$T_{\text{idle},i,k} = T_{\text{round}} - T_{i,k} \quad (15)$$

Energy consumption comprises computational and communication components:

$$E_{\text{cmp},i,k} = \sigma \alpha_i c_i d_i \zeta_{i,k}^2 \quad (16a)$$

$$E_{\text{com},i,k} = \delta_i T_{\text{com},i,k} \quad (16b)$$

$$E_{i,k} = E_{\text{cmp},i,k} + E_{\text{com},i,k} \quad (16c)$$

Here,  $\alpha_i$  and  $\delta_i$  are energy coefficients. Edge nodes are incentivized based on their contributions. For edge node  $i$ :

$$u_{i,k} = p_{i,k} \zeta_{i,k} - \lambda_e E_{i,k} \quad (17)$$

Here,  $p_{i,k}$  is the price per CPU cycle and  $\lambda_e$  reflects the importance of energy costs. The system aims to optimize model accuracy while minimizing costs. Given a budget  $\psi_0$ , the remaining budget after  $k$  rounds is:

$$\psi_k = \psi_0 - \sum_{k=1}^K \sum_{i=1}^N \delta_{i,k} p_{i,k} \zeta_{i,k} \quad (18)$$

The utility function of the learning process is:

$$u = \lambda_a A(\omega_{g,K}) - \lambda_t \sum_{k=1}^K T_k + \psi_K \quad (19)$$

Here,  $A(\omega_{g,K})$  denotes model accuracy,  $\lambda_a$  and  $\lambda_t$  are weight parameters.

### II. 3 PROBLEM FORMATION AND ANALYSIS

This section elaborates on the strategies of the parameter server and edge nodes to optimize edge learning while ensuring robustness against Byzantine failures. The strategies aim to balance utility, computational efficiency and budget allocation under privacy constraints. The optimization problem is defined for both edge nodes and the parameter server. The key objective is to maximize the utility for both entities while maintaining efficiency in computation and communication. Each edge node  $i$  aims to maximize its utility  $u_{i,k}$  by adjusting its computational contribution  $\zeta_{i,k}$  during the  $k$ -th training round. The problem is formulated as:

$$\left. \begin{array}{l} \text{OP}_{i,k} : \max_{\zeta_{i,k}} u_{i,k}, \\ \text{subject to : } \zeta_{i,k} \in (0, \zeta_{i,\max}], \\ u_{i,k} \geq 0 \end{array} \right\} \quad (21)$$

The utility  $u_{i,k}$  is a function of the received bonus, computation energy, and communication energy is given in equation (17). The parameter server seeks to optimize its pricing strategy  $p_{i,k}$  to maximize utility  $u$ . The optimization problem is given as:

$$\left. \begin{array}{l} \text{OP}_{PS} : \max_{p_{i,k}} u, \\ \text{subject to : } \sum_{k=1}^K \sum_{i=1}^N \delta_{i,k} p_{i,k} \zeta_{i,k} \leq \psi_0 \end{array} \right\} \quad (22)$$

Here,  $\psi_0$  is the total budget and  $\delta_{i,k}$  indicates whether edge node  $i$  participates in round  $k$ . The optimal strategies for edge nodes and the parameter server are analysed to address both honest and dishonest nodes. Honest nodes participate in training only if their utility is positive. The optimal CPU frequency for an honest edge node  $i$  is determined by:

$$\zeta_{i,k}^* = \frac{p_{i,k}}{2\lambda_e \sigma \alpha_i c_i d_i} \quad (23)$$

Here,  $\alpha_i$ ,  $c_i$  and  $d_i$  represent hardware coefficients and data size respectively. The maximum utility is:

$$v_{i,k}^* = \frac{p_{i,k}^2}{4\lambda_e \sigma \alpha_i c_i d_i} - \lambda_e \zeta_{i,k} T_{\text{com},i,k} \quad (24)$$

Dishonest nodes include lazy and malicious nodes. Lazy nodes generate random updates without training, while malicious nodes send harmful updates. Their behaviour is modelled as:

$$\omega_{i,k}^\sigma = \omega_{i,k}^0 + \phi \quad (25)$$

Here,  $\phi$  is random noise. Their utility function is:

$$v_{i,k} = p_{i,k} \zeta_{i,k} - \lambda_e \zeta_{i,k} T_{\text{com},i,k} \quad (26)$$

The parameter server aims to minimize idle time while ensuring efficient training. Idle time for node  $i$  is given in equation (15). The pricing strategy is optimized to satisfy:

$$T_{\text{idle},k} = 0 \quad (27)$$

The incentive mechanism ensures participation and fairness. Edge nodes receive bonuses proportional to their contributions, and malicious nodes are identified and excluded. The utility of the parameter server over  $K$  rounds is expressed as:

$$v = \lambda_a A(\omega_{g,K}) - \lambda_t \sum_{k=1}^K T_k + \psi_K \quad (28)$$

Here,  $A(\omega_{g,K})$  is the model accuracy and  $\psi_K$  is the remaining budget. The energy consumption of edge node  $i$  is given in (16a), (16b) and (16c). Time efficiency is optimized by aligning training times across nodes, ensuring:

$$r_{\text{eff}} = \frac{\sum_{i=1}^N T_{i,k}}{NT_{\text{round}}} \approx 1 \quad (29)$$

### III. HIERARCHICAL REINFORCEMENT LEARNING DESIGN

Write HRL is employed to optimize the incentive mechanism in edge learning systems, ensuring robustness and efficiency. This section elaborates on the three-layer HRL framework, agent-specific designs and its advantages over traditional DRL. Edge learning environments present unique challenges. It includes dishonest edge nodes which has lazy and malicious nodes degrade system performance. Privacy Concerns is used as server access to edge node raw data and hardware details is restricted. Dynamic Environments are used as training data distributions and resource availability shift over time. To address these challenges, the HRL approach decomposes complex tasks into three sub-tasks handled by dedicated DRL agents Price volume determination, Bonus distribution and Edge node selection.

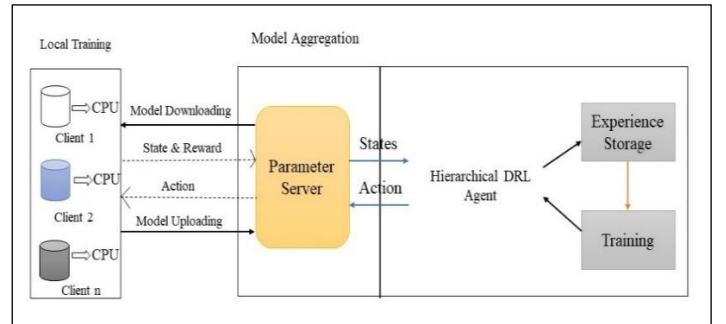


Figure 1: Edge Learning Operational Process.  
Source: Authors, (2025).

The Figure 1 illustrates the architecture of the proposed framework for edge learning using a Hierarchical DRL Agent. It highlights three main components: Local Training, Model Aggregation and Hierarchical DRL Agent. In the Local Training phase, multiple edge nodes (referred to as clients) independently train local models using their private datasets. Each client performs computations locally to preserve privacy and avoid data transfer.

After training, the clients upload their locally updated models to a central Parameter Server. The server manages model aggregation by collecting updates from all participating edge nodes and integrating them to update the global model. This global model is then sent back to the clients through model downloading, ensuring continuous and iterative learning. The Parameter Server interacts directly with the Hierarchical DRL Agent for incentive mechanism optimization. The server provides real-time states and rewards to the DRL agent which evaluates the system's performance and sends back actions to guide the incentive mechanisms and edge node participation. The Hierarchical DRL Agent has two submodules Experience Storage, which records interaction history for further learning and Training which continuously improves the DRL policy based on past experiences. This design enables robust decision-making allowing the system to select reliable edge nodes and reward contributions. It also ensures efficient and fair resource utilization, resulting in improved global model accuracy and system performance.

The HRL framework comprises three agents, first is the Exterior Agent (Price Volume Calculator) which determines the overall budget allocation, second is the Middle Agent (Price Partition Distributor) which allocates the budget across edge nodes to minimize idle time and the third is the Inner Agent (Edge Node Selector) which selects participating edge nodes, expelling malicious ones. Each agent interacts with its environment and learns from experience tuples  $(s, a, r, s')$ , where  $s$  represents the state,  $a$  the action,  $r$  the reward and  $s'$  the subsequent state. The state, action, and reward functions for each agent are defined as follows. Exterior Agent is used as Price Volume Calculator which combines historical and current information.

$$s_k^E = \{\zeta_{k-L}, \dots, \zeta_{k-1}, p_{k-L}, \dots, p_{k-1}, T_{k-L}, \dots, T_{k-1}, \psi_k, k\} \quad (30)$$

Here,  $\zeta$ ,  $p$ , and  $T$  denote CPU frequencies, pricing strategies, and training times, respectively, from the past  $L$  rounds.

Action: Sets the total budget:

$$a_k^E = \{p_{total,k}\} \quad (31)$$

Reward: Encourages long-term utility:

$$r_k^E = \lambda_a (A(\omega_k) - A(\omega_{k-1})) - \lambda_t T_k + \psi_k \quad (32)$$

Here,  $\lambda_a$  and  $\lambda_t$  are weight parameters for accuracy improvement and training time.

State: Takes the total budget as input:

$$s_k^M = \{p_{total,k}\} \quad (33)$$

Action: Allocates the budget proportionally among nodes:

$$a_k^M = \{\rho_{1,k}, \dots, \rho_{N,k}\}, \quad \text{where } \sum_{i=1}^N \rho_{i,k} = 1. \quad (34)$$

Reward: Encourages time consistency:

$$r_k^M = -\sum_{i=1}^N T_{idle,i,k} \quad (35)$$

Here,  $T_{idle,i,k}$  is the idle time of edge node  $i$ .

State: Incorporates model weights, price allocations, and remaining budget:

$$s_k^I = \{p_{1,k}, \dots, p_{N,k}, \omega'_{1,k}, \dots, \omega'_{N,k}, \omega'_g, \psi_k, k\} \quad (36)$$

Action: Determines the probability of node participation:

$$a_k^I = \{v_{1,k}, \dots, v_{N,k}\}, \quad v_{i,k} \in [0,1] \quad (37)$$

Reward: Balances accuracy and budget consumption:

$$r_k^I = \lambda_a (A(\omega_{k+1}) - A(\omega_k)) - \sum_{i=1}^N v_{i,k} p_{i,k} \zeta_{i,k} \quad (38)$$

Each agent employs Proximal Policy Optimization (PPO) for training. The workflow includes Initializing policy parameters, collecting experience tuples  $(s, a, r, s')$  and Updating actor and critic networks to optimize rewards. The PPO loss functions are:

$$L_{actor}(\theta) = E \left[ \min \left( r(\theta) A_t, \text{clip}(r(\theta), 1 - \delta, 1 + \delta) A_t \right) \right] \quad (39)$$

$$L_{critic} = \sum (r_t + \gamma V(s_{t+1}) - V(s_t))^2 \quad (40)$$

Here,  $r(\theta)$  is the probability ratio and  $A_t$  the advantage. Advantages of HRL include Task Decomposition which Simplifies optimization by dividing tasks into manageable sub-tasks, Enhanced Exploration expands the action space across three layers and Robustness adapts to dynamic environments and identifies malicious nodes.

#### IV. RESULTS AND DISCUSSIONS

In This section evaluates the effectiveness of the proposed HRL system, Chiron. The evaluation involves comprehensive experiments designed to assess global model accuracy, time efficiency, and system utility in diverse environments. Robustness against dishonest edge nodes and scalability under varying system conditions is also analysed. The experiments utilize real-world datasets and models under systematically controlled settings. The datasets include MNIST, Fashion-MNIST and CIFAR-10. Models of CNNs are MNIST and Fashion-MNIST which are two 5x5 convolutional layers followed by max pooling and CIFAR-10 of LeNet with three 5x5 convolutional layers followed by max pooling. The edge node settings are CPU cycle requirements for processing one bit are  $c_i \sim U(1,2)$  GHz. Communication times  $T_{com,i} \sim U(10,20)$  seconds. Implementation Framework has DRL agents which are implemented using the Tianshou framework with PPO. Actor and critic learning rates decay by 95% every 20 rounds. Three primary metrics are employed to assess performance, first is the Global Model Accuracy  $A(\omega_g)$  which is evaluated using test datasets. Second is the Time Efficiency  $r_{eff}$  which measures valid training time utilization:

$$r_{eff} = \frac{\sum_{i=1}^N T_{i,k}}{NT_{round}} \quad (41)$$

Here,  $T_{i,k}$  is the training time of edge node  $i$  in round  $k$ . Third is the server utility  $u$  which combines accuracy, time efficiency and budget usage is given in equation (19). Chiron's performance is compared with a DRL-based baseline and a greedy approach. Server Utility is used as Chiron achieves higher utility across budgets. Chiron maintains accuracy without sacrificing performance for budget constraints. Chiron achieves nearly 100%-time efficiency, minimizing idle times. Experiments with 10 to 100 edge nodes highlight Chiron's scalability are Utility Trends where Chiron's utility remains above 25, while baselines drop significantly with more nodes, Time efficiency exceeds 80% preserving budget for additional rounds. Chiron's performance is evaluated in environments with malicious and lazy nodes. Malicious Nodes are Chiron outperforms baselines, maintaining accuracy and utility even when 70% of nodes are malicious. In Lazy Nodes Chiron resists budget wastage from lazy nodes, remaining robust up to 60% laziness. Mixed Environments has Chiron which excels with honest, malicious and lazy nodes achieving the best metrics. In Budget Utilization Chiron's hierarchical design prevents budget overuse, enabling sustainable training. Malicious Node Exclusion include the inner agent accurately filters harmful updates, preserving model quality. Long-Term Optimization has adaptive pricing strategies ensure robust utility growth. Chiron consistently outperforms baselines in accuracy, utility and robustness. The results validate the efficacy of hierarchical reinforcement learning in addressing the challenges of edge learning environments.

The Figure 2 shows the accuracy versus number of rounds for three methods: Chiron, DRL-Based, and Greedy. Chiron achieves the highest accuracy across all rounds, starting at 0.6 and reaching almost 0.95 at round 50. The DRL-Based method performs slightly lower, beginning at 0.6 and gradually improving to 0.85 at round 50. The Greedy method exhibits the slowest improvement, starting at 0.55 and reaching approximately 0.8 by round 50. From the graph, we see that Chiron consistently outperforms the other methods in accuracy throughout the training rounds. The difference between Chiron and the DRL-Based method is noticeable, especially after round 20, with a gap of about 0.05 to 0.1. Similarly, the gap between Chiron and the Greedy method widens with increasing rounds, highlighting Chiron's superior learning capability. DRL-Based maintains a steady and moderate improvement, while Greedy shows the least effective performance. This indicates that Chiron is more efficient in learning and adapting compared to the other approaches.

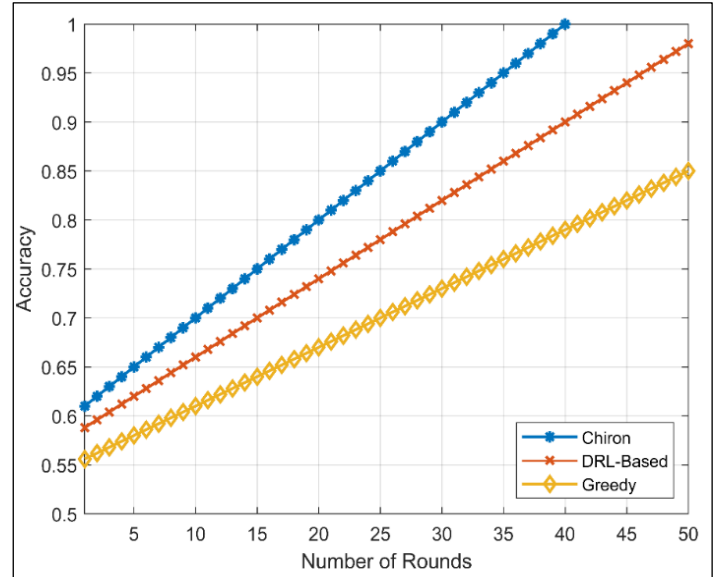


Figure 2: Accuracy versus number of rounds.  
Source: Authors, (2025).

The Figure 3 shows the Performance under CIFAR-10 when varying the total budgets for Server Utility vs. Total Budget for three methods: Chiron, DRL-Based, and Greedy. Chiron consistently achieves the highest server utility at every budget level. At a budget of 50, its utility starts at around 30, increasing linearly to reach nearly 70 at a budget of 300. DRL-Based is average, you get around an initial 25 utility that grows to approximately 60 for about 300 in budget. The impulse approach is the least efficient, achieving a utility of 20 and approximately 55 at the highest budget. We observe that Chiron consistently outperforms all the other methods for all budget levels. As the budget is increased, the difference between Chiron and DRL-Based grows, resulting in a utility gap of 5 to 10 points—between candidate budgets that range from 0 to 60. Also, the ever-growing distance between Chiron and Greedy confirms Chiron's effective resource utilization. These two methods turned out to provide the slowest improvement, as we can see that the utility curve for the Greedy method also starts to flatten shortly after the budget has approached the 300 mark. The well-shown trends demonstrated are reflecting Chiron's better optimization strategies represented by DRL-Based and Greedy approaches.

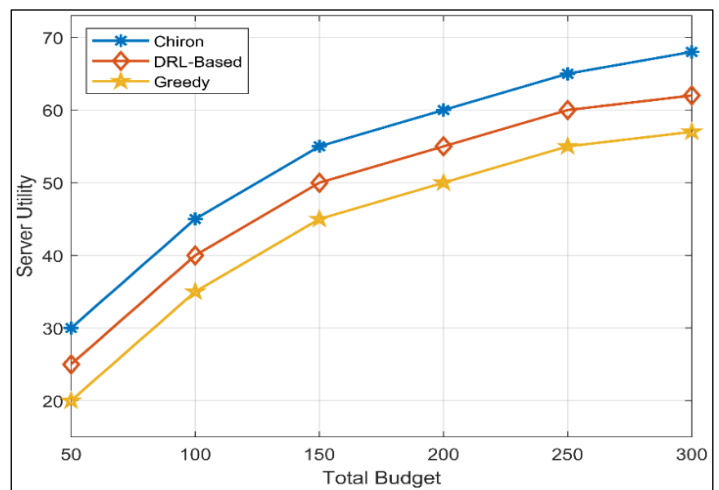


Figure 3: Performance under CIFAR-10 when varying the total budgets for server utility.  
Source: Authors, (2025).



The Figure 4 illustrates the Performance under CIFAR-10 when varying the total budgets for Global Model Accuracy vs. Total Budget for three methods: Chiron, DRL-Based, and Greedy. Chiron achieves the highest accuracy at all budget levels. It starts at approximately 0.7 with a budget of 50 and steadily increases to about 0.87 at a budget of 300. The DRL-Based method performs moderately. It starts at 0.7 similar to Chiron, but grows more slowly, reaching around 0.82 at a budget of 300. The Greedy method has the lowest accuracy. It starts at 0.65, then moves up gradually to around 0.78 with the highest budget. Times mention that Chiron always outperforms the others in terms of accuracy, thus it better utilizes the budget. Over the time period considered, the worst gap between Chiron and DRL-Based is around 0.05 as the budget increases. The same can also be said for the gap between Chiron and Greedy, as throughout the tests there is a consistent gap of 0.1 to 0.12. These trends highlight Chiron's better optimization as well as Chiron's ability to improve the models performance across all budget levels while DRL-Based gets moderate gains and Greedy simply can't obtain high accuracy. In budget-constrained environments, maximizing resource-use efficiency is essential, and this only supports the importance of that.

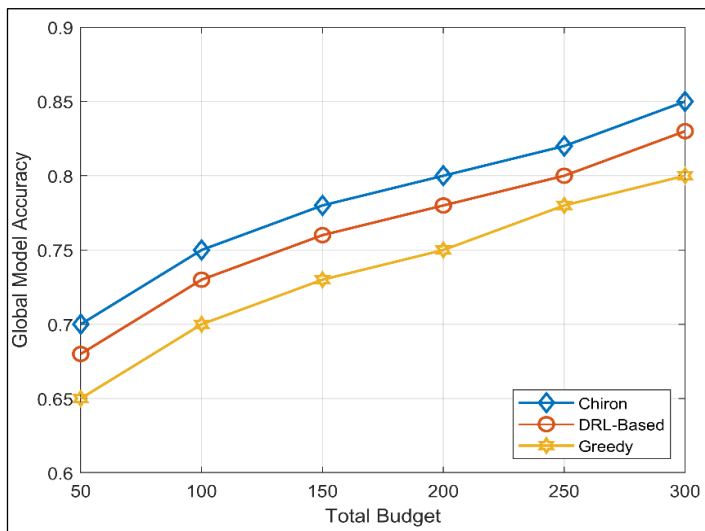


Figure 4: Performance under CIFAR-10 when varying the total budgets for Global Model Accuracy.  
Source: Authors, (2025).

The Figure 5 shows Performance under CIFAR-10 when varying the total budgets for time efficiency versus total budget for three methods: Chiron, DRL-Based, and Greedy. Chiron starts at a time efficiency of around 0.85 for a budget of 50 and steadily increases to nearly 0.97 at a budget of 300. DRL-Based begins at approximately 0.8 and gradually rises to about 0.9 as the budget increases. Greedy starts at 0.75 and increases modestly to around 0.87 by the end of the budget range. The results highlight that Chiron outperforms the other methods in time efficiency across all budget levels. The difference between Chiron and DRL-Based is noticeable, with a gap of approximately 0.05 to 0.07 throughout. Similarly, Chiron maintains a significant advantage over Greedy, with a time efficiency difference of about 0.1 at most budget levels. The Greedy method shows the slowest improvement, indicating less efficient use of resources to minimize idle time. These trends underline Chiron's ability to achieve high time efficiency, particularly as the budget increases, making it the most effective method for optimizing resource utilization.

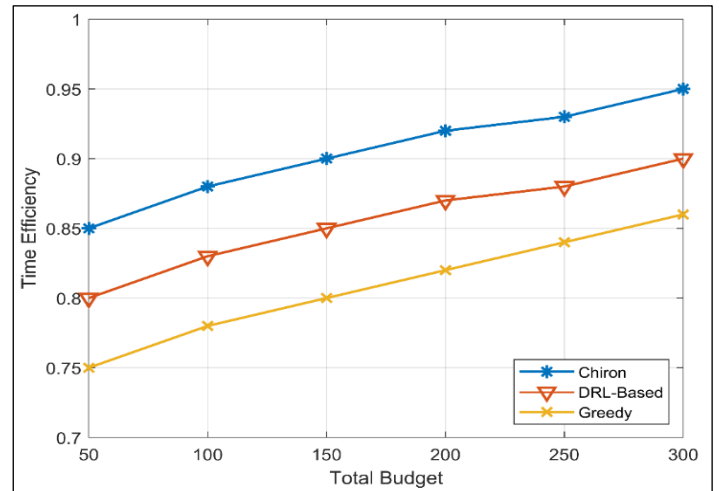


Figure 5: Performance under CIFAR-10 when varying the total budgets for Time Efficiency.  
Source: Authors, (2025).

The Figure 6 shows accuracy versus percentage of malicious nodes for three methods: Chiron, DRL-Based, and Greedy. Chiron starts with an accuracy of 0.85 when there are no malicious nodes. Its accuracy gradually declines to approximately 0.65 as malicious nodes increase to 70%. The DRL-Based method begins at an accuracy of 0.8 and decreases more sharply, reaching around 0.6 at 70% malicious nodes. The Greedy method consistently delivers the worst performance, beginning at 0.75 and falling to 0.5 when 70% of the nodes are malicious. This shows that under the all conditions, Chiron achieves the highest accuracy indicates its strong robustness to malicious node. Chiron's resultant accuracy in comparison to conjectured DRL-Based model varies between 0.05 to 0.1 throughout the range, which indicates Chiron's improved resistance against adversarial malicious behaviour. It can be seen that the Greedy method has the steepest decline in the accuracy, which shows that it is vulnerable to malicious nodes. With increasing number of malicious nodes, Chiron's optimization and fault tolerance enables it to out perform Greedy as the gap increases. This analysis highlights that Chiron demonstrates proficiency in robustness to noisy environments in comparison to the other methods.

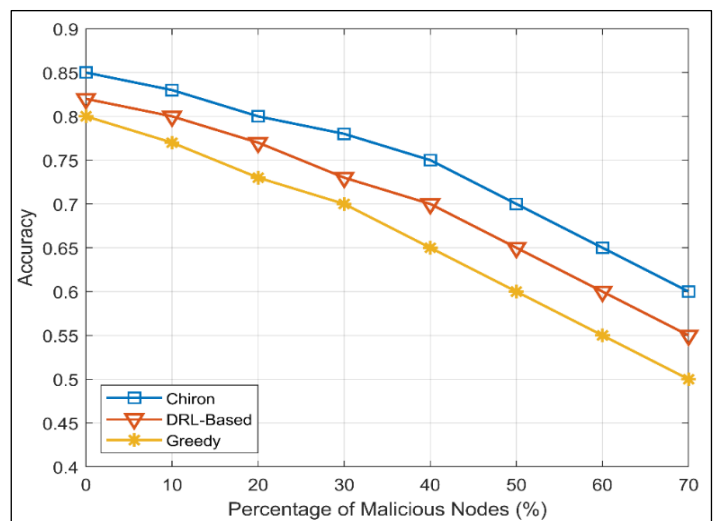


Figure 6: Accuracy versus Percentage of Malicious Nodes.  
Source: Authors, (2025).

The Figure 7 depicts idle time versus number of edge nodes for three methods: Chiron, DRL-Based, and Greedy. Chiron has the lowest idle time across all edge node counts. Its idle time starts at about 10 seconds for 10 edge nodes and increases linearly to approximately 30 seconds for 100 edge nodes. DRL-Based exhibits moderate idle time, starting at 12 seconds for 10 nodes and growing steadily to about 45 seconds for 100 nodes. The Greedy method performs the worst, starting at 15 seconds and rising sharply to nearly 70 seconds for 100 edge nodes. This analysis highlights the relative shrug-ability of Chiron with respect to idle time with increasing edge nodes. This gap is even bigger when comparing Chiron and DRL-Based, culminating in a 15 seconds difference at 100 edge nodes. Likewise, the difference between Chiron and Greedy becomes. Similar to before, we have a huge gap of almost 40 seconds between Chiron and Greedy at 100 nodes. This shows that Chiron handles idle time efficiently even at a large scale and is more efficient and scalable than DRL-Based approaches and Greedy approaches. This highlights the benefits of Chiron in efficiently utilizing resources and reducing latency in distributed edge learning systems.

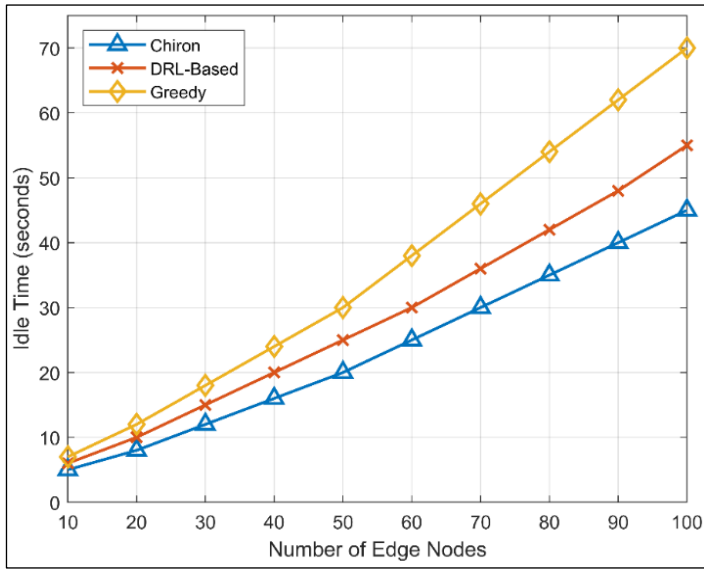


Figure 7: Ideal time versus Number of Edge Nodes.  
Source: Authors, (2025).

The Figure 8 presents the convergence of DRL agents over episodes for three agents: the inner agent, middle agent, and exterior agent. In subplot (a), the Inner Agent begins with a reward close to 0 in the initial episodes. The reward steadily increases to approximately 20 by the 50th episode, showing a smooth convergence pattern. Subplot (b) depicts the Middle Agent, where the reward starts near 0 and rises steadily, converging at around 15 by episode 50. Subplot (c) shows the Exterior Agent, whose reward also starts near 0, increases steadily and converges at about 12 by the 50th episode. These plots demonstrate that all three agents successfully learn and converge within the 50 episodes. The inner agent achieves the highest reward, indicating it has the most significant impact or effectiveness in the system. The middle agent converges at a slightly lower reward, while the exterior agent achieves the lowest reward. This suggests a hierarchical distribution of complexity and contribution among the agents. The steady increase in rewards across episodes also reflects stable training and effective optimization strategies for all agents. Overall, the figure highlights that the DRL framework effectively enables each agent to achieve its respective learning objectives.

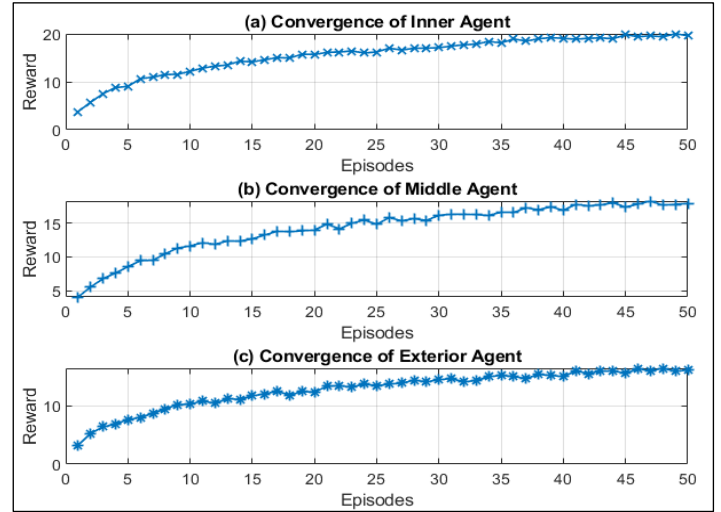


Figure 8: Convergence of DRL Agents.  
Source: Authors, (2025).

The Figure 9 illustrates global model accuracy versus percentage of malicious nodes for three methods: Chiron, DRL-Based, and Greedy. Chiron starts at an accuracy of 0.85 when there are no malicious nodes and gradually decreases to approximately 0.7 as malicious nodes increase to 70%. DRL-Based begins with an accuracy of 0.8 and declines steadily, reaching around 0.6 at 70% malicious nodes. Greedy has the lowest accuracy, starting at 0.75 and dropping sharply to approximately 0.55 by the end. The results highlight Chiron's superior performance in maintaining accuracy under increasing malicious nodes. The difference between Chiron and DRL-Based grows as malicious nodes increase, with a gap of about 0.1 at higher percentages. Similarly, the gap between Chiron and Greedy is even more pronounced, emphasizing Chiron's robustness in hostile environments. DRL-Based shows moderate resistance, though Greedy performs poorly, especially as the percentage of malicious nodes grows. This comparison clearly demonstrates Chiron's effectiveness in mitigating the impact of malicious behaviour and maintaining reliable model accuracy.

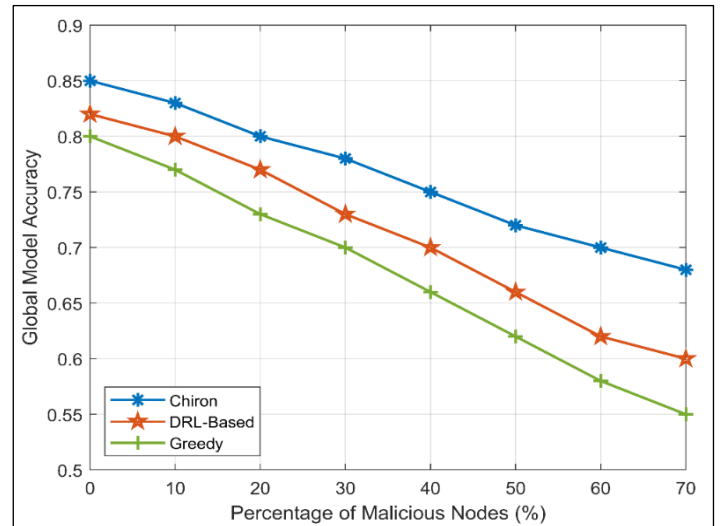


Figure 9: Global model accuracy versus percentage of malicious nodes in malicious environment.  
Source: Authors, (2025).

The Figure 10 shows global model accuracy versus percentage of lazy nodes for three methods: Chiron, DRL-Based,

and Greedy. Chiron starts with an accuracy of 0.85 at 0% lazy nodes and gradually decreases to around 0.7 when lazy nodes reach 70%. DRL-Based begins with an accuracy of approximately 0.8 and declines steadily, reaching 0.65 at 70% lazy nodes. Greedy starts at 0.75 and drops more sharply, reaching 0.6 at the maximum percentage of lazy nodes. This figure demonstrates Chiron's superior robustness against lazy nodes, maintaining higher accuracy across all percentages. The gap between Chiron and DRL-Based grows as lazy nodes increase, reaching about 0.05 at 70%. Similarly, the gap between Chiron and Greedy is even more significant, with a difference of approximately 0.1 at higher percentages. DRL-Based performs moderately but struggles more as the proportion of lazy nodes increases. Greedy shows the steepest decline, indicating its inability to handle high levels of laziness. These results emphasize Chiron's effectiveness in minimizing the impact of lazy nodes and maintaining reliable model accuracy in such scenarios.

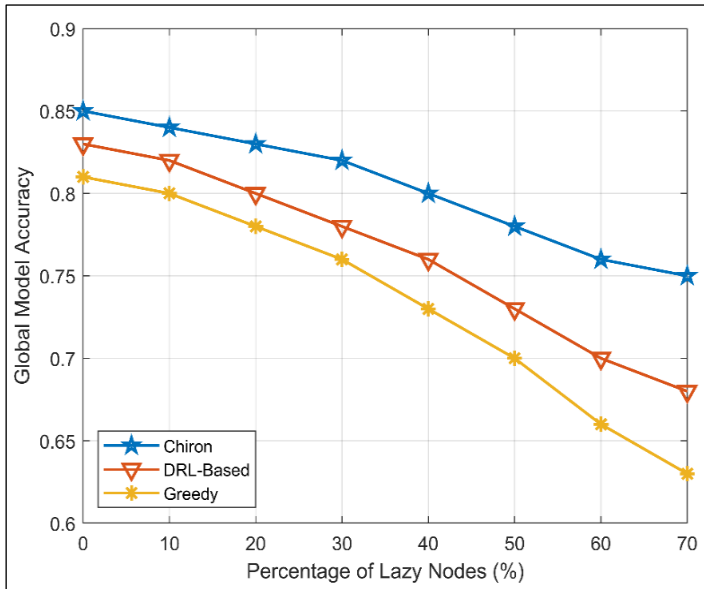


Figure 10: Global model accuracy versus percentage of lazy nodes in lazy environment.  
Source: Authors, (2025).

The Figure 11 shows server utility versus number of edge nodes for three methods: Chiron, DRL-Based, and Greedy. Chiron achieves the highest server utility for all edge node counts. It starts at around 20 for 10 edge nodes and steadily increases to approximately 90 for 100 edge nodes. DRL-Based has moderate server utility. It begins at around 18 for 10 edge nodes and grows to approximately 80 at 100 edge nodes. The Greedy method has the lowest performance, starting at around 15 for 10 edge nodes and reaching only about 70 for 100 edge nodes. This graph highlights Chiron's superior ability to maximize server utility as the number of edge nodes increases. The gap between Chiron and DRL-Based widens as more edge nodes are added, reaching a difference of about 10 utility units at 100 edge nodes. Similarly, the difference between Chiron and Greedy grows significantly, reaching nearly 20 utility units at the same point. The Greedy method consistently lags behind, reflecting its inefficiency in resource allocation compared to the other methods. This analysis underscores Chiron's advantage in optimizing server utility, especially in large-scale distributed systems. It performs better in leveraging additional edge nodes, demonstrating its robustness and scalability.

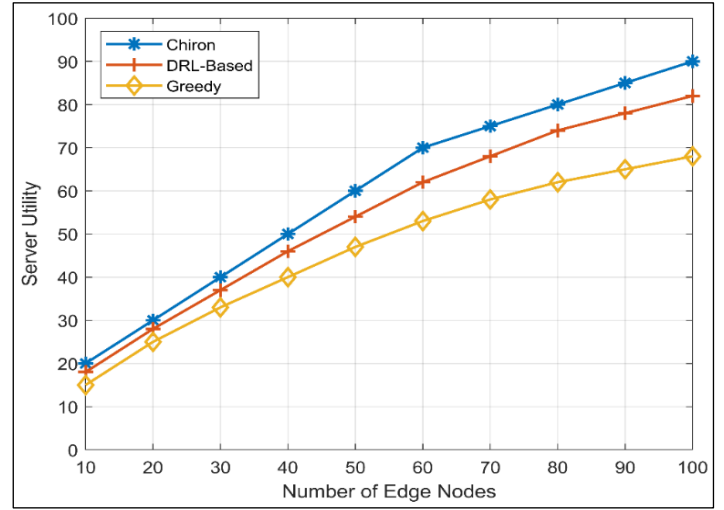


Figure 11: Server utility versus number of edge nodes  
Source: Authors, (2025).

## V. CONCLUSIONS

The research addresses the crucial problem of designing an efficient incentive mechanism for edge learning systems, emphasizing three primary objectives. The first is to incorporate model performance metrics into the optimization process to guarantee high-quality outputs. The second is ensuring system sustainability by implementing long-term optimization strategies. Finally, it focuses on identifying and mitigating the effects of malicious and lazy edge nodes to enhance the system's robustness. To achieve these objectives, the paper introduces a HRL framework comprising three distinct layers. This design decomposes the complex task into three sub-tasks: pricing determination for long-term utility maximization, bonus distribution for short-term optimization and edge node selection for excluding underperforming or malicious participants. This three-tiered approach ensures that the system remains efficient, adaptive and robust against dishonest behaviours in the dynamic edge learning environment proposed method demonstrates substantial improvements compared to state-of-the-art mechanisms.

Experimental evaluations on real-world datasets, like CIFAR-10, reveal an increase in system accuracy and total utility by 14.96% and 12.66%, respectively. By expelling lazy and malicious nodes, the system maintains higher reliability and performance consistency. Additionally, the framework ensures effective budget utilization and scalability, making it suitable for future network scenarios like beyond 5G (B5G). The researchers emphasize the importance of continuing exploration in areas like advanced node behaviour analysis, energy-aware strategies and integration into emerging network architectures. This secures the practical implications of the HRL-based incentive mechanism, which balances efficiency, robustness and sustainability in edge learning systems. By addressing existing limitations, it paves the way for more reliable and effective distributed machine learning frameworks.

## VI. AUTHOR'S CONTRIBUTION

**Conceptualization:** Gowtham R, Vatsala Anand, Yadati Vijaya Suresh, Kasetty Lakshmi Narasimha, R. Anil Kumar, V.Saraswathi

**Methodology:** Gowtham R, Vatsala Anand, Yadati Vijaya Suresh, Kasetty Lakshmi Narasimha, R. Anil Kumar, V.Saraswathi.

**Investigation:** Gowtham R, Vatsala Anand, Yadati Vijaya Suresh, Kasetty Lakshmi Narasimha, R. Anil Kumar, V.Saraswathi.

**Discussion of results:** Gowtham R, Vatsala Anand, Yadati Vijaya Suresh, Kasetty Lakshmi Narasimha, R. Anil Kumar, V.Saraswathi.

**Writing – Original Draft:** Gowtham R, Vatsala Anand, Yadati Vijaya Suresh, Kasetty Lakshmi Narasimha, R. Anil Kumar, V.Saraswathi.

**Writing – Review and Editing:** Gowtham R, Vatsala Anand, Yadati Vijaya Suresh, Kasetty Lakshmi Narasimha, R. Anil Kumar, V.Saraswathi.

**Resources:** Gowtham R, Vatsala Anand, Yadati Vijaya Suresh, Kasetty Lakshmi Narasimha, R. Anil Kumar, V.Saraswathi.

**Supervision:** Gowtham R, Vatsala Anand, Yadati Vijaya Suresh, Kasetty Lakshmi Narasimha, R. Anil Kumar, V.Saraswathi.

**Approval of the final text:** Gowtham R, Vatsala Anand, Yadati Vijaya Suresh, Kasetty Lakshmi Narasimha, R. Anil Kumar, V.Saraswathi.

## VII. REFERENCES

- [1]M. S. Murshed, C. Murphy, D. Hou, N. Khan, G. Ananthanarayanan, and F. Hussain, "Machine learning at the network edge: A survey," *ACM Computing Surveys (CSUR)*, vol. 54, no. 8, pp. 1–37, 2021.
- [2]Y. Yu, X. Li, X. Leng, L. Song, K. Bu, Y. Chen, J. Yang, L. Zhang, K. Cheng, and X. Xiao, "Fault management in software-defined networking: A survey," *IEEE Communications Surveys & Tutorials*, vol. 21, no. 1, pp. 349–392, 2018.
- [3]Y. Liu et al., "Optimizations on resource constrained federated learning with diverse clients," 2024.
- [4]Y. Sun, H. Ochiai, and H. Esaki, "Decentralized deep learning for multi-access edge computing: A survey on communication efficiency and trust worthiness," *IEEE Transactions on Artificial Intelligence*, vol. 3, no. 6, pp. 963–972, 2021.
- [5]W. Y. B. Lim, N. C. Luong, D. T. Hoang, Y. Jiao, Y.-C. Liang, Q. Yang, D. Niyato, and C. Miao, "Federated learning in mobile edge networks: A comprehensive survey," *IEEE communications surveys & tutorials*, vol. 22, no. 3, pp. 2031–2063, 2020.
- [6]F. Akhtar, S. A. Lodhi, S. S. Khan, and F. Sarwar, "Incorporating permaculture and strategic management for sustainable ecological resource management," *Journal of environmental management*, vol. 179, pp. 31–37, 2016.
- [7]Y.-J. Gong, J. Zhang, H. S.-H. Chung, W.-N. Chen, Z.-H. Zhan, Y. Li, and Y.-H. Shi, "An efficient resource allocation scheme using particle swarm optimization," *IEEE Transactions on Evolutionary Computation*, vol. 16, no. 6, pp. 801–816, 2012.
- [8]M. A. Khan, Shalu, Q. N. Naveed, A. Lasisi, S. Kaushik, and S. Kumar, "A multi-layered assessment system for trustworthiness enhancement and reliability for industrial wireless sensor networks," *Wireless Personal Communications*, vol. 137, no. 4, pp. 1997–2036, 2024.
- [9]Y. Tang, "Transport efficiency increase for axfood's transport carriers in central gothenburg," *rapport nr.: Masters Thesis*, no. 2003, 2004.
- [10]M. T. Hammi, B. Hammi, P. Bellot, and A. Serhrouchni, "Bubbles of trust: A decentralized blockchain-based authentication system for iot," *Computers & Security*, vol. 78, pp. 126–142, 2018.
- [11]Z. Wang, X. Chen, and Z. Zhou, "Joint Resource Allocation and Incentive Design for Federated Learning in Wireless Networks," *IEEE Transactions on Wireless Communications*, vol. 20, no. 3, pp. 2121–2132, Mar. 2021.
- [12]J. Zhang, L. Liu, and H. Tang, "Contract-Based Incentive Mechanisms for Federated Learning," *IEEE Transactions on Network Science and Engineering*, vol. 7, no. 3, pp. 1227–1240, Jul.–Sep. 2020.
- [13]Z. Tang, Y. Zhao, and R. Liu, "Auction-Based Federated Learning Incentive Mechanisms," *IEEE Transactions on Mobile Computing*, vol. 19, no. 11, pp. 2598–2612, Nov. 2020.
- [14]L. Li, J. Wang, and X. Zhang, "Efficient Resource Allocation in Heterogeneous Edge Networks," *IEEE Transactions on Cloud Computing*, vol. 8, no. 3, pp. 853–865, Jul.–Sep. 2020.
- [15]J. Huang, S. Zhou, and Z. Niu, "Optimized Task Scheduling for Edge Computing," *IEEE Transactions on Parallel and Distributed Systems*, vol. 29, no. 7, pp. 1604–1617, Jul. 2018.
- [16]X. Chen, L. Pu, and Z. Wang, "Resource Optimization in Federated Learning Systems," *IEEE Transactions on Mobile Computing*, vol. 22, no. 5, pp. 781–792, May 2023.
- [17]Y. Liu, S. Guo, and Y. Zhan, "Chiron: Robustness-Aware Incentive Mechanism for Edge Learning," *IEEE Transactions on Mobile Computing*, vol. 23, no. 8, pp. 8508–8518, Aug. 2024.
- [18]Z. Tang, Y. Zhao, and R. Liu, "Resource Management for Federated Edge Learning," *IEEE Internet of Things Journal*, vol. 9, no. 3, pp. 2271–2284, Mar. 2022.
- [19]P. Blanchard, E. M. Lupu, and R. Shen, "Byzantine-Robust Federated Learning," *IEEE Transactions on Neural Networks and Learning Systems*, vol. 31, no. 3, pp. 1012–1024, Mar. 2020.
- [20]J. Xie, L. Yang, and Y. Chen, "Reputation-Based Robustness in Federated Learning," *IEEE Transactions on Communications*, vol. 69, no. 10, pp. 6712–6721, Oct. 2021.
- [21]J. Kang, R. Yu, and Z. Xie, "Blockchain for Secure and Efficient Edge Learning," *IEEE Communications Surveys & Tutorials*, vol. 22, no. 2, pp. 1141–1164, Second Quarter 2020.
- [22]C. Fung, C. Zhang, and S. S. Lee, "Robust Federated Learning with Adaptive Aggregation," *IEEE Transactions on Artificial Intelligence*, vol. 2, no. 2, pp. 132–144, Apr. 2021.
- [23]A. Vezhnevets, S. Osindero, and T. Schaul, "FeUdal Networks for Hierarchical Reinforcement Learning," *Proceedings of the International Conference on Machine Learning*, 2017, pp. 3540–3549.
- [24]Z. Tang, R. Liu, and Y. Zhao, "Task Allocation in Distributed Systems Using HRL," *IEEE Transactions on Systems, Man, and Cybernetics: Systems*, vol. 51, no. 9, pp. 5031–5042, Sep. 2021.
- [25]X. Chen, L. Pu, and Z. Niu, "HRL for Federated Learning Optimization," *IEEE Transactions on Parallel and Distributed Systems*, vol. 33, no. 4, pp. 859–871, Apr. 2022.





ISSN ONLINE: 2447-0228

ITEGAM-JETIA

Manaus, v.11 n.52, p. 243-252. March./April., 2025.

DOI: <https://doi.org/10.5935/jetia.v11i52.1677>RESEARCH ARTICLE  
ACCESS

OPEN

# ENHANCING REAL-TIME ANIMATION: ENSURING DISTINCTIVENESS IN CROWD DYNAMICS THROUGH PHYSICS-BASED COLLISION AVOIDANCE

Imane DRIDI <sup>1</sup>, Cherif FOUDIL <sup>2</sup><sup>12</sup> LESIA Laboratory, Institute of Science Department of Computer Science, Mohamed Khider University, Biskra, Algeria.<sup>1</sup> <https://orcid.org/0009-0009-7958-5462> , <sup>2</sup> <http://orcid.org/0000-0003-1539-835X> Email: [imane.dridi@univ-biskra.dz](mailto:imane.dridi@univ-biskra.dz), [cherif.foudil@univ-biskra.dz](mailto:cherif.foudil@univ-biskra.dz)

## ARTICLE INFO

### Article History

Received: March 03, 2025

Revised: March 20, 2025

Accepted: March 15, 2025

Published: April 31, 2025

### Keywords:

Animation variety,  
Collision prevention,  
Newton's laws and the laws of momentum,  
Optimization pool object algorithm  
Occlusion culling algorithm.

## ABSTRACT

Crowds are essential in daily activities, performing as dynamic systems of human interaction. They involve numerous individuals collecting in specified locations for diverse activities, whether in urban environments, public events, or social interactions. In virtual environments, animated crowds frequently display repetitive behaviors and a deficiency in movement diversity, leading to unrealistic simulations. It is imperative to provide distinctive and diverse actions for each character, avoiding visual duplication to augment realism. This paper introduces a method to enhance crowd variety by ensuring distinct and realistic character movements. We propose providing various motion types to prevent the duplication of cloned characters. Our approach creates a set of animations and utilizes techniques to control character velocity, ensuring distinctive and convincing movements. Furthermore, we present collision prevention methods based on Newton's Laws, the conservation of momentum, and the laws of kinetic energy. Ray-casting determines collision velocities by considering each character's mass and velocity without external forces. We implement a hybrid pool object approach and occlusion culling techniques to optimize real-time performance, increasing FPS (framed per second) and reducing computational load. These experiments evaluate the efficacy of our technique under different conditions. The results demonstrate the method's effectiveness and flexibility in dynamic environments.



Copyright ©2025 by authors and Galileo Institute of Technology and Education of the Amazon (ITEGAM). This work is licensed under the Creative Commons Attribution International License (CC BY 4.0).

## I. INTRODUCTION

A virtual crowd involves individual virtual entities that reflect behaviours identical to those of their adjacent neighbours, each possessing distinct actions and properties. Animators categorize the crowd into numerous entities and regulate the crowd's collective behaviours, the groups' movements, and the conduct of each virtual entity. Monitoring identical characters performing the same behaviour makes it feasible to regulate crowd movement, navigate around obstacles, and facilitate interactions with 3D characters or virtual humans.

Real-time crowd simulation is a technique for animating the movement of large groups of characters within a virtual environment. As the crowd moves, each character dynamically interacts with others based on predefined behaviours, such as avoiding collisions or navigating obstacles. These interactions are defined by algorithms that adjust character paths to maintain personal space, avoid obstructions, and respond to environmental changes. It results in an evolving, natural collective behaviour that unfolds in real time, allowing characters to react continuously to their surroundings and each other. The challenge lies in executing these processes instantly, ensuring fluid and realistic movement in virtual settings like games and simulations.

Our crowd animation technique produces distinct locomotion cycles for each character, creating diverse movements that enhance realism and complexity within the scene. Beyond movement variation, we introduce a technique to prevent character collisions, ensuring smooth and natural interactions among individuals in the crowd. Our approach is based on Newton's laws of motion, incorporating principles of momentum and kinetic energy conservation under the assumption of no external forces. By applying these physical principles, our method accurately computes the final velocities of characters after interactions, maintaining realistic and natural movement.

This integration of dynamic animation and collision avoidance leads to a more immersive and cohesive crowd simulation, making character behaviour more believable in complex virtual environments. Motion has a significant role in capturing crowds' diversity since virtual characters' physical appearance is often limited. To address this, many researchers have developed animation methods. For example, one study [1] aims to minimize memory usage while generating and animating various crowd characters.

This approach involves two main steps: first, simplifying and segmenting virtual character data into essential body parts; second, integrating installation and peeling information into a shared texture space for the new characters. Rigging and skinning data are incorporated into global textures through UV parameterization, allowing all created characters to share a single set of rigging and skinning textures for each gender or age variant (male, female, child). It reduces memory for efficient large-scale crowd simulations but may introduce artefacts, impacting animation quality and crowd smoothness [1].

The study in [2] includes different approaches to improve crowd simulation in important areas. It utilizes a multi-domain planning method and uses steps instead of depending exclusively on the speeds and placements of the character roots. The animation focuses on frame-based solutions to avoid foot-sliding artefacts and synthesizes character movements to ensure they follow the provided paths. In addition, the research introduces a distinctive rendering method based on joint impostors, which is validated by the results of validation experiments. The authors in [3] introduces a data-driven optimization strategy for dynamically adjusting individual agent velocities in response to real-world crowd movement patterns. It improves the realism of the simulated pedestrian behaviours.

The study in [4] focuses on minimizing memory usage and optimizing the rendering step using two complementing architectures. The first is a skeleton linked to octrees for each limb, which determines the amount of detail for geometry and animation. The second structure is scene tiling, which determines the level of detail required for geometry, animation, and character behaviour. A quad-tree is constructed on top of this tiling to improve rendering optimization, allowing geometry from many characters to be combined in locations away from the camera. Furthermore, this tiling functions as an evaluating mechanism, increasing the effectiveness of collision avoidance calculations.

The method presented in [5] uses Gaussian Process Dynamical Models to generate probabilistic low-dimensional poses for motion. Sampling trajectories through Monte Carlo Markov Chains creates infinite motion variants, including blended versions, without costly non-linear interpolation in the mesh domain. This approach allows for the efficient generation of diverse and realistic motion variations, offering animation flexibility while maintaining computational efficiency. The ability to generate such diverse movements without the overhead of

complex interpolation techniques makes it a valuable tool for realistic and dynamic motion synthesis in various applications. The output variations generated by the method in [5] remain relatively similar to the input movements while allowing for changes in poses and timings.

The goal is to create infinite variations for each blended motion using a motion parameterization approach. This approach provides control for customizing motion and simulations, but parameterizing motion capture and controlling variations can be complex and less effective for complex movements.

In addition, to create a diversified heterogeneous crowd, [6] presents a multi-agent reinforcement learning-based method that incorporates a variety of input settings. This approach demonstrates generalized crowd navigation, allowing for the simulation of diverse individual behaviours within the crowd. The system can account for complex agent interactions by utilizing reinforcement learning, generating realistic and dynamic crowd movements. This method enhances the ability to simulate large crowds with varying characteristics, ensuring a more natural representation of human behaviour in crowded environments. These techniques benefit applications in gaming, virtual reality, and crowd management simulations, where realistic and diverse animations are necessary.

The study in [7] presents a local collision avoidance algorithm for uncrewed surface vehicles (USVs) based on the International Regulations for Preventing Collisions at Sea (COLREGs). The algorithm is divided into three main sections: collision risk assessment, which evaluates the potential for collisions; steering occasion determination, which identifies the need for course adjustments; and navigation waypoint updates, which modify the vehicle's path to avoid obstacles. This approach ensures safe navigation for USVs in complex environments by considering real-time collision risks and applying the rules of maritime navigation to maintain safe distances from other vessels and obstacles.

The algorithm uses the closest point of approach (CPA) method to evaluate collision risk within an analytically defined angle range, assessing potential threats from other vessels or obstacles. The steering occasion determination calculates a supplemental steering angular velocity, allowing the USV to adjust its course and maintain a safe distance. The navigation waypoint update generates temporary waypoints, ensuring compliance with COLREGs for safe passing and crossing situations. Finite state machines (FSMs) control these three components, coordinating the decision-making process. This method guarantees adherence to COLREGs, reduces collision risks, manages dynamic situations, and enhances USV efficiency.

Nevertheless, incorporating COLREGs may elevate computational requirements, thus affecting performance. Moreover, environmental factors limit the algorithm's practical application. In contrast, [8] used a rule-based Bayesian Network approach to model collision issues for ships and marine structures. This method offers clear reasoning and high visibility, making it easier to understand the decision-making process while providing stability in the system's behaviour.

However, it may lead to uncertain or inconsistent ship behaviour due to the inherent conditions required for state transitions. For example, conflicts can arise between the triggering situations for specific behaviours, which may result in unexpected or incorrect decisions. These conflicts can cause system failures or degrade the algorithm's reliability, especially when dealing with complex or dynamic maritime scenarios. Additionally, the algorithm's ability to handle intricate situations

is limited, which affects its overall performance in real-world applications. The challenge of analyzing and resolving these complicated scenarios means that while intuitive and interpretable, the rule-based approach may not always be the most effective solution in dynamic environments where rapid and flexible decision-making is required [9], [10]. As a result, alternative approaches or hybrid systems might be necessary to improve robustness and adaptability in collision avoidance algorithms for maritime navigation.

The authors in [11] proposed an innovative approach for modelling agent movements in crowd simulations with deep reinforcement learning (DRL). Based on environmental awareness, this technique emphasizes the development of agents' navigation strategies, including locomotion and obstacle avoidance. This research substantially advances the field by establishing a parametric framework for developing crowd simulation environments, thus allowing performance evaluation across numerous scenarios.

The authors of [12] present the CrowdMoGen framework employs a dual-phase approach for generating crowd motion based on text input. The Crowd Scene Planner employs a Large Language Model (LLM) to analyze textual descriptions and generate motion plans, specifying both semantic (activities) and spatial (trajectories) characteristics.

The Collective Motion Generator employs a diffusion-based model, incorporating InputMixing and Control Attention approaches, to synthesize character movements that realistically conform to intended dynamics. This method facilitates zero-shot motion generation, obviating the necessity for paired training data. Consequently, CrowdMoGen improves adaptability and authenticity in crowd animation.

In this paper [13], authors proposed an approach incorporates Anisotropic Fields (AFs) to address the limitations of replicating homogenous behaviors. By capturing the uncertainty and variability in crowd motions, it enhances realism and behavioral diversity in simulations. The produced AFs are integrated into the crowd simulation engine, influencing agent decision-making processes. The method examines video data in real crowds to identify movement patterns and transform them into AFs. This approach involves capturing individual motions and calculating local directional preferences to create AFs that represent observed behaviors.

This paper addresses a significant challenge in real-time crowd simulation: preventing unintended character movements in virtual environments and optimizing real-time performance by combining the pooling and culling algorithms to improve the efficiency and quality of interactive models. We aim to ensure consistent frame rates, reduce the computational load of hardware (CPU, GPU and memory), and ensure precise navigation for realistic interactions while maintaining movement within a reasonable range of animations.

This approach improves visual realism and ensures a more convincing crowd simulation experience. We apply Newton's laws of motion, momentum, and kinetic energy to improve collision detection and avoidance. By estimating and modifying character movement in real-time, we can prevent collisions while maintaining physical realism, resulting in smoother, more realistic character interactions and a more realistic virtual environment. This approach ensures that characters move and interact in a way consistent with the laws of physics, contributing to an immersive simulation.

## II. MODELING VIRTUAL HUMAN ANIMATION

Simulating different crowds is important for real-time applications such as games, animated films, and navigation systems. These applications benefit from added features and details that improve the visual quality of the virtual environment and its elements, thereby enhancing the overall realism and performance of the system. It is essential to explore how animation variation and collision avoidance can generate a range of motions by creating unique movements for each character model, improving FPS (frames per second) stability by reducing the rendering load and making the FPS calculations consistent. This approach allows for the production of diverse animations, ensuring each character moves in its distinct way. Applying animation diversity is crucial in creating a crowd that highlights each character's individuality, contributing to a more dynamic and realistic crowd simulation (see Figure 1).

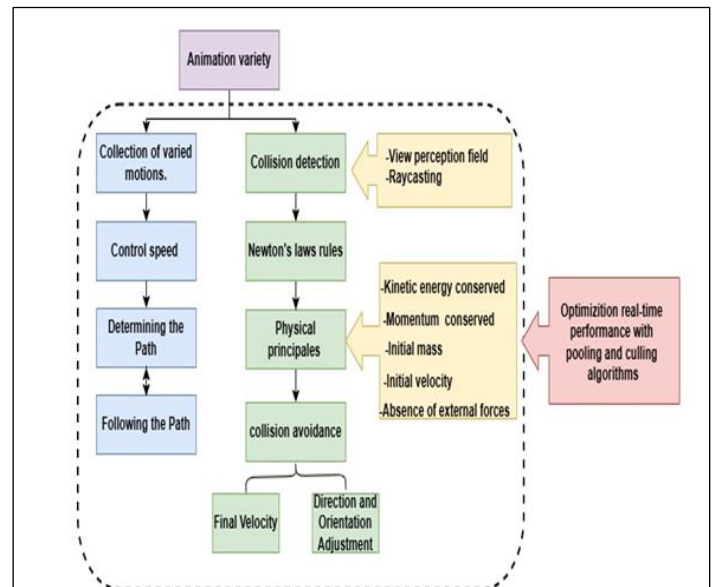


Figure 1: Animation and collision avoidance approach in crowd simulation.

Source: Authors, (2025).

### II.1 ANIMATION APPROACH

We utilise an animator controller and scripting to create diverse and unique movements for our models. The animator controller efficiently manages and blends multiple animations. At the same time, scripting allows us to activate animations based on specific conditions or user interactions, giving each model its personality and individuality. This approach ensures that our models move realistically and interactively, enabling walking, running, jumping, turning, and idling (see Figure 2).

We developed a collection of animated clips and integrated them with scripting in the animator component to achieve this. This setup triggers animations based on defined conditions or user inputs, ensuring fluid and lifelike character behaviours. We efficiently assign and control various movement patterns by constructing multiple animations with distinct attributes and motions. Additionally, we enhance diversity by seamlessly blending animations, resulting in more dynamic and natural motion transitions. Our animation system is enhanced by C# scripting, ensuring accurate animation behaviours while preserving clarity and flexibility. Through custom scripting algorithms, we introduce realistic variations in motion. A key aspect of this process involves dynamically generating velocity



values to regulate animation speed, ensuring smooth transitions between different movements. These velocity-based transitions create a seamless animation flow, enhancing realism and immersion. We initially position models randomly in different directions to ensure a varied animation cycle for different virtual characters. Each model is assigned a unique animation type with specific speed parameters and the ability to jump to a certain height. These techniques generate diverse locomotion cycles, resulting in more visually realistic crowd movement.

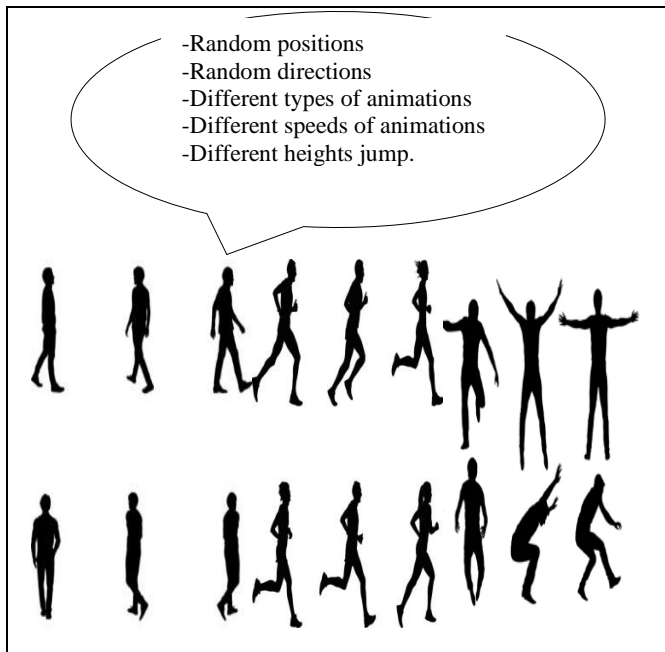


Figure 2: Animation and collision avoidance approach in crowd simulation. Employing a variety of animation styles for different models, each with its own speed.

Source: Authors, (2025).

## II.2 MOVEMENT PATH VISUALIZATION

Creating a unique animation style for characters in a virtual world or interactive environment is crucial for defining their personalities and improving the fluidity of their movements. Blending various animations with controlled movement along predefined paths allows characters to be represented distinctly and dynamically. This method ensures that each character moves uniquely, engaging and consistent with their role in the virtual world, which adds depth and realism to the overall experience. We explore a strategy demonstrating how our crowd can distinguish its animation style.

### Algorithm: Character animation with paths

**Input:** character, movement, velocity, position list of points.

**Output:** a path to follow.

- Determinate the initial position of the path
- Determinate the destination position of the path
- Determinate the movement.
- Determinate the velocity
- Determinate the path
- Following the path

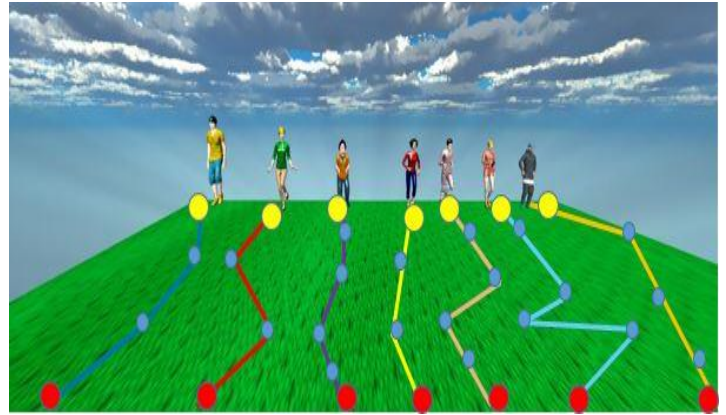


Figure 3: Various animations with different speeds to follow the path sequence.

Source: Authors, (2025).

It includes animating characters with diverse movements and controlling their speed along a specified path. In our environment, we set a starting point and a final destination for each character, guiding them through a path to reach their goal effectively. A key aspect of this strategy is using varied motion styles to reflect the characters' personalities and actions. These styles encompass a range of movements, including idle states, walking, strolling with a briefcase, performing a feminine gait, a unique older man's walk, walking with joy, rhythmic hip-hop dancing, texting while walking, and running. Each motion style adds depth and individuality to the characters, ensuring they are dynamic and realistic in different situations, ultimately enhancing engagement and realism within the virtual environment (see Figure 3).

In addition to animation variation, controlling the movement speed and path traversal is another critical factor. Each model is defined to perform particular types of movement and can change how it moves along a predetermined path. The animation is controlled by a speed parameter ranging from 1 to 50 (m/s). These speed decisions are precisely selected to ensure the movement appears realistic and visually appealing, enhancing the overall sense of motion within the defined parameters. As a result, each character's movement feels distinct, representing their characteristics and activities. A character's movement speed may also reflect its emotional condition and give additional depth to the animation. We ensure that each character moves effortlessly and naturally by blending different animations with varying movement speeds. The variations in speed and animation styles emphasize their individuality, making their behaviours more noticeable.



Figure 4: Enhancing visual animation diversity across various templates in an urban context.

Source: Authors, (2025).



This method not only improves the visual dynamic of the environment but also enhances transmitting emotions and intentions through character movements and animations (see Figure 4).

### II.3 CROWD COLLISION DETECTION APPROACH

We present a comprehensive description of our approach, which aims to improve and achieve realistic results in collision avoidance within crowds. Collision avoidance is a critical challenge in crowd simulation, as it ensures individuals within the environment move without unrealistic interactions. Addressing this issue is essential for creating an efficient crowd system. Many researchers have proposed various methods to implement collision avoidance behaviour in crowd simulations.

The algorithm used is based on a technique called Raycasting, Newton's Laws, along with the principles of momentum and kinetic energy conservation for collision detection and possibly for determining visibility or field of view:

- Raycasting Basics: It estimates the intersection between our models during their movements from the projection of the current character's position to the other character. It involves casting a ray (a straight line) from a specific point (often a character's position) in a particular direction (e.g., direction of movement or field of view). The ray continues until it intersects with an object in the scene or reaches a maximum distance.

- Collision Detection: Raycasting is a technique used in character movement to detect collisions with nearby objects. When a character moves forward, a ray is cast in the direction of movement. This ray checks for obstacles within its path, such as objects or other characters. If the ray intersects with an object, it indicates a potential collision, allowing the game to respond appropriately by stopping the character or adjusting its movement. This method is efficient for real-time environments, enabling accurate collision detection without complex geometry calculations.

- Field of View Representation: Raycasting can also assess what is visible from a character's perspective. By casting rays in several directions within a defined field of view, we can determine which objects or entities fall within that area and are visible to the character. Based on this information, we calculate the mass and initial speed (e.g., WalkSpeed, RunSpeed) to apply to the character's movement.

- Collided characters: The raycasting method determines if characters have collided after a set number of time steps. It calculates the distance between them, considers their masses and velocities, and selects the faster character. By casting rays along the movement path, the method checks for potential collisions. If a collision is detected, the model can adjust the characters' positions or velocities based on their masses and speeds, ensuring realistic interaction and response to obstacles or other characters.

- We applied Newton's Laws, along with the principles of momentum and kinetic energy conservation, to model the dynamics of motion and calculate the final velocities and direction changes for each character during collisions. These physical laws govern the interactions between objects and are essential for accurately simulating realistic motion. The conservation of momentum ensures that the total momentum before and after a collision remains constant, while kinetic energy conservation applies to elastic collisions where no energy is lost.

These principles apply without external forces, allowing us to predict the results of character collisions with high accuracy and realism.

Where,  $p_1, K_1, p_2, K_2, p'_1, K'_1, p'_2$  and  $K'_2$  are the momentum and kinetic energy of character 1 and character 2 before and after the collision, respectively [14].

Table 1: Determination of the final velocity of the characters after the sensing collision by the raycasting technique, Newton's laws, the concepts of momentum and conservation of kinetic energy.

Scenarios	Various mass and velocity cases.	The velocities at the time of collision.	Final velocities after collision detection.
Scenario1	$M \gg m$ And $V_M > V_m$	$v'_M = v_M$ $= \frac{v_M(M-m)}{M+m}$	$v'_M = v_M$ $v'_m = 2v_M$
Scenario2	$M = m$ And $V_M \neq V_m$	$v'_m = \frac{2M * v_M}{M+m}$	$v'_M = 0$ $v'_m = v_M$
Scenario3	$M > m$ And $V_M < V_m$	$v'_M = v'_M$ $v'_m = v'_m$	$v'_M = v'_M$ $v'_m = v'_m$
Scenario4	$M = m$ And $V_M = V_m$		$v'_M = v'_M$ $v'_m = v'_m$

Source: Authors, (2025).

$$p_1 + p_2 = p'_1 + p'_2 = cte \quad (1)$$

$$K_1 + K_2 = K'_1 + K'_2 = cte \quad (2)$$

When our two characters collided at two different velocities,  $v_M$  and  $v_m$  and two different masses,  $M$  for the heavier object and  $m$  for the lesser one, along with the sum of the two momenta, the sum of the two kinetic energies is conserved in elastic collisions.

The two conservation equations are written as follows:

$$\frac{1}{2}Mv_M^2 + \frac{1}{2}mv_m^2 = \frac{1}{2}Mv'^2_M + \frac{1}{2}mv'^2_m \quad (3)$$

$$Mv_M + mv_m = Mv'_M + mv'_m \quad (4)$$

Where the final velocities of both objects  $v'_M$ , and  $v'_m$  are given. The sums of the velocities before and after the collision for each object are equal when the two equations are rearranged with the velocities of one object on one side of Eq. (3) and Eq. (4) and those of the other on the opposite side, then dividing the rearranged Eq. (3) with the rearranged Eq. (4) [14].

$$v_M + v'_M = v_m + v'_m \quad (5)$$

The ultimate velocities following the collision are determined by solving the set of linear Eq. (4) and Eq. (5):

$$v'_M = \frac{(M-m)v_M + 2mv_m}{M+m} \quad (6)$$

$$v'_m = \frac{(m-M)v_M + 2Mv_M}{M+m} \quad (7)$$

Depending on the values of  $m$  and  $M$  for our colliding characters in Eq. (4) and Eq. (5), we disregard the smallest value and get the final velocities  $v'_M$  and  $v'_m$  (Table 1). We derive a valid method for collisions from Newton's Laws, the laws of momentum, and kinetic energy conservation. It provides a way to

determine the final velocities after detection collision using the Raycasting technique without external net forces, according to each character's initial masse and velocity (see Figure 5). In the second scenario, when the masses are equal, the final velocity of this character will be reduced to a small value for some seconds. At this time, the second character will change its direction and take the velocity of the first character to move. After steps of seconds, both of them will take their first velocity. To ensure that we examine all possible conditional cases that could occur between characters, we have added two additional cases based on the same previous data. In these two situations, the end velocity used to predict the occurrence of a collision is the same as the initial velocity of the two characters before the collision.

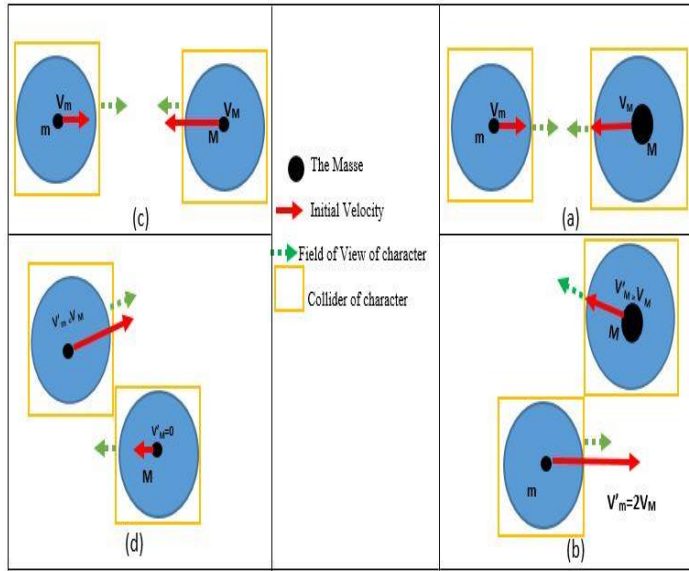


Figure 5: Examples of two cases of collision  
Source: Authors, (2025).

Perception with no collision of the first Scenario. (b) Final velocities are determined according to the initial different velocities and masses of characters by Newton's Laws, as well as the concepts of momentum and kinetic energy conservation after detection collision by the Raycasting technique. (c) Perception with no collision of the second Scenario. (d) Final velocities are determined according to the different initial velocities and equal masses of characters by Newton's Laws, as well as the concepts of momentum and kinetic energy conservation after detection collision by the Raycasting technique.

#### Algorithm: Collision detection

**Input:** initial masse, direction, initial velocity, ray range, characters, character controller, positions, and orientations.

**Output:** final velocity, final direction and rotation. distance

**If** (collision occurs) **then**

- Calculate distance.

**-If** ( $V_M > V_m$  and  $M > m$ ) **then**

( $v'_M = v_M$  and  $v'_m = 2 v_M$ )

**-Else if** ( $V_M > V_m$  and  $M = m$ ) **then**

( $v'_M = 0$  and  $v'_m = v_M$ )

**-Else if** ( $V_M > V_m$  and  $m > M$ ) **then**

( $v'_m = v_m$  and  $v'_M = 2 v_m$ )

**-Else if** ( $V_M > V_m$  and  $m = M$ ) **then**

( $v'_m = 0$  and  $v'_M = v_m$ )

**-Else if** ( $V_M < V_m$  and  $M > m$ ) **then**

( $v'_m = v_m$  and  $v'_M = 2 v_m$ )

**-Else if** ( $V_M < V_m$  and  $m > M$ ) **then**

( $v'_m = v_m$  and  $v'_M = v_M$ )

**-Else if** ( $V_M = V_m$  and  $m = M$ ) **then**

( $v'_m = v_m$  and  $v'_M = v_M$ )

**-End if**

-Change direction.

-Change rotation.

**End if**

### III. CROWD SYSTEM RESULTS AND DISCUSSION

Virtual humans simulated on a Windows 10 computer with an Intel i7 processor running at 2.80 GHz, an NVIDIA GeForce GTX 780 graphics card, and 8 GB of RAM. The pedestrian system utilizes shader files for rendering the models and C# scripts to simulate the behaviour of virtual individuals within Unity 3D, version 2018.3.2f1 (64-bit).

The crowd system enhances the visual experience by including diverse character movements, rendering the simulation more dynamic and realistic. These movements are specifically selected to ensure that the virtual humans behave naturally in various scenarios. Combining high-quality shaders, detailed character animations, and realistic behaviours allows a seamless and immersive simulation of crowded environments. This setup offers a strong platform for real-time simulation and visualization of extensive pedestrian systems, providing valuable insights for various applications such as crowd control and urban planning.

#### III.1 CROWD DENSITY AND ANIMATION VARIATION IN OPEN ENVIRONMENT

To ensure a variety of movements among the crowd, we set the models in an open environment where each model has specific motions and behaviours while avoiding collisions. The actions include idle poses, jumping, walking, strolling with a briefcase, feminine gait, an older adult's unique motion, walking with joy, performing rhythmic hip-hop dancing, walking while texting, and running. Each model can perform specific movements that vary along a predetermined path. The animations are set to a specific speed, ranging from 1 to 50 units per second.

Different Scenarios	Number of characters	Number of animations type applied	Range of movements speed applied	Frame per seconds(ms)
Scenario1	7	11	[1 m/s, 50 m/s]	60
Scenario2	14	22	[1 m/s, 50 m/s]	59.1
Scenario3	21	33	[1 m/s, 50 m/s]	58.7
Scenario4	63	99	[1 m/s, 50 m/s]	55

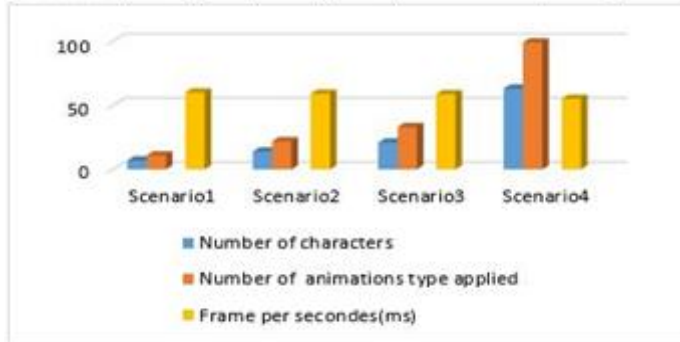


Figure 6: The performance evaluation of our approach across four different scenarios involved examining how adding various types of animations with different speed values affects the changes in FPS values.

Source: Authors, (2025).

These speed values are determined to achieve realism and visual attractiveness, enhancing overall movement dynamics within the specified parameters. As a result, each model's movement represents its unique characteristics and activities (see Figure 6).

In another approach, we manage character animations in scenarios where collisions occur between them (Figure 7). Each character is animated with various movements and speeds, allowing for realistic, interactive collisions. We use collision detection algorithms based on Newton's Laws to effectively manage these collisions, focusing on momentum and kinetic energy conservation.

This method accurately calculates the final velocities of characters after a collision by utilizing raycasting techniques. The algorithm considers each character's initial mass and velocity to

compute the result, providing no external forces are applied. It ensures that character interactions behave realistically, with adjustments to their velocities reflecting the laws of physics. By incorporating these principles, we achieve a more immersive and believable simulation of collisions between characters. This approach is beneficial for creating dynamic environments where characters interact with one another in real time, such as in crowd simulations.

### III.2 THE PERFORMANCE EVALUATION OF OUR ANIMATION VARIATION APPROACH BY EXPLORING THE MAXIMUM COMBINATIONS OF ELEMENTS

To ensure the precision of our animation results, we identify combinations of elements that increase diversity. We begin by selecting key factors such as each character's movement type and speed variations. The process calculates the possible ways to combine these factors at each time step. We can generate a wide range of character behaviours by identifying the maximum combinations for these elements across multiple scenarios.

This approach ensures diverse and realistic animations, allowing characters to interact in varied ways. It also enhances the simulation by accounting for different kinds of motion and speeds in dynamic environments, where:

- **H** : It represents the maximum number of characters our model utilises for simulation and animation.
- **T** : It represents the maximum number of animation types each character uses in the simulation or model.
- **V** : It represents the maximum number of speed values assigned to each character in the simulation.
- **Max\_Combinations\_Anim**: It represents the value of the maximum feasible combination of terms for each model, which contributes to the overall variety and diversity of animations within the simulation.

$$H \times T \times V = \text{Max\_Combinations\_Anim}$$

The maximum feasible combination of model terms that contribute to the variety of animations in the simulation:  
 $(18 \times 10 \times 50) \times 5 = 9000.$  (c)

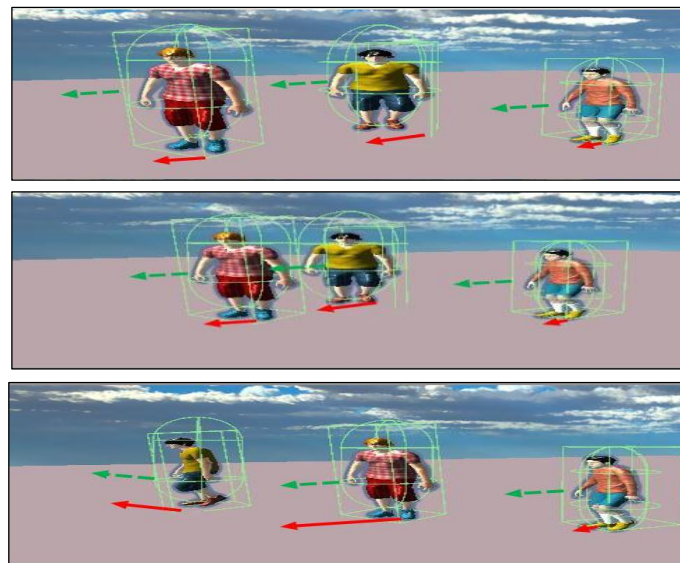


Figure 7: The scenario of crowd animation with collision detection: (a) Perception with collision: The green arrow represents the character's field of view, while the red arrow indicates the velocity before the collision. (b) Collision detection between two characters. (c) After the collision is detected using the Raycasting technique, the red arrow shows the final velocities, which are determined based on the characters' initial velocities and masses by Newton's Laws and the principles of momentum and kinetic energy conservation.

Source: Authors, (2025).



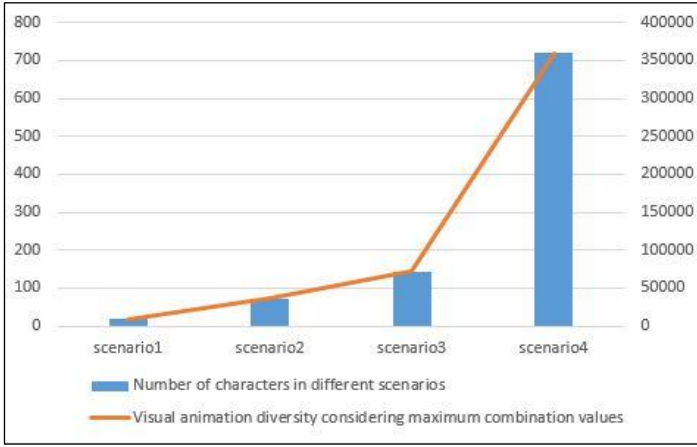


Figure 8: Exploring the maximum feasible combinations of elements in our diverse animations based on the number of characters involved.

Source: Authors, (2025).

We realized that our algorithm could generate various motion types by combining key factors such as the number of characters and the range of movement types at different speeds. As the number of characters in various scenarios increases, so does the potential for diverse motion combinations. For instance, using 1080 characters, our algorithm can produce approximately 540000 unique combinations. This feature significantly increases the range of feasible character movements, making the simulation more dynamic and varied. We can introduce additional character types and movement styles to enhance this variety further, resulting in more complex and visually realistic animations.

This expansion improves the realism of individual character interactions and significantly improves the overall quality of crowd simulations. By providing these combinations, we can create a more immersive and immersive experience, offering a wider range of diverse animations for large-scale crowd scenes and dynamic environments.

Table 2: The maximum combination values improve the visual animation diversity of various templates in different scenarios.

Number of characters in different scenarios	Visual animation diversity considering maximum combination values
Scenario1,H=18	9000
Scenario2,H=72	36000
Scenario3,H=144	72000
Scenario4,H=720	360000

Source: Authors, (2025).

### III.3 EVALUATION OF THE PERFORMANCE OF POSSIBLE COMBINATIONS OF OUR APPROACH FOR CHANGING ANIMATIONS USING A PARTICULAR NUMBER OF ELEMENT SETS FOR DIFFERENT CHARACTERS.

The following process presents how to increase animation variation by selecting elements simultaneously. We determine the number of combinations for different terms across various contexts, considering factors like character types, movement styles, and speeds. This approach maximizes diversity in animations, allowing for more dynamic and varied character behaviours in different simulation scenarios.

$$C_H^h \cdot C_T^t \cdot C_V^v = \text{Possible\_Animation\_Variety}$$

To begin, we assign specific labels to each item associated with an account, ensuring accurate identification and categorization for efficient processing and analysis.

- **H** represents the maximum number of characters while **h** denotes the number of characters under consideration in a given scenario.

- **T** represents the total number of animation types used by our models, while **t** specifies the specific type of animation applied to a particular model.

- **V** refers to the maximum height value of speed animation for our characters, representing the highest possible speed in the animation. Meanwhile, **v** denotes the specific speed value assigned to each character during their animation, allowing for variation in movement and enhancing the realism of character actions.

- **Possible\_Animation\_Variety** indicates the number of possible combinations of these different terms, such as character types, animations, and speeds that contribute to the overall variety and diversity of animations in our simulation or model.

Next, we determine the number of combinations in our scene based on the various terms defining the animation variety for our ten distinct models. To do this, we define the following variables:

**H** = 10 for the total number of characters, and **h** = 1 for the characters considered.

**T** = 10 for the total number of animation types utilized by our models, with **t** = 1, **t** = 4 specifying the types of animation used by the model during its animation.

**V** = 50 represents the height value of the speed animation for our characters, and **v** = 1 signifies the specific speed value assigned to each model.

Using these variables, we can calculate the total number of unique animation combinations within our scene. The combination of these elements (character types, animation styles, and speed values) results in a wide variety of possible motion sequences for each character. This allows us to generate a more dynamic and diverse simulation, ensuring that each character behaves in a unique and realistic way. The formula derived from these variables will provide the total number of animation possibilities for the crowd, enhancing realism and interaction within the simulation.

Possible combinations are:

$$(C_{10}^1 \cdot (C_{10}^1 + C_{10}^4) \cdot (C_{50}^1)) \times 18 = (10 \cdot (10 + 210) \cdot (50)) \times 18 = 1980000.$$

## IV. OPTIMAZING REAL TIME PERFORMANCE

The reason for measuring the efficacy of crowd simulation depends on an accurate characterization of the aims of the crowd simulation tasks. Computer simulations of crowd behaviour may emphasize different performance metrics depending on the objectives of the application [15]. Some studies [16] [17] [18] propose simulating virtual crowd systems that are identical to real crowds. This enables them to clarify the operational dynamics of real crowds and identify potential risks within the system. Thus, their performance indicators reflect the accuracy of the simulation, its similarity to actual crowd behaviour, and the behaviour of individual agents.



Enhancing our real-time model's efficiency requires reducing computational and rendering complexity in character animation. We achieve this by combining techniques such as object pooling, frustum culling, and occlusion culling, ensuring smooth performance even with several animated characters displayed simultaneously. It produces greater frame rates and less latency.

#### IV. 1 OBJECT POOLING FOR PERFORMANCE OPTIMIZATION

This method involves creating a collection of inactive characters, which are subsequently utilized as required. This method reduces memory allocations and enhances performance as animated characters increase. Rather than repeatedly creating and eliminating characters, which incurs significant computational costs, we utilize pre-existing objects, thus minimizing memory overhead and garbage collection, ultimately improving real-time performance.

##### Algorithm: pooling for performance optimization

**Input:** 3D character models, collection size, distance between characters, velocity range, mass range  
**Output:** different animations, avoid collision, reduce memory allocation, optimize real-time

```

For each character in the allocation set do
    Instantiate character number
    Sets the character inactive
    Adjust character size and rotation.
    Incorporate characters into the collection list.
end for
For each character in the allocation set do
    Iterates through the collection
    Activate available character
    Give a unique random position
    Apply different animations at varying speeds.
    Avoid collision
end for
For each character stored in the collection list do
    Iterates through collection list
    Return the first inactive object
end for

```

#### IV. 2 FRUSTUM CULLING FOR PERFORMANCE OPTIMIZATION

This technique prevents the display of characters outside the camera's vision by specifying the camera's perspective, defined as the frustum. Only characters within this viewpoint are rendered, enhancing performance by conserving computational resources and reducing the GPU load. By verifying if the animated character is within the camera's field of vision, we can selectively deactivate or activate them, optimizing resource utilization and improving rendering efficiency.

#### IV. 3 OCCLUSION CULLING FOR PERFORMANCE OPTIMIZATION

This method determines if a character, although within the camera's field of vision, has been hidden or occluded by other objects. It prevents the engine from displaying characters

hidden by different elements. Eliminating the rendering of hidden characters conserves computational resources. This approach increases FPS and improves performance by eliminating unnecessary rendering.

#### IV. 4 PERFORMANCE OPTIMIZATION OF HYBRID METHODS

Our method simulates multiple characters, each having distinct motions and velocities. We utilize Newton's Laws, laws of momentum, and the conservation of kinetic energy to prevent collisions between the models. It enables the computation of final velocities after collision detection using the Raycasting method, without external net forces, depending on each character's starting mass and velocity.

Then, we implement a hybrid approach that combines the pool object algorithm with frustum culling and occlusion culling approaches to enhance the frames per second during character movement. This technique improves real-time FPS performance, eliminates insignificant computations and rendering for characters unavailable to the camera, and decreases frequent memory allocation and deallocation.

By integrating these methods, we achieve significant results: our models perform at consistent frame rates, eliminate using resources on invisible characters and objects, minimize unnecessary frame computations, and prevent the rendering of occluded objects by analyzing the scene's geometry and identifying disabled characters (see figure 9).

##### Algorithm: object pooling and culling algorithms

##### for performance optimization

**Input:** 3D character models, collection size, distance between characters, velocity range, mass range, primary camera reference, Fractional camera culling  
**Output:** different animations, avoid collision, reduce memory allocation, optimize real time, reducing the processing load

Algorithm pooling for performance optimization  
 For each active character in the collection set do

```

    Obtains renderer
    Checks character within frustum
    Detects hiding character
    If the object is visible and not occluded
      remains active
    else
      remains inactive
    end if

```

end for

Measure object-main camera distance.

Perform Raycast

Check if another object blocks the character.

Deactivate objects that are not visible

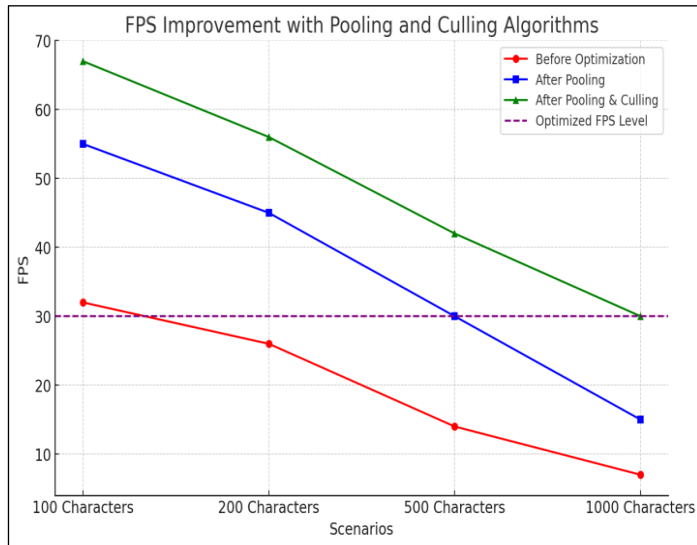


Figure 9: Improvement of FPS performance with pooling and culling optimisation algorithms.  
Source: Authors, (2025).

## V. CONCLUSIONS

We propose in this paper a method to enhance the diversity of crowd animation by integrating numerous animation styles and assigning each character distinct movements with varying velocities. This approach involves establishing unique animation cycles specific to each character model, facilitating a diverse array of movements during the simulation. Our method aim to obtain a more dynamic and realistic representation of crowd animation in virtual spaces while avoiding characters appearing too similar to each other. The study considers several human genders and age groups, ensuring that each character exhibits distinct movements.

Furthermore, we introduce an algorithm that utilizes Ray-casting for collision prevention between characters. Based on fundamental physics principles such as Newton's laws, momentum conservation, and kinetic energy conservation, the algorithm calculates the final velocities of characters during potential collisions, ensuring realistic and accurate results in crowd simulations. This results in more convincing and realistic crowd visualizations.

Additionally, we implement a hybrid approach that combines the object pooling algorithm with frustum culling and occlusion culling techniques. This method stabilizes frames per second in real-time and enhances performance, producing significant results by reducing the number of active objects processed. It ensures that only characters actively contributing to rendering and animation are considered, optimizing overall simulation efficiency.

As a prospective enhancement, we plan to improve our system by integrating crowd behavior principles to enhance simulation realism. Additionally, we aim to apply reinforcement learning for character animation and obstacle avoidance, enabling adaptive crowd navigation across diverse scenarios. This will facilitate effective autonomous navigation for multiple agents in more complex environments.

## VII. REFERENCES

- [1] Ruiz, S., Hernández, B., Alvarado, A., & Rudomín, I. (2013). Reducing memory requirements for diverse animated crowds. In *Proceedings of Motion on Games* (pp. 77-86).
- [2] Beacco, A. (2014, October 16). Simulation, Animation and Rendering of Crowds in Real-Time. Simulation, Animation and Rendering of Crowds in Real-Time. <https://upcommons.upc.edu/handle/2117/95561>.
- [3] Liu, P., Chao, Q., Huang, H., Wang, Q., Zhao, Z., Peng, Q., ... & Jin, X. (2022). Velocity-based dynamic crowd simulation by data-driven optimization. *The Visual Computer*, 38(9), 3499-3512.
- [4] Toledo, L., De Gyves, O., & Rudomín, I. (2014). Hierarchical level of detail for varied animated crowds. *The Visual Computer*, 30, 949-961.
- [5] Boukhayma, A., & Boyer, E. (2017, October). Controllable variation synthesis for surface motion capture. In *2017 International Conference on 3D Vision (3DV)* (pp. 309-317). IEEE.
- [6] Hu, K., Haworth, B., Berseth, G., Pavlovic, V., Faloutsos, P., & Kapadia, M. (2021). Heterogeneous crowd simulation using parametric reinforcement learning. *IEEE Transactions on Visualization and Computer Graphics*.
- [7] Wang, D., Zhang, J., Jin, J., & Mao, X. (2021). Local collision avoidance algorithm for a unmanned surface vehicle based on steering maneuver considering colregs. *Ieee Access*, 9, 49233-49248.
- [8] Yu, Q., Liu, K., Yang, Z., Wang, H., and Yang, Z. (2021). Geometrical risk evaluation of the collisions between ships and offshore installations using rulebased Bayesian reasoning. *Reliability Eng. System Saf.* 210, 107474. doi:10.1016/j.res.2021.107474
- [9] Tam, C., Bucknall, R., and Greig, A. (2009). Review of collision avoidance and path planning methods for ships in close range encounters. *J. Navigation* 62 (3), 455–476. doi:10.1017/S0373463308005134.
- [10] Wang, C., Wang, N., Xie, G., and Su, S. F. (2022). "Survey on collision-avoidance navigation of maritime autonomous surface ships," in *Offshore robotics* (Singapore: Springer), 1–33. doi:10.1007/978-981-16-2078-2\_1
- [11] Li, Y., Chen, Y., Liu, J., & Huang, T. (2025). Efficient crowd simulation in complex environment using deep reinforcement learning. *Scientific Reports*, 15(1), 5403.
- [12] Guo, X., Zhang, M., Xie, H., Gu, C., & Liu, Z. (2024). Crowdmogen: Zero-shot text-driven collective motion generation. *arXiv preprint arXiv:2407.06188*.
- [13] Li, Y., Liu, J., Guan, X., Hou, H., & Huang, T. (2025). Introducing anisotropic fields for enhanced diversity in crowd simulation. *The Visual Computer*, 1-16.
- [14] Hernández, A. G. Y., & Alberú, M. del P. S. (2021). Modeling the Interaction of an Elastic Collision between two Objects. *Journal of Physics: Conference Series*, 1929(1), 012016. <https://doi.org/10.1088/1742-6596/1929/1/012016>
- [15] Li, Y., Chen, Y., Liu, J., & Huang, T. (2025). Efficient crowd simulation in complex environment using deep reinforcement learning. *Scientific Reports*, 15(1), 5403.
- [16] Rempe, D., Luo, Z., Bin Peng, X., Yuan, Y., Kitani, K., Kreis, K., ... & Litany, O. (2023). Trace and pace: Controllable pedestrian animation via guided trajectory diffusion. In *Proceedings of the IEEE/CVF Conference on Computer Vision and Pattern Recognition* (pp. 13756-13766).
- [17] Colas, A., van Toll, W., Zibrek, K., Hoyet, L., Olivier, A. H., & Pettré, J. (2022, May). Interaction fields: Intuitive sketch-based steering behaviors for crowd simulation. In *Computer Graphics Forum* (Vol. 41, No. 2, pp. 521-534).
- [18] Panayiotou, A., Kyriakou, T., Lemonari, M., Chrysanthou, Y., & Charalambous, P. (2022, July). Ccp: Configurable crowd profiles. In *ACM SIGGRAPH 2022 conference proceedings* (pp. 1-10).



## RESEARCH ARTICLE

## OPEN ACCESS

# PROCESS OPTIMIZATION AS A TOOL FOR ANALYZING PERFORMANCE INDICATORS OF ADDITIONAL TAXI-OUT AND TAXI-IN TIME OF THE BRAZILIAN AIRSPACE CONTROL SYSTEM

Alessandro Soares de Freitas<sup>1</sup>, Edilson Marques Magalhaes<sup>2</sup>

<sup>1</sup>Student in the Postgraduate Program in Process Engineering at the Federal University of Pará,

<sup>2</sup>General Coordinator of the Galileo Institute of Technology and Education of the Amazon – ITEGAM

<sup>3</sup>Professor in the Postgraduate Program in Process Engineering at the Federal University of Pará.

<sup>1</sup> <http://orcid.org/0000-0005-2663-6765> , <sup>2</sup> <http://orcid.org/0000-0003-3056-0757> 

Email: [alessandrosoaresfreitas@hotmail.com](mailto:alessandrosoaresfreitas@hotmail.com), [magalhaes@ufpa.br](mailto:magalhaes@ufpa.br).

## ARTICLE INFO

**Article History**

Received: March 13, 2025

Revised: March 20, 2025

Accepted: March 15, 2025

Published: April 31, 2025

**Keywords:**

Air Traffic,  
Performance Indicators,  
Process Optimization,  
Business Process Management.

## ABSTRACT

This study aims to improve the efficiency of Brazilian air traffic by analyzing the Brazilian Airspace Control System (SISCEAB) performance indicators. The methodology used combined alternative data sources, namely BIMTRA, TATIC FLOW, and VRA, which were employed to examine the impact of different variations in taxiing times. Specifically, Additional Taxi-Out Time (KPI 02) and Additional Taxi-In Time (KPI 13) were analyzed to identify discrepancies among these data sources and determine the most precise combination. The results indicate that airport layout, gate distribution, and runway threshold selection significantly impacted taxiing times. Statistical analysis revealed substantial variations in unimpeded taxi times across different gates and runway thresholds, emphasizing optimizing operational flows. Based on these findings, integrating BIMTRA and VRA is recommended for more accurate KPI measurement. Therefore, this study contributes to implementing operational enhancements, optimizing airport operation flow, and leading to a more efficient management of Brazilian air traffic.



Copyright ©2025 by authors and Galileo Institute of Technology and Education of the Amazon (ITEGAM). This work is licensed under the Creative Commons Attribution International License (CC BY 4.0).

## I. INTRODUCTION

The increasing complexity and competitiveness of the air traffic sector impose significant operational challenges on organizations responsible for airspace control. In Brazil, the Department of Airspace Control (DECEA) establishes processes and methods to enhance organizational planning in Air Traffic Management (ATM) [1].

However, the lack of reliable data for analyzing performance indicators compromises operational efficiency assessment, particularly regarding Additional Taxi-Out Time (KPI 02) and Additional Taxi-In Time (KPI 13).

The absence of consolidated data sources and the difficulty in accessing reliable information limits the ability to diagnose and improve airport operations, directly impacting performance management and the efficiency of air navigation services.

Process optimization contributes to safety and air traffic organization, creating a more efficient operational environment. Within the ATM context, performance indicators play a key role in providing a comprehensive view of operational performance,

enabling comparisons between airports. Their analysis is crucial for improving performance-based management and enhancing navigation service efficiency [2].

Thus, implementing process optimization strategies emerges as a fundamental approach to continuous sector improvement. The systematic review and enhancement of methods, procedures, and workflows create significant opportunities for reducing operational costs and promoting economic and environmental sustainability.

This study proposes optimizing the Brazilian Airspace Control System (SISCEAB) performance through a critical evaluation of key performance indicators and available data sources. The research analyzes taxi time variability and the influence of variable combinations on KPI calculations, aiming to identify discrepancies and opportunities for process improvement.

This study's main contribution lies in identifying alternative and reliable data sources for evaluating operational performance and establishing a benchmarking framework for the databases currently used in air traffic monitoring. This structured approach



enables an in-depth analysis of the Key Performance Areas (KPA) for Efficiency, facilitating more accurate airport comparisons.

Additionally, this study proposes enhancements for performance-based management, focusing on Efficiency and sustainability in airport operations. Considering that fuel costs account for approximately 41% of airline operating expenses, optimizing these processes can generate significant cost reductions and mitigate environmental impacts [3].

Therefore, this research advances theoretical knowledge on process optimization and performance indicator analysis within the ATM context and proposes practical solutions to improve the Efficiency of Brazilian airspace control. By addressing complex operational challenges, this study contributes to a safer, more effective, and sustainable air traffic management system in the country.

## II. THEORETICAL REFERENCE

### II.1 AIR TRAFFIC

#### II.1.1 Characterization of the Brazilian Airspace Control System

The Brazilian Airspace Control System (SISCEAB) is a critical infrastructure designed to ensure the safety and efficiency of air traffic. It comprises control towers, area control centers, radar systems, and advanced communication networks, coordinating operations from takeoff to landing.

The integration of international regulations, rigorous procedures, and technological advancements highlights the system's complexity. Challenges such as increasing air traffic and the introduction of unmanned aircraft drive ongoing research efforts aimed at enhancing efficiency and safety.

##### II.1.1.1 Responsible Organizations

The Brazilian Airspace Control System (SISCEAB) is responsible for managing and controlling airspace, as well as providing air navigation services throughout the country. It is a comprehensive and effective system that ensures the organization and safety of air traffic flow [4].

The Aeronautics Command Directive (DCA) establishes the flexible use of Brazilian airspace and assigns the Department of Airspace Control (DECEA) the responsibility for controlling and administering an area of 8,511,965 km<sup>2</sup> of national territory, including the oceanic region up to the 10°W meridian, totaling 22 million km<sup>2</sup> [5].

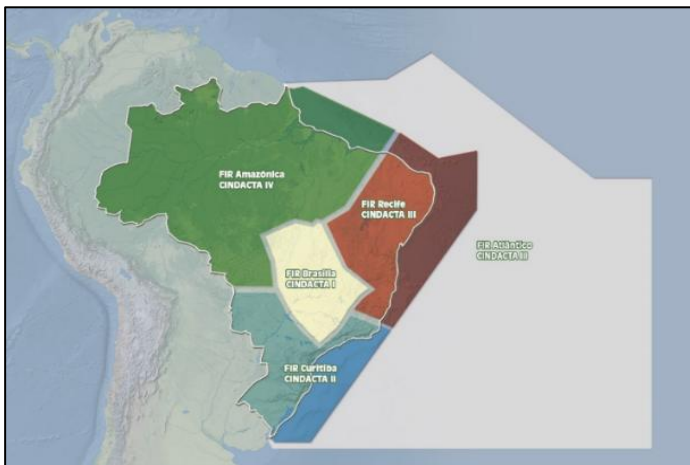


Figure 2: Air Traffic Control Jurisdiction in Brazil.  
Source: Authors, (2025).

The Air Navigation Management Center (CGNA), a unit under DECEA, is responsible for balancing demand and capacity at airports and control sectors, working in collaboration with airlines, Air Navigation Service Providers (ANSPs), and control centers to optimize air traffic flow in Brazil [6].

Brazilian controlled airspace is divided into five Flight Information Regions (FIRs), managed by the Integrated Air Defense and Air Traffic Control Centers (CINDACTA), ensuring supervision and operational safety of air traffic within national territory.

##### II.1.1.1 Air Traffic Management

Air traffic refers to the coordinated movement of aircraft within airspace, regulated by specific systems and procedures to ensure safety, efficiency, and order in operations. This complex system involves Air Traffic Control (ATC), airports, navigation systems, communication networks, and regulations that maintain the smooth and secure flow of operations, both on the ground and in the air [7].

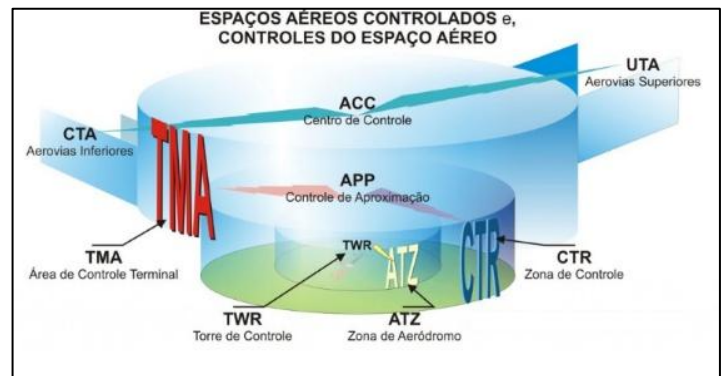


Figure 3: Operational Authority Jurisdiction.  
Source: Authors, (2025).

Air Traffic Management (ATM) aims to dynamically and integratively coordinate air traffic and airspace, ensuring safety, efficiency, and cost-effectiveness in operations, while fostering collaboration among stakeholders [7][8].

ATM is directly related to air traffic demand, influencing flight planning and managing delays in landings and takeoffs at airports. Its structure is based on three key components: Air Traffic Service (ATS), Airspace Management (ASM) and Air Traffic Flow Management (ATFM).

Air Traffic Flow Management (ATFM) is a service designed to ensure safe, organized, and efficient traffic, enabling Air Traffic Control (ATC) to operate at full capacity, in accordance with the declared capacity set by the competent authority [8][9]. ATFM seeks to balance capacity and demand, making the definition and understanding of key operational parameters essential for service efficiency. Its measures aim to maximize available capacity, adjusting the traffic flow along a route or at an aerodrome, preventing operational imbalances [10].

##### II.1.2 Performance-Based Management

The evaluation of organizational performance focuses on financial aspects, quality, and productivity, categorized into strategic goals (long-term objectives), tactical goals (process and personnel monitoring), and operational goals (real-time evaluation) [11][12].



The International Civil Aviation Organization (ICAO) develops air navigation principles and promotes global transportation, encouraging performance benchmarking and the use of Key Performance Indicators (KPIs) to optimize sector management [13].

In Brazil, performance-based management seeks to optimize and efficiently utilize air traffic controllers' workforce, prioritizing performance, capacity, and resource management [14].

Performance indicators play a fundamental role in measuring results, ensuring higher quality and efficiency in decision-making and risk mitigation [15]. These indicators are classified as objective (unambiguous measurement) and subjective (requiring contextual interpretation) [16]. Their proper application enhances strategic decision-making and optimizes available resources [17].

Additionally, these indicators help in defining priorities and continuously evaluating processes, enabling adjustments and effective monitoring of organizational impacts [18]. In the corporate sector, they support structured strategic planning [19] and establish technical foundations for regulatory recommendations and program implementation [20].

In the air transport sector, performance analysis is becoming increasingly relevant, highlighting the importance of indicators for evaluating revenues, costs, and airport operations [21]. Identifying the relationship between demand, airport capacity, and flight punctuality underscores the importance of operational planning [22].

KPIs are essential for continuous improvement, providing an objective view of organizational performance. They monitor, communicate objectives, motivate teams, and drive improvements, serving as essential tools for efficient and sustainable management [23].

The definition of Key Performance Areas (KPA) represents management methodologies that reflect an organization's strategic vision [24]. The critical elements for process management include monitoring and effective process control, with the identification of relevant KPIs being essential for evaluating the analyzed processes [25].

KPIs represent key metrics in quantifying process performance and are widely recognized as fundamental elements in planning and control. Their relevance lies in providing critical information that supports more precise decision-making [26],[27].

The Department of Airspace Control (DECEA) adopted ICAO's 2016 performance indicators through DOC 9750-NA/963 – 2016-2030 (Global Air Navigation Plan - GANP), which established 19 KPIs aimed at verifying whether these indicators accurately express the intent of specific objectives [28].

Thus, metrics can represent past, present, and future performance, correlating with organizational objectives to support a more effective performance management strategy.

### II.1.3 Application of the Business Process Management Cycle

Business Process Management (BPM) is an approach that has gained increasing interest among administrators and managers due to its ability to optimize organizational outcomes. The collaborative nature of BPM emerged in the 1990s, introducing a new administrative approach focused on restructuring and improving organizational processes [29].

BPM is widely recognized in specialized literature as an essential strategy for improving operational efficiency. According to [30], early studies highlighted the importance of process

reengineering as an effective means to transform organizations and achieve substantial performance gains.

The theory of processes, as proposed by [31], provides the foundation for BPM by viewing organizational activities as interconnected elements aimed at continuous optimization. At the same time, the continuous improvement perspective promotes an incremental approach to enhancing efficiency and quality [32].

In the context of organizational innovation, [33] emphasizes the importance of adopting innovative practices aligned with BPM, encouraging the integration of advanced technologies, such as automation and process analytics.

The practical application of BPM is supported by numerous benefits, including: Increased operational efficiency, Improved process visibility and control, Greater adaptability to business environment changes, Enhanced quality and consistency of products and services. These aspects are widely discussed in [34] and [35].

Furthermore, [36] highlights the growing relevance of process automation and the integration of emerging technologies, such as artificial intelligence and predictive analytics, within BPM. These innovations reflect the continuous development and adaptation of BPM to the modern business landscape.

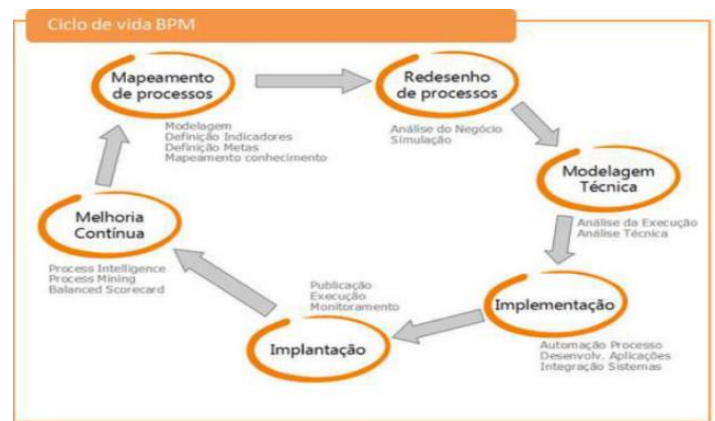


Figure 4: BPM Cycle.

Source: [36].

## III. MATERIALS AND METHODS

In 2016, DECEA initiated a study to implement performance-based management as a method for measuring results. The initial findings were published in the SISCEAB Performance Report 2017, marking a significant milestone in the analysis of performance-based management in Brazil.

From this standpoint, airports were selected based on their relevance and flight volume within Brazilian airspace. In the São Paulo Terminal Control Area (TMA – SBXP), the international airports of Guarulhos (SBGR), Congonhas (SBSP), and Campinas (SBKP) were chosen due to their status as major national hubs. Additionally, Belém Val-de-Cans International Airport (SBBE) and Manaus Eduardo Gomes International Airport (SBEG) were included in the Northern Region because of their high traffic volume, significant cargo transportation, and important strategic infrastructure. This thoughtful selection allows for a comprehensive analysis of national air traffic, encompassing both key connection hubs and regional logistics centers.

The calculation of Key Performance Indicators (KPIs) in this study follows the ATM indicators methodology from SISCEAB. Airlines aim to optimize their gate-to-gate operational costs through flight efficiency by using KPI 02 and KPI 13 to measure discrepancies in unimpeded times. were included in the

Northern Region due to their high movement volume, cargo transportation, and strategic infrastructure. This strategic selection enables a comprehensive analysis of national air traffic, covering both key connection hubs and regional logistics centers.

The calculations of the Key Performance Indicators (KPIs) in this study follow the methodology of ATM indicators from SISCEAB [37]. Airlines, through flight efficiency, aim to optimize gate-to-gate operational costs by using KPI 02 and KPI 13 to measure discrepancies in unimpeded times

It is important to highlight that taxi time is defined as the difference between gate departure and takeoff for KPI 02, and the difference between landing and gate arrival for KPI 13.

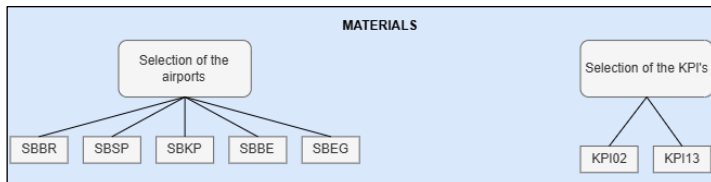


Figure 5: Selection of Airports and KPI's.  
Source: Authors, (2025).

The variability of these times directly impacts the planning of air operations. Thus, taxi time indicators are essential for airlines and airport administrators, as they support the optimization of operational efficiency by providing data-driven insights based on reliable sources.

The study adopted a retrospective, documentary, exploratory, descriptive, and analytical approach, using data from the Airspace Control Institute (ICEA), under the jurisdiction of DECEA, as well as the ATM Performance Reports from SISCEAB and ANAC (2023).

The research covers all Air Navigation Service Providers (ANSPs) in Brazil that use the TATIC FLOW System, with the sample comprising records of landings and takeoffs from scheduled commercial flights registered in this system in 2023 at airports monitored under the Aeronautics Command Plan and selected for this study [38].

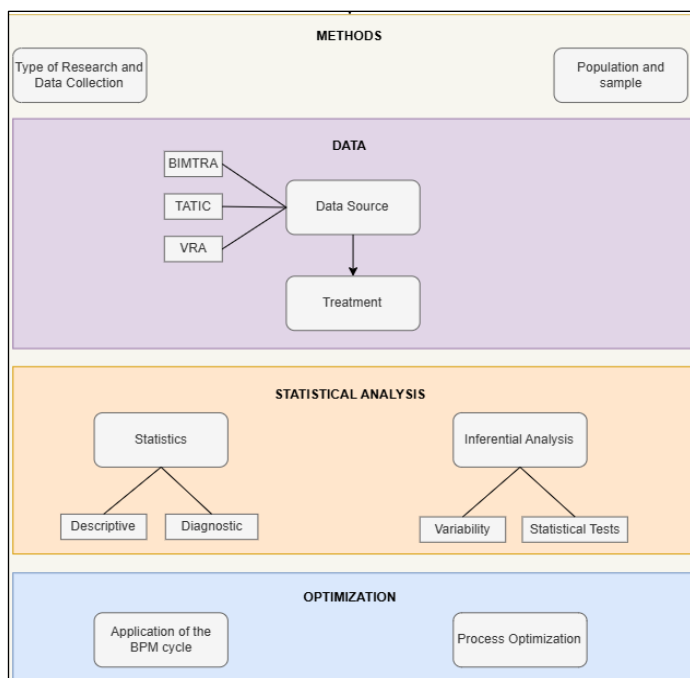


Figure 6: Methodology.  
Source: Authors, (2025).

The data sources used in the study included TATIC FLOW, the Air Traffic Movement Information Database (BIMTRA), and the Active Scheduled Flight (VRA) system, which are used to measure air traffic control tower (TWR) performance and assess the operational efficiency of the selected indicators. Data processing involved the preparation, organization, and cleaning of the collected information, ensuring its quality and reliability before analysis.

Thus, two datasets were constructed from commercial flight records based on movements registered in the TATIC FLOW System: the first dataset analyzed KPI 02, containing 290.133 records, of which 0.57% (1,649 records) were excluded due to negative times or values exceeding 40 minutes. The second dataset, related to Additional Taxi-In Time (KPI 13), included 291.170 records, with 0.39% (1,138 records) removed for not meeting the established criteria.

Additionally, cross-validation was performed between the BIMTRA, TATIC FLOW, and VRA systems to ensure data consistency. In other words, the same movement recorded in the TATIC FLOW system was also found in BIMTRA and VRA, allowing for accurate comparisons.

After applying the exclusion criteria, 288.484 takeoff movements and 290.032 landing movements were considered, ensuring a solid foundation for subsequent analyses. Statistical analysis was essential for data interpretation and followed complementary steps to ensure a detailed and robust approach. Initially, a descriptive and diagnostic analysis of the data was conducted, identifying patterns and discrepancies through graphs, measures of central tendency, and dispersion statistics.

Next, variability analysis was performed using metrics such as variance, standard deviation, and interquartile range to assess data fluctuation. To test hypotheses, non-parametric statistical tests such as Mann-Whitney and Kruskal-Wallis were applied. The choice of tests was based on the most suitable approach given the characteristics of the data, including distribution, variability, and independence, ensuring a systematic and reliable analysis.

A Business Process Management (BPM) cycle was applied, focusing on optimizing efficiency and the quality of organizational processes. This cycle involved six key phases: Planning, Analysis, Modeling, Implementation, Monitoring, and Process Optimization.

#### IV. RESULTS AND DISCUSSIONS

The application of the BPM Cycle was designed to integrate new data sources for obtaining ATM performance indicators in Brazil. During the Planning phase, processes and responsible parties were identified using flow diagrams and quality tools, such as the Cause-and-Effect diagram.

This highlighted the need for more reliable sources to enhance the accuracy of indicator calculations. In the Process Analysis phase, we evaluated inefficiencies and explored new data sources, including BIMTRA and VRA. Key variables, such as takeoff (ATOT) and gate departure (AOBT) for KPI 02, as well as gate arrival (AIBT) and landing (ALDT) for KPI 13, were analyzed. These variables are crucial for measuring taxi times and improving the accuracy of calculations.

Table 1: Combination for KPI 02.

Combination	Metric 01	Metric 02
1ª Combination	ATOT (TATIC FLOW)	AOBT (TATIC FLOW)
2ª Combination	ATOT (TATIC FLOW)	AOBT (VRA)
3ª Combination	ATOT (BIMTRA)	AOBT (TATIC FLOW)
4ª Combination	ATOT (BIMTRA)	AOBT (VRA)

Source: Authors, (2025).

The Process Modeling phase proposed four combinations of data sources for each KPI, allowing for comparisons and greater efficiency in the indicators, as shown in Tables 01 and 02.

Table 2: Combination for KPI 13.

Combination	Metric 01	Metric 02
1ª Combination	AIBT (TATIC FLOW)	ALDT (TATIC FLOW)
2ª Combination	AIBT (TATIC FLOW)	ALDT (BIMTRA)
3ª Combination	AIBT (VRA)	ALDT (TATIC FLOW)
4ª Combination	AIBT(VRA)	ALDT (BIMTRA)

Source: Authors, (2025).

For the statistical tests, significance levels were considered as described in Table 3.

Table 3: Test Statistic.

p-Value	Level of Significance
*	< 0.05
**	< 0.01
***	< 0.001
ns	>= 0.05

Source: Authors, (2025).

Process implementation integrates advanced technologies and training to optimize activities, reducing manual interventions.

Process Monitoring established a control system to measure KPI effectiveness, ensuring agile adjustments and identifying opportunities for continuous improvement.

Finally, Process Optimization leveraged monitored data for operational adjustments and refinement of analyses, enhancing efficiency and adaptability to organizational needs. Using KPIs and dashboards ensured data-driven decision-making, reinforcing the application of the BPM Cycle in air traffic management.

Table 4 presents the number of landings and takeoffs per airport in 2023.

Table 4: Movimento de aeronaves.

Operação	Aeroporto				
	SBGR	SBSP	SBKP	SBBE	SBEG
Decolagem	110.095	91.557	59.518	14.365	12.949
Pouso	110.904	92.202	59.738	14.335	12.853
<b>Total</b>	<b>220.999</b>	<b>183.759</b>	<b>119.256</b>	<b>28.700</b>	<b>25.802</b>

Source: Authors, (2025).

Guarulhos Airport (SBGR) recorded the highest number of operations, totaling 220.999 movements, followed by Congonhas (SBSP) with 183.759 and Campinas (SBKP) with 119.256. In the North Region, Belém (SBBE) and Manaus (SBEG) had lower volumes, with 14.365 and 12.949 takeoffs and 14.335 and 12.853 landings, respectively. These figures highlight the concentration of traffic in the country's main TMAs, particularly in São Paulo, while also emphasizing the lower operational demand in Northern airports, despite their strategic importance in air transport and logistics.

The analysis of Taxi-Out Times revealed an average close to 15 minutes and a median around 14 minutes, indicating slight asymmetry in the distribution, as the mean is slightly higher. The standard deviation ranges between 0.0035 and 0.0038, suggesting moderate variation but no significant fluctuations, reinforcing operational consistency.

Comparing different data sources, the 3rd and 4th combinations showed similar averages and medians, demonstrating that the use of TATIC or BIMTRA does not

significantly impact the recorded times. Thus, the analysis suggests that the Taxi-Out process is stable and predictable, supporting efficient air traffic management, as shown in Figure 6.

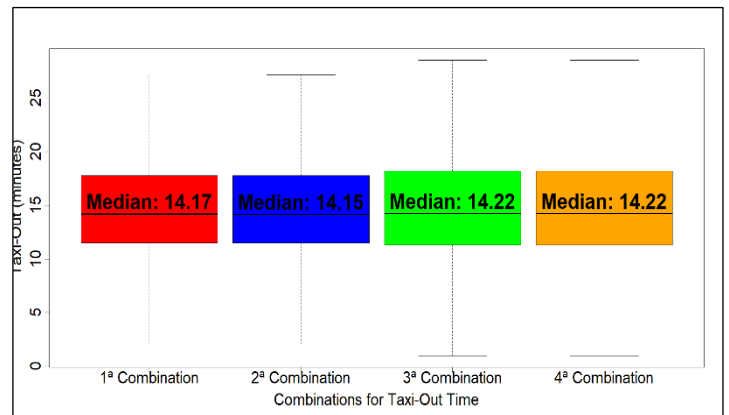


Figure 6: Taxi-Out Time.

Source: Authors, (2025).

The variability analysis of Taxi-In Time at the studied airports revealed significant differences among the data source combinations, as shown in Figure 7.

In the 1st and 2nd combinations, which considered only variants from the TATIC source, the mean values were 2m46s and 2m49s, respectively, while the medians were 1m45s and 1m46s, suggesting the presence of outliers that increase the mean. The standard deviation of 0.13s indicates that most values are concentrated near the median.

In the 3rd and 4th combinations, the distributions were more symmetrical, with means of 6m06s and 6m09s and medians of 5m23s and 5m25s, respectively. The standard deviation remained low at 0.14s, suggesting greater homogeneity. Overall, the 1st and 2nd combinations exhibited higher positive skewness due to extreme values, whereas the 3rd and 4th combinations were more balanced.

The low standard deviations reflect high consistency in the recorded times. However, the outliers in the 1st and 2nd combinations should be further investigated, as they may be related to atypical operational conditions. Additionally, the average Taxi-In times in the 3rd and 4th combinations, around 6 minutes, indicate the need for a comparative analysis with industry benchmarks to identify potential improvements in operational efficiency.

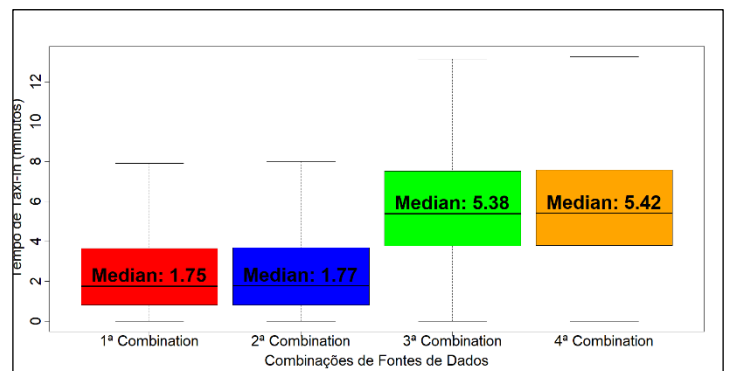


Figure 7: Taxi-In Time.

Source: Autor, (2024).

The analysis of Taxi-Out Time at the studied airports revealed significant variations across locations, reflecting traffic

volume and the operational complexity of each airport, as shown in Figure 8 and Figure 9.

Congonhas (SBSP) recorded the highest average time (16m13s), followed by Guarulhos (SBGR) with 15m42s, while lower-traffic airports, such as Belém (SBBE) and Manaus (SBEG), had shorter times (11m27s and 13m, respectively).

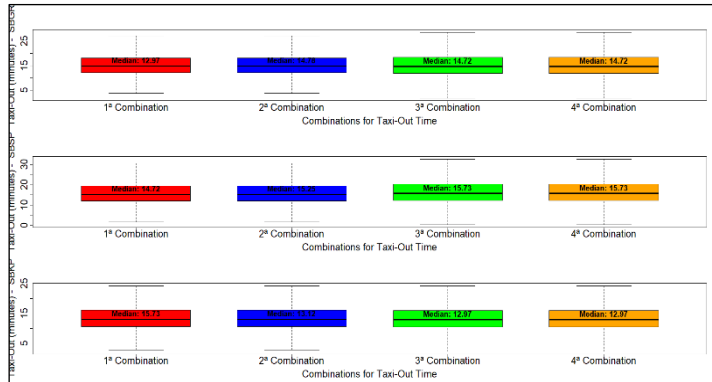


Figure 8: *Taxi-Out* Time for SBGR, SBSP and SBKP.  
Source: Authors, (2025).

The medians follow the same pattern, with SBSP and SBGR recording the highest values (15m15s and 14m47s), while SBBE and SBEG showed more stable times (11m04s and 12m22s).

The standard deviation, which measures time dispersion, was higher in SBSP (0.00384) and SBGR (0.00335), indicating greater variability, possibly due to high slot demand. In contrast, SBBE (0.00226) and SBEG (0.00229) had lower dispersion, suggesting higher operational efficiency.

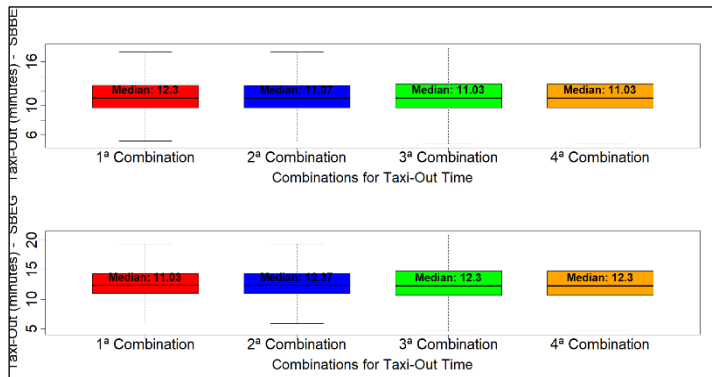


Figure 9: *Taxi-Out* Time for SBBE and SBEG.  
Source: Authors, (2025).

The analysis of Taxi-In Times at the studied airports, as shown in Figure 10 and Figure 11, revealed distinct patterns in central tendency and dispersion. Guarulhos (SBGR) recorded the highest average times, reaching 3m56s in the 1st combination and 7m54s in the 3rd, reflecting a higher traffic volume and potential congestion. In contrast, Manaus (SBEG) had the lowest times, with 1m15s in the 1st combination, suggesting faster and more efficient taxiing.

The medians confirm this trend, with SBGR at 2m45s and SBEG at just 28s in the 1st combination, indicating greater dispersion in SBGR, where some flights experience significant delays. The standard deviation further reinforces this variability, being higher in SBGR (0.00257 in the 3rd combination) and lower in SBEG and SBKP, suggesting greater operational predictability at these airports.

These results highlight areas for improvement, such as traffic management adjustments and infrastructure optimization at

SBGR, while SBEG can serve as a model for airports seeking greater efficiency and reduced taxiing times.

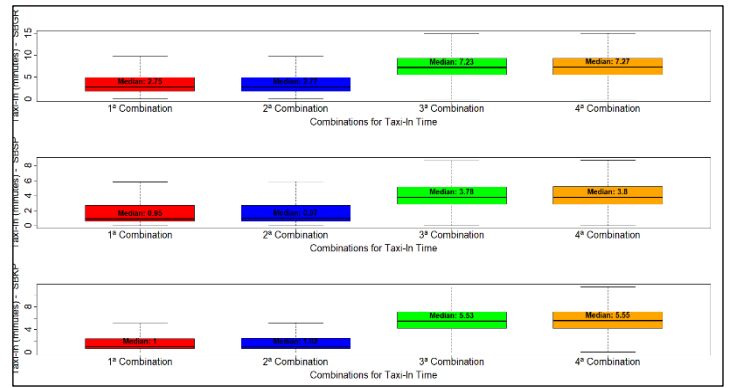


Figure 10: *Taxi-In* Time for SBGR, SBSP and SBKP.  
Source: Authors, (2025).

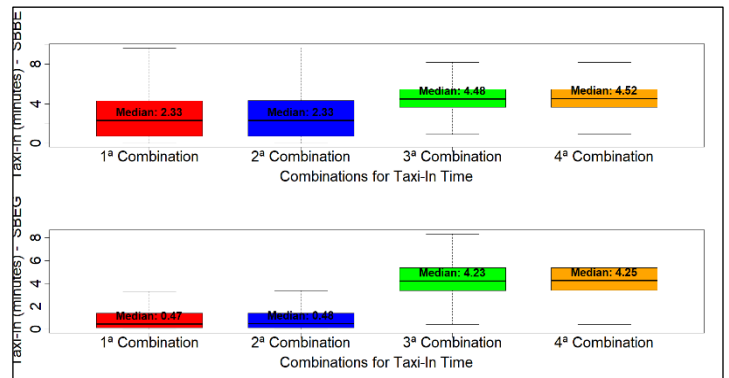


Figure 11: *Taxi-In* Time for SBBE and SBEG.  
Source: Authors, (2025).

In this context, the study aimed to verify the existence of significant differences in taxiing times across the analyzed airports.

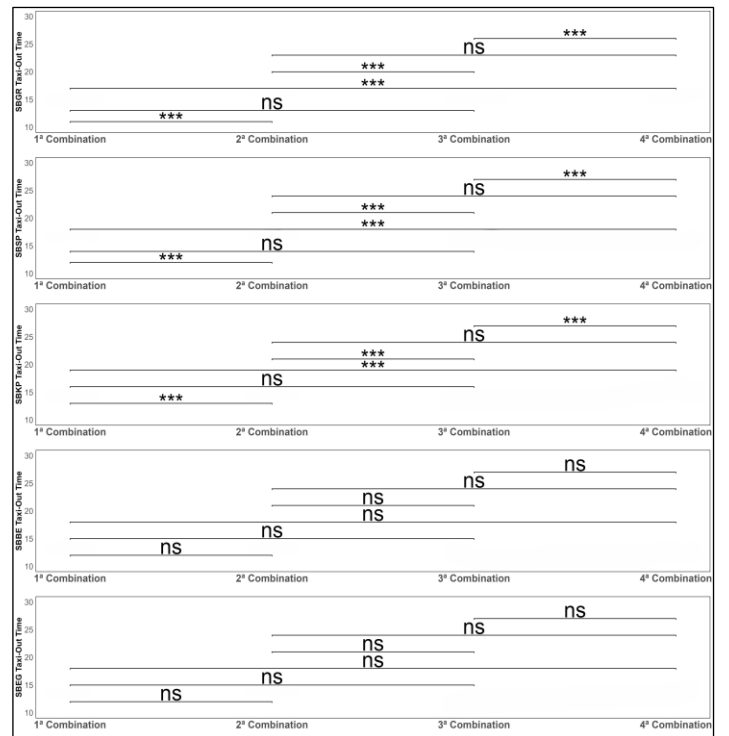


Figure 12: Combinations for *Taxi-Out* Time  
Source: Authors, (2025).



Figure 12 showed statistically significant differences in Taxi-Out Time between certain combinations of data sources for airports SBGR, SBSP, and SBKP. In contrast, at Belém (SBBE) and Manaus (SBEG) airports, these variations were not as pronounced.

SBGR, recognized as one of the busiest airports in Brazil, exhibited low p-values, indicating considerable variability in taxi times due to its complex operations and high traffic volume. Congonhas (SBSP) also demonstrated significant differences, likely influenced by the high volume of domestic flights and infrastructure limitations. Campinas (SBKP), an essential hub for both cargo and passenger transport, also showed variations in taxi times, reflecting its connectivity for domestic and international flights.

In contrast, Belém (SBBE) and Manaus (SBEG) had no statistically significant differences between data combinations, possibly due to their lower traffic volumes and operational stability. Nevertheless, taxiing times at these airports are still affected by infrastructure, weather conditions, and logistical operations.

Given the relevant differences in taxiing times observed at SBGR, SBSP, and SBKP, operational efficiency could be enhanced by considering factors such as airport layout, taxiing routes, runway holding times, and distances between gates and runway thresholds. The key performance indicators (KPIs) associated with these times provide valuable insights to optimize air traffic flow, reduce excessive taxiing durations, and improve overall airport efficiency.

The analysis of Taxi-In Time comparisons (Figure 11) revealed statistically significant differences across all airports except for the comparisons between the 1st and 2nd datasets, as well as the 3rd and 4th datasets, as illustrated in Figure 13.

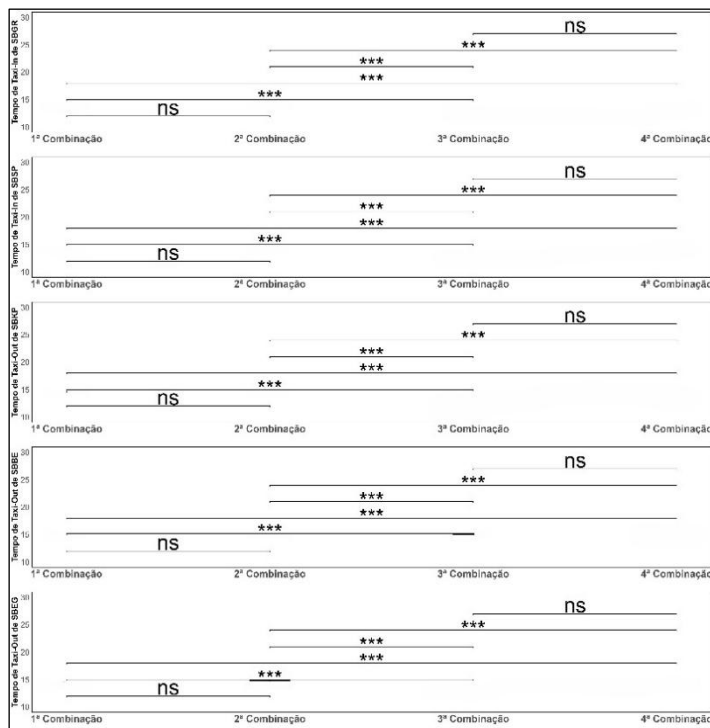


Figure 13: Combinations for *Taxi-In* Time.

Source: Authors, (2025).

At SBGR, SBSP, and SBKP, the comparisons between the 1st and 2nd combinations did not show significant differences ( $p = 0.61, 0.51, \text{ and } 0.49$ , respectively).

However, when comparing the 1st combination with the 3rd and 4th, highly significant differences were observed ( $p < 2e-16$ ), while the comparison between the 3rd and 4th combinations was not significant ( $p = 0.92, 0.91, \text{ and } 0.93$ ), indicating a higher similarity between the latter two.

At SBBE and SBEG airports, the results followed a similar pattern. Comparisons between the 1st and 2nd combinations, as well as between the 3rd and 4th combinations, showed no significant differences ( $p \approx 0.99-1.00$ ). However, when the 3rd and 4th combinations were compared to the 1st, the differences were highly significant ( $p < 2e-16$ ), suggesting that the 1st and 2nd combinations are more homogeneous, while the 3rd and 4th differ significantly.

These results indicate that while some combinations are statistically similar, others reflect more pronounced variations in Taxi-In Times, influenced by differences in data sources and the operational dynamics of the airports.

Additionally, considering the distances between gates and runway thresholds was essential, as they directly impact additional taxi time, affecting the airports' operational efficiency.

From this perspective, the study also aimed to assess whether taxi time variations, as combined from different data sources, would impact the efficiency of unimpeded taxi time indicators when considering different gate and runway threshold combinations.

For Guarulhos Airport (SBGR), the existence of two runways for landing and takeoff operations 10R/28R and 10L/28L was verified, as described in the airport chart (Figure 14).

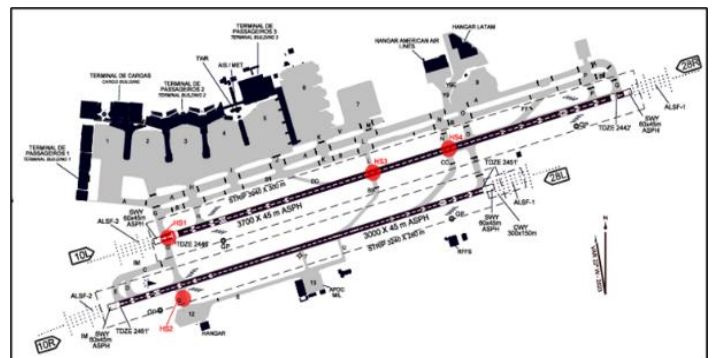


Figure 14: SBGR Airport Chart.

Source: Adapted from [39], (2025).

For departures, the most frequently used threshold was 10L, accounting for 75,04% (82.624) of movements, followed by 28R, 10R, and 28L, with 23,94% (26.353), 0,92% (1.012), and 0.10% (106) movements, respectively. For arrivals, 110.994 movements were recorded, with runway 10R handling the highest volume at 81.729 operations, while 28L registered 25.907 landings. Runways 10L and 28R had lower volumes, with 2.611 and 657 landings, respectively.

SBGR presented 462 possible gate and runway threshold combinations, a significant number that reflects its importance as the busiest airport in the country. The analysis of gate distribution revealed that demand was concentrated in six distinct aprons, with the combinations featuring the highest volume of landings and takeoffs selected for each of them.

Gate 207 with runway threshold 10L was the most frequent combination, recording 2.125 takeoffs (1,93%), followed by gates 309 (2.009; 1,82%), 102R (1.979; 1,80%), 401 (1.414; 1,28%), 501 (654; 0,60%), and 604 (288; 0,26%).

At runway threshold 28R, the most utilized gates were 102R, 209, 309, 401, 507R, and 606. Gate 209 led with 765

recorded takeoffs (0,70%), followed by gates 311 (711; 0,28%), 102R (648; 0,59%), 401 (547; 0,50%), 507R (189; 0,17%), and 606 (111; 0,10%). For arrivals (landings), 552 gate and runway threshold combinations were identified. Gate 208 was the busiest, with 2.183 landings (1,97%), followed by gates 310 (2.051; 1,85%), 102R (1.873; 1,69%), 401 (1.531; 1,38%), 504R (553; 0,50%), and 612L (181; 0,16%), all combined with runway 10R.

At runway threshold 28L, gates 102R, 209, 309, 401, 507R, and 606 recorded the highest landing volumes. Gate 209 was the most utilized (765 landings; 0,69%), followed by gates 309 (707; 0,64%), 102R (648; 0,58%), 401 (528; 0,48%), 507R (173; 0,15%), and 606 (58; 0,05%). Figure 15 revealed significant differences between the gates and runway threshold 10L in most comparisons, indicating relevant operational variations. Gates 102R, 207, 309, 401, and 501 showed consistent differences among themselves, reflecting distinct impacts on taxi times.

However, the comparison between gates 501 and 604 resulted in  $p = 0.07$ , suggesting no significant difference, possibly due to operational similarities or physical proximity. These findings reinforce the need to consider gate variability in airport planning, optimizing operational efficiency and air traffic flow.

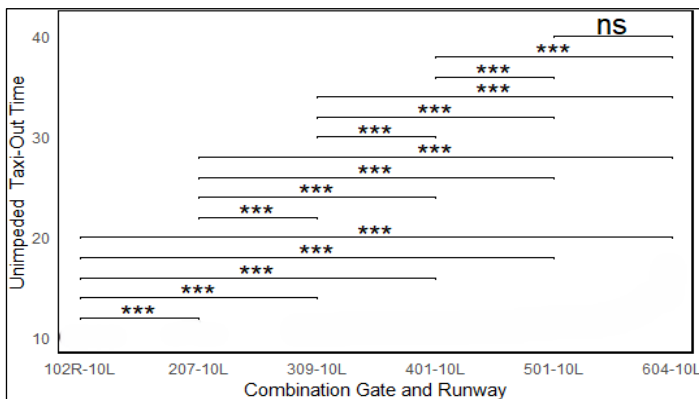


Figure 15: Combination of gate and runway 10L for KPI 02.  
Source: Authors, (2025).

The analysis of Unimpeded Taxi-Out Times for gates using runway threshold 28R revealed statistically significant differences among gates 102R, 209, 311, 401, 507R, and 604, as presented in Figure 16.

These variations indicate relevant operational differences, suggesting that gate allocation directly influences taxi time efficiency. The results reinforce the need for strategic adjustments in gate utilization to optimize airport resource management and improve operational flow at runway threshold 28R.

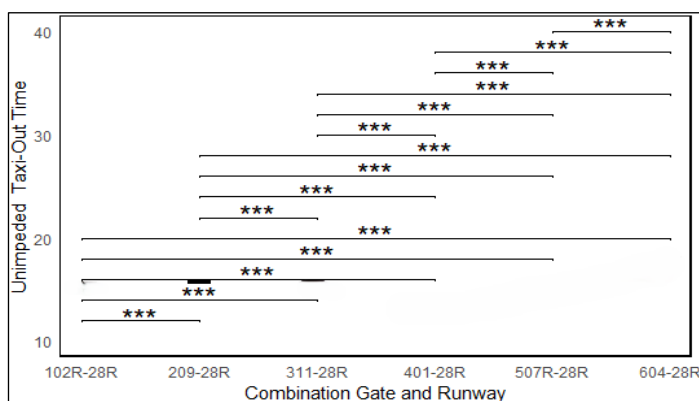


Figure 16: Combination of gate and runway 28R for KPI 02.  
Source: Authors, (2025).

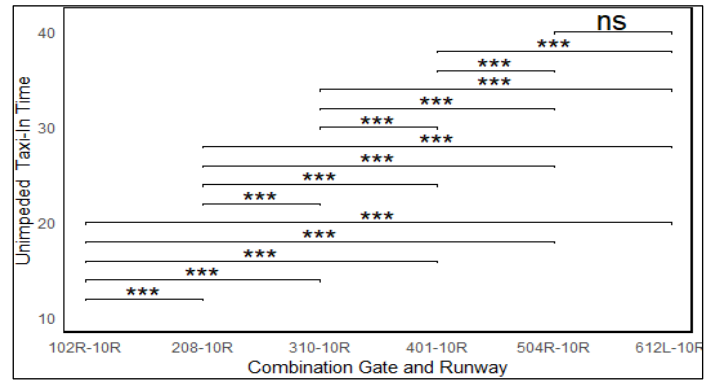


Figure 17: Combination of gate and runway 10R for KPI 13.  
Source: Authors, (2025).

Figure 17 showed the combination of gate and runway threshold at threshold 10R, revealing statistically significant differences among gates 102R, 208, 310, 401, 504R, and 612L, with  $p < 0.001$  for most comparisons. The exception was the comparison between gates 504R and 612L ( $p = 0,48$ ), which showed no significant difference.

Figure 18 described the combinations of gate and runway threshold 28L, revealing statistically significant differences among gates 102R, 209, 309, 401, 507R, and 606, except for the comparison between gates 507R and 606 ( $p = 0.94$ ), which showed no relevant variation. For all other combinations,  $p$ -values were below 0.001.

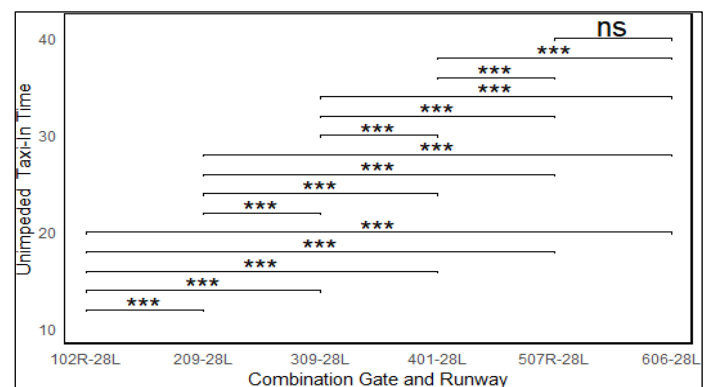


Figure 18: Combination of gate and runway 28L for KPI 13.  
Source: Authors, (2025).

At Congonhas Airport (SBSP), landing and takeoff operations take place on two runways: 17R/35L and 17L/35R, as described in the airport chart (Figure 19).

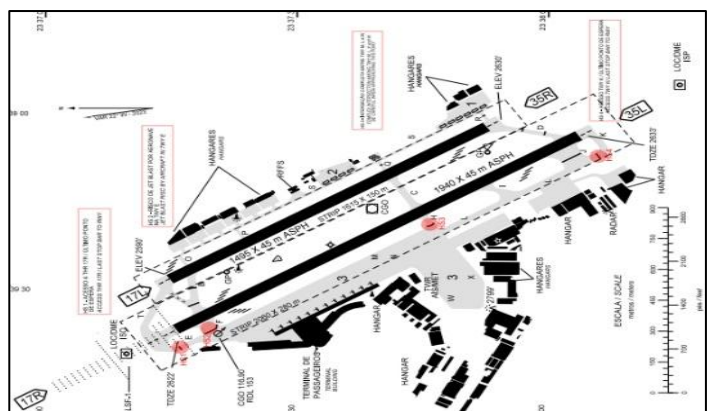


Figure 19: SBSP Airport Chart.  
Source: Adapted from [39], (2025).

Runway threshold 17R was the most frequently used for takeoffs, accounting for 59,47% (54.449 movements), followed by 35L (38,55%; 35.296 movements), 17L (1,10%; 1.006 movements), and 35R (0,88%; 806 movements). For landings, threshold 17R also predominated, with 59,81% (55.145 movements), highlighting its significance in the distribution of air traffic at SBSP. The gate layout for Apron 3 at Congonhas Airport (SBSP) covered 84,75% (100) of possible modifications and 99,97% of movements (91.532). The apron has 30 gates, organized into six groups of five gates each, with each group represented by the gate with the highest number of movements.

SBSP identified 118 gate and runway threshold combinations for takeoffs, with gate 05 standing out, recording 2.622 departures (2,86%) when combined with runway 17R. At threshold 35L, gates 04, 06, 11, 16, 22, and 26 were analyzed as they had the highest traffic volumes. Gate 06 led with 1.712 recorded takeoffs (1,87%), followed by gates 04 (1.704; 1,86%), 11 (1.573; 1,72%), 16 (1.030; 1,12%), 22 (976; 1,07%), and 26 (915; 1,00%).

For arrivals, 130 gate and runway threshold combinations were identified, with gate 04 standing out, recording 2.644 landings (2,87%) when combined with runway 17R. Additionally, movements recorded at threshold 35L were analyzed, where gates 04, 06, 11, 16, 22, and 26 had high traffic volumes. Gate 04 had the highest number of recorded landings, with 1.753 arrivals (1,90%), followed by gates 06 (1.726; 1,87%), 11 (1.608; 1,74%), 16 (1.005; 1,09%), 21 (910; 0,98%), and 26 (843; 0,91%).

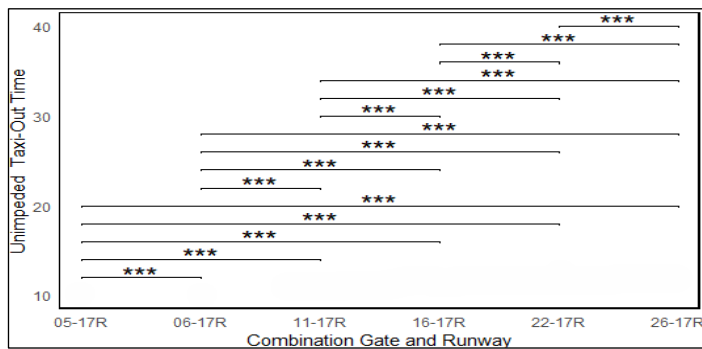


Figure 20: Combination of gate and runway 17R for KPI 02.  
Source: Authors, (2025).

Figure 20 presents the analysis of Unimpeded Taxi-Out Times for each gate and runway threshold combination, revealing statistically significant differences for gates 05, 06, 11, 16, 22, and 26 when compared to runway threshold 17R.

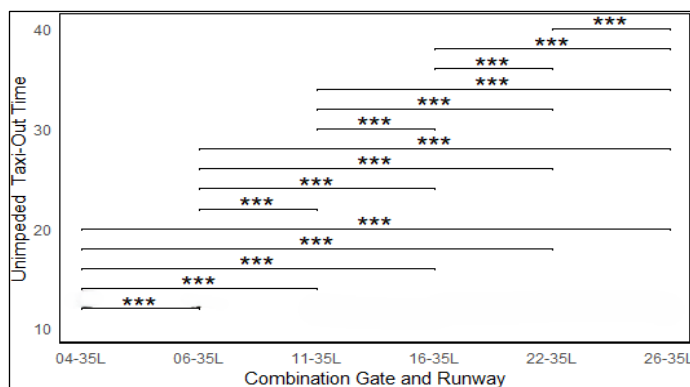


Figure 21: Combination of gate and runway 35L for KPI 02.  
Source: Authors, (2025).

Figure 21 presented the combinations among the six groups, highlighting significant differences. In other words, variations were observed in the medians of the Unimpeded Taxi-Out Times for gates 04, 06, 11, 16, 22, and 26 at runway threshold 35L.

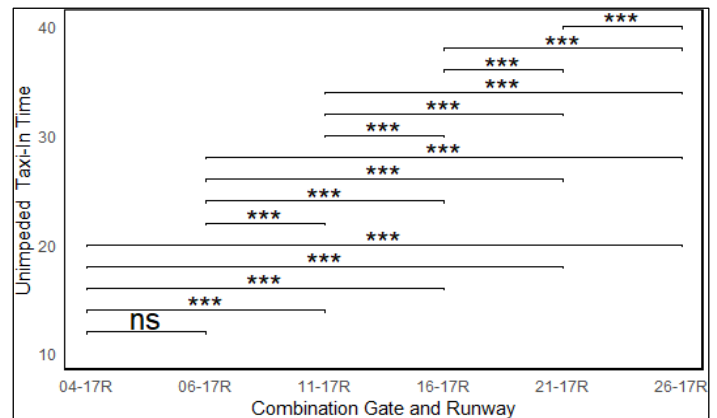


Figure 22: Combination of gate and runway 17R for KPI 13.  
Source: Authors, (2025).

Figure 22 shows the combination of gate and runway threshold, revealing significant differences in the medians of gates 05, 06, 11, 16, 21, and 26 at runway threshold 17R. Except for the comparison between gates 04 and 06, where no significant difference was observed, all other combinations exhibited substantial variations in taxi times, with  $p$ -values below 0,001 in all comparisons.

Figure 23 presents the combinations of gate and runway threshold 35L, highlighting gates 04, 06, 11, 16, 22, and 26. Statistically significant differences were found among the medians.

The only exception was observed between gates 04 and 16, where no significant difference was found ( $p = 1.00$ ). For all other comparisons,  $p$ -values were below 0,001, indicating highly significant differences and reinforcing the heterogeneity in taxi times among the analyzed groups.

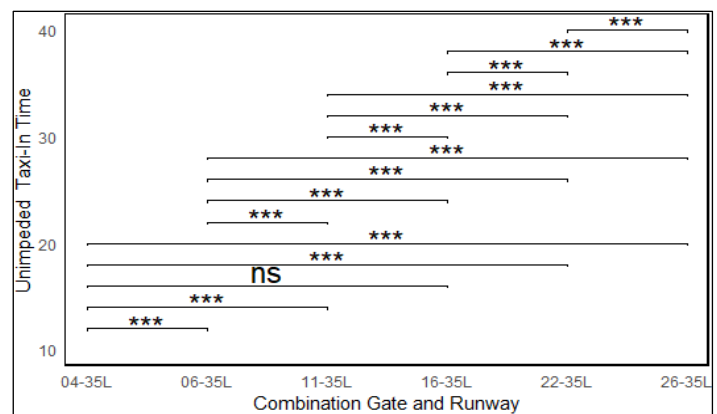


Figure 23: Combination of gate and runway 35R for KPI 13.  
Source: Authors, (2025).

Campinas Airport (SBKP) has a single runway for landing and takeoff operations (15/33, Figure 24).

For takeoff operations, runway threshold 15 was the most utilized, accounting for 69,61% of the total (41.430 movements), while threshold 33 recorded 30,39% (18.088 movements). Similarly, threshold 15 predominated for landing operations, with 68,75% of movements (41.069 records).



These data highlight a clear operational preference for runway threshold 15 for landings and takeoffs, emphasizing its importance in the distribution of air traffic flows.

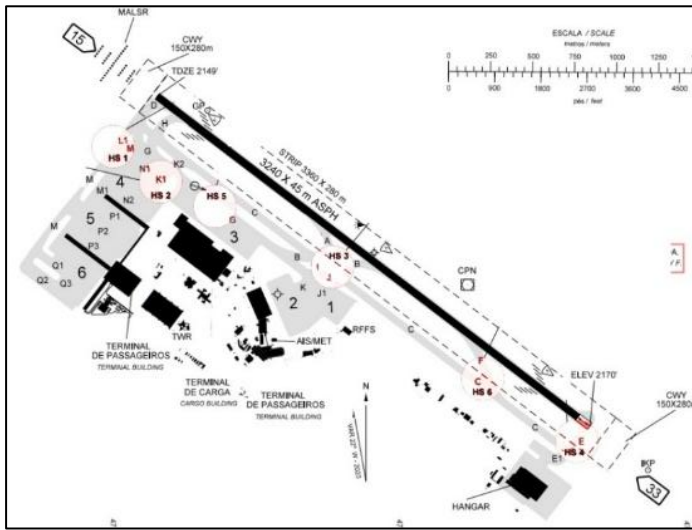


Figure 24: SBKP Airport Chart.  
Source: Adapted from [39], (2025).

SBKP identified 177 gate and runway threshold combinations for takeoffs, with gate C02 standing out, recording 1.732 departures (2,91%) when combined with runway 15.

For threshold 33, gates B02, B13A, C02, M5, R7, and R9 were analyzed as they had the highest traffic volumes. Gate C02 led with 757 recorded takeoffs (1,27%), followed by B02 (631; 1,06%), B13A (293; 0,49%), M5 (139; 0,23%), R7 (129; 0,22%), and R9 (89; 0,15%).

For arrivals, 184 gate and runway threshold combinations were identified, with gate B02 standing out, recording 1.501 landings (2,51%) when combined with runway 15.

Similarly, gate and threshold combinations for runway 33 were analyzed, selecting gates B11, C04, C05, M5, R7, and T04, which had the highest traffic volumes. Gate C04 had the highest number of recorded movements, with 776 operations (1,30%), followed by C05 (661; 1,10%), B11 (290; 0,48%), R7 (136; 0,23%), M5 (128; 0,21%), and T04 (28; 0,05%).

Figure 25 reveals statistically significant variations in the medians of Unimpeded Taxi-Out Times for gates B02, B13A, C02, M5, R7, and R9 in relation to runway threshold 15. However, some differences among M5, R7, and R9 were not significant, as indicated by the *p-values*.

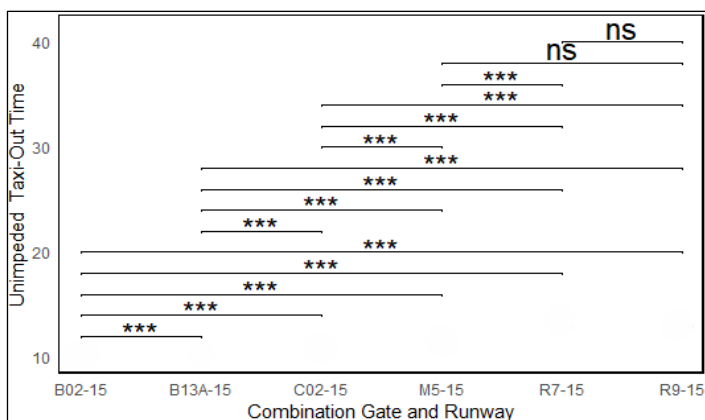


Figure 25: Combination of gate and runway 15 for KPI 02.  
Source: Authors, (2025).

Figure 26 revealed statistically significant differences in the medians of Unimpeded Taxi-In Times for gates T3, R8, M5, C06, B02, and B13A in relation to runway threshold 15. The only exception was the comparison between T3 and R8 ( $p = 0.85$ ), which showed no relevant variation.

Combinations involving M5, C06, B02, and B13A exhibited consistent differences among themselves, with *p-values* below 0,001, highlighting the variability in KPI 13 as a function of the gates and the runway threshold used.

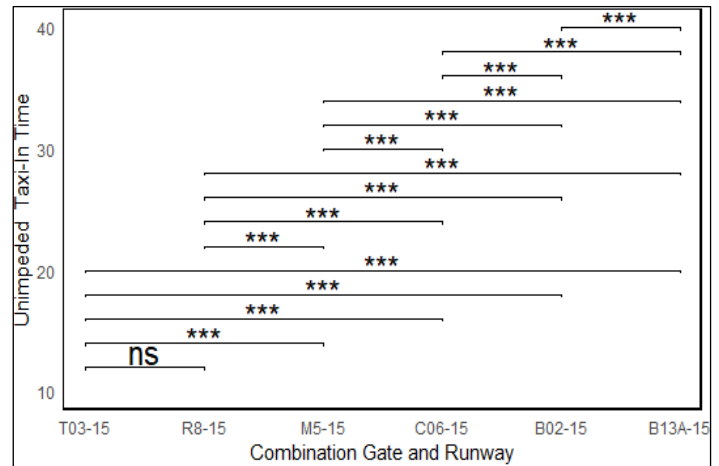


Figure 26: Combination of gate and runway 15 for KPI 13.  
Source: Authors, (2025).

For Belém Airport (SBBE), the existence of two runways for landing and takeoff operations 06/24 and 02/20 was verified (Figure 27).

It was verified that, for both takeoffs and landings, runway threshold 06 was the most utilized, accounting for 90,94% (13.064) and 92,28% (13.229) of movements, respectively.

The analysis of gate and runway threshold combinations at Belém Airport (SBBE) identified 72 combinations for departures and 63 for arrivals, with aprons 3 and 4 concentrating 98,30% of departure movements (14.121 records in 2023). These aprons contain 12 gates, divided into six groups of two, represented by the gates with the highest traffic volumes.

Gate 04 recorded 1.969 departures (13,71%) and gate 05 had 1.959 departures (13,64%), both combined with runway threshold 06. For threshold 02, gates 02, 04, 05, 07, 08, and 12 had the highest departure volumes, with gate 04 leading (160 records; 1,11%), followed by gates 05 (150; 1,04%), 02 (147; 1,02%), and 12 (145; 1,01%).

For arrivals (landings), gate 04 was also the busiest, with 1.942 recorded landings (13,54%), followed by gate 05 (1.915; 13,36%), both combined with runway threshold 06. For threshold 02, gates 02, 04, 05, 07, 10, and 12 recorded the highest landing volumes, with gate 05 being the most utilized (163 records; 1,14%), followed by gates 04 (150; 1,05%) and 02 (134; 0,46%).

The data indicate that gates 04 and 05 were the most active for both departures and arrivals, highlighting an operational concentration and a decreasing distribution among other gates, reflecting strategic traffic management patterns at SBBE.



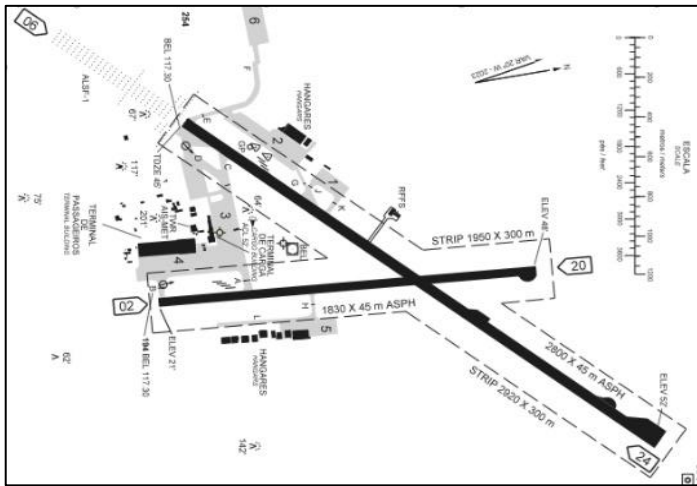


Figure 27: SBBE Airport Chart.  
Source: Adapted from [39], (2025).

Figure 28 presents the analysis of Unimpeded Taxi-Out Times for each gate and runway threshold combination, revealing statistically significant differences.

Observing the combinations of gates 02, 04, 05, 07, 08, and 12 with runway threshold 06, the differences in the medians of Unimpeded Taxi-Out Times were found to be highly significant, as indicated by the *p-values*. This result suggests that, for runway threshold 06, there are substantial variations in taxi times depending on the gate used, reflecting operational and logistical differences for each combination.

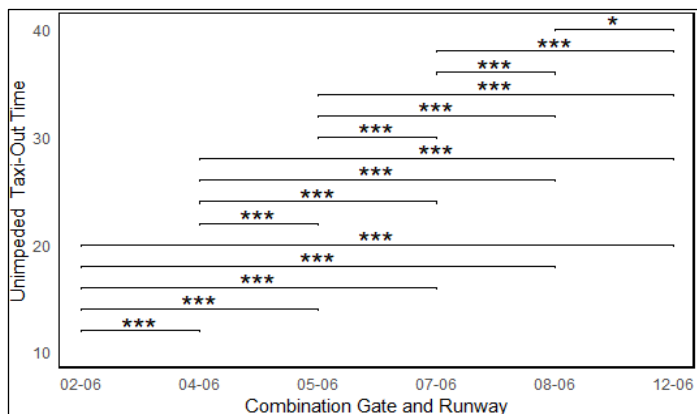


Figure 28: Combination of gate and runway 06 for KPI 02.  
Source: Authors, (2025).

Figure 29 presents the analysis of combinations among gates 02, 04, 05, 07, 08, and 12, considering runway threshold 06, revealing statistically significant differences in the medians of Unimpeded Taxi-Out Times in most comparisons. The exceptions were the combinations between gates 02 and 07, 04 and 07, 07 and 08, and 08 and 12, which showed no statistically relevant variations.

These results indicate that, although some combinations did not exhibit significant differences, Unimpeded Taxi-Out Times show substantial variations among the analyzed gates. Notably, gate 12 stood out for having the largest observed difference, suggesting a significant impact on operational efficiency depending on the configuration used.

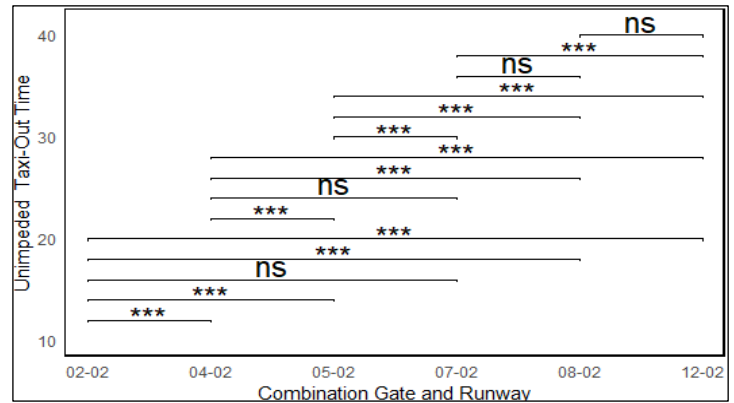


Figure 29: Combination of gate and runway 02 for KPI 02.  
Source: Authors, (2025).

The analysis of runway threshold 02 revealed statistically significant differences among the median times of the analyzed gates, as shown in Figure 30.

Comparisons between gates 02 and 04, 02 and 05, 02 and 07, 02 and 10, and 02 and 12 presented *p-values* < 0.001, indicating significant variations in Unimpeded Taxi-In Times for these combinations. The only exception was the comparison between gates 10 and 12, which did not show a statistically significant difference.

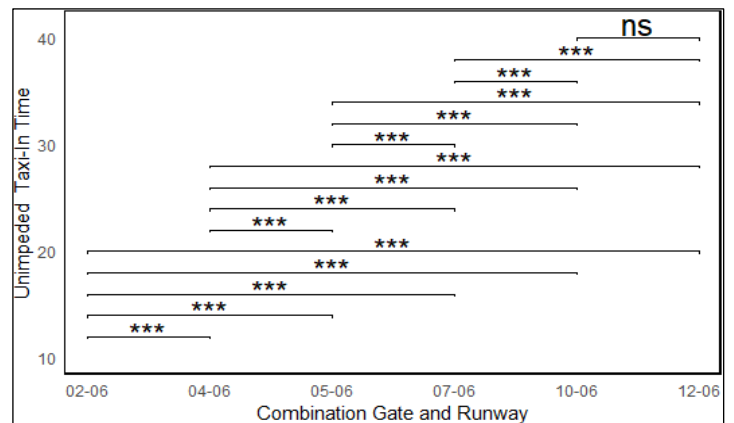


Figure 30: Combination of gate and runway 06 for KPI 13.  
Source: Authors, (2025).

Figure 31 illustrates the runway threshold 02 combination, revealing statistically significant variations among gates 02, 04, 05, 07, 10, and 12, except for comparisons between gates 04 and 12, and gates 07 and 10, which showed no relevant differences.

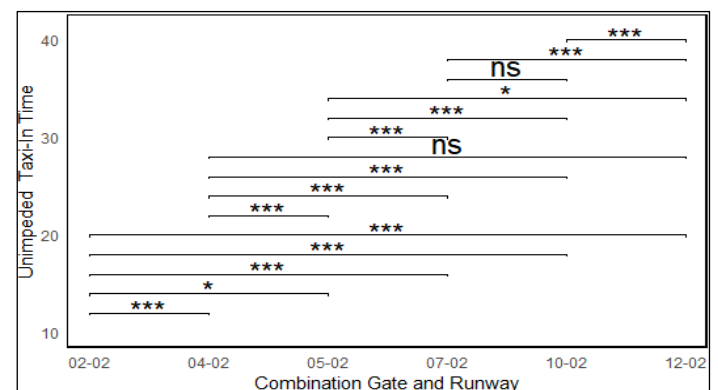


Figure 31: Combination of gate and runway 02 for KPI 13.  
Source: Authors, (2025).

The results indicate that Taxi-In Unimpeded Times differ substantially among gate combinations, notably between gates 02 and 10 ( $p < 0.001$ ), and between gate 05 and other gates, demonstrating statistically significant differences. On the other hand, gates 04 and 12 showed similar taxi times, as did gates 07 and 10, whose comparison yielded a  $p$ -value of 0,3988, suggesting comparable taxi-in times. At Manaus Airport (SBEG), there is a single runway (11/29) used for both landing and take-off operations (Figure 32).

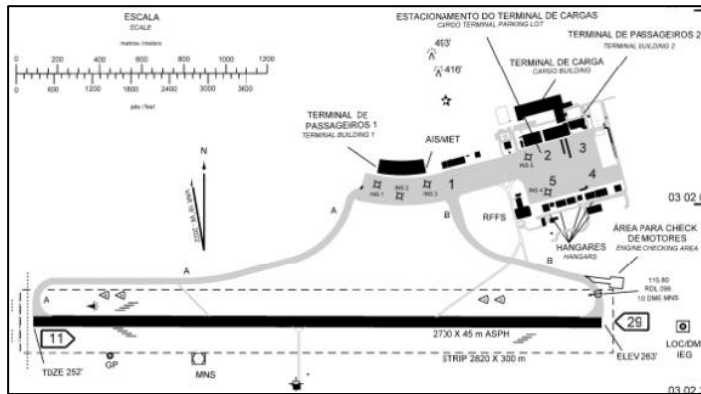


Figure 32: SBEG Airport Chart.  
Source: Adapted from [39], (2025).

For departures, runway threshold 11 was the most frequently used, representing 94,49% of the operations (12.235 movements), whereas runway threshold 29 accounted for only 5,51% (714 movements). In landings, runway threshold 11 also predominated, accounting for 97,02% of operations (12.470 movements), while runway threshold 29 was utilized in just 2,98% of cases (383 movements). These data indicate a strong operational preference for runway threshold 11, both for takeoffs and landings, possibly influenced by factors such as prevailing winds, airport infrastructure, and the established air traffic flow patterns.

At SBEG, 67 combinations of gates and runway thresholds were identified for departures and 78 for arrivals. Apron 1 concentrated 87,79% of departures (11.369 movements in 2023) and is configured with 18 gates divided into 6 groups of 3, each represented by the gate with the highest activity. The most frequently used combination for commercial flights was gate B18 with runway threshold 11, totaling 1.764 departures (13,62%). In the analysis of operations using runway threshold 29, gates B18, E15, R20, R21, R23, and R26 were selected due to their higher traffic volumes. Gate R20 registered 121 movements (0,93%), followed by gates R21 (81; 0,63%), B18 (70; 0,54%), R23 (36; 0,28%), E15 (31; 0,24%), and R26 (13; 0,10%).

For arrivals (landings), 78 combinations of gates and runway thresholds were identified, notably gate B18, which received 1,774 landings (13,80%), followed by gates C17 (1.725; 13,42%), R20 (1.052; 8,18%), R26 (600; 4,67%), F14 (485; 3,77%), and R22 (268; 2,08%), all operating with runway threshold 11. Similarly, for runway threshold 29, gates B18, C17, F14, R20, R22, and R25 were selected due to their higher landing volumes.

Figure 33 shows gate-runway threshold combinations at SBEG, revealing statistically significant differences among gates A19, B18, E15, R21, R24, and R25 for runway threshold 11. Comparisons between gates A19 and B18 indicated statistically relevant differences ( $p < 0.001$ ), suggesting distinct taxi times between these gates. The same pattern was observed for gate E15, which demonstrated significant variations compared to gates A19 and B18.

Significant differences were also identified in comparisons among gates R21, R24, and R25, all presenting extremely low  $p$ -values ( $p < 0.001$ ), reinforcing the substantial variation in taxi times across the analyzed gates.

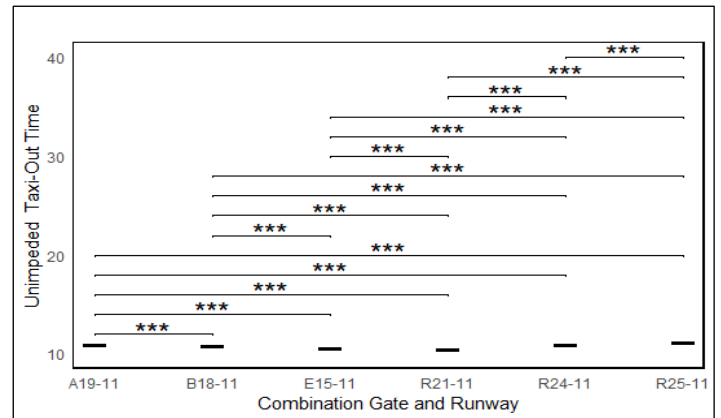


Figure 33: Combination of gate and runway 11 for KPI 02.  
Source: Authors, (2025).

Figure 34 presents gate-runway threshold 29 combinations, revealing statistically significant differences. Comparisons indicated substantial variations among median unimpeded taxi-out times for gates B18, E15, R20, R21, R23, and R26. However, no significant differences were observed in the combinations between gates B18 and R23, B18 and R26, and E15 and R26, suggesting these gates have similar taxi times.

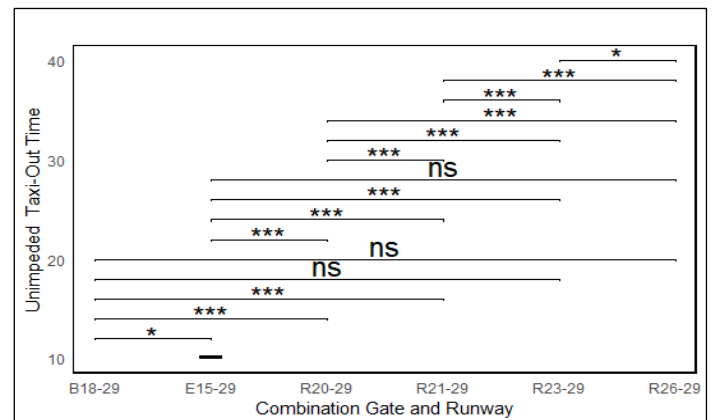


Figure 34: Combination of gate and runway 29 for KPI 02.  
Source: Authors, (2025).

Figure 35 shows the gate-runway threshold 11 combinations, revealing statistically significant differences.

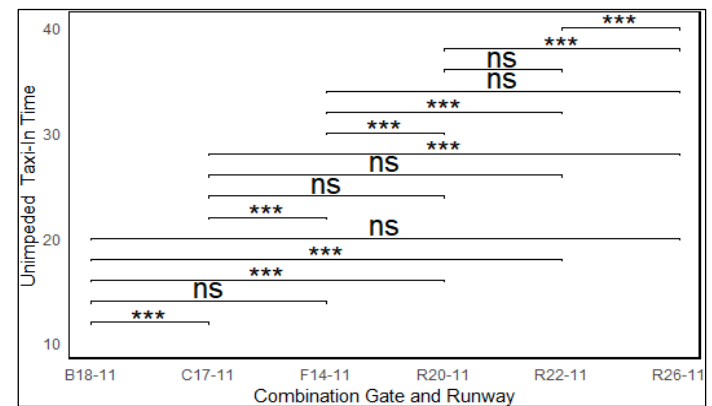


Figure 35: Combination of gate and runway 11 for KPI 13.  
Source: Authors, (2025).

Gates B18, C17, F14, R20, R22, and R26 showed variations in median unimpeded taxi-in times, indicating distinct operational impacts among these combinations. However, no significant differences were observed in comparisons between gates B18 and F14, B18 and R26, C17 and R20, C17 and R22, F14 and R26, and R20 and R22, suggesting these gate pairs have similar taxi times.

Finally, Figure 36 describes gate-runway threshold 29 combinations, revealing statistically significant differences. Gates B18, C17, F14, R20, R22, and R25 showed variations in median unimpeded taxi-in times, indicating operational discrepancies among these combinations. However, no significant differences were observed in comparisons between gates B18 and F14, B18 and R20, C17 and R25, and R20 and R22, suggesting similar taxi times among these gate pairs.

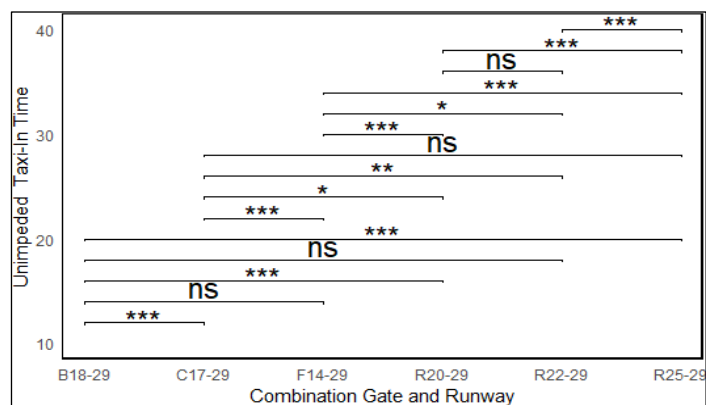


Figure 36: Combinação de Gate e Runway 29 para KPI 13.

Source: Authors, (2025).

## V. CONCLUSIONS

The assessment of key performance indicators of the Brazilian Airspace Control System (SISCEAB) was essential to this study. It highlighted that out of the 19 KPIs and 7 IDBRs described in MCA 100-22, only 10 KPIs and 1 IDBR are currently monitored by DECEA.

An analysis of data sources (TATIC FLOW, BIMTRA, and VRA) revealed significant discrepancies in the records, underscoring the necessity for an integrated approach to enhance the accuracy of KPI 02 and KPI 13.

The selection of data sources directly influences the reliability of indicators, while operational and environmental factors may impact taxi time variability.

The analysis found that BIMTRA and VRA provide greater representativeness and accuracy in calculations despite their inherent limitations.

The study revealed an overall efficiency of 0,35% for KPI 02 and 207% for KPI 13. When examining KPI 02 individually, the airport combinations displayed similar efficiencies, except for SBEG, which notably achieved 3,15%. Regarding KPI 13, the efficiency results varied considerably across airports: SBGR had an efficiency of 163%, SBSP reached 298%, SBKP recorded 453%, SBBE obtained 92%, and SBEG stood out significantly at 800%.

The optimal data source combination for KPI 02 includes take-off time (ATOT) from BIMTRA and gate departure (AOBT) from VRA, whereas for KPI 13, gate arrival time (AIBT) from VRA and landing time (ALDT) from BIMTRA proved to be most effective.

Therefore, integrating these data sources enables more accurate and reliable measurements, optimizing air traffic

management, reducing congestion, and improving operational efficiency, particularly at high-flow airports.

It is recommended to use these databases jointly as the most effective strategy for enhancing KPI 02 and KPI 13, thus contributing to more efficient and secure airport operations management.

## VI. AUTHOR'S CONTRIBUTION

**Conceptualization:** Alessandro Soares de Freitas, Edilson Marques Magalhaes

**Methodology:** Alessandro Soares de Freitas, Edilson Marques Magalhaes

**Investigation:** Alessandro Soares de Freitas, Edilson Marques Magalhaes

**Discussion of results:** Alessandro Soares de Freitas, Edilson Marques Magalhaes

**Writing – Original Draft:** Alessandro Soares de Freitas, Edilson Marques Magalhaes

**Writing – Review and Editing:** Alessandro Soares de Freitas, Edilson Marques Magalhaes

**Supervision:** Alessandro Soares de Freitas, Edilson Marques Magalhaes

**Approval of the final text:** Alessandro Soares de Freitas, Edilson Marques Magalhaes

## VII. ACKNOWLEDGMENTS

The authors sincerely express their deepest gratitude and appreciation to the department, institution, and all individuals whose support and contributions were instrumental in the successful completion of this study.

## VIII. REFERENCES

- [1] NSCA 351-1, *Brazilian Air Force Command System Standard: Brazilian Airspace Control System (SISCEAB)*. Rio de Janeiro: DECEA, 2024.
- [2] A. D. Silva *et al.*, "ATM performance report of the Airspace Control System (SISCEAB)," DECEA, 2019.
- [3] ANAC, "Air Transport Yearbook." in *National Civil Aviation Agency. Air Transport Indicators Panel 2022*, ANAC, 2024.
- [4] DCA 351-7, *Air Force Command Guideline: Guideline for Airspace Control*, DECEA, Rio de Janeiro, Brazil, 2025.
- [5] DCA 100-2, *Guideline of the Air Force Command: Flexible Use of Airspace*, DECEA, Rio de Janeiro, Brazil, 2017.
- [6] *Aeroespaço*, Special Edition commemorating the 10th anniversary of CGNA, DECEA, Rio de Janeiro, Brazil, Dec. 2017.
- [7] DCA 351-2, *Guideline of the Air Force Command: National ATM Operational Concept*, DECEA, Rio de Janeiro, Brazil, 2021.
- [8] ICA 100-22, *Instruction of the Air Force Command: Air Traffic Service*, DECEA, Rio de Janeiro, Brazil, 2023.
- [9] L. P. Oliveira, "System for optimizing Brazilian air traffic management with the Collaborative Trajectory Options Program," Undergraduate Thesis, University of Brasília (UNB), Brasília, Brazil, 2018.
- [10] P. C. F. Barbosa, *Imbalance of aerodrome runway capacities: A calculation for obtaining the maximum per type of operation*, M.S. thesis, Professional Master's Program in National Network Mathematics, Graduate Studies, Research, Extension, and Culture Office, Pedro II College, Rio de Janeiro, Brazil, 2021.

- [11] R. Tezza, A. C. Bornia, and I. H. Vey, "Performance measurement systems: A review and classification of the literature," *Management & Production*, vol. 17, pp. 75–93, 2010.
- [12] A. C. Fernandes, "Analysis and forecasting of Brazilian air traffic performance indicators," Undergraduate Thesis, Aeronautics Institute of Technology, São José dos Campos, Brazil, 2022.
- [13] DECEA, "ATM performance report of the Airspace Control System (SISCEAB)," DECEA, 2023.
- [14] DECEA, "ATM performance report of the Airspace Control System (SISCEAB)," DECEA, 2024.
- [15] A. C. R. A. Duarte, "Implementation of operational safety indicators in Cape Verde aviation," M.S. thesis, Master's Program in Air Transport Operations, Higher Institute of Education and Sciences, Lisbon, Portugal, 2023.
- [16] O. T. Muniz, *Performance Management*, 1st. Rio de Janeiro, Brazil: SESES, 2016.
- [17] P. M. Jannuzzi, *Social Indicators in Brazil*, 6th. ed. Campinas, Brazil: Alínea Publishing, 2017.
- [18] L.O. Bahia, *Reference guide for the construction and analysis of indicators*, 1st ed. Brasília, Brazil: ENAP, 2021.
- [19] R. B. Santana and V. A. G. Zanoni, "Brazilian housing indicators: comparative analysis of the historical series 1995-2018," *Cadernos Metr pole*, vol. 24, no. 53, pp. 409–428, 2022.
- [20] H. O. Gomes *et al.*, "The impact of Embraer's intellectual property assets indicators on strategic decision-making for the company," *Peer Review*, vol. 5, no. 5, pp. 353–365, 2023.
- [21] A. C. Fernandes, "Analysis and forecasting of Brazilian air traffic performance indicators," Undergraduate Thesis, Aeronautics Institute of Technology, São José dos Campos, Brazil, 2022.
- [22] B. Bubalo, *Airport Capacity and Performance in Europe: A Study of Transport Economics, Service Quality and Sustainability*, Ph.D. dissertation, Department of Economics, University of Hamburg, Hamburg, Germany, 2021.
- [23] Francischini, A. S. N., and Francischini, P. G. *Performance Indicators*. 1st ed. Rio de Janeiro, Brazil: Alta Books, 2017.
- [24] A. W. Dougall and M. Mmola, "Identification of key performance  reas in the Southern African surface mining delivery environment". *Journal of the Southern African Institute of Mining and Metallurgy*, V. 115, n. 111, pp. 1001-1006, 2015.
- [25] P. Gackowiec *et al.* "Review of Key Performance Indicators for Process Monitoring in the Mining Industry." *Energies*, V. 13, n. 20, pp. 30-59, 2020.
- [26] R. Domigues *et al.*, "Key performance indicators in marketing," *Iberian Journal of Information Systems and Technologies*, no. E35, pp. 128–140, 2020.
- [27] F. R. M. S. Montenegro and A. L. C. Callado, "Contingency factors and the use of performance indicators associated with the Balanced Scorecard perspectives," *Revista Gest o Organizacional*, vol. 12, no. 1, pp. 73–91, 2019.
- [28] ICAO, *Global Air Navigation Plan (GANP)*, 7th ed. Montreal, Canada: ICAO, 2021.
- [29] R. L. Pereira, "Management of the methodology for air traffic controllers' shift scheduling: a perspective based on EUROCONTROL concepts," M.S. thesis, Graduate Program in International Security and Defense, Superior War College, Rio de Janeiro, Brazil, 2022.
- [30] M. Hammer and J. Champy, *Reengineering the Corporation: A Manifesto for Business Revolution*, New York, NY, USA: HarperCollins Publishers, 1993.
- [31] T. H. Davenport, *Process Reengineering: How to Innovate in the Company Through Information Technology*, 4th ed. Rio de Janeiro, Brazil: Campus, 1994.
- [32] M. Imai, Kaizen: The Path of Continuous Improvement, Sa o Paulo, Brazil: McGraw-Hill, 1986.
- [33] J. Tidd and J. Bessant, *Innovation and Business Process Management*, 5th ed. , Porto Alegre, Brazil: Bookman, 2015.
- [34] J. Jeston and J. Nelis, *Business Process Management: Practical Guidelines to Successful Implementations*, 5th ed. Abingdon, UK: Routledge, 2018.
- [35] P. Harmon, *Business Process Change: A Guide for Business Managers and BPM and Six Sigma Professionals*, 2<sup>a</sup> ed., Burlington, MA: Morgan Kaufmann, 2010.
- [36] W. van der Aalst, *Process Mining: Data Science in Action*, 2nd ed. Heidelberg, Germany: Springer, 2016.
- [37] MCA 100-22, Air Force Command Manual: ATM Indicators Methodology of SISCEAB. Rio de Janeiro, Brazil: DECEA, 2020.
- [38] PCA 100-3, Brazilian Air Force Command Plan: ATM Performance Plan. DECEA, Rio de Janeiro, Brazil, 2024.
- [39] Adapted from SBGR ADC Chart (AISWEB), (2024). file:///C:/Users/LAB%2020%20ITEGAM/Downloads/sbgr\_adc-sbgr\_adc\_20240905.pdf





## RESEARCH ARTICLE

## OPEN ACCESS

# QUANTUM COMPUTING: APPROACHES, SCALABILITY, AND THE FUTURE OF EMERGING TECHNOLOGIES

Manoel Socorro Santos Azevedo<sup>1</sup>, Marcelo Weber Schiller<sup>2</sup>, João Paulo Modesto Damiano<sup>3</sup>, Cristiano Peniche Ceccon<sup>4</sup> and Antonio Gabriel Nunes Martins<sup>5</sup>

<sup>1,2,3,4,5</sup> Escola Superior de Tecnologia – EST-UEA. Manaus-Amazonas, Brazil.

<sup>1</sup><https://orcid.org/0000-0002-0611-2906> , <sup>2</sup><https://orcid.org/0000-0002-5677-0309> , <sup>3</sup><https://orcid.org/0009-0009-1218-2378> 

<sup>4</sup><https://orcid.org/0009-0001-1278-7467> , <sup>5</sup><https://orcid.org/0009-0002-9432-7479> 

Email: [mazevedo@uea.edu.br](mailto:mazevedo@uea.edu.br), [mschiler@uea.edu.br](mailto:mschiler@uea.edu.br), [jpmd.eng22@uea.edu.br](mailto:jpmd.eng22@uea.edu.br), [cpc.eng23@uea.edu.br](mailto:cpc.eng23@uea.edu.br), [agnm.eng23@uea.edu.br](mailto:agnm.eng23@uea.edu.br)

## ARTICLE INFO

**Article History**

Received: March 13, 2025

Revised: March 20, 2025

Accepted: March 15, 2025

Published: April 31, 2025

**Keywords:**

Quantum Computing,  
Nuclear Magnetic Resonance,  
MRV,  
Educational Quantum Computing.

## ABSTRACT

Quantum computing is an emerging field that promises to revolutionize science and technology by offering exponentially superior processing capabilities compared to classical computing. This paper analyzes three main approaches to quantum computer development: IBM's scalable and modular systems, D-Wave's practical solutions for optimization problems, and Nuclear Magnetic Resonance (NMR)-based computers designed for education and research. We explore the technological advancements, practical applications, challenges, and future prospects of these approaches, demonstrating how they collectively pave the way for a future where quantum computing becomes indispensable.



Copyright ©2016 by authors and Galileo Institute of Technology and Education of the Amazon (ITEGAM). This work is licensed under the Creative Commons Attribution International License (CC BY 4.0).

## I. INTRODUCTION

Quantum computing is fundamentally redefining the limits of science and technology. Unlike classical computing, which operates with binary bits (000 or 111), quantum computing uses qubits. These units of quantum information exploit unique properties of quantum mechanics, such as **superposition**, **entanglement**, and **quantum interference**, enabling calculations to occur simultaneously across multiple states. This exponential processing power positions quantum computing as a revolutionary tool to address scientific, industrial, and societal challenges previously considered insurmountable [1].

The potential applications of quantum computing are vast, encompassing areas like molecular simulation for drug and material design, highly secure quantum cryptography systems, logistical optimization, and large-scale data analysis. However, realizing this potential has required the development of different approaches to harness the principles of quantum computing for practical and theoretical advancements.

In recent years, three main approaches have emerged:

1. **IBM** focuses on scalable, hybrid quantum-classical systems, striving to solve large-scale, high-complexity

problems. The company has pioneered milestones such as the Eagle (127 qubits) and Condor (1121 qubits) processors and aims to build systems exceeding 4000 qubits by 2025 [2].

2. **D-Wave** specializes in optimization solutions, addressing specific industrial challenges with practical and immediate applications. Systems like Advantage2, with over 1200 qubits, have proven instrumental in logistics and geophysics [3].
3. **NMR-based quantum computers** provide an accessible entry point for education and research, allowing students and scientists to explore fundamental quantum principles [4].

While these advancements are remarkable, quantum computing still faces significant challenges, including **error mitigation**, **coherence maintenance**, and **scalability**. Additionally, democratizing access to this technology by reducing costs and increasing availability remains a critical barrier [5].

This paper presents a comprehensive analysis of these approaches, discussing their contributions to advancing science and industry and their potential to shape the future of technology. IBM leads with scalable solutions, D-Wave delivers practical results, and

NMR systems provide educational opportunities, collectively transforming quantum computing into a foundational technology of the 21st century.

## II. THEORETICAL REFERENCE

### II.1 QUANTUM COMPUTING OVERVIEW

Quantum computing relies on qubits, the fundamental units of quantum information, which differ from classical bits due to their ability to exist in a superposition of states [4]. Mathematically, a qubit is described as a linear combination of two basis states, represented as  $|0\rangle$  and  $|1\rangle$ , defined by the equation [5]:

$$|\psi\rangle = \alpha|0\rangle + \beta|1\rangle, \text{ where } |\alpha|^2 + |\beta|^2 = 1 \quad (1)$$

This property allows qubits to process multiple states simultaneously, resulting in exponentially greater computational power compared to classical bits.

Qubit scalability is a critical factor in quantum systems' performance. While classical systems are limited to linear state processing, quantum systems can represent  $2^n$  states simultaneously, where  $n$  is the number of qubits. For example, a system with 5 qubits can represent 32 states simultaneously, while a 1000-qubit system can explore  $2^{1000}$  states.

Table 1: Classical and Quantum Capability Comparison.

Number of Qubits	Classical Capability	Quantum Capability ( $2^n$ )
2	2 states	$2^2 = 4 \text{ states}$
3	3 states	$2^3 = 8 \text{ states}$
5	5 states	$2^5 = 32 \text{ states}$
1000	1000 states	$2^{1000}$

Source: Authors, (2025).

Table 1 illustrates a comparison between the capabilities of classical and quantum systems, highlighting the exponential growth of quantum computational power relative to classical systems. While a classical system with  $n$  bits can represent  $n$  states, a quantum system with  $n$  qubits can explore  $2^n$  states simultaneously, as shown in the table. For instance, 5 qubits allow access to 32 states at once, whereas 1,000 qubits can explore  $2^{1000}$  states, demonstrating the superior scalability of quantum systems.

These properties make quantum computing ideal for solving problems deemed intractable for classical computers, such as molecular simulations, industrial process optimization, and advanced cryptographic algorithms.

### II.2 TECHNOLOGICAL APPROACHES

Three distinct technological approaches are shaping the development of quantum computing: IBM's scalable systems, D-Wave's optimization solutions, and Nuclear Magnetic Resonance (NMR)-based systems for education and research. Each approach has unique focuses, features, and challenges.

#### II.2.1 IBM: SCALABLE MODULAR SYSTEMS

IBM leads innovation in hybrid quantum systems, integrating classical and quantum processors to tackle high-complexity problems [6],[7]. Highlights include:

- **Advances:** Processors like Eagle (127 qubits) and Condor (1121 qubits), aiming for over 4000 qubits by 2025.
- **Applications:** Molecular simulations for drug development, material modeling, and artificial intelligence algorithms.
- **Challenges:** Error mitigation and quantum coherence maintenance in large-scale systems.

#### II.2.2 D-WAVE: PRACTICAL OPTIMIZATION SOLUTION

D-Wave adopts a specialized approach, focusing on optimization problems via quantum annealing. Key features include:

- **Advances:** The Advantage2 system with over 1200 qubits, providing practical solutions to industrial challenges.
- **Applications:** Logistics, such as supply chain optimization, and geophysics, including subsurface mapping.
- **Challenges:** Limited scalability and inability to execute universal algorithms [94†source] .

#### II.2.3 NMR-BASED QUANTUM COMPUTER

Nuclear Magnetic Resonance (NMR)-based systems offer an accessible alternative for teaching and research in quantum computing. Main characteristics:

- **Advances:** Models like SpinQ Gemini (2 qubits) and Triangulum (3 qubits), accessible for academic use.
- **Applications:** Teaching fundamental algorithms like Grover's and Deutsch-Jozsa, and experimenting with basic quantum principles.
- **Challenges:** Limited scalability and precision, hindering large-scale practical applications.

## III. TECHNOLOGICAL APPROACHES

### III.1 IBM: SCALABLE MODULAR SYSTEMS

IBM is recognized for its leadership in developing scalable, modular quantum processors that address complex scientific and industrial needs [8],[9].

- **Advances:**
  - Launch of the Eagle processor (127 qubits) in 2021, followed by the Osprey (433 qubits) in 2022 and Condor (1121 qubits) in 2023.
  - A roadmap targeting over 4000 qubits by 2025 through modular architecture that combines multiple quantum processors.
- **Applications:**
  - **Molecular Simulations:** Designing new drugs and materials through precise chemical simulations.
  - **Artificial Intelligence:** Developing advanced algorithms for big data analysis.
- **Challenges:**

- **Error Mitigation:** Ensuring reliability in large-scale quantum operations.
- **Coherence Maintenance:** Preserving quantum states in complex systems.
- **Integration:** Combining classical and quantum systems effectively.

### III.2 D-WAVE: PRACTICAL OPTIMIZATION SOLUTIONS

D-Wave distinguishes itself by focusing exclusively on optimization problems, providing practical tools for real-world industrial challenges [3].

- **Characteristics:**
  - Advantage2 system, with over 1200 qubits, offers 20 times greater performance for complex optimization problems.
  - Utilizes quantum coupling technology to address logistical and geophysical challenges.
- **Applications:**
  - **Geophysics:** Partnerships with companies like Aramco for seismic data processing and detailed subsurface mapping.
  - **Logistics:** Supply chain optimization and resource allocation.
- **Challenges:**
  - **Limited Scope:** Optimized for specific problems, lacking capabilities for general quantum algorithms.
  - **Scalability:** Expansion depends on hardware and error mitigation advancements.

### III.3 NMR-BASED QUANTUM COMPUTERS: EDUCATION AND RESEARCH

NMR-based systems provide an alternative for education and research, leveraging nuclear spin qubits manipulated through radiofrequency pulses [5].

- **Characteristics:**
  - Models like the SpinQ Gemini (2 qubits) and Triangulum (3 qubits) enable basic quantum operations.
  - Designed to democratize access to quantum computing for academic institutions.
  -
- **Applications:**
  - **Education:** Introducing fundamental quantum algorithms, such as Grover's and Deutsch-Jozsa.
  - **Research:** Validating quantum theories and experimenting with quantum principles.
- **Challenges:**

- **Limited Scalability:** Restricted to small systems.
- **Precision:** Challenges in maintaining coherence and achieving stable results.

### III.4 GRAPH GENERATION DESCRIPTION

To visualize the comparative analysis of quantum technologies, a graph was created using Python and the Matplotlib library. The graph highlights two key evaluation criteria: scalability and impact on applications, for IBM, D-Wave, and NMR technologies. The following steps outline the methodology used to generate the visualization:

- **Data Preparation:**
  - A dataset was defined, representing the scalability and application impact of each technology on a scale from 1 to 10.
  - Scalability refers to the capacity of each technology to expand its qubit count and handle complex problems.
  - Impact evaluates the practical relevance of the technologies in scientific, industrial, and educational contexts.
- **Graph Configuration:**
  - A two-dimensional scatter plot was chosen to represent the data.
  - Each technology (IBM, D-Wave, and NMR) was assigned a unique color for visual distinction.
- **Labeling and Customization:**
  - Labels were added to each point on the graph to identify the technologies.
  - The graph was customized with appropriate titles, axis labels, and a grid for better readability.
- **Execution Environment:**
  - The graph was generated in a Python environment with the Matplotlib library, ensuring compatibility and reproducibility.
- **Visualization Output:**
  - The resulting graph illustrates the distinct characteristics of each technology, emphasizing IBM's scalability, D-Wave's practical applications, and NMR's accessibility for research and education.

The graph provides a clear visualization of the comparative analysis, highlighting the unique roles of IBM, D-Wave, and NMR-based quantum technologies in advancing quantum computing. This approach ensures transparency and reproducibility while avoiding the direct inclusion of source code in the article.

### IV.COMPARATIVES ANALYSIS: IBM, D-WAVE, AND NUCLEAR MAGNETIC RESONANCE (NMR) QUANTUM COMPUTING

The comparative analysis of quantum technologies was conducted based on specific criteria evaluating their features, applications, and limitations. This section outlines the methods used to collect, organize, and analyze data on IBM, D-Wave, and NMR-based systems.

IV.1 EVALUATION CRITERIA

The comparison of technologies followed three main criteria:

- **Scalability:**
  - Assessment of each technology's ability to increase the number of qubits and support more complex applications.
  - Includes examining system architectures and modularity.
- **Impact on Applications:**
  - Measurement of each technology's practical relevance in scientific, industrial, and educational contexts.
  - Includes areas such as logistics, molecular simulation, and teaching of fundamental quantum concepts.
- **Technological Challenges:**
  - Analysis of the main obstacles faced by each approach, such as error mitigation, maintaining quantum coherence, and hardware limitations.

IV.2 DATA COLLECTION AND ORGANIZATION

Data were collected from the following sources:

- **Scientific Articles and Reports:** Including technical information and performance updates published by companies and institutions related to these technologies [9],[10].
- **Primary Sources:** Data on IBM's quantum processors (Eagle and Condor), D-Wave's Advantage2 systems, and NMR devices such as SpinQ Gemini and Triangulum were extracted directly from technical documentation [5], [6].
- **External References:** Publications describing practical applications, such as supply chain optimization and educational experiments, were used [11],[12].

The data were organized into tables and graphs to facilitate comparative analysis and visualization, following the structure presented in this Section.

IV.3 ANALYSIS AND COMPARISON

Data were analyzed in three main steps:

- **Scalability:**

- IBM leads with scalable systems, such as Condor (1121 qubits), aiming to surpass 4000 qubits by 2025.
- D-Wave offers moderate scalability, with 1200 qubits optimized for specific problems.
- NMR systems are limited in scalability, with a maximum capacity of 3 qubits.

● **Impact on Applications:**

- IBM stands out in scientific and industrial applications, including material modeling and artificial intelligence.
- D-Wave has significant impact in optimization areas, such as logistics and geophysics.
- NMR systems mainly contribute to teaching and initial research.

● **Technological Challenges:**

- IBM faces challenges in error mitigation and integration with classical systems.
- D-Wave relies on hardware advancements to expand its application.
- NMR systems have limitations in precision and coherence maintenance.

IV.4 DATA VISUALIZATION

The comparisons were synthesized into a table and a graph to illustrate the differences and complementarities of the technologies:

Table 2: Summary Comparison of Quantum Technologies

Technology	Main Focus	Scalability	Impact on Applications	Technological Challenges
IBM	Universal Computing	High	Broad scientific impact	Error mitigation
D-Wave	Optimization	Moderate	Industrial optimization	Hardware advancement
NMR	Education and Research	Low	Teaching and research	Precision limitations

Source: Authors, (2024).

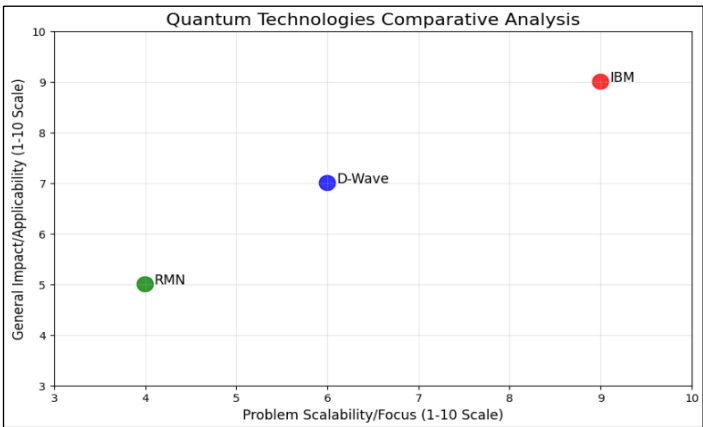


Figure 1: Comparative Analysis of Quantum Technologies.

Source: Authors, (2025).

The Figure presents a two-dimensional graph with scalability and impact criteria for the three technologies, highlighting differences in their applications and limitations. Table



2 provides a summary comparison of different quantum technologies, highlighting their main focus, scalability, impact on applications, and technological challenges. For instance, IBM focuses on universal computing with high scalability and broad scientific impact, though it faces challenges related to error mitigation. D-Wave, primarily aimed at optimization, offers moderate scalability and contributes to industrial advancements, while NMR focuses on education and research with low scalability due to precision limitations. These distinctions are further visualized in Figure 1, which plots scalability against general impact, emphasizing the varying strengths and challenges across these technologies (Table 2).

#### IV.5 METHODOLOGY CONCLUSION

The criteria and methods described ensure a robust analysis, enabling an understanding of how IBM, D-Wave, and NMR technologies are positioned in the current quantum landscape. The use of tables and graphs complements the analysis, providing a clear and objective view of each approach's strengths and challenges.

#### V. CONCLUSION

The approaches developed by IBM, D-Wave, and NMR-based systems exemplify the diverse and transformative potential of quantum computing. IBM excels in scalable solutions for complex challenges, D-Wave provides targeted tools for optimization, and NMR systems enable education and foundational research. Together, these approaches are shaping a future where quantum computing becomes a cornerstone of technological and scientific innovation. Quantum computing requires continued interdisciplinary collaboration, involving physicists, engineers, and computer scientists, to overcome its challenges. Its evolution will not only redefine problem-solving capabilities but also create new paradigms for advancing science, technology, and society.

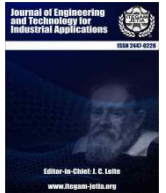
#### VI. REFERENCES

- [1] R. M. Silveira, "Internet quântica: realidade ou sonho," in Poster de conferência: 10ª Conferência Ibero Americana Computação Aplicada, 2023.
- [2] A. Nunes Oliveira, E. V. de Oliveira, A. Costa Santos, and C. Jorge Villas-Boas, "Algoritmos quânticos com IBMQ Experience: Algoritmo de Deutsch-Jozsa," Caderno Brasileiro de Ensino de Física, vol. 44, 2022.
- [3] P. J. Souza, T. M. Mendonça, E. V. d. Oliveira, and C. J. Villas-Boas, "Computação Quântica Adiabática: Do Teorema Adiabático ao Computador da D-Wave," Revista Brasileira de Ensino de Física, vol. 43, p. e20210049, 2021.
- [4] M. A. Nielsen and I. L. Chuang, Quantum Computation and Quantum Information. Cambridge, U.K.: Cambridge University Press, 2000.
- [5] Y. d. C. Lourenço and A. G. d. A. Ferreira, "Introdução à conceitos básicos de informação quântica utilizando Ressonância Magnética Nuclear (RMN)," Resumos, 2023.
- [6] M. E. F. Caçula, "Computação Quântica: Estado Atual e Aplicações Futuras," Revista Capará, vol. 6, pp. e93-e93, 2024.
- [7] M. V. M. Brasão and M. R. d. O. M. S. Santos, "Uso de computadores quânticos para resolução de problemas NP," 2020.
- [8] B. C. Capoferri, G. D. Rameh, H. M. Frezzatti, and L. S. Makuta, "A História da Computação Quântica".
- [9] O. Pessoa Jr, "Uma axiomatização operacional da teoria quântica".
- [10] T. N. F. dos Reis, A. M. Sousa, D. B. Melo, and J. P. Costa, "A revolução quântica: transformações, desafios e potenciais da nova era computacional," SAS &

Tec CEST (Saúde, Ambiente, Sustentabilidade e Tecnologia), vol. 2, pp. 96-126, 2024.

[11] G. F. d. Jesus, M. H. F. da Silva, T. G. Dourado, L. Q. Galvão, F. G. de Oliveira Souza, and C. Cruz, "Computação quântica: uma abordagem para a graduação usando o Qiskit," Revista Brasileira de Ensino de Física, vol. 43, p. e20210033, 2021.

[12] M. A. Nielsen and I. L. Chuang, Quantum Computation and Quantum Information. Cambridge, U.K.: Cambridge University Press, 2000.



## RESEARCH ARTICLE

## OPEN ACCESS

## FUZZY IRRIGATION MODEL IN PROTECTED CROP BASED ON EXPERT KNOWLEDGE

Alain Godo Alonso<sup>1</sup>, Dennis Villavicencio Quintero<sup>2</sup>, Emilio Cabrera Hernández<sup>3</sup> and Ivan Santana Ching<sup>4</sup><sup>1</sup> SORBA.ai, Jacksonville, FL, USA<sup>2, 3, 4</sup> University "Marta Abreu" of Las Villas, Santa Clara, Cuba<sup>1</sup><http://orcid.org/0000-0002-1501-0696> , <sup>2</sup><http://orcid.org/0000-0002-5433-6947> , <sup>3</sup><http://orcid.org/0000-0003-3142-7253> <sup>4</sup><http://orcid.org/0000-0001-5089-520X> Email: [alaindga@gmail.com](mailto:alaindga@gmail.com), [dvillavicencio@uclv.cu](mailto:dvillavicencio@uclv.cu), [emcabrera@uclv.cu](mailto:emcabrera@uclv.cu), [ching@uclv.edu.cu](mailto:ching@uclv.edu.cu)

## ARTICLE INFO

*Article History*

Received: March 13, 2025

Revised: March 20, 2025

Accepted: March 15, 2025

Published: April 31, 2025

*Keywords:*Irrigation model,  
Protected crop,  
Artificial intelligence,  
Fuzzy system,  
Expert knowledge.

## ABSTRACT

Fuzzy logic is a subfield of Artificial Intelligence that allows human knowledge to be expressed naturally, through linguistic variables and values, and an inference process very similar to the one it uses daily. The present research uses expert criteria to design and evaluate a model based on a fuzzy system to predict the irrigation time of the protected crop of cucumber (*Cucumis sativus* L.). The variables temperature, soil moisture and lighting are used for the model construction, which is coupled to an existing IoT technology in the various crops company "Valle del Yabú", serving as a support system for decision making. The prototype is created and simulated in MATLAB, then transferred to a Raspberry Pi 4 Model B, using the Python programming language. Tests using a database collected during one crop cycle show a 10.07% reduction in water usage compared to the standard irrigation currently implemented by the company.



Copyright ©2025 by authors and Galileo Institute of Technology and Education of the Amazon (ITEGAM). This work is licensed under the Creative Commons Attribution International License (CC BY 4.0).

## I. INTRODUCTION

Agriculture is the main food source in all world countries [1]. The global demand for food means greater pressure on water resources [2], and agriculture is by far the largest consumer of water, accounting for around 70 % of all water withdrawals for irrigation, with a figure that can be as high as 95 % in some developing countries [3].

The agriculture industry is becoming more data-centric and requires more advanced and accurate information and technologies [4]. The difference between the demand and supply of water in agriculture is considered a problem that must be solved through advanced technologies to optimize resource use [5]. A precision or smart irrigation system is a sustainable method of saving water to maximize crop yields and reduce the unwanted environmental impacts of irrigation [6].

Worldwide there are numerous advances in terms of different technologies applied to agriculture for better performance in general, through the use of the Internet of Things (IoT) [7], robotics [8], or Artificial Intelligence (AI) techniques [9], to cite just a few examples.

The various crops company "Valle del Yabú", is the main productive center of the province of Villa Clara, there is the base business unit (UEB, acronym in Spanish) for protected and semi-protected crops, which has several of these premises to produce vegetables, which have a semi-automated irrigation system.

Despite the good results obtained today in greenhouses, the institution's experts indicate that better resource optimization can be achieved [10], either in favor of reducing consumption or increasing production. Taking the best of previous related works [11],[12], this research aims to contribute to this scientific problem in search of a viable solution, which only requires the knowledge of experts.

For this purpose, fuzzy logic is among the most widely used AI tools in current agriculture [13] when it is necessary to raise production results and optimize resources, especially in processes that require a knowledge base that is normally only available to experts on the subject, but that through the simple use of everyday language can be collected and put in a position to be improved and expanded. Numerous recent uses in the literature show the potential of this technique in a general way [14-17] and more attached to the topic of intelligent irrigation specifically [18-21].

The case study, cucumbers (*Cucumis sativus* L.), are among the most cultivated vegetables in the world, and due to their widespread use, there is a rich variety of these fruits [22].

Regardless of its genotype, there is a general trend of this crop (and of most plantations) towards certain conditions necessary for favorable growth, the most influential variables are ambient temperature, relative humidity, soil moisture, lighting, pH, and electrical conductivity [22],[23]. Only a few variants modified for certain climates escape generality [22].

The created model interacts in a deployed IoT system, using the ThingBoard platform, which is open-source software for the collection, processing, visualization, and management of data from devices [24],[25]. The communication protocol used is MQTT, developed by the OASIS organization, which is a standard communication protocol designed for the IoT [26],[27].

The programming languages MATLAB and Python are used in favor of building the model. MATLAB is an environment highly used by the scientific community, and Python is one of the favorite programming languages for AI development due to its syntactic simplicity and versatility. Both have an extensive amount of tools for AI development [28-31].

## II. LOGIC AND FUZZY SYSTEM FOR IRRIGATION MODEL

The fuzzy system (FS) designed has four fundamental standard functional blocks Figure 1 [32]. Intentionally, from the first stage, the design was made in MATLAB due to the great potential of the Fuzzy Logic Toolbox, and because the prototype is achieved in a highly visual, fast, and efficient way. The version used was MATLAB 2022a.

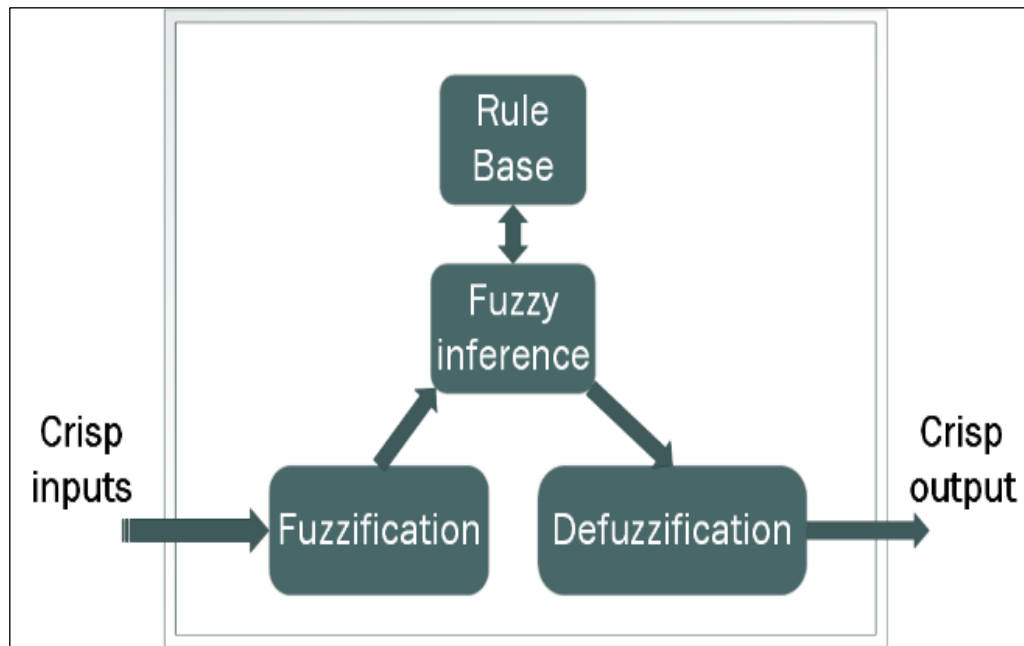


Figure 1: Fundamental functional blocks of a fuzzy system of quantitative input and output.

Source: Authors, (2025).

A fundamental point in the FS is the definition of both the input and output variables. To select the inputs used in cucumber (*Cucumis sativus* L.) production, the environmental variables that have the most influence and are available in the IoT system installed in the greenhouses were chosen.

The selected input variables were: ambient temperature, soil moisture, and lighting. The only output variable needed was: irrigation time, which corresponds to the duration of the suggestion given to the operator at the time of the irrigation schedule. Was only modified the time and not the frequency of irrigation because it is expected that the crops have a fixed daily frequency of four times.

### II.1 DESIGN OF THE FUZZY LOGIC

#### II.1.1 MEMBERSHIP FUNCTIONS

The memberships proposed here consist of triangular and trapezoidal functions for the FS inputs and output, respectively. The figure below shows the independent value ( $x$ ) versus the degree of membership ( $\mu$ ) for both.

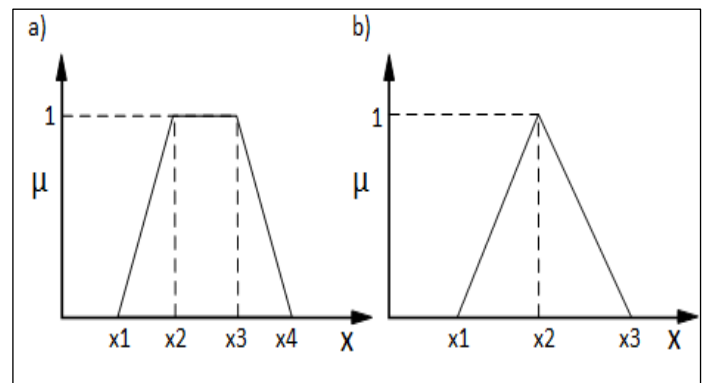


Figure 2: Membership functions: a) trapezoidal b) triangular.

Source: Authors, (2025).

As can be seen in Figure 2 a) due to its shape, the trapezoid is determined by four critical points. The universe of discourse was partitioned using this function into three subspaces, and it was applied in a general way to the variables: temperature, soil moisture, and lighting (input variables). In this way, each linguistic variable is associated with a value as shown in the following table:

Table 1: Variables and linguistic values of system inputs.

	Linguistic value		
Temperature	Cold	Favorable	Hot
Soil Moisture	Dry	Favorable	Wet
Lighting	Dark	Medium	High

Source: Authors, (2025).

As can be seen in Figure 2 b) due to its shape, the triangle is determined by three critical points. The universe of discourse was partitioned using this function into five subspaces, and it was applied to the only output variable: irrigation time. In this way, each linguistic variable is associated with a value as shown in the following Table 2:

Table 2: Variables and linguistic values of system output.

	Linguistic value				
Irrigation Time	Zero (Z)	Short (S)	Medium (M)	Long (L)	Very Long (VL)

Source: Authors, (2025).

## II.1.2 FUZZY RULE SET

To build the knowledge base of the system, Mamdani's rules were used [32]:

$$\text{IF } x_1 \text{ is } \tilde{A}_1^k, x_2 \text{ is } \tilde{A}_2^k \text{ and } x_3 \text{ is } \tilde{A}_3^k \text{ THEN } y^k \text{ es } \tilde{B}^k \quad (1)$$

$$k = 1, 2, 3, \dots, r$$

Where  $\tilde{A}_1^k$  and  $\tilde{A}_2^k$  are the representation of the fuzzy set for the k-th antecedent and  $\tilde{B}^k$  is the fuzzy set of the k-th consequence.

A system of three inputs and three linguistic values, as is the case, to be fully expressed with only conjunction operators, must have, according to the multiplication rule,  $3 * 3 * 3 = 27$  rules. Fuzzy standard operations were selected as connectors, (2) as a conjunction operator, and (3) for the aggregation of the rules. Let  $\tilde{A}$  and  $\tilde{B}$  be two fuzzy sets:

$$\mu_{\tilde{A} \cup \tilde{B}}(x) = \mu_{\tilde{A}}(x) \vee \mu_{\tilde{B}}(x) = \max(\mu_{\tilde{A}}(x), \mu_{\tilde{B}}(x)) \quad (2)$$

$$\mu_{\tilde{A} \cap \tilde{B}} = \mu_{\tilde{A}}(x) \wedge \mu_{\tilde{B}}(x) = \min(\mu_{\tilde{A}}(x), \mu_{\tilde{B}}(x)) \quad (3)$$

Tables 3, 4, and 5 express the set of rules used for the system, based on one of the three possible linguistic values of the soil moisture variable.

Table 3: Rules for the duration of irrigation at dry soil moisture.

	Lighting		
Temperature	Dark	Medium	High
Cold	VL	VL	VL
Favorable	M	L	L
Hot	Z	S	S

Source: Authors, (2025).

Table 4: Rules for the duration of irrigation at favorable soil moisture.

	Lighting		
Temperature	Dark	Medium	High
Cold	M	M	M
Favorable	P	M	M
Hot	Z	P	M

Source: Authors, (2025).

Table 5: Rules for the duration of irrigation at favorable wet moisture.

	Lighting		
Temperature	Dark	Medium	High
Cold	Z	Z	Z
Favorable	Z	Z	Z
Hot	Z	Z	Z

Source: Authors, (2025).

## II.1.3 INFERENCE AND DEFUZZIFICATION METHOD

The implication mechanism used is also standard and responds to operation (3). The system is of the Mamdani type, so operator (2) was used for the aggregations. The method used for defuzzification is the centroid method. The center of gravity of the resulting set is the final output of the system, this is the estimated irrigation time, finally expressed as a numerical value.

## II.2 DESIGN OF THE FUZZY SYSTEM FOR EMBEDDED HARDWARE

The device selected to deploy the system was a Raspberry Pi 4 Model B. The board is part of the IoT system mounted in the greenhouses of the "Valle del Yabú", where its function is precisely to receive data from sensors, process them and output the estimated irrigation time, which acts as an Agricultural Decision System Support (ADSS). The deployed sensors Figure 3 measure a variety of environmental variables, but of these, they are only inputs to the system, the three necessities for its operation.



Figure 3: Sensor node.

Source: Authors, (2025).

The sensor readings come to the Raspberry Pi by sending packets using the MQTT protocol, and once the prediction is made, the result is transmitted using the same protocol. The ThingsBoard platform oversees establishing the necessary broker for communication and allows the visualization of both the behavior of the variables involved, as well as the suggested irrigation time in real-time, which the operator must consider when scheduling the time. The platform resides in another Raspberry Pi of the same model, exclusively dedicated to serving as a server for the IoT system.

Each node or sensing device has a publication topic called "Node". Under this topic, and with the use of a dictionary of six variables, the information is transmitted to the broker. The Raspberry Pi is subscribed to that topic, and after using the necessary variables as inputs to the FS, it returns another one that



contains only the output of the model. The architecture shown in Figure 4 describes the data flow in a general way.

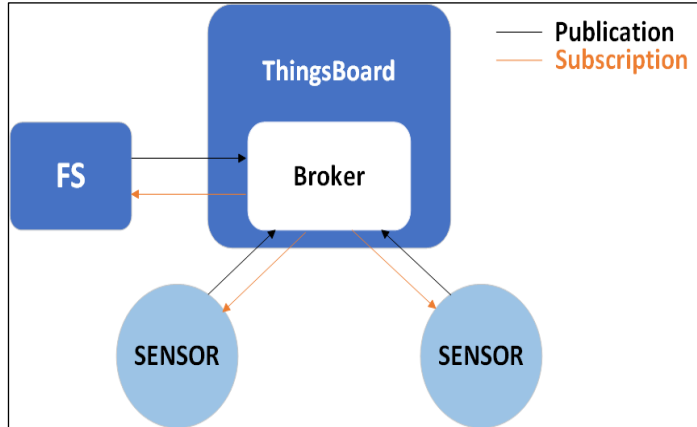


Figure 4: Architecture for the coupling to the IoT system. The FS is isolated from the coordinator node.

Source: Authors (2023).

### II.2.1 FUZZY SYSTEM PROGRAMMING

To program the FS scripts in the embedded hardware, the Python programming language in its version 3.11 was used and the Anaconda distribution was used as a work environment, due to its ease in managing packages in the field of data science. The third-party modules used were: scikit-fuzzy and paho-mqtt. As a complement, the pandas and matplotlib modules were also needed to manage data structures and visualize the results respectively.

## III. GETTING THE IRRIGATION SYSTEM

The model obtained is an FS 3-1, it has three inputs and a single output. The system was built in MATLAB, using Fuzzy Logic Toolbox, and named: "FSsystem". Its general configuration is shown in Figure 5.

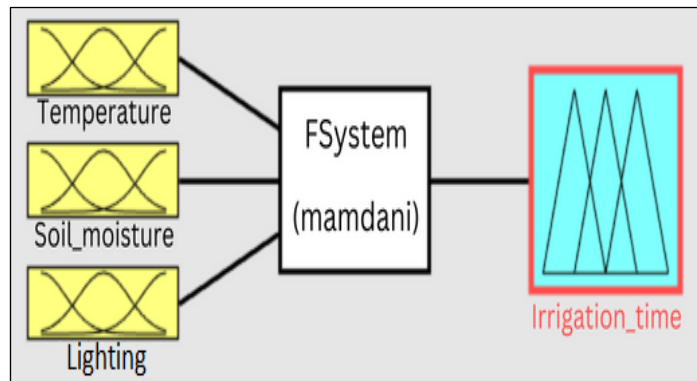


Figure 5: Obtaining fuzzy logic in MATLAB.

Source: Authors (2023).

The membership functions were conceived from the reviewed literature and the criteria of the UEB experts of protected and semi-protected crops of the "Valle del Yabú".

Due to the use of only trapezoidal and triangular membership functions, the assignment of critical points was determined in a highly relational and intuitive way. Each input variable in Tables 6 and 7 presented a "Favorable" or "Normal" range that describes the set of fuzzy values that favor plant growth, with a plateau of unitary membership value, which alludes to the

possible threshold or tolerance that exists in the quantitative description of the range, which by nature presents uncertainty.

The other two extreme ranges, with consistent linguistic values, describe the limit conditions for the variable to which analysis is made, presenting in the same way, a plateau of unitary membership value to compensate for the diffuse character of said limits.

On the other hand, the output variable Table 8, when representing fixed amounts of irrigation of a practical nature, could be eliminated from uncertainty plateaus, and therefore the triangular function remained as a result of its description.

The input variables are expressed in Celsius degrees (°C), percentage ratio (%), and luminous flux per unit area (lux) correspondingly. The output variable "Irrigation\_time" is expressed in minutes (min).

Table 6: Critical points of the "Temperature" membership function.

	Cold	Favorable	Hot
Critic points	[0 0 14 20]	[14 20 30 40]	[30 40 50 50]

Source: Authors, (2025).

Table 7: Critical points of the "Soil\_moisture" membership function.

	Dry	Favorable	Wet
Critic points	[0 0 17 22]	[17 22 26 50]	[26 50 60 60]

Source: Authors, (2025).

Table 8: Critical points of the "Lighting" membership function.

	Dark	Medium	High
Critic points	[0 0 0.45 1]	[0.45 1 13000 175000]	[13000 175000 21000 21000]

Source: Authors, (2025).

Table 9: Critical points of the "Irrigation\_time" membership function.

	Z	S	M	V	VL
Critic points	[0 0 7.5]	[0 7.5 15]	[7.5 15 22.5]	[15 22.5 30]	[22.5 30 30]

Source: Authors, (2025).

### III.1 FUZZY RULE SET

The rules described for the FS are analyzed in Tables 3, 4 and 5. Of the set of 27 total rules, many of these presented logical redundancy, therefore, taking advantage of the idempotent nature of the conjunction operator, the existing rules were reduced to 15, making use of the property expressed in equation (3).

$$\text{IF } B_1 = B_2 = B_3 = \dots B_n$$

$$A \cup B_1 \cup B_2 \cup B_3 \cup \dots B_n = A \quad (3)$$

In this way, the rules that express the system become more coherent and attached to natural language, for example, Table 10 summarizes a simple expression: "If Soil\_moisture is wet then Irrigation\_time is zero" (Rule 1). Table 5 shows the rules obtained. The symbol "x" means "don't care" the value of the linguistic variable.

Table 10: Reduced rules for the FIS.

Rule	Input			Output
	Temperature	Soil Moisture	Lighting	Irrigation time
1	x	Wet	x	Z
2	Cold	Favorable	x	M
3	Favorable	Favorable	High	S
4	Favorable	Favorable	Medium	M
5	Favorable	Favorable	Dark	M
6	Hot	Favorable	High	Z
7	Hot	Favorable	Medium	S
8	Hot	Favorable	Dark	L
9	Cold	Dry	x	VL
10	Favorable	Dry	High	M
11	Favorable	Dry	Medium	L
12	Favorable	Dry	Dark	L
13	Hot	Dry	High	Z
14	Hot	Dry	Medium	S
15	Hot	Dry	Dark	VL

Source: Authors, (2025).

### III.2 INFERENCE AND DEFUZZIFICATION METHOD

By using the proposed inference and defuzzification methods, the FS responded as shown in Figure 6. An example is observed for the intermediate values of the universe of discourse, activating rules 1 and 4, unifying the sets obtained employing the operator (1), and quantifying the response by the centroid method, to obtain an estimated irrigation time of 13.4 min.

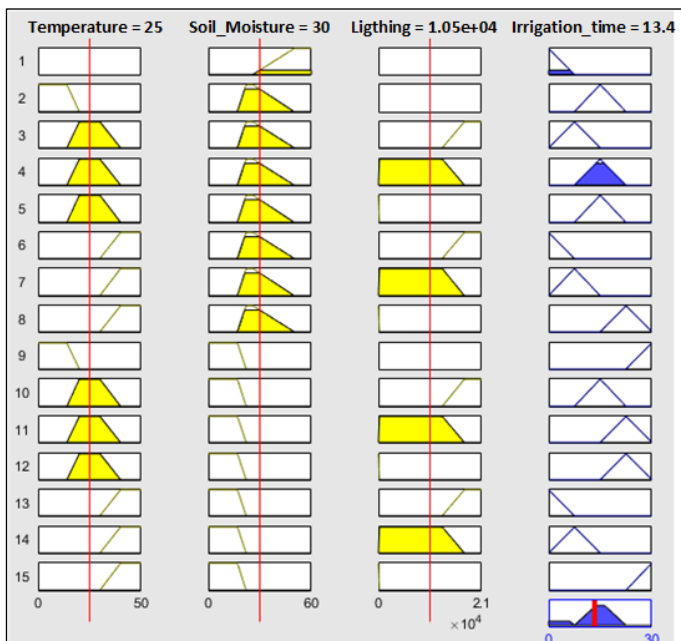


Figure 6: Simulation of the FS in Fuzzy Logic Toolbox.

Source: Authors, (2025).

Given the configuration of the system and its defuzzification method, the minimum possible time that the FS can suggest is 2.4 min, and a maximum of 27.5 min.

The behavior of the output, concerning temperature and lighting, is complex, and as expected, highly dependent on soil moisture. There is a natural gradient to the increase in irrigation time with the decrease in soil moisture, for the same surface level.

Figure 7 shows these two variables compared, for different soil moisture references. The first of these graphs a), shows visually and in a more evident way, the maximum point of 27.5 min, which is between the temperature values of 0 and 10, and which is independent of lighting, which is expected behavior. On the other hand, the last graph d) shows rule number two of the FS obtained, in which regardless of the variations of the remaining parameters, the irrigation time is 2.4 min, which corresponds to the minimum point of our system.

The valleys or plateaus presented by the levels are coherent with those existing in the membership functions because describe the range of uncertainty or error rate of the linguistic values.

### III.3 INFERENCE AND DEFUZZIFICATION METHOD

After a prototype, the FS was embedded in the Raspberry Pi 4 Model B, which serves as a data analysis server in the mentioned IoT system (Figure 4). The script that integrates the model was transferred to the SD card, and it was configured as a process to be executed in an infinite loop at each boot of the device.

To verify the correct rewriting between both languages, graphs of the membership functions of both the input and output variables of the system were generated, using the matplotlib module.

To verify the correct transfer of the rules, as well as the inference and defuzzification methods, a random test database with 3000 points was generated, which were compared to those returned by the FS created in MATLAB using a script that made use of the Python random module. The test presented 100% compatibility between the datasets.

The verification of the FS obtained for the embedded hardware was preceded by the verification of its correct coupling to the IoT technology. In the ThingsBoard platform of the main node, a new device named "Raspberry AI" was created in charge of the administration of the Raspberry Pi of this project. Random test data was sent to it, and upon verification of receipt, the dashboard was configured for the final consumer. The window that the operator can observe is shown in Figure 8.

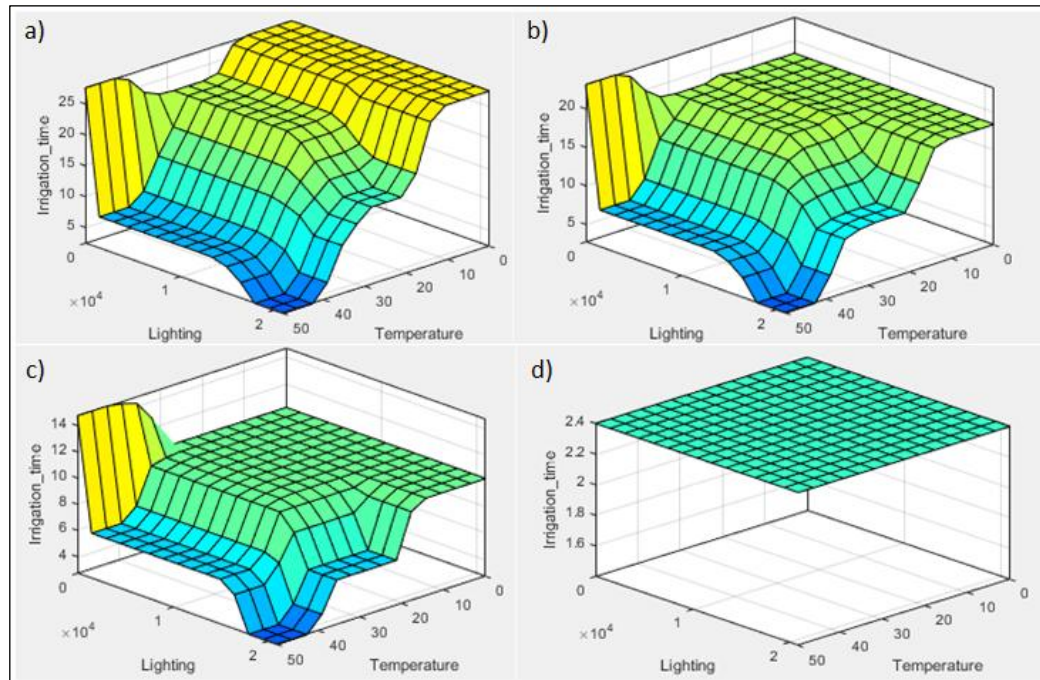


Figure 7: Surfaces in the Fuzzy Logic Toolbox. References of soil moisture: a) 0%, b) 20%, c) 40%, d) 60 %.  
Source: Authors, (2025).

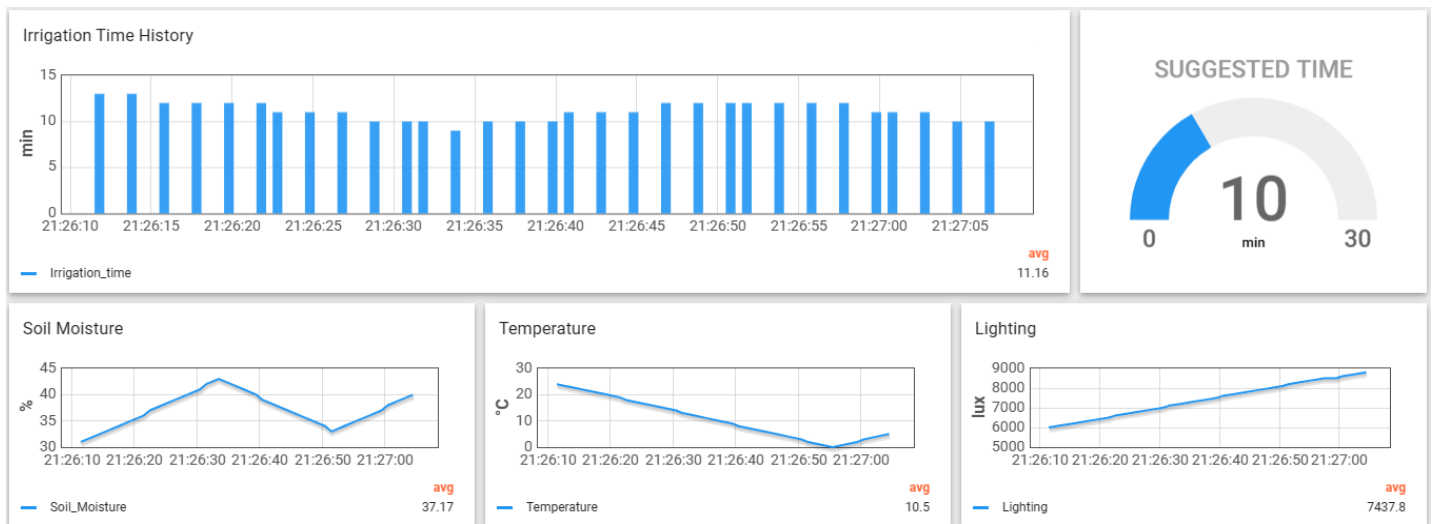


Figure 8: ThingsBoard visualization dashboard.  
Source: Authors (2023).

History charts are configurable in the sample range and interval they can display. These serve to provide a notion of the behavior of variables over time. As additional data, each one shows in the lower right part the average behavior of the variable. In the upper right part of the entire window, there is a widget to show the FS irrigation prediction in real-time.

The display panel is displayed on a Kuman 7" 1280x800 screen, connected to the central Raspberry Pi that the ThingsBoard platform server has. When programming the watering time of the pumping, the operator must make use of it, and based on your experience and the suggestion given, set the end time. One of the last tests carried out on the embedded FS was the measurement of the time it took the Raspberry Pi to process and send a single data packet with the required information. After using the time module and measuring the execution time interval of 1000 sends, the average delay was 1.71 seconds. This period is much lower than the data collection rate of the IoT deployment, which is 15 min.

#### IV. EVALUATION

In a lapse of time of a month, the IoT network was installed in one greenhouse. During this period, samples of the input variables of the system were taken.

Table 11 shows an analysis of the stored data, specifically for the center's irrigation schedules. Four data packets are received every hour since the nodes are transmitted with a frequency of 15 min. The number of samples is not uniform, nor does it correspond to the 112 that do not exist in total, this is due to possible losses, either due to transmission problems of the sensing nodes or reception of the platform, disconnection of the devices due to lack of power supply or other inconveniences.

The range of the variables, minimum and maximum possible value, is framed in the universe of discourse of the membership functions of the designed FS. Even if the sensing of a variable exceeds these limits, no error will occur, since the

embedded FS was built so that any of these values can be interpreted by extreme linguistic values.

Beyond the irrigation schedules, it is interesting to explore the behavior of the variables globally, that is, of the entire sample. When observing the standard deviations in Table 12, these present a significantly small value compared to the values in which the variable in question oscillates.

This fact is typical of greenhouses, given their controlled environment. On the other hand, the mode and the mean represent two indicators of great interest for our FS. These are a measure of the trend of environmental conditions in the crop cycle, which are little fluctuating as previously shown by the standard deviation. The fact that the mode for illumination is 0 lux, for the sample data set, indicates that most of the IoT system operation occurred at nighttime.

By substituting these points of interest in the FS using the Fuzzy Logic Toolbox, the results of Figure 9 are obtained. The model estimates the same irrigation time currently made by the operators: 15 minutes. This indicates that, on average, the FS expresses the same level of knowledge as the experts, resulting from their accumulated experience. Outside the threshold close to the trend of the variables, the FS expresses "new experiences".

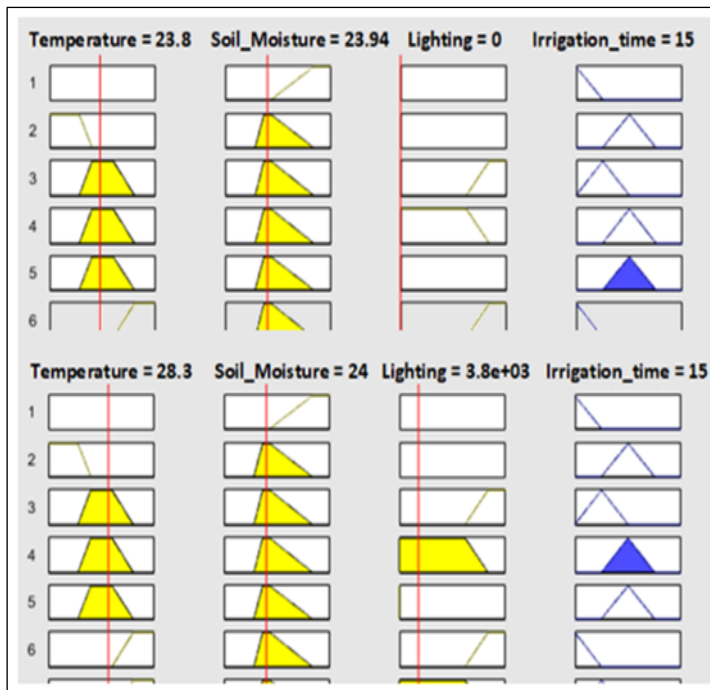


Figure 9: Evaluation of central tendency values in Fuzzy Logic Toolbox.

Source: Authors, (2025).

Table 11: The extreme behavior of the input variables during the sample period for irrigation schedules.

Schedules	Temperature (°C) (Min-Max)	Soil Moisture (%) (Min-Max)	Lighting (lux) (Min-Max)	Samples
8 AM	22.6 – 30.1	1.72 – 37.52	1309 -	109
10 AM	27.2 – 36.9	11.78 –	4391 -	108
1 PM	32.2 – 42.5	12.45 –	410 -	56
3 PM	28.9 – 46.1	13.75 –	591 -	44

Source: Authors (2023).

Table 12: General behavior of the input variables during the sample period.

	Temperature (°C)	Soil Moisture (%)	Lighting (lux)
<b>Min - Max</b>	21.6 – 47.8	0.32 – 40.61	0 - 20723
<b>Variance</b>	29.97	44.98	29408484.7
<b>Standard</b>	5.47	6.71	5422.96
<b>Mode</b>	23.8	23.94	0
<b>Mean</b>	28.27	24.0	3800.07

Source: Authors (2023).

The 2182 samples collected, without discriminating hours, were processed by the FSsystem module, and the prediction was obtained for each triad of values. The Pearson correlation matrix is plotted in Figure 10. Irrigation time is inversely proportional to the three FS inputs. Although the correlation is not necessarily indicative of a cause-effect, it shows that to a greater extent, the achieved model is dependent on soil temperature and moisture, and to a lesser extent on lighting.

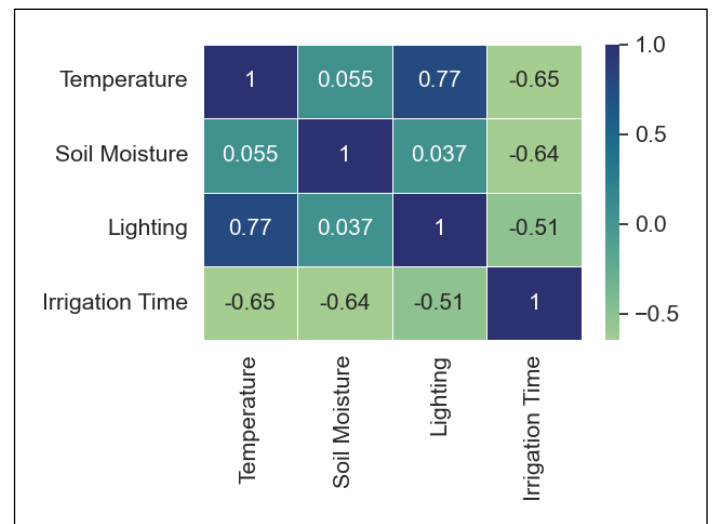


Figure 10: Pearson correlation of the processed samples.

Source: Authors, (2025).

With the use of the processed data the graph of the behavior of the inputs and the output of the FS for the irrigation schedules are constructed (Figure 11). The notable correlation between temperature and lighting in the greenhouse can be qualitatively observed, which can be related quantitatively to the results obtained in Figure 10 (0.77 units of Pearson correlation).

Since the soil moisture has a lower range of oscillation, the changes in the FS predictions move around according to the other conditions: the temperature and lighting, because both are the most fluctuating and time-dependent variables. These fluctuating variables are highly dependent on the time of day. From all this information it can be concluded that, despite having built the FS giving greater weight to the soil moisture variable, in practice, for our case study, the most determining variable so far is temperature.

It is observed that the general tendency of the suggested time is to decrease as the day progresses, which is evident quantitatively in the averages of Table 13, except in the last hour. The FS decreases its output and limits the minimum and maximum values to the pair. The model notices a greater need for irrigation in the first shift, and then the prediction of all the others falls below what the standard time establishes. The final result is that in accumulation, the model reduces resource use from 4755 to 4276 min, meaning 10.07%.



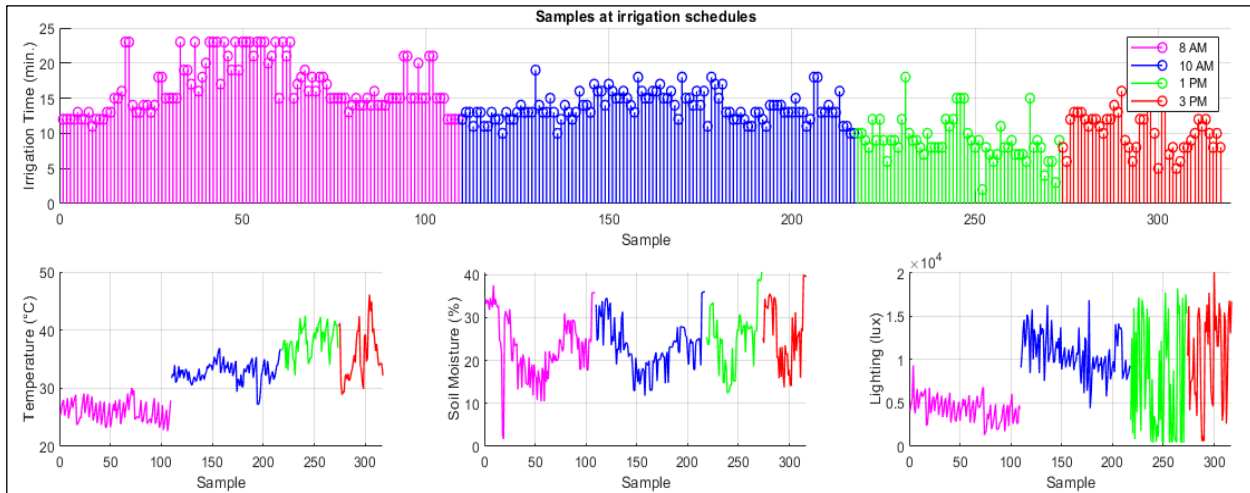


Figure 11: Graph of the inputs and output of the FS of the samples for the irrigation schedules.

Source: Authors, (2025).

Table 13: Irrigation times in study hours.

	Schedules			
	8 AM	10 AM	1 PM	3 PM
<b>Minimum time (FS)</b>	11 min	10 min	2 min	5 min
<b>Maximum time (FS)</b>	23 min	19 min	18 min	16 min
<b>Mean time (FS)</b>	16.75 min	13.75 min	8.98 min	10.5 min
<b>Standard time</b>	15 min	15 min	15 min	15 min
<b>Total time (FS)</b>	1826 min	1485 min	503 min	462 min
<b>Standard total time</b>	1635 min	1620 min	840 min	660 min
<b>Accumulated time (FS)</b>	4276 min			
<b>Standard accumulated</b>	4755 min			

Source: Authors, (2025).

## V. DISCUSSION

The use of an FS as a solution to the modeling of the irrigation system is a more manageable and interpretable alternative in contrast to the methods of Fuzzy Cognitive Maps in previous works made for the institution [11],[12]. The main knowledge engine of the system, the membership function and fuzzy rules are obtained directly from the knowledge of experts. The model built from the use of fuzzy logic is not specific, nor exclusive, for the case study, but rather the proposed methodology allows the same procedures to be applied to any other variety in protected cultivation at the center.

Much of the reviewed literature makes use of an FLC, as a solution to the problem of the intelligent irrigation system, controlling the irrigation system either by closing or opening a valve or by continuously establishing the irrigation time using timers. Faced with this, the FS designed as ADSS has the disadvantage of having a delayed action. The final action element, the irrigation system, is activated by the operator, and once the process is started its interruption is manual. In the time frame of the programmed irrigation, the climatic conditions can have abrupt changes, such as those caused by a sudden rain, which affects the system variables, and although the prediction changes accordingly, the FS cannot impose the new state.

The computational cost of the FS is negligible concerning other AI techniques, and this is evidenced by the short average response time for receiving, processing, and sending data. This feature makes it versatile and less dependent on large hardware

resources. The IoT architecture where the model is coupled presents great modularity, since by isolating a node for data processing, the main node that serves as server and orchestrator is not saturated by the execution of algorithms. From the reviewed literature, the implementation of the model in architectures such as those presented in [18],[20] would entail a computational overload, since the UEB has a total of 42 cultivation houses, a considerable number of threads to be processed by the node coordinator.

## VI. CONCLUSIONS

In this research, an irrigation model based on fuzzy logic was designed, specifically a fuzzy system, for embedded hardware, for the optimization of water resources. Based on the work carried out, the following conclusions were reached:

- The interpretability of the FS makes the model practical. The selection of trapezoidal membership functions and their consequent unit plateaus in the fuzzification process of the FS entries allowed the expression of the error presented by the linguistic values according to expert criteria:
- The model obtained is computationally light, with an average response time between reception, processing and sending of 1.71 seconds, making it suitable for the chosen hardware.
- The FS shows satisfactory behavior, taking the same standard decision as the operators for the trend of the samples collected, and suggesting, in general, a reduction of 10.07% of the irrigation time, that is, a proportional saving of resources.

## VII. AUTHOR'S CONTRIBUTION

**Conceptualization:** Alain Godo Alonso.

**Methodology:** Alain Godo Alonso and Ivan Santana Ching.

**Investigation:** Alain Godo Alonso.

**Discussion of results:** Alain Godo Alonso, Dennis Villavicencio Quintero and Emilio Cabrera Hernández.

**Writing – Original Draft:** Alain Godo Alonso.

**Writing – Review and Editing:** Alain Godo Alonso and Ivan Santana Ching

**Resources:** Ivan Santana Ching.

**Supervision:** Ivan Santana Ching.

**Approval of the final text:** Alain Godo Alonso, Dennis Villavicencio Quintero, Emilio Cabrera Hernández and Ivan Santana Ching.

## VIII. ACKNOWLEDGMENTS

Special thanks to the Internet of Things and Artificial Intelligence for Automation Group from the University "Marta Abreu" of Las Villas (UCLV) and the workers and specialists at the various crops company "Valle del Yabú".

## IX. REFERENCES

- [1] A. O. Bula, "Importancia de la agricultura en el desarrollo socio-económico," Aug. 2020, Accessed: Oct. 16, 2022. [Online]. Available: <http://rephip.unr.edu.ar/xmlui/handle/2133/18616>
- [2] A. Mérida García, I. Fernández García, E. Camacho Poyato, P. Montesinos Barrios, and J. A. Rodríguez Díaz, "Coupling irrigation scheduling with solar energy production in a smart irrigation management system," *J. Clean. Prod.*, vol. 175, pp. 670–682, Feb. 2018, doi: 10.1016/j.jclepro.2017.12.093.
- [3] "United Nations World Water Development Report 2021. Valuing Water." <https://www.unesco.org/reports/wwdr/2021/en> (accessed Oct. 16, 2022).
- [4] N. Khan, R. L. Ray, G. R. Sargani, M. Ihtisham, M. Khayyam, and S. Ismail, "Current Progress and Future Prospects of Agriculture Technology: Gateway to Sustainable Agriculture," *Sustainability*, vol. 13, no. 9, p. 4883, Apr. 2021, doi: 10.3390/su13094883.
- [5] L. S. Pereira, P. Paredes, and N. Jovanovic, "Soil water balance models for determining crop water and irrigation requirements and irrigation scheduling focusing on the FAO56 method and the dual Kc approach," *Agric. Water Manag.*, vol. 241, p. 106357, Nov. 2020, doi: 10.1016/j.agwat.2020.106357.
- [6] B. Mason, M. Rufi-Salís, F. Parada, X. Gabarrell, and C. Gruden, "Intelligent urban irrigation systems: Saving water and maintaining crop yields," *Agric. Water Manag.*, vol. 226, p. 105812, Dec. 2019, doi: 10.1016/j.agwat.2019.105812.
- [7] M. S. Farooq and S. Akram, "IoT in agriculture: Challenges and opportunities," *J. Agric. Res.*, p. 25, 2021.
- [8] L. F. Oliveira, A. P. Moreira, and M. F. Silva, "Advances in Agriculture Robotics: A State-of-the-Art Review and Challenges Ahead," *Robotics*, vol. 10, no. 2, p. 52, Mar. 2021, doi: 10.3390/robotics10020052.
- [9] A. Kumar and S. K. Pillai, "Applications of artificial intelligence in agriculture," vol. 10, p. 8, 2021.
- [10] R. Mesa, "Incremento de la producción de *Solanum lycopersicum* L. cv. Aegean en cultivo protegido mediante alternativa de manejo del riego," Thesis, Universidad Central "Marta Abreu" de Las Villas. Facultad de Ciencias Agropecuarias. Departamento de Ingeniería Agrícola, 2019. Accessed: Oct. 16, 2022. [Online]. Available: <http://dspace.uclv.edu.cu:8089/xmlui/handle/123456789/10866>
- [11] A. Madruga, "Modelado de riego de *Solanum lycopersicum* L. en cultivo protegido basado en mapas cognitivos difusos," Thesis, Universidad Central "Marta Abreu" de Las Villas. Facultad de Ingeniería Eléctrica. Departamento de Automática y Sistemas Computacionales, 2019. Accessed: Oct. 16, 2022. [Online]. Available: <http://dspace.uclv.edu.cu:8089/xmlui/handle/123456789/12435>
- [12] A. Méndez, "Diseño de modelo de riego en el cultivo protegido de tomate para el manejo de los requerimientos hídricos," Thesis, Universidad Central "Marta Abreu" de Las Villas, Facultad de Ingeniería Eléctrica, Departamento de Automática y Sistemas Computacionales, 2019. Accessed: Oct. 16, 2022. [Online]. Available: <http://dspace.uclv.edu.cu:8089/xmlui/handle/123456789/11344>
- [13] I. Zambon, M. Cecchini, G. Egidi, M. G. Saporito, and A. Colantoni, "Revolution 4.0: Industry vs. Agriculture in a Future Development for SMEs," *Processes*, vol. 7, no. 1, p. 36, Jan. 2019, doi: 10.3390/pr7010036.
- [14] R. Ben Ali, S. Bouadila, and A. Mami, "Development of a Fuzzy Logic Controller applied to an agricultural greenhouse experimentally validated," *Appl. Therm. Eng.*, vol. 141, pp. 798–810, Aug. 2018, doi: 10.1016/j.applthermaleng.2018.06.014.
- [15] G. Lavanya, C. Rani, and P. Ganeshkumar, "An automated low cost IoT based Fertilizer Intimation System for smart agriculture," *Sustain. Comput. Inform. Syst.*, vol. 28, p. 100300, Dec. 2020, doi: 10.1016/j.suscom.2019.01.002.
- [16] S. Remya and R. Sasikala, "Classification of rubberized coir fibres using deep learning-based neural fuzzy decision tree approach," *Soft Comput.*, vol. 23, no. 18, pp. 8471–8485, Sep. 2019, doi: 10.1007/s00500-019-03961-0.
- [17] S. Nosratabadi, S. Ardabili, Z. Lakner, C. Mako, and A. Mosavi, "Prediction of Food Production Using Machine Learning Algorithms of Multilayer Perceptron and ANFIS," *Agriculture*, vol. 11, no. 5, p. 408, May 2021, doi: 10.3390/agriculture11050408.
- [18] B. Alomar and A. Alazzam, "A Smart Irrigation System Using IoT and Fuzzy Logic Controller," in 2018 Fifth HCT Information Technology Trends (ITT), Dubai, United Arab Emirates: IEEE, Nov. 2018, pp. 175–179. doi: 10.1109/CTIT.2018.8649531.
- [19] R. S. Krishnan et al., "Fuzzy Logic based Smart Irrigation System using Internet of Things," *J. Clean. Prod.*, vol. 252, p. 119902, Apr. 2020, doi: 10.1016/j.jclepro.2019.119902.
- [20] H. Benyezza, M. Bouhedda, and S. Rebouh, "Zoning irrigation smart system based on fuzzy control technology and IoT for water and energy saving," *J. Clean. Prod.*, vol. 302, p. 127001, Jun. 2021, doi: 10.1016/j.jclepro.2021.127001.
- [21] D. K. Widyawati and A. Ambarwari, "Fuzzy Logic Design to Control the Duration of Irrigation Time in the Greenhouse," *IOP Conf. Ser. Earth Environ. Sci.*, vol. 1012, no. 1, Art. no. 1, Apr. 2022, doi: 10.1088/1755-1315/1012/1/012086.
- [22] J. Badgery-Parker, L. James, J. Jarvis, and D. S. Parks, *Commercial Greenhouse Cucumber Production*. NSW Agriculture, 2019.
- [23] Á. D. Casaca, "Guías Tecnológicas de Frutas y Vegetales," p. 13, 2005.
- [24] M. Henschke, X. Wei, and X. Zhang, "Data Visualization for Wireless Sensor Networks Using ThingsBoard," in 2020 29th Wireless and Optical Communications Conference (WOCC), Newark, NJ, USA: IEEE, May 2020, pp. 1–6. doi: 10.1109/WOCC48579.2020.9114929.
- [25] thingsboard, "ThingsBoard - Open-source IoT Platform," ThingsBoard. <https://thingsboard.io/> (accessed Oct. 26, 2022).
- [26] "MQTT - The Standard for IoT Messaging." <https://mqtt.org/> (accessed Oct. 27, 2022).
- [27] B. Mishra and A. Kertesz, "The Use of MQTT in M2M and IoT Systems: A Survey," *IEEE Access*, vol. 8, pp. 201071–201086, 2020, doi: 10.1109/ACCESS.2020.3035849.
- [28] S. Mihajlović, A. Kupusinac, D. Ivetić, and I. Berković, "The Use of Python in the field of Artificial Intelligence," p. 5, 2020.
- [29] "MATLAB - MathWorks." <https://www.mathworks.com/products/matlab.html> (accessed Oct. 18, 2022).
- [30] "Our Community," Python.org. <https://www.python.org/community/> (accessed Oct. 17, 2022).
- [31] P. Kim, *MATLAB Deep Learning*. Berkeley, CA: Apress, 2017. doi: 10.1007/978-1-4842-2845-6.

[32] T. J. Ross, Fuzzy Logic with Engineering Applications, 1st ed. Wiley, 2017.  
doi: 10.1002/9781119994374.

[33] L. F. Oliveira, A. P. Moreira, and M. F. Silva, "Advances in Agriculture Robotics: A State-of-the-Art Review and Challenges Ahead," Robotics, vol. 10, no. 2, Art. no. 2, Mar. 2021, doi: 10.3390/robotics10020052.